UNIVERSITÀ
DEGLI STUDI
DI PADOVA

Head Office: Università degli Studi di Padova

Department of Chemical Sciences

Ph.D. COURSE IN MOLECULAR SCIENCES
CURRICULUM CHEMICAL SCIENCES
XXXIV SERIES

Macrocyclic Ligands for the Chelation of Theranostic Radiometals

Coordinator: Prof. Leonard J. Prins
Supervisor: Prof. Valerio Di Marco

Ph.D. Student: Marianna Tosato

“For me chemistry represented an indefinite cloud of future powers which enveloped my life to come in black volutes torn by fiery flashes.”

“Per me la chimica rappresentava una nuvola indefinita di potenze future che avvolgeva il mio avvenire in nere volute lacerate da bagliori di fuoco.”

Primo Levi

Abstract

When appropriately harnessed the radioactive emission of metallic radioisotopes can be exploited to image, treat and monitor cancer. The combination of imaging and therapy in a 'matched pair' of radioisotopes gives rise to the concept of 'theranostic', an emerging clinical management paradigm where patient treatment is planned according to an individually tailored therapeutic regime.

Although in past decades only a few radiometals were employed due to the difficulty inherent to their production, nowadays an increasingly wide variety of rare metallic radionuclides are available, providing larger choice among decay energy and properties, and thus having the potential to improve diagnostic and therapeutic routes according to patient needs, as defined by the principle of personalized medicine. These theranostic pairs include the exotic silver-103/104/111 ($^{103/104/111}$Ag) and mercury-197m/g ($^{197m/g}$Hg) and the non-standard lead-203/212 ($^{203/212}$Pb) and copper-64/67 ($^{64/67}$Cu).

To successfully deliver the radiation to the desired molecular target, radiometal ions need to be securely bound by a chelator coupled to a biologically active molecule. However, to date, no *in vivo* stable [$^{103/104/111}$Ag]Ag^{+} and [$^{197g/m}$Hg]Hg^{2+} chelates exist to harness their theranostic power. Moreover, existing ligands do not perform well *in vivo* for $^{64/67}$Cu as the stability of [$^{64/67}$Cu]Cu^{2+}-complexes can be thwarted by the biologically triggered redox switching between Cu^{2+} and Cu^{+} that may bring upon demetallation processes. As a consequence, the unbound radiometal can spread through the body leading to a loss of selectivity for the target to be imaged or treated. Analogously, the issues of [$^{203/212}$Pb]Pb^{2+}-dissociation combined with the stable complexation of its daughter radionuclide bismuth-212 remain unsolved.

The aim of this thesis is to explore novel chelating agents for the borderline-soft theranostic couples [$^{103/104/111}$Ag]Ag^{+}, [$^{64/67}$Cu]$Cu^{2+/+}$, [$^{203/212}$Pb]Pb^{2+} and [$^{197g/m}$Hg]Hg^{2+}, to circumvent the shortcomings in their stable complexation and to facilitate their clinical translation. For this purpose, a family of polyazamacrocycles bearing sulfanyl arms was designed and synthesized. To optimize the coordination properties of the chelators several structural parameters were tuned such as different pendant coordinating arms and a wide range of macrocyclic scaffold rings. The aqueous coordination chemistry of the corresponding metal complexes was investigated assessing their thermodynamic stability, formation and dissociation kinetics and structural properties. Radiolabelling experiments were performed with the corresponding radioisotopes to evaluate the complexation efficiency in extremely

diluted conditions. As a final evaluation of the potential of the proposed ligands for theranostic applications, *in vitro* stability assays were executed with the resultant radiometal complexes.

Riassunto

Se opportunamente sfruttata, l'emissione radioattiva di radioisotopi metallici può essere utilizzata per la diagnosi, il trattamento e il monitoraggio del cancro. La combinazione di *imaging* e terapia in una 'coppia abbinata' di radioisotopi dà origine al concetto di 'teranostico', un paradigma di gestione clinica emergente in cui il trattamento del paziente è pianificato secondo un regime terapeutico personalizzato.

Mentre nei decenni passati venivano impiegati solo pochi radiometalli, a causa della difficoltà insita nella loro produzione, oggigiorno è disponibile una varietà sempre più ampia di radionuclidi metallici rari, che offrono una scelta più varia di energie e proprietà di decadimento, e quindi hanno il potenziale di migliorare i percorsi diagnostici e terapeutici secondo le esigenze del paziente, così come definito dal principio della medicina personalizzata. Queste coppie teranostiche includono i radionuclidi esotici, argento-103/104/111 ($^{103/104/111}$Ag) e mercurio-197m/g ($^{197m/g}$Hg) e quelli non-standard, piombo-203/212 ($^{203/212}$Pb) e rame-64/67 ($^{64/67}$Cu).

Per indirizzare con successo la radiazione al bersaglio molecolare desiderato, gli ioni radiometallici devono essere fortemente legati da un chelante coniugato ad una molecola biologicamente attiva. Tuttavia, ad oggi, non esistono chelati stabili *in vivo* per [$^{103/104/111}$Ag]Ag^+ e [$^{197g/m}$Hg]Hg^{2+} che consentano di sfruttare il loro potenziale teranostico. Inoltre, i leganti esistenti non sono adatti *in vivo* per $^{64/67}$Cu poiché la stabilità dei complessi di [$^{64/67}$Cu]Cu^{2+} può essere compromessa dalla riduzione di Cu^{2+} a Cu^+, innescata biologicamente, che può portare a processi di demetallazione. Di conseguenza, il radiometallo non legato può diffondersi attraverso il corpo portando a una perdita di selettività per il sito *target* che dev'essere visualizzato o trattato. Analogamente, restano irrisolti i problemi della dissociazione di [$^{203/212}$Pb]Pb^{2+} combinati con il complessamento stabile del suo radionuclide figlio bismuto-212.

Lo scopo di questa tesi è quello di esplorare nuovi agenti chelanti per le coppie teranostiche *borderline-soft* [$^{103/104/111}$Ag]Ag^+, [$^{64/67}$Cu]$Cu^{2+/+}$, [$^{203/212}$Pb]Pb^{2+} e [$^{197g/m}$Hg]Hg^{2+}, per risolvere i problemi legati al loro complessamento non sufficientemente stabile e per facilitare la loro traslazione clinica. A tale scopo è stata progettata e sintetizzata una famiglia di poliazamacrocicli contenenti donoratori solforati. Per ottimizzare le proprietà di coordinazione dei chelanti sono stati variati diversi parametri strutturali come le catene laterali, ed è stata considerata un'ampia gamma di *scaffold* macrociclici. La chimica di coordinazione acquosa dei complessi metallici corrispondenti è stata studiata valutandone la stabilità termodinamica, la cinetica di formazione e dissociazione e le proprietà strutturali.

Sono stati eseguiti esperimenti di radiomarcatura con i radioisotopi corrispondenti per valutare l'efficienza di complessamento in condizioni estremamente diluite. Come valutazione finale del potenziale dei leganti proposti per applicazioni teranostiche, sono stati eseguiti saggi di stabilità *in vitro* dei complessi radiometallici risultanti.

Table of Contents

List of Tables

List of Figures

List of Schemes

List of Symbol and Abbreviations

α	Alpha
β^+	Positron
β^-	Beta
γ	Gamma
AAZTA	1,4-Bis(carboxymethyl)-6-(bis[carboxymethyl])-amino-6-methylperhydro-1,4-diazepine
ADF	Amsterdam Density Functional
ASA	Activation Strain Analysis
ASM	Activation Strain Model
BBN	Bombesin
BFC	Bifunctional Chelator
bispa	6,6′-[{9-Hydroxy-1,5-bis(methoxycarbonyl)-2,4-di(pyridin-2-yl)-3,7-diazabicyclo[3.3.1]nonane-3,7-diyl}bis-(methylene)]-dipicolinic acid
Bq	Bequerel
CB-DO2A	1,4,7,10-Tetraazabicyclo[5.5.2]tetradecane-4,10-diacetic acid
CB-TE2A	1,4,8,11-Tetraazabicyclo[6.6.2]-hexadecane-4,11-diacetic acid
CE	Counter Electrode
CE	Conversion Electron
CHX-DTPA	Cyclohexane-1,2-diamine-N,N,N′,N′-tetraacetate
COSMO	Conductor-like Screening Model
COSY	Correlation Spectroscopy
CN	Coordination Number
CSD	Cambridge Structural Database
CT	Computed Tomography
CV	Cyclic Voltammetry
Cyc4Me	1,4,7,10-Tetramethyl-1,4,7,10-tetrazacyclododecane
Cyclen	1,4,7,10-Tetraazacyclododecane
Cyclam	1,4,8,11-Tetrazacyclotetradecane
DATA	6-Amino-1,4-diazepine triacetic acid
dedpa	1,2-[{6-(Carboxylato)pyridin-2-yl}methylamino]-ethane
DEPA	7-[2-(Bis-carboxymethylamino)-ethyl]-4,10-biscarboxymethyl-1,4,7,10-tetraazacyclododec-1-yl-acetic acid

DFO	Deferoxamine
DFT	Density Functional Theory
DMSA	Dimercaptosuccinic acid
DO4S	1,4,7,10-Tetrakis[2-(methylsulfanyl)ethyl]-1,4,7,10-tetraazacyclododecane
DO4S4Me	(2S,5S,8S,11S)-2,5,8,11-Tetramethyl-1,4,7,10-tetrakis[2-(methylsulfanyl) ethyl]-1,4,7,10-tetraazacyclododecane
DO3S	1,4,7-Tris[2-(methylsulfanyl)ethyl]-1,4,7,10-tetraazacyclododecane
DO3SAm	1,4,7-Tris[2-(methylsulfanyl)ethyl]-10-acetamido-1,4,7,10-tetraazacyclodo - decane
DO2A2S	1,7-Bis[2-(methylsulfanyl)ethyl]-4,10,diacetic acid-1,4,7,10-tetraazacyclodo-decane
DOT-*n*-Bu	1,4,7,10-Tetra-*n*-butyl-1,4,7,10-tetraazacyclododecane
DOTA	1,4,7,10-Tetraazacyclododecane-1,4,7,10-tetraacetic acid
DOTP	1,4,7,10-Tetraazacyclododecane-1,4,7,10-tetramethylene phosphonic acid
DNA	Deoxyribonucleic Acid
DTPA	1,1,4,7,7-Diethylenetriaminepentaacetic acid
EC	Electron Capture
ECC	Ethylenecysteamine cysteine
EDA	Energy Decomposition Analysis
EDC	Ethyl Cysteinate Dimer
EGFR	Epidermal Growth Factor Receptor
EGTA	Ethylene glycol bis(2-aminoethyl ether)-N,N,N′,N′-tetraacetic acid
EPR	Electron Paramagnetic Resonance
ET	Electron Transfer
eV	Electronvolt
FDA	Food and Drug Administration
FSC	Fusarinine C
I	Ionic strength
IC	Internal Conversion
ISOL	Isotope Separation On-Line
iTLC	Instant Thin-Layer Chromatography
GRP	Gastrin-Releasing Peptide
HBED	N,N′-Bis(2-hydroxybenzyl)ethylenediamine-N,N′-diacetic acid
HEPES	2-[4-(2-hydroxyethyl)piperazin-1-yl]ethanesulfonic acid
HMQC	Heteronuclear Multiple Quantum Coherence
HOMO	Highest Occupied Molecular Orbital

HPGe	High Purity Germanium
HPLC	High-Performance Liquid Chromatography
HSAB	Hard-Soft Acid Base Theory
HSQC	Heteronuclear Single Quantum Coherence
KS-MO	Kohn-Sham Molecular Orbital
HER-2	Human Epidermal Growth Factor Receptor 2
LET	Linear Energy Transfer
LMCT	Ligand to Metal Charge-Transfer
LUMO	Lowest Unoccupied Molecular Orbital
LSV	Linear Scan Voltammetry
macropa	N,N′-bis[(6-carboxy-2-pyridil)methyl]-4,13-diaza-18-crown-6
Me4-Cyclen	(2S,5S,8S,11S)-2,5,8,11-Tetramethyl-1,4,7,10-tetraazacyclododecane
MO	Molecular Orbital
MSH	α-Melanocyte Stimulating Hormone
NET	Neuroendocrine Tumours
NMR	Nuclear Magnetic Resonance
NODAGA	1,4,7-Triazacyclononane,1-glutaric acid-4,7-acetic acid
NOESY	Nuclear Overhauser Effect Spectroscopy
NOTA	1,4,7-Triazacyclononane-1,4,7-triacetic acid
PBS	Phosphate-Buffered Saline
PEPA	1,4,7,10,13-Pentaazocyclopentadecane pentaacetic acid
PET	Positron Emission Tomography
PES	Potential Energy Surface
PRTT	Peptide Receptor-Targeted Therapy
PSMA	Prostate-Specific Membrane Antigen
RCY	Radiochemical Yield
RIBE	Radiation-Induced Bystander Effect
ROS	Reactive Oxygen Species
RNS	Reactive Nitrogen Species
SCE	Saturated Calomel Electrode
SDS-PAGE	Sodium Dodecyl Sulfate - PolyAcrylamide Gel Electrophoresis
SFO	Symmetry-Adapted Fragment Orbitals
SPECT	Single Photon Emission Computed Tomography
SP	Substance P
SST	Somatostatin
STO	Slater-Type Orbital

TACD	1,5,9-Triazacyclododecane
TACD3S	1,5,9-Tris[2-(methylsulfanyl)ethyl]-1,5,9-triazacyclododecane
TAT	Targeted Alpha Therapy
TE4S	1,4,8,11-Tetrakis[2-(methylsulfanyl)ethyl]-1,4,8,11-tetrazacyclotetradecane
TETA	1,4,8,11-Tetraazacyclotetradecane-1,4,8,11-tetraacetic acid
TCMC	1,4,7,10-Tetraazacyclododecane-1,4,7,10-tetraacetic amide
TFA	Trifluoroacetic Acid
THP	Tris(3,4-hydroxypyridinone)
TLC	Thin Layer Chromatography
TOCSY	Total Correlation Spectroscopy
TRI	1,4,7,10-Tetrazacyclotridecane
TRI4S	1,4,7,10-Tetrakis[2-(methylsulfanyl)ethyl]-1,4,7,10-tetrazacyclotridecane
TRT	Targeted Radionuclide Therapy
TSP	3-(Trimethylsilyl)propionic acid
UHPLC	Ultra-High-Performance Liquid Chromatography
VT	Variable Temperature
WE	Working Electrode
ZORA	Zeroth-Order Regular Approximation

Chapter 1

Introduction

The Chapter reviews the fundamental principles of the application of radioactivity to nuclear medicine. An overview of the most commonly employed radionuclides for both cancer therapy and diagnosis, including their type of emission, production routes and coordination chemistry is discussed. Illustrative biological studies are also reported.

1.1 Radioactivity for Tumour Diagnosis and Therapy

Targeted radionuclide therapy (TRT) has emerged as a powerful approach for the treatment of cancer due to its specificity and minimal invasiveness compared to traditional chemotherapy significantly increasing the quality of life of patients during and after treatment.[1] This strategy relies on an alpha (α), beta (β^-), or Meitner-Auger radiation-emitting nuclide fused to a biologically active targeting molecule that has the ability to selectively accumulate into specific disease sites while sparing the nearby healthy tissues.[2–5]

A benefit of radiolabelled drugs is the possibility to identify the sites of disease, assess the therapeutic efficacy and monitor the disease progression using imaging techniques, *i.e.* single photon emission computed tomography (SPECT) and positron emission tomography (PET), exploiting either gamma (γ) rays or annihilation photons that are produced by positron (β^+) emitters, respectively.[6] The combination of both imaging and therapeutic radiation in a 'matched pair' of radioisotopes gives rise to the concept of theranostic.[7] This approach represents an emerging clinical management paradigm where patient treatment is performed according to an individually tailored therapeutic regime.

1.2 Radiopharmaceutical Design

Metallic radioisotopes provide a large choice of suitable radionuclides thanks to the variety of half-life and decay modes. However, the stability and hence the biological safety of radiopharmaceuticals containing these radionuclides must be guaranteed by the formation of stable complexes with a bifunctional chelator (BFC) coupled to the targeting moiety *via* a covalent linkage. [4,8–12] A general scheme of a metal-based radiopharmaceutical is illustrated in **Figure 1.1**.

1.2.1 The Central Role of The Chelating Agents

After the injection, it is imperative that the radiopharmaceutical deliver the radionuclide to its biological target without any radiometal loss. This would result in high background activity levels, which limit the target visualization, and an unintended radiation burden on healthy tissues.[12–15] For such reason, BFCs must display high thermodynamic stability and kinetic inertness toward the radionuclide to prevent dissociation, transchelation and transmetallation reactions in biological media. Fast complexation under mild conditions is also essential to allow the use of heat- and pH-sensitive biovectors (*e.g.*, antibody).[4,12,16–18]

BFCs not only coordinate the metallic radionuclide but also offer an anchoring point for the incorporation of the tumour-targeting moiety. Representative coupling strategies exploit

carboxylic acids or activated esters for amide couplings (*e.g.*, N-hydroxysuccinimide NHS-ester, tetrafluorophenyl TFP-ester), isothiocyanates and maleimides for thiourea and thiol couplings, or click chemistry. These approaches are summarized in **Figure 1.2**. Moreover, they can be used to modulate the pharmacokinetics of the whole radiolabelled drug, in particular when low-molecular-weight vectors (*e.g.*, small molecules or peptides) are used.[6,12] A great advantage of this modular strategy is the possibility to tune each component to optimize the performance of the whole drug.

1.2.2 Tumour-Targeting Vectors

Targeting vectors command the biodistribution and pharmacokinetics of the whole radiolabelled drug. To selectively direct the radiation to the target sites, the bioactive molecule should exhibit elevated affinity for receptors that are over-expressed on target cells but are absent or minimally expressed on healthy cells.[19] Minimal renal and hepatic accumulation, high thermal and *in vivo* stability are also required.

Small molecules, peptides, antibodies, antibody fragments and nanoparticles are commonly used as targeting agents. It is worth to underline that each class of biomolecules has different biological properties, *i.e.* different biological half-lives, that must be matched with the physical properties of the radionuclide. For example, because of their large size (~150 kDa), antibodies have prolonged biological half-lives (days to weeks) that must be matched with long-lived radiometals to allow tumour accumulation and non-specific clearance.[19] Frequently employed antibodies are *Trastuzumab* for human epidermal growth factor receptor 2 (HER-2) targeting, *Rituximab* for CD20 targeting and *Cetuximab* for epidermal growth factor receptor (EGFR) targeting.

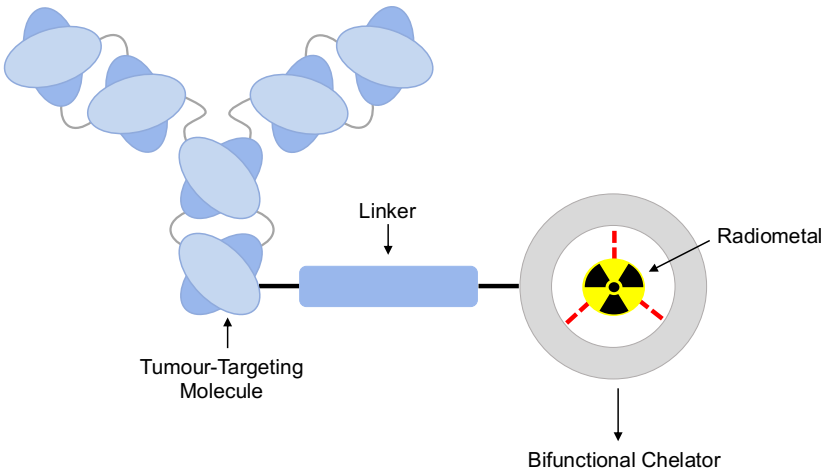

Figure 1.1. General structure of a metal-based radiopharmaceutical consisting of four components (radiometal, bifunctional chelator, linker and targeting vector).

Contrarily, due to their lower molecular weight, peptides experience fast tumour localization, thus they are well suited to short-lived radioisotopes. In fact, unbound peptide radiotracers rapidly clear from circulation, resulting in high tumour-to-background ratios.[19] A caveat to this point is that exceptionally high rates of circulation and clearance can preclude sufficient tumour accumulation.

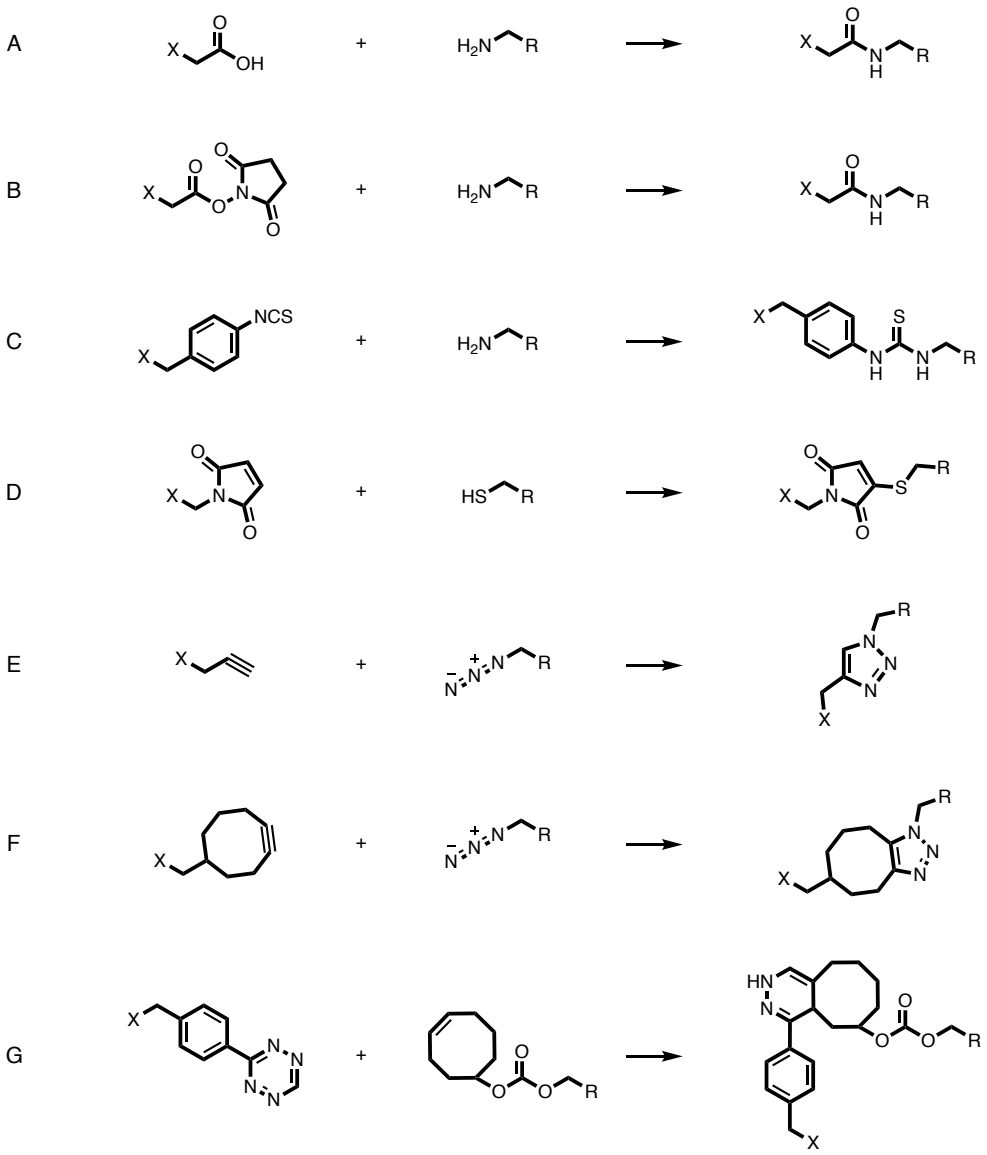

Figure 1.2. Representative conjugation strategy for the attachment of the BFC to the targeting vector: (A) amide coupling with coupling reagents (*e.g.*, 1-ethyl-3-(3-dimethylaminopropyl) carbodiimide or O-(7-azabenzotriazol-1-yl)-N,N,N',N'-tetramethyluronium hexafluorophosphate), (B) amide coupling with activated ester, (C) thiourea formation, (D) thioether formation, (E) copper catalyzed azide-alkyne [3+2] cycloaddition, (F) strain-promoted azide-alkyne [3+2] cycloaddition and (G) inverse electron demand Diels-Alder [4+2] cycloaddition.[4,12]

Commonly employed peptides are PSMA-specific peptides for prostate-specific membrane antigen (PSMA) targeting, bombesin (BNN) fragments for gastrin-releasing peptide (GRP) receptor targeting, Arg-Gly-Asp (RGD) analogues for integrin targeting and 1,4,7,10-tetraazacyclododecane-1,4,7,10-tetraacetic acid (DOTA)-conjugated octreotide analogues (*e.g.*, DOTATATE, DOTATOC, and DOTANOC) for somatostatin (SST) receptor targeting.[19] Representative structures of targeting vectors discussed throughout this Chapter are shown in **Figure 1.3**.

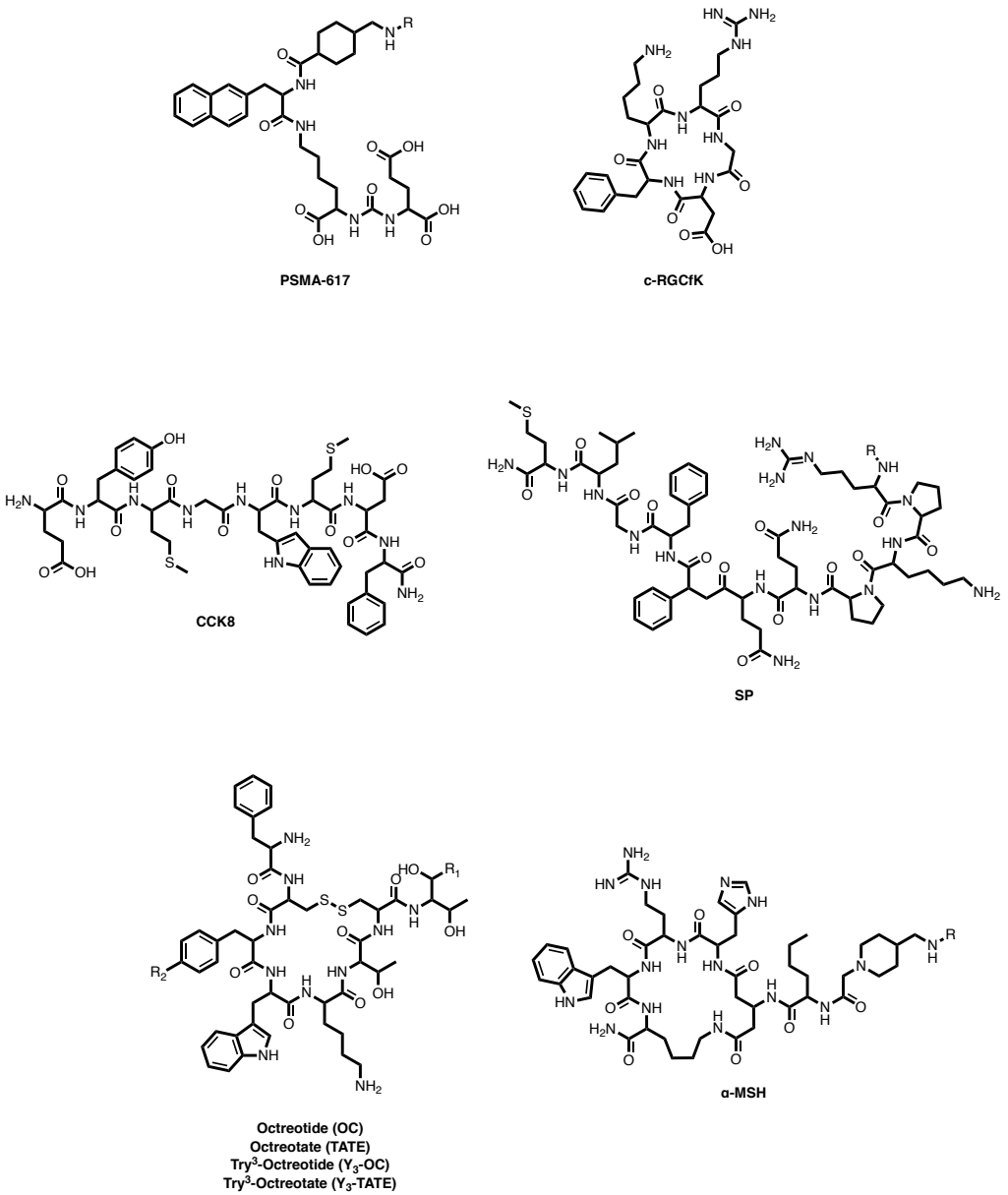

Figure 1.3. Structures of selected targeting vectors: PSMA-617, cyclic-RGCfK, CCK8, substance P, octreotide (R_1 = R_2 = H)/octreotate (R_1 = O, R_2 = H)/Try^3-octreotide (R_1 = H, R_2 = OH)/Try^3-octreotate (R_1 = O, R_2 = OH) and α-melanocyte stimulating hormone.

1.3 Radiometals for Cancer Therapy

In therapeutic radiopharmaceuticals, the radionuclide decays *via* emission of high-energy ionizing non-penetrating radiation (β^-, α-particles, and Meitner-Auger electrons) that, if properly directed, can provoke cell death. Depending on their linear energy transfer (LET*), therapeutic particles can irradiate tumour volumes of multicellular, cellular and subcellular dimensions with different ionization densities. β^- particles possess a low LET compared to α-particles and Meitner-Auger electrons (0.2 keV/μm) which translates into a long penetration pathway (0.5-10 mm, 100 to 500 cell diameters).[19] This makes the β^- emission appropriate for the treatment of larger or poorly vascularized tumour masses as cells that are not directly targeted could receive a dose from the crossfire irradiation from a neighbouring targeted cell ('crossfire effect').[6] Conversely, the use of a β^- emitter to treat metastatic tumours may cause damage to neighbouring healthy cells. α-Particle or Meitner-Auger electron therapy may be preferable in this scenario. Due to their high LET (80 keV/μm for α-emitters and 4-26 keV/μm for Meitner-Auger emitters), a highly localized energy deposition within the cell clusters (α-emitters) or single cancer cells (Meitner-Auger electron emitters), while sparing surrounding normal tissues, can be achieved.[4,6,20,21]

The different LET also translates into a different mechanism of cell destruction: low LET emitters primarily induce the cell death through a direct mechanism, causing non-repairable deoxyribonucleic acid (DNA) breaks (single-strand, double-strand breaks or base-pair modifications). Contrarywise, with α-particles and Meitner-Auger electrons, the formation of reactive oxygen species (ROS), *e.g.*, hydroxyl radical (•OH), ionized water (H_2O^+), superoxide ($O_2{\bullet}^-$) and H_2O_2, as well as reactive nitrogen species (RNS), *e.g.*, nitric oxide (•NO), nitrogen dioxide ($NO_2{\bullet}$), and peroxynitrite anion ($ONOO^-$), is the predominant pathway.[4,12,22,23] This is an advantage over β^--emitters, as the presence of hypoxic regions within the tumour is a major cause of failure of β^--therapy.[24–26] It is worth to note that also nontargeted effects, namely radiation-induced bystander effect (RIBE) can play a certain role in radiation-induced cell death. Therefore, the choice of the proper radionuclide for tumour therapy should be made based on the decay characteristics of the radionuclide and the tumour size to be treated. Moreover, the biological half-life of the targeting agent and the availability of the radionuclide at high quality have also to be considered.

An overview of the most employed radiometals for therapeutic and diagnostic applications, including their type of emission, production routes and coordination chemistry, is discussed in the following sections. **Table 1.1** summarize the reported radiometals and their decay properties while the structures of the discussed chelators are shown in **Figure 1.4** - **1.5**.

* The linear energy transfer is a measure of atom ionization *per* unit length.

1.3.1 Alpha-Emitting Radionuclides for Targeted Alpha Therapy

α-Particles are double charged helium nuclei ($^{4}He^{2+}$) consisting of two protons and two neutrons.[6] Their high positive charge and heavy mass makes them suitable for the treatment of small metastatic tumours or circulating malignant cells as they can deposit a high energy (5-9 MeV) in a short path (50-100 μm, < 10 cell diameters).[19] The cytotoxicity of α-emitters is also independent of cell cycle or oxygen concentration, providing an advantage for treating hypoxic, often radiation-resistant tumours.[27,28]

Most of the α-emitters decay *via* the emission of multiple α-particles which can theoretically be useful to increase the effectiveness of the radiation treatment.[6] However, the fate of the daughter isotopes is generally a concern in targeted alpha therapy (TAT). Indeed, each α-emission has an associated recoil energy (100-200 keV) that could break any coordination bonds (~ 5 eV) causing the detachment of daughter from the BFC and resulting in the non-directed circulation of potentially radiotoxic radionuclides.[6]

Notwithstanding this issue, the interest in α-emitters is nowadays growing mostly due to the fact that excellent responses to TAT have been obtained in patients resistant to β^- therapy.[6,29–31] α-Emitting radionuclides suitable for TAT application include actinium-225 (^{225}Ac), bismuth-212/213 ($^{212/213}Bi$), lead-212 (^{212}Pb), terbium-149 (^{149}Tb) and thorium-227 (^{227}Th).[32,33] The decay properties of these promising α-emitters, their production, chelation and selected biological studies are briefly reviewed in the following paragraphs.

Actinium-225. ^{225}Ac ($t_{1/2}$ 10.0 d) is one of the most potent α-emitters. It decays generating stable bismuth-209 (^{209}Bi) through a cascade of six daughter isotopes (**Figure 1.6**), producing in total four α and three β^- emissions.[6,34]

^{225}Ac can be produced from stockpiles of thorium-229 (^{229}Th, $t_{1/2}$ 7340 y), a daughter nuclide of uranium-223 (^{223}U), or by accelerator-based methods.[34] These include proton irradiation of radium-226 (^{226}Ra) targets or spallation of thorium-232 (^{232}Th).[6,35,36]

The chemistry of actinium is virtually unexplored, as there are no stable isotopes.[4] Actinium is found almost exclusively as a trivalent cation (Ac^{3+}); it is a hard acid according to the Pearson's Hard Soft Acid Base (HSAB) theory, and it can form stable complexes with hard donors such as O or N. Its preference for large coordination number (CN 8-12) makes it well-matched with large polydentate macrocyclic chelators of high denticity.[34,37] To date, the most promising [^{225}Ac]Ac^{3+} chelators are N,N′-bis[(6-carboxy-2-pyridyl)methyl]-1,7-diaza-18-crown-6 (macropa) and (2,2′,2″,2‴-(1,10-dioxa-4,7,13,16-tetraazacyclooctadecane-4,7,13,16-tetrayl)-tetraacetic acid (crown) which can stably bind [^{225}Ac]Ac^{3+} at submicromolar concentration in less than 10 min at room temperature.[6,38,39]

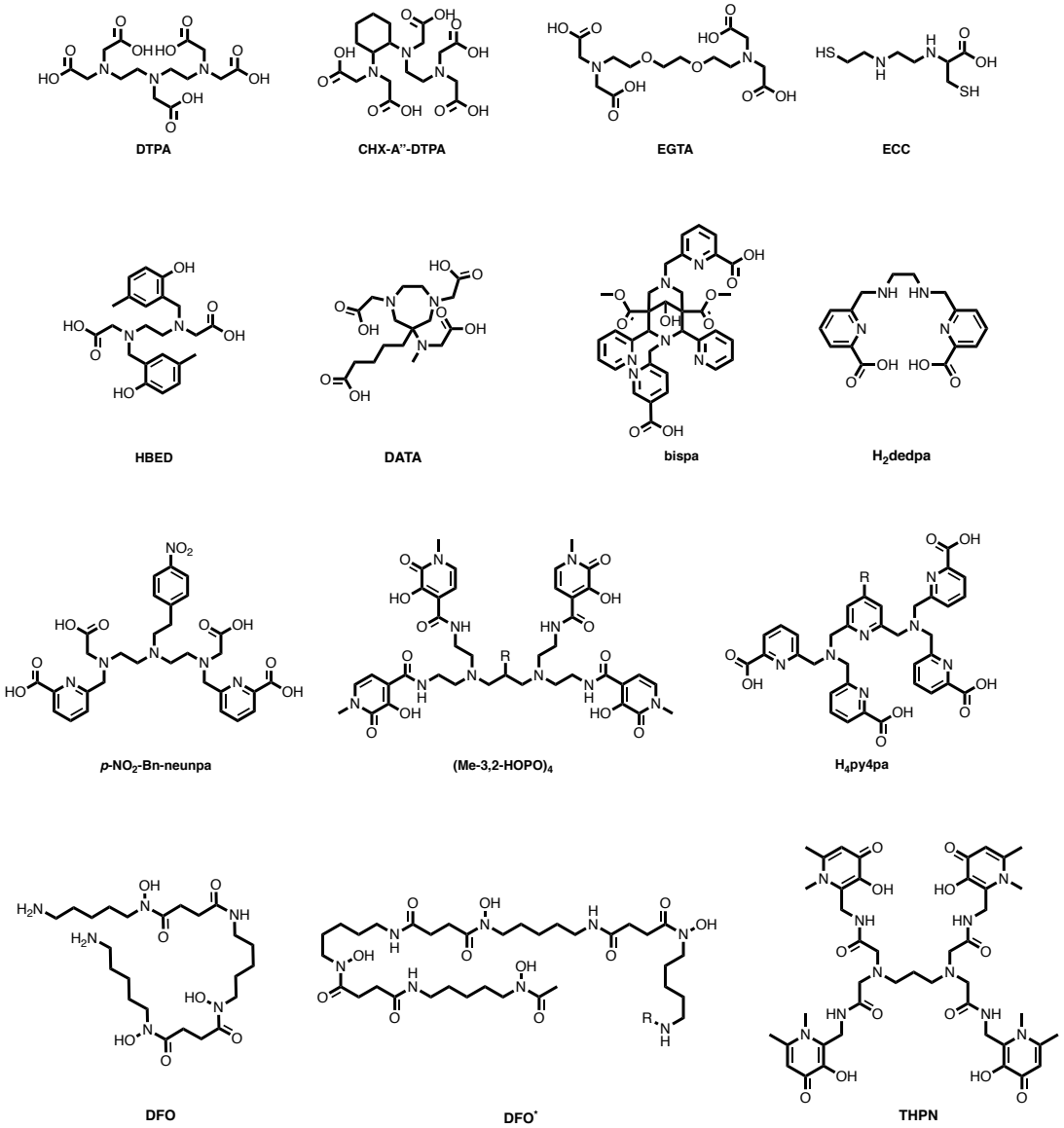

Figure 1.4. Structure of acyclic chelators discussed in this Chapter.

Other macrocycles such as 1,4,7,10,13-pentaazacyclopentadecane-N,N',N'',N''',N''''-pentaacetic acid (PEPA) or 1,4,8,11-tetraazacyclotetradecane-1,4,8,11-tetraacetic acid (TETA) suffer either from low labelling yield or poor *in vivo* stability.[27] Also the acyclic ligands, [6,6'-({9-hydroxy-1,5-bis(methoxycarbonyl)-2,4-di(pyridin-2-yl)-3,7-diazabicyclo[3.3.1] nonane -3,7-diyl}bis(-methylene))dipicolinic acid] (bispa), and H_4py4pa have shown promise as they can label [^{225}Ac]Ac^{3+} in less that 30 min at ambient temperature.[6,40] DOTA, even if it requires high temperature (95°C) and long reaction times to reach quantitative labelling, remains the 'gold standard' for [^{225}Ac]Ac^{3+} chelation in preclinical and clinical studies.[12,27]

Several monoclonal antibodies were tested in preclinical models of colon and breast cancer as well as for neuroblastoma treatment with ^{225}Ac.[39–42] For example, clinical trials with DOTA conjugates have been performed with [^{225}Ac]Ac-DOTATOC for the treatment of neuroendocrine tumours (NETs), [^{225}Ac]Ac-substance P for the therapy of glioblastoma and [^{225}Ac]Ac-PSMA-617 for metastatic castration-resistant prostate cancer.

Bismuth-212/213. ^{213}Bi ($t_{1/2}$ 45.6 min) is a short-lived α-emitter. It decays through two different pathways (**Figure 1.7**): *via* α-emission (E_α 5.8 MeV, I_α 2%) to thallium-209 (^{209}Tl, $t_{1/2}$ 2.17 min, $E_{\beta^-\,ave}$ 650 keV, I_{β^-} 99%) and β^- emission ($E_{\beta^-\,ave}$ 435 keV, I_{β^-} 98%) to polonium-213 (^{213}Po, $t_{1/2}$ 4.2 μs, E_α 8.375 MeV).[4,6,43] Its daughters, *i.e.* ^{213}Po and ^{209}Tl, then decay to the long-lived bismuth-209 (^{209}Bi, $t_{1/2}$ $1.9\cdot10^{19}$ y).[44] The decay of ^{213}Bi is also accompanied by a photon emission (E_γ 440 KeV, I_γ 26%) that can be used for dosimetry studies and/or to monitor its biodistribution *via* SPECT.[44]

^{213}Bi is commonly produced using the ^{225}Ac/^{213}Bi generator.[44–47] Alternative routes include proton, neutron or deuteron irradiation of ^{226}Ra targets.

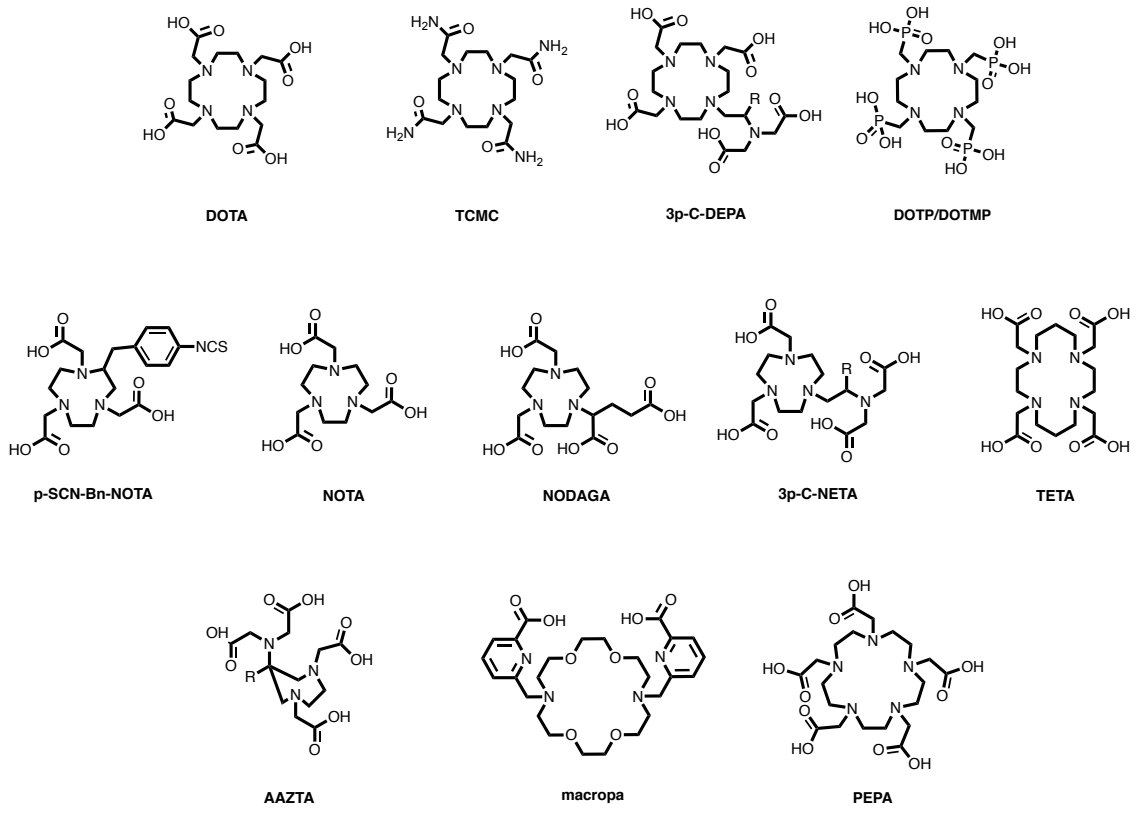

Figure 1.5. Structure of macrocyclic chelators discussed in this Chapter.

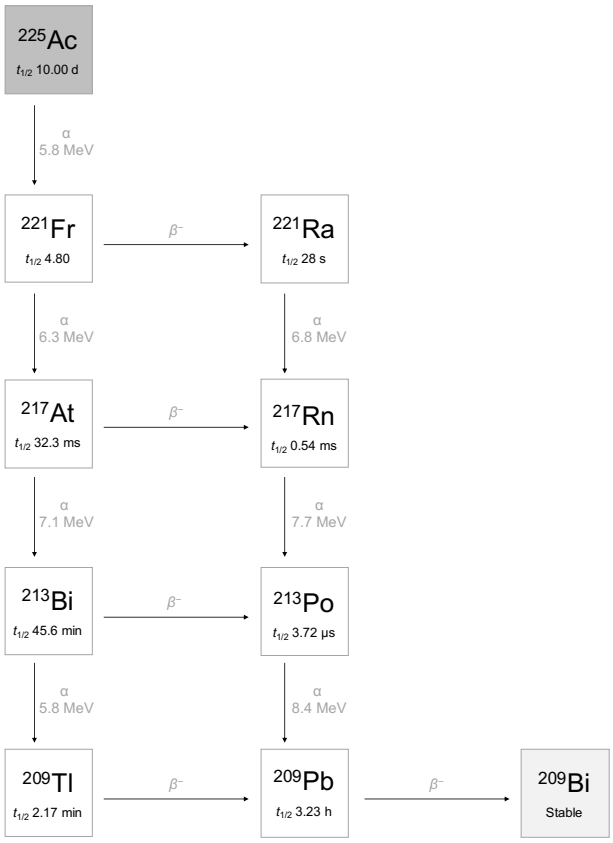

Figure 1.6. Decay chain of actinium-225.

^{212}Bi ($t_{1/2}$ 60.6 min) is another medically relevant bismuth radioisotope which predominantly decays *via* β^- emission (E_{β^-} 771 keV, I_{β^-} 64%) to the α-emitter polonium-212 (^{212}Po, $t_{1/2}$ 0.3 µs). A minor route involves the α-decay ($E_{\alpha,\ ave}$ 6.21 MeV, I_α 36%) to thallium-208 (^{208}Tl, $t_{1/2}$ 3.05 min) (**Figure 1.8**). ^{212}Bi production relies on generators, employing the parent ^{224}Ra ($t_{1/2}$ 3.6 d).[19]

Bismuth is typically found in its +3 oxidation state (Bi^{3+}) with CN of 5-8.[48] Being a borderline cation, it has a high affinity for O- and N-containing ligands but it also forms stable complexes with S and halogens.[4] DOTA and diethylenetriaminepentaacetic acid (DTPA) form highly thermodynamically stable Bi^{3+} complexes which however suffer from *in vivo* instability, thus resulting in high [^{213}Bi]Bi^{3+} uptake in the kidneys. Enhanced stability has been obtained with the acyclic *trans*-cyclohexyl chelator CHX-A''-DTPA and two DOTA and 1,4,7-triazacyclononane-1,4,7-triacetic acid (NOTA) derivatives, *i.e.* 3p-C-DEPA and 3p-C-NETA, which can label [^{213}Bi]Bi^{3+} at room temperature in less than 30 min.[12]

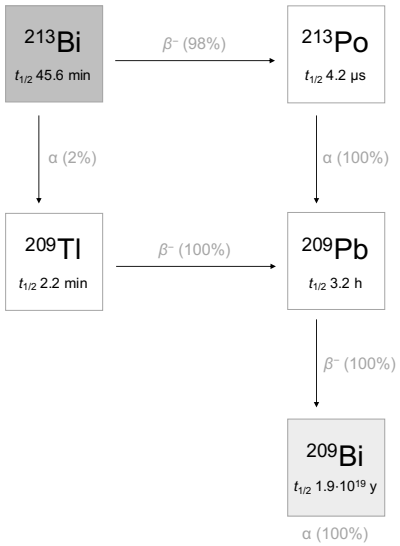

Figure 1.7. Decay chain of bismuth-213.

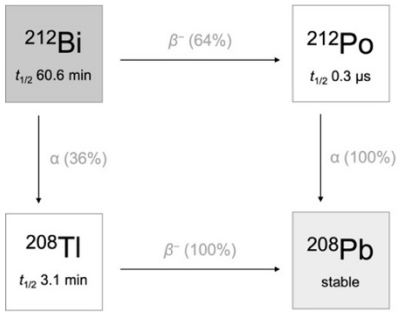

Figure 1.8. Decay chain of bismuth-212.

Also the phosphorous-containing cyclen-based ligand 1,4,7,10-tetraazacyclododecane-1,4,7,10-tetramethylene phosphonic acid (DOTP) forms a stable complex with [^{213}Bi]Bi^{3+} at ambient temperature which was demonstrated to be more stable in human serum compared to [^{213}Bi]Bi-DOTA or [^{213}Bi]Bi-CHX-A''-DTPA.[6,27,49] Even though the short half-life of ^{213}Bi requires the use of fast-circulating bioconjugates, many *in vivo* studies used monoclonal antibodies. [^{213}Bi]Bi^{3+} constructs have been evaluated for the treatment of acute myeloid leukemia (*e.g.*, [^{213}Bi]Bi-Lintuzumab), melanoma (*e.g.*, *Trastuzumab*, neural/glial antigen 2), bladder cancer (*e.g.*, *Cetuximab*) and leukemia (*e.g.*, anti-CD45).[50–53] [^{213}Bi]Bi^{3+}-peptide conjugates have also been studied for the treatment of gliomas (substance P analogues) and NETs (*e.g.*, Try^3-octreotide).

Lead-212. ^{212}Pb ($t_{1/2}$ 10.6 h) is a β^- emitter (E_{β^-} 570 keV, I_{β^-} 100%) investigated for TAT because it is the parent radionuclide of the α-emitter ^{212}Bi ($t_{1/2}$ 60.6 m).[4] It also forms an ideal theranostic pair with the SPECT radioisotope lead-203 (^{203}Pb, $t_{1/2}$ 51.9 h, E_γ 279.1 keV, I_γ 81%). A detailed description of lead decay properties, production and chelation is given in **Chapter 5**.

Even though different chelation issues have still to be satisfied, ^{212}Pb has been investigated for peptide receptor-targeted therapy (PRTT) using melanocyte-stimulating hormone, Try^3-octreotate or PSMA ligands as well as in radioimmunotherapy.[54–58] [^{212}Pb]Pb-TCMC-trastuzumab was used in the first human dose-escalation clinical trial and was well tolerated.[27,59]

Terbium-149. ^{149}Tb ($t_{1/2}$ 4.12 h, E_α 3970 keV, I_α 17%) is the only α-emitter that possesses a single α-emission in its decay chain (**Figure 1.9**). ^{149}Tb also emits β^+ particles suitable for PET imaging ($E_{\beta^+\,\text{ave}}$ 728 keV, $I_{\beta^+\,\text{ave}}$ 7%), which may allow approximate dose quantification during therapy. It also represents a theranostic quadruplet with its isotopes ^{151}Tb, ^{155}Tb and ^{161}Tb.[6] ^{149}Tb is mostly produced by proton-induced spallation of tantalum targets *via* the ^{nat}Ta(p,x)^{149}Tb nuclear reaction followed by on-line mass separation.[60–62] Beyond spallation, ^{149}Tb can also be produced *via* the ^{152}Gd(p,4n)^{149}Tb reaction.

Terbium is commonly found in the 3+-oxidation state (Tb^{3+}), and it has a high affinity for oxygen donors, forming 8- or 9-coordinated complexes dominated by electrostatic interactions.[6] Terbium-based radiotracers virtually solely use DOTA as it forms highly stable complexes with Tb^{3+} but a high temperature (95°C) is required for the radiolabelling. Quantitative incorporation at room temperature can be achieved with DTPA and its derivative CHX-A''-DTPA.[63] To date only limited but very encouraging preclinical applications are reported: for example, [^{149}Tb]Tb-DOTA-folate was found to delay tumour growth whilst [^{149}Tb]Tb-CHX-A''DTPA-rituximab demonstrated tumour-free survival in mice.[27,33,62]

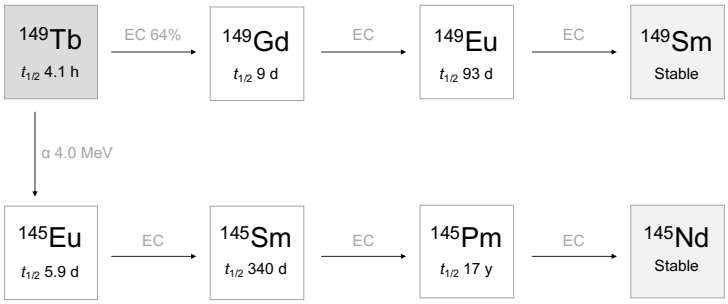

Figure 1.9. Decay chain of terbium-149.

Thorium-227. ^{227}Th ($t_{1/2}$ 18.7 d, E_α 6.0 MeV) decays *via* the emission of five α- and two β^--particles to the stable ^{207}Pb (**Figure 1.10**). ^{227}Th can be produced from the β^- decay of ^{227}Ac ($t_{1/2}$ 21.8 y), accessible *via* legacy material of ^{231}Pa stockpiles, a decay product of ^{235}U.[6] Thorium is generally found in the +4-oxidation state (Th^{4+}), and it is a strong Lewis acid with a high affinity for oxygen donors. It commonly forms octa and nona-coordinated complexes. DOTA forms stable complexes with [^{227}Th]Th^{4+} even if high temperatures are required for the labelling. To date, the current standard for [^{227}Th]Th^{4+} chelation is (Me-3,2-HOPO)$_4$. Among the most relevant preclinical data, [^{227}Th]Th-mesothelin and [^{227}Th]Th-PSMA have demonstrated excellent antitumour activity in lung and prostate cancer xenograft models in mice, thus supporting the initiation of two clinical trials (NCT03507452 and NCT03724747).[64–66]

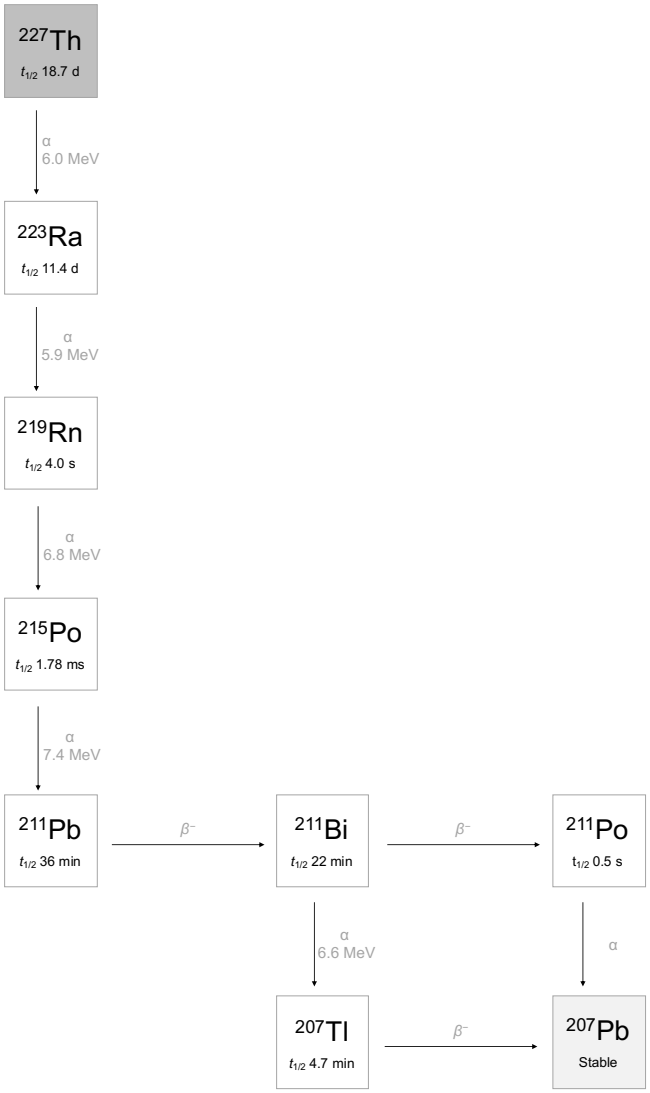

Figure 1.10. Decay chain of thorium-227.

Table 1.1. Summary of the decay properties of therapeutic and diagnostic radiometals discussed in this Chapter.

Emission		Radioisotope	Half-life $t_{1/2}$	Decay	Branching ratio [%]	E_{ave} [keV]
Therapeutic Radiometals	α-Emitters	^{225}Ac	10.0 d	α	100	5800
		^{213}Bi	45.6 min	β^-	98	435
				α	2	5800
		^{212}Bi	60.6 min	β^-	64	771
				α	36	6210
		^{212}Pb	10.6 h	β^-		100
				α	36	6300
		^{227}Th	18.7 d	α	100	6000
		^{149}Tb	4.1 h	α β^+ EC	17 7 76	4000 (α) 728 (β^+)
	Meitner-Auger Electron Emitters	^{119}Sb	38.2 h	EC	-	8.9 23.7 [(a)]
		^{197g}Hg	2.67 d	EC	-	16.1 23.2 [(a)]
		^{197m}Hg	23.8 h	IT EC	91 9	13.5 19.4 [(a)]
	β^--Emitters	^{47}Sc	3.35 d	β^-	100	162.0
		^{67}Cu	61.8 h	β^-	100	141
		^{177}Lu	6.7 d	β^-	100	134
		^{161}Tb	6.9 d	β^- IC	- -	151 0.9 [(a)]
		^{90}Y	64.0 h	β^-	100	934
Diagnostic Radiometals	β^+ Emitters (PET)	^{44}Sc	4.04 h	β^+	94	632
		^{68}Ga	1.13 h	β^+ EC	89 11	830
		^{86}Y	14.7 h	β^+ EC	32 68	664
		^{152}Tb	17.5 h	β^+ EC	20 80	1142
	γ-Emitters (SPECT)	^{67}Ga	78.2 h	EC	100	-
		^{111}In	67.2 h	EC	100	6.8 [(a)]
		^{155}Tb	5.3 d	EC	100	-

[(a)] Meitner-Auger electrons/decay.

1.3.2 Meitner-Auger Emitters for Meitner-Auger Electrons Therapy

Meitner-Auger electrons are low-energy electrons (1-10 keV) emitted to fill the vacancies produced in the shell of atoms after electron capture (EC) and/or internal conversion (IC). Meitner-Auger electrons possess short path lengths in tissues (< 10 μm, 1-2 cell diameters) and a very high LET (~ 4-26 keV/μm). This allows to confine the cytotoxic effects to the immediate vicinity of the decay site, making them highly powerful for the treatment of small micrometastatic tumours or single cancer cells.[6,67] Although Meitner-Auger emitting radionuclides are the least investigated among the three types of therapeutic radiation, an increasing number of radionuclides are nowadays being considered.[68–71] Two promising Meitner-Auger emitters are antimony-119 (^{119}Sb) and mercury-197 (^{197}Hg).

Antimony-119. ^{119}Sb ($t_{1/2}$ 38.2 h) decays purely *via* EC, emitting 23.7 Meitner-Auger electrons per decay (E_{ave} 8.9 keV/decay).[72] It also possesses a same element matching pair, *i.e.* ^{117}Sb ($t_{1/2}$ 2.80 h, E_γ 158.45 keV, I_γ 86%) which can be used for SPECT imaging. ^{119}Sb can be produced by proton irradiation of tin target *via* the ^{119}Sn(p,n)^{119}Sb nuclear reaction or using the ^{119m}Te/^{119}Sb generator (^{119m}Te $t_{1/2}$ 4.70 d).[73] To date the chelation chemistry of antimony for nuclear medicine applications is unexplored.[6]

Mercury-197m/g. ^{197m}Hg (^{197m}Hg, $t_{1/2}$ 23.8 h, E_γ 134 keV, I_γ 34%) and ^{197g}Hg (^{197g}Hg, $t_{1/2}$ 64.14 h, E_γ 77 keV, I_γ 19%; E_γ 279 keV, I_γ 6%) are γ-emitting radionuclides suitable for SPECT imaging and of additional interest because of the therapeutic potential of their Meitner-Auger and conversion electron emission.[6,74] A detailed description of mercury radioisotopes decay properties, production and chelation is given in **Chapter 6**.

1.3.3 β^--Emitters for Cancer Therapy

Beta particles (β^-) are electrons emitted from the nucleus of a radioactive atom during its decay.[6] Owing to their intermediate energies (0.1-2.3 MeV) and long tissue ranges (0.5-12 mm), resulting in the lowest LET (0.2 keV/μm) of all therapeutic particles, these emitters are very appropriate for the treatment of mid-to-large-size tumours.[6]
The low energy deposited *per* cell produces few irradiation events which lead to partial DNA damage that can be easily repaired. Consequently, very high doses of the radiopharmaceutical (GBq/cycle) have to be administered to have a therapeutic effect in patients.[75,76] This dose is 100-fold larger than those typically used with α-emitters (1-100 MBq/cycle). Differently from the latter, β^--emitting radionuclides have simpler decay schemes and very low recoil energies (~ 10 eV). This minimizes the likelihood of a daughter-nuclide-loss event. An overview of the decay properties production, chelation and *in vivo* studies with β^- emitters are briefly discussed in the following paragraphs.

Copper-67. ^{67}Cu ($t_{1/2}$ 61.8 h) is a pure β^--emitter ($E_{\beta^- ave}$ 141 keV, I_{β^-} 100%) which decays to stable ^{67}Zn. Its decay also involves the co-emission of three γ-rays suitable for SPECT (E_γ 91.2 keV, I_γ 7%; E_γ 93.3 keV, I_γ 16% and E_γ 184.5 keV, I_γ 49%).
^{67}Cu can be produced by high energy proton irradiation of zinc targets *via* the ^{68}Zn(p,2p)^{67}Cu or ^{70}Zn (p, α)^{67}Cu reactions or by fast neutron bombardment through the ^{67}Zn(n,p)^{67}Cu nuclear reaction in high flux reactors.[6] The former reaction is the most exploited as it can be performed using cyclotrons; however, the simultaneous production of ^{64}Cu, which is extremely challenging to isolate and remains in solution for several days, represents the

major drawback.[6] Alternative productions pathways are the $^{64}Ni(\alpha,p)^{67}Cu$ or ^{68}Zn (d,2pn)^{67}Cu reactions.[77,78] Copper has very rich coordination chemistry and can be found in nature in its metallic form (Cu^0) or as monovalent (Cu^+) or divalent (Cu^{2+}) cation. The latter is the prevalent form for radiopharmaceutical development. The coordination chemistry and the current challenges for its *in vivo* stabilization are described in **Chapter 4**.

Lutetium-177. ^{177}Lu ($t_{1/2}$ 6.6 d) decays *via* the emission of low energy β^--particles useful for therapy ($E_{\beta^- ave}$ 134 keV, I_{β^-} 100%).[79] In addition it emits two γ rays ($E_{\gamma,max}$ 208 keV, I_γ 11%; $E_{\gamma,max}$ 113 keV, I_γ 6.6%) that can be used for SPECT imaging and dosimetry calculations.[5,79] ^{177}Lu can be produced in medium flux reactors *via* irradiation of enriched ^{176}Lu through the $^{176}Lu(n,\gamma)^{177}Lu$ reaction.[5,79] However, a shortcoming of this method is the production of carrier-added activity. This can be overcome using a reactor-based strategy *via* the $^{176}Yb(n,\gamma)^{177}Yb \rightarrow {}^{177}Lu$ pathway.

Lutetium is the last lanthanide, and its most common oxidation state is the +3 (Lu^{3+}). It commonly forms 8- to 9-coordinate complexes with oxygen-donating groups due to their ionic-donating compatibility.[79] The most commonly used chelators for $[^{177}Lu]Lu^{3+}$ chelation are DOTA and DTPA analogues.[12] The former necessitates heating to reach quantitative labelling so that if heat-sensitive bioconjugates are employed, DTPA is generally used to rapidly radiolabel at ambient temperature. ^{177}Lu has been an intense area of research in recent years and has culminated in the first ^{177}Lu-based drug, Lutathera® ($[^{177}Lu]$Lu-DOTATATE), which received FDA approval for treatment of somatostatin receptor-positive gastroenteropancreatic neuroendocrine tumours.[19]

Scandium-47. ^{47}Sc ($t_{1/2}$ 3.35 d, $E_{\beta^- ave}$ 162 keV, I_{β^-} 100%) is a low-energy pure β^--emitter. Even if its γ emission can be exploited for associated SPECT imaging (E_γ 159.3 keV, I_γ 68%), it forms a theranostic pair with the PET isotope ^{44}Sc ($t_{1/2}$ 3.97 h, $E_{\beta^+ ave}$ 632 keV, I_{β^+} 94%).[63] ^{47}Sc can be produced by neutron irradiation of enriched $^{47}TiO_2$ target *via* $^{47}Ti(n,p)^{47}Sc$ reaction.[80] Alternatively, ^{47}Sc is accessible *via* the $^{46}Ca(n,\gamma)^{47}Ca \rightarrow {}^{47}Sc$ pathway.[19]

Scandium is commonly found in the 3+-oxidation state (Sc^{3+}), and it forms 6- to 8-coordinate complexes with O-containing ligands. A high propensity to hydrolyse (pH > 2.5) is the consequence of the high acid dissociation constant of hydrated Sc^{3+} ($Sc^{3+}{}_{(aq)} \rightarrow ScOH^{2+}{}_{(aq)}$, pK_a = 4.3) and poses labelling challenges.[19] Precipitation as $Sc(OH)_3$ occurs at neutral-to-basic pH (pH 7-11).[19]

DOTA forms a highly stable Sc^{3+} complex but requires high temperatures (70-90°C) to obtain radiometal incorporation.[81] On the other hand, the acyclic chelator DTPA is a satisfactory

alterantive to DOTA. Ethylene glycol-bis(2-aminoethylether)-N,N,N′,N′-tetraacetic acid (EGTA) can quantitatively label [^{47}Sc]Sc^{3+} at mild temperatures in less than 10 min.[82] Moreover, 1,4 - bis(carboxymethyl) - 6 - [bis(carboxymethyl)]amino - 6 - methylperhydro - 1,4 -diazepine (AAZTA) was also reported to radiolabel [^{44}Sc]Sc^{3+} very efficiently forming a highly thermodynamically stable and kinetically inert complex at room temperature.[83] Due to the lack of reliable ^{47}Sc supply, only limited preclinical evaluations are reported to date. However, its therapeutic capacity combined with its theranostic pair ^{44}Sc is encouraging for its clinical future.

Terbium-161. ^{161}Tb ($t_{1/2}$ 6.9 d) has a unique decay profile which combines a low-energy β^--emission ($E_{\beta^-\,ave}$ 154 keV, I_{β^-} 100%) and a Meitner-Auger electron cascade (0.9 electron/decay, E_{ave} 5.1 keV).[72] ^{161}Tb can stand itself as a theranostic isotope thanks to the emission of low-energy γ rays (E_γ 48.9 keV, I_γ 17%; E_γ 74.5 keV, I_γ 10%) imageable through SPECT, or it can also be used as a theranostic quadruplet with ^{152}Tb and ^{155}Tb. ^{161}Tb can be produced by neutron irradiation of enriched gadolinium target *via* the ^{160}Gd(n,γ)^{161}Gd → ^{161}Tb reaction.[84]

Terbium chelation chemistry has already been described for ^{149}Tb (*vide supra*). ^{161}Tb has gained attention due to the similar decay properties with respect to ^{177}Lu. However, the coemission of Meitner-Auger electrons is expected to enhance its therapeutic effectiveness.[84,85] In fact, [^{161}Tb]Tb-PSMA-617 has revealed higher anticancer efficacy than the ^{177}Lu analogue.

Yttrium-90. ^{90}Y ($t_{1/2}$ 64 h) decays solely *via* β^- emission ($E_{\beta^-\,ave}$ 934 keV, I_{β^-} 100%). Even though the pure β^- emission is a key advantage of ^{90}Y therapy, dosimetry calculations are challenging due to the lack of γ-emission: the use of ^{86}Y is an attractive option due to the identical chemical behaviour, which would mitigate concern over non-representative image information.[19]

^{90}Y is commercially produced in a ^{90}Sr/^{90}Y generator system (^{90}Sr, $t_{1/2}$ 28.8 y).[5] Direct ^{90}Y production *via* the ^{89}Y(n,γ)^{90}Y reaction has also been demonstrated but this method results in low specific activity due to the chemically identical target.[86] The ^{90}Zr(n,p)^{90}Y reaction was also studied but the target cost and the need for fast neutrons have smothered progress of this method.[86]

Y generally exhibits the +3-oxidation state (Y^{3+}) and can achieve coordination numbers as high as 10. Y^{3+} is considered a hard Lewis acid and consequently it prefers hard donor atoms such as O and N.[87] Despite its slow radiolabelling kinetics and heating requirements, DOTA is the current 'gold standard' chelators for ^{90}Y.[12] CHX-A''-DTPA is also employed.

The most popular ^{90}Y radiopharmaceutcals are the FDA-approved Zevalin®, a [^{90}Y]-labelled monoclonal antibody ([^{90}Y]Y-tiuxetan-ibritumomab) used in β^--therapy of B-cell non-Hodgkin's lymphoma[4] and yttrium-90-bearing microspheres (SIR-spheres, TheraSphere®) for brachytherapy of hepatocellular carcinoma.[88–91]

1.4 Radiometals for Tumour Diagnosis

Nuclear imaging can be used to non-invasively diagnose and monitor cancer exploiting the photons emitted directly or indirectly through positron emission.[19] Single-photon emission computer tomography (SPECT) and positron emission tomography (PET) are the established imaging modalities.[4] The former approach relies on a γ-emitting radionuclide which emissions are recorded by detector cameras.[4,19] Because only single-emission events are detected, SPECT devices require a collimator for decay localization and sharp image construction.[19] Consequently, low energy γ-photons (100-250 keV) are required for SPECT as they can be easily filtered by collimators and attenuated by the SPECT detector. On the other hand, PET employs positron (β^+)-emitting radionuclides.[4,12] After emission, the positron collides with a nearby electron and, annihilating, release two near-coincident (180°) 511 keV γ rays (**Figure 1.11**). [4,12,19] The latter are detected by a circular array of PET scanner coincidence detectors and, after image reconstruction, it is possible to calculate the radiotracer location by determining the point of anniihilation.[4,19,92] Compared to SPECT, PET exhibits higher resolution and sensitivities (up to 10^{-12} M, compared to 10^{-6} M for SPECT).[4,93] However, due to the absence of anatomical perspective, SPECT and PET are often combined with computed tomography (CT) to surpass this limitation.[19 27]

The γ-emitter technetium-99m (^{99m}Tc) is the workhorse of medical imaging, used in about 70-80% of all radiodiagnostic SPECT scans, whilst fluorine-18 (^{18}F, $t_{1/2}$ 109 min) is the archetypical PET isotope.[4,94,95] Nonetheless, tremendous effort has been made towards the production of alternative SPECT and PET metallic radioisotopes. These are briefly discussed in the following paragraphs.

1.4.1 PET Radiometals

Copper-64. ^{64}Cu ($t_{1/2}$ 12.7 h) decays *via* β^+ emission (18%), electron capture (43%) and β^- emission (39%).[87,96] ^{64}Cu can also provide a matched element PET imaging pair with the pure β^- emitter ^{67}Cu ($t_{1/2}$ 62 h) (*vide supra*).[97] ^{64}Cu can be produced *via* proton irradiation of enriched ^{64}Ni through the ^{64}Ni(p,n)^{64}Cu reaction.[94] Its challenging chelation chemistry is discussed in **Chapter 4**.

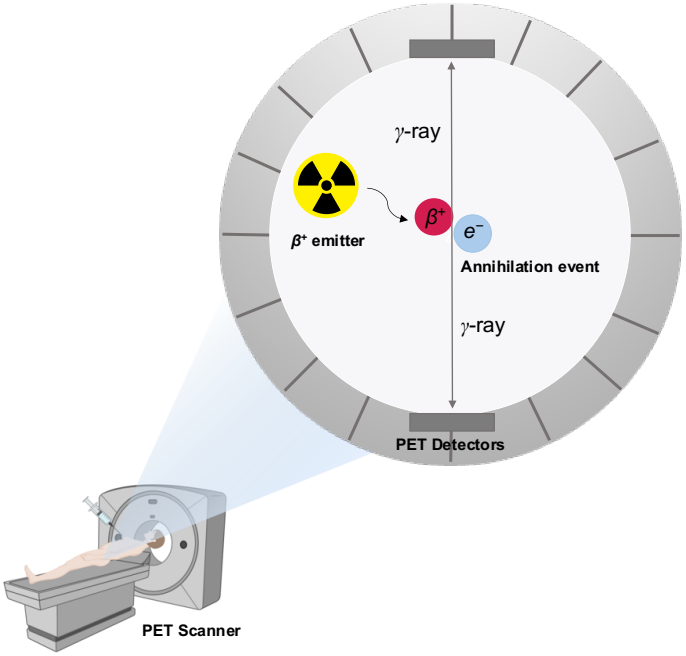

Figure 1.11. Representation of PET imaging.

Gallium-68. ^{68}Ga ($t_{1/2}$ 67.7 min) is a β^+ emitter ($E_{\beta^+,\,max}$ 1.9 MeV, I_{β^+} 89%) that can be produced using the ^{68}Ge/^{68}Ga generator system.[4,87] The half-life of the parent ^{68}Ge ($t_{1/2}$ 270 d) allows the generator to be used for up to one year, with two or three elutions *per* day, obviating the need for an on-site cyclotron.[98]

Gallium can be found in aqueous solution exclusively in its +3 oxidation state (Ga^{3+}), and free hydrated $[Ga(H_2O)_6]^{3+}$ is stable only under acidic conditions.[87] A major challenge of gallium-based radiotracers is its propensity to form hydroxide species. Indeed, at pH > 4 insoluble $Ga(OH)_3$ forms. At pH > 7, $[Ga(H_2O)_6]^{3+}$ hydrolyses to $[Ga(OH)_4]^-$ which may result in demetallation of its complexes.[87] Ga^{3+} is classified as a hard acidic cation that prefers hard donor ligands as O or N and forms 4- to 6-coordinate complexes.[87,93,99] DOTA has been extensively used with gallium radioisotopes despite the non-optimal match.[12] The pyridine-containing DOTA derivative PCTA appears to be an improvement, achieving quantitative incorporation at room temperature and maintaining high stability.[100] NOTA is an excellent chelate-match with Ga^{3+} and it can stably radiolabel ^{68}Ga at ambient temperature. This behaviour is preserved with its analogues 1,4,7-triazacyclononane,1-glutaric acid-4,7-acetic acid (NODAGA) and *p*-SCN-Bn-NOTA.[100–102]

Many acyclic ligands have also been reported: N,N′-bis[2-hydroxybenzyl]ethylenediamine-N,N′-diacetic acid (HBED) demonstrated outstanding stability and it can quantitatively radiolabel radioactive gallium at room temperature with high specific activity, demonstrating high resistance to decomplexation.[103–106] Tris(3,4-hydroxypyridinone) (THP) possesses a

high affinity for Ga^{3+} which has demonstrated superior [^{68}Ga]Ga^{3+} labelling with respect to DOTA, NOTA and HBED.[19] Numerous other chelators have been studied with Ga^{3+}: dedpa, 6-amino-1,4-diazepine triacetic acid (DATA), deferoxamine (DFO) but also sulfur-based ligands, including [9]aneN3 analogues, ethylenecysteamine cysteine (ECC) and ethyl cysteinate dimer (EDC) shown promise for ^{68}Ga imaging.[107,108] ECC and EDC were shown to be useful in [^{68}Ga]Ga^{3+}-based renal and cerebral blood flow imaging.

^{68}Ga radiotracers are the vanguard of nuclear drug development, as evidenced by the approval of [^{68}Ga]Ga-DOTATATE (NETSPOT®) for imaging SST receptor-expressing neuroendocrine tumours, as well as the clinical attention to [^{68}Ga]Ga-DOTATOC, [^{68}Ga]Ga-DOTANOC, [^{68}Ga]-Ga-PSMA-617 *etc*.[19,109–113]

Scandium-44. ^{44}Sc is a long-lived PET radionuclide ($t_{1/2}$ 4.04 h, E_{β^+} 632 keV, I_{β^+} 94%).[114] ^{44}Sc is considered a diagnostic match for the β^- emitters ^{90}Y and ^{177}Lu, due to the chemical similarities of rare-earth metals.[19] It also represents a matched theranostic pair with ^{47}Sc (*vide supra*).

^{44}Sc can be produced *via* the ^{44}Ca(p,n)^{44}Sc reaction or through the ^{44}Ti/^{44}Sc generator, even if the production of the parent ^{44}Ti remain challenging, requiring high-flux protons due to the low ^{45}Sc(p,2n)^{44}Ti reaction cross section.[115,116]

Scandium chelation chemistry has already been described for ^{47}Sc (*vide supra*). Thanks to the compatibility with commercially available and widely employed DOTA, a variety of *in vivo* studies have been performed. DOTATATE, DOTANOC, DOTAPuromycin, DOTA-cRGD and DOTA-PSMA-617 are examples of bioconjugates investigated.[19,117–121]

Yttrium-86. ^{86}Y ($t_{1/2}$ 14.7 h) decays *via* the emission of a high energy β^+ particle (E_{β^+} 1.2 MeV, I_{β^+} 32%), and γ emission (E_γ 1.08 MeV, I_γ 68%) and it forms a theranostic pair with pure β^- emitter ^{90}Y.[4,93,94]

^{86}Y can be produced by irradiating $SrCO_3$ or SrO with protons *via* the ^{86}Sr(p,n)^{86}Y reaction.[87] The drawback of this approach is the need for enriched ^{86}Sr to minimize the coproduction of $^{87/88}$Y, thus necessitating a careful recycling strategy of the target material.[122] Other production strategy include the ^{86}Sr(p,n)^{86}Y, ^{88}Sr(p,3n)^{86}Y, ^{90}Zr(p,2p3n)^{86}Y reactions as well as the indirect route ^{89}Y(p,4n)^{86}Zr → ^{86}Y.[19]

Yttrium chelation chemistry has already been described for ^{90}Y (*vide supra*). Notable studies with ^{86}Y have been conducted with [^{86}Y]Y-DOTATOC, [^{86}Y]Y-DOTA-PSMA, [^{86}Y]Y-CHX-A″-DTPA-bevacizumab, [^{86}Y]Y-CHX-A″-DTPA-antimindin/RG-1, [^{86}Y]Y-CHX-A″-DTPA-cetuximab, and [^{86}Y]Y-CHX-A″-DTPA-panitumomab.[19]

Zirconium-89. ^{89}Zr ($t_{1/2}$ 78.4 h) is a β^+ emitter (E_{β^+} 902 keV, I_{β^+} 23%,) with an ideal half-life for labelling antibodies in immuno-PET imaging.[123] ^{89}Zr can be produced by proton irradiation of natural yttrium targets *via* the ^{89}Y(p,n)^{89}Zr reaction.[95]

Zr forms an extremely acidic hydrated Zr^{4+} cation with a marked preference for multidentate ligands with hard donor atoms such as anionic oxygen from carboxylic acid or phosphinic acid residues. Zr^{4+} prefers to form octadentate complexes.[87,124] The bacterial iron siderophore DFO is the widely employed [^{89}Zr]Zr^{4+} chelator even if preclinical results in mice show considerable bone uptake, thus suggesting the [^{89}Zr]Zr-DFO instability. Polyhydroxiamate-based ligands have also been investigated.[125–127] For example, stability improvements were obtained by adding an additional hydroxamate donor in DFO, obtaining DFO*. Also other scaffolds based on naturally occurring siderophores were examined. Among those fusarinine C (FSC) has shown excellent short-term stability.[7] Hydroxypyridinonate-based ligands, *i.e.* HOPO and THPN, were also explored as replacements for DFO. HOPO can label [^{89}Zr]Zr^{4+} in 1 h at room temperature, and the resulting complex was found to be stable in human serum for 7 days.[128–130] With THPN, the labelling reaction is even shorter as it requires 30 min at room temperature. However, the bone uptake for [^{89}Zr]Zr-THPN is comparable to [^{89}Zr]Zr-DFO.

Thanks to its half-life, ^{89}Zr is generally matched with antibody constructs. *Pertuzumab* and *Trastuzumab* for breast and ovarian cancer, huJ591 for prostate cancer, *Cetuximab* for colorectal cancer, and *Pembrolizumab* for cell lung cancer conjugates were investigated in clinical trials.[7]

Terbium-152. ^{152}Tb ($t_{1/2}$ 17.5 h) is a β^+ emitter ($E_{\beta^+,\,ave}$ 1142 keV, E_{β^+} 20%) suitable for PET imaging. ^{152}Tb production occurs *via* proton-induced spallation of tantalum targets and isotope mass separation. Alternative routes involved the ^{152}Gd(p,n)^{152}Tb and ^{155}Gd(p,4n)^{152}Tb reactions.[131,132] Terbium chelation chemistry has already been described for ^{155}Tb (*vide supra*).

1.4.2 SPECT Radiometals

Gallium-67. ^{67}Ga ($t_{1/2}$ 78.2) is a low-energy γ-emitter suitable for SPECT imaging (E_γ 93 keV, I_γ 39%; E_γ 184 keV, I_γ 21%; E_γ 300 keV, I_γ 17%).[19] Moreover, the emission of Meitner-Auger electrons has prompted some interest in ^{67}Ga therapy.[133]

^{67}Ga is produced through proton irradiation of zinc targets *via* the ^{67}Zn(p,n)^{67}Ga reaction or *via* the ^{67}Zn(d,2n)^{67}Ga, ^{64}Zn(α,n)^{67}Ga, and ^{65}Cu(α,2n)^{67}Ga routes.[19] Gallium chelation chemistry has already been described for ^{68}Ga (*vide supra*).

Indium-111. ^{111}In ($t_{1/2}$ 2.8 d) decays *via* electron capture (I_{EC} 100%) by emission of two γ-rays (E_γ 171 keV, I_γ 91%; E_γ 245 keV, I_γ 94%) suitable for SPECT imaging.[87] ^{111}In also emits Meitner-Auger electrons and has been considered for Meitner-Auger electron therapy. ^{111}In is commercially produced *via* the ^{111}Cd(p,n)^{111}In reaction or the ^{112}Cd(p,2n)^{111}In reaction in natural cadmium target.

Indium is a group 13 element, and it is only stable in the +3-oxidation state (In^{3+}). It is a fairly hard acidic cation with preferences for hard donor atoms in 7-8 coordinated complexes.[87] Despite its slow radiolabelling kinetics and required heating, DOTA is the current 'gold standard' for ^{111}In chelation together with CHX-A''-DTPA.[12] ^{111}In has been successfully introduced into different clinically-approved pharmaceuticals: Octreoscan® ([^{111}In]In-CHX-A''-DTPA-pentetreotide.), ProstaScint® ([^{111}In-In-CHX-A''-DTPA-capromab), CEA-Scan® ([^{111}In]In-CHX-A''-DTPA-arcitumonab), MPI indium DTPA In-111 ([^{111}In]In-CHX-A''-DTPA), and In-111 oxyquinoline ([^{111}In]In-oxyquinoline).[19]

Terbium-155. ^{155}Tb ($t_{1/2}$ 128 h) is a low energy γ emitter (E_γ 87 keV, I_γ 32%; E_γ 105 keV, I_γ 25%) for SPECT imaging. ^{155}Tb production occur *via* proton-induced spallation of tantalum targets and isotope mass separation.[6] An alternative route involved the ^{155}Gd(p,n)^{155}Tb or the ^{159}Tb(p,5n)^{155}Dy → ^{155}Tb reactions. Terbium chelation chemistry has already been described for ^{155}Tb (*vide supra*).

1.5 References

1 G. Sgouros, L. Bodei, M. R. McDevitt and J. R. Nedrow, *Nat. Rev. Drug Discov.*, 2020, **19**, 589-608.

2 M. Neves, A. Kling and A. Oliveira, *J. Radioanal. Nucl. Chem.*, 2005, **266**, 377-384.

3 S. Lacerda, M. P. Campello, F. Marques, L. Gano, V. Kubıček, P. Fousková, É. Tóth and I. Santos, *Dalton Trans.*, 2009, 4509-4518.

4 C. Ramogida and C. Orvig, *Chem. Commun.*, 2013, **49**, 4720-4739.

5 S. Liu, *Adv. Drug Deliv. Rev.*, 2008, **60**, 1347-1370.

6 I. Carbo-Bague and C. F. Ramogida, in *Encyclopedia of Inorganic and Bioinorganic Chemistry*, 2021.

7 E. Boros and A. B. Packard, *Chem Rev.*, 2019, **119**, 870-901.

8 L. Li, M. de G. Jaraquemada-Peláez, H.T. Kuo, H. Merkens, N. Choudhary, K. Gitschalter, U. Jermilova, N. Colpo, C. Uribe-Munoz, V. Radchenko, P. Schaffer, K. S. Lin, F. Benard and C. Orvig, *Bioconjugate Chem.*, 2019, **30**, 1539-1553.

9 R. Ševčíková, P. Lubal, M. P. C. Campello and I. Santos, *Polyhedron*, 2013, **62**, 268-273.

10 S. Spreckelmeyer, C. F. Ramogida, J. Rousseau, K. Arane, I. Bratanovic, N. Colpo,

U. Jermilova, G. M. Dia, I. Dud, M. de G. Jaraquemada-Peláez, F. Bénar, P. Schaffer and C. Orvig, *Bioconjugate Chem.*, 2017, **28**, 2145-2159.

11 J. Notni, J. Simecek and H.J. Wester, *ChemMedChem*, 2014, **9**, 1107-1115.

12 E. W. Price and C. Orvig, *Chem. Soc. Rev.*, 2014, **43**, 260-290.

13 S. Litau, U. Seibold, A. Vall-Sagarra, G. Fricker, B. Wängler and C. Wängler, *ChemMedChem*, 2015, **10**, 1200-1208.

14 C. S. Cutler, H. M. Hennkens, N. Sisay, S. Huclier-Markai and S. Jurisson, *Chem Rev.*, 2013, **113**, 858-883.

15 K. Vermeulen, M. Vandamme, G. Bormans and F. Cleeren, *Semin. Nucl. Med.*, 2019, **49**, 339-356.

16 L. M. P. Lima, Z. Halime, R. Marion, N. Camus, R. Delgado, C. Platas-Iglesias and R. Tripier, *Inorg. Chem.*, 2014, **53**, 5269-5279.

17 L. Dai, C. M. Jones, W. T. K. Chan, T. A. Pham, X. Ling, E. M. Gale, N. J. Rotile, W. C. S. Tai, C. J. Anderson, P. Caravan and G. L. Law, *Nat. Commun.*, 2018, **9**, 857.

18 A. Rodríguez-Rodríguez, Z. Halime, L. M. P. Lima, M. Beyler, D. Deniaud, N. Le Poul, R. Delgado, C. Platas-Iglesias, V. Patinec and R. Tripier, *Inorg. Chem.*, 2016, **55**, 619-632.

19 T. I. Kostelnik and C. Orvig, *Chem Rev.*, 2019, **119**, 902-956.

20 B. Olsen, H. Thisgaard, S. Vogel, M. Thomassen, T. A. Kruse, D. Needham and P. Flemming *Eur. J. Nanomedicine*, 2013, **5**, 4.

21 C. Boswell and M. Brechbiel, *Nucl. Med. Biol.*, 2007, **34**, 757-778.

22 W. Volkert, W. Goeckeler, G. Ehrhardt and A. Ketring, *J. Nucl. Med. Med.*, 1991, **32**, 174-185.

23 J. Reisz, N. Bansal, J. Qian, W. Zhao and C. M. Furdui, *Antioxid Redox Signal*, 2014, **21**, 260-292.

24 A. I. Kassis, *Semin. Nucl. Med.*, 2008, **38**, 358-366.

25 M. Bache, M. Kappler, H. M. Said, Staab A. and D. Vordermark *Curr. Med. Chem.*, 2008, **15**, 322-338.

26 W. Tinganelli, N. Y. Ma, C. Von Neubeck, A. Maier, C. Schicker, W. Kraft-Weyrather and M. Durante, *J Radiat Res*, 2013, **54**, Suppl 1: i23-30.

27 H. Yang, J. J. Wilson, C. Orvig, Y. Li, D. S. Wilbur, C. Ramogida, V. Radchenko and P. Schaffer, *J. Nucl. Med.*, 2021, 121, 262687.

28 G. Sgouros, J. C. Roeske, M. R. McDevitt, S. Palm, B. J. Allen, D. R. Fisher, A. B. Brill, H. Song, R. W. Howell and G. Akabani, *J. Nucl. Med.*, 2010, **51**, 311-328.

29 A. Afshar-Oromieh, H. Hetzheim, W. Kübler, C. Kratochwil, F. L. Giesel, T. A. Hope, M. Eder, M. Eisenhut, K. Kopka and U. Haberkorn, *Eur. J. Nucl. Med. Mol. Imaging.*, 2016, **43**, 1611-1620.

30 C. Kratochwil, F. L. Giesel, F. Bruchertseifer, W. Mier, C. Apostolidis, R. Boll, K. Murphy, U. Haberkorn and A. Morgenstern, *Eur J Nucl Med Mol Imaging*, 2014, **41**, 2106-2119.

31 L. Marcu, E. Bezak and B. J. Allen, *Crit. Rev. Oncol. Hematol.*, 2018, **123**, 7-20.

32 S. Poty, L. C. Francesconi, M. R. McDevitt, M. J. Morris, *J Nucl Med*, 2018, **59**, 878-884.

33 G. J. Beyer, M. Miederer, S. Vranjes-Duric, J. J. Comor, G. Kunzi, O. Hartley, R. Senekowitsch-Schmidtke, D. Soloviev and F. Buchegger, *Eur J Nucl Med Mol Imaging*, 2004, **31**, 547-554.

34 M. Miederer, D. Scheinberg and M. McDevitt, *Adv. Drug Deliv. Rev.*, 2008, **60**, 1371-1382.

35 A. Morgenstern, C. Apostolidis, C. Kratochwil, M. Sathekge, L. Krolicki and F. Bruchertseifer, *Curr. Radiopharm.*, 2018, **11**, 200-208.

36 A. K. H. Robertson, B. L. McNeil, H. Yang, D. Gendron, R. Perron, V. Radchenko, S. Zeisler, P. Causey and P. Schaffer, *Inorg. Chem.*, 2020, **59**, 12156-12165.

37 L. L. Chappell, K. A. Deal, E. Dadachova and M. W. Brechbiel, *Bioconjugate Chem*, 2000, **11**, 510-519.

38 H. Yang, C. Zhang, Z. Yuan, C. Rodriguez-Rodriguez, A. Robertson, V. Radchenko, R. Perron, D. Gendron, P. Causey, F. Gao, F. Bénard and P. Schaffer, *Chemistry*, 2020, **26**, 11435-11440.

39 N. A. Thiele and J. J. Wilson, *Cancer Biother Radiopharm*, 2018, **33**, 336-348.

40 L. Li, J. Rousseau, M. de Guadalupe Jaraquemada-Peláez, X. Wang, A. Robertson, V. Radchenko, P. Schaffer, K.S. Lin, F. Bénard and C. Orvig, *Bioconjugate Chem*, 2020, **32**, 1348-1363.

41 F. E. Escorcia, E. Henke, M. R. McDevitt, C. H. Villa, P. Smith-Jones, R. G. Blasberg, R. Benezra and D. A. Scheinberg, *Cancer Res.*, 2010, **70**, 9277-9286.

42 M. Miederer, M. R. McDevitt, P. Borchardt, I. Bergman, K. Kramer, N.K. V Cheung and D. A. Scheinberg, *Clin. Cancer Res.*, 2004, **10**, 6985-6992.

43 R. M. De Kruijff, H. T. Wolterbeek and A. G. Denkova, *Pharmaceuticals*, 2015, **8**, 321-336.

44 A. Morgenstern, C. Apostolidis, C. Kratochwil, M. Sathekge, L. Krolicki and F. Bruchertseifer, *Curr Radiopharm.*, 2018, **11**, 200-208.

45 D. Horváth, F. Travagin, N. Guidolin, F. Buonsanti, G. Tircsó, I. Tóth, F. Bruchertseifer, A. Morgenstern, J. Notni, G. B. Giovenzana and Z. Baranyai, *Inorg. Chem. Front.*, 2021, **8**, 3893-3904.

46 M. Makvandi, E. Dupis, J. W. Engle, F. M. Nortier, M. E. Fassbender, S. Simon, E. R. Birnbaum, R. W. Atcher, K. D. John, O. Rixe and J. P. Norenberg, *Target Oncol.*, 2018, **13**, 189-203.

47 P. J. Blower, *Dalton Trans.*, 2015, **44**, 4819-4844.

48 R. Shannon, *Acta Cryst.*, 1976, **32**, 751-767.

49 J. Šimeček, P. Hermann, C. Seidl, F. Bruchertseifer, A. Morgenstern, H.J. Wester and J. Notni, *EJNMMI Res.*, 2018, **8**, 78.

50 T. L. Rosenblat, M. R. McDevitt, D. A. Mulford, N. Pandit-Taskar, C. R. Divgi, K. S. Panageas, M. L. Heaney, S. Chanel, A. Morgenstern, G. Sgouros, S. M. Larson,

D. A. Scheinberg and J. G. Jurcic, *Clin. Cancer Res.*, 2010, **16**, 5303-5311.

51 C. Raja, P. Graham, S. M. A. Rizvi, E. Song, H. Goldsmith, J. Thompson, A. Bosserhoff, A. Morgenstern, C. Apostolidis, J. Kearsley, R. Reisfeld and B. J. Allen, *Cancer Biol Ther.*, 2007, **6**, 846-852.

52 B. J. Allen, C. Raja, S. Rizvi, Y. Li, W. Tsui, P. Graham, J. F. Thompson, R. A. Reisfeld and J. Kearsley, *Cancer Biol Ther.*, 2005, **4**, 1318-1324.

53 N. Fichou, S. Gouard, C. Maurel, J. Barbet, L. Ferrer, A. Morgenstern, F. Bruchertseifer, A. Faivre-Chauvet, E. Bigot-Corbel, F. Davodeau, J. Gaschet and M. Chérel, *Front. Med.*, 2015, **2**, 76.

54 T. A. R. Stallons, A. Saidi, I. Tworowska, E. S. Delpassand and J. J. Torgue, *Mol Cancer Ther.*, 2019, **18**, 1012-1021.

55 Y. Miao, M. Hylarides, D. R. Fisher, T. Shelton, H. Moore, D. W. Wester, A. R. Fritzberg, C. T. Winkelmann, T. Hoffman and T. P. Quinn, *Clin. Cancer Res.*, 2005, **11**, 5616-5621.

56 C. Zhang, K.S. Lin and F. Bénard, *Mol Imaging*., 2017, **16**, 1536012117737919.

57 S. R. Banerjee, I. Minn, V. Kumar, A. Josefsson, A. Lisok, M. Brummet, J. Chen, A. P. Kiess, K. Baidoo, C. Brayton, R. C. Mease, M. Brechbiel, G. Sgouros, R. F. Hobbs and M. G. Pomper, *J. Nucl. Med.*, 2020, **61**, 80-88.

58 J. C. Dos Santos, M. Schäfer, U. Bauder-Wüst, W. Lehnert, K. Leotta, A. Morgenstern, K. Kopka, U. Haberkorn, W. Mier and C. Kratochwil, *Eur J Nucl Med Mol Imaging*, 2019, **46**, 1081-1091.

59 R. F. Meredith, J. J. Torgue, T. A. Rozgaja, E. P. Banaga, P. W. Bunch, R. D. Alvarez, J. M. Straughn, M. C. Dobelbower and A. M. Lowy, *Am J Clin Oncol.*, 2018, **41**, 716-721.

60 C. Umbricht, U. Köster, P. Bernhardt, N. Gracheva, K. Johnston, R. Schibli, N. P. van der Meulen and C. Müller, *Sci. Rep.*, 2019, **9**, 17800.

61 C. Müller, K. Zhernosekov, U. Koster, K. Johnston, H. Dorrer, A. Hohn, N.T. van der Walt, A. Turler and R. Schibli, *J. Nucl. Med.*, 2012, **53**, 1951-1959.

62 C. Müller, J. Reber, S. Haller, H. Dorrer, U. Köster, K. Johnston, K. Zhernosekov, A. Türler and R. Schibli, *Pharmaceuticals*, 2014, **7**, 353-365.

63 C. Müller, E. Fischer, M. Behe, U. Köster, H. Dorrer, J. Reber, S. Haller, S. Cohrs, A. Blanc, J. Grünberg, M. Bunka, K. Zhernosekov, N. van der Meulen, K. Johnston, A. Türler and R. Schibli, *Nucl. Med. Biol.*, 2014, **41**, 58-65.

64 U. B. Hagemann, C. Ellingsen, J. Schuhmacher, A. Kristian, A. Mobergslien, V. Cruciani, K. Wickstroem, C. A. Schatz, C. Kneip, S. Golfier, R. Smeets, S. Uran, H. Hennekes, J. Karlsson, R. M. Bjerke, O. B. Ryan, D. Mumberg, K. Ziegelbauer and A. S. Cuthbertson, *Clin. Cancer Res.*, 2019, **25**, 4723-4734.

65 S. Hammer, U. B. Hagemann, S. Zitzmann-Kolbe, A. Larsen, C. Ellingsen, S. Geraudie, D. Grant, B. Indrevoll, R. Smeets, O. Von Ahsen, A. Kristian, P. Lejeune, H. Hennekes, J. Karlsson, R. M. Bjerke, O. B. Ryan, A. S. Cuthbertson and D. Mumberg,

Clin. Cancer Res., 2020, **26**, 1985-1996.

66 V. Frantellizzi, L. Cosma, G. Brunotti, A. Pani, A. Spanu, S. Nuvoli, F. De Cristofaro, L. Civitelli and G. De Vincentis, *Cancer Biother. Radiopharm.*, 2020, **35**, 437-445.

67 A. Morgenroth, C. Dinger, B. D. Zlatopolskiy, E. Al-Momani, G. Glatting, F. M. Mottaghy and S. N. Reske, *Nucl Med Biol*, 2011, **38**, 1067-1077.

68 J. Fonslet, B. Q. Lee, T. A. Tran, M. Siragusa, M. Jensen, T. Kibedi, A. E. Stuchbery and G. W. Severin, *Phys. Med. Biol.,* 2017, **63**, 015026.

69 P. Bernhardt, E. Forssell-Aronsson, L. Jacobsson and G. Skarnemark, *Acta Oncol.*, 2001, **40**, 602-608.

70 M. Sadeghi, *J Mod Phys.*, 2010, **1**, 217-225.

71 C. Müller, J. Reber, S. Haller, H. Dorrer, P. Bernhardt, K. Zhernosekov, A. Türler and R. Schibli, *Eur. J. Nucl. Med. Mol. Imaging*, 2014, **41**, 476-485.

72 A. Ku, V. J. Facca, Z. Cai and R. M. Reilly, *EJNMMI Radiopharm. Chem.*, 2019, **4**, 27.

73 H. Thisgaard and M. Jensen, *Med. Phys.*, 2008, **35**, 3839-3846.

74 P. Randhawa, A. P. Olson, S. Chen, K. L. Gower-Fry, C. Hoehr, J. W. Engle, C. F. Ramogida and V. Radchenko, *Curr Radiopharm.*, 2021,**14**, 394-419.

75 J. Strosberg, G. El-Haddad, E. Wolin, A. Hendifar, J. Yao, B. Chasen, E. Mittra, P. L. Kunz, M. H. Kulke, H. Jacene, D. Bushnell, T. M. O'Dorisio, R. P. Baum, H. R. Kulkarni, M. Caplin, R. Lebtahi, T. Hobday, E. Delpassand, E. Van Cutsem, A. Benson, R. Srirajaskanthan, M. Pavel, J. Mora, J. Berlin, E. Grande, N. Reed, E. Seregni, K. Öberg, M. Lopera Sierra, P. Santoro, T. Thevenet, J. L. Erion, P. Ruszniewski, D. Kwekkeboom and E. Krenning, *N. Engl. J. Med.*, 2017, **376**, 125-135.

76 D. A. Pryma, B. B. Chin, R. B. Noto, J. S. Dillon, S. Perkins, L. Solnes, L. Kostakoglu, A. N. Serafini, M. H. Pampaloni, J. Jensen, T. Armor, T. Lin, T. White, N. Stambler, S. Apfel, V. A. DiPippo, S. Mahmood, V. Wong and C. Jimenez, *J. Nucl. Med.*, 2019, **60**, 623-630.

77 S. F. Hosseini, M. Aboudzadeh, M. Sadeghi, A. Ahmadi Teymourlouy and M. Rostampour, *Appl. Radiat. Isot.*, 2017, **127**, 137-141.

78 J. Kozempel, K. Abbas, F. Simonelli, A. Bulgheroni, U. Holzwarth and N. Gibson, *Radiochim. Acta*, 2012, **100**, 419-423.

79 C. S. Cutler, H. M. Hennkens, N. Sisay, S. Huclier-Markai and S. S. Jurisson, *Chem Rev.*, 2013, **113**, 858-883.

80 K. L. Kolsky, V. Joshi, L. F. Mausner and S. C. Srivastava, *Appl. Radiat. Isot.*, 1998, **49**, 1541-1549.

81 S. Huclier-Markai, A. Sabatie, S. Ribet, V. Kubíček, M. Paris, C. Vidaud, P. Hermann and C. S. Cutler, *Radiochim. Acta*, 2011, **99**, 653-662.

82 M. Połosak, A. Piotrowska, S. Krajewski and A. Bilewicz, *J. Radioanal. Nucl. Chem.*, 2013, **295**, 1867-1872.

83 S. Aime, L. Calabi, C. Cavallotti, E. Gianolio, G. B. Giovenzana, P. Losi, A. Maiocchi, G. Palmisano and M. Sisti, *Inorg. Chem.*, 2004, **43**, 7588-7590.

84 S. Lehenberger, C. Barkhausen, S. Cohrs, E. Fischer, J. Grünberg, A. Hohn, U. Köster, R. Schibli, A. Türler and K. Zhernosekov, *Nucl. Med. Biol.*, 2011, **38**, 917-924.

85 H. Uusijärvi, P. Bernhardt, F. Rösch, H. R. Mäcke and E. Forssell-Aronsson, *J. Nucl. Med.*, 2006, **47**, 807-814.

86 I. A. Abbasi, J. H. Zaidi, M. Arif, S. Waheed and M. S. Subhani, *Radiochim. Acta*, 2006, **94**, 381-384.

87 T. J. Wadas, E. H. Wong, G. R. Weisman and C. J. Anderson, *Chem. Rev.*, 2010, **110**, 2858-2902.

88 M. A. Westcott, D. M. Coldwell, D. M. Liu and J. F. Zikria, *Adv. Radiat. Oncol.*, 2016, **1**, 351-364.

89 L. Wei, X. Zhang, F. Gallazzi, Y. Miao, X. Jin, M. W. Brechbiel, H. Xu, T. Clifford, M. J. Welch, J. S. Lewis and T. P. Quinn, *Nucl. Med. Biol.*, 2009, **36**, 345-354.

90 P. McQuade, Y. Miao, Y. Yoo, T. P. Quinn, M. J. Welch and J. S. Lewis, *J. Med. Chem.*, 2005, **48**, 2985-2992.

91 G. B. Biddlecombe, B. E. Rogers, M. De Visser, J. J. Parry, M. De Jong, J. L. Erion and J. S. Lewis, *Bioconjug. Chem.*, 2007, **18**, 724-730.

92 I. Verel, G. Visser and G. van Dongen, *J. Nuc. Med.*, 2005, **46**, 164S-171S.

93 B. M. Zeglisa and J. S. Lewis, *Dalton Trans.*, 2011, **40**, 6168-6195.

94 S. Bhattacharyya and M. Dixita, *Dalton Trans.*, 2011, **40**, 6112-6128.

95 J. P. Holland, M. J. Williamson and J. S. Lewis, *Mol. Imaging*, 2010, **9**, 1-20.

96 S. V. Smith, *J. Inorg. Biochem.*, 2004, **98**, 1874-1901.

97 P. J. Blower, J. S. Lewis and J. Zweit, *Nucl. Med. Biol.*, 1996, **23**, 957-980.

98 M. Fani, J. André and H. Mäcke, *Contrast Media Mol Imaging*, 2008, **3**, 67-77.

99 C. J. Anderson and M. J. Welch, *Chem Rev.*, 1999, **99**, 2219-2234.

100 C. L. Ferreira, E. Lamsa, M. Woods, Y. Duan, P. Fernando, C. Bensimon, M. Kordos, K. Guenther, P. Jurek and G. E. Kiefer, *Bioconjug. Chem.*, 2010, **21**, 531-536.

101 I. Velikyan, H. Mäcke and B. Langstrom, *Bioconjug. Chem.*, 2008, **19**, 569-573.

102 J. Lee, K. Garmestani, C. Wu, M. W. Brechbiel, H. K. Chang, C. W. Choi, O. A. Gansow, J. A. Carrasquillo and C. H. Paik, *Nucl. Med. Biol.*, 1997, **24**, 225-230.

103 M. Eder, B. Wängler, S. Knackmuss, F. LeGall, M. Little, U. Haberkorn, W. Mier and M. Eisenhut, *Eur. J. Nucl. Med. Mol. Imaging*, 2008, **35**, 1878-1886.

104 M. Eder, A. V. Krivoshein, M. Backer, J. M. Backer, U. Haberkorn and M. Eisenhut, *Nucl. Med. Biol.*, 2010, **37**, 405-412.

105 M. Eder, S. Knackmuss, F. Le Gall, U. Reusch, V. Rybin, M. Little, U. Haberkorn, W. Mier and M. Eisenhut, *Eur. J. Nucl. Med. Mol. Imaging*, 2010, **37**, 1397-1407.

106 J. Schuhmacher, G. Klivényi, R. Matys, M. Stadler, T. Regiert, H. Hauser, J. Doll,

W. Maier-Borst and M. Zöller, *Cancer Res.*, 1995, **55**, 115-123.

107 R. J. Motekaitis, A. E. Martell, S. A. Koch, J. W. Hwang, D. A. Quarless and M. J. Welch, *Inorg. Chem.*, 1998, **37**, 5902-5911.

108 J. Notni, K. Pohle, J. A. Peters, H. Görls and C. Platas-Iglesias, *Inorg. Chem.*, 2009, **48**, 3257-3267.

109 J. Calais, W. Fendler, M. Eiber, E. Wolin, R. Slavik, M. Barrio, P. Gupta, A. Quon, C. Schiepers and M. Auerbach, *J. Nucl. Med.*, 2017, **58**, 172-178.

110 S. Zolghadri, M. Naderi, H. Yousefnia, B. Alirezapour and D. Beiki, *Asia Ocean. J. Nucl. Med. Biol.*, 2018, **6**, 41-49.

111 I. Velikyan, A. Sundin, J. Sörensen, M. Lubberink, M. Sandström, U. Garske-Román, H. Lundqvist, D. Granberg and B. Eriksson, *J. Nucl. Med.*, 2014, **55**, 204-210.

112 V. Ambrosini, D. Campana, L. Bodei, C. Nanni, P. Castellucci, V. Allegri, G. C. Montini, P. Tomassetti, G. Paganelli and S. Fanti, *J. Nucl. Med.*, 2010, **51**, 669-673.

113 D. Campana, V. Ambrosini, R. Pezzilli, S. Fanti, A. M. M. Labate, D. Santini, C. Ceccarelli, F. Nori, R. Franchi, R. Corinaldesi and P. Tomassetti, *J. Nucl. Med.*, 2010, **51**, 353-359.

114 E. García-Toraño, V. Peyrés, M. Roteta, A. I. Sánchez-Cabezudo, E. Romero and A. Martínez Ortega, *Appl. Radiat. Isot.*, 2016, **109**, 314-318.

115 T. S. Carzaniga, M. Auger, S. Braccini, M. Bunka, A. Ereditato, K. P. Nesteruk, P. Scampoli, A. Türler and N. van der Meulen, *Appl. Radiat. Isot.*, 2017, **129**, 96-102.

116 D. V. Filosofov, N. S. Loktionova and F. Rösch, *Radiochim. Acta*, 2010, **98**, 149-156.

117 E. Koumarianou, D. Pawlak, A. Korsak and R. Mikolajczak, *Nucl. Med. Rev.*, 2011, **14**, 85-89.

118 N. P. van der Meulen, M. Bunka, K. A. Domnanich, C. Müller, S. Haller, C. Vermeulen, A. Türler and R. Schibli, *Nucl. Med. Biol.*, 2015, **42**, 745-751.

119 S. Eigner, D. R. B. Vera, M. Fellner, N. S. Loktionova, M. Piel, O. Lebeda, F. Rösch, T. L. Roß and K. E. Henke, *Mol. Imaging Biol.*, 2013, **15**, 79-86.

120 C. A. Umbricht, M. Benešová, R. M. Schmid, A. Türler, R. Schibli, N. P. van der Meulen and C. Müller, *EJNMMI Res.*, 2017, **7**, 9.

121 H. Honarvar, C. Müller, S. Cohrs, S. Haller, K. Westerlund, A. E. Karlström, N. P. van der Meulen, R. Schibli and V. Tolmachev, *Nucl. Med. Biol.*, 2017, **45**, 15-21.

122 M. Sadeghi, M. Aboudzadeh, A. Zali and B. Zeinali, *Appl. Radiat. Isot.*, 2009, **67**, 1392-1396.

123 M. Deri, B. Zeglis, L. Francesconi and J. Lewis, *Nucl. Med. Biol.*, 2013, **40**, 3-14.

124 D. S. Abou, T. Ku and P. M. Smith-Jones, *Nucl. Med. Biol.*, 2011, **38**, 675-681.

125 C. Zhai, D. Summer, C. Rangger, G. M. Franssen, P. Laverman, H. Haas, M. Petrik, R. Haubner and C. Decristoforo, *Mol. Pharm.*, 2015, **12**, 2142-2150.

126 D. Summer, J. Garousi, M. Oroujeni, B. Mitran, K. G. Andersson, A. Vorobyeva, J. Löfblom, A. Orlova, V. Tolmachev and C. Decristoforo, *Mol. Pharm.*, 2018, **15**, 175-185.

127 M. Patra, A. Bauman, C. Mari, C. A. Fischer, O. Blacque, D. Häussinger, G. Gasser and T. L. Mindt, *Chem. Commun.*, 2014, **50**, 11523-11525.

128 M. A. Deri, S. Ponnala, P. Kozlowski, B. P. Burton-Pye, H. T. Cicek, C. Hu, J. S. Lewis and L. C. Francesconi, *Bioconjug. Chem.*, 2015, **26**, 2579-2591.

129 M. A. Deri, S. Ponnala, B. M. Zeglis, G. Pohl, J. J. Dannenberg, J. S. Lewis and L. C. Francesconi, *J. Med. Chem.*, 2014, **57**, 4844-4860.

130 C. Buchwalder, C. Rodríguez-Rodríguez, P. Schaffer, S. K. Karagiozov, K. Saatchi and U. O. Häfeli, *Dalton Trans.*, 2017, **46**, 9654-9663.

131 G. F. Steyn, C. Vermeulen, F. Szelecsényi, Z. Kovács, A. Hohn, N. P. van der Meulen, R. Schibli and T. N. van der Walt, *Nucl. Instruments Methods Phys. Res. Sect. B Beam Interact. with Mater. Atoms*, 2014, **319**, 128-140.

132 D. Nayak, S. Lahiri, A. Ramaswami, S. B. Manohar and N. R. Das, *Appl. Radiat. Isot.*, 1999, **51**, 631-636.

133 M. F. Othman, N. R. Mitry, V. J. Lewington, P. J. Blower and S. Y. A. Terry, *Nucl. Med. Biol.*, 2017, **46**, 12-18.

Chapter 2

Polyazamacrocyles Bearing Sulfanyl Arms for the Chelation of Borderline and Soft Radiometals

This chapter contains an adaptation of a published work, and is reproduced in part, with permission from Tosato, M.; Verona, M.; Doro, R.; Dalla Tiezza, M.; Orian, L.; Andrighetto, A.; Pastore, P.; Marzaro, G.; Di Marco, V. Toward Novel Sulfur-Containing Derivatives of Tetraazacyclododecane: Synthesis, Acid-Base Properties, Spectroscopic Characterization, DFT Calculations, and Cadmium(II) Complex Formation in Aqueous Solution, *New J. Chem.*, **2020**, 44, 8337-8350, Copyright 2020 Royal Society of Chemistry, (https://pubs.rsc.org/en/content/articlelanding/2020/nj/d0nj00310g).

This chapter also comprehends part of a submitted manuscript and is reproduced in part with the permission from Tosato, M.; Pelosato, M.; Franchi, S.; Isse, A. A.; May, N. V.; Zanoni, G.; Mancin, F.; Pastore, P.; Badocco, D.; Asti, M.; Di Marco, V., When Ring Makes the Difference: Coordination Properties of Cu^{2+}/Cu^{+} Complexes with Sulfur-Pendant Polyazamacrocycles for Radiopharmaceutical Applications, **2022**.

2.1 Introduction and Aim

Despite in past decades only a restricted number of radionuclides were available, recent advances in medical radioisotope production routes boosted their variety. Different non-standard theranostic radiometal pairs classified as soft or borderline cations, according to Pearson's Hard-Soft Acid-Base (HSAB) theory, have recently attracted a great deal of interest as their incorporation in radiopharmaceuticals has the potential to open new opportunities for both therapy and imaging according to patient needs, as defined by the principle of personalized medicine.

These new theranostic pairs include [$^{103/104/111}$Ag]Ag^{+}, [$^{64/67}$Cu]$Cu^{2+/+}$, [$^{197g/m}$Hg]Hg^{2+}, and [$^{203/212}$Pb]Pb^{2+}. However, to date, no efficient chelators have been hitherto proposed, and no radiopharmaceuticals exist for mercury and silver and the issue of stabilizing copper and lead *in vivo* has not yet been fully addressed: to harness their theranostic power, efficient ligands must be developed.

For this purpose, a new family of macrocyclic chelators that can potentially stabilize both borderline and soft cations was rationally designed and synthesized hereby (**Figure 2.1**). The design tenet has considered that, while the chemical softness of Ag^{+}, Cu^{+} and Hg^{2+} dictates a preference for soft Lewis base donors such as S, Cu^{2+} and Pb^{2+} are borderline cations and can form stable complexes with a variety of ligands bearing N, O, S, or P atoms. To fulfil these requirements, a mix of N, O and S donors were inserted in different macrocyclic structures. The 'first-generation' series of macrocycles are structurally homologous varying in the nature of the pendant arms which modulate their relative basicity and their chemical softness properties and are based on the 1,4,7,10-tetrazacycodedecane (cyclen) backbone (**Figure 2.1**). 1,4,7,10-tetrakis[2-(methylsulfanyl)ethyl]-1,4,7,10-tetraazacyclododecane (DO4S) possesses four S donor atoms in the side chains and was originally designed by Mäcke *et al*. while 1,4,7-tris[2-(methylsulfanyl)ethyl]-1,4,7,10-tetraazacyclododecane (DO3S) has one non-alkylated nitrogen that could be used as reacting site to later covalently attaching a biovector.[1] In 1,4,7-tris[2-(methylsulfanyl)ethyl]-10-acetamido-1,4,7,10-tetraazacyclododecane (DO3SAm), an amide chain was introduced to mimic the electronic and steric effect of the subsequent *N*-alkylation of DO3S when conjugated to a tumour-targeting molecule.[67] DO2A2S possesses two opposite sulfur atoms and two carboxylates, which enhance water solubility and still allow an easy functionalization, thus it represents a hybrid between DO4S and the commonly employed DOTA. (2*S*,5*S*,8*S*,11*S*) - 2,5,8,11 - tetramethyl - 1,4,7,10 - tetrakis [2 - (methylsulfanyl) ethyl] - 1,4,7,10 - tetra - azacyclododecane (DO4S4Me) is a chiral analogue of DO4S and was designed to enforce the preorganization and enhance the rigidity of the donor atoms by introducing chiral methyl

groups on the polyamine backbone. This modification was inspired by a family of chiral DOTA derivatives which have demonstrated higher thermodynamic stability and faster labelling properties with copper-64 and lutetium-177 compared to their DOTA analogues.[2] Finally, 1,4,7,10-tetra-*n*-butyl-1,4,7,10-tetraazacyclododecane (DOT-*n*-Bu) was considered to highlight the effects of sulfanyl pendant arms on the properties of these ligand series.

As subtle changes of the chelator structure, site of conjugation, and donor arms can cause drastic changes in the stability of their radiometal complexes, on their radiolabelling properties and *in vivo* stability, a 'second-generation' series of polyazamacrocycles incorporating sulfanyl pendants was designed to evaluate the impact of a larger macrocyclic backbone and a different array of N/S donor atoms of the corresponding metal complexes (**Figure 2.1**): 1,5,9-tris[2-(methylsulfanyl)ethyl]-1,5,9-triazacyclododecane (TACD3S) possesses the same number of atoms in the ring as DO4S but fewer overall donors (3N3S *vs.* 4N4S), while 1,4,7,10-tetrakis[2-(methylsulfanyl)ethyl]-1,4,7,10-tetrazacyclotridecane (TRI4S) and 1,4,8,11-tetrakis[2-(methylsulfanyl)ethyl]-1,4,8,11-tetrazacyclotetradecane (TE4S) have the same number of nitrogens and sulfanyl pendants as DO4S but a progressively larger ring size.

It is worth to note that, despite different coordinating arms have been appended on polyazamacrocyclic scaffolds (*e.g.*, carboxylic, phosphonic, phosphinic, acetamido, amino, alcoholic, alkylic, arylic), ligand bearing one or more sulfur-containing functional groups have been rarely considered in the literature so far.[3–12] For example, Shinoda *et al.* inserted a sulfonic substituent to enhance water solubility, while Lacerda, Lewin *et al.* studied DOTA derivatives in which an acetate pendant arm was replaced by ethane-thiol.[9,13,14] Lacerda, Ševčíková *et al.* studied the 1-monosubstituted ethanethiol cyclen, and showed that it has rather different acidity constants, thermodynamic and kinetic metal-complexing properties with respect to cyclen.[15,16]

First- and second-generation chelators behave as Brønsted bases in water. As metal-ion complexation and protonation are concurrent processes, the knowledge of the acid-base behaviour of the different ionizable protons must be firstly addressed to evaluate the metal complexation ability of these ligands.

This Chapter describes the synthesis and the acid-base properties of the first- and second-generation chelators. The latter study was performed by potentiometry and UV-Vis spectroscopy as well as *via* Nuclear Magnetic Resonance (1D ^{1}H NMR and 2D ^{1}H-^{1}H COSY, ^{1}H-^{1}H TOCSY, NOESY, ^{1}H-^{13}C HMQC and ^{1}H-^{13}C HSQC). Density functional theory (DFT) calculations were also performed to investigate the conformations and the thermodynamics of protonation equilibria and to interpret the electronic transitions on a molecular orbital basis.

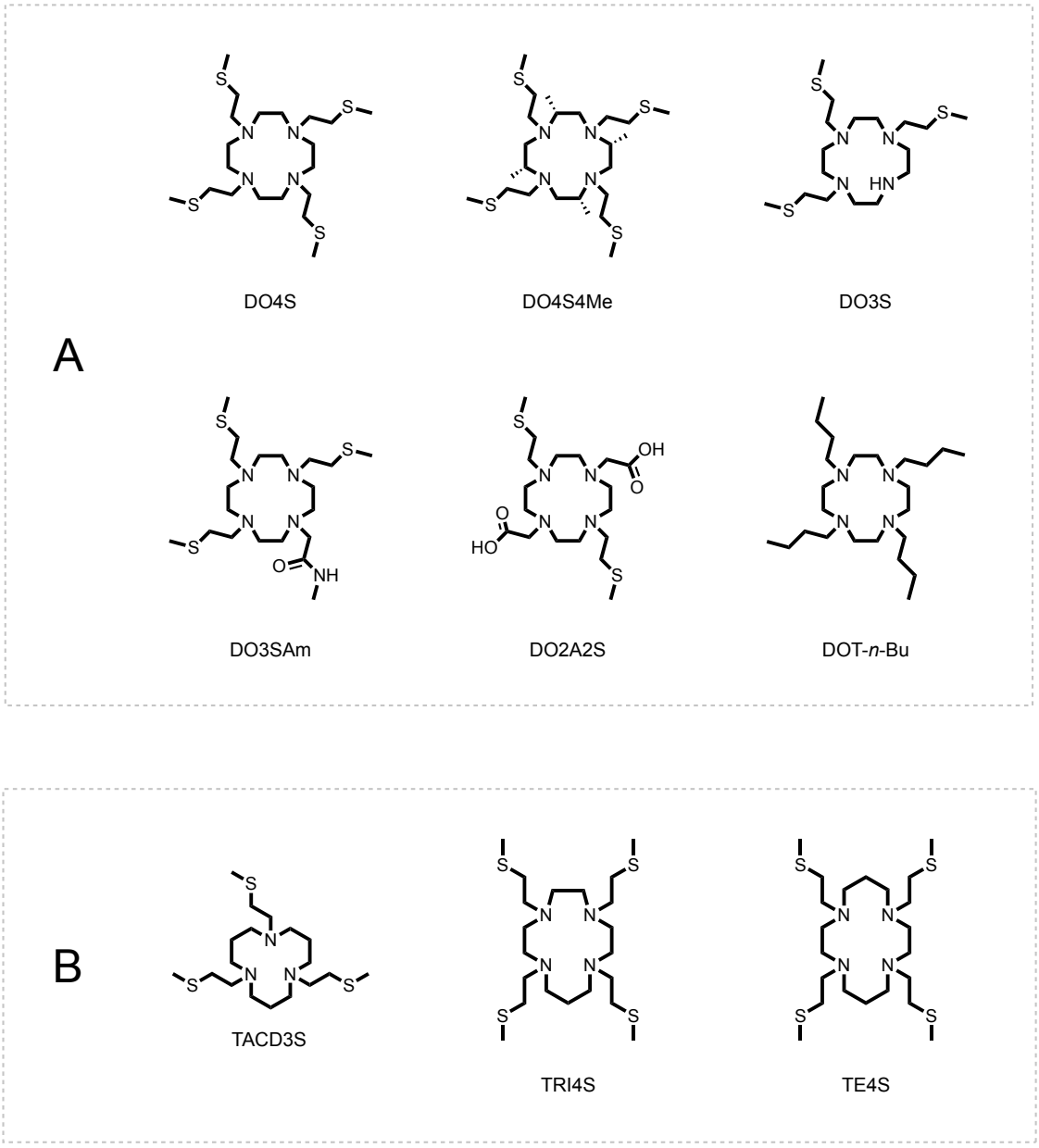

Figure 2.1. Structure of (A) first- (DO4S, DO4S4Me, DO3S, DO3SAm, DO2A2S and DOT-*n*-Bu) and (B) second-generation (TACD3S, TRI4S and TE4S) series of sulfanyl-bearing polyazamacrocycles.

2.2 Results and Discussion

2.2.1 Synthesis of First and Second-Generation Ligands

The homo-substituted cyclen derivatives, *i.e.* DO4S and DOT-*n*-Bu, were obtained by complete alkylation of cyclen with the appropriate halide (2-chloroethyl methyl sulfide and bromobutane, respectively) in the presence of potassium carbonate in acetonitrile at 60°C (**Scheme 2.1**). Using a lower amount of alkylating agent and a lower temperature it was possible to obtain an incomplete substitution, yielding DO3S (**Scheme 2.1**).

DO4S4Me was obtained by complete alkylation of Me4-cyclen with 2-chloroethyl methyl sulfide in presence of potassium carbonate in acetonitrile at 40°C (**Scheme 2.1**). The larger steric bulk of M4-cyclen reduced the rate of alkylation when compared to cyclen. Consequently, to speed up the reaction an *in situ* Finklestein reaction was performed by adding potassium iodide.

DO3SAm (**Scheme 2.2**) was synthesized starting from cyclen that was monosubstituted with ethyl bromoacetate and then exhaustively alkylated with 2-chloroethyl methyl sulfide in the usual conditions. Treatment of compound (**2**) with methylamine directly afforded the desired amide derivative.

DO2A2S (**Scheme 2.3**) was synthesized from the commercially available cyclen derivative, *i.e.* di-tert-butyl 2,2′-(1,4,7,10-tetraazacyclododecane-1,7-diyl) diacetate (**3**), that was alkylated using the same reaction condition above reported. Trifluoroacetic acid (TFA)-mediated deprotection allowed to obtain the final product. TACD3S, TRI4S and TE4S were synthesized similarly to DO4S by direct complete alkylation of the parent macrocycles (1,5,9-triazacyclododecane - TACD, 1,4,7,10-tetrazacyclotridecane - TRI and 1,4,8,11-tetrazacyclotetradecane - cyclam, respectively) with an excess of 2-chloroethly methyl sulfide in acetonitrile at 60°C for 24 hours according to **Scheme 2.4**.

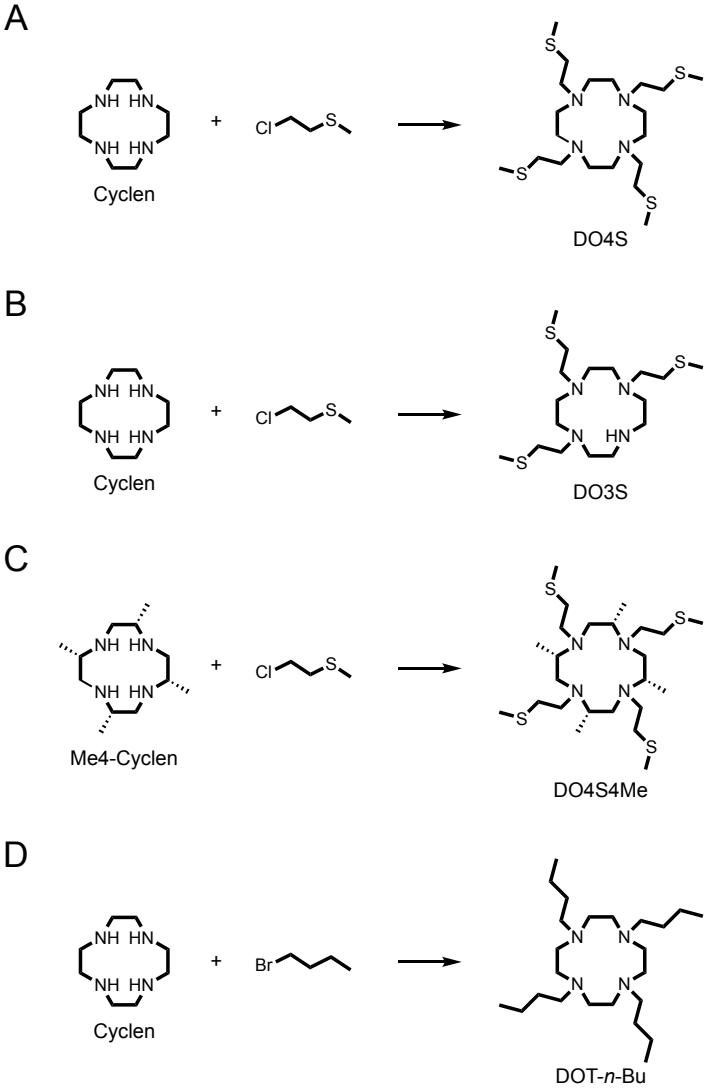

Scheme 2.1. Synthesis of pure sulfur-bearing cyclen derivatives (DO4S, DO3S, DO4S4Me) and DOT-*n*-Bu. Reaction conditions: (A) 2-chloroethyl methyl sulfide, K_2CO_3, CH_3CN, 60°C, 24 h; (B) 2-chloroethyl methyl sulfide, K_2CO_3, CH_3CN, 40°C, 5 days; (C) 2-chloroethyl methyl sulfide, K_2CO_3, KI, CH_3CN, 40°C, 52 h and (D) bromobutane, K_2CO_3, CH_3CN, 60°C, 24 h.

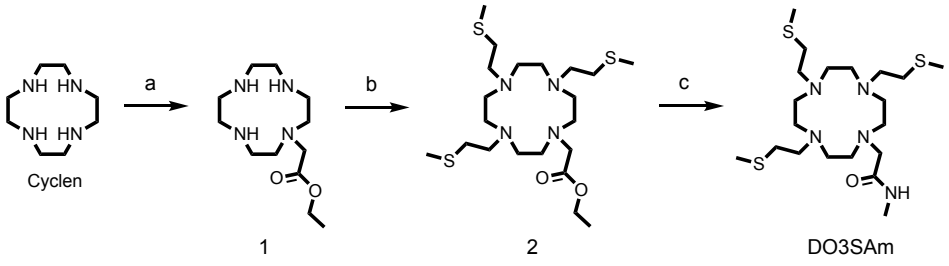

Scheme 2.2. Synthesis of DO3SAm. Reaction conditions: a) ethyl bromoacetate, CH_3CN, 0°C, 2 h and RT, 24 h; b) 2-chloroethyl methyl sulfide, K_2CO_3, CH_3CN, 60°C, 24 h; c) ethanolic methylamine solution 8.03 M, RT, 72 h.

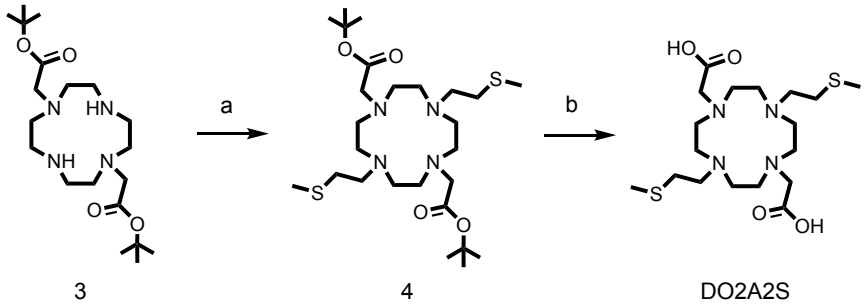

Scheme 2.3. Synthesis of DO2A2S. Reaction conditions: a) 2-chloroethyl methyl sulfide, K_2CO_3, CH_3CN, 60°C, 24 h; b) TFA, CH_2Cl_2, RT, 24 h.

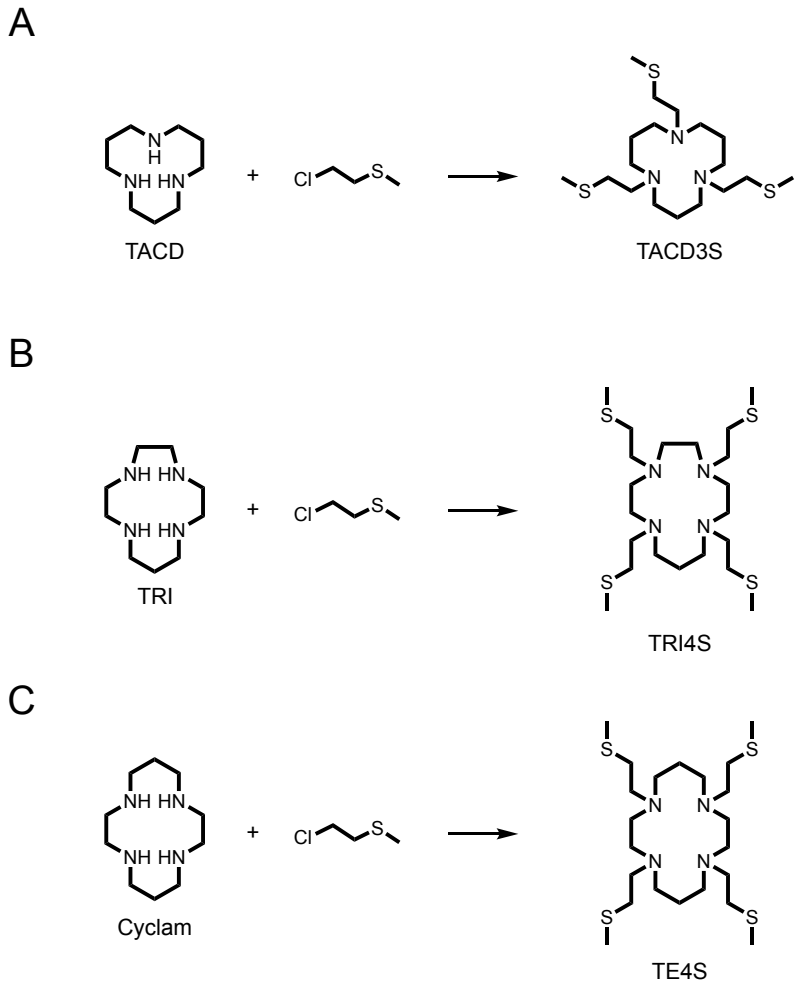

Scheme 2.4. Synthesis of (A) TACD3S, (B) TRI4S and (C) TE4S. Reaction conditions: 2-chloroethyl methyl sulfide, K_2CO_3, CH_3CN, 60°C, 24 h.

2.2.2 Protonation Equilibria of First-Generation Ligands

The protonation constants of cyclen, DO4S, DO4S4Me, DO3S, DO3SAm, DO2A2S and DOT-*n*-Bu were studied in aqueous solution by combined potentiometric titrations and UV-Vis spectroscopy at 25°C and ionic strength (*I*) equal to 0.15 M $NaNO_3$. The obtained values are summarized in **Table 2.1** while the corresponding protonation speciation diagrams are presented in **Figure 2.2**.

Values for cyclen agree very well with those reported in the literature at 25°C and at ionic strengths similar to $NaNO_3$ 0.15 M (pK_{a3} = 9.69 and pK_{a4} = 10.66 in *I* = $NaClO_4$ 0.15 M; pK_{a3} = 9.6 and pK_{a4} = 10.6 in *I* = $NaNO_3$ 0.1 M).[17,18] No pK_a values were obtained so far for any of the other ligands investigated herein, with the partial exception of DO4S, for which pK_{a3} = 6.22 and pK_{a4} = 11.26 in 1:1 water/methanol.[1] Despite DO4S, DO4S4Me, DO3S, DO3SAm and DOT-*n*-Bu possess four ionizable amino groups, only two acidity constants, *i.e.* pK_{a3} and pK_{a4}, were accurately determined by pH-potentiometric measurements (**Table 2.1**).[19] For DO2A2S, which contains six protonable sites (four amines and two carboxylates), the last three pK_a values were obtained (**Table 2.1**).[19] According to the proton content of the examined solutions and the results of potentiometric and spectrophotometric titrations, the lowest determined pK_a was assigned to the deprotonation reaction $H_3L^+ \rightleftharpoons H_2L + H^+$ (pK_{a4}). The last two pK_a values are too similar, and only their sum (pK_{a5} + pK_{a6}) was experimentally determined. The deprotonation sequence is likely similar to those reported for DOTA and DOTA-like ligands: the first proton should be lost from the COOH group while the last two from the ammonium ions in opposite position.[20] The other acidity constants are very low (< 2) because of the electrostatic repulsion between the positive charges resulting from the progressive protonation of the amino groups on the macrocyclic backbone. In fact, for cyclen, Cabani *et al.* found a pK_{a2} of 1.41 (referred to the $H_3L^{3+} \rightleftharpoons H_2L^{2+} + H^+$ equilibrium)[17], whereas Kodama *et al.* estimated pK_{a1} (referred to the $H_4L^{4+} \rightleftharpoons H_3L^{3+} + H^+$ equilibrium) and pK_{a2} to be 0.8 and 1.6, respectively, at 35°C and *I* = 0.2 M $NaClO_4$.[21] For DO2A2S, protonations were unfavored also due to its capability to form intramolecular hydrogen bonds (*vide infra*). Those acidity constants, namely pK_{a2} for DO4S, DO3S, and DO3SAm, and pK_{a3} for DO2A2S, were therefore determined using in-batch UV-Vis spectrophotometric titrations at very acidic conditions (pH < 2), where pH-potentiometry cannot give reliable results. The pK_{a2} for DO4S, DO3S, and DO3SAm certainly belong to the amino groups, whilst the pK_{a3} for DO2A2S likely corresponds to the deprotonation of an acetate arm. The pK_{a3} and pK_{a4} values of several cyclen derivatives are graphically shown in **Figure 2.3**. Whereas the values of pK_{a4} for these ligands are relatively similar, those of pK_{a3} vary by more than two orders of magnitude and correlate with the nature and the number of the substituents on the nitrogen atoms.

Table 2.1. Dissociation constants (pK_a values) of first-generation ligands, DOT-*n*-Bu and cyclen at T = 25°C and I = 0.15 M $NaNO_3$. Unless otherwise stated values were obtained by potentiometry. The reported uncertainty was obtained by the fitting procedure and represents one standard deviation unit.

Ligand	Equilibrium [a]	pK_a			
DO4S	$H_3L^{3+} \rightleftharpoons H_2L^{2+} + H^+$	1.9	±	0.3	[b]
	$H_2L^{2+} \rightleftharpoons HL^+ + H^+$	7.29 6.8	± ±	0.03 0.2	[c]
	$HL^+ \rightleftharpoons L + H^+$	10.14 10.1	± ±	0.05 0.2	[c]
DO4S4Me	$H_2L^{2+} \rightleftharpoons HL^+ + H^+$	7.9 7.3	± ±	0.2 0.5	[c]
	$HL^+ \rightleftharpoons L + H^+$	10.46 10.8	± ±	0.07 0.9	[c]
DO3S	$H_3L^{3+} \rightleftharpoons H_2L^{2+} + H^+$	2.0	±	0.1	[b]
	$H_2L^{2+} \rightleftharpoons HL^+ + H^+$	7.54 7.2	± ±	0.01 0.1	[c]
	$HL^+ \rightleftharpoons L + H^+$	10.86 11.3	± ±	0.09 0.4	[c]
DO3SAm	$H_3L^{3+} \rightleftharpoons H_2L^{2+} + H^+$	1.9	±	0.2	[b]
	$H_2L^{2+} \rightleftharpoons HL^+ + H^+$	7.8	±	0.1	
	$HL^+ \rightleftharpoons L + H^+$	10.42	±	0.07	
DO2A2S	$H_4L^{2+} \rightleftharpoons H_3L^+ + H^+$	1.79	±	0.08	[b]
	$H_3L^+ \rightleftharpoons H_2L + H^+$	3.44 3.1	± ±	0.06 0.2	[c]
	$H_2L \rightleftharpoons HL^- + H^+$	18.30	±	0.02	
	$HL^- \rightleftharpoons L^{2-} + H^+$	18.6	±	0.3	[c]
DOT-*n*-Bu	$H_2L^{2+} \rightleftharpoons HL^+ + H^+$	8.62	±	0.04	
	$HL^+ \rightleftharpoons L + H^+$	9.94	±	0.04	
Cyclen	$H_4L^{4+} \rightleftharpoons H_3L^{3+} + H^+$		0.8		[d]
	$H_3L^{3+} \rightleftharpoons H_2L^{2+} + H^+$		1.6		[d]
	$H_2L^{2+} \rightleftharpoons HL^+ + H^+$	9.51	±	0.01	
	$HL^+ \rightleftharpoons L + H^+$	10.63	±	0.02	

[a] L denotes the ligand in its deprotonated form.
[b] No ionic strength control.
[c] Obtained by UV-Vis spectroscopy.
[e] From ref. [22], I = 0.5 mol/L KNO_3, T = 25°C.

The pK_{a3} order cyclen > tetramethylcyclen > DOT-*n*-Bu can be explained by the increase of the steric hindrance of the sidearms, which destabilize the alkyl-ammonium ion by decreasing its water solvation. If the alkyl groups are replaced by sulfanyl arms, the pK_{a3} values are unexpectedly further reduced by around one log unit, and a pK_{a3} order DO3SAm > DO3S > DO4S can be observed. This 'pK_{a3} effect' was attributed to the presence of the sulfur atoms on the side chains: these atoms, due to their polarizability and dimension, may hinder the motion of the chains around the ring, causing an increased distortion of the latter. As a result, the two charged nitrogens in the H_2L^{2+} species can undergo increased electrostatic repulsion compared to the same species of non-sulfanyl ligands.

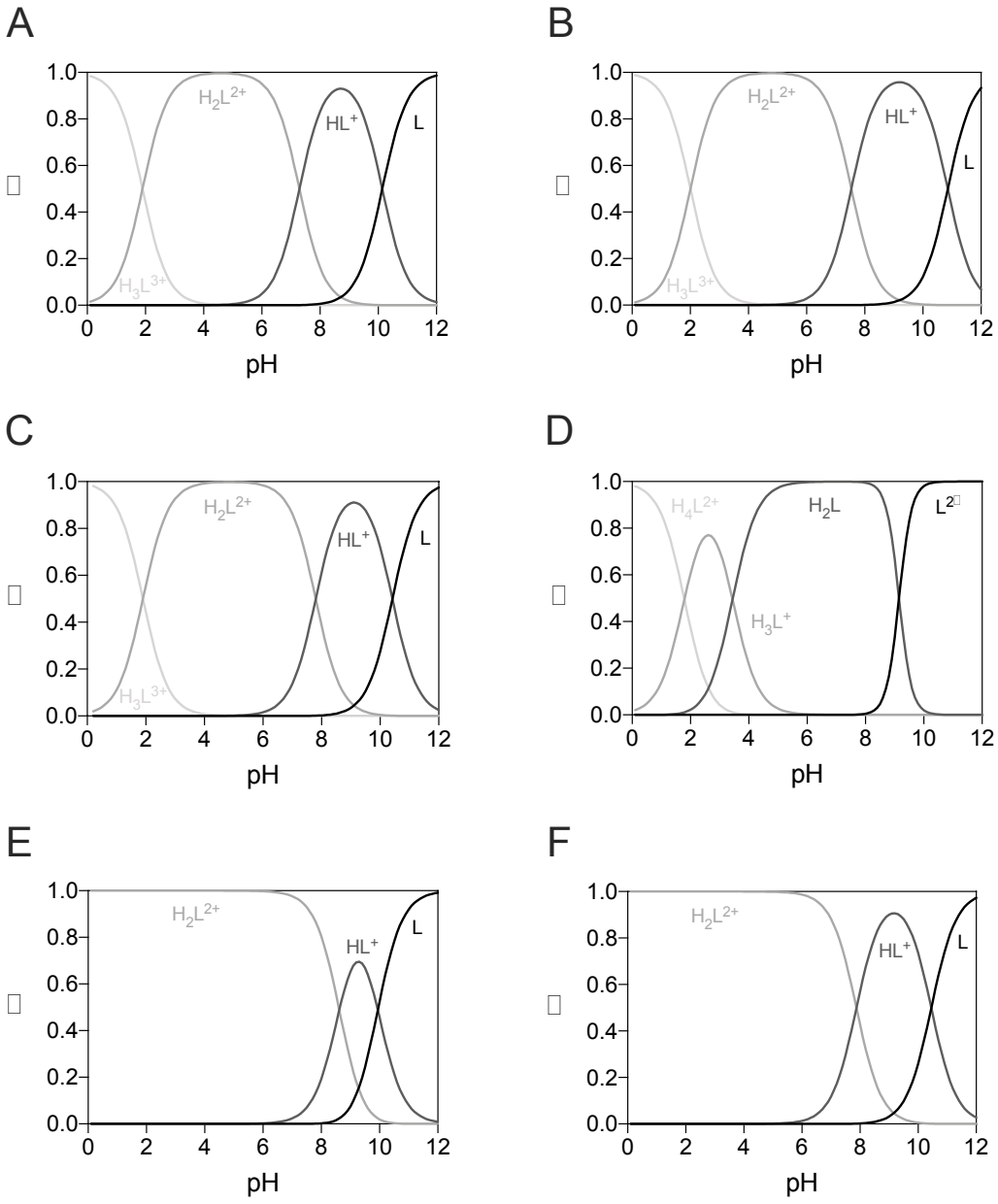

Figure 2.2. Speciation diagram of (A) DO4S, (B) DO3S, (C) DO3SAm, (D) DO2A2S, (E) DOT-*n*-Bu and (F) DO4S4Me.

For the monoprotonated species HL^+, no electrostatic repulsions are expected for both distorted and non-distorted rings. As a consequence, pK_{a3} should change whereas pK_{a4} should not, as it was experimentally observed. The presence of several conformers for sulfanyl derivatives and/or their inertia was also observed by NMR (*vide infra*).

The deprotonation paths and the conformations were investigated by DFT calculations choosing DO4S and DO3S as 'model' ligands.

A conformational analysis was at first performed for deprotonated cyclen. Nine structures (**Table A1** - **Appendix A**) were selected and analysed at the ZORA-OPBE/TZ2P//ZORA-OPBE/DZP level. The most stable structure has all four nitrogen atoms above the molecular plane and the hydrogens point alternately inside and outside the cyclic moiety. There are several possibilities for the monoprotonation of this neutral form (**Table A2** - **Appendix A**), but the extra stabilization by solvation is most efficient when three hydrogen atoms point outside the ring. On the other hand, in the most stable structure of diprotonated cyclen (with charges on opposite sides), the hydrogens point alternately inside and outside the ring. These calculations indicate that, upon protonation/deprotonation, cyclen changes its conformation. The values computed for pK_{a3} and pK_{a4} are given in **Table A3** (**Appendix A**) and they are in good agreement with the experimental findings.

Calculations for DO3S were performed by considering fully extended alkyl chains since this conformation allows a systematic comparison among the different isomers. For the neutral ligand, the most stable structure has the hydrogen atom pointing inside the ring (**Table 2.2**). For the monoprotonated form, an inner H bond forms in the minimum. Lastly, in the diprotonated structures, the acid hydrogen atoms favour the two tertiary nitrogens because of the inductive effects. Three preferential deprotonation mechanisms were considered (**Table A4** - **Appendix A**). In path A, the most kinetically favourable deprotonated species (starting from the double charged species) is formed when the outer hydrogen leaves. The neutral structure is achieved by the deprotonation of the last acid proton.

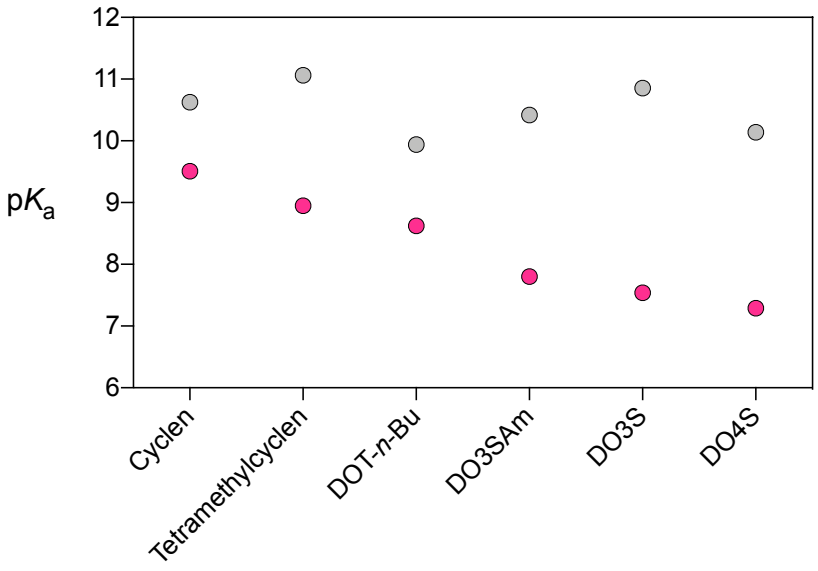

Figure 2.3. Values of pK_{a3} (pink) and pK_{a4} (grey) at T = 25°C and I = 0.15 M $NaNO_3$ for cyclen and its alkyl, amido and sulfanyl derivatives. Values for cyclen and tetramethylcyclen were obtained by Hancock *et al*. at T = 25°C and I = 0.1 M $NaNO_3$.[18,23]

Computed pK_{a3} and pK_{a4} values are, in the best case, two log units distant from the experimental values (7.54 and 10.86, respectively) but the trend and the ΔpK_a are nicely reproduced by both methods. Similarly, path C considers a different starting diprotonated species (two tertiary nitrogens are charged), and the subsequent deprotonation leads to an H-bond formation. Paths B and C imply the formation of the H-bonded monoprotonated structure: the enhanced stability favours the formation of the conjugated bases for the first acidity constant but disfavours the subsequent deprotonation. The main consequence is the underrate of pK_{a3} and an important overrate of pK_{a4}. It is likely that mixed paths occur in aqueous solutions and, as for cyclen, conformation changes may occur upon deprotonation for DO3S. As regards DO4S, the complete alkylation of the four nitrogens with the alkyl chains significantly reduces the number of possible structures (**Table 2.3**) but, on the other hand, increases the degrees of freedom due to the pendants. This might be the cause of the decreased accuracy of the calculated pK_a values when going from cyclen to DO4S (**Table A5** - **Appendix A**). The pK_{a3} shows a significant discrepancy when compared to experimental findings; however, the pK_{a4} accuracy is comparable to the previous cases. Like for DO3S, the pK_a trends are conserved.

2.2.3 Solution Structure of First-Generation Ligands: NMR Investigation

The ^{1}H-NMR spectra of the first-generation ligands were obtained in aqueous solution at various pH/pD. In all cases, the spectral interpretation considered the acid-base properties reported in **Table 2.1**, which allowed to define the differently protonated forms predominating at each pH/pD. The pK_a increase (up to ~ 0.6 log units) predicted by the relation of Rule and La Mer, when D_2O replaces H_2O as solvent, was also taken into account.[24] The ^{1}H-NMR spectra of DO4S over the pH range of 2-12 are shown in **Figure 2.4**, and spectral data are summarized in **Table A6** (**Appendix A**). The spectra obtained at pD ≤ 4.5 are identical, in agreement with the pK_a values given in **Table 2.1**, as only the diprotonated form (H_2L^{2+}) exists in these acidic conditions. Besides the terminal methyl groups (SCH_3), which appear as a sharp singlet at 2.20 ppm, all other protons give broad multiplets at 2.94 ppm and 3.28 ppm which were assigned to SCH_2 and NCH_2 respectively, based on the integration values and the bidimensional ^{1}H-^{1}H COSY, ^{1}H-^{13}C HMQC and NOESY spectra (**Figure 2.5**). The latter show that all functional groups are spatially close to each other and that many protons are exchanging. The spectrum at pD 9.8 is very different than those at acidic pD, suggesting that the expected deprotonation $H_2L^{2+} \rightleftharpoons HL^+ + H^+$ causes significant conformational changes. Furthermore, signals of HL^+ are much sharper than those of H_2L^{2+}: likely, fewer conformers exist for HL^+ than for H_2L^{2+}, and/or they are exchanging faster on the NMR timescale.

Table 2.2. Electronic and Gibbs free energies (in gas-phase and in water) for the neutral, monoprotonated and diprotonated forms of DO3S. All the energies are in kcal/mol and are relative to the most stable structure (in bold); level of theory: (COSMO)-ZORA-OPBE/TZ2P//ZORA-OPBE/DZP.

	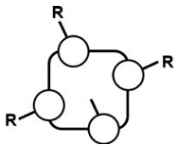	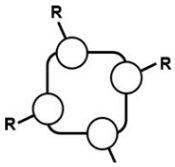	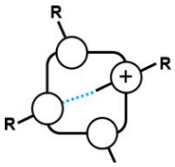
ΔE	**0.0**	6.1	4.2
ΔE_{H2O}	**0.0**	8.0	2.4
ΔG	**0.0**	7.0	4.9
ΔG_{H2O}	**0.0**	8.9	3.1
Point Group	$\mathbf{C_1}$	C_1	C_1
	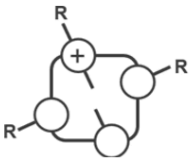	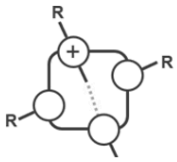	
ΔE	5.7	**0.0**	6.7
ΔE_{H2O}	2.1	**0.0**	1.0
ΔG	5.4	**0.0**	7.4
ΔG_{H2O}	1.8	**0.0**	1.8
Point Group	C_1	$\mathbf{C_1}$	C_1
	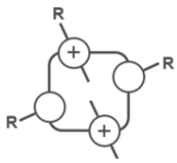	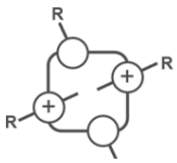	
ΔE	5.0	**0.0**	
ΔE_{H2O}	0.0	**0.0**	
ΔG	2.7	**0.0**	
ΔG_{H2O}	–2.3	**0.0**	
Point Group	C_1	$\mathbf{C_1}$	

Table 2.3. Electronic and Gibbs free energies (in gas-phase and in water) for the neutral, monoprotonated and diprotonated forms of DO4S. All energies are in kcal/mol and are relative to the most stable structure (in bold); level of theory: (COSMO)-ZORA-OPBE/TZ2P//ZORA-OPBE/DZP.

	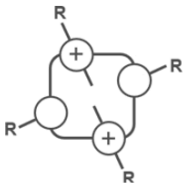	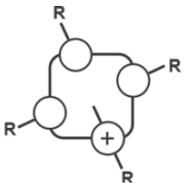	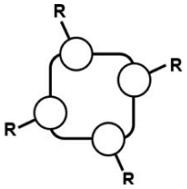
ΔE	134.6	29.1	**0.0**
ΔE_{H2O}	–0.1	–6.4	**0.0**
ΔG	154.7	39.2	**0.0**
ΔG_{H2O}	20.1	3.7	**0.0**
Point Group	C_2	C_1	$\mathbf{C_4}$

The faster exchange of HL^+ conformers might be related to the 'pK_{a3} effect' (*vide supra*), because the release of one proton from H_2L^{2+}, by eliminating the electrostatic repulsions, can reduce the kinetic barriers of the conformational changes.

The ^{1}H-^{1}H COSY, ^{1}H-^{13}C HMQC, and NOESY spectra at pD 9.8 (**Figure 2.5**) allowed to assign all the protons (**Table A6** - **Appendix A**). Both patterns of H_2L^{2+} and HL^+ are observed at pD 7.7 (**Figure 2.4**), where the deprotonation $H_2L^{2+} \rightleftharpoons HL^+ + H^+$ occurs. This result, together with the signal enlargement, indicates that this deprotonation is a surprisingly slow process on the NMR timescale. Slowness can be due to the inertia of the conformers and to the possibly required conformation changes occurring upon deprotonation, as suggested by the DFT calculations (*vide supra*). At the largest examined pD (10.8), small downfield shifts of the signals, especially for the NCH_2 protons of the sidearms, are observed with respect to pD 9.8, giving some evidence of the occurrence of the deprotonation $HL^+ \rightleftharpoons L + H^+$. This process should be fast according to the sharpness of the signals and the absence of multiple patterns. As well, the modest shifts of the NMR signals suggest that the conformers and the exchanging rates of L are similar to those of HL^+.

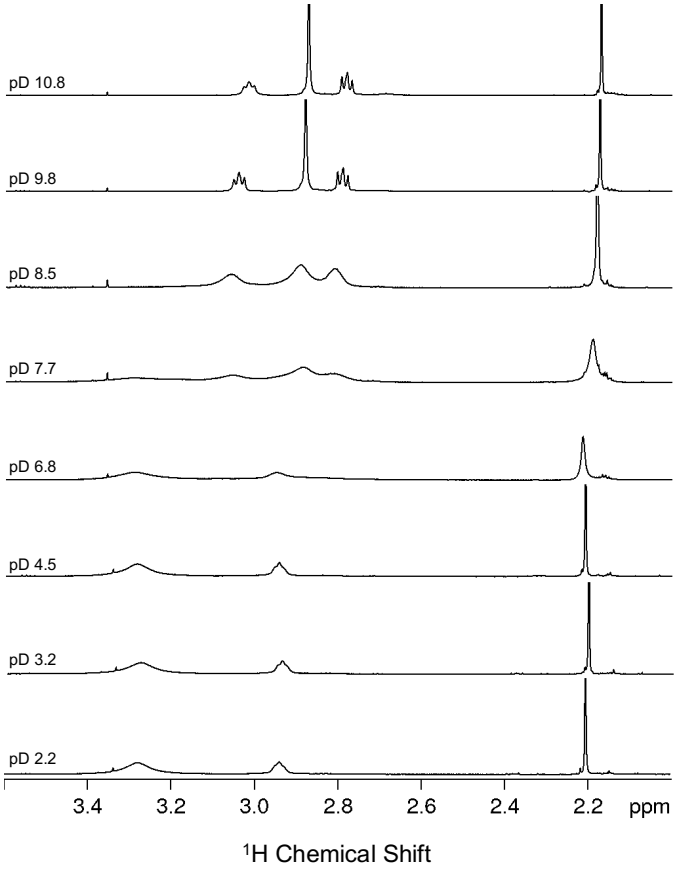

Figure 2.4. Variable-pD ^{1}H-NMR spectra of DO4S (600 MHz, D_2O, T = 25°C, C_{DO4S} = 1·10^{-3} M).

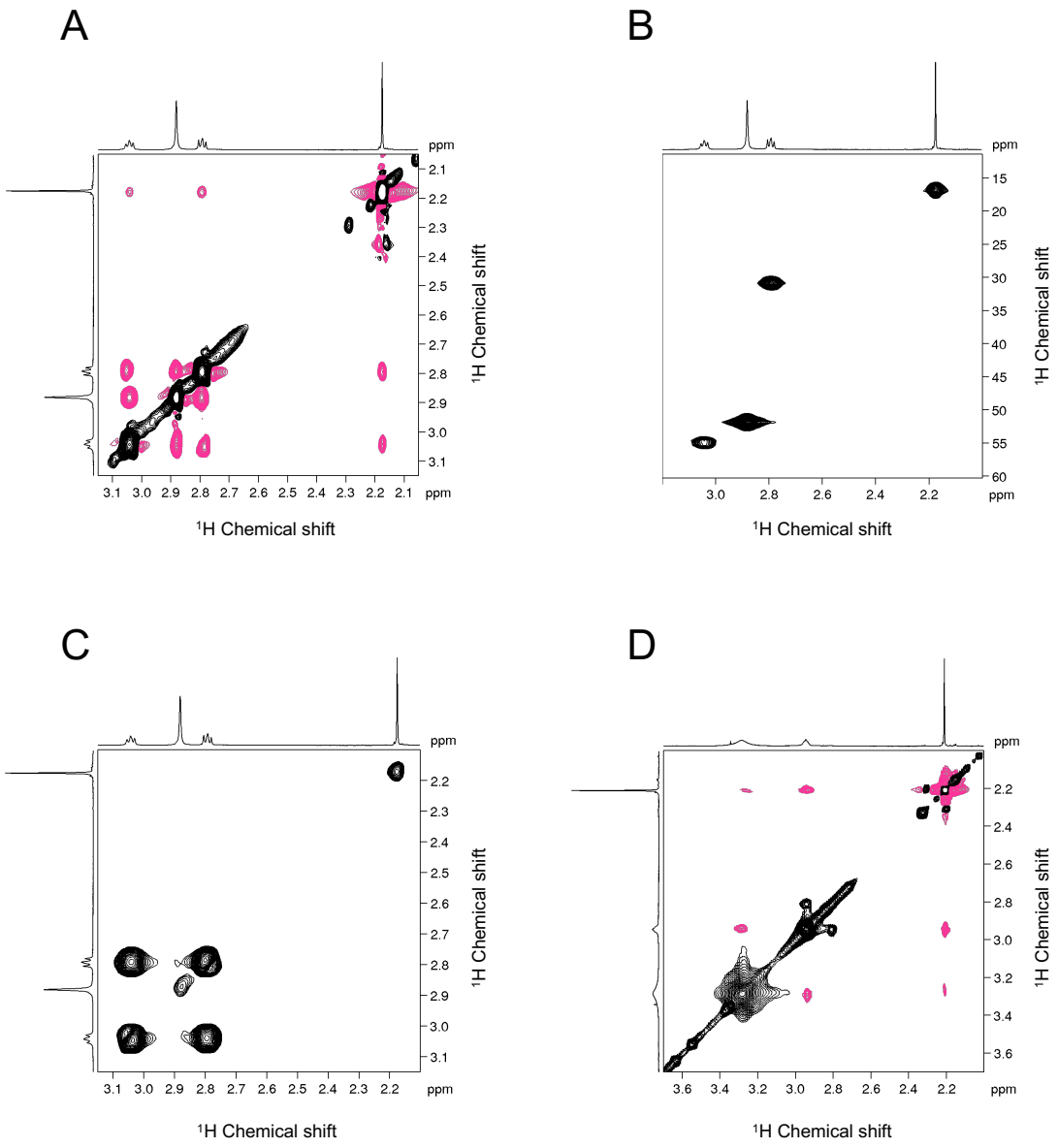

Figure 2.5. (A) NOESY, (B) ^{1}H-^{13}C HMQC and (C) ^{1}H-^{1}H COSY spectrum of monoprotonated DO4S and (D) NOESY spectra of diprotonated DO4S.

The ^{1}H-NMR spectra of DO3S at various pD are shown in **Figure 2.6** and spectral data are summarized in **Table A7** (**Appendix A**). At all pD values, the NMR patterns are much more complicated than for DO4S, as the molecule bearing three sulfanyl arms is not as symmetric as that bearing four. Among the three arms, only two (N_1 and N_7) are chemically equivalent, whereas the third (N_4) is different and this justifies the presence of two different sharp singlets for SCH_3 at 2.20 ppm, having an intensity ratio 2:1, and of many broad multiplets for the other protons (SCH_2, NCH_2 arm and NCH_2 ring) at all the investigated pD. Signals were

assigned based on the integration values and the bidimensional ^{1}H-^{1}H COSY, ^{1}H-^{13}C HMQC and NOESY spectra (**Figure 2.7**). The NOESY spectra both in acidic and alkaline solution show correlation peaks for SCH_3, thus indicating that also for DO3S the mean molecular conformation should have the sulfanyl arms sufficiently close to the ring.

Several pD-dependent features of DO4S NMR signals can be found for DO3S, too: signals become sharper at basic pD, substantial changes in the spectra are observed at pD values where the deprotonation $H_2L^{2+} \rightleftharpoons HL^{+} + H^{+}$ occur (between 7.4 and 9.6), and less marked changes are visible at pD 10.8 where the deprotonation $HL^{+} \rightleftharpoons L + H^{+}$ takes place.

The ^{1}H-NMR spectra of DO3SAm are shown in **Figure 2.6** and spectral data are summarized in **Table A8** (**Appendix A**). This ligand is identical to DO3S with the exception that the secondary amine of DO3S is alkylated with an amide pendant. Despite the subtle structural changes from DO3S to DO3SAm, the spectra are different. For example, peak shapes and chemical shifts change considerably for DO3SAm when the pD is varied in the range where the deprotonation $HL^{+} \rightleftharpoons L + H^{+}$ occurs (from pD 9.3 to 11.8), whereas for DO3S these differences are much less evident. This suggests that the amide side chain has a marked effect on the average conformation of DO3SAm with respect to DO3S.

The ^{1}H-NMR spectra of DOT-*n*-Bu are shown in **Figure 2.8** and spectral data are summarized in **Table A9** (**Appendix A**). It is interesting to compare these spectra with those of DO4S (**Figure 2.4**) which differs from DOT-*n*-Bu only by the presence of sulfur on the sidearms. The *n*-butyl proton' signals in DOT-*n*-Bu, except those directly linked with N, are almost insensible to the pD variations, whereas those of sulfanyl arms in DO4S experience a significant downfield shift while increasing the pD. It is worth noting that also the signals of amidic NCH_3 for DO3SAm are unaffected by the change of the solution proton content (**Figure 2.6**). The peak broadness and the spectral fine structure do not change for DOT-*n*-Bu when the deprotonation $H_2L^{2+} \rightleftharpoons HL^{+} + H^{+}$ takes place, whereas, as previously reported, for DO4S this reaction is slow on the NMR timescale, and ^{1}H-NMR spectra change markedly. Furthermore, protons of the *n*-butyl sidearms in DOT-*n*-Bu give narrow peaks at all pD values, whereas those of sulfanyl arms in DO4S give broad signals at all pD except in alkaline solutions. This suggests that DOT-*n*-Bu conformers can undergo fast fluxional changes both in the diprotonated and monoprotonated species, whereas for DO4S the diprotonated form is more rigid.

This difference can again be related to the 'pK_{a3} effect': in general, the NMR results indicate that sulfur atoms have a strong influence on the average conformation and/or on the kinetics of conformers interconversion of DO4S, DO3S and DO3SAm.

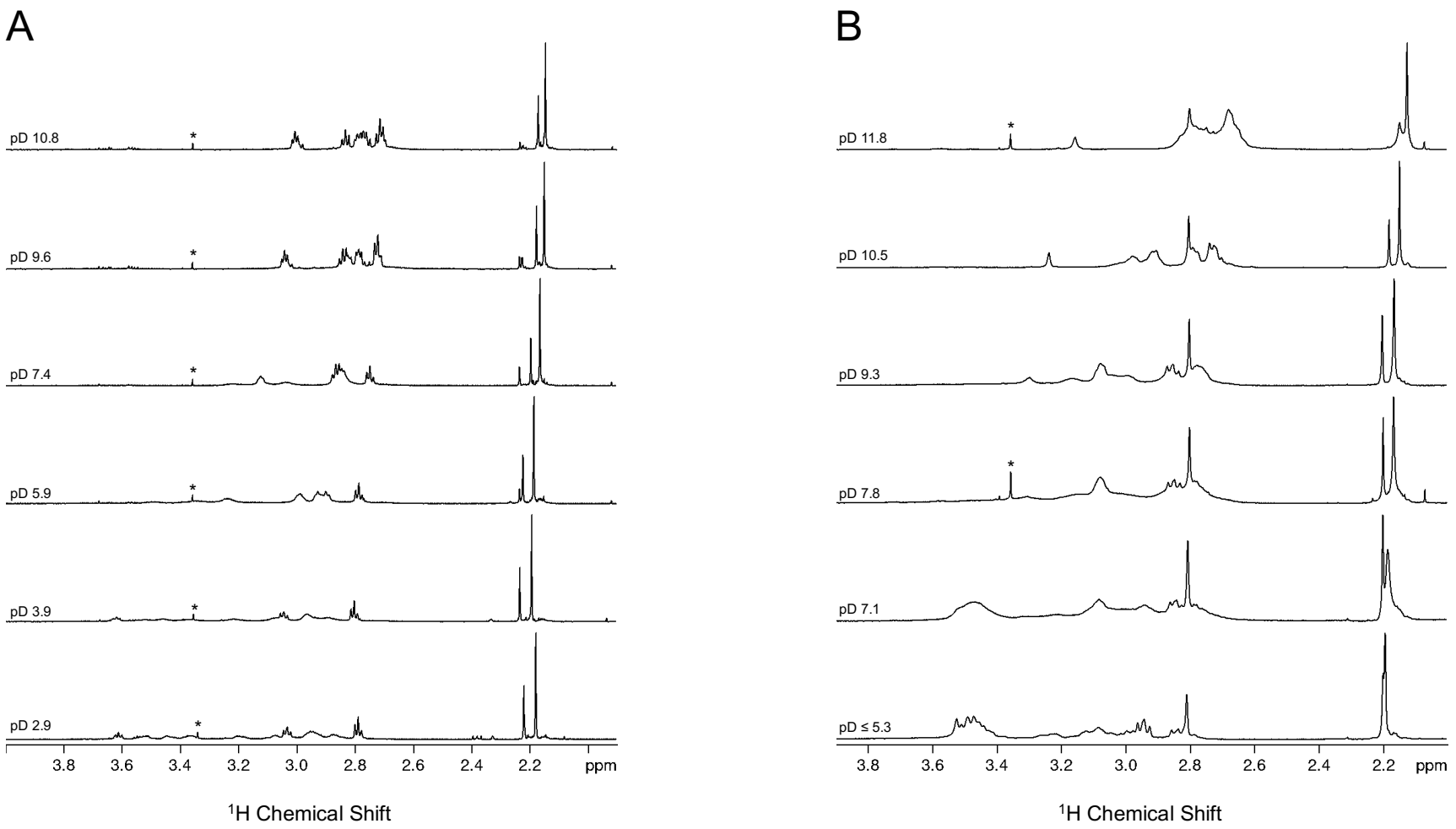

Figure 2.6. Variable-pD ^{1}H-NMR spectra of (A) DO3S (600 MHz, D_2O, T = 25°C, C_{DO3S} = $6.0 \cdot 10^{-4}$ M) and (B) DO3SAm (400 MHz, D_2O, T = 25°C, C_{DO3SAm} = $1.0 \cdot 10^{-3}$ M). For (A) the signals at 2.30-2.40 ppm are produced by the internal reference and those at 3.60-3.70 ppm (pD ≥ 7.4) are due to impurities. Peaks marked with an asterisk are residual methanol.

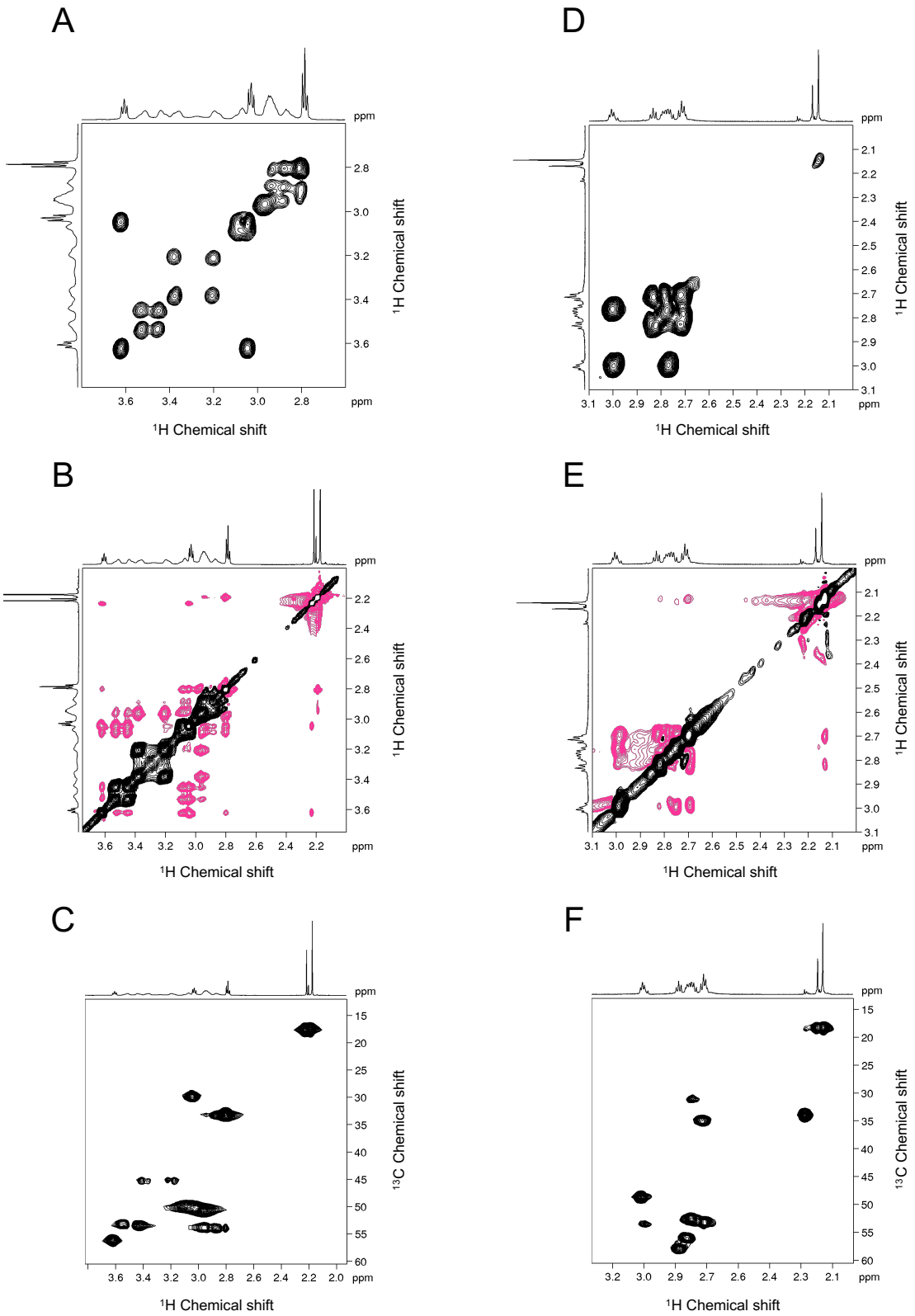

Figure 2.7. (A) ^{1}H-^{1}H COSY, (B) NOESY and (C) ^{1}H-^{13}C HMQC spectrum of diprotonated DO3S; (D) ^{1}H-^{1}H COSY, (E) NOESY and (F) ^{1}H-^{13}C HMQC of monoprotonated DO3S.

The ^{1}H-NMR spectra of DO2A2S at various pD are shown in **Figure 2.9**, while signal assignations are resumed in **Table A10** (**Appendix A**). At acidic pD (2.5), where the triprotonated form (H_3L^+) predominates, all signals can be assigned on the basis of the ^{1}H-^{1}H COSY and ^{1}H-^{13}C HMQC spectra shown in **Figure 2.10**. By increasing the pD to 3.2 and then to higher values, where H_2L starts to form, the NMR spectra of DO2A2S change significantly: not only all peaks become broader, indicating the presence of more conformers and/or of slower rates for their interconversion, but also several peak shifts occur. The SCH_2 protons and the vicinal NCH_2 ones experience a rather large upfield shift, whereas the NCH_2 protons of the acetate arms (and to a minor extent also some ring protons) are unexpectedly downfield shifted. A poorly visible, indeed still downfield shift was reported also for some DOTA protons by Desreux *et al.*,[25] but the authors did not comment on this result, which could be due to the formation of intramolecular hydrogen bonds between the deprotonated acetate arms and the protonated nitrogen atoms of the ring. Other considerable changes occur in DO2A2S spectra at pD larger than 9.1, where HL^- and L^{2-} form. At pD 10.4 even the SCH_3 signals become very broad so that the deprotonation appears to be a slow process on the NMR timescale or, alternatively, the conformational changes produced by deprotonation are slow.

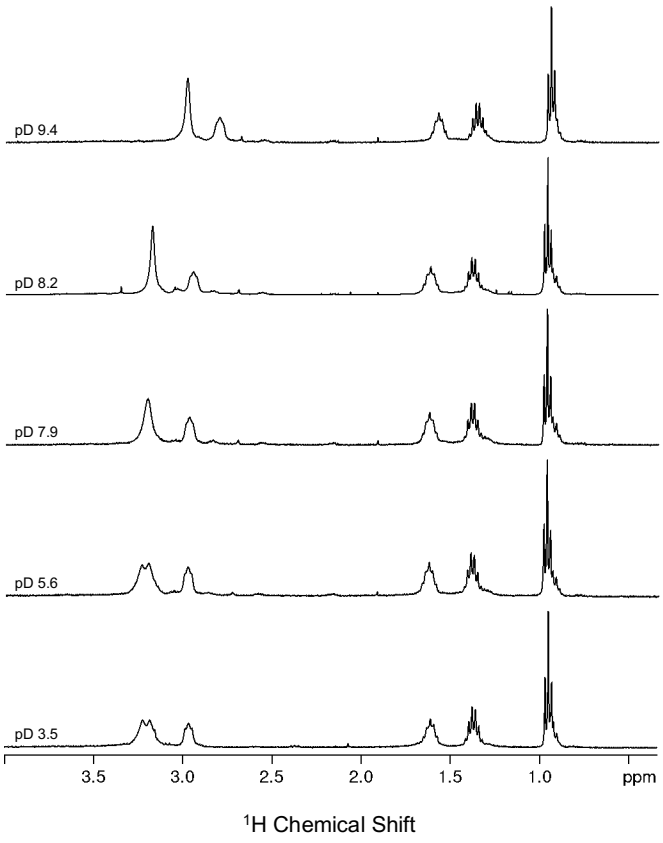

Figure 2.8. Variable-pD ^{1}H-NMR spectra of DOT-*n*-Bu (400 MHz, D_2O, T = 25°C, $C_{DOT\text{-}n\text{-}Bu}$ = 8.0·10^{-4} M).

The ^{1}H-NMR spectra of DO4S4Me over the pH range of 2-11 are shown in **Figure A1** (**Appendix A**), and spectral data are summarized in **Table A11** (**Appendix A**). The signal attribution was based on the integration values and the bidimensional ^{1}H-^{1}H COSY spectra (**Figure 2.11**). The spectra obtained at pH < 7.55 are identical as only the diprotonated form (H_2L^{2+}) exists in these conditions. Besides the chiral methyl groups (CH_3) on the cyclen ring and the terminal methyl groups (SCH_3) on the sidearms, which appear as a sharp doublet at 1.20 ppm and a singlet at 2.20 ppm, all other protons give broader multiplets (**Table A11** - **Appendix A**). The NOESY spectra of H_2L^{2+} show that all functional groups are spatially close to each other and that many protons are exchanging, similarly to its achiral analogue DO4S. Differently from DO4S, the spectra in alkaline environments are similar to those in acidic conditions thus suggesting that the deprotonation $H_2L^{2+} \rightleftharpoons HL^{+} + H^{+}$ do not cause noteworthy conformational rearrangements. However, in a similar manner of DO4S, the enlargements of the peaks at pH 7.55 and 8.88, where the deprotonation $H_2L^{2+} \rightleftharpoons HL^{+} + H^{+}$ occurs, indicates that the latter is a slow process with respect to the NMR timescale.

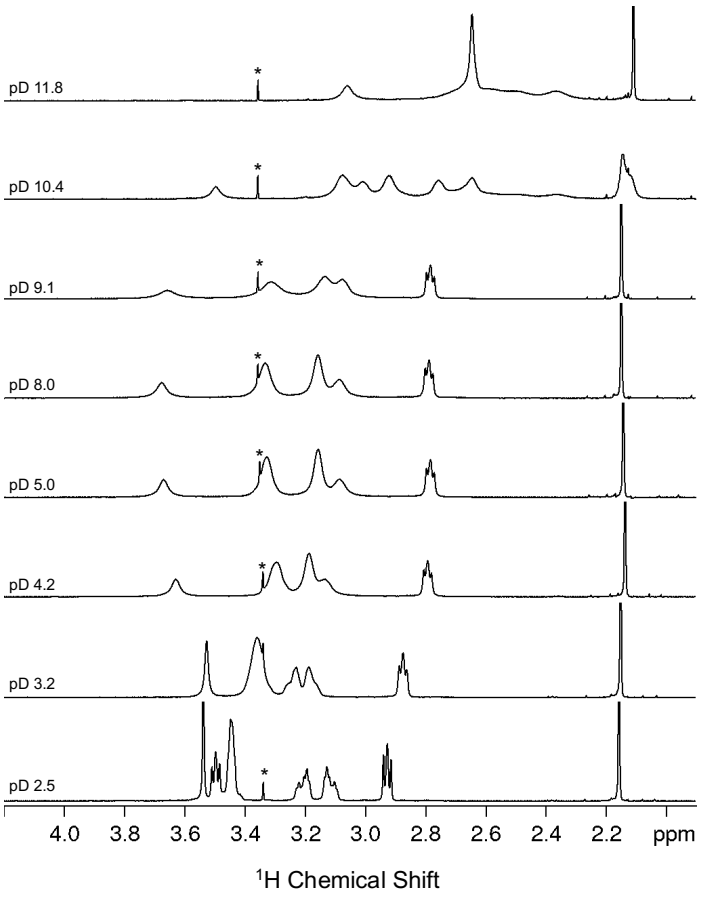

Figure 2.9. Variable-pD ^{1}H-NMR spectra of DO2A2S (600 MHz, D_2O, T = 25°C, C_{DO2A2S} = 2·10^{-3} M). Peaks marked with an asterisk are residual methanol impurities.

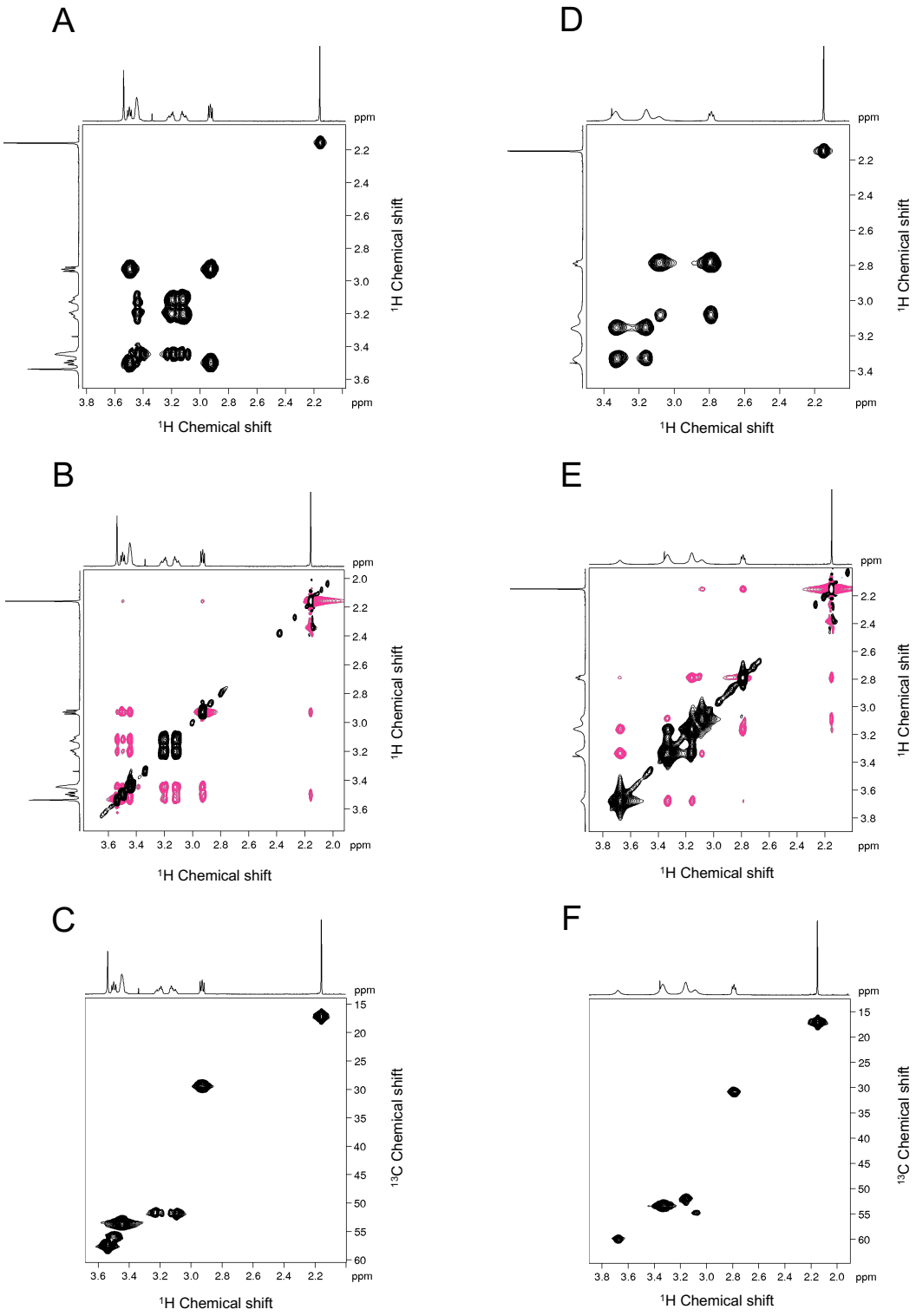

Figure 2.10. (A) ^{1}H-^{1}H COSY, (B) NOESY and (C) ^{1}H-^{13}C HMQC spectrum of triprotonated DO2A2S; (D) ^{1}H-^{1}H COSY, (E) NOESY and (F) ^{1}H-^{13}C HMQC spectrum of diprotonated DO2A2S.

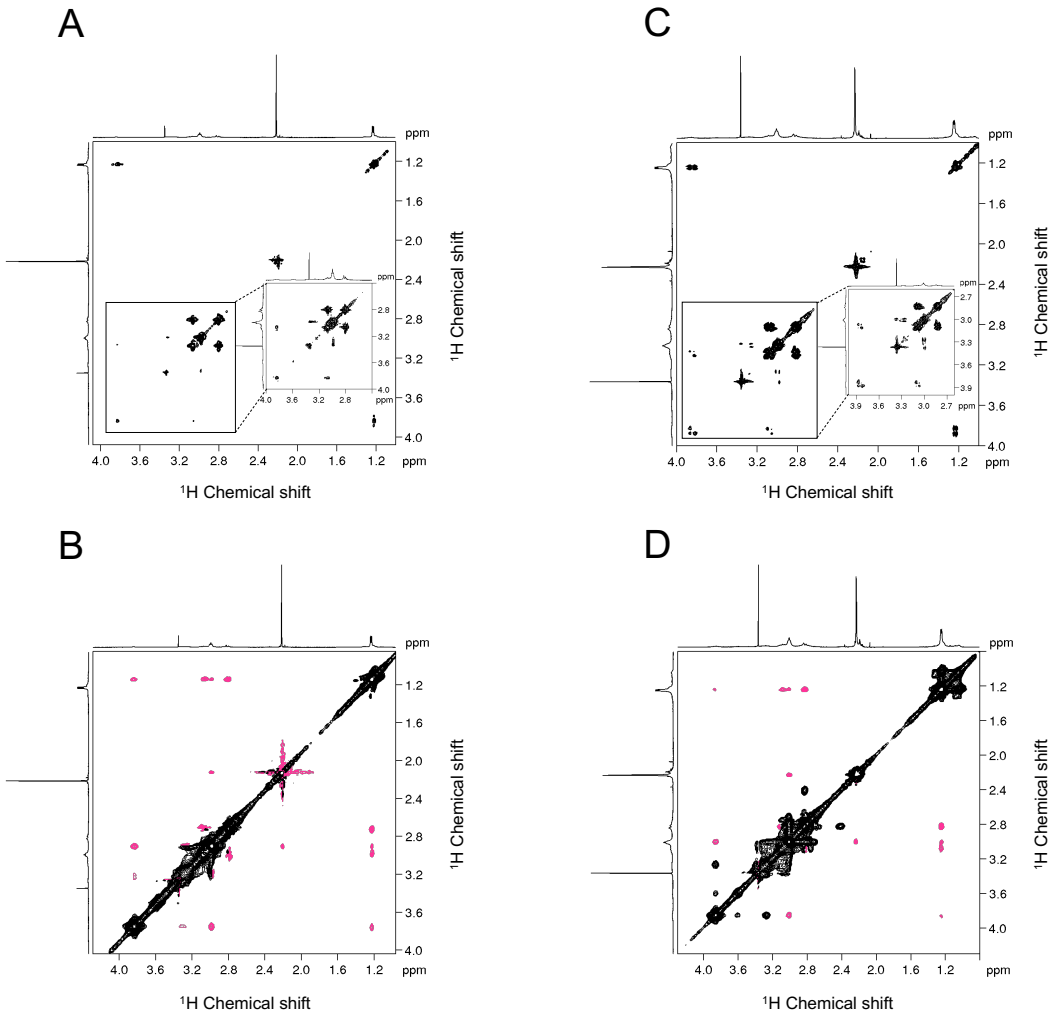

Figure 2.11. (A) ^{1}H-^{1}H COSY and (B) NOESY spectrum of diprotonated DO4S4Me; (C) ^{1}H-^{1}H COSY and (D) NOESY spectrum of monoprotonated DO4S4Me.

2.2.4 Solution Structure of First-Generation Ligands: UV-Vis Investigation

Representative UV-Vis spectra of the first-generation ligands at various pH values are reported in **Figure 2.12** and **Figure A2** (**Appendix A**). No significant absorption can be observed above 300 nm, whereas below this wavelength, the spectra display a weak peak, especially at acidic pH (*e.g.*, $\varepsilon \approx 2.7 \cdot 10^2$ L/mol·cm at pH 2.32 for DO4S) centred at around 280 nm, and a very strong absorption below 250 nm throughout the investigated pH range (*e.g.*, $\varepsilon \approx 1.8 \cdot 10^3$ L/mol·cm at 230 nm at pH 2.32 and $\varepsilon \approx 3.0 \cdot 10^3$ L/mol·cm ^{1} at pH 9.09 for DO4S). For all ligands, an absorbance increase can be detected by increasing the pH. Data clearly show that the increase is maximum at pH close to the pK_a values (**Figure 2.12**) and this property allows to elaborate the UV-Vis data to determine the protonation constants.

The obtained values are resumed in **Table 2.1**, and it is worth to note that they are in good agreement with those obtained by potentiometry.

The comparison of these spectra with those of cyclen (**Figure A2** - **Appendix A**) indicates that all ligands display similar absorption properties. Notably, the presence of the sulfide side arms causes an increase in the absorbances with respect to cyclen. This could be justified considering the synergic effect of the electron-donor character of the sulfur-containing alkyl chains and their intrinsic absorption features as, according to Fehnel *et al.*, alkyl thioethers absorb below 250 nm.[26]

The absorption spectra of cyclen, DO3S and DO4S in different protonation states were computed at COSMO-ZORA-SAOP/QZ4Pae//OPBE/DZP level, to elucidate the electronic transitions occurring in these ligands. Computed spectra are shown in **Figure A3**, and the relevant absorptions are reported in **Table A12** (**Appendix A**). Transitions are almost always pure monoelectronic, and the lowest excitation involves the HOMO and the LUMO. For cyclen, the HOMO-LUMO absorption changes from 201 to 219 and 225 nm when passing from H_2L^{2+} to HL^{+} and then to L (**Table A12**), *i.e.*, when increasing the pH.

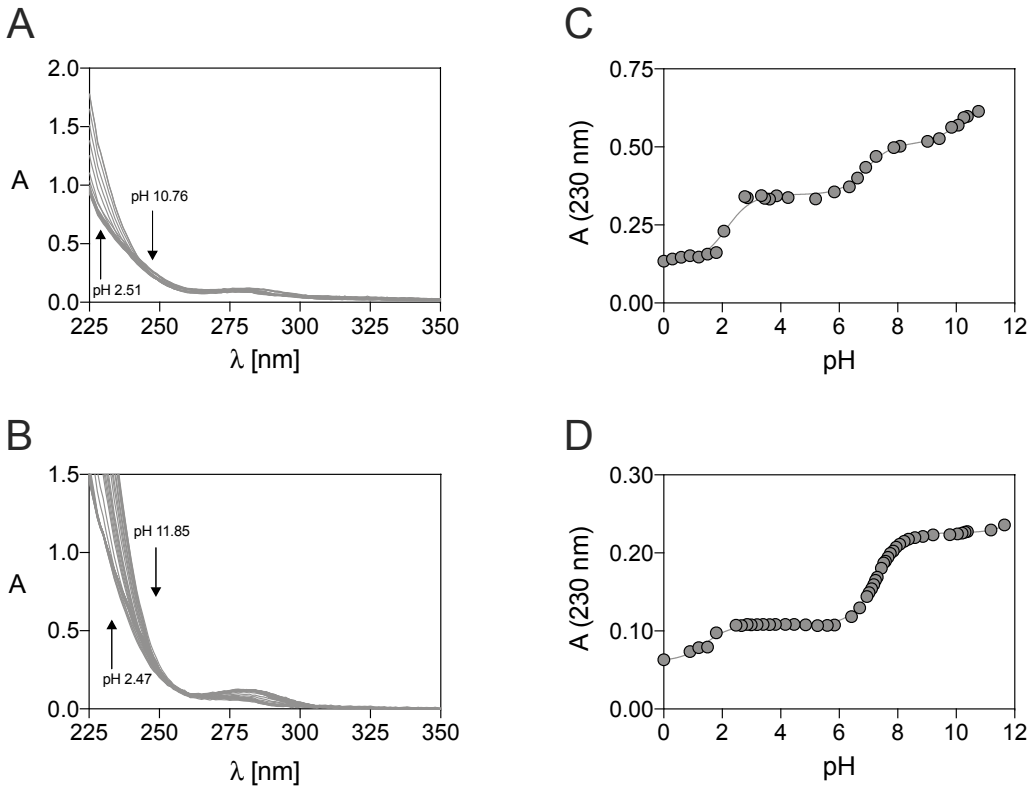

Figure 2.12. Variable-pH UV-Vis spectra of (A) DO4S (C_{DO4S} = 4.03·10^{-4} M), (B) DO3S (C_{DO3S} = 1.01·10^{-3} M) and (C, D) corresponding experimental points and fitting line of absorbance *vs.* pH at selected λ.

Conversely, for DO3S and DO4S, the HOMO-LUMO excitations vary from 260 to 254 and 278 nm and from 261 to 255 and 287 nm, respectively. Notably, the bathochromic shift associated with the pH increase experimentally observed is reproduced.

The HOMO and LUMO are shown in **Figure 2.13** and **Figure A4** (**Appendix A**). It appears that the HOMO-LUMO transition in cyclen can be mainly ascribed to the ring amines, whereas in DO3S and DO4S the transitions involve both the chain and the ring moieties. Particularly, the HOMO-LUMO is a ring-to-arms transition in the neutral forms and becomes an arm-to-arm transition upon protonation. Despite the higher energy transitions still maintaining an almost pure monoelectronic character, they are energetically very close and have comparable oscillator strength and this precludes a precise assignment of the experimental peaks. Nevertheless, the bathochromic shift is computed also for the strongest computed absorptions, in nice agreement with the experimental results.

2.2.5 Protonation Equilibria and Solution Structure of Second-Generation Ligands

Combined potentiometric, ^{1}H-NMR and UV-Vis spectrophotometric titrations in aqueous solution were used to determine the protonation constants of TACD3S, TRI4S and TE4S at 25°C with ionic strength adjusted to 0.15 M $NaNO_3$. The stepwise deprotonation constants (pK_a) are outlined in **Table 2.4** and compared with those of DO4S and structurally related ligands (tetramethyl-cyclen and tetramethyl-cyclam) or with the parent unsubstituted macrocycles (TACD, TRI and cyclam). The protonation speciation diagrams for TACD3S, TRI4S and TE4S are presented in **Figure 2.14**.

For all the investigated chelators, the constants for the deprotonation of HL^{+} and H_2L^{2+} (**Table 2.4**) can be assigned to the deprotonation of two opposite or adjacent nitrogen atoms of the azamacrocyclic rings. The other deprotonation constants (*i.e.* those for H_3L^{3+} and, if applicable, for H_4L^{4+}) were always found to be very high ($pK_a < 2$, **Table 2.4**), primarily due to the Coulombic repulsion between the positive charges resulting from the protonated amines that are forced into proximity by the cyclic nature of the ligands.

Comparing TRI4S and TE4S with DO4S, the slight differences in the pK_a values are related to the different ring sizes and the relative position of the nitrogen atoms. For TE4S, the higher pK_a values with respect to those of DO4S likely reflect the larger separation between the nitrogen atoms afforded by the larger backbone, which lowers the charge-charge repulsion, allowing a better stabilization of the proton binding.

Unexpectedly, the tertiary nitrogen atoms of TRI4S are less basic than those of DO4S and TE4S. Simple charge-repulsion arguments do not explain this trend, which should be thus justified by conformational effects resulting from the asymmetry of the molecule.

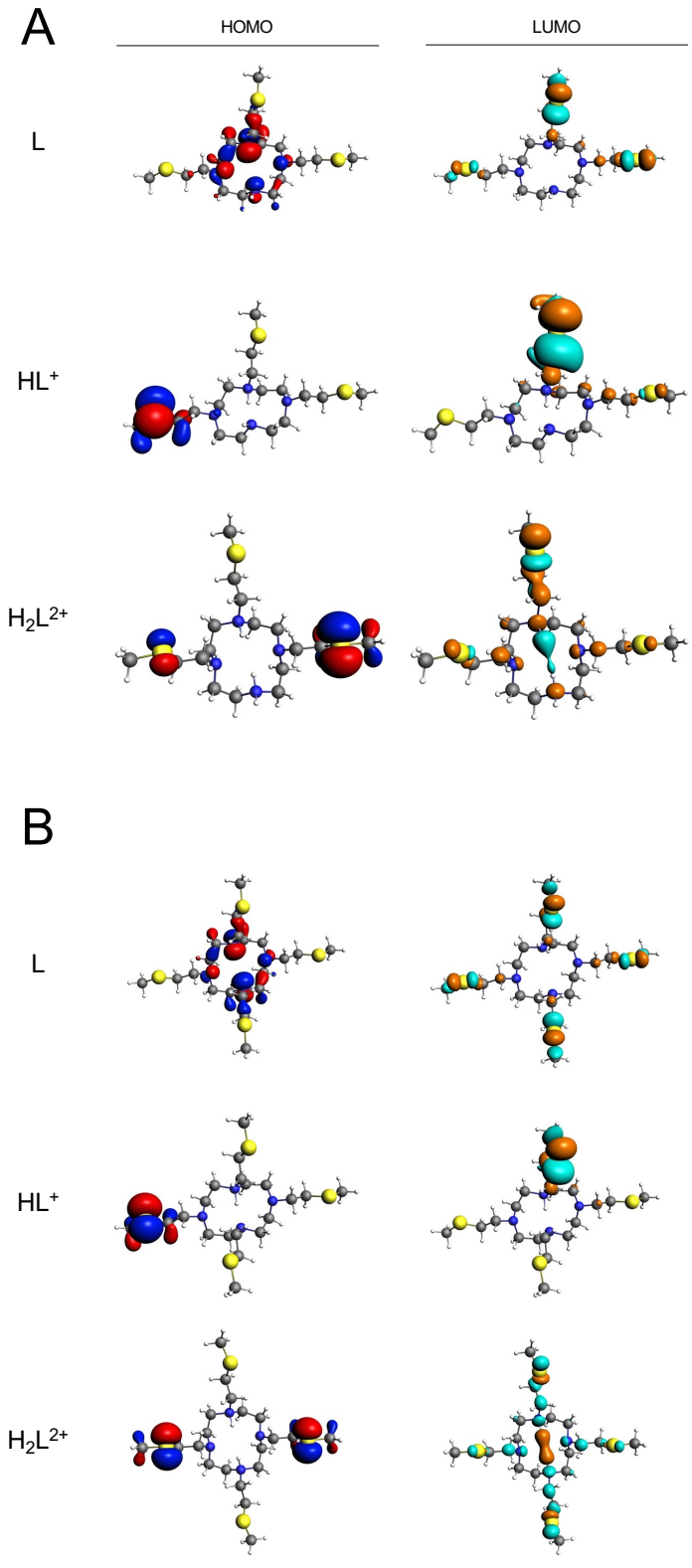

Figure 2.13. HOMO and LUMO of the differently protonated species of (A) DO3S and (B) DO4S (level of theory: COSMO-ZORA-SAOP/QZ4Pae//ZORA-OPBE/DZP).

Although TACD3S and DO4S possess the same number of atoms in the macrocyclic scaffold, the former is significantly more acidic. In TACD3S the tertiary amines are separated by a larger distance with respect to DO4S, but the lower number of possible microstates (where protons are localized on different nitrogens) leads to a lower stability of the protonated species for the former ligand, thus explaining the observed behaviour.

As previously found for DO4S and its derivatives (*vide supra*), a decrease of pK_a was also observed (especially for the deprotonation of H_2L^{2+}) with all the investigated second-generation ligands when compared to the bare macrocycles or the non-sulfanyl analogues. While the former effect can be explained by the consequence of the destabilization of the protonated species resulting from the decrease in water solvation after the *N*-alkylation, the latter is attributed to the presence of the sulfur atoms on the sidearms.

Table 2.4. Dissociation constants (pK_a values) of second-generation ligands at T = 25°C and I = 0.15 M $NaNO_3$. The pK_a values of the corresponding unsubstituted macrocycles and other structurally related compounds are reported for comparison purposes. Unless otherwise stated, the values were obtained by pH-potentiometry.

Ligand	Equilibrium [#]		
	$HL^+ \rightleftharpoons L + H^+$	$H_2L^{2+} \rightleftharpoons HL^+ + H^+$	$H_3L^{3+} \rightleftharpoons H_2L^{2+} + H^+$
TACD3S	9.60 ± 0.02 9.6 ± 0.2 [§]	5.57 ± 0.05 5.41 ± 0.06 [§] 5.29 ± 0.03 [*]	1.62 ± 0.07 [§]
DO4S [a, b]	10.14 [a]	7.29 [a]	1.9 [b]
TRI4S	9.76 ± 0.03 9.4 ± 0.1 [§]	6.69 ± 0.03 6.0 ± 0.3 [§] 6.10 ± 0.05 [*]	1.5 ± 0.1 [§]
TE4S	10.60 ± 0.01 10.9 ± 0.3 [*]	7.73 ± 0.05 7.5 ± 0.2 [*]	1.7 ± 0.2 [§]
TACD [c]	12.6	7.57	2.41
Cyclen [a, b]	10.63 [a]	9.51 [a]	1.6 [b]
Tetramethyl-cyclen [d]	11.06	8.95	–
TRI [e]	11.02	9.96	1.96
Cyclam [f]	11.3	10.23	1.43
Tetramethyl-cyclam [f]	9.34	8.99	2.58

[#] L represents the deprotonated form of each chelator. The reported uncertainty was obtained by the fitting procedure and represents one standard deviation unit.
[§] Obtained from ^{1}H-NMR data, no ionic strength control.
[*] Obtained from UV-Vis data, no ionic strength control.
[a, b] From ref. [19], I = 0.15 M $NaNO_3$, and ref. [27], no ionic strength control, T = 25°C.
[c] From ref. [28], I = 0.15 M KNO_3, T = 25°C.
[d] From ref. [29], I = 0.2 M $NaClO_4$, T = 25°C.
[e] From ref. [30], I = 0.1 M $NaNO_3$, T = 25°C.
[f] From ref. [31], I = 0.1 M $NaNO_3$, T = 25°C.

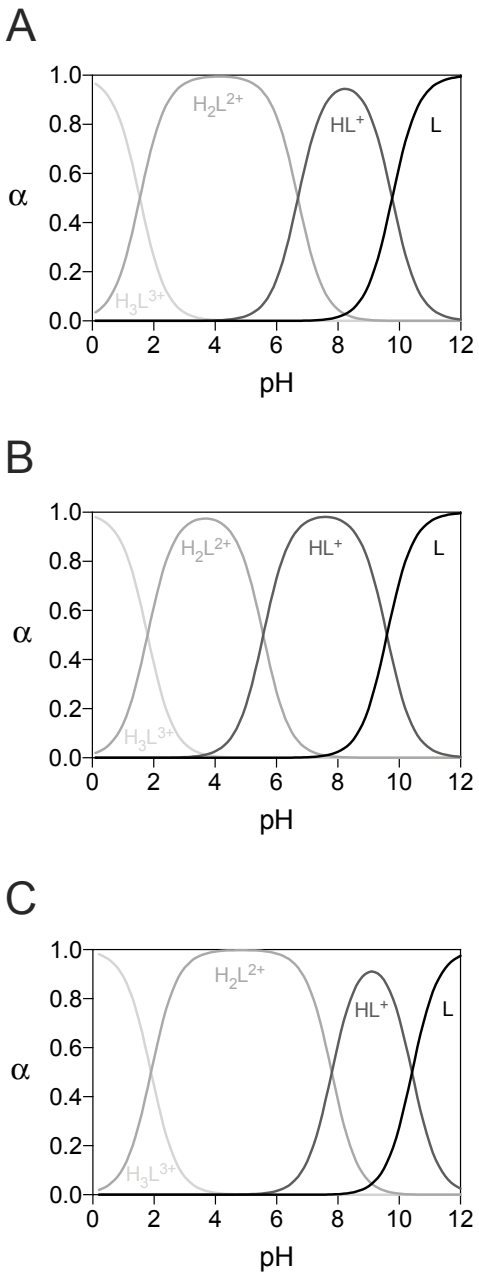

Figure 2.14. Speciation diagram of (A) TACD3S, (B) TRI4S and (C) TE4S.

^{1}H-NMR spectroscopy was employed to confirm some pK_a values and to determine the most acidic ones (pK_a << 2, not accessible by potentiometric measurements). In addition, it was also used to gain insights into the solution structure and the dynamics of the protonation/deprotonation processes of the second-generation ligands. The pK_a values determined by NMR are reported as well in **Table 2.4**. Some minor discrepancies between the deprotonation constants obtained by NMR and potentiometry can be attributed to the uncontrolled ionic strength during NMR experiments.

The ^{1}H-NMR spectra of TACD3S, TRI4S and TE4S and the ^{1}H chemical shift variations as a function of pH are shown in **Figure 2.15** - **2.17**. The signal assignments, supported by bidimensional spectra of **Figure 2.18** - **2.21**, are reported in **Table A13** - **A15** (**Appendix A**). For TACD3S, at the most acidic pH, the S-bound methyl and methylenic protons resonate as a singlet and a triplet at 2.15 and 2.92 ppm, respectively (**Figure 2.15** and **Table A13** - **Appendix A**). Both the ring and side-arms nitrogen-bound protons resonate as a triplet at 3.55 and 3.49 ppm, respectively, while the methylenic protons of the ring appear as a quintet at 2.33 ppm. Upon increasing the pH, no significant shifts were detected for the SCH_3 signals as they are far from the (de)protonation sites (**Figure 2.15**), whereas all the other resonances shift upfield because of the increase of the electron density on the nitrogens after their deprotonations (**Figure 2.15** and **Figure 2.17**). The same behaviour was observed for TRI4S and TE4S, too.

In TRI4S, the molecular asymmetry generated from the propyl chain induces the splitting of the signals of the sidearms at the lowest investigated pH. According to the ^{1}H-^{1}H TOCSY spectra (**Figure 2.18**), the SCH_3 protons resonate as two singlets at 2.16 and 2.17 ppm (an enlargement of the SCH_3 signals is shown in **Figure 2.22**), the SCH_2 protons as two triplets at 2.87 and 2.93 ppm and the NCH_2 ones as two triplets at 3.21 and 3.50 ppm. The latter signal is overlapped with those of the N-bound ^{1}H of the propyl chain and half of the methylenic protons located on opposite sides of the ring (and equal two by two through the σ_v' symmetry plane); the second half of the latter resonates as a triplet at 3.67 ppm. The NCH_2 ^{1}H opposite to the propyl chain are as well equivalent due to the σ_v' symmetry plane. These protons and the CH_2 ones laying on σ_v' resonate as a singlet at 3.34 ppm and a non-splitted multiplet at 2.25 ppm, respectively. At higher pH, the spectra become complicated as all the SCH_2 and NCH_2 signals overlap, making the exact attribution difficult.

Due to the higher symmetry of TE4S with respect to TRI4S, the signals in the ^{1}H NMR spectra of the former are less complicated at acidic pH while a similar coalescence is observed at basic pH (**Figure 2.17** and **Table A15** - **Appendix A**).

For all the investigated ligands, the N-bound methylenic protons of the ring experience a greater chemical shift variation than those of the side chains when the pH was increased from the most acidic to the most basic (*e.g.*, $\Delta\delta_{NCH_2,\ ring} \approx 0.7$ ppm *vs.* $\Delta\delta_{NCH_2,\ arms} \approx 0.5$ ppm for TACD3S and TE4S). The same effect is also observed when the methylenic protons of the ring are compared with those bound to S (*e.g.*, $\Delta\delta_{CH_2,\ ring} \approx 0.4$ ppm *vs.* $\Delta\delta_{SCH_2,\ arms} \approx 0.1$ ppm for TACD3S) despite being at the same distance from the protonation sites. This effect might be related to the relaxation of the structural constrain, caused by the H^+-H^+ repulsions, after the deprotonation: this is higher for the ring than for the side chains, because the latter are not confined into a cyclic structure.

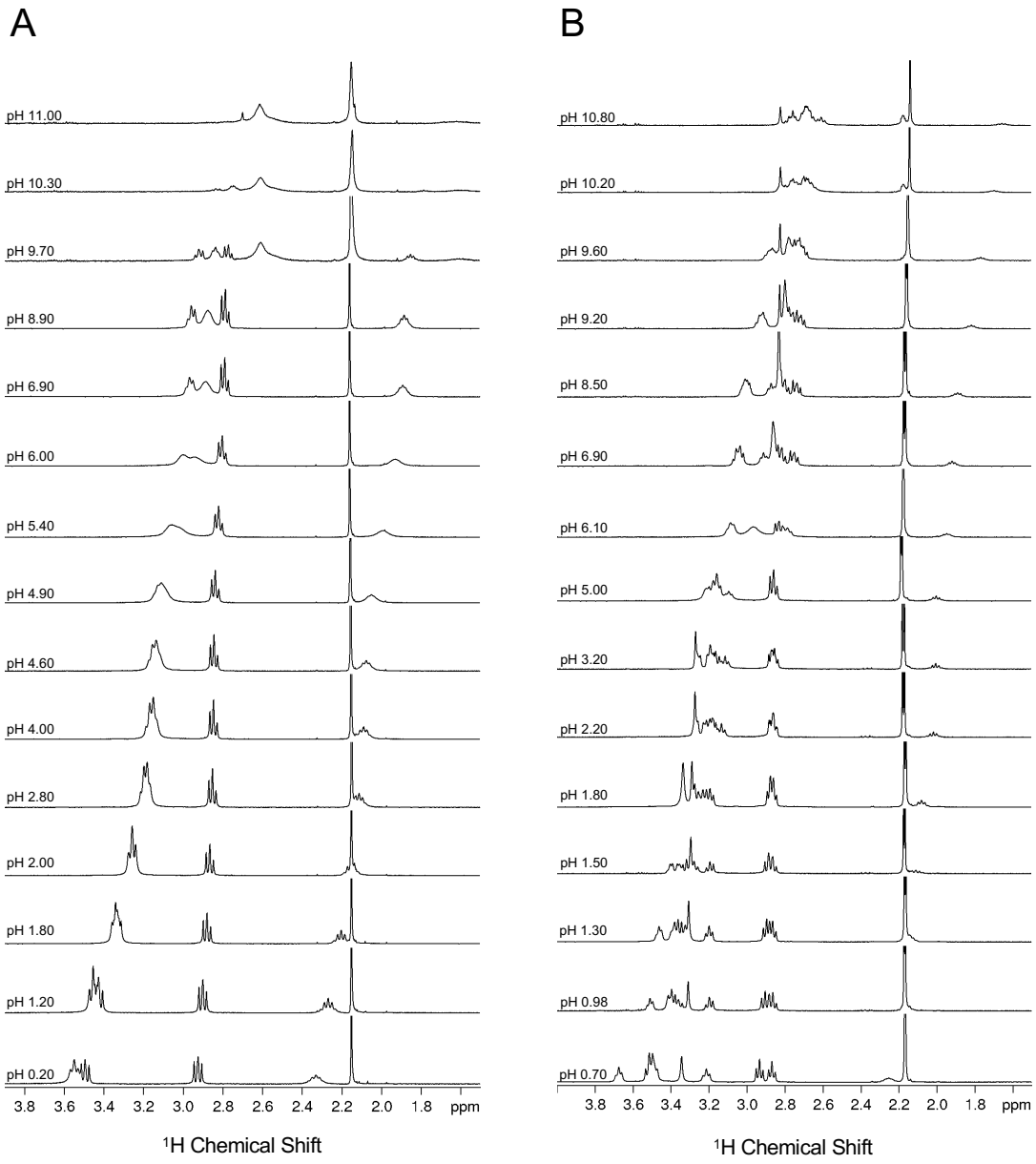

Figure 2.15. Variable-pH ^{1}H NMR spectra (400 MHz, T = 25°C, H_2O + 10% D_2O) of (A) TACD3S (C_{TACD3S} = 9.8·10^{-4} M) and (B) TRI4S (C_{TRI4S} = 9.1·10^{-4} M).

According to the sharpness of the signals and the absence of multiple patterns, all the deprotonation processes ($H_3L^{3+} \leftrightharpoons H_2L^{2+} + H^+ \leftrightharpoons HL^+ + H^+$) should be fast on the NMR timescale (**Figure 2.15** and **Figure 2.16**). An exception is represented by the last deprotonation step of TACD3S, which appears markedly slower since both patterns of HL^+ and L, together with a signal enlargement, can be observed (**Figure 2.15**). The estimated molar ratio between these two species obtained by the integration of NMR signals is in good agreement with the values calculated by potentiometry. Moreover, the sharpness of the signals also indicates that the conformational equilibria within a single species are fast on the

NMR timescale (except for TACD3S in its totally deprotonated form). On the contrary, it is worth to note that in the cyclen-based analogue, *i.e.* DO4S, the multiplets were sharp only in its neutral form (*vide supra*). The lower energetic barrier of the conformer interconversion, resulting from the added CH_2 spacer in the ring of TACD3S, TRI4S and TE4S, could justify this difference.

As regards the UV-Vis analysis, the electronic spectra of TACD3S, TRI4S and TE4S display a strong absorption in the UV region (below 250 nm) which showed an absorbance increase close to the pK_a values (**Figure 2.23**), similarly to DO4S and its derivatives (*vide supra*). UV-Vis data were fitted to determine the pK_a values (**Table 2.4**) which agree reasonably well with those obtained from potentiometric titrations and NMR.

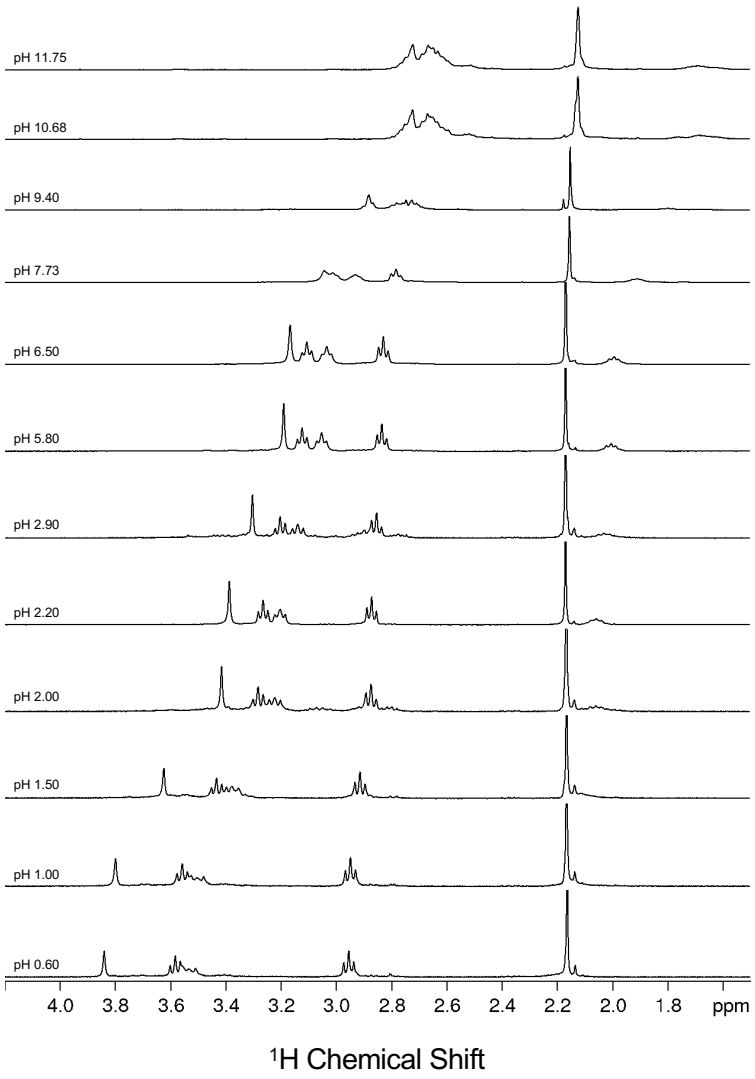

Figure 2.16. Variable-pH ^{1}H NMR spectra of TE4S (400 MHz, T = 25°C, H_2O + 10% D_2O, $C_{TE4S} = 9.7 \cdot 10^{-4}$ M).

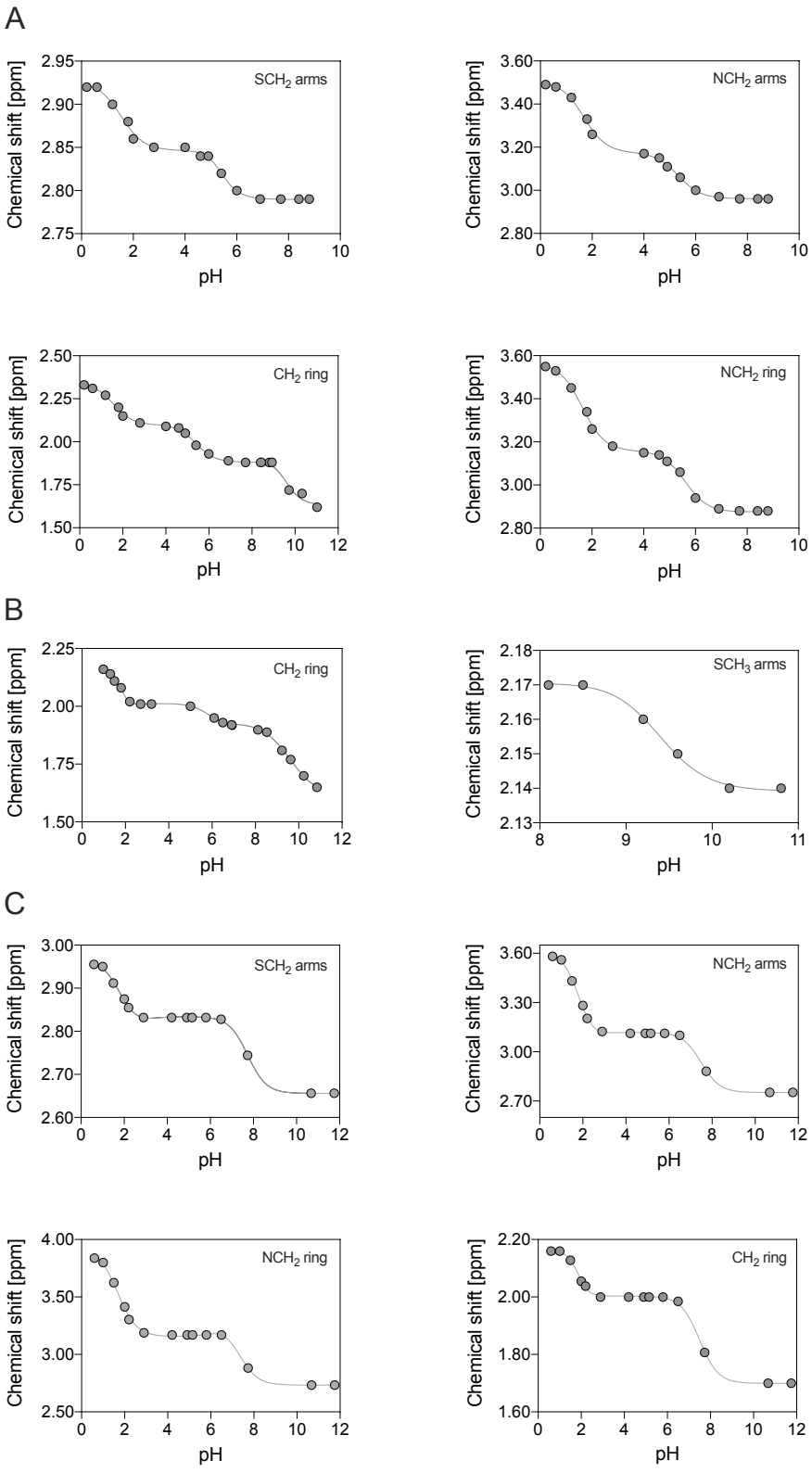

Figure 2.17. Representative ^{1}H-NMR titration curves and corresponding fitting lines of (A) TACD3S (data points were taken from **Figure 2.15**), (B) TRI4S (data points were taken from **Figure 2.15**) and (C) TE4S (data points were taken from **Figure 2.16**).

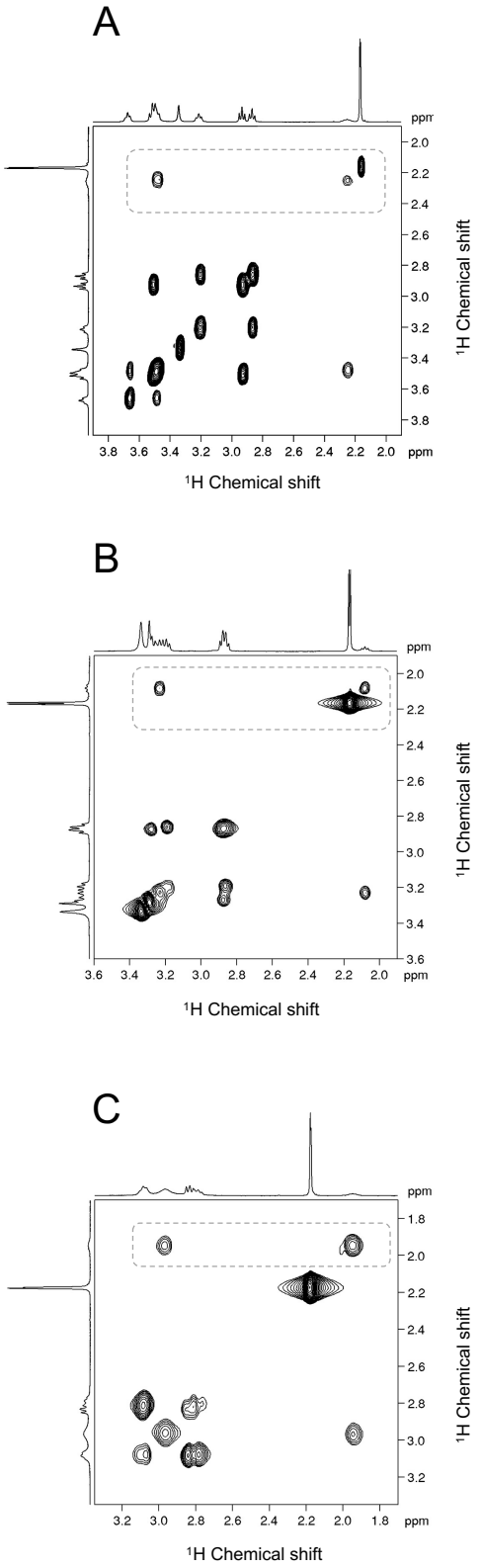

Figure 2.18. ^{1}H-^{1}H TOCSY spectra of TRI4S at (A) pH 0.7, (B) pH 1.8 and (C) pH 6.1.[†]

[†] Intensity scale for ring CH_2 signal is different from those used for the others.

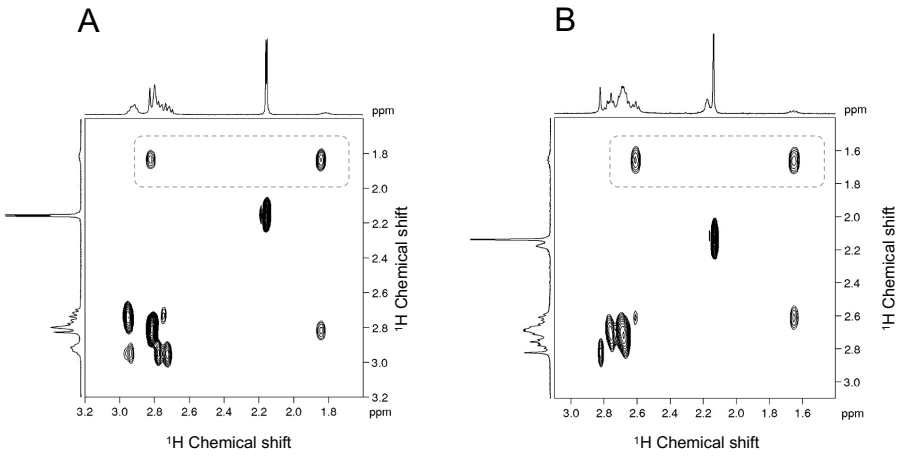

Figure 2.19. ^{1}H-^{1}H TOCSY spectra of TRI4S at (A) pH 9.2 and (B) pH 10.8.†

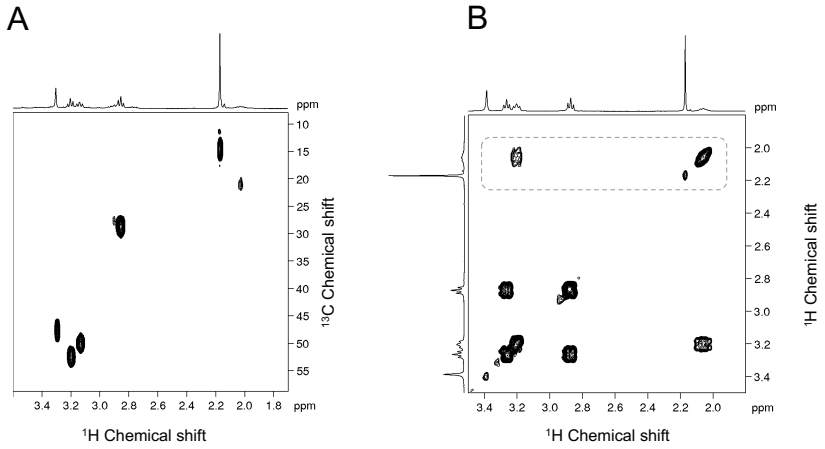

Figure 2.20. (A) ^{1}H-^{13}C HSQC and (B) ^{1}H-^{1}H TOCSY spectra of TE4S at pH 1.7.†

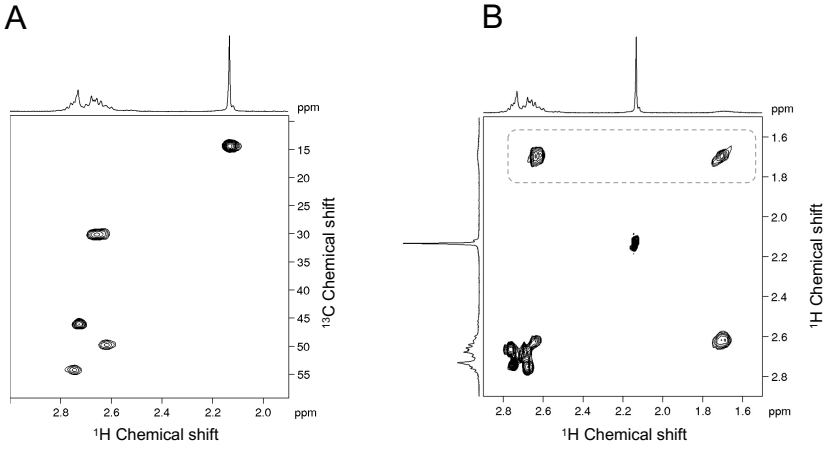

Figure 2.21. (A) ^{1}H-^{13}C HSQC and (B) ^{1}H-^{1}H TOCSY spectra of TE4S at pH 12.†

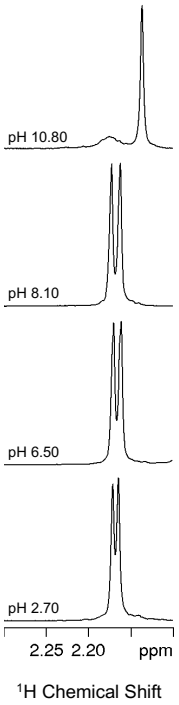

Figure 2.22. Enlargement of SCH_3 spectral region of TRI4S.

2.3 Experimental Section

2.3.1 Ligand Synthesis

Materials and methods. All solvent and starting materials were purchased from commercial suppliers and used without further purifications. 1,4,7,10-Tetrazacyclododecane (cyclen), 1,5,9-triazacyclododecane (TACD), 1,4,7,10-tetrazacyclotridecane (TRI), and 1,4,8,11-tetrazacyclotetradecane (cyclam) were purchased from Chematech. (2*S*,5*S*,8*S*,11*S*)-2,5,8,11-tetramethyl-1,4,7,10-tetraazacyclododecane (Me4-cyclen) was synthesized according to previously reported procedures.[32] Thin layer chromatography (TLC) was performed on pre-coated plates of silica gel 60 with fluorescent indicator UV254 (0.2 mm, Macherey-Nagel); column chromatography was done with silica gel 60 (0.063-0.100 mm, Merck) or on high purity grade silica gel (60 Å, 230-400 mesh, 40-63 µm, Sigma-Aldrich). The ^{1}H, ^{13}C, ^{19}F NMR spectra were recorded at room temperature on a Bruker 400-AMX or 600 MHz spectrometers. Chemical shifts (δ) are reported as parts per million (ppm) relative to the residual solvent peak and coupling constants (*J*) in hertz (Hz). Multiplicity is given as follows: s = singlet, d = doublet, t = triplet, q = quartet, qn = quintet, m = multiplet, br = broad peak. High-resolution mass spectra (HRMS, ESI) were recorded with an Applied Biosystem Mariner System 5220 or Agilent Technologies LC/MSD Trap SL mass spectrometer.

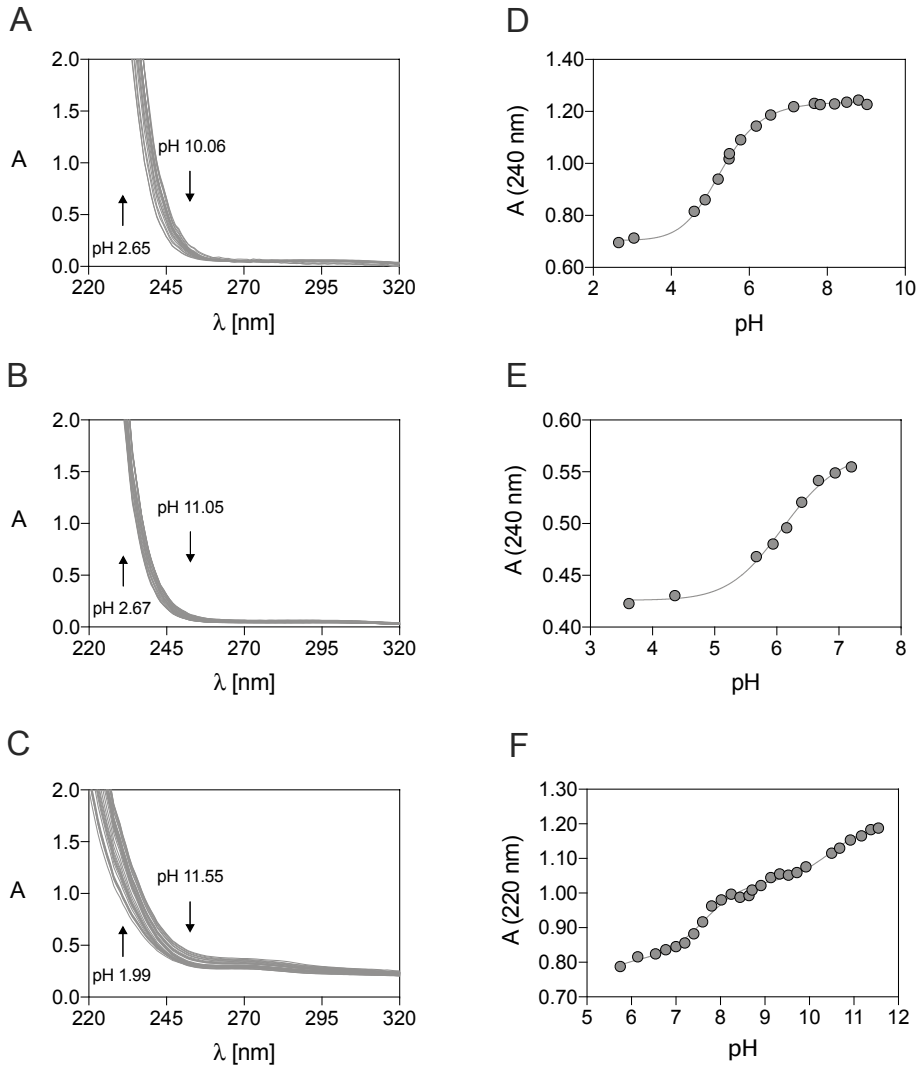

Figure 2.23. UV-Vis spectra of (A) TACD3S (C_{TACD3S} = 1.43·10^{-3} M), (B) TRI4S (C_{TRI4S} = 5.6·10^{-4} M), (C) TE4S (C_{TE4S} = 5.4·10^{-4} M) and (D, E, F) corresponding experimental points and fitting line of absorbance *vs.* pH at selected λ.

1,4,7,10-Tetrakis[2-(methylsulfanyl)ethyl]-1,4,7,10-tetraazacyclododecane (DO4S). DO4S was synthesized with slight variation from the literature procedure.[1] A solution of cyclen (0.51 g, 3.00 mmol, 1.0 eq.) in CH_3CN (45 mL) was added with K_2CO_3 (3.82 g, 24.00 mmol, 8.0 eq.) and 2-chloroethyl methyl sulfide (1.66 g, 15.00 mmol, 5.0 eq.). The mixture was stirred at 60°C under nitrogen atmosphere for 24 h and the reaction was monitored by TLC. After completion of the reaction, the mixture was filtered and solvent evaporated under reduced pressure to give a brown oil purified by silica-gel chromatography ($CHCl_3$/CH_3OH 9:1 + 0.5% $NH_{3\,(aq)}$) to obtain DO4S (0.72 g, 51% yield). ^{1}H-NMR (400 MHz, $CDCl_3$): δ 3.15-2.95 (m, 24 H, NCH_2), 2.72 (m, 8 H, SCH_2), 2.18 (s, 12 H, SCH_3). ^{13}C-NMR (600 MHz, D_2O, pD 10.8): δ 17.6 (SCH_3), 32.0 (SCH_2), 53.2 (NCH_2), 56.2 (NCH_2). ESI/MS$^+$: *m/z* $[M+H]^+$ 469.2507 (found); 469.2527 (calculated for $C_{20}H_{45}N_4S_4$).

1,4,7-Tris[2-(methylsulfanyl)ethyl]-1,4,7,10-tetraazacyclododecane (**DO3S**). A solution of cyclen (0.50 g, 2.70 mmol, 1.0 eq.) in CH_3CN (20 mL) was added with K_2CO_3 (1.5 g, 10.8 mmol, 4.0 eq.) and 2-chloroethyl methyl sulfide (1.11 g, 10.00 mmol, 3.7 eq.). The mixture was stirred at 40°C under nitrogen atmosphere for 5 days and the reaction was monitored by TLC. After completion of the reaction, the mixture was filtered and solvent evaporated under reduced pressure to give a brown oil purified by silica-gel chromatography ($CHCl_3/CH_3OH$ 9:1) to obtain DO3S (0.25 g, 20% yield). ^{1}H-NMR (400 MHz, $CDCl_3$): δ 2.90-2.50 (m, 28 H, NCH_2 + SCH_2), 2.14 (s, 3 H, SCH_3), 2.12 (s, 6 H, SCH_3). ^{13}C-NMR (600 MHz, D_2O, pD 2.9): δ 18.0 (SCH_3), 30.2 (N_4-SCH_2), 33.7 (N_1, N_7-SCH_2), 45.7 (NCH_2), 51.1 (NCH_2), 53.9 (NCH_2), 54.3 (NCH_2), 56.4 (NCH_2). ESI/MS^+ *m/z* $[M+H]^+$: 395.2470 (found); 395.2337 (calculated for $C_{17}H_{39}N_4S_3$).

1-[1-(Ethoxycarbonyl)methyl]-1,4,7,10-tetraazacyclododecane (**1**). A solution of ethyl bromoacetate (0.17 g, 1.00 mmol, 1.0 eq.) in CH_3CN (30 mL) was added dropwise for 30 min to an ice-cooled solution of cyclen (0.52 g, 3.00 mmol, 3.0 eq.) in CH_3CN (30 mL). After 2 h the reaction mixture was allowed to warm to room temperature and further stirred for 24 h. After completion of the reaction, the mixture was filtered and the solvent was removed under reduced pressure to give **2** as a yellow oil purified by silica gel chromatography ($CHCl_3/CH_3OH$ 9:1 + 1% $NH_{3\,(aq)}$) (0.11 g, 44% yield). ^{1}H-NMR (400 MHz, $CDCl_3$): δ 4.13-4.03 (q, *J* = 7.31, 2 H), 3.32 (s, 2 H), 2.75-2.67 (m, 8 H), 2.58-2.47 (m, 8 H), 1.22-1.15 (t, *J* = 7.17, 3 H).

1,4,7-Tris[2-(methylsulfanyl)ethyl]-10-[1-(ethoxycarbonyl)methyl]-1,4,7,10-tetraazacyclododecane (**2**). A solution of **1** (0.11 g, 0.44 mmol, 1.0 eq.) in CH_3CN (13 mL) was added with K_2CO_3 (0.55 g, 3.96 mmol, 9.0 eq.) and 2-chloroethyl methyl sulfide (0.22 g, 1.98 mmol, 4.5 eq.). The reaction mixture was stirred at 60°C for 24 h. After completion of the reaction, the mixture was filtered, and solvent evaporated to give **2** as a brown oil purified by silica-gel chromatography ($CHCl_3/CH_3OH$ 9:1 + 0.5% $NH_{3\,(aq)}$) (0.15 g, 72% yield). ^{1}H-NMR (400 MHz, $CDCl_3$): δ 4.17-4.07 (q, *J* = 7.36, 2 H), 3.37 (s, 2 H), 2.85-2.52 (m, 28 H), 2.09 (s, 9 H), 1.27-1.21 (t, *J* = 7.13, 3 H).

1,4,7-Tris[2-(methylsulfanyl)ethyl]-10-methylacetamido-1,4,7,10-tetraazacyclododecane (**DO3SAm**). A solution of **2** (0.08 g, 0.17 mmol) in ethanolic methylamine solution (6 mL, 8.03 M in EtOH) was stirred in a sealed vial for 72 h at room temperature. After evaporation, the residue was purified by silica-gel chromatography ($CHCl_3/CH_3OH$ 9:1 + 0.5% $NH_{3\,(aq)}$) to give pure DO3SAm (0.08 g, quantitative yield) as a colourless oil. ^{1}H-NMR (400 MHz, $CDCl_3$): δ 8.75-8.70 (m, 1 H), 3.04 (s, 2 H), 2.78-2.75 (d, *J* = 4.40, 3 H), 2.72-2.45 (m, 28 H),

2.09 (s, 3 H), 2.07 (s, 6 H). ESI/MS$^+$: *m/z* $[M+H]^+$ 466.2815 (found); 466.2708 (calculated for $C_{20}H_{44}N_5OS_3$).

1,7-Bis[2-(methylsulfanyl)ethyl]-1,4,7,10-tetraazacyclododecane-4,10-diacetic acid ditertbutyl ester (**4**). A solution of di-tert-butyl 2,2′-(1,4,7,10-tetraazacyclododecane-1,7-diyl) diacetate (**3**) (0.52 g, 1.30 mmol, 1.0 eq.) in CH_3CN (40 mL) was added with K_2CO_3 (1.08 g, 7.80 mmol, 6.0 eq.) and 2-chloroethyl methyl sulfide (0.43 g, 3.90 mmol, 3.0 eq.). The reaction mixture was stirred at 60°C under nitrogen atmosphere for 24 h. After reaction, the mixture was filtered and solvent evaporated to give **4** as a brown oil purified by chromatography on silica gel ($CHCl_3/CH_3OH$ 9:1 + 0.5% $NH_{3\ (aq)}$) (0.65 g, 90% yield). ^{1}H-NMR (400 MHz, $CDCl_3$): δ 3.28 (s, 4 H), 2.88-2.80 (m, 8 H), 2.70-2.54 (m, 16 H), 2.11 (s, 6 H), 1.45 (s, 18 H).

1,7-Bis[2-(methylsulfanyl)ethyl]-1,4,7,10-tetraazacyclododecane-4,10-diacetic acid (**DO2A2S**). A solution of **4** (0.65 g, 1.18 mmol) in CH_2Cl_2 (20 mL) at 0°C was added with TFA (6 mL) dropwise and the reaction mixture was stirred at room temperature for 24 h. The solvent was removed under reduced pressure to give DO2A2S as white solid (0.52 g, quantitative yield). ^{1}H-NMR (400 MHz, D_2O): δ 3.32 (s, 4 H), 3.30-3.00 (m, 20 H), 2.79-2.72 (m, 4 H); 2.11 (s, 6 H). ^{13}C-NMR (400 MHz, CD_3OD): δ 15.32 (SCH_3), 27.97 (SCH_2), 50.05 (NCH_2), 51.87 (NCH_2), 53.90 (NCH_2), 55.43 (NCH_2). ^{19}F-NMR (400 MHz, CD_3OD): no signal. ESI/MS$^+$: *m/z* $[M+H]^+$ 437.2813 (found); 437.2256 (calculated for $C_{18}H_{37}N_4O_4S_2$).

1,4,7,10-Tetra-*n*-butyl-1,4,7,10-tetraazacyclododecane (**DOT-*n*-Bu**). A solution of cyclen (0.17 g, 1.00 mmol, 1.0 eq.) in CH_3CN (20 mL) was added with K_2CO_3 (0.82 g, 6.00 mmol, 6.0 eq.) and 1-bromobutane (0.55 g, 4.00 mmol, 4.0 eq.). The reaction mixture was stirred at 60°C for 24 h. The mixture was filtered, and solvent evaporated to give DOT-*n*-Bu as a brown oil purified by silica-gel chromatography ($CHCl_3/CH_3OH$ 9:1) (0.18 g, 45% yield). ^{1}H-NMR (400 MHz, $CDCl_3$): δ 2.61 (s, 16 H), 2.40-2.30 (t, *J* = 7.52, 12 H), 1.50-1.36 (m, 8 H), 1.34-1.32 (q, *J* = 7.17, 8 H), 0.92-0.86 (t, *J* = 6.45, 12 H). ESI/MS$^+$: *m/z* $[M+H]^+$ 397.4363 (found); 397.4270 (calculated for $C_{24}H_{53}N_4$).

(2S,5S,8S,11S) - 2,5,8,11 - Tetramethyl - 1,4,7,10-tetrakis[2-methylsulfanyl) ethyl] - 1,4,7,10-tetraazacyclododecane (**DO4S4Me**)**.** Me4-cyclen (50 mg, 0.219 mmol, 1.0 eq.), K_2CO_3 (305 mg, 2.19 mmol, 10 eq.) and KI (10.7 mg, 0.0645 mmol, 0.29 eq.) were suspended in CH_3CN and 2-chloroethyl methyl sulfide (121 mg, 0.110 mL, 1.10 mmol, 5.0 eq.) was added. The suspension was heated to 40°C for 52 h and triethylamine (0.5 mL) was added. The solution was cooled to room temperature and filtered. The solvent was

evaporated, and the crude was purified by preparative HPLC[‡] to yield DO4S4Me (103 mg, 90% yield) as yellowish oil. ^{1}H-NMR (600 MHz, CD_3CN): δ 3.77-3.60 (m, 8 H, NCH_2), 3.28-3.05 (m, 8 H, NCH_2), 2.99-2.83 (m, 8 H, SCH_2), 2.65-2.59 (m, 4 H, NCH_2), 2.18 (s, 12 H, SCH_3), 1.24 (d, *J* = 6.06 Hz, 12 H, CH_3). ^{13}C-NMR (150 MHz, CD_3CN): δ 53.86 (NCH_2), 52.18 (NCH_2), 50.05 (NCH_2), 30.43 (SCH_2), 15.91 (SCH_3), 12.00 (CH_3). ESI-MS$^+$: m/z $[M+H]^+$ 525.3141 (found); 525.3148 (calculated for $C_{24}H_{52}N_4S_4$).

1,5,9-Tris(2-(methylsulfanyl)ethyl)-1,5,9-triazacyclododecane (**TACD3S**)**.** 1,5,9-Triaza cyclododecane (171 mg, 1.0 mmol, 1.0 eq.) and K_2CO_3 (989 mg, 6.5 mmol, 6.5 eq.) were added to CH_3CN (15 mL) in a pressure tube flushed with nitrogen. 2-chloroethyl methyl sulfide was added to the mixture (399 µL, 4.0 mmol, 4.0 eq.) and the pressure tube was heated to 60°C under stirring for 24 hours. The mixture was then evaporated under reduced pressure and the product was purified by flash column chromatography on silica (eluent $CHCl_3$: CH_3OH 9: 1 + 0.5% $NH_{3\,(aq)}$ 30%). The product was collected as a yellowish paste (247 mg, 63% yield). ^{1}H NMR (500 MHz, $CDCl_3$): δ 2.59 (s, CH_2CH_2S, 12 H), 2.53 (t, NCH_2, *J* = 6.13 Hz, 12 H), 2,11 (s, SCH_3, 9 H), 1.59 (qn, CH_2, *J* = 12.3 Hz, 6 H). ^{13}C NMR (126 MHz, $CDCl_3$): δ 53.36 (NCH_2CH_2S), 49.23 ($NCH_2CH_2CH_2N$), 32.14 (NCH_2CH_2S), 21.40 ($NCH_2CH_2CH_2N$), 15.81 (SCH_3). ESI-MS$^+$: *m*/*z* $[M+H^+]$ 394.2478 (found); 394.2379 (calculated for $C_{18}H_{40}N_3S_3$).

1,4,7,10-Tetrakis(2-(methylsulfanyl)ethyl)-1,4,7,10-tetrazacyclotridecane (**TRI4S**)**.** 1,4,7,10-Tetraazacyclotridecane (448 µL, 1.0 mmol, 1.0 eq.) and K_2CO_3 (898 mg, 6.5 mmol, 6.5 eq.) were added to CH_3CN (15 mL) in a pressure tube flushed with nitrogen. 2-chloroethyl methyl sulfide was added to the reaction mixture (448 µL, 4.5 mmol, 4.5 eq.) and the pressure tube was heated to 60°C under stirring for 24 hours. The mixture was then evaporated under reduced pressure and the product was purified by flash column chromatography on silica (eluent $CHCl_3$: CH_3OH 9 : 1 + 0.5% $NH_{3\,(aq)}$ 30%). The product was collected as a yellowish paste (182 mg, 38% yield). ^{1}H NMR (500 MHz, $CDCl_3$): δ 2.73-2.58 (m, 32 H, CH_2), 2.169 (s, 6 H, SCH_3), 2.167 (s, 6 H, SCH_3), 1.63 (t, *J* = 12.30 Hz, 2 H,

[‡] Analytical and preparative HPLC of DO4S4Me were performed on a Shimadzu LC20 HPLC-system equipped with a prominence UV-Vis detector, FRC-10A fraction collector, and a Shimadzu 2020 ESI-MS detector. For analytical and preparative HPLC a ReprosilPur120 ODS-3 3 µm 150 Å ~ 3 mm column and a Reprosil-Pur 120 ODS-3 5 µm 30 Å ~ 20 mm column were used, respectively. The methods use a binary gradient with solvent A, water + 0.1% TFA, and solvent B, 90% CH_3CN + 10% water + 0.085% TFA. Analytical method: flow rate, 1.0 mL/min; oven temperature 40°C; UV set to 254 and 280 nm; gradient, 2 min at 5% B followed by a gradient over 4 min from 5% B to 100% B. After 8 min, a gradient from 100% B to 5% B over 1 min followed. These conditions were kept constant for another 7 min. Preparative method: flow rate, 10 mL/min; oven temperature 40°C; UV set to 254 and 280 nm; gradient, 2 min at 5% B followed by a gradient over 7 min from 5% B to 100% B. After 7 min, a gradient from 100% B to 5% B over 1 min followed. These conditions were kept constant for another 2 min. ESI-MS was set at a positive mode and mass spectra were recorded in the 100−1500 *m*/*z* range. A fraction collector was set to the compound mass and a sample volume of 5-10 mL *per* fraction was collected.

$NCH_2\underline{CH_2}CH_2N$). ^{13}C NMR (126 MHz, $CDCl_3$): δ 54.98 (CH_2), 54.58 (CH_2), 52.46 (CH_2), 52.35 (CH_2), 51.63 (CH_2), 50.95 (CH_2), 31.89 (CH_2SCH_3), 31.65 (CH_2SCH_3), 23.35 ($NCH_2\underline{CH_2}CH_2N$), 15.86 ($SCH_3$). ESI-$MS^+$: *m*/*z* [$M+H^+$] 483.2784 (found); 483.2678 (calculated for $C_{21}H_{47}N_4S_4$).

1,4,8,11-Tetrakis(2-(methylsulfanyl)ethyl)-1,4,8,11-tetrazacyclotetradecane (**TE4S**)**.** 1,4,8,11-Tetraazacyclotetradecane (200 mg, 1 mmol, 1.0 eq.) and K_2CO_3 (1.17 g, 8.5 mmol, 8.5 eq.) were added to CH_3CN (15 mL) in a pressure tube flushed with nitrogen. 2-chloroethyl methyl sulfide was added to the reaction mixture (528 µL, 5.3 mmol, 5.3 eq.) and the pressure tube was heated to 60°C under stirring for 24 hours. The mixture was then evaporated under reduced pressure and the product was purified by flash column chromatography on silica (eluent $CHCl_3$: CH_3OH 9 : 1 + 0.5% $NH_{3\,(aq)}$ 30%). The product was collected as a yellowish paste (211 mg, 42% yield). ^1H NMR (500 MHz, $CDCl_3$): δ 2.81-2.69 (m, 32 H, CH_2), 2.22 (s, 12 H, SCH_3), 1.77 (qn, *J* = 13.80 Hz, 4 H, $NCH_2\underline{CH_2}CH_2N$). ^{13}C NMR (126 MHz, $CDCl_3$): δ 54.56 (CH_2), 51.22 (CH_2), 50.39 (CH_2), 31.23 (CH_2SCH_3), 23.01 ($NCH_2\underline{CH_2}CH_2N$), 14.46 ($SCH_3$). ESI-$MS^+$: *m*/*z* [$M+H^+$] 497.2935 (found); 497.2835 (calculated for $C_{22}H_{49}N_4S_4$).

2.3.2 Potentiometric Titrations

A Metrohm 715 Dosimat burette and a Metrohm 713 pH-meter were used for the automatic titrations. All solutions were prepared by using ultrapure water (Millipore Milli-Q/plus or Purelab Chorus, Veolia). The samples in the potentiometric cell (3 mL) were thermostated at 25.0 ± 0.1°C with a Haake F3 cryostat, and CO_2 was completely removed by bubbling purified nitrogen for ~ 15 min before the measurements. A 0.1 M HNO_3 solution was prepared from the concentrated one (Aristar - VWR Chemicals, 69%) and standardized against Na_2CO_3 (Aldrich, 99.95 - 100.5%). The HNO_3 solution was used to calibrate the glass electrode (Hamilton pH 0 - 14) before each titration and to standardize the 0.1 M NaOH (Fluka, 99% min) solutions. The latter were protected against carbonatation, and each NaOH solution was used for a maximum of three weeks.

The ligand stock solutions were prepared by dissolving each compound in water at a concentration of ~ $3\cdot10^{-3}$ M, and HNO_3 (C_{H^+} ~ $4.2\cdot C_L$) was co-added to facilitate the solubilization and avoid carbonatation. Water solubility of the studied ligands depends on pH, and in all cases except DO2A2S minimal values occur at basic (> 10) pH values, where solubility is ~ $1\cdot10^{-3}$ M for DO4S, DO3S, and DO3SAm, and ~ $5\cdot10^{-4}$ M for DOT-*n*-Bu. The water solubility for DO2A2S is larger than $1\cdot10^{-3}$ M at any pH. The solubility constants (K_s) of the deprotonated ligand forms (L) were estimated from the pH at which precipitation starts

and from the stoichiometric ligand concentration. Results for TACD3S, TRI4S and TE4S were $1.5 \cdot 10^{-4}$ M, $1.9 \cdot 10^{-4}$ M and $1.3 \cdot 10^{-4}$ M, respectively. The stability of the ligands at room temperature in aqueous solutions with and without added HNO_3 and $NaNO_3$ 0.15 M was confirmed by NMR, ESI-MS and UV-Vis measurements performed up to three weeks after solution preparation. All solutions were stored in the fridge (4°C) when not in use. NaOH was used to titrate all solutions, added in the cell at ligand concentrations ranging from $7 \cdot 10^{-4}$ to $2 \cdot 10^{-3}$ M. At least five independent replicate titrations were performed for each ligand. All solutions contained $NaNO_3$ (Carlo Erba, 99% min) with a total NO_3^- concentration equal to 0.15 M, to keep constant the ionic strength during the measurements. Due to the calibration method, the pH was measured in terms of proton concentration and not of proton activity ($pH = -\log[H_3O^+]$).

2.3.3 UV-Vis Titrations

The absorption spectra of the ligands were recorded on a Cary 60 UV-Vis spectrophotometer (Agilent) in the range from 200 to 800 nm using a 1 cm path length optical Torlon fiber probe or a quartz spectrophotometric cell of 1 cm path length. The pH was measured using a combined glass electrode (Mettler Toledo pH-meter) daily calibrated with commercial buffer solutions (pH 4.01 and 7.01 at 25°C). In highly acidic solutions (pH < 2), the pH was computed from the H^+ concentration ($pH = -\log C_{H^+}$).

2.3.4 NMR Titrations

NMR spectra were collected at 25°C using a 400 MHz Bruker Avance III HD spectrometer or 600 MHz Bruker spectrometer. 3-(Trimethylsilyl) propionic acid (TSP) sodium salt (Sigma Aldrich, 99%) was used as internal reference. The solutions were prepared in D_2O (Sigma Aldrich, 99.9% D) or H_2O + 10% D_2O at a ~ 0.5 - $2 \cdot 10^{-3}$ M concentration. Water signal was suppressed using presaturation or excitation sculpting suppression pulse scheme, respectively.[33] Proper additions of DNO_3 (Aldrich, 65% in D_2O, 99%D) or CO_2-free NaOD (Aldrich, 40% in D_2O, 99.5% D) in D_2O were performed to set the pH. The latter was measured with the same pH-meter and electrode used for potentiometric titrations. In highly acidic solutions (pH < 2), the pH was computed from the H^+ concentration ($pH = -\log C_{H^+}$). In pure D_2O, 0.41 log units were added to the instrumental pH values to account for isotopic effects, *i.e.* pD values instead of pH ones were considered.[34] All data were collected and processed with Topspin 3.5 using standard Bruker processing parameters with Topspin 4.1.1 software.

2.3.5 Data Treatment

The acidity constants of each ligand (pK_a) are referred to the equilibrium $H_hL^{n+} \rightleftharpoons H_{h-1}L^{(n-1)+} + H^+$ and were refined using the least-squares fitting program PITMAP.[35] The water ionization constant (pK_w, $2H_2O \rightleftharpoons H_3O^+ + OH^-$) was calculated by the same program at T = 25°C and I = $NaNO_3$ 0.15 M, and it resulted equal to 13.54 on average. The errors quoted are the standard deviations calculated by the PITMAP program.[35]

2.3.6 Density Functional Theory Calculations

All DFT calculations were performed with Amsterdam Density Functional (ADF) software.[36–38] The chosen exchange-correlation density functional is the general gradient approximation (GGA) OPBE,[39,40] and the scalar relativistic effects have been included with the zeroth-order regular approximation (ZORA).[41–43] This approach has been adopted in view of studying the heavy metal complexes of the ligands since it is not much more computationally demanding than non-relativistic calculations. OPBE potential has been successfully used to study the energetics and the reaction mechanisms of organic compounds.[44–46] The combined basis sets are uncontracted sets of Slater-type orbitals (STOs): geometry optimizations were carried out with the double-ζ quality basis set augmented with one set of polarization functions on each atom (DZP). Frequency calculations were then performed to assess the stationary nature of the minima. The final energy evaluation was done using the triple-ζ quality basis set augmented with two sets of polarization functions on each atom (TZ2P).[47] Frozen core approximation was used in both sets of calculations up to 1*s* for C, N and S. This level of theory is denoted ZORA-OPBE/TZ2P//ZORA-OPBE/DZP.

All calculations were performed in gas-phase and in water; for the latter case, the solvation effects were quantified using the COSMO (COnductor-like Screening MOdel) approach (level of theory: COSMO-ZORA-OPBE/TZ2P//ZORA-OPBE/DZP).[48–51] For water, a solvent-excluding surface was used with an effective radius and relative dielectric constant of 2.94 Å and 8.9, respectively. The empirical parameter in the scaling function in the COSMO equation was set to 0.0. The radii of the atoms were taken to be MM3 radii, divided by 1.2, giving 1.350 Å for H, 1.700 Å for C, 1.792 for S and 1.608 Å for N.[48] Symmetry constrained geometry optimizations were performed as indicated by the point group label in the text.

The protonation constants of selected ligands were calculated with two distinct methods, reported as ‘method 1’ and ‘method 2’, which are based on two different thermodynamic cycles shown in **Scheme 2.5**.[52–55] ‘Method 1’ is the mere dissociation of the acid proton in order to form the conjugate base (no hydronium ions are involved).

From **Scheme 2.5**, eq. 1 is obtained:

$$\Delta G_{aq}=G_{gas}(H^+)+G_{gas}(A^{q-1})G_{gas}(AH^q)+\Delta G_{solv}(H^+)+\Delta G_{solv}(A^{q-1})-\Delta G_{solv}(AH^q)+RT\ln 24.46 \quad (1)$$

where $G_{gas}(H^+)$ = −6.28 kcal/mol based on the statistical thermodynamics and the Sackur-Tetrode derivation, and the contribution $RT\ln 24.46$ is a transformation term required by the change of the gas-phase reference state of 1 atm/L to 1 M in liquid-phase and at 25°C. Then, pK_a is derived from eq. 2:

$$pK_a = \frac{\Delta G_{aq}}{RT\ln 10} \quad (2)$$

'Method 2' (**Scheme 2.5**) considers a water molecule, and the dissociation includes the formation of the hydronium ion. In this case, ΔG_{aq} is computed with eq. 3:

$$\Delta G_{aq}=G_{gas}(H_3O^+)+G_{gas}(A^{q-1})-G_{gas}(AH^q)-G_{gas}(H_2O)+\Delta G_{solv}(H_3O^+)+\Delta G_{solv}(A^{q-1})+\Delta G_{solv}(AH^q) -\Delta G_{solv}(H_2O) \quad (3)$$

The value of pK_a is then derived by eq. 4:

$$pK_a = \frac{\Delta G_{aq}}{RT\ln 10} - \log[H_2O] \quad (4)$$

The log[H_2O] term must be added because of the definition of the K_a, here expressed using the hydronium ion instead of the proton H^+. Both $\Delta G_{solv}(H_3O^+)$ and $\Delta G_{solv}(H_2O)$ were obtained by experimental data and the values used in this work are −110.2 kcal/mol and −6.32 kcal/mol, respectively.[52] In 'method 2', the evaluation of pK_a is more accurate than in 'method 1'. This is mainly ascribed to the quality of the thermodynamic data for the hydronium ion (the intrinsic errors are smaller). TD-DFT calculations were carried out on the optimized geometries using all electron QZ4P basis sets for all the atoms. The approximate exchange potential obtained with the statistical averaging of (model) orbital potentials (SAOP) was employed to calculate the excitation energies.[56,57] This functional was successfully employed to study the properties of excited states.[58–60] Solvent effects were taken into account with the Conductor-like Screening Model (COSMO), as implemented in the ADF program. This level of theory is denoted COSMO-ZORA-SAOP/QZ4Pae//ZORA-OPBE/DZP.

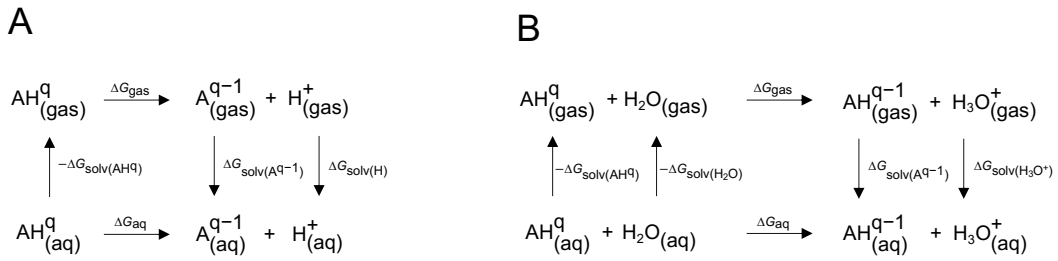

Scheme 2.5. Thermodynamic cycles used to calculate pK_a with method (A) 1 and (B) 2.

2.4 Conclusions

This chapter describes the development of novel macrocyclic ligands that can potentially stabilize medically relevant borderline-soft theranostic radiometals, *i.e.* [$^{103/104/111}$Ag]Ag^+, [$^{64/67}$Cu]$Cu^{2+/+}$, [$^{203/212}$Pb]Pb^{2+} and [$^{197g/m}$Hg]Hg^{2+}, in attempt to circumvent the current shortcomings in their stable *in vivo* chelation.

Two series of sulfur-bearing macrocycles were designed and synthesized, making several modifications on the pendant arms and the polyamine backbone to explore the effect of the donor atoms, ring size, rigidity and presence of chirality on the corresponding metal complexes. Their acid-base equilibria at 25°C in aqueous 0.15 M $NaNO_3$ were investigated employing pH-potentiometry as well as UV-Vis and NMR spectroscopies. DFT calculations were performed to investigate the conformations, the thermodynamics of protonation equilibria and to rationalize the relevant electronic transitions.

In the following chapters, the candidacy of these ligands for nuclear medicine applications will be evaluated by examining their coordination chemistry, assessing their radiolabelling performances with [^{111}Ag]Ag^+ (**Chapter 3**), [^{64}Cu]$Cu^{2+/+}$ (**Chapter 4**), [^{203}Pb]Pb^{2+} (**Chapter 5**) and [^{197}Hg]Hg^{2+} (**Chapter 6**) radionuclides and testing the *in vitro* stability of the resulting radioactive complexes in simulated biological environments.

Author Contributions

M. Tosato designed all the ligands described in this Chapter (except for DO4S4Me which was proposed by Prof. D. Häussinger and R. Vogel). M. Tosato and M. Verona synthesized the first-generation ligands. R. Vogel synthesized DO4S4Me. G. Zanoni synthesized the second-generation ligands. Prof. G. Marzaro and Prof. F. Mancin were responsible for the supervision of the ligands' synthesis. M. Tosato performed the potentiometric titrations with assistance from the Master's students R. Doro and S. Franchi. UV-Vis spectrophotometric and NMR measurements were conducted by M. Tosato and by the Master's students

E. Berberi and S. Franchi. All students worked under the supervision of M. Tosato. Data analysis were performed by M. Tosato. DFT calculations were performed by Dr M. Dalla Tiezza, supervised by Prof. L. Orian. Prof. V. Di Marco oversaw and supervised the study. Both manuscripts were written by M. Tosato.

2.5 References

1 T. Gyr, H. R. Mäcke and M. Hennig, *Angew. Chemie*, 1997, **36**, 2786-2788.

2 L. Dai, C. M. Jones, W. T. K. Chan, T. A. Pham, X. Ling, E. M. Gale, N. J. Rotile, W. C. S. Tai, C. J. Anderson, P. Caravan and G. L. Law, *Nat. Commun.*, 2018, **9**, 857.

3 S. Chilla, C. Henoumont, L. Vander Elst, R. Muller and S. Laurent, *Isr. J. Chem.*, 2017, **57**, 800-808.

4 N. Pfannkuchen, M. Meckel, R. Bergmann, M. Bachmann, C. Bal, M. Sathekge, W. Mohnike, R. P. Baum and F. Rösch, *Pharmaceuticals*, 2017, **10**, 45.

5 I. Lukeš, J. Kotek, P. Vojtíšek and P. Hermann, *Coord. Chem. Rev.*, 2001, **216**, 287-312.

6 S. Hassfjell, K. O. Kongshaug and C. Rømming, *Dalton Trans.*, 2003, 1433-1437.

7 M. Försterová, I. Svobodová, P. Lubal, P. Táborský, J. Kotek, P. Hermann and I. Lukeš, *Dalton Trans.*, 2007, 535-549.

8 F. Cuenot, M. Meyer, E. Espinosa, A. Bucaille, R. Burgat, R. Guilard and C. Marichal-Westrich, *Eur. J. Inorg. Chem*, 2008, **2008**, 267-283.

9 S. Shinoda, *Chem. Soc. Rev.*, 2013, **42**, 1825-1835.

10 T. Fricke, Š. Chrápavá and B. König, *Synth. Commun.*, 2002, **32**, 3595-3602.

11 Y. Habata, Y. Oyama, M. Ikeda and S. Kuwahara, *Dalton Trans.*, 2013, **42**, 8212-8217.

12 Y. Habata, M. Ikeda, S. Yamada, H. Takahashi, S. Ueno, T. Suzuki and S. Kuwahara, *Org. Lett.*, 2012, **14**, 4576-4579.

13 S. Lacerda, M. P. Campello, F. Marques, L. Gano, V. Kubıček, P. Fousková, É. Tóth and I. Santos, *Dalton Trans.*, 2009, 4509-4518.

14 A. Lewin, J. P. Hill, R. Boetzel, T. Georgiou, R. James, C. Kleanthous and G. R. Moore, *Inorganica Chim. Acta*, 2002, **331**, 123-130.

15 S. Lacerda, M. P. Campello, I. C. Santos, I. Santos and R. Delgado, *Polyhedron*, 2007, **26**, 3763-3773.

16 R. Ševčíková, P. Lubal, M. P. C. Campello and I. Santos, *Polyhedron*, 2013, **62**, 268-273.

17 S. Cabani, N. Ceccanti, R. Pardini and M. Tine, *Polyhedron*, 1999, **18**, 3295-3303.

18 R. Hancock, M. Shaikjee and S. Dobson, *Inorganica Chim. Acta.*, 1988, **154**, 10.

19 M. Tosato, M. Verona, R. Doro, M. Dalla Tiezza, L. Orian, A. Andrighetto, P. Pastore, G. Marzaro and V. Di Marco, *New J. Chem.*, 2020, **44**, 8337-8350.

20 G. Anderegg, F. Arnaud, R. Delgado and K. Popov, *Pure Appl. Chem.*, 2005, **77**, 1445-1495.

21 M. Kodama and E. Kimura, *J. Chem. Soc., Dalton Trans.,* 1980, **327**, 327-333.

22 A. P. Leugger, L. Hertli and T. A. Kaden, *Helv. Chim. Acta*, 1978, **61**, 2296-2306.
23 R. Hancock, P. Wade, M. Ngwenya, A. S. De Sousa and K. V. Damu, *Inorg. Chem*, 1990, **29**, 1968-1974.
24 C. K. Rule and V. K. La Mer, *J. Am. Chem. Soc*, 1938, **60**, 1974-1986.
25 J. Desreux, E. Merciny and M. Loncin, *Inorg. Chem*, 1981, **20**, 987-991.
26 E. A. Fehnel and M. Carmack, *J. Am. Chem. Soc*, 1949, **71**, 84-93.
27 M. Tosato, M. Dalla Tiezza, N. V. May, A. A. Isse, S. Nardella, L. Orian, M. Verona, C. Vaccarin, A. Alker, H. Mäcke, P. Pastore and V. Di Marco, *Inorg. Chem.*, 2021, **60**, 11530-11547.
28 L. J. Zompa, *Inorg. Chem.*, 1978, **17**, 2531-2536.
29 M. Kodama and E. Kimura, *J. Chem. Soc., Dalton Trans.*, 1976, 1720-1724.
30 A. Bianchi, M. Micheloni and P. Paoletti, *Coord. Chem. Rev.*, 1991, **110**, 17-113.
31 B. S. Nakani, J. J. B. Welsh and R. D. Hancock, *Inorg. Chem.*, 1983, **22**, 2956-2958.
32 T. Müntener, F. Thommen, D. Joss, J. Kottelat, A. Prescimone and D. Häussinger, *ChemComm*, 2019, **55**, 4715-4718.
33 T. L. Hwang and A. J. Shaka, *J. Magn. Reson. Ser. A*, 1995, **112**, 275-279.
34 A. K. Covington, M. Paabo, R. A. Robinson and R. G. Bates, *Anal. Chem.*, 1968, **40**, 700-706.
35 V. Di Marco, PhD Thesis, Univeristy of Padova, 1998.
36 G. te Velde, F. M. Bickelhaupt, E. J. Baerends, C. Fonseca Guerra, S. J. A. van Gisbergen, J. G. Snijders and T. Ziegler, *J. Comput. Chem.*, 2001, **22**, 931-967.
37 C. Fonseca Guerra, J. G. Snijders, G. te Velde and E. J. Baerends, *Theor. Chem. Acc*, 1998, **99**, 391-403.
38 ADF 2018, SCM, Theoretical Chemistry; Vrije Universiteit, Amsterdam: The Netherlands, http://www.scm.com.
39 N. C. Handy and A. J. Cohen, *Mol. Phys.*, 2001, **99**, 403-412.
40 J. P. Perdew, K. Burke and M. Ernzerhof, *Phys. Rev. Lett.*, 1996, **77**, 3865-3868.
41 E. van Lenthe, E. J. Baerends and J. G. Snijders, *J. Chem. Phys*, 1994, **101**, 9783-9792.
42 E. van Lenthe, E. J. Baerends and J. G. Snijders, *J. Chem. Phys.*, 1993, **99**, 4597-4610.
43 E. van Lenthe, A. Ehlers and E. J. Baerends, *J. Chem. Phys*, 1999, **110**, 8943-8953.
44 M. Bortoli, M. Dalla Tiezza, C. Muraro, G. Saielli and L. Orian, *Molecules*, 2019, **24**, 1250.
45 G. Ribaudo, M. Bellanda, I. Menegazzo, L. P. Wolters, M. Bortoli, G. Ferrer-Sueta, G. Zagotto and L. Orian, *Chem. Eur. J*, 2017, **23**, 2405-2422.
46 F. Zaccaria, L. P. Wolters, C. F. Guerra and L. Orian, *J. Comput. Chem.2*, 2016, **37**, 1672-1680.
47 E. van Lenthe and E. J. Baerends, *J. Comput. Chem.*, 2003, **24**, 1142-1156.
48 N. L. Allinger, X. Zhou and J. Bergsma, *J. Mol. Struct. THEOCHEM*, 1994, **312**, 69-83.
49 J. Ho, A. Klamt and M. L. Coote, *J. Phys. Chem. A*, 2010, **114**, 13442-13444.
50 A. V. Marenich, C. J. Cramer and D. G. Truhlar, *J. Phys. Chem. B*, 2009, **113**, 6378-6396.

51 C. C. Pye and T. Ziegler, *Theor. Chem. Acc.*, 1999, **101**, 396-408.

52 D. M. Camaioni and C. A. Schwerdtfeger, *J. Phys. Chem. A*, 2005, **109**, 10795-19797.

53 A. T. P. Carvalho, P. A. Fernandes and M. J. Ramos, *J. Comput. Chem.*, 2006, **27**, 966-975.

54 R. Casasnovas, J. Ortega-Castro, J. Frau, J. Donoso and F. Muñoz, *Int. J. Quantum Chem.*, 2014, **114**, 1350-1363.

55 A. M. Rebollar-Zepeda, T. Campos-Hernández, M. T. Ramírez-Silva, A. Rojas-Hernández and A. Galano, *J. Chem. Theory Comput.*, 2011, **7**, 2528-2538.

56 O. V. Gritsenko, P. R. T. Schipper and E. J. Baerends, *Chem. Phys. Lett.*, 1999, **302**, 199-207.

57 P. R. T. Schipper, O. V. Gritsenko, S. J. A. van Gisbergen and E. J. Baerends, *J. Chem. Phys.*, 2000, **112**, 1344-1352.

58 A. Donoli, A. Bisello, R. Cardena, M. Crisma, L. Orian and S. Santi, *Organometallics*, 2015, **34**, 4451-4463.

59 S. Scuppa, L. Orian, A. Donoli, S. Santi and M. Meneghetti, *J. Phys. Chem. A*, 2011, **115**, 8344-8349.

60 L. Orian, S. Scuppa, S. Santi and M. Meneghetti, *Phys. Chem. Chem. Phys.*, 2013, **15**, 12971.

Chapter 3

Highly Stable Silver(I) Complexes with Polyazamacrocyles Bearing Sulfide Arms: A Step Toward Silver Labelled Radiopharmaceuticals

This chapter is an adaptation of published work, and is reproduced in part, with permission from Tosato, M.; Asti, M.; Dalla Tiezza, M.; Orian, L.; Häussinger, D.; Vogel, R.; Köster, U.; Jensen, M.; Andrighetto, A.; Pastore, P.; Di Marco, V. Highly Stable Silver(I) Complexes with Cyclen-Based Ligands Bearing Sulfide Arms: A Step Towards Silver-111 Labelled Radiopharmaceuticals, *Inorg. Chem.*, **2020**, 59, 10907-10919**,** Copyright 2020 American Chemical Society (https://pubs.acs.org/doi/10.1021/acs.inorgchem.0c01405). This chapter includes also a manuscript in preparation, reproduced in part with the permission from Tosato, M.; Franchi, S.; Köster, U.; Jensen, M.; Dalla Tiezza, M.; Orian, L.; Asti, M.; Di Marco, V. *et al.* From 12- to 14-Member Thioether Functionalized Polyazamacrocycles: Searching for a Chelator to Selectively Complex and Stabilize Theranostic Silver. Expected submission: April 2022.

This research was supported by the ISOLPHARM_Ag and ISOLPHARM_EIRA project funded by the Legnaro National Laboratories of the Italian Institute of Nuclear Physics (*Istituto Nazionale di Fisica Nucleare - Laboratori Nazionali di Legnaro*, INFN-LNL, Italy).

3.1 Introduction

A great deal of progress toward a patient-specific treatment has been made in recent years boosted by the theranostic approach in which the same radiopharmaceutical is used to diagnose and subsequently treat cancer. Among the candidate theranostic radiometals, silver is regarded to be very promising as it possesses a combination of isotopes capable of both imaging and therapy. Silver-111 (^{111}Ag, $t_{1/2}$ 7.47 d) could be used for cancer therapy due to its medium-energy β^- emission ($E_{\beta^-, max}$ 1.04 MeV) and for associated SPECT imaging thanks to its two low energy γ rays (E_γ 245.4 keV, I_γ 1.24%; E_γ 342.1 keV, I_γ 6.7%).[1–5] On the other hand, the β^+-emitters silver-103g (^{103g}Ag, $t_{1/2}$ 65.7 min, β^+ 27%, EC 73%) and silver-104g (^{104g}Ag, $t_{1/2}$ 69.2 min, β^+ 15%, EC 85%) could be exploited as PET imaging analogues.[1,6] Furthermore, the relatively long $t_{1/2}$ of ^{111}Ag matches well with the biological half-lives of antibodies (2-3 weeks), making this isotope interesting for use in radioimmunotherapy.[7,8]

The production of ^{111}Ag can be accomplished *via* neutron irradiation of palladium targets, to give the short-lived palladium-111 (^{111}Pd, $t_{1/2}$ 23.4 min) by ^{110}Pd(n,γ)^{111}Pd reaction.[5,9,10] Short-lived ^{111}Pd then decays to ^{111}Ag.[3] For the production of ^{111}Ag from natural palladium, the neutron capture of palladium-108 (^{108}Pd) to palladium-109 (^{109}Pd) with the subsequent decay to stable silver-109 (^{109}Ag) is the most important parasitic reaction since this isotope limits the final specific activity. To yield no-carrier-added ^{111}Ag, enriched palladium-110 (^{110}Pd) targets must be used. Direct production *via* ^{110}Pd(d,n)^{111}Pd is also possible with access to medium energy deuteron beams (10-20 MeV).[1] As an alternative route, the ^{111}Ag production *via* Isotope Separation On-Line (ISOL) technique is currently investigated at the Legnaro National Laboratories of the Italian Institute of Nuclear Physics in the framework of the ISOLPHARM project.[11,12] Moreover, ^{111}Ag can also be recovered from irradiated thorium targets during the production of the medically-interesting α-emitter actinium-225 (^{225}Ac).[5]

Only limited preclinical applications of ^{111}Ag are reported in the literature so far: Chattopattay *et al.* examined the therapeutic management of arthritis with ^{111}Ag-labelled hydroxyapatite and Lapi *et al.* investigated the use of ^{111}Ag as a radiotracer to determine the biodistribution and stability of silver-based antimicrobials.[2,3] However, no previous research has investigated ^{111}Ag for application in nuclear medicine: a key step to attaining this goal is to develop suitable ligands that can act as BFCs forming sufficiently stable Ag^+ complexes under *in vivo* conditions. As reported in **Chapter 1** and **Chapter 2**, tri- and tetraazamacrocyclic ligands with coordinating pendant arms (*e.g.*, DOTA, DO2A, CB-DO2A, NOTA, *etc.*[13–17]) exhibit both high thermodynamic stability and kinetic inertness towards several metal ions due to their constrained geometries and partially preorganized coordination sites, and have been widely investigated as BFCs for a large variety of hard radionuclides so far (*e.g.*, lutetium-177, gallium-68, indium-111 *etc.*).[18,19] However, these

ligands are not predicted to be the chelators of election for Ag^+ since its soft character would prevent the formation of stable coordination bonds with hard-donor groups like the carboxylates of DOTA and similar analogues. For this purpose, the series of macrocyclic chelators described in **Chapter 2** was designed to form highly stable complexes with soft metal cations and are considered herein as potential Ag^+ chelating agents.[20]

In this chapter, the complexation behaviour of the first- and second-generation ligands toward Ag^+ is discussed. DOTA and the unsubstituted macrocycles were also included for comparison, to evaluate the effects of the introduction of sulfanyl side chains on the properties of the resulting Ag^+ complexes and the role of sulfur donors in the metal coordination, and because their complex formation with Ag^+ has been hitherto never reported in aqueous solution (data are available only for cyclen and only in some organic solvents).[21] Experimental studies were performed by pH- and pAg-potentiometry, UV-Vis and NMR (1D ^{1}H-NMR and 2D ^{1}H-^{1}H COSY/TOCSY, NOESY, ^{1}H-^{13}C HMQC/HSQC) spectroscopies. DFT calculations provided insight into the structure of selected Ag^+ complexes. In addition to the non-radioactive chemistry, radiolabelling studies were performed to assess the ability of the first- and second-generation macrocycles to complex [^{111}Ag]Ag^+ under extremely low concentrations. Transmetallation, stability in phosphate-buffered saline (PBS) and competition experiments with biologically relevant metal cations were also conducted. The selectivity of the ligands towards Ag^+ was evaluated through competition with stable Pd^{2+} and Cd^{2+}. The former can be an impurity originating from the target material when ^{111}Ag is produced *via* the ^{110}Pd(n,γ)^{111}Pd reaction while the latter represents the main isobaric impurity of ISOL-produced ^{111}Ag. Lastly, to unambiguously evaluate the potential of these ligands as chelating agents in radiopharmaceutical design, the *in vitro* human serum stability assays of the corresponding [^{111}Ag]Ag^+ complexes were also accomplished.

3.2 Results and Discussion

3.2.1 Thermodynamics of Silver Complexes with First-Generation Ligands

The equilibrium constants of Ag^+ complexes with the first-generation ligands were determined by potentiometry and UV-Vis spectroscopy and are summarized in **Table 3.1** while the corresponding distribution diagrams are shown in **Figure 3.1**.[§] The formation constants for DO3SAm, DO2A2S, DOTA, and cyclen were all accessible by pH-potentiometric titrations, whereas additional potentiometric measurements with silver electrode were required to obtain reliable equilibrium constants for DO4S, DO4S4Me and

[§] Preliminary NMR measurements of solution containing Ag^+ and the ligands at different pH ($C_{Ag^+} = C_L = 1 \cdot 10^{-3}$ M) demonstrated that all the complexation reactions were quickly enough to be investigated by potentiometry.

DO3S due to the very high complex stability which caused the complexation to start at very low pH (< 2). This result was attributed to the absence of competitive protonation equilibria on SCH_3, allowing this functional group to strongly bind metal ions also at very acidic pH. By increasing the pH, the successive formation of the monoprotonated, *i.e.* $[AgHL]^{2+}$, and the deprotonated complexes, *i.e.* $[AgL]^{+}$, for DO4S, DO4S4Me, DO3S, DO3SAm takes place.** For DO2A2S, also the diprotonated complex, *i.e.* $[AgH_2L]^{+}$, was found. Diagrams change with overall ligand and metal concentration, but at physiological pH, the main complex is always the fully deprotonated one.

The equilibrium constants for Ag^{+}-DO4S, Ag^{+}-DO4S4Me and Ag^{+}-DO2A2S complexes were also confirmed by UV-Vis spectrophotometric titrations (**Table 3.1**). Representative UV-Vis spectra of solutions containing ligand and Ag^{+} at various pH values are reported in **Figure 3.2**.

Table 3.1. Equilibrium constants (logβ) and pAg^{+} values for the complexes formed between Ag^{+} and the first-generation ligands in I = $NaNO_3$ 0.15 M at T = 25°C. If not differently stated, values were obtained by pH-potentiometric titrations. The reported uncertainty was obtained by the fitting procedure and represents one standard deviation unit.

Ligand	Equilibrium reaction [a]	logβ				pAg^{+} [d]
DO4S	$Ag^{+} + H^{+} + L \rightleftharpoons [AgHL]^{2+}$	21.03	±	0.04	[b]	14.5
	$Ag^{+} + L \rightleftharpoons [AgL]^{+}$	16.51	±	0.03		
		16.9	±	0.1	[c]	
DO4S4Me	$Ag^{+} + H^{+} + L \rightleftharpoons [AgHL]^{2+}$	20.76	±	0.01	[b]	15.3
	$Ag^{+} + L \rightleftharpoons [AgL]^{+}$	18.00	±	0.07		
		17.9	±	0.2	[c]	
DO3S	$Ag^{+} + H^{+} + L \rightleftharpoons [AgHL]^{2+}$	22.09	±	0.04	[b]	13.3
	$Ag^{+} + L \rightleftharpoons [AgL]^{+}$	16.12	±	0.01		
		15.81	±	0.09	[c]	
DO3SAm	$Ag^{+} + H^{+} + L \rightleftharpoons [AgHL]^{2+}$	20.16	±	0.05		12.9
	$Ag^{+} + L \rightleftharpoons [AgL]^{+}$	15.48	±	0.05		
DO2A2S	$Ag^{+} + 2H^{+} + L^{2-} \rightleftharpoons [AgH_2L]^{+}$	22.82	±	0.09		11.2
		23.2	±	0.5	[c]	
	$Ag^{+} + H^{+} + L^{2-} \rightleftharpoons [AgHL]$	19.63	±	0.06		
		19.6	±	0.3	[c]	
	$Ag^{+} + L^{2-} \rightleftharpoons [AgL]^{-}$	13.71	±	0.06		
DOTA	$Ag^{+} + H^{+} + L^{4-} \rightleftharpoons [AgHL]^{2-}$	16.6	±	0.2		6.9
	$Ag^{+} + L^{4-} \rightleftharpoons [AgL]^{3-}$	9.1	±	0.2		
Cyclen	$Ag^{+} + L \rightleftharpoons [AgL]^{+}$	6.60	±	0.02		6.0

[a] L denotes the ligand in its totally deprotonated form.
[b] Obtained by pAg-potentiometric titrations.
[c] Obtained by UV-Vis spectrophotometric titrations.
[d] pAg values calculated at $C_{Ag^{+}} = 1 \cdot 10^{-6}$ M, $C_L = 1 \cdot 10^{-5}$ M at pH 7.4.

** *Caveat!* The formalism M-L (where L is a general ligand) will be used throughout the text to indicate the complex formed by the metal cation M and the ligand L, while the formula $[M_m(H_hL_l)]^{n-}$ will refer to the single species with the specified stoichiometry and protonation state.

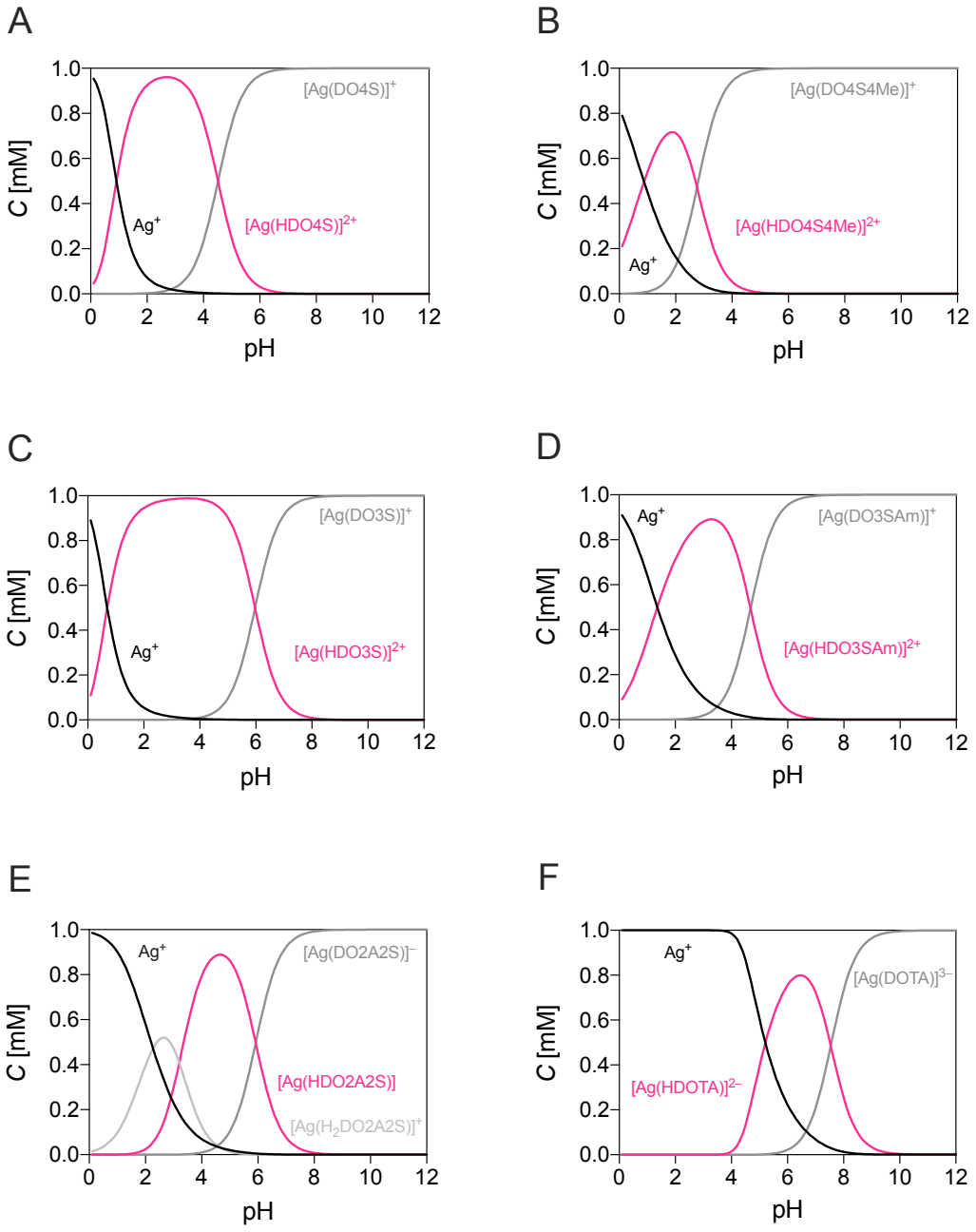

Figure 3.1. Distribution diagrams of (A) Ag^+-DO4S, (B) Ag^+-DO4S4Me, (C) Ag^+-DO3S, (D) Ag^+-DO3SAm, (E) Ag^+-DO2A2S and (F) Ag^+-DOTA at $C_{Ag^+} = C_L = 1 \cdot 10^{-3}$ M.

For all ligands, the presence of Ag^+ causes a bathochromic and hyperchromic effect on the absorption band, which is accountable for the complexation event and was attributed to a charge-transfer (CT) transition. The UV-Vis band changed also according to the proton content of the complexes, exhibiting a redshift and a general absorbance increase when the pH becomes more basic. The absorbance *vs*. pH graphs at selected wavelengths are shown

in **Figure 3.2**. It is noteworthy that these graphs well resemble the distribution diagrams of the deprotonated complex ([AgL]) of all ligands. This indicates that the main chromophore at the considered wavelength corresponds to [AgL] (*e.g.*, for Ag^+-DO4S $\varepsilon_{(250\ nm,\ pH\ 4)} \approx 1.8 \cdot 10^3$ L/mol·cm and $\varepsilon_{(250\ nm,\ pH\ 10.00)} \approx 2.2 \cdot 10^3$ L/mol·cm; for Ag^+-DO2A2S $\varepsilon_{(250\ nm,\ pH\ 10.08)} \approx 2.4 \cdot 10^3$ L/mol·cm and $\varepsilon_{(250\ nm,\ pH\ 4.35)} \simeq 1.2 \cdot 10^3$ L/mol·cm).

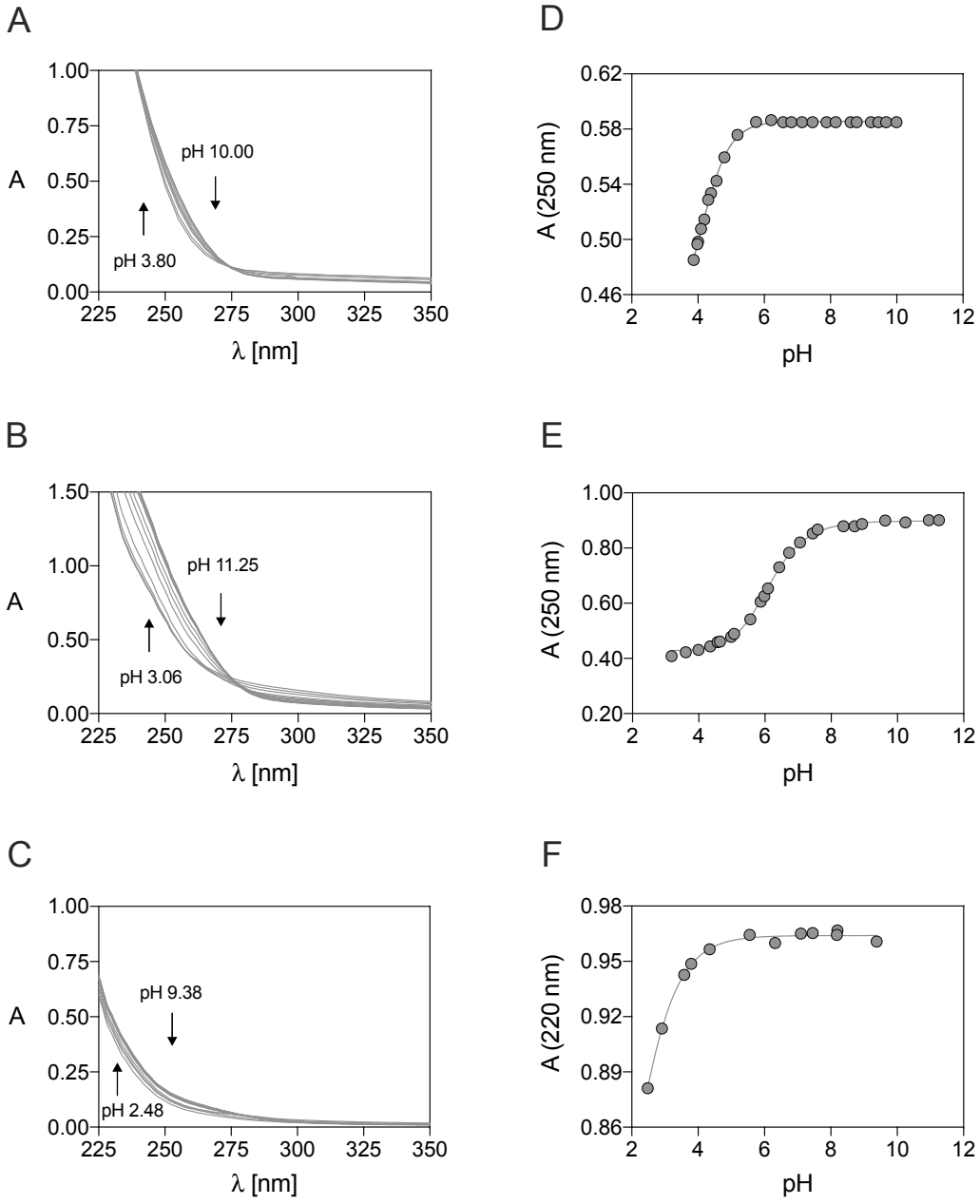

Figure 3.2. UV-Vis spectra of (A) Ag^+-DO4S ($C_{Ag^+} = C_{DO4S} = 2.7 \cdot 10^{-4}$ M), (B) Ag^+-DO2A2S ($C_{Ag^+} = C_{DO2A2S} = 3.7 \cdot 10^{-4}$ M), (C) Ag^+-DO4S4Me ($C_{Ag^+} = C_{DO4S4Me} = 1.14 \cdot 10^{-4}$ M) and (D, E, F) corresponding experimental points and fitting line of absorbance *vs.* pH.

3.2.2 Thermodynamics of Silver Complexes with Second-Generation Ligands

Cyclam and some derivatives bearing methyl groups on the nitrogen atoms and/or on the carbon backbone, as well as other 14- or 15-member tetraazamacrocyclic ligands, can stabilize the unusual oxidation state of silver, *i.e.* Ag^{2+}, through the $2Ag^{+} + L \rightleftharpoons [AgL]^{2+} + Ag$ disproportionation reaction.[22–27] While this ability is not preserved in cyclen (*vide supra*), TACD and TRI seem to be capable to stabilize the +2-oxidation state. Indeed, at pH > 5, 1:1 metal-to-ligand solutions became orange-to-brown upon the addition of Ag^{+}, with the subsequent formation of a grey-to-brown precipitate. UV-vis spectra of Ag-TACD or Ag-TRI at 2:1 metal-to-ligand molar ratio shown two absorption maxima at λ_{max} ~ 255 and 431 nm for the former and λ_{max} ~ 283 and 430 nm for the latter, consistent with the presence of Ag^{2+} complexes. Thus, these systems were not studied further as this peculiarity hampered the determination of the stability constants of their Ag^{+} complexes. Contrarily, neither colour change nor the formation of metallic silver were detected with the second-generation ligands. In these cases, the absence of any electronic absorption in the visible region combined with the successful NMR characterization (*vide infra*) demonstrated that the introduction of sulfanyl side chains avoids the stabilization of Ag^{2+}, thus preventing dismutation of Ag^{+} to Ag^{2+} and Ag. The formation constants of Ag^{+} complexes with the second-generation ligands were therefore determined by potentiometry. UV-Vis spectrophotometric competitive titrations with Cu^{2+} and pAg-potentiometric measurements were also employed with TACD3S and TRI4S (**Figure B1** - **Appendix B**). This was due to the very high complex stability of Ag^{+}-TACD3S and Ag^{+}-TRI4S which caused the complexation to start at very low pH as previously found with some first-generation ligands. The obtained logβ are summarized in **Table 3.2** while the corresponding distribution diagrams are shown in **Figure 3.3**.[††]

Similarly to the cyclen analogue, *i.e.* DO4S, TRI4S and TE4S form the monoprotonated and the deprotonated complexes ($[AgHL]^{2+}$ and $[AgL]^{+}$) while for TACD3S also the diprotonated and the hydroxo-complex ($[AgH_2L]^{3+}$ and $[AgL(OH)]$[‡‡]) were detected. It is readily apparent that the increase of the ring size while maintaining the same number of nitrogen donors in TRI4S and TE4S does not affect the speciation of the resulting Ag^{+} complexes. On the other hand, with TACD3S, the different number and the spatial arrangement of the ring's nitrogen donors might allow the formation of a lower-repulsion conformation of the diprotonated complex, $[AgH_2L]^{3+}$, with respect to 4N macrocycles, thus justifying its detection.

[††] Similarly to the first-generation ligands, preliminary NMR measurements of solution containing Ag^{+}-TACD3S, Ag^{+}-TRI4S and Ag^{+}-TE4S at different pH ($C_{Ag^+} = C_L = 1 \cdot 10^{-3}$ M) were performed to assess the kinetic of the complexation reactions. All the reactions resulted fast, taking no longer than a few minutes.

[‡‡] [Ag(TACD3S)(OH)] is an electrically neutral species that might result less water-soluble than the analogous charged complexes: its existence is thus consistent with the formation of a precipitate observed at pH > 9.

Table 3.2. Equilibrium constants (logβ) and pAg^+ for the complexes formed between Ag^+ and the second-generation ligands in I = $NaNO_3$ 0.15 M at T = 25°C. If not differently stated, values were obtained by pH-potentiometric titrations. The reported uncertainty was obtained by the fitting procedure and represents one standard deviation unit.

Ligand	Equilibrium	logβ				pAg^+ [(d)]
TACD3S	$Ag^+ + L + 2H^+ \rightleftharpoons [AgH_2L]^{3+}$	20.79	±	0.09	[(a)]	10.6
	$Ag^+ + L + H^+ \rightleftharpoons [AgHL]^{2+}$	17.93 18.2	± ±	0.06 0.2	[(b)]	
	$Ag^+ + L \rightleftharpoons [AgL]^+$	11.78 12.4	± ±	0.06 0.1	[(b)]	
	$Ag^+ + L + H_2O \rightleftharpoons [AgL(OH)] + H^+$	2.3	±	0.1		
TRI4S	$Ag^+ + L + H^+ \rightleftharpoons [AgHL]^{2+}$	20.53	±	0.07	[(c)]	12.4
	$Ag^+ + L \rightleftharpoons [AgL]^+$	13.8 13.85	± ±	0.1 0.09	[(b)]	
TE4S	$Ag^+ + L + H^+ \rightleftharpoons [AgHL]^{2+}$	20.06	±	0.05		10.3
	$Ag^+ + L \rightleftharpoons [AgL]^+$	12.89	±	0.03		

[(a)] Obtained by pAg-potentiometry.
[(b)] Obtained by NMR spectroscopy.
[(c)] Obtained by Ag^+-Cu^{2+} UV-Vis spectrophotometric competition.
[(d)] pAg values calculated at $C_{Ag^+} = 1 \cdot 10^{-6}$ M, $C_L = 1 \cdot 10^{-5}$ M at pH 7.4.

3.2.3 Comparison of the Thermodynamic Stability of Silver Complexes with First- and Second-Generation Ligands

As already reported, one of the features that a ligand has to possess to represent a promising chelator for nuclear medicine applications is the formation of extremely stable complexes with the radionuclide of interest. In order to compare the Ag^+ complex stability of the examined ligands, the thermodynamic data were used to compute the pAg^+ values, *i.e.* the cologarithm of free metal concentration ($pAg^+ = -\log[Ag^+]$): the higher the pAg^+, the stronger the complex.[28–30]

The pAg^+ values determined at physiological pH values are reported in **Table 3.1** - **3.2** and graphically compared in **Figure 3.4**. According to these values, DO4S4Me forms the most stable complexes with Ag^+, especially at physiological pH.

A relatively minor pAg^+ difference of about one log unit can be observed also between DO4S and DO3S, which can be assigned to a statistical effect taking place in presence of the fourth thioether chain which promotes the complexation in the former. The introduction of the amide pendant arm into the DO3S frame does not remarkably reduce the thermodynamic stability of the complex (the pAg^+ of DO3SAm is 0.4 log units lower than that of DO3S), suggesting that the pendant arm, linking the chelator to the targeting moiety, only slightly affects the complex formation.

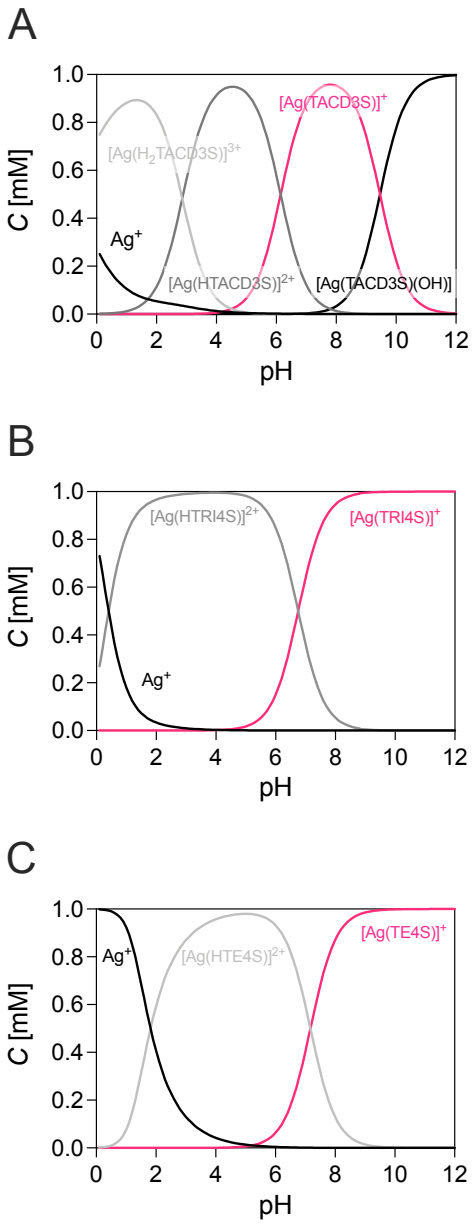

Figure 3.3. Distribution diagrams of (A) Ag^+-TACD3S, (B) Ag^+-TRI4S and (C) Ag^+-TE4S at $C_{Ag^+} = C_L = 1 \cdot 10^{-3}$ M.

The ligand functionalized with two sulfanyl arms, *i.e.* DO2A2S, forms Ag^+ complexes which are around 2 log units less stable than those bearing three arms, *i.e.* DO3S and DO3SAm, but its pAg^+ values at physiological pH are still 4-5 log units larger than those of DOTA and cyclen. The trend shown in **Figure 3.4** strongly suggests that complex stability is ruled by the number of sulfide-donating groups appended on the cyclen moiety.

Variation of the ring dimension and the nitrogen donor array (*i.e.* number of C atoms between two N of the ring) has a noteworthy effect on the complexes' stability. The progressive increase of the ring size from a 12- to a 14-member ring, *i.e.* from DO4S to TE4S, is

unfavourable in terms of the stability of the resulting Ag^+ complexes, as the pAg^+ of TRI4S and TE4S are 2 and 4 orders of magnitude lower than that of DO4S, respectively. This could be related to the worst complementary between the size of the silver cation and increasingly larger ring cavities, thus resulting in the observed stability drop.

A stability reduction was also obtained with TACD3S (**Figure 3.4**). It is worth to note that, Ag^+-TACD3S complexes are less stable than Ag^+-DO3S: as these two ligands possess the same number of sulfur donors, it appears that the number of amines groups and their spatial arrangement are the structural features that alter the stability of corresponding Ag^+ complexes.

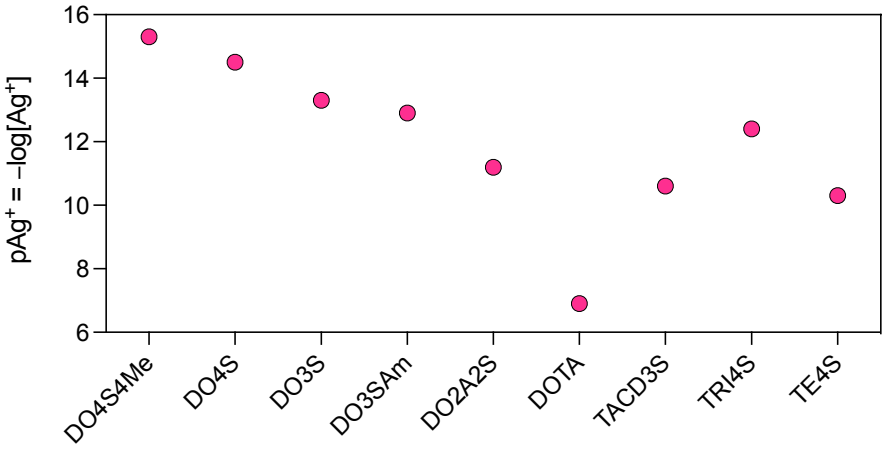

Figure 3.4. Comparison of the pAg^+ values at physiological pH for the Ag^+ complexes formed with the first- and second-generation ligands.

3.2.4 Structure of Ag^+ Complexes with First-Generation Ligands: DFT Calculations

DFT calculations have been carried out for the $[AgL]^+$ complexes formed by DO4S, DO4S4Me, and DO3S, and for the $[AgHL]^{2+}$ complex formed by DO4S. DO4S and DO3S were considered to evaluate the coordination role of the sulfanyl side chains while, for DO4S4Me, a different stiffness of the cyclen backbone is expected, due to the presence of methyl groups. The crystallographic structure deposited with the NAXJIF identifier in the Cambridge Structural Database (CSD) was used as DO4S starting structure.[31] DO3S and DO4S4Me initial geometries were obtained by modifying DO4S. The obtained results are shown in **Figure 3.5**.

It is well known that in general Ag^+ forms linear complexes. However, in the $[AgL]^+$ complexes formed by DO4S, DO4S4Me, and DO3S, the metal *d* molecular orbitals (MO) energy pattern closely resembles the distinctive order typical of a distorted square-planar coordination system, where two pnictogen and two chalcogen atoms act as Lewis bases and

each ligand atom behaves like a 2-electron donor system. Furthermore, an in-depth analysis of the correlation diagrams and the evaluation of the metal-ligand overlap integrals show a variation of the interaction strength between the ligands and the Ag^+ center symmetry-adapted fragment orbitals (SFO). The stronger interaction unravels the nature of the principal bonding force, involving the empty 5*s* Ag orbital and four *p* orbitals (**Figure 3.5**) belonging to two opposite-side N atoms (*i.e.* N_1 and N_7 on the cyclen ring) and the corresponding S atoms. The fragments' combination forms the inner valence HOMO−7 (Ag^+-DO4S, Ag^+-DO4S4Me), HOMO−8 (Ag^+-DO3S) bonding and LUMO+2 (Ag^+-DO4S, Ag^+-DO3S), LUMO+3 (Ag^+-DO4S4Me) anti-bonding pair. HOMO and LUMO have also a smaller contribution formed from the combination of a ligand SFO due to the other two opposite N atoms (N_4 and N_{10} on the cyclen ring), and the 5*s* empty orbital of Ag^+ (**Figure 3.5**). Due to a poorer overlap and a higher energy gap, the involved interaction is less significant compared to the former one and therefore the arms involving these orbitals do not effectively coordinate the metal center. For these systems, the valence orbitals show no noteworthy combination between metal and ligand but are mainly formed by the almost unperturbed *d* metal orbitals and a few distant orbitals on the ligand pendants.

The $[AgHL]^{2+}$ complex formed by DO4S shows a slightly different bonding mode, because, after the insertion of a proton, the metal ion slips away from the center of the cyclen ring increasing the distortion of the original square-planar coordination. The bonding and anti-bonding pair are formed by the HOMO−7 and LUMO, respectively. The ligand contribution is similar to the $[AgL]^+$ form (**Figure 3.5**) but with a reduced contribution of both the chalcogens. However, in this case, Ag^+ is closer to the N_4 nitrogen and this can contribute significantly through a dumbbell-shaped orbital pointing directly towards the silver atom.

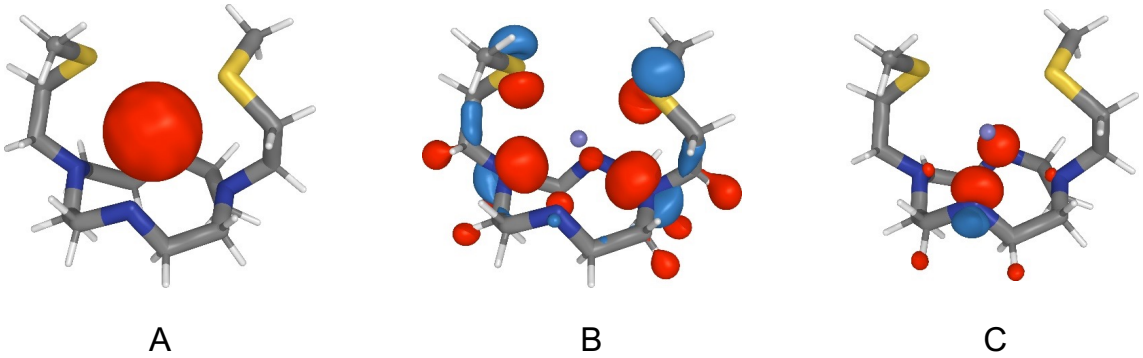

Figure 3.5. Significant symmetry-adapted fragment orbitals (SFO) for the $[AgL]^+$ complex formed by DO4S. The extended sulfide sidearms from N_4 and N_{10} have been hidden for the sake of clarity: (A) SFO representing the 5*s* orbital located on the Ag^+ center, (B) ligand SFO involved in the main bonding orbital and (C) ligand SFO involved in the weaker bonding interaction.

The activation strain analysis (ASA) and the energy decomposition analysis (EDA) have been used to better outline the difference in the bonding nature among the considered ligands in gas-phase (**Table 3.3**). The deformation energies ΔE_{strain} directly reflect the ligand size: the bigger the ligand, the higher the strain. DO3S is more stable in the gas phase because of the reduced strain, but an additional important effect could be delineated upon removal of a non-metal-coordinated sulfanyl pendant arm: the higher electrostatic interaction ΔV_{elstat} contributes to increase the overall stabilizing energy ΔE_{int}. Analogously, the addition of methyl groups in DO4S4Me also contributes to an over-stabilization due to more effective electrostatic interactions. Nevertheless, this effect is counterbalanced in the gas phase by a significant increase in the steric repulsion ΔE_{strain} as reported above. In all three systems, the orbital interaction term ΔE_{oi} does not seem to play a crucial role.

The stability order elucidated experimentally in solution was however reversed, likely because the conformational effects characterizing these systems have been neglected in the calculations. Compared to $[AgL]^+$, in $[AgHL]^{2+}$ a greater ΔE_{int} and a less stabilizing electrostatic interaction ΔV_{elstat} can be observed. This originates from the more unsymmetrical cyclic scaffold due to the formation of an internal H-bond between NH^+ and the opposite N. This feature has been found also in the free ligand and has been already discussed in **Chapter 2**. The higher (less stabilizing) ΔV_{elstat} is mainly caused by the localized charge on the N_{10} nitrogen.

Strain and interaction contributions for $[AgHL]^{2+}$ sum up to a generally more unstable protonated form compared to the deprotonated ones. As a result, the pK_a due to the deprotonation of $[AgHL]^{2+}$ to form $[AgL]^+$ is relatively small (*e.g.*, for DO4S p$K_{a,\,[AgHL]}$ = 4.16 = 21.029 – 16.513, see **Table 3.1**), and it is much smaller than that due to the deprotonation of the free ligand with the same charge +2 (*e.g.*, for DO4S p$K_{a,\,H_2L}$ = 7.29).[20]

Table 3.3. Activation strain analysis (ASA) and energy decomposition analysis (EDA) for the $[AgL]^+$ complexes formed by DO4S, DO4S4Me, and DO3S, and for the $[AgHL]^{2+}$ complex formed by DO4S. All the energies are in kcal/mol.

Ligand	Complex	ΔE	ΔE_{strain}	ΔE_{int}	ΔE_{Pauli}	ΔE_{oi}	ΔV_{elstat}
DO4S	$[AgL]^+$	–98.4	6.7	–105.1	101.6	–82.8	–123.9
DO4S	$[AgHL]^{2+}$	–19.8	11.7	–31.5	121.4	–93.4	–59.5
DO4S4Me	$[AgL]^+$	–97.4	9.2	–106.6	104.9	–84.5	–127.0
DO3S	$[AgL]^+$	–101.8	5.7	–107.5	105.5	–83.1	–129.9

3.2.5 Solution Structure of Ag^+ Complexes with First-Generation Ligands: NMR Investigation

The ^{1}H-NMR spectra of D_2O solutions containing Ag^+ and DO4S in the pD range 2 - 10 are shown in **Figure 3.6** while the spectral data are summarized in **Table B1** (**Appendix B**). At pD > 6.0 all spectra are identical: this finding agrees with thermodynamic results according to which only the $[Ag(DO4S)]^+$ complex exists at neutral-to-basic pH. Based on the integration values and the bidimensional ^{1}H-^{13}C HMQC spectrum (**Figure 3.7**), the singlet at 2.22 ppm and the triplet at 2.84 ppm were assigned to SCH_3 and SCH_2, respectively, whereas the broad singlet centred around at 2.77 ppm was attributed to both ring and arms NCH_2. Spectra are consistent with the formation of a highly symmetric complex as they exhibit only three resonances, as also observed by Mäcke *et al.* for the same complex in organic solvent.[32] Upon the coordination of the metal ion, changes in chemical shifts and coupling patterns of $[Ag(DO4S)]^+$ were observed with respect to the free ligand (**Figure 3.8**).[20] This result, combined with the equivalence of all carbon atoms of the side chains, would suggest that all the four sulfur donor atoms are involved in the coordination of Ag^+.

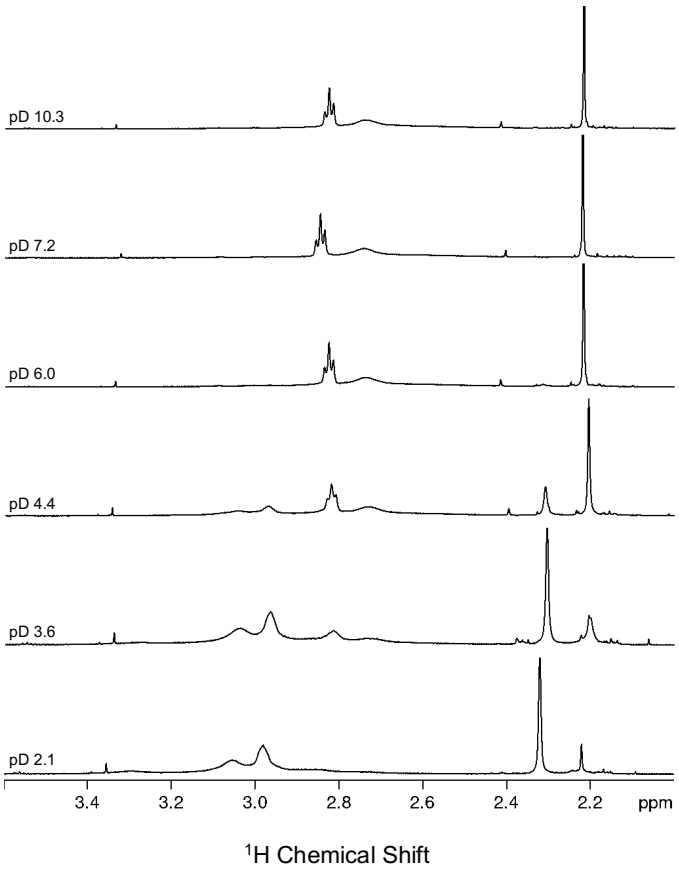

Figure 3.6. Variable-pD ^{1}H NMR spectra of Ag^+-DO4S (600 MHz, T = 25°C, D_2O, $C_{Ag^+} = C_{DO4S} = 1.1 \cdot 10^{-3}$ M).

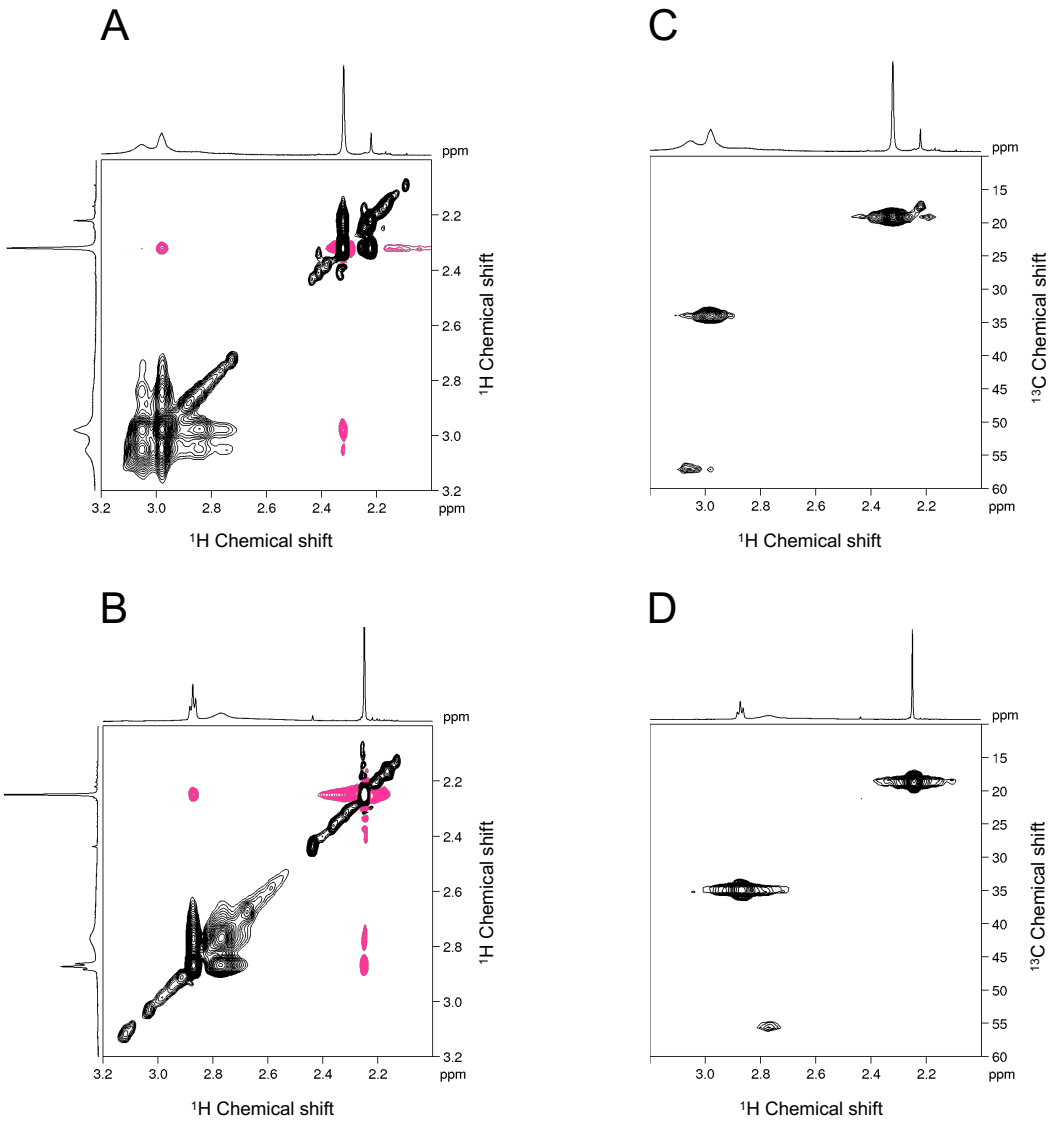

Figure 3.7. NOESY spectrum of (A) $[Ag(HDO4S)]^{2+}$ and (B) $[Ag(DO4S)]^{+}$; ^{1}H-^{13}C HMQC spectrum of (C) $[Ag(HDO4S)]^{2+}$ and (D) $[Ag(DO4S)]^{+}$.

However, according to the DFT calculations (*vide supra*), and to the X-ray crystal structure of $[Ag(DO4S)]^{+}$ obtained by Mäcke *et al*. (**Figure 3.9**), only two sulfur atoms are simultaneously interacting with the Ag^{+} *core* and the coordination is completed by the nitrogen atoms of the heterocyclic ring.[32] Therefore, it is more reasonable to assume that, while in the solid-state only two sulfurs are effectively bound to the metal ion, all four pendant arms are exchanging fast on the NMR timescale thus becoming chemically equivalent in solution. Also, the spatial-coupling in the NOESY spectra of the complex (**Figure 3.7**) is remarkably different with respect to that of the free ligand: while the SCH_3 are close to all functional groups in the unbound ligand, they become coupled only to SCH_2 protons upon the Ag^{+} coordination.

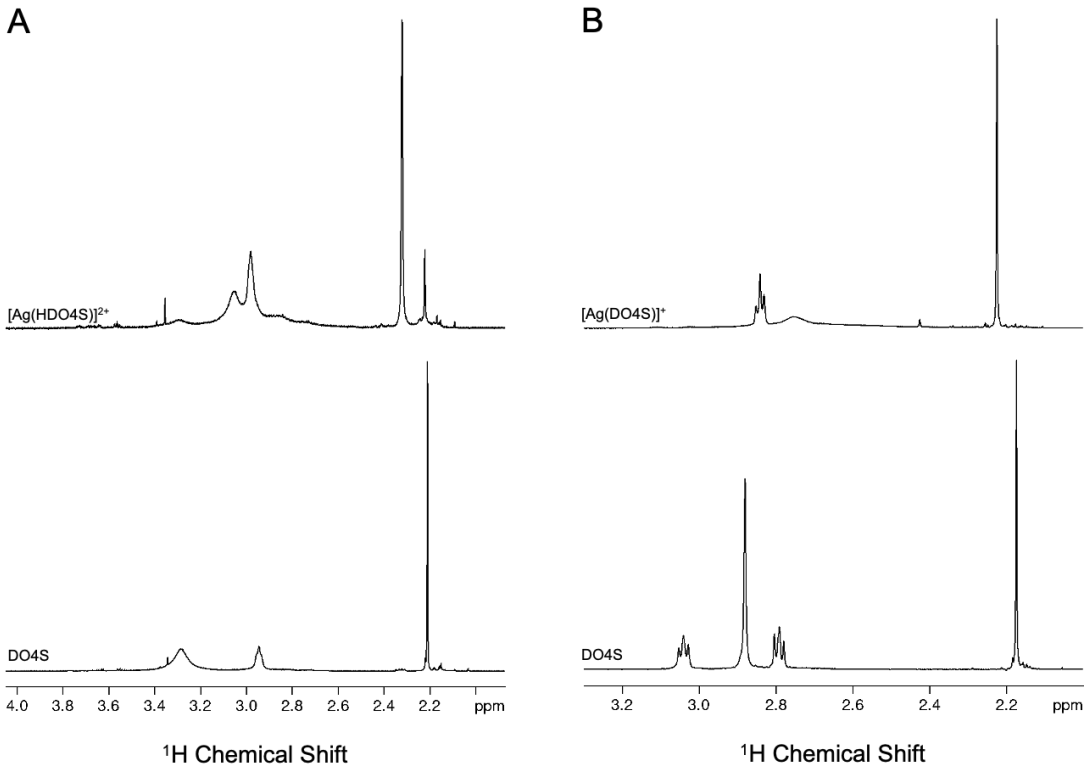

Figure 3.8. Comparison of the ^{1}H NMR spectra of (A) diprotonated DO4S and $[Ag(HDO4S)]^{2+}$ and (B) monoprotonated DO4S and $[Ag(DO4S)]^{+}$.

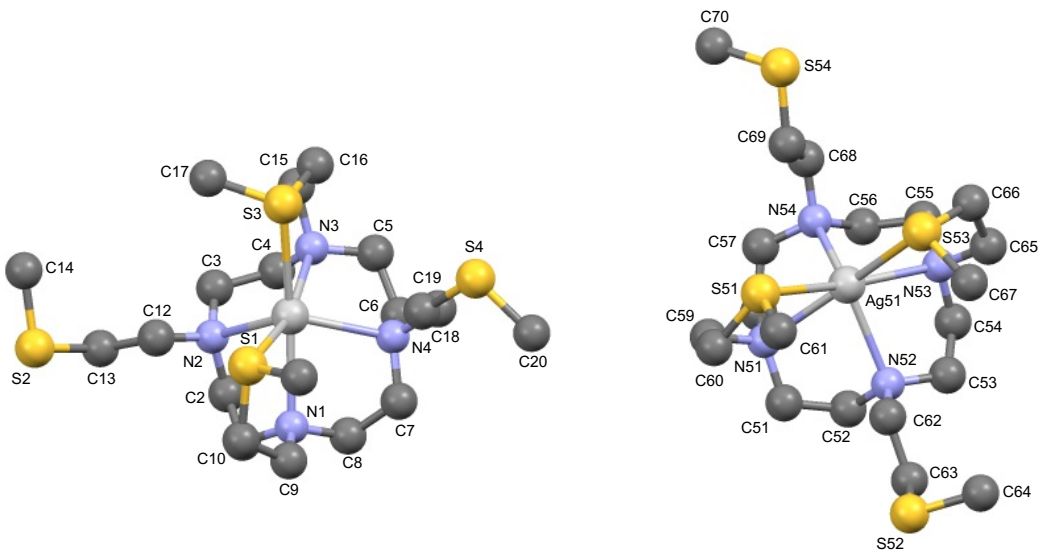

Figure 3.9. X-ray structure of $[Ag(DO4S)](PF_6)$ obtained by Mäcke *et al.*: there are two molecules in the asymmetric unit that are chemically equivalent but differ in the orientation of the terminal methyl group on the coordinated sulfur atoms.[32]

Apparently, the coordination of the metal ion prevents the folding of the side chains which remain far from the ring. Moreover, both the broadness of the NCH_2 signal and the exchange cross-peaks (black) in the NOESY spectra (**Figure 3.7**) strongly suggest a fluxional behaviour of the complex in solution. When the ^{1}H-NMR spectra at pD > 6.0 are compared with those at lower pD, several differences can be evidenced. This finding can be attributed to the predominance of different complexes species in the two conditions, namely $[Ag(DO4S)]^+$ and $[Ag(HDO4S)]^{2+}$, respectively. As seen in the DFT section, different structural features are expected for these species, and these are reflected on the spectra. According to the integration values and the ^{1}H-^{13}C HMQC and NOESY spectra (**Figure 3.7**), the singlet at 2.32 ppm in the spectrum at pD 2.1 was attributed to SCH_3, while the multiplets at 2.98 ppm and 3.05 ppm were attributed to SCH_2 and NCH_2, respectively. The singlet at 2.20 ppm was associated with the SCH_3 protons of the free ligand. Interestingly, all the signals of $[Ag(HDO4S)]^{2+}$ are broader than those of $[Ag(DO4S)]^+$ so that more conformers and/or slower rates of interconversion are occurring for the former than for the latter. However, similar upfield-downfield shifts for both complexes with respect to the free ligand are observed (**Figure 3.8**). At pD 3.6 and 4.4 (**Figure 3.6**), where $[Ag(HDO4S)]^{2+}$ and $[Ag(DO4S)]^+$ coexist, the patterns of both complexes can be recognized, indicating that the deprotonation $[Ag(HDO4S)]^{2+} \rightleftharpoons [Ag(DO4S)]^+ + H^+$ is relatively slow. As reported in **Chapter 2**, also for the free ligand the deprotonation $H_2L^{2+} \rightleftharpoons HL^+ + H^+$ was slow, and it was attributed to structural changes occurring by the proton loss.[20]

The ^{1}H NMR spectra of Ag^+-DO3S are shown in **Figure 3.10** while signal assignment is summarized in **Table B2** (**Appendix B**). The spectra change with pD only in the 5.4 - 7.8 range: below pD 5.4 and above pD 7.8 no further changes can be evidenced. This behaviour agrees with the thermodynamic data according to which two different complexes exist at acidic and at neutral-to-basic conditions, *i.e.* $[Ag(HDO3S)]^+$, respectively. At acidic pD, the presence of a small amount of unbound ligand can also be recognized (**Figure B2** - **Appendix B**). An important difference can be evidenced between the $[AgL]^+$ signals of DO3S and of DO4S: for the former, two different singlets for SCH_3 protons, at 2.23 and 2.19 ppm, can be observed which implies that the $[AgL]^+$ complex formed by DO3S is asymmetric. It can be assumed that the DO3S arm bound to N_4 cannot engage in the metal binding because there is no counter arm on N_{10}, thus resulting chemically different from the other two. As for Ag^+-DO4S, the signal enlargement of the Ag^+-DO3S complex indicate the presence of intramolecular dynamic exchange processes. Semiquantitative data can be obtained from the ^{1}H NMR spectra by calculating the relative integral between the signals of the complexes and those of the free ligand. For DO4S the relative amount of $[Ag(HDO4S)]^{2+}$ and free ligand are 86% and 14%, respectively, at pD 2.1 whereas for DO3S the corresponding percentages are 91% and 9% at pH 3. Considering the uncertainty of the

NMR integration values and the isotopic and solvent effects, these values are in good agreement with those calculated on the basis of the thermodynamic data of **Table 3.1** (94% and 6% for DO4S and 90% and 10% for DO3S, respectively, at the two-given pH).

The ^{1}H NMR spectra of Ag^{+}-DO3SAm are shown in **Figure B3** (**Appendix B**) while signal assignment is summarized in **Table B3** (**Appendix B**). Similar ^{1}H NMR spectra were expected for DO3S and DO3SAm as the two ligands are identical apart from the N-alkylation with the amide group in the latter. This is partly true at pD > 4 but not at more acidic conditions, as for DO3SAm all signals are much more enlarged. This indicates that $[Ag(HDO3SAm)]^{2+}$ has more conformers than $[Ag(HDO3S)]^{2+}$, and/or that the former experiences slower exchange reactions. The ^{1}H-NMR spectra of solutions containing Ag^{+} and DO2A2S are shown in **Figure 3.11**; signal assignment is summarized in **Table B4** (**Appendix B**) as deduced from ^{1}H-^{13}C HMQC (**Figure 3.12**). In alkaline solution (pD > 7.8) the spectra are identical as only $[Ag(DO2A2S)]^{-}$ exists in these conditions, whereas at lower pD the spectra change because of the presence of [Ag(HDO2A2S)] and/or of $[Ag(H_2DO2A2S)]^{+}$.

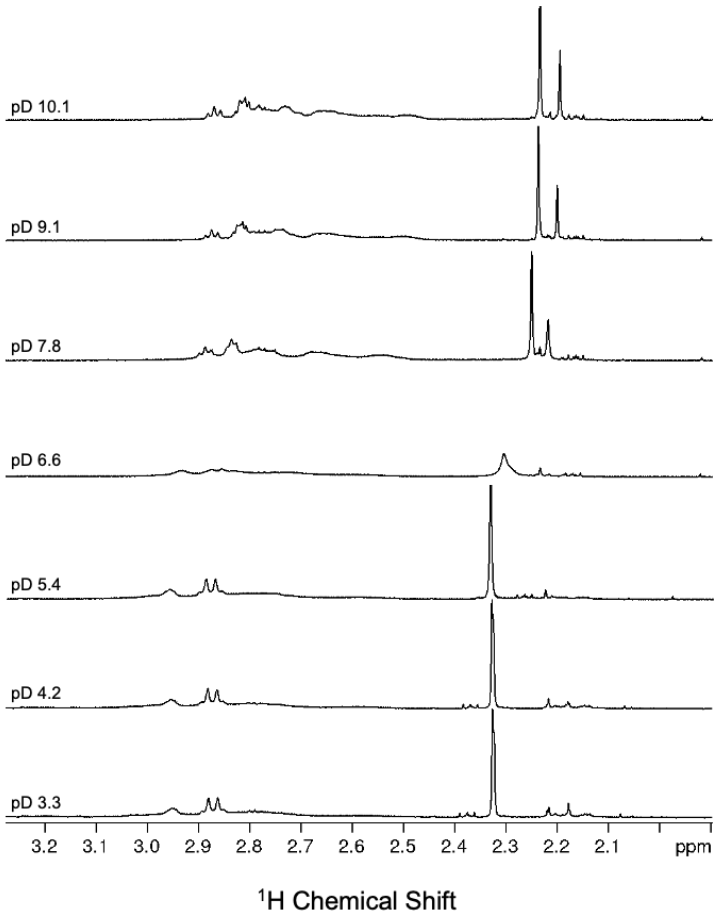

Figure 3.10. Variable-pD ^{1}H NMR spectra of Ag^{+}-DO3S (600 MHz, T = 25°C, D_2O, $C_{Ag^{+}} = 9.3 \cdot 10^{-4}$ M, $C_{DO3S} = 9.4 \cdot 10^{-4}$ M).

Both ring and sidearms NCH_2 protons give broad multiplets indicating a highly flexible structure as demonstrated by the in-phase correlation peaks (black) in the NOESY spectra (**Figure 3.12**). SCH_3 and SCH_2 signals are downfield shifted with respect to the free ligand suggesting the role of the transannular S-donor atoms in the coordination of Ag^+. It is worth noting that, despite in the free ligand the NCH_2 protons of the acetate arms were unexpectedly downfield shifted (**Chapter 2**) when Ag^+ is coordinated, all the signals are shielded when pD increase, due to the higher electron density associated with the deprotonation process. This suggests that the metal ion prevents the intramolecular interaction between the deprotonated acetate arms and the protonated nitrogen atoms of the ring. Differently from the other chelators, when Ag^+ is coordinated by DO2A2S, the SCH_3 protons become spatially close to the protons of the carboxylic chain and the NCH_2 and SCH_2 protons of the sulfanyl side chain, as indicated by the NOESY spectrum (**Figure 3.12**). Moreover, except for the signal shifts, the spectra remain almost identical at all pD values, so that the protonation/deprotonation (from $[Ag(H_2DO2A2S)]^+$ to $[Ag(DO2A2S)]^-$) does not change markedly the structure of the complex.

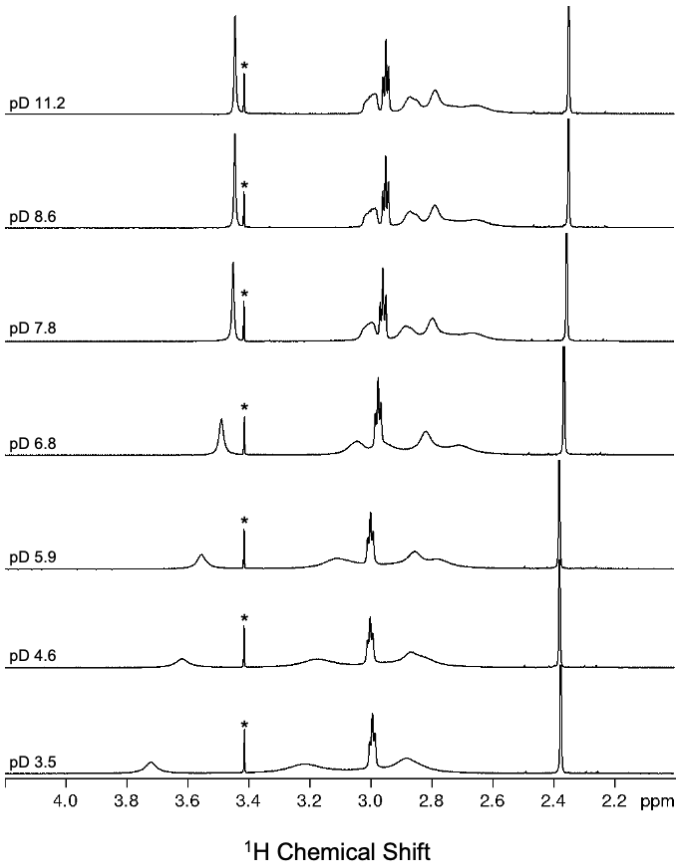

Figure 3.11. Variable-pD ^1H NMR spectra of Ag^+-DO2A2S (600 MHz, T = 25°C, D_2O, $C_{Ag^+} = C_{DO2A2S} = 2.0 \cdot 10^{-3}$ M). The signals marked with an asterisk are related to methanol impurities.

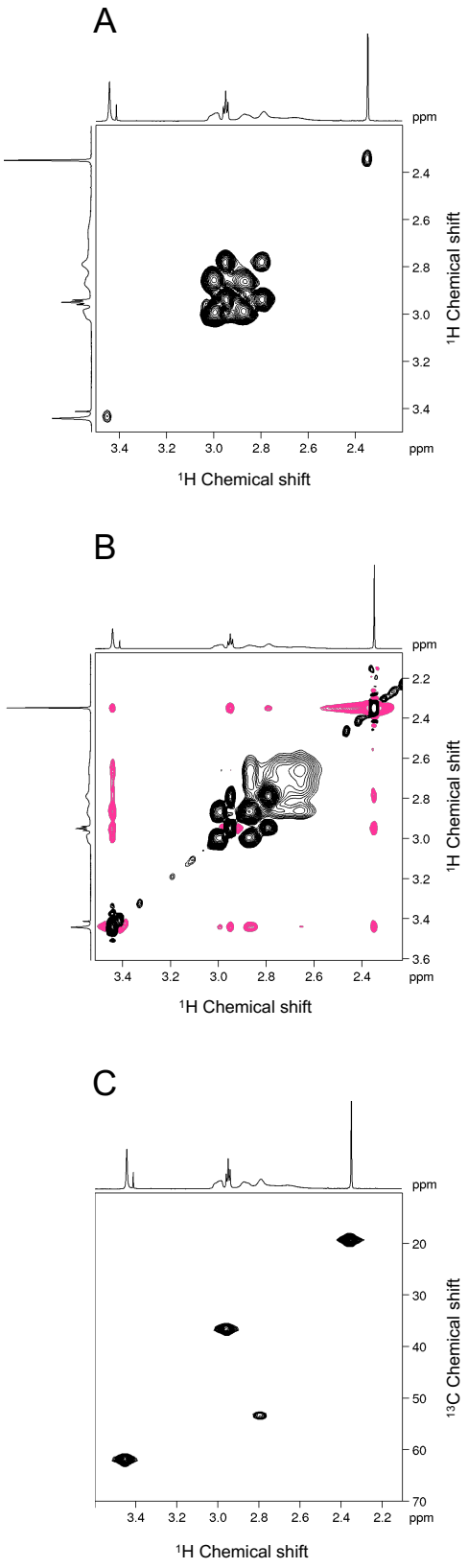

Figure 3.12. (A) ^{1}H-^{1}H COSY, (B) NOESY and (C) ^{1}H-^{13}C HMQC spectrum of $[Ag(DO2A2S)]^-$.

The same pH-dependent behaviour was also observed for Ag^+-DOTA solutions as the spectra are almost the same at different pH where differently protonated complexes (*i.e.* $[Ag(HDOTA)]^{2-}$ to $[Ag(DOTA)]^{3-}$) exist (**Figure 3.13**). At increasingly acidic pH, the signals of the free DOTA can also be recognized, in agreement with potentiometric data. It is worth to note that differently from the other sulfur bearing macrocyclic complexes, Ag^+ causes a noticeable splitting pattern of the methylene protons of the DOTA ring which may arise from their non-equivalence upon Ag^+ binding to all the nitrogen donors (**Figure 3.13**). The acetate arms are likely not involved in the complexation as their corresponding methylenic protons do not change markedly with respect to the free DOTA (**Figure B4** - **Appendix B**), as also expected considered the non-preference of Ag^+ for hard-donor groups.

The ^{1}H-NMR spectra of Ag^+-DO4S4Me are reported in **Figure 3.14**. Signal assignment is summarized in **Table B5** (**Appendix B**) as deduced also from the ^{1}H-^{1}H COSY spectra (**Figure 3.15**). Clearly, the coordination of Ag^+ causes significant changes in the spectra (**Figure B5** - **Appendix B**); in particular, a large number of narrow signals can be detected in the Ag^+-DO4S4Me solutions. This feature represents the most marked difference with respect to the spectra obtained for other Ag^+-ligand solutions, where few and broader peaks were detected.

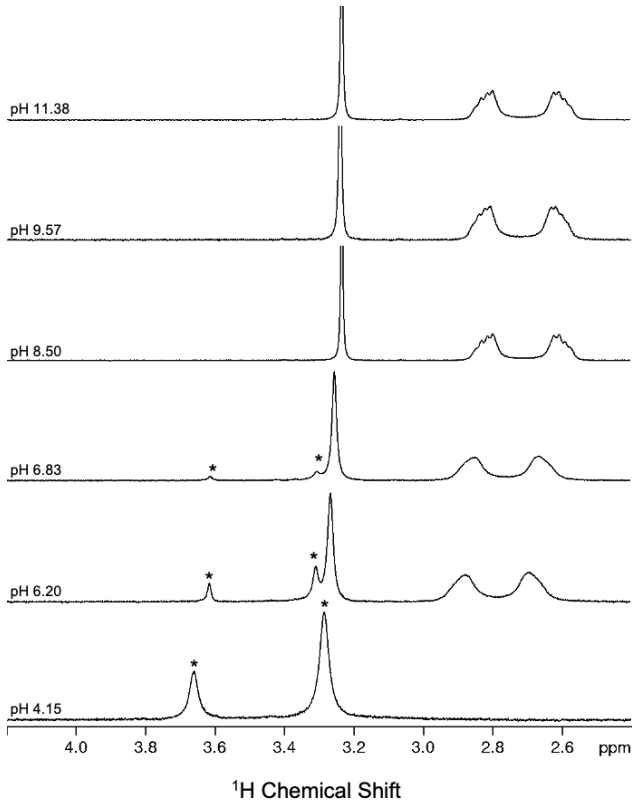

Figure 3.13. Variable-pH ^{1}H NMR spectra of Ag^+-DOTA (400 MHz, T = 25°C, H_2O + 10% D_2O, $C_{Ag^+} = C_{DOTA} = 1.8 \cdot 10^{-3}$ M). The signals of free DOTA are marked with asterisks.

DO4S4Me forms an asymmetric complex with Ag^+, and NMR indicates that it is characterized by a slowed-down fluxional interconversion compared to its achiral analogue. Namely, the chiral methyl groups on the cyclen ring induce the formation of a more rigid complex structure and rise the energetic barrier of interconversion between conformers. Two signals (at around 2.4 ppm, area ratio among 3.5:1 and 3:1) appear for the SCH_3 protons, and less clearly still two signals with the same ratio appear also for the ring methyl protons (0.9 ppm). This feature might be explained by the formation of two conformers in solution, which are not exchanging on the NMR timescale; the alternative hypothesis, *i.e.* that one of the four sulfur atoms is chemically different from the other three, is also possible. However, it is not supported by DFT according to which the chalcogen atoms are equivalent two-by-two (*vide supra*). At pH 2 the appearance of a new ring CH_3 signal at 1.08 ppm and of (at least) one additional SCH_3 peak at 2.37 ppm evidence that a different complex coexists, which is identified as $[Ag(HDO4S4Me)]^{2+}$ according to the thermodynamic data.

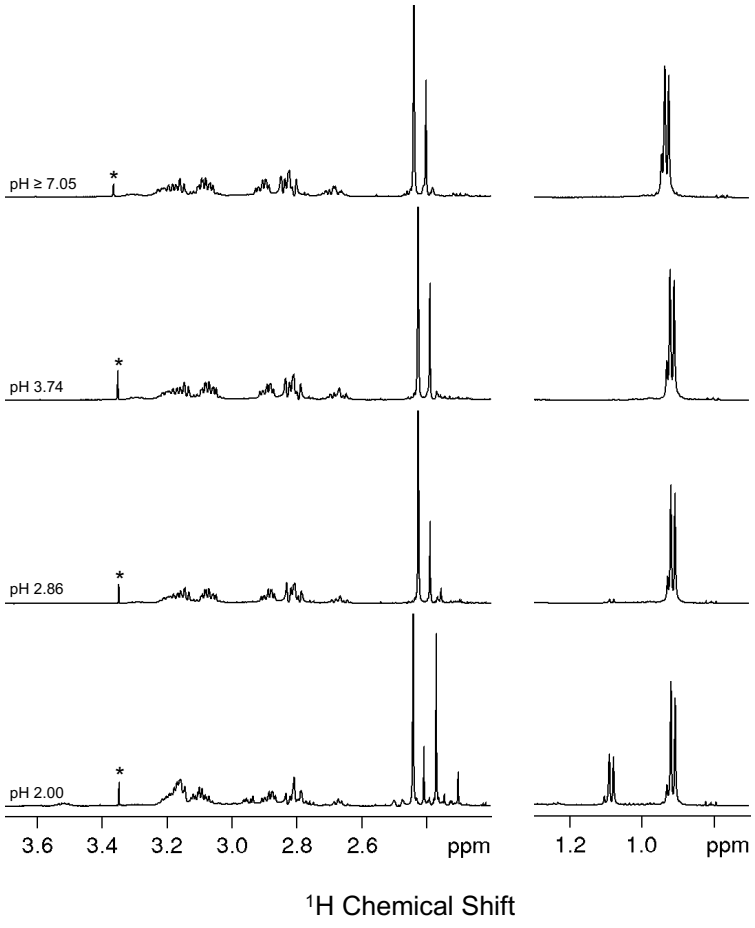

Figure 3.14. Variable-pH ^1H NMR spectra of Ag^+-DO4S4Me (600 MHz, T = 25°C, H_2O + 10% D_2O, C_{Ag^+} = $C_{DO4S4Me}$ = $1.1 \cdot 10^{-3}$ M). The signals marked with asterisks are related to methanol impurities.

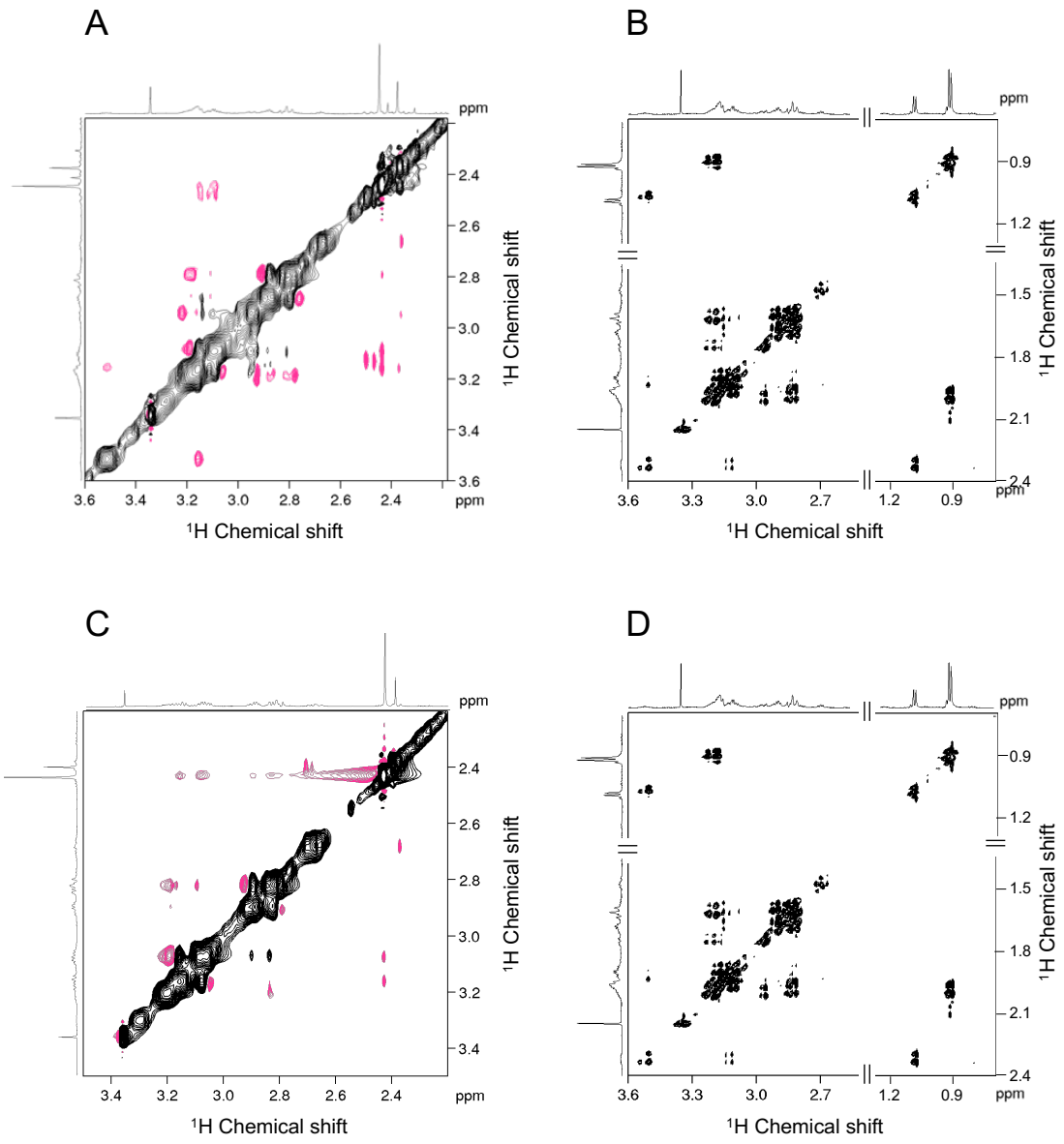

Figure 3.15. (A) NOESY and (B) ^{1}H-^{1}H COSY spectrum of a mixture of $[Ag(DO4S4Me)]^{+}$ and $[Ag(HDO4S4Me)]^{+}$; (C) NOESY and (D) ^{1}H-^{1}H COSY spectrum of $[Ag(DO4S4Me)]^{+}$.

3.2.6 Solution Structure of Ag^{+} Complexes with Second-Generation Ligands: NMR Investigation

The ^{1}H NMR spectra of the Ag^{+} complexes with the second-generation ligands at various pH were collected to further corroborate the speciation model and to gain insight into the structural variation produced by the different macrocyclic backbones with respect to the 12-member analogue DO4S. The ^{1}H NMR spectra of Ag^{+}-TAC3S and Ag^{+}-TRI4S are shown in **Figure 3.16** while those of Ag^{+}-TE4S are reported in **Figure 3.17**. Signal attributions are

summarized in **Table B6** - **B8** (**Appendix B**), based on the integration values and the bidimensional spectra (^{1}H-^{1}H COSY, ^{1}H-^{1}H TOCSY and ^{1}H-^{13}C HSQC) displayed in **Figure 3.18** - **3.19**. The spectra of solutions containing Ag^+ are markedly different from those of the free ligands (**Figure 2.20**), thus demonstrating the formation of the metal complexes throughout the investigated pH, while the pH-dependent spectral variations are indicative of the formation of the differently protonated complexes (**Figure 3.3**).

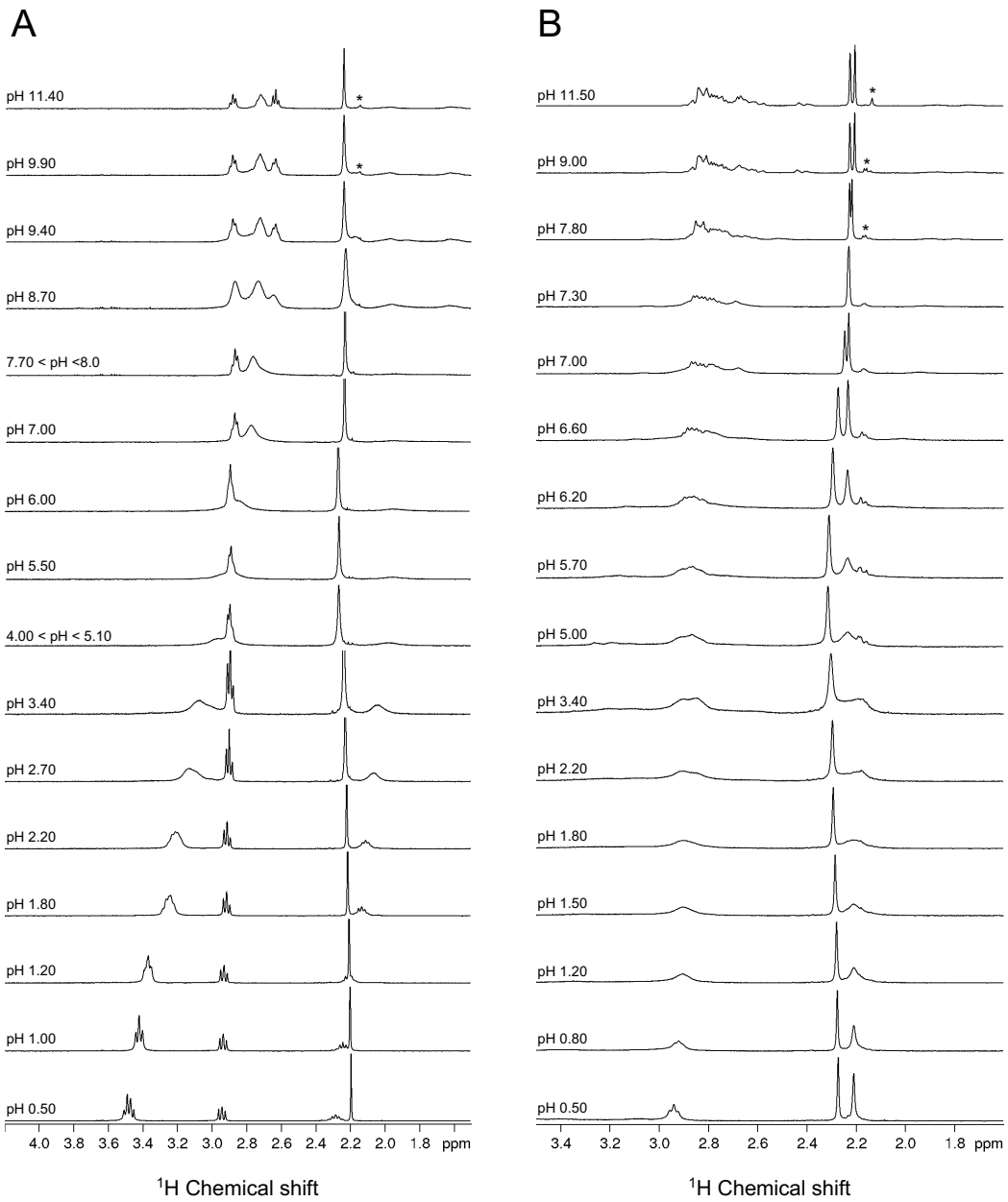

Figure 3.16. Variable-pH ^{1}H NMR spectra of (A) Ag^+-TACD3S (400 MHz, T = 25°C, H_2O + 10% D_2O, C_{Ag^+} = C_{TACD3S} = $8.90 \cdot 10^{-4}$ M) and (B) Ag^+-TRI4S (C_{Ag^+} = C_{TRI4S} = $1.11 \cdot 10^{-3}$ M). Signals marked with asterisks have been attributed to the free ligand.

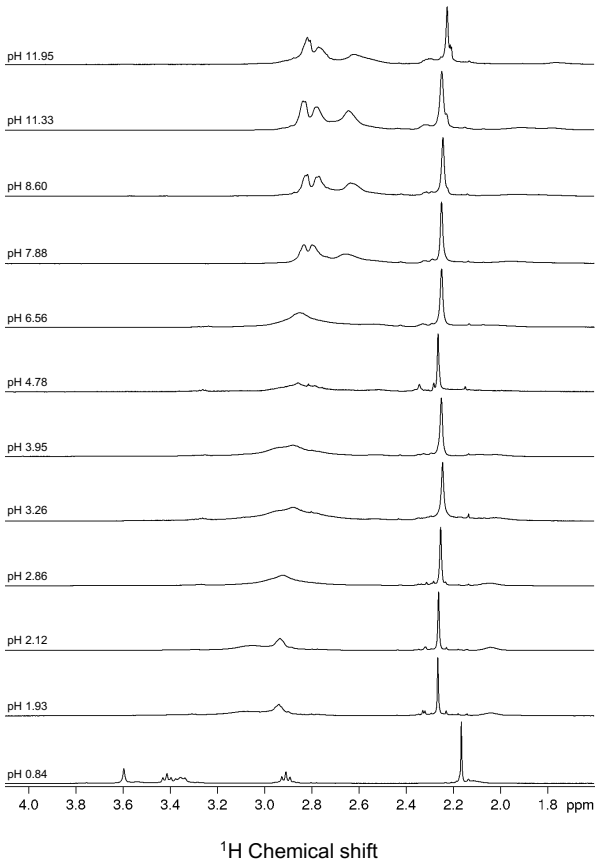

Figure 3.17. Variable-pH ^{1}H NMR spectra of Ag^+-TE4S (400 MHz, T = 25°C, H_2O + 10% D_2O, $C_{Ag^+} = C_{TE4S} = 1.15 \cdot 10^{-3}$ M).

Similarly to DO4S, for Ag^+-TACD3S, the methyl groups of the side chains (SCH_3) always resonate as a singlet (**Figure 3.16**), which is deshielded with respect to those of the free ligand (**Figure 3.20**), suggesting that all the S donors are involved in the coordination sphere as they are simultaneously bound to Ag^+ or in rapid exchange with respect to the NMR timescale. While the SCH_2 protons of the sidechains are detectable at all pH, even if the fine structure of the triplet is recognizable only at acidic pH, those related to methylene protons (NCH_2) of the ring and side chains are always overlapped. Only at pH > 9, where [Ag(TACD3S)(OH)] exists, they are split into a multiplet and a triplet, respectively. Contrarily, all the N-bound protons are shielded in the complexes with respect to the free protonated ligand (**Figure 3.20**). Considering the same net charge (*e.g.*, H_2L^{2+} *vs.* $[AgHL]^{2+}$), an H^+ is 'replaced' by Ag^+ in the complex: while the protons are located solely on the N atoms, it is reasonable to assume that the silver ion is simultaneously bound by both N and S donors. Therefore, the N in the free ligand experience a lower electron density than the complex, justifying the observed trend.

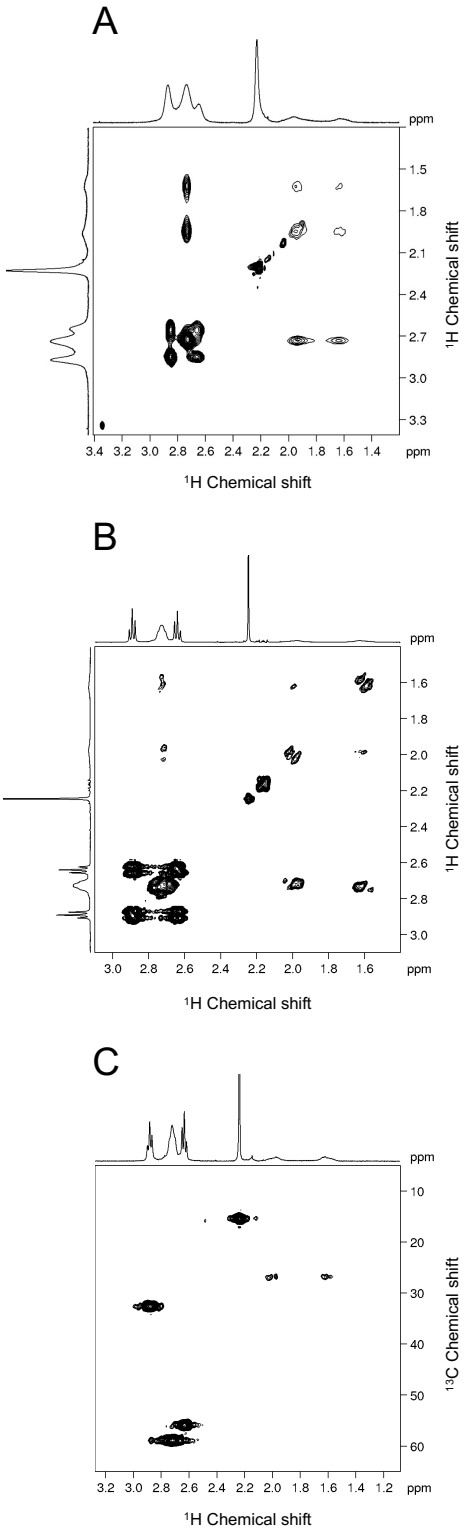

Figure 3.18. ^{1}H-^{1}H TOCSY spectrum of (A) [Ag(TACD3S)]$^{+}$, (B) ^{1}H-^{1}H TOCSY and (C) ^{1}H-^{13}C HSQC spectrum of [Ag(TACD3S)(OH)].

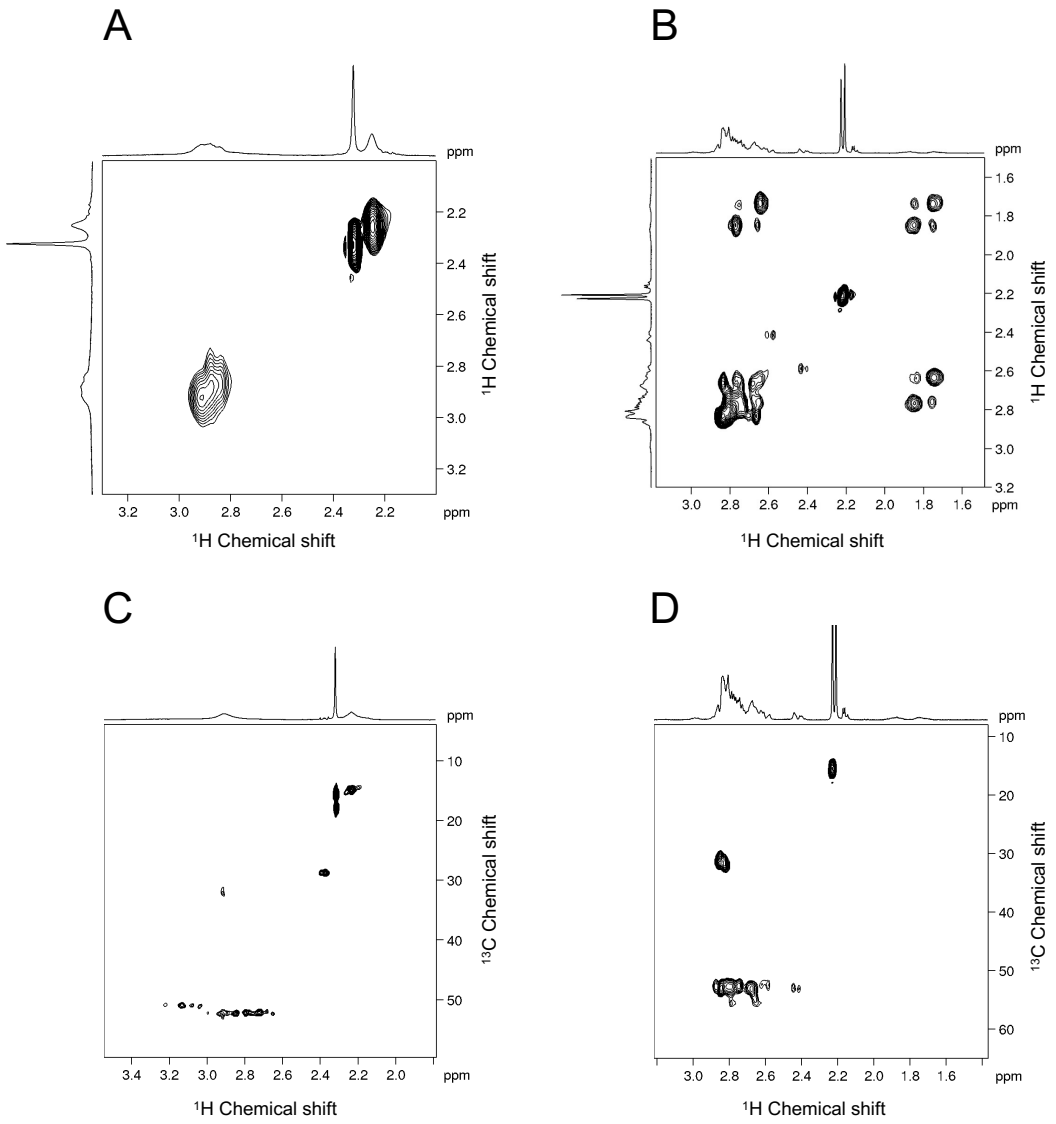

Figure 3.19. ^{1}H-^{1}H TOCSY spectrum of (A) $[Ag(HTRI4S)]^{2+}$ and (B) $[Ag(TRI4S)]^+$; (C) ^{1}H-^{13}C HSQC spectrum of Ag^+-TRI4S at pH 1 and (D) $[Ag(TRI4S)]^+$.

An exception to this shielding effect is represented by the neutral species TACD3S and [Ag(TACD3S)(OH)] as the NCH_2 signals of the latter resonate at chemical shifts similar, or slightly greater, than those of the free ligand. This supports the hypothesis that the nitrogen donors are involved in the metal complexation.

It is worth to note that in the deprotonated complexes' forms, *i.e.* $[Ag(TACD3S)]^+$ and [Ag(TACD3S)OH], the axial and equatorial methylene protons of the ring ($NCH_2\underline{CH_2}CH_2N$) became magnetically non-equivalent after the complexation as they resonate as two-splitted coupling peaks. As regards the pH-dependent chemical shift variation of these protons, the trend between free and complex ligand is not regular and is probably strictly dependent on the conformational changes induced by the complex formation.

Similar spectral variations with respect to the free ligand can also be found with the other ligands (**Figure 3.20**).

For the Ag^+-TRI4S, the SCH_3 protons resonate as two singlets of equal area at all the explored pH: in the deprotonated complex, *i.e.* $[Ag(TRI4S)]^+$, both signals are comparatively narrow, while in $[Ag(HTRI4S)]^{2+}$ one is much broader than the other (**Figure 3.21**). It should be noted that the difference in chemical shift between the two signals is greater than those detected for free ligand (**Chapter 2**), thus suggesting that all the S donors are involved in the coordination of Ag^+ on average (as these signals changed in chemical shift and broadness with respect to the free ligand), but in a different geometry: they seem to be equivalent at two-by-two and exchanging with different dynamics in $[Ag(HTRI4S)]^{2+}$ as the peaks' broadness is different. The signals of the SCH_2 and NCH_2 protons of the side chains and the ring are always overlapped in a single multiplet, which is exceptionally broad in $[Ag(HTRI4S)]^{2+}$. The methylene protons of the propyl chain of the ring became recognizable at pH > 6 and splitted into two extremely broad multiplets of equal area in $[Ag(TRI4S)]^+$.

The higher molecular symmetry of TE4S with respect to TRI4S appears to be translated in the corresponding complexes as all protons gave a few and very broad multiplets, except for the SCH_3 groups which resonate as a fairly narrow singlet (**Figure 3.17**). At the lowest investigated pH, the spectrum represents those of the free ligand as, under this condition, Ag^+ is not bound, in agreement with the potentiometric data.

All the protonation/deprotonation equilibria of the differently protonated Ag^+ complexes with the second-generation ligands are fast on the NMR timescale, as only mediated signals can be observed. At highly acidic pH, where the free ligand should co-exist with the protonated complexes (*vide supra*), no distinct signals for the complexes and the unbound chelator are distinguishable: this indicates that also these species are in fast exchange with respect to the NMR timescale, making the protonated complexes very labile.

To verify these results and to exclude the presence of other protonated species, ^1H NMR spectra of solutions containing an excess of ligand (metal-to-ligand ratio equal to 1:2) (**Figure B6** - **Appendix B**) were collected. The spectra, in the presence of ligand excess, are similar to those obtained with a metal-to-ligand ratio equal to 1:1 and the signals characteristic of the free ligands do not emerge.[§§] However, all the signals are more shifted towards those of the free ligand: this can be rationalized considering that the observed spectra are a weighted average on the abundance of the species existing in solution. These observations further substantiate the hypothesis that a rapid exchange between the free ligand and protonated complex occurs at acidic pH.

[§§] Contrarily, the excess free ligand is not in exchange with the deprotonated complex, or it is in slow exchange with respect to the NMR timescale as its signals are always recognizable (**Figure B6** - **Appendix B**).

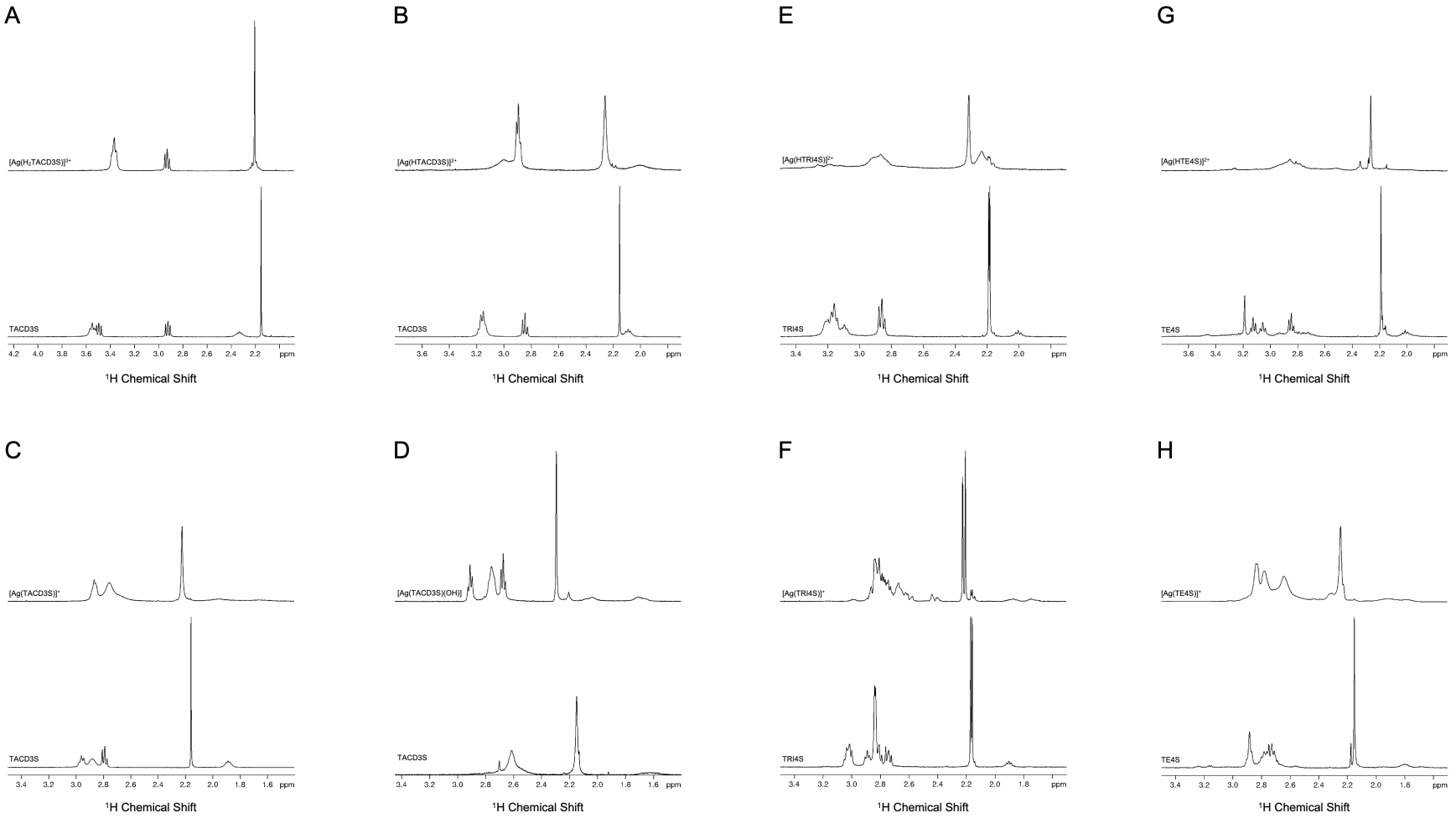

Figure 3.20. Comparison of the ^{1}H NMR spectra of (A) triprotonated TACD3S and $[Ag(H_2TACD3S)]^{3+}$, (B) diprotonated TACD3S and $[Ag(HTACD3S)]^{2+}$, (C) monoprotonated TACD3S and [Ag(TACD3S)], (D) neutral TACD3S and [Ag(TACD3S)(OH)], (E) diprotonated TRI4S and $[Ag(HTRI4S)]^{+}$, (F) monoprotonated TRI4S and $[Ag(TRI4S)]^{+}$, (G) diprotonated TE4S and $[Ag(HTE4S)]^{+}$ and (H) monoprotonated TE4S and [Ag(TE4S)].

It is intriguing to note that in Ag^+-DO4S, the protonation/deprotonation equilibria of the different complexes as well as the equilibria with the free ligand were slower on the NMR timescale as the patterns of both complexes ($[Ag(HDO4S)]^{2+}$ and $[Ag(DO4S)]^+$) or the free DO4S were recognisable in the pH region where they co-exist (*vide supra*). This can be ascribed to the larger ring sizes (or the less N) of the second-generation ligands which make proton exchange faster.

With all the second-generation ligands, the chemical shift of the SCH_3 groups undergoes minimal variations (< 0.1 ppm) with the proton content, with an increasing upfield shift at pH < 5. This can be explained considering that, at acidic pH, the chemical shifts decrease due to the presence of the free ligand in exchange with the complex (*vide supra*) while, at higher pH, the signals are progressively shielded due to the increase in electron density after the deprotonation processes. These reactions are also responsible for the upfield shift experiences by the SCH_2 and NCH_2 protons of the side chains and the ring with pH (**Figure B7** - **Appendix B**). Data fitting of the chemical shift variation as a function of pH allows to obtain the log*K* values of the monoprotonated complex reported in **Table 3.2**, which agree with the values obtained from the pH-potentiometric titrations (*vide supra*).

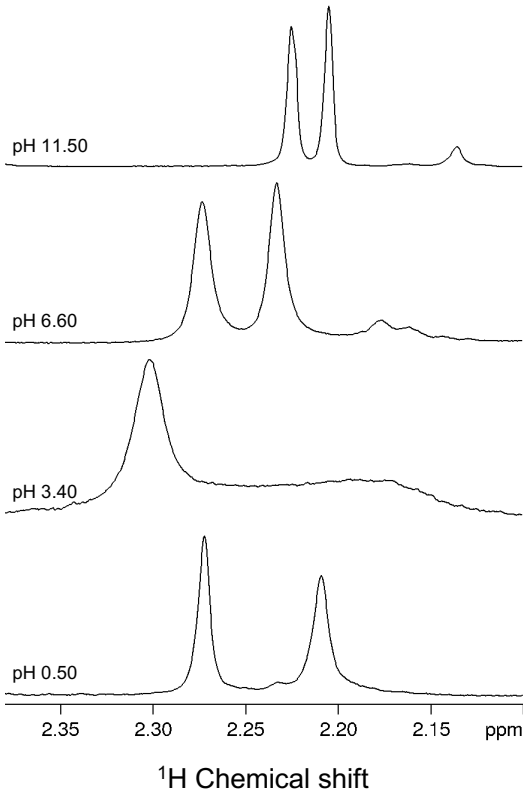

Figure 3.21. Enlargement of the SCH_3 region of Ag^+-TRI4S at different pH.

3.2.7 Variable-Temperature NMR of Silver Complexes: Insight into the Solution Dynamics

With the exception of [Ag(TACD3S)(OH)] and $[Ag(TRI4S)]^+$ which showed rather narrow resonances, all the complexes with the pure sulfur-bearing ligands (DO4S, TACD3S, TRI4S and TE4S), either in their protonated or deprotonated forms, gave broad resonances, indicating a great solution dynamics. To gain insight into the fluxional nature of these complexes and to obtain additional information on their structure, variable-temperature (VT) ^{1}H NMR were performed.

With increasing temperature, the signals of S-bound protons (SCH_3 and SCH_2) of $[Ag(H_2TACD3S)]^{3+}$ do not vary significantly, while all the other peaks become narrower and the spectral fine structure emerges at $T \geq 45$°C (**Figure 3.22**). This behaviour suggests different dynamics between the sulfur and nitrogen donors. In particular, all sulfurs seem to be involved on average in the coordination sphere of the Ag^+ ion, either because they are simultaneously bound to it or always in fast exchange in the explored temperature range. The dynamic exchange behaviour of the sidechains is further supported by the absence of satellite peaks due to the scalar coupling between ^{107}Ag/^{109}Ag*** and ^{1}H, compatible with a rapid intramolecular donor dissociation. Clearly, it is also possible that the couplings are not detected due to the conformation of the H-C-S-Ag bond angles, which could make zero the coupling constant, $J_{H\text{-}Ag}$. The N donors are involved in conformational equilibria that make the NCH_2 and CH_2 protons of the ring equivalent: it can be concluded that the nitrogen donors are simultaneously bound to both H^+ and Ag^+ and in exchange with each other. On the other hand, in $[Ag(TACD3S)]^+$ (**Figure 3.22**), all the signals become very broad and almost coalescing at the lowest investigated temperature while, with the temperature increase, they became faintly narrower. Rising the temperature, the CH_2 protons of the propylic chain of the ring become equivalent at $T \geq 45$°C, while the NCH_2 ones always resonate as a broad singlet, which tends to overlap the one resulting from the SCH_2 protons. It can be concluded that all the N donors are equivalent and simultaneously involved in a dynamic Ag^+ binding. The equivalence of the three N atoms represents a difference with respect to the $[AgDO4S]^+$ complex, in which the N were equivalent only to two-by-two (*vide supra*): this could be due to the different symmetry of the macrocyclic ring of the two chelators and, in particular, can be related to the absence of two opposite N atoms in TACD3S.

*** ^{107}Ag: 51.82% natural abundance, nuclear spin I = ½, magnetogyric ratio $-1.087 \cdot 10^7$ rad/T·s, relative sensitivity (^{1}H = 1.00) $6.62 \cdot 10^{-5}$. ^{109}Ag: 48.18% natural abundance, nuclear spin I = ½, magnetogyric ratio $-1.25 \cdot 10^7$ rad/T·s, relative sensitivity (^{1}H = 1.00) $1.01 \cdot 10^{-5}$.

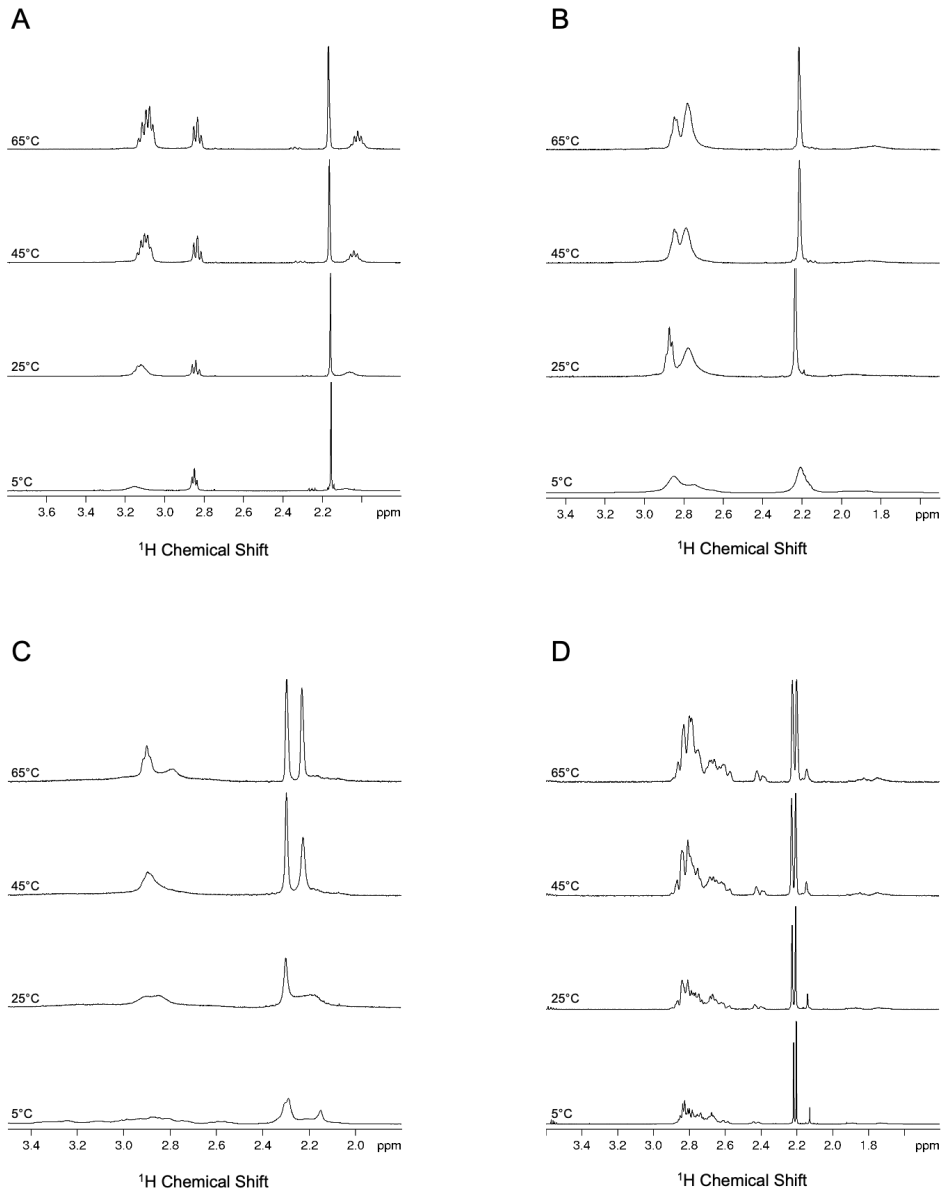

Figure 3.22. VT-NMR of (A) $[Ag(H_2TACD3S)]^{3+}$, (B) $[Ag(TACD3S)]^{+}$, (C) $[Ag(HTRI4S)]^{2+}$ and (D) $[Ag(TRI4S)]^{+}$.

A further difference is also related to the absence of temperature-dependent variation of the SCH_3 signals of $[Ag(DO4S)]^{+}$ (**Figure 3.23**). The same considerations made above for $[Ag(H_2TACD3S)]^{3+}$ are therefore arguable for $[Ag(DO4S)]^{+}$ too.

A different solution behaviour was obtained with $[Ag(HTRI4S)]^{2+}$ (**Figure 3.22**) as, with the temperature increases (T > 45°C), the SCH_3 and SCH_2 signals became markedly narrower. This implies that the S donors are exchanging on the NMR timescale. The different broadness of the signals corroborates the initial hypothesis (*vide supra*) that the two pairs of S are differently involved in the Ag^{+} binding. On the contrary, in $[Ag(HDO4S)]^{2+}$ the SCH_3 are all equivalent: this difference between TRI4S and DO4S could be initiated by the different

symmetry of the ligands, which in TRI4S makes the side chains not equivalent. However, in analogy with $[Ag(HDO4S)]^{2+}$, it is reasonable to assume that in $[Ag(HTRI4S)]^{2+}$ only two opposite side chains are instantaneously bound to Ag^+. All the N donors could be involved in the coordination of both Ag^+ and H^+ and in exchange or only bound to H^+.

The ^1H NMR spectrum of $[Ag(TRI4S)]^+$ (**Figure 3.22**) does not undergo noteworthy changes with increasing temperature. This confirms the more rigid nature of this complex compared to the others and the absence of conformational dynamics. The greater stiffness compared to $[Ag(DO4S)]^+$ could be caused by the introduction of the asymmetric propyl chain of the ring as this non-dynamic behaviour was found only with this non-symmetric ligand. In fact, when the propylic group-containing chelator has a more symmetrical structure, *i.e.* TACD3S and TE4S, the ^1H NMR spectra are affected by the temperature variations (**Figure 3.22**). The same change observed for $[Ag(DO4S)]^+$ were found also for $[Ag(TE4S)]^+$ as the temperature increase generated sharper signals. No variations were detected for the SCH_3 ones.

The variation of the macrocyclic structure therefore not only severely modifies the thermodynamic stability of the resulting complexes but also hugely affect their intramolecular dynamic properties.

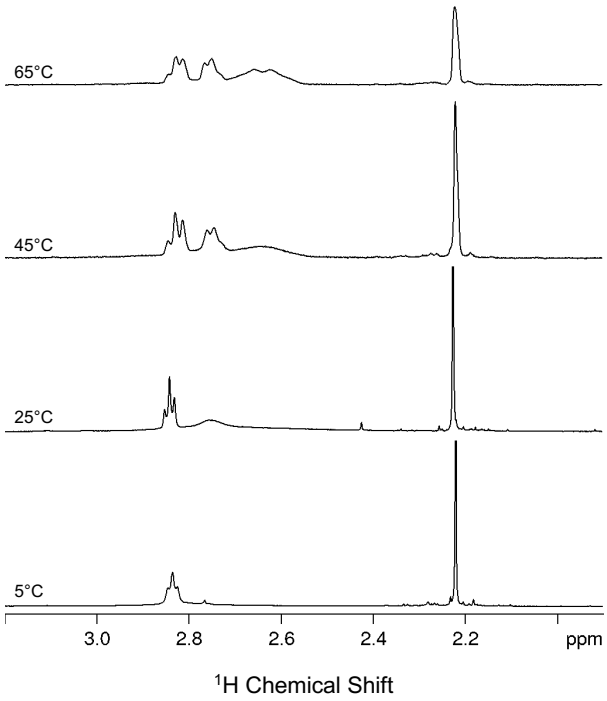

Figure 3.23. VT-NMR of $[Ag(DO4S)]^+$.

3.2.8 Silver-111 Radiolabelling

3.2.8.1 Radiolabelling with First-Generation Ligands

The ability of the first-generation ligands forming the most stable complexes with Ag^+, *i.e.* DO4S and DO4S4Me, of labelling $[^{111}Ag]Ag^+$ under extremely diluted conditions was examined. Results of radiolabelling are summarized in **Table 3.4**.[†††]

For DO4S at pH 4 with a $2 \cdot 10^{-5}$ M ligand concentration, a quantitative yield both at room temperature and at 50°C was achieved in 5 minutes. The incorporation of $[^{111}Ag]Ag^+$ remained quantitative at pH 7, whereas it became lower than 75% at pH 2. This behaviour was expected from thermodynamic data according to which some free metal ions exist at very acidic pH values. The radionuclide incorporation by DO4S4Me in the same conditions was similar, even if the temperature appears to be a relevant parameter as at ambient temperature a lower yield of 76% was obtained at pH 4. Concentration-dependent radiolabelling at 50°C and pH 4 indicated that for both ligands the complexation was quantitative in 5 minutes with a minimum concentration of $2 \cdot 10^{-5}$ M (corresponding to 20 nmol). Efficiency became lower when the ligand concentration was reduced and, despite thermodynamic data predict a slightly stronger complex formation for DO4S4Me than for DO4S, the labelling experiments demonstrated the former to be moderately less efficient than the latter. Indeed, according to the temperature effect evidenced on the complex formation for DO4S4Me, this ligand might react with Ag^+ more slowly than DO4S, so that the addition of a rigid chiral backbone onto the DO4S structure with the intention of increasing its stability may also hamper the labelling kinetics at the lowest concentrations.

Table 3.4. $[^{111}Ag]Ag^+$ radiochemical yields (in %) for DO4S and DO4S4Me. All yields are given within the experimental uncertainties of the cyclone device of 5% and refer to a labelling time of 5 min and to ~ 1 MBq ^{111}Ag activity.

Ligand	Ligand Molarity [M]	Temperature [°C]	pH	Yields [%]
DO4S	$1 \cdot 10^{-6}$	50	4	85
	$1 \cdot 10^{-5}$	50	4	87
	$2 \cdot 10^{-5}$	50	4	100
	$2 \cdot 10^{-5}$	50	2	75
	$2 \cdot 10^{-5}$	50	7	100
	$2 \cdot 10^{-5}$	RT	4	100
DO4S4Me	$1 \cdot 10^{-6}$	50	4	53
	$1 \cdot 10^{-5}$	50	4	92
	$2 \cdot 10^{-5}$	50	4	100
	$2 \cdot 10^{-5}$	RT	4	76

[†††] Because of the low amount of ^{111}Ag available at that time, only one data point was collected for each experiment.

3.2.8.2 Radiolabelling with Second-Generation Ligands

The capability of the second-generation ligands to label [^{111}Ag]Ag^{+} was assessed by exploring the effect of the ligand concentration on the complexes formation under mild reaction conditions (pH 7, RT, 5 min), compatible with thermolabile or pH-sensitive biovectors. DO4S was considered for comparison purposes. The results are shown in **Figure 3.24**.

Quantitative (> 99%) incorporation of [^{111}Ag]Ag^{+} was obtained at room temperature at 10^{-4} M of both DO4S and TRI4S chelators. An almost comparable behaviour was obtained decreasing the ligand concertation to 10^{-5} M and 10^{-6} M as the RCY dropped sequentially to 45% and 19% for DO4S and 63% and 18% for TRI4S. A 100-fold and 10-fold lower ligand concentration gave quantitative yield when the reaction mixtures were heated at 50°C (**Figure 3.24**). Unexpectedly, TACD3S and TE4S showed no labelling neither at room temperature nor after prolonged heating albeit using the highest ligand concentration assessed (10^{-3} M).

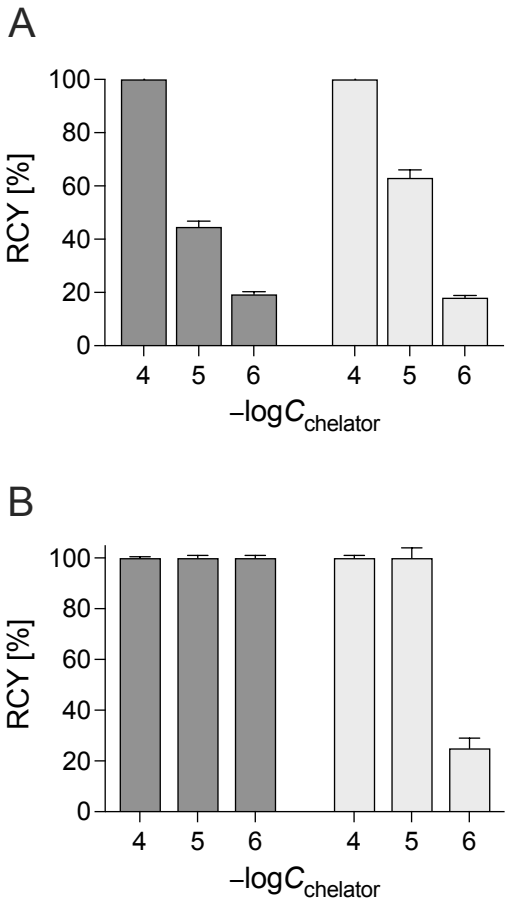

Figure 3.24. Concentration-dependent radiolabelling of DO4S (left) and TRI4S (right) with [^{111}Ag]Ag^{+} (1 MBq) at pH 7 after 5 min at (A) room temperature and (B) 50°C.

3.2.9 Competitions with Cadmium and Palladium

The selectivity of the ligands towards Ag^+ was evaluated through competition with stable Cd^{2+} which represents the main isobaric contaminant of ISOL-produced ^{111}Ag, as well as with stable Pd^{2+} which can be an impurity originating from the target material when ^{111}Ag is produced *via* the $^{110}Pd(n,\gamma)^{111}Pd$ reaction.

As shown in **Table 3.5**, an almost complete labelling was obtained when $[^{111}Ag]Ag^+$ and the ligands were mixed in the presence of a 2-fold molar excess of Cd^{2+}.

Competition experiments with Pd^{2+} demonstrated that the presence of 1-fold molar excess of competitor with respect to the ligand does not affect the labelling efficiency of DO4S. Conversely, the RCY dropped to 75% with TRI4S. A further increase in the palladium content reduced the incorporation yield to 67% for DO4S while TRI4S was not able to label $[^{111}Ag]Ag^+$. With a 100-fold molar excess of Pd^{2+}, no incorporation of Ag was observed.

3.2.10 *In Vitro* Stability Assays

Since the kinetic inertness plays a decisive role in determining the *in vivo* integrity of metal-based radiopharmaceuticals, stability assays are useful for predicting the fate of radiometallic complexes in biological environments. Therefore, the stability of the $[^{111}Ag]Ag^+$ complexes formed by the first- and second-generation ligands was investigated *vs.* time after incubation in suitable media to mimic the biological environment (**Table 3.5**).

Table 3.5. Labelling efficiency in the presence of an excess of Cd^{2+} and Pd^{2+} and stability of $[^{111}Ag]Ag^+$-labelled chelators at room temperature with a 5-fold molar excess of Zn^{2+} or in phosphate-buffered saline (PBS, pH 7.4).

Assay	*n*(M^+)/*n*(chelator)	$[^{111}Ag][Ag(DO4S)]^+$	$[^{111}Ag][Ag(DO4S4Me)]^+$	$[^{111}Ag][Ag(TRI4S)]^+$
Cd^{2+} Competition	2	95	96	[a]
Pd^{2+} Competition	1	100	[a]	75
	10	67	[a]	0
	100	< 1	[a]	0
	Incubation time [h] [b]	**$[^{111}Ag][Ag(DO4S)]^+$**	**$[^{111}Ag][Ag(DO4S4Me)]^+$**	**$[^{111}Ag][Ag(TRI4S)]^+$**
Zn^{2+} Stability	24	100	100	[a]
	48	100	100	[a]
PBS Stability	2	100	90	100
	24	94	88	100
	48	94	88	100

[a] Not tested under this condition.
[b] Values are reported as % of intact complex.

A check of metal-transmetallation possibly occurring *in vivo* was performed with Zn^{2+}, and very encouraging results were obtained, as the $[^{111}Ag]Ag^{+}$ complexes were completely intact (100%) over time in the presence of a 5-fold Zn^{2+} excess.

In phosphate-buffered saline (PBS) the stability was 94%, 88% and 100% over 48 h for $[^{111}Ag][Ag(DO4S)]^{+}$, $[^{111}Ag][Ag(DO4S4Me)]^{+}$ and $[^{111}Ag][Ag(TRI4S)]^{+}$ respectively, thus demonstrating high stability under the employed conditions.

Lastly, to unambiguously evaluate the potential of these ligands as chelating agents in radiopharmaceutical design, the *in vitro* human serum stability assays of the corresponding $[^{111}Ag]Ag^{+}$ complexes were also accomplished. As shown in **Figure 3.25**, the obtained results surprisingly indicate a great instability of $[^{111}Ag][Ag(TRI4S)]^{+}$ as no $[^{111}Ag]Ag^{+}$ remain bound after 1 hour. $[^{111}Ag][Ag(DO4S)]^{+}$ demonstrated a modest stability as, after 6 hours of incubation in human serum, there is a significant decomplexation.

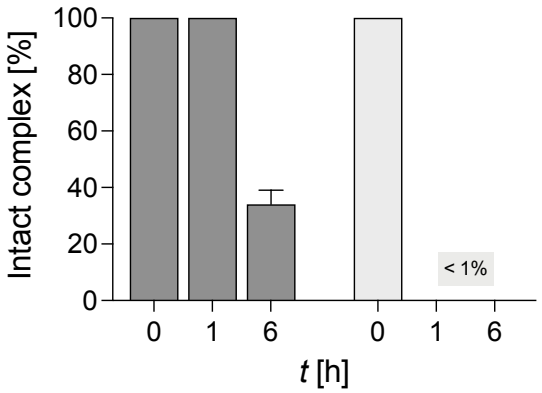

Figure 3.25. Human serum stability of $[^{111}Ag][Ag(DO4S)]^{+}$ (left) and $[^{111}Ag][Ag(TRI4S)]^{+}$ (right) at 37°C, over 6 hours.

3.3 Experimental Section

3.3.1 Materials and Methods

All solvent and reagents were purchased from commercial suppliers (Sigma-Aldrich, Fluka, VWR Chemicals) and were used without further purification. 1,4,7,10-Tetrazacyclododecane (cyclen), 1,5,9-triazacyclododecane (TACD), 1,4,7,10-tetrazacyclotridecane (TRI), 1,4,8,11-tetrazacyclotetradecane (cyclam) and 1,4,7,10-tetraazacyclododecane-1,4,7,10-tetraacetic (DOTA) were purchased from Chematech. First- and second-generation ligands were synthesized according to the procedures reported in **Chapter 2**.

3.3.2 Thermodynamic Measurements

Potentiometry. The potentiometric measurements were carried out at 25.0 ± 0.1°C as reported in detail in **Chapter 2**. Nitric acid, carbonate-free sodium hydroxide and ligand stock solutions were prepared following the same protocol previously described. Silver solutions were prepared from analytical grade nitrate salt (Aldrich, > 99.98% min). Ligand and Ag^+ were introduced in the titration cell in concentration ranging from 8.5 to $2.0 \cdot 10^{-3}$ M. The metal-to-ligand molar ratio varied from 0.5:1 to 2:1. The solutions were acidified with a known volume of HNO_3 to adjust the pH around 2, and the titrations were then carried out by the addition of known volumes of NaOH stock solution over the pH range 2-12. Additional potentiometric titrations were performed at a constant pH 0.5-2 (by HNO_3) using Ag^+ as titrant. In these cases, the combined glass electrode was replaced by a silver electrode (Crison) and an Ag/AgCl/KCl 3 M double junction electrode (Crison) was used as reference. The ionic strength was fixed to 0.15 M using sodium nitrate ($NaNO_3$) as background electrolyte. Each experiment was performed independently at least five times.

UV-Vis Spectroscopy. Variable-pH UV-Vis spectrophotometric measurements were performed as reported in **Chapter 2**. UV-Vis spectrophotometric titrations with Cu^{2+} as a competitor were performed at pH 3.7 (formic/formate buffer) without control of the ionic strength. Batch titration points were prepared adding varying amounts of Cu^{2+} to a solution containing the preformed Ag^+ complex ($C_{Ag} = C_L \sim 1 \cdot 10^{-4}$ mol/L). Different metal-to-metal ratios, between 0 and 4, were attained. Due to the slow kinetics of the transmetallation reactions at room temperature, solutions were brought to the equilibrium through heating at 65°C before the UV-Vis spectra measurements. The equilibrium was considered to be reached when the UV-vis spectra did not change.

NMR Spectroscopy. Variable-pH ^{1}H-NMR spectra and bidimensional spectra were recorded as reported in **Chapter 2**. Variable-temperature ^{1}H NMR spectra of the Ag^+ complexes were recorded at different temperatures using a 400 MHz Bruker Avance III HD spectrometer or a 600 MHz Bruker DMX 600. The temperature limits investigated were set between 5°C and 65°C. These temperatures were selected to protect the probe from damage due to freezing of the solvent and breaking of the NMR tube or boiling and leaking solvent.

Data Treatment. The overall equilibrium constants ($\log\beta_{pqr} = [M_pL_qH_r]/[M]^p[L]^q[H]^r$) were obtained by refinement of the thermodynamic data using the PITMAP software and are referred to the overall equilibria $pM^{m+} + qH^+ + rL^{l-} \leftrightarrows M_pH_qL_r^{pm+q-rl}$, where M is the metal ion and L the non-protonated ligand molecule.[33] The errors quoted are the standard deviations

calculated by the fitting program. The constants for ligand protonation and, in the case of the competition-titrations, also of the Cu^{2+} complexes, were taken from **Chapter 2** and **Chapter 4**.[20,34,35]

3.3.3 Density Functional Theory Calculations

All density functional theory (DFT)[36,37] calculations were performed with the Amsterdam Density Functional (ADF) program.[38–40] Scalar relativistic effects were accounted for using the zeroth-order regular approximation (ZORA). For geometry optimizations, carried out with no symmetry constraint and using analytical gradient techniques, the OPBE[41,42] density functional was used, in combination with the TZP basis set for Ag and DZP basis set for lighter elements.[43] This potential has proved to provide good structural properties and energies even in presence of heavy nuclei.[44–46] All structures were verified by frequency calculations: all normal modes have real frequencies. To achieve higher accuracy for energies, single point calculations were performed on the optimized structures using OPBE and the TZ2P basis set for all elements. TZ2P basis set is a large, uncontracted set of Slater-type orbitals (STOs). It is of triple-ζ quality and has been augmented with two sets of polarization functions on each atom: 2*p* and 3*d* in the case of H, 3*d* and 4*f* in the case of C, N and S, 5*p* and 4*f* in the case of Ag. The frozen-core approximation was employed: up to 1*s* for C, N, S and up to 3*d* for Ag. Solvent (water) effects have been accounted using the Conductor-like Screening Model (COSMO).[47–51] A radius of 1.93 Å and a relative dielectric constant of 78.39 were used. The empirical parameter in the COSMO equation was considered to be 0.0. The radii of the atoms are the classical MM3 radii divided by 1.2.
In order to gain insight into the nature of the bonding between Ag^+ and the ligands, the activation strain model[52] was used, which provides a meaningful description of structural and reactivity properties of chemical species.[53–56] In the activation strain analysis (ASA), the energy relative to the involved fragments (Ag^+ and ligand), ΔE, is decomposed into the strain energy ΔE_{strain} and the interaction energy ΔE_{int} (eq. 1):

$$\Delta E = \Delta E_{strain} + \Delta E_{int} \quad (1)$$

ΔE_{strain} is the energy associated with deforming the fragments from their equilibrium geometry into the geometry they have in the metal complex. It can be divided into a contribution stemming from each fragment. ΔE_{int} is the actual interaction energy between the deformed fragments. ΔE_{int} can also be further analyzed in the framework of the Kohn-Sham Molecular Orbital (MO) model using a quantitative energy decomposition (EDA) of the bond into

electrostatic attraction, Pauli repulsion (or exchange repulsion), and stabilizing orbital interactions (Eq. 2):

$$\Delta E_{int} = \Delta V_{elstat} + \Delta E_{Pauli} + \Delta E_{oi} \quad (2)$$

3.3.4 Silver-111 Radiolabelling, Competitions and *In Vitro* Stability Assays

Caution! ^{111}Ag is a radionuclide that emits ionizing radiation, and it was manipulated in a specifically designed facility under appropriate safety controls.

^{111}Ag Production. 2.54 mg of metallic Pd powder, enriched to 98.6% in ^{110}Pd (Oak Ridge National Lab, batch 214301) was enclosed in a quartz ampoule and irradiated for 4 days in a thermal neutron flux of about $1.1 \cdot 10^{15}$ 1/cm^2·s in the beam tube V4 of the high flux reactor at Institut Laue-Langevin in Grenoble, France. Thermal neutron capture on ^{110}Pd produces short-lived ^{111}Pd which β-decays with 23.4 minutes half-life to ^{111}Ag. The samples were shipped to the Hevesy Lab, Risø, Denmark for radiochemical separation of the non-carrier-added ^{111}Ag. The purification procedure was performed as reported in the literature or with slight variations.[57]

^{111}Ag Radiolabelling. Stock solutions of the ligands (10^{-3} M) were prepared in ultrapure H_2O and diluted appropriately to give serial dilution series (10^{-4}-10^{-6} M).
First-generation ligands. To evaluate the effect of the ligand concentration, an aliquot of the post-processed [^{111}Ag]Ag$^+$ eluate stock solution (~ 1 MBq, 1 M HCl) was incubated with a solution containing the ligand (DO4S or DO4S4Me) at the proper concentration diluted in 1.5 M sodium acetate buffer (pH 4). The influence of the temperature on the reaction yield was evaluated by incubating the reaction mixtures containing [^{111}Ag]Ag$^+$ (1 MBq) and the ligand (20 nmol) at different temperatures (RT or 50°C) in acetate buffer (1.5 M, pH 4) for 5 min. To determine the ligand efficiency at different pH, the reaction mixtures ([^{111}Ag]Ag$^+$ 1 MBq, 20 nmol of the ligand) were buffered with KH_2PO_4 1.5 M and Na_2HPO_4 1.5 M (pH 7), or diluted with HCl 0.01 M (pH 2). Radiolabelling was monitored *via* thin layer chromatography (TLC) using RP-silica gel plates. The TLC were developed by water: methanol (25 : 75 volume ratio) + ammonium acetate 5% as eluent. Under these conditions, Ag$^+$ complexes are retained at the origin (R_f = 0) while free Ag$^+$ moves with the solvent front (R_f = 1). The TLC plate was exposed to a multi-sensitive medium phosphor screen (Perkin Elmer) for 3 min using a Cyclone Plus Storage Phosphor System (Perkin Elmer).
Second-generation ligands. Concentration-dependent radiolabelling were performed by addition of [^{111}Ag]Ag$^+$ (12.5 µL, 1 MBq, 0.3 M HCl) to a solution containing the ligand

(20 µL, 10^{-3} - 10^{-5} M) diluted in 0.1 M Na_2HPO_4 (100 µL) at room temperature and 50°C. All radiolabelling reactions were repeated at least in duplicate.
Radiolabelling was monitored *via* thin layer chromatography (TLC) using Silica Gel 60 F254 aluminium plates and a mixture of $CHCl_3/CH_3OH/H_2O/CH_3COOH$ 50/20/4/1% as mobile phase. Under these conditions, free Ag^+ is retained at the origin (R_f = 0) while Ag^+ complexes has R_f = 0.5. The TLC plates were analyzed using the same set up described above.

Metal Competition Assays. Metal competition studies were performed by labelling DO4S and DO4S4Me with [^{111}Ag]Ag^+ ($2 \cdot 10^{-5}$ M ligand, pH 4, 50°C, 5 min) in presence of a 2:1 metal-to-ligand excess of Cd^{2+}. Competitions studies with Pd^{2+} were performed by labelling DO4S and TRI4S with [^{111}Ag]Ag+ (10^{-4} M ligand, pH 7, RT, 5 min) in presence of a 1:1, 10:1 and 100:1 metal-to-ligand excess of Pd^{2+}.

***In Vitro* Stability Assays.** The stability of the [^{111}Ag]Ag-labelled complexes was checked in presence of Zn^{2+}, in PBS and in human serum by adding a 5:1 metal-to-ligand molar ratio excess of Zn^{2+} or diluting the radiolabelled complex solutions with an equal volume of PBS or human serum (1:1 *v*/*v* dilution), respectively. The solutions were incubated at 37°C. The metal-complexes stability was monitored over time *via* TLC using the same protocol described for the radiolabelling studies (*vide supra*).

3.4 Conclusions

Despite its potential as a theranostic radionuclide, the labelling chemistry of silver remains virtually unexplored so far and the development of chelating agents that form sufficiently stable complexes with this metal ion *in vivo* remains a challenge.
In this Chapter, several sulfur-containing ligands were considered as Ag^+ chelators. Potentiometric and spectroscopic results showed that the first-generation series formed a highly stable [AgL] complex at physiological pH, but complex stability was remarkably high also in acidic solutions where protonated species (*e.g.*, [AgHL]) predominated.
Overall results indicated that the sulfanyl pendant arms play an essential role in the metal coordination, enhancing the stability of the Ag^+-complexes with respect to carboxylate containing arms of the commonly employed azamacrocycles (*e.g.*, DOTA). The ligands bearing four sulfide arms, *i.e.* DO4S and DO4S4Me, were demonstrated to form the most stable complexes. DO3S and DO3SAm, despite bearing three sulfide chains instead of four, formed not much weaker complexes: this finding was explained by DFT calculations, NMR measurements, and X-ray structure of [Ag(DO4S)]PF_6,[32] which indicated that only the two opposite sulfur atoms can simultaneously coordinate the metal ion. The highest stability

displayed by the compounds bearing four sulfide arms can thus be attributed to statistical effects.

The formation of a distorted tetrahedral structure around Ag^+ was demonstrated through DFT calculations. Among the eight possible coordinating groups of DO4S, only the two opposite N atoms (*i.e.* N_1 and N_7 on the cyclen ring) and the corresponding sulfide arms were bound to Ag^+. A weaker coordination by the remaining two nitrogens was also computed to occur. In solution, a highly fluxional behaviour due to sidearms exchange and/or macrocyclic ring turn was revealed by NMR.

Variation of the ring size and the nitrogen donor array dramatically influence the thermodynamic stability of the resulting complexes as a drop of stability was found from the 12-member ring, *i.e.* DO4S, to the 14-member ring, *i.e.* TE4S (pAg^+_{DO4S} = 14.5 *vs.* pAg^+_{TE4S} = 10.3) and the 3N analogue, *i.e.* TACD3S (pAg^+_{TACD3S} = 10.6).

The variation of the macrocyclic backbone also had a consequence on the solution dynamic of the corresponding Ag^+ complexes as the deprotonation/protonation equilibria were always found to be fast with the second-generation ligands, probably as an effect of the larger ring size or its lower tensions. However, the alteration of the backbone properties seems to maintain unchanged the fluxional behaviour found in solution with the first-generation ligands, in particular as regards the intramolecular exchanges of sulfur donors. Intriguingly, the introduction of asymmetry in TRI4S give raise to a more static Ag^+ complex.

Radiolabelling data showed that the metal ion was rapidly and efficiently bound by DO4S at various pH and at room temperature. DO4S4Me, on the other hand, gave quantitative radiolabelling only at a higher temperature, suggesting that the addition of a rigid chiral backbone onto the DO4S structure with the intention of increasing its stability hamper the labelling kinetics.

The ring properties noticeably also influence the labelling yield when radioactive silver-111 is handled as, while TRI4S maintained an efficient labelling behaviour, TACD3S and TE4S demonstrated to be not able to bind the metal ion under extremely dilute conditions.

Human serum stability assays revealed that $[^{111}Ag][Ag(DO4S)]^+$ was moderately stable while $[^{111}Ag][Ag(TRI4S)]^+$ demonstrated to be unstable under simulated biological conditions. It follows that the *in vitro* stabilities/inertness of the silver complex are strongly correlated with their thermodynamic properties.

Author Contributions

M. Tosato designed the experiments, analyzed and interpreted the data. M. Tosato performed the pH/pAg potentiometric titrations with assistance from the Master's students R. Doro, M. Covolo and S. Franchi. UV-Vis and NMR spectroscopic measurements were

conducted by M. Tosato and by the students F. Bordignon and S. Franchi. All students worked under the supervision of M. Tosato. DFT calculations were performed by Dr M. Dalla Tiezza, supervised by Prof. L. Orian. R. Vogel and Prof. D. Häussinger designed and synthesized DO4S4Me. Prof. U. Köster was responsible of the production of silver-111. Prof. M. Jensen was responsible of the separation of silver-111. Radiochemistry experiments were performed by M. Tosato and Dr M. Asti at the Hevesy Laboratory, Department Health Technology, Technical University of Denmark (DTU), Roskilde, Denmark. Dr M. Asti was responsible of the radiochemistry experiments. Prof. V. Di Marco oversaw and supervised the study. Both manuscripts were written by M. Tosato.

3.5 References

1 A. Hermanne, S. Takacs, F. Tarkanyi and R. Bolbos, *Nucl. Instruments Methods Phys. Res. B*, 2004, **217**, 193-201.

2 T. A. Aweda, O. Ikotun, T. Mastren, C. L. Cannon, B. Wright, W. J. Youngs, C. Cutler, J. Guthrie and S. E. Lapi, *MedChemComm*, 2013, **4**, 1015-1017.

3 S. Chattopadhyay, K. V. Vimalnath, S. Saha, A. Korde, H. D. Sarma, S. Pal and M. K. Das, *Appl. Radiat. Isot.*, 2008, **66**, 334-339.

4 M. Neves, A. Kling and R. M. Lambrecht, *Appl. Radiat. Isot.*, 2002, **57**, 657-664.

5 T. Mastren, V. Radchenko, J. W. Engle, J. W. Weidner, A. Owens, L. E. Wyant, R. Copping, M. Brugh, N. Meiring, E. R. Birnbaum, K. D. John and M. E. Fassbender, *Anal. Chim. Acta*, 2018, **998**, 75-82.

6 N. Ukon, M. Aikawa, Y. Komori and H. Haba, *Nucl. Inst. Methods Phys. Res. B*, 2018, **426**, 13-17.

7 T. M. Illidge and S. Brock, *Curr. Pharm. Des.*, 2000, **6**, 1399-1418.

8 D. K. Hazra, G. T. Stevenson and K. S. Kan, *Cell Biophys.*, 1995, **26**, 183-186.

9 R. Alberto, P. Blauenstein, I. Novak-Hofer, A. Smith and P. A. Schubiger, *Appl. Radiat. Isot.*, 1992, **43**, 869-872.

10 M. Khalid, A. Mushtaq and M. Z. Iqbal, *Appl. Radiat. Isot.*, 2000, **52**, 19-22.

11 A. Andrighetto, M. Tosato, M. Ballan, S. Corradetti, F. Borgna, V. Di Marco, G. Marzaro and N. Realdon, *J. Radioanal. Nucl. Chem.*, 2019, **332**, 73-77.

12 M. Tosato, S. Nardella, D. Badocco, P. Pastore, A. Andrighetto, N. Realdon and V. Di Marco, *Appl. Radiat. Isot.*, 2020, **164**, 109263.

13 R. Delgado, R. Felix, L. M. P. Lima and D. W. Price, *Dalton Trans.*, 2007, **26**, 2734-2745.

14 D. J. Stigers, R. Ferdani, G. R. Weisman, E. H. Wong, C. J. Anderson, J. A. Golen, C. Moore and A. L. Rheingold, *Dalton Trans.*, 2010, **39**, 1699-1701.

15 R. Ferdani, D. J. Stigers, A. L. Fiamengo, L. Wei, B. T. Y. Li, J. A. Golen, A. L. Rheingold, G. R. Weisman, E. H. Wong and C. J. Anderson, *Dalton Trans.*, 2012, **41**,

1938-1950.

16 M. Roger, L. M. P. Lima, M. Frindel, C. Platas-Iglesias, J. F. Gestin, R. Delgado, V. Patinec and R. Tripier, *Inorg. Chem.*, 2013, **52**, 5246-5259.

17 P. Comba, L. Grimm, C. Orvig, K. Rück and H. Wadepohl, *Inorg. Chem*, 2016, **55**, 12531-12543.

18 R. Ševčík, J. Vaněk, R. Michalicová, P. Lubal, P. Hermann, I. C. Santos, I. Santos and M. P. C. Campello, *Dalton Trans.*, 2016, **45**, 12723-12733.

19 S. Lacerda, M. P. Campello, F. Marques, L. Gano, V. Kubıček, P. Fousková, É. Tóth and I. Santos, *Dalton Trans.*, 2009, **23**, 4509-4518.

20 M. Tosato, M. Verona, R. Doro, M. Dalla Tiezza, L. Orian, A. Andrighetto, P. Pastore, G. Marzaro and V. Di Marco, *New J. Chem.*, 2020, **44**, 8337-8350.

21 S. L. Whitbread, S. Politis, A. K. W. Stephens, J. B. Lucas, R. Dhillon, S. F. Lincoln and K. P. Wainwright, *J. Chem. Soc., Dalton Trans.,* 1996, **7**, 1379-1384.

22 M. O. Kestner and A. L. Allred, *J. Am. Chem. Soc.*, 1972, **94**, 7189-7190.

23 E. K. Barefield and M. T. Mocella, *Inorg. Chem.*, 1973, **12**, 2835-2439.

24 K. B. Mertes, *Inorg. Chem.*, 1978, **17**, 49-52.

25 H. N. Po, E. Brinkman and R. J. Doedens, *Acta Crystallogr.*, 1991, **47**, 2310-2312.

26 H. N. Po, S. C. Shen and R. J. Doedens, *Acta Crystallogr.*, 1993, **49**, 1914-1916.

27 A. Honda, S. Kakihara, S. Ichimura, K. Tomono, M. Matsushita, R. Yamamoto, E. Kikuta, Y. Tamaki and K. Miyamura, *Inorganica Chim. Acta*, 2021, **524**, 120431.

28 Z. D. Liu, H. H. Khodr, D. Y. Liu, S. L. Lu and R. C. Hider, *J. Med. Chem.*, 1999, **42**, 4814-4823.

29 G. Crisponi and V. M. Nurchi, *Chelation Therapy in the Treatment of Metal Intoxication*, 2016, 35-61.

30 M. Tosato and V. Di Marco, *Biomolecules*, 2019, **9**, 269.

31 C. R. Groom, I. J. Bruno, M. P. Lightfoot and S. C. Ward, *Acta Crystallogr. Sect. B Struct. Sci. Cryst. Eng. Mater.*, 2016, **72**, 171-179.

32 T. Gyr, H. R. Mäcke and M. Hennig, *Angew. Chemie*, 1997, **36**, 2786-2788.

33 V. Di Marco, PhD Thesis, Univeristy of Padova, 1998.

34 M. Tosato, M. Asti, M. Dalla Tiezza, L. Orian, D. Häussinger, R. Vogel, U. Köster, M. Jensen, A. Andrighetto, P. Pastore and V. Di Marco, *Inorg. Chem.*, 2020, **59**, 10907-10919.

35 C. F. J. Baes and R. E. Mesmer, *The Hydrolysis of cations*, 1976.

36 P. Hohenberg and W. Kohn, *Phys. Rev.*, 1964, **136**, B864-B871.

37 W. Kohn and L. J. Sham, *Phys. Rev.*, 1965, **140**, A1133-A1138.

38 G. te Velde, F. M. Bickelhaupt, E. J. Baerends, C. Fonseca Guerra, S. J. A. van Gisbergen, J. G. Snijders and T. Ziegler, *J. Comput. Chem.*, 2001, **22**, 931-967.

39 C. Fonseca Guerra, J. G. Snijders, G. te Velde and E. J. Baerends, *Theor. Chem. Acc*,

1998, **99**, 391-403.

40 ADF2018, SCM, Theoretical Chemistry; Vrije Universiteit, Amsterdam: The Netherlands, http://www.scm.com.

41 N. C. Handy and A. J. Cohen, *Mol. Phys.*, 2001, **99**, 403-412.

42 J. P. Perdew, K. Burke and M. Ernzerhof, *Phys. Rev. Lett.*, 1996, **77**, 3865-3868.

43 E. van Lenthe and E. J. Baerends, *J. Comput. Chem.*, 2003, **24**, 1142-1156.

44 M. Bortoli, M. Dalla Tiezza, C. Muraro, G. Saielli and L. Orian, *Molecules*, 2019, **24**, 1250.

45 G. Ribaudo, M. Bellanda, I. Menegazzo, L. P. Wolters, M. Bortoli, G. Ferrer-Sueta, G. Zagotto and L. Orian, *Chem. Eur. J*, 2017, **23**, 2405-2422.

46 F. Zaccaria, L. P. Wolters, C. F. Guerra and L. Orian, *J. Comput. Chem.2*, 2016, **37**, 1672-1680.

47 C. C. Pye and T. Ziegler, *Theor. Chem. Acc.*, 1999, **101**, 396-408.

48 A. V. Marenich, C. J. Cramer and D. G. Truhlar, *J. Phys. Chem. B*, 2009, **113**, 6378-6396.

49 J. Ho, A. Klamt and M. L. Coote, *J. Phys. Chem. A*, 2010, **114**, 13442-13444.

50 N. L. Allinger, X. Zhou and J. Bergsma, *J. Mol. Struct. THEOCHEM*, 1994, **312**, 69-83.

51 S. Grimme, C. Bannwarth and P. Shushkov, *J. Chem. Theory Comput.*, 2017, **13**, 1989-2009.

52 F. M. Bickelhaupt and E. J. Baerends, *Kohn-Sham Density Functional Theory: Predicting and Understanding Chemistry*, John Wiley & Sons, Inc., 2007.

53 L. Orian, L. P. Wolters and F. M. Bickelhaupt, *Chem. Eur. J.*, 2013, **19**, 13337-13347.

54 L. Orian, J. van Stralen and F. M. Bickelhaupt, *Organometallics*, 2007, **26**, 3816-3830.

55 M. Dalla Tiezza, F. M. Bickelhaupt and L. Orian, *Chem Open*, 2019, **8**, 143-154.

56 M. Dalla Tiezza, F. M. Bickelhaupt and L. Orian, *ChemPhysChem*, 2018, **19**, 1766-1773.

57 R. Bauer, E. Danielsen, L. Hemmingsen, M. J. Bjerrum, Ö. Hansson and K. Singh, *J. Am. Chem. Soc.*, 1997, **119**, 157-162.

Chapter 4

Copper Coordination Chemistry of Sulfur-Rich Macrocycles: An Attempt to Hinder the Reductive-Induced Demetallation in $^{64/67}$Cu-Based Radiopharmaceuticals

This chapter contains an adaptation of a published work, and is reproduced in part, with permission from Tosato, M.; Dalla Tiezza, M.; May, N. V.; Isse, A. A.; Nardella, S.; Orian, L.; Verona, M.; Vaccarin, C.; Alker, A.; Mäcke, H.; Pastore, P.; Di Marco, V. Copper Coordination Chemistry of Sulfur Pendant Cyclen Derivatives: An Attempt to Hinder the Reductive-Induced Demetalation in $^{64/67}$Cu Radiopharmaceuticals, *Inorg. Chem.*, **2021**, 60, 15, 11530 - 11547, Copyright 2021 American Chemical Society (https://pubs.acs.org/doi/10.1021/acs.inorgchem.1c01550).

This chapter comprehends an adaptation of a submitted manuscript and is reproduced in part with the permission from Tosato, M.; Pelosato, M.; Franchi, S.; Isse, A. A.; May, N.V.; Zanoni, G.; Mancin, F.; Pastore, P.; Badocco, D.; Asti, M.; Di Marco, V., When Ring Makes the Difference: Coordination Properties of Cu^{2+}/Cu^{+} Complexes with Sulfur-Pendant Polyazamacrocycles for Radiopharmaceutical Applications, **2022**.

This chapter comprises also a manuscript in preparation, reproduced in part with the permission from Tosato, M.; Verona, M.; Favaretto, C.; Talip, Z.; van der Meulen, N.; Di Marco, V.; Asti, M. *et al.* Expected submission: March 2022. This research was supported by the ISOLPHARM_EIRA project funded by INFN-LNL (Italy).

4.1 Introduction

A great deal of research has been conducted during the past decades to develop radiopharmaceuticals for non-invasive imaging and treatment of tumours. In particular, copper has received much interest because it possesses several radioisotopes (copper-60, copper-61, copper-62, copper-64, copper-67) with half-life and emission properties suitable for diagnostic and therapeutic applications.[1–3] Copper-64 (^{64}Cu, $t_{1/2}$ 12.7 h) is the most versatile since its unique decay profile, which combines electron capture (I_{EC} 43%) with associated Meitner-Auger electrons, β^+ (I_{β^+} 18%, $E_{\beta^+,\,max}$ 655 keV) and β^- emission (I_{β^-} 39%, $E_{\beta^-,max}$ 573 keV), makes it suitable for PET imaging and, in principle, radiotherapy by using the same radiopharmaceutical.[4–6] On the other hand, the β^- emitter copper-67 (^{67}Cu, $t_{1/2}$ 61.9 h, I_{β^-} 100%, $E_{\beta^-,max}$ 141 keV) is a promising candidate for therapy as well as for SPECT imaging due to its γ-rays emission (E_γ 93 keV, I_γ 16%; E_γ 185 keV, I_γ 49%).[7–9]

The theranostic approach of using both ^{64}Cu and ^{67}Cu could allow low-dose scouting scans to obtain dosimetry information, followed by higher dose therapy in the same patient, thus bringing a major step towards personalized medicine.[10]

As described in **Chapter 1**, to obtain the site-specific delivery of the emitted radiation, the copper radioisotopes must be firmly coordinated by a BFC appended to a tumour-targeting biomolecule.[11–13] However, the biologically-induced reduction of Cu^{2+} to Cu^+ is a potential pathway for the demetallation of [$^{64/67}$Cu]Cu^{2+} radioconjugates, as unstable and labile cuprous species can trigger the dissociation of the complexes.[4,14–17] As a result, the unbound radiometal can spread through the body leading to a loss of selectivity for the target to be imaged or treated.[17] Therefore, it is important for a BFC selected for $^{64/67}$Cu to be able to firmly complex both Cu^{2+} and Cu^+ or to stabilise Cu^{2+} to prevent this reduction pathway.[14,16,18–24]

Given the borderline character of Cu^{2+} according to Pearson's Hard-Soft Acid-Base theory (HSAB), the investigated BFCs for its chelation are mostly confined to polyazamacrocyclic scaffolds with pendant carboxylate arms such as 1,4,7,10-tetraazacyclododecane-1,4,7,10-tetraacetic acid (DOTA), 1,4,8,11-tetraazacyclotetradecane-1,4,8,11-tetraacetic acid (TETA) (**Figure 4.1**), and their derivatives. These ligands form Cu^{2+} complexes with excellent thermodynamic stability but suffer from marked kinetic lability which causes *in vivo* demetallation.[2,6,19,25,26] To overcome this limit, constrained or reinforced polyaza chelators such as 1,4,7,10-tetraazabicyclo[5.5.2]tetradecane-4,10-diacetic acid (CB-DO2A), 1,4,8,11-tetraazabicyclo[6.6.2]-hexadecane-4,11-diacetic acid (CB-TE2A), and other derivatives were developed (**Figure 4.1**).[1,2,6,14,27–30] The increased rigidity of the ligand backbone makes these complexes less prone to dissociation but also causes slow formation rates, thus needing harsh labelling conditions such as high temperature and prolonged

reaction time. While still practicable for bioconjugates of some targeting vectors, these severe labelling conditions preclude the use of thermo-sensitive biomolecules (*e.g.*, antibodies). Besides the high kinetic inertness obtainable through structurally constrained derivatives, also 1,4,7-triazacyclononane-1,4,7-triacetic acid (NOTA) as well as its 1-glutaric acid derivative (NODAGA), and sarcophagine chelators (**Figure 4.1**) have demonstrated remarkable inertness combined with mild labelling conditions.[31]

The quest of novel BFCs for $^{64/67}$Cu that combine high *in vivo* stability and kinetic inertness, with quantitative and fast radiolabelling in mild conditions and no demetallation upon Cu^{2+}/Cu^{+} reduction, is still a significant challenge.[32] With regards to the latter decomplexation pathway, only a few attempts have been made to develop BFCs able to securely bind both Cu^{2+} and Cu^{+}.[23,33,34] In light of this, it was hypothesized herein that the series of polyazamacrocyclic ligands bearing sulfide pendant chains described in detail in **Chapter 2** could stabilize both copper oxidation states as they simultaneously incorporate functional groups with different chemical softness.

In this chapter, the kinetic, thermodynamic, and structural investigation of the Cu^{2+} and Cu^{+} complexes of the first- and second-generation ligands is reported. This study was performed with natural copper through UV-Vis, Electron Paramagnetic Resonance (EPR) and NMR spectroscopies, X-ray crystallography, and electrochemical methods (potentiometric titrations, cyclic voltammetry, and electrolysis), and the results were supported by accurate relativistic DFT calculations. Furthermore, to fully assess the potential of these macrocycles for nuclear medicine applications, radiolabelling with $[^{64}Cu]Cu^{2+}$ and *in vitro* stability assays of the corresponding $[^{64}Cu]Cu^{2+}$-complexes were also performed.

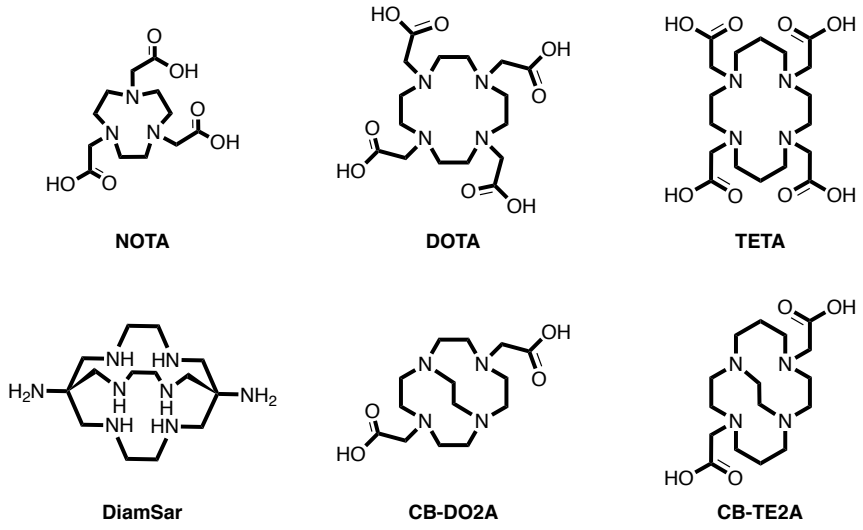

Figure 4.1. Structure of selected state-of-the-art copper chelators (NOTA, DOTA, TETA, DiamSar, CB-DO2A and CB-TE2A).

4.2 Results and Discussion

4.2.1 Complexation Kinetics of Cupric Complexes with First-Generation Ligands

Preliminary evaluation of the complex formation between Cu^{2+} and the first-generation ligands demonstrated that these reactions can be remarkably slow. As the attainment of rigorous thermodynamic data requires solutions to be at equilibrium, time conditions for reaching equilibrium were explored as a function of pH and at room temperature before performing the thermodynamic measurements.

The UV-Vis spectra and the time course of the complexation reaction between Cu^{2+} and the investigated sulfide-bearing chelators are shown in **Figure 4.2**, **Figure 4.3,** and **Figure 4.4**. DOTA was also included for comparison purposes (**Figure 4.5**).

At concentrations of ~ 10^{-4} M for both Cu^{2+} and ligand, the complex formation was always found to be instantaneous (< 10 s) at neutral pH, whilst at pH 4.8 it was complete (> 99%) in a few seconds for DO2A2S and DOTA and within ~ 1 h for DO4S, DO3S, and DO3SAm. The reactions became progressively slower under increasingly acidic conditions, as resumed in **Table C1** (**Appendix C**): at pH 2.0, DOTA and DO2A2S reached the equilibrium in a few hours, whilst for the other chelators, the equilibrium was established only after ~ 10 days.

Other experiments were performed which showed that the reaction rates increased proportionally with the concentration of the reactants (**Table C2** - **Appendix C**).

The marked difference between the complex formation rate of the pure sulfide-bearing chelators and the carboxylate-ones can be rationalized by analyzing the role that the acetate arms play in the complexation event. These negatively charged pendants can interact with the incoming Cu^{2+} ions forming an out-of-cage intermediate, which is later transformed into an in-cage product where the metal ion is coordinated by the nitrogens and the donor atoms of the pendants so that the overall reaction can be accelerated by increasing the local concentration of the metal ion close to the ligand cavity.[35,36]

This ability has been indicated for DOTA, and it appears to be absent when all carboxylates are replaced by sulfanyl groups. If the pH decreases, protonated species become increasingly predominant (**Chapter 2**). In these forms, the protons induce an electrostatic repulsion towards the Cu^{2+} ions and block the access of the metal ion into the ligand cavity, progressively slowing down the complex formation.

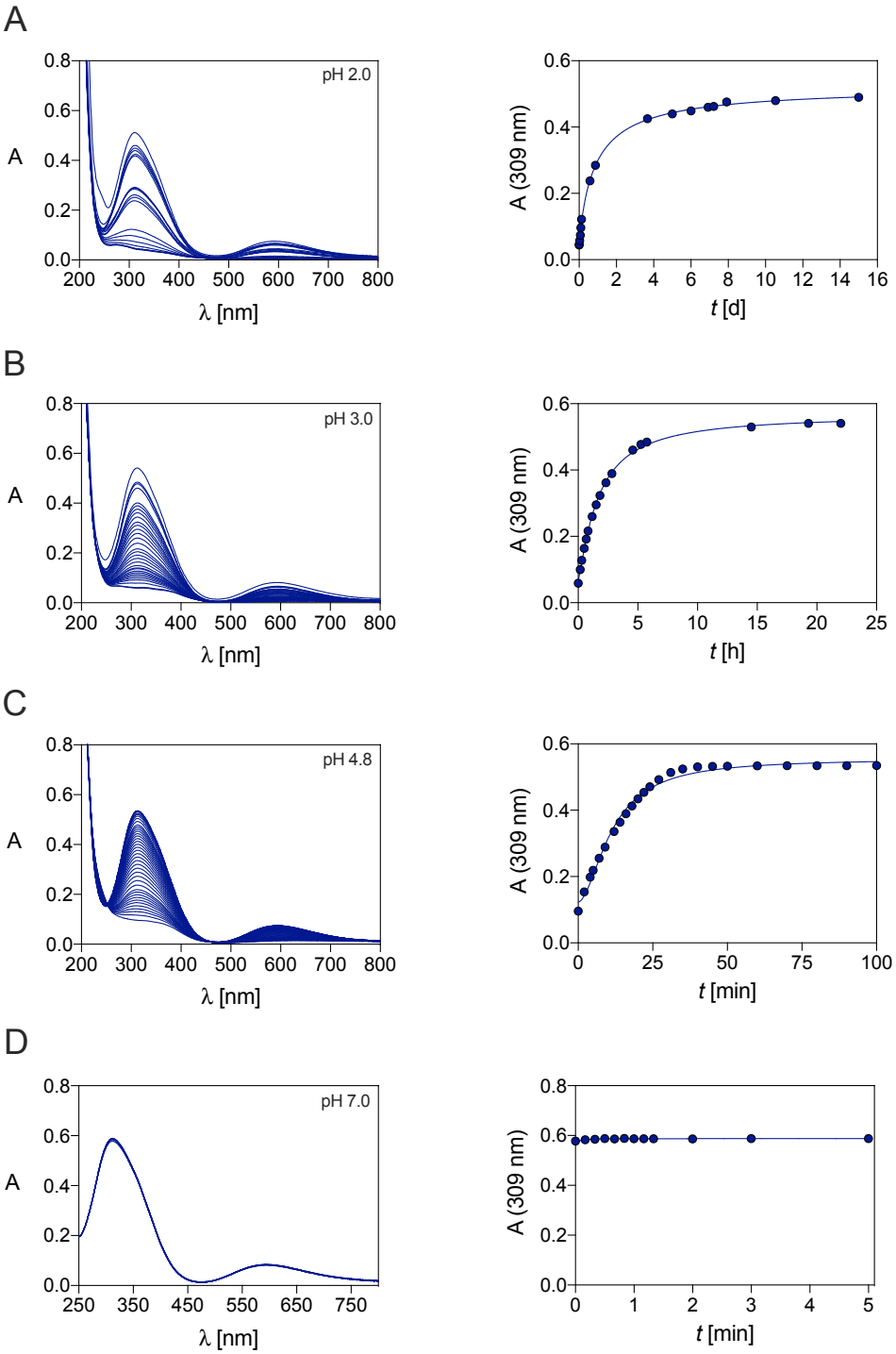

Figure 4.2. UV-Vis spectra (left) and time course (right) of the Cu^{2+}-DO4S complex formation at (A) pH 2.0 (C_{DO4S} = $C_{Cu^{2+}}$ = $1.2 \cdot 10^{-4}$ M), (B) pH 3.0 (C_{DO4S} = $C_{Cu^{2+}}$ = $1.5 \cdot 10^{-4}$ M), (C) pH 4.8 (C_{DO4S} = $C_{Cu^{2+}}$ = $1.3 \cdot 10^{-4}$ M) and (D) pH 7.0 (C_{DO4S} = $C_{Cu^{2+}}$ = $1.5 \cdot 10^{-4}$ M).

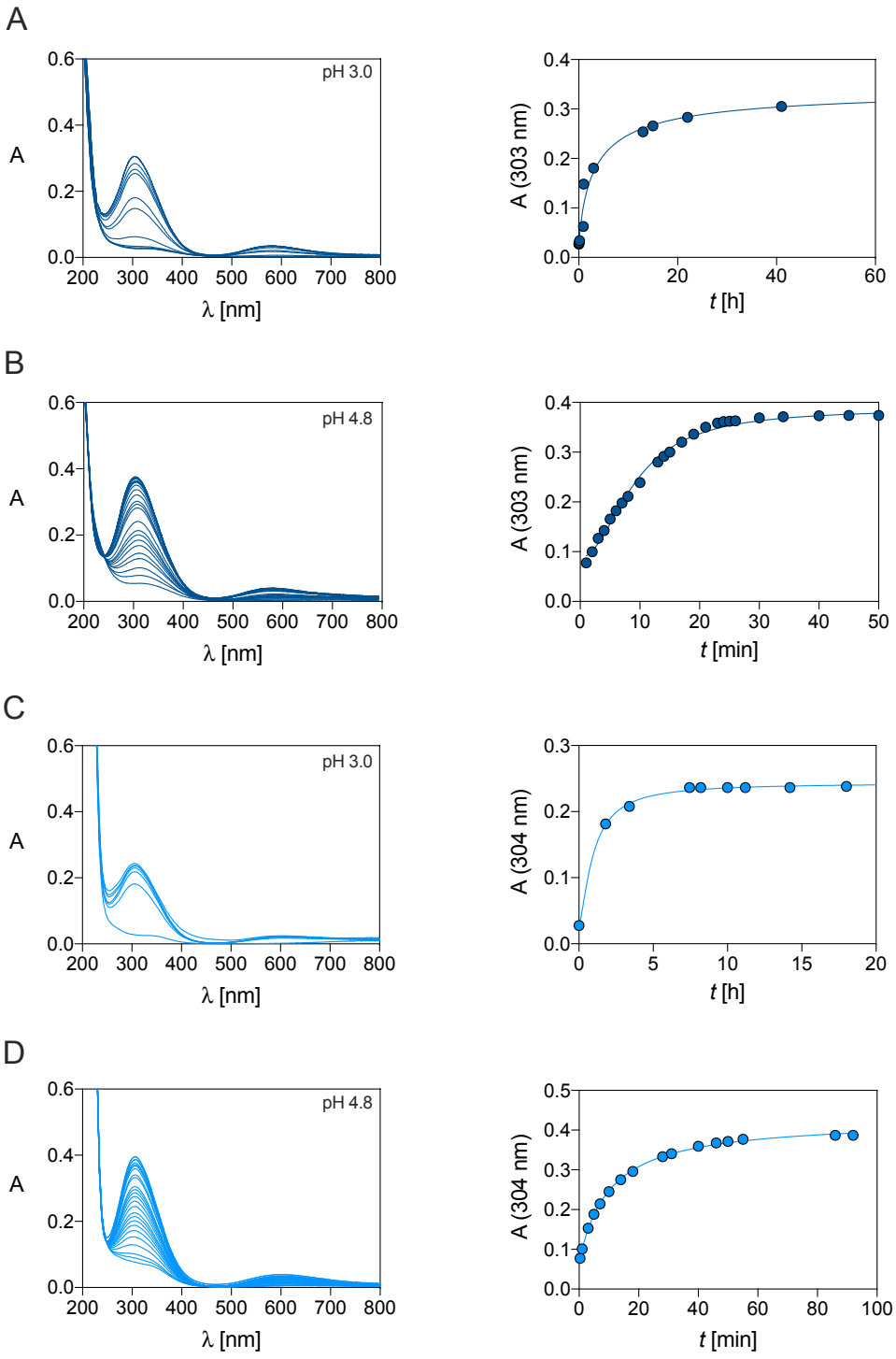

Figure 4.3. UV-Vis spectra (left) and time course (right) of the Cu^{2+} complex formation with (A) DO3S at pH 3.0 ($C_{DO3S} = C_{Cu^{2+}} = 1.0 \cdot 10^{-4}$ M), (B) DO3S at pH 4.8 ($C_{DO3S} = C_{Cu^{2+}} = 1.2 \cdot 10^{-4}$ M), (C) DO3SAm at pH 3.0 ($C_{DO3SAm} = C_{Cu^{2+}} = 8.0 \cdot 10^{-5}$ M) and (D) DO3SAm at pH 4.8 ($C_{DO3SAm} = C_{Cu^{2+}} = 1.1 \cdot 10^{-4}$ M).

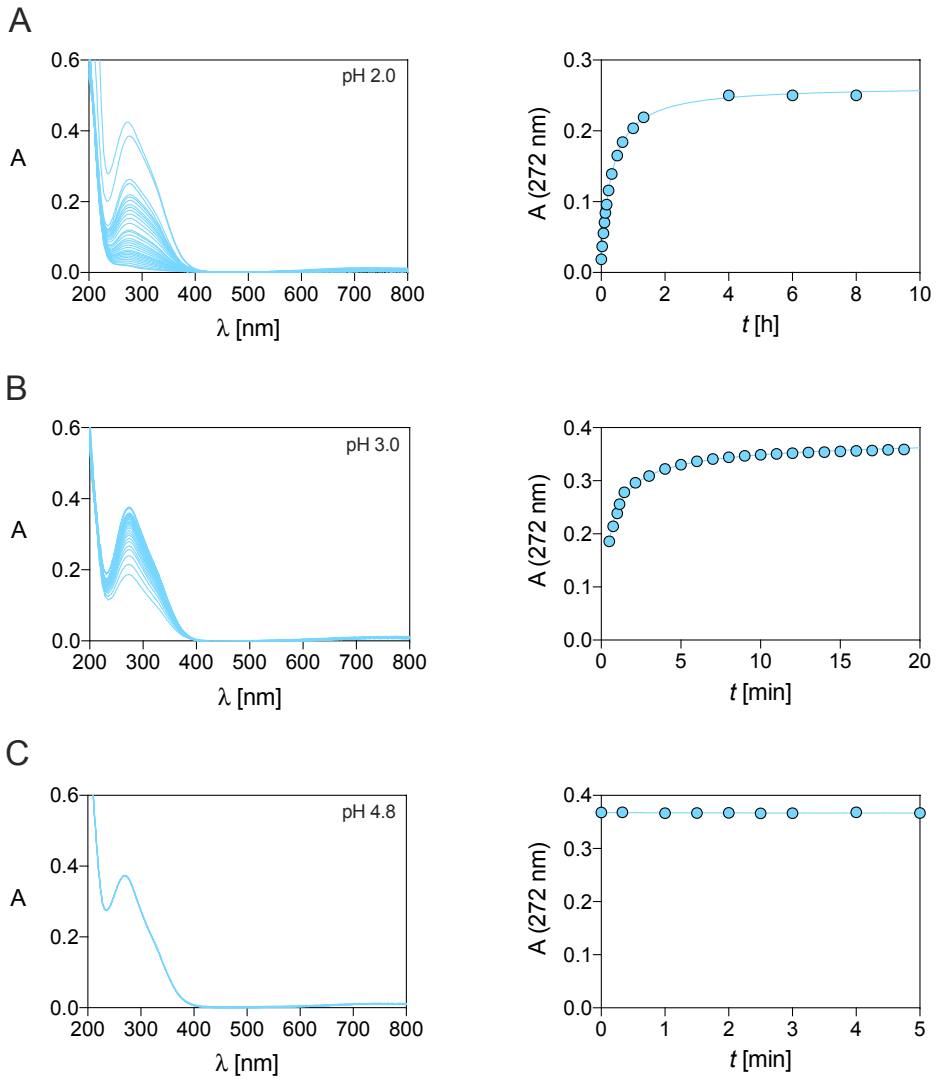

Figure 4.4. UV-Vis spectra (left) and time course (right) of the Cu^{2+}-DO2A2S complex formation at (A) pH 2.0 (C_{DO2A2S} = $C_{Cu^{2+}}$ = $8.0 \cdot 10^{-5}$ M), (B) pH 3.0 (C_{DO2A2S} = $C_{Cu^{2+}}$ = $8.0 \cdot 10^{-5}$ M) and (C) pH 4.8 (C_{DO2A2S} = $C_{Cu^{2+}}$ = $1.1 \cdot 10^{-4}$ M).

4.2.2 Complexation Kinetics of Cupric Complexes with Second-Generation Ligands

For TRI4S and TE4S, reaction times from seconds to many hours were found (**Figure 4.6** and **Table C1** - **Appendix C**). The complex formation rate strongly decreased upon decreasing the pH, reflecting the dissimilar reactivity of the differently protonated ligands species predominating at different pH (**Chapter 2**): higher protonation states correspond to higher electrostatic repulsion between Cu^{2+} and the ring cavity where the donor atoms are located, as reported for DO4S and its derivatives (*vide supra*).

The increased ring size in TRI4S and TE4S significantly accelerates the formation of the Cu^{2+} complexes when compared with the cyclen-analogue, *i.e.* DO4S (**Table C1** - **Appendix C**). This complexation rate enhancement could be explained by the lower electrostatic repulsion between the metal ion and the nitrogen donors driven by the larger ring.

TACD3S was found not to be able to complex Cu^{2+} except at nearly neutral pH, where the reaction rate resulted comparable to that of the other ligands.

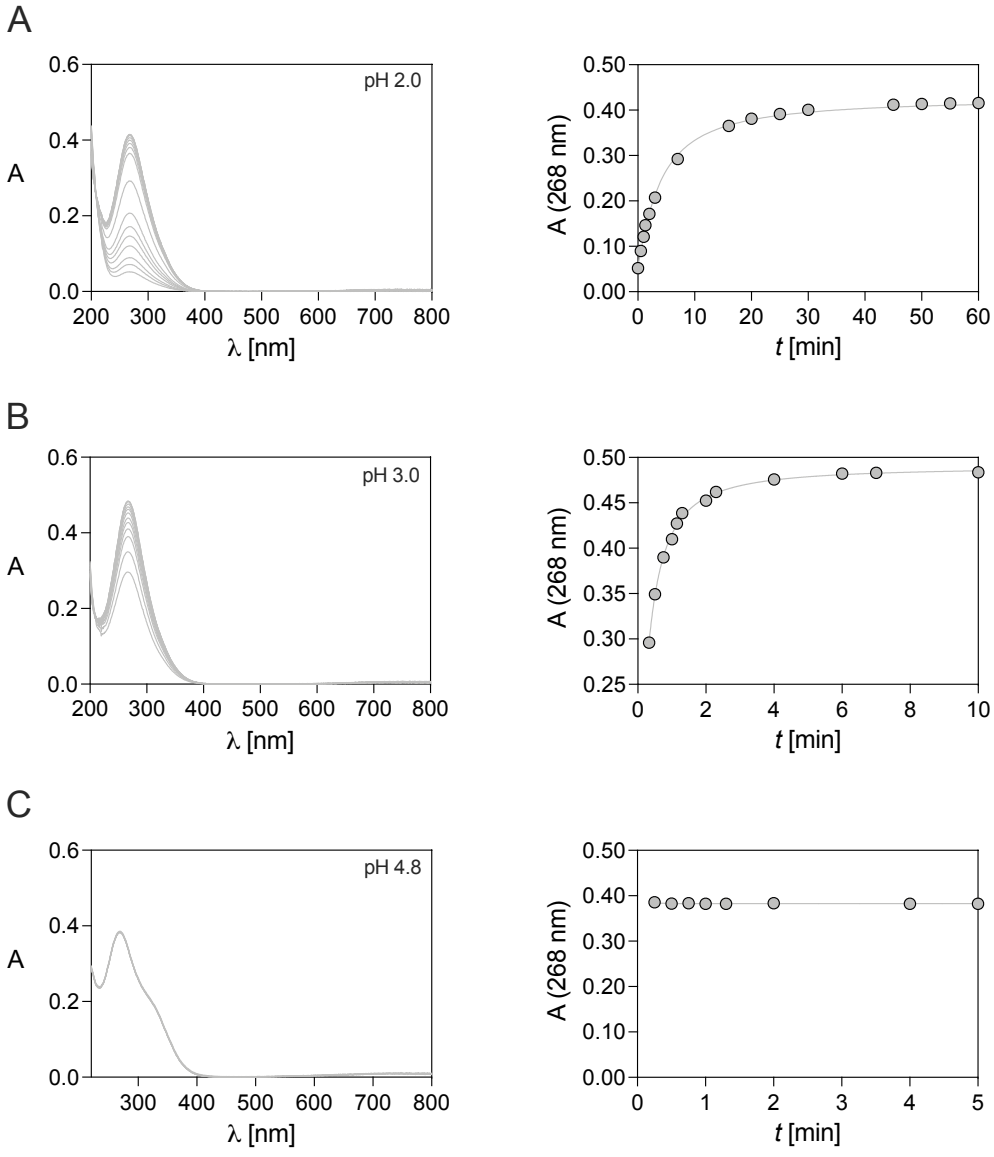

Figure 4.5. UV-Vis spectra (left) and time course (right) of the Cu^{2+}-DOTA complex formation at (A) pH 2.0 (C_{DOTA} = $C_{Cu^{2+}}$ = $1.0 \cdot 10^{-4}$ M), (B) pH 3.0 (C_{DOTA} = $C_{Cu^{2+}}$ = $1.0 \cdot 10^{-4}$ M) and (C) pH 4.8 (C_{DOTA} = $C_{Cu^{2+}}$ = $1.0 \cdot 10^{-4}$ M).

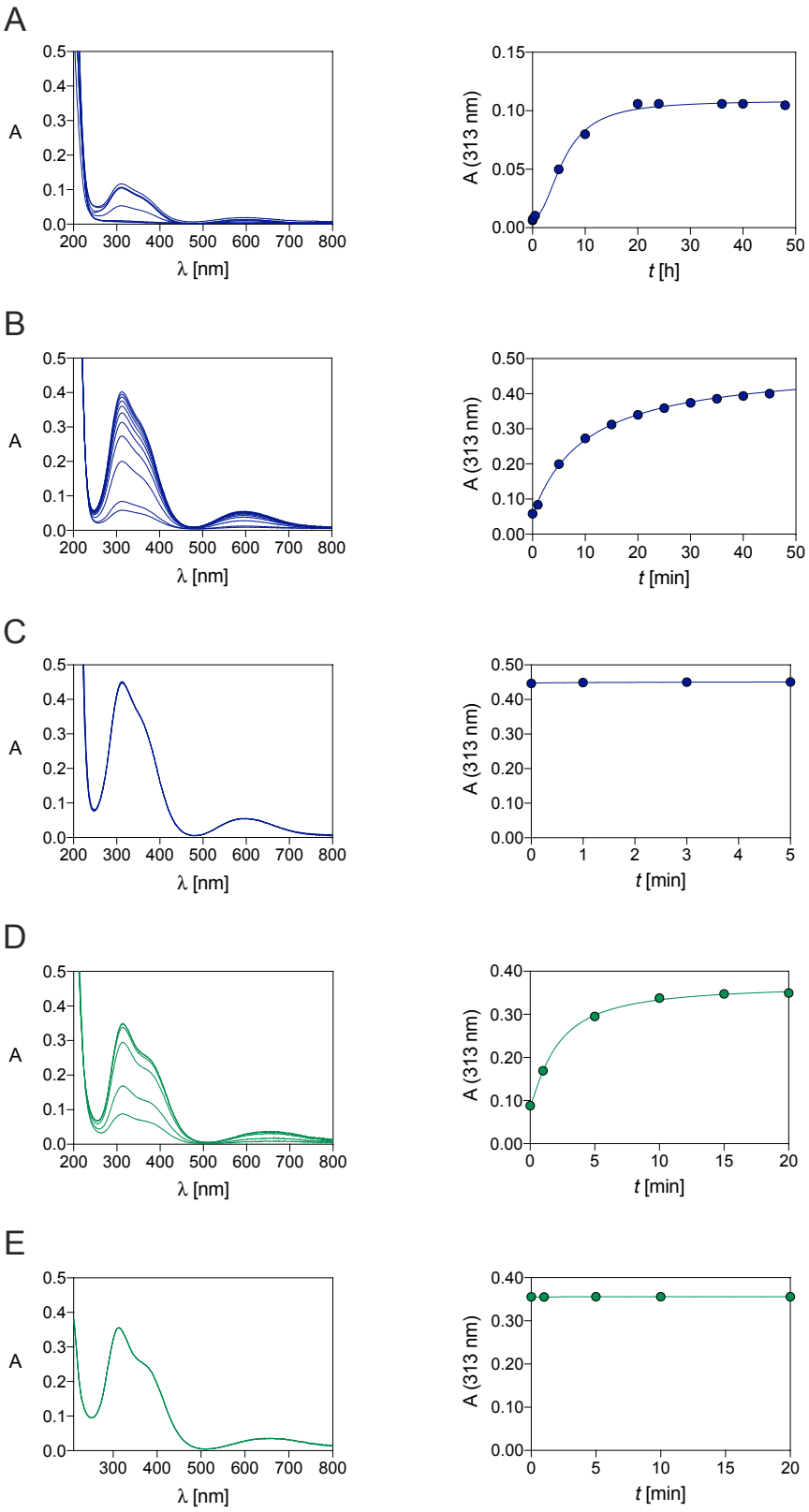

Figure 4.6. UV-Vis spectra (left) and time course of the Cu^{2+} complexation (right) by TRI4S at (A) pH 2.0, (B) pH 3.7 and (C) pH 7.5 (C_{TRI4S} = $C_{Cu^{2+}}$ = $1.0 \cdot 10^{-4}$ M) and TE4S at (D) pH 3.7 and (E) pH 7.5 (C_{TE4S} = $C_{Cu^{2+}}$ = $7.0 \cdot 10^{-5}$ M).

4.2.3 Thermodynamics of Cupric Complexes with First-Generation Ligands

The slow equilibration at acidic pH and the high stability of the Cu^{2+} complexes formed by the first-generation ligands hampered the determination of the equilibrium constants by conventional pH-potentiometry. Therefore, UV-Vis spectrophotometric out-of-cell titrations under strongly acidic conditions, direct in-cell UV-Vis titrations, potentiometric titrations at pH > 4, and spectrophotometric Ag^{+}-Cu^{2+} competition experiments were performed.

Figure 4.7 and **Figure C1** (**Appendix C**) report the electronic spectra of solutions containing Cu^{2+}-DO4S, Cu^{2+}-DO3S, Cu^{2+}-DO3SAm and Cu^{2+}-DO2A2S at equilibrium at pH < 2 and pH > 2, respectively, while the spectroscopic data are summarized in **Table C3** (**Appendix C**).

The marked absorbance variations at pH < 2 can be interpreted by the complex formation. At pH larger than ~ 2, only very minor changes were detected in the spectra of Cu^{2+}-DO4S, Cu^{2+}-DO3S, and Cu^{2+}-DO3SAm, suggesting that the speciation does not change in the investigated pH range.

UV-Vis titrations performed at different metal-to-ligand molar ratios demonstrated that only a 1:1 metal-to-ligand complex exists as deduced from the sharp inflection point at ~ 1:1 molar ratio in the titration curves (**Figure 4.8**). The formation of only one Cu^{2+} complex in the pH range 4-11 was also indicated by pH-potentiometric titrations. According to both spectrophotometric and potentiometric data, this complex is $[CuL]^{2+}$. For Cu^{2+}-DO2A2S, the formation of the deprotonated 1:1 metal-to-ligand complex, *i.e.* [CuL], was also confirmed, but an additional species, $[CuHL]^{+}$, was detected at pH below ~ 4. The overall stability constants determined are given in **Table 4.1** and the corresponding distribution diagrams are shown in **Figure 4.9**.

Competitive Ag^{+}-Cu^{2+} titrations were also performed to determine the Cu^{2+}-ligand stability constants with an independent method, as the constants of Ag^{+}-ligand complexes have been previously determined (**Chapter 3**). The electronic spectra of the preformed Ag^{+} complex with DO4S, DO3S, DO3SAm, and DO2A2S immediately after the addition of 0.2 - 4 equivalents of Cu^{2+} and at equilibrium are shown in **Figure C2** (**Appendix C**). As a slow kinetics of the transmetallation reactions was detected at room temperature, the solutions containing Ag^{+}, Cu^{2+}, and the chelator were forced to equilibrium through heating. The increase of the absorptions at the characteristic wavelengths of the Cu^{2+} complexes clearly reflects their formation (**Figure C2** - **Appendix C**). The stability constants calculated by competitive titrations (**Table 4.1**) agree well with those obtained from UV-Vis spectrophotometric measurements.

4.2.4 Thermodynamics of Cupric Complexes with Second-Generation Ligands

UV-Vis spectrophotometric titrations at equilibrium conditions were performed to determine the Cu^{2+}-complexes formation constants with TACD3S, TRI4S and TE4S. The slow equilibration timing evidenced at acidic pH (*vide supra*) forced the employment of out-of-cell titrations at pH ≤ 4 together with the direct in-cell ones (pH > 4). The high binding Cu^{2+} affinity of TRI4S obviated the use of conventional pH-potentiometric technique, while for TE4S also pH-potentiometry was employed. The Cu^{2+} addition to solutions containing any second-generation chelator causes the appearance of two absorption bands in the UV-Vis spectra, which are accountable for the metal complexation event (**Figure C3** - **Appendix C**). These bands change in intensity but not in shape with pH, so that the formation of the same Cu^{2+} complex in all the pH range was deduced. In fact, the fitting procedure indicated the presence of only one complex having stoichiometry $[CuL]^{2+}$. UV-Vis titrations at different metal-to-ligand molar ratios, which showed saturation at equimolar metal-to-ligand molar ratio (**Figure 4.8**), and potentiometric titrations (at pH ≥ 2 for TE4S, at pH ≥ 4 for TRI4S), further confirmed this speciation model. The overall stability constants are reported in **Table 4.1** while the distribution diagrams are shown in **Figure 4.9**.

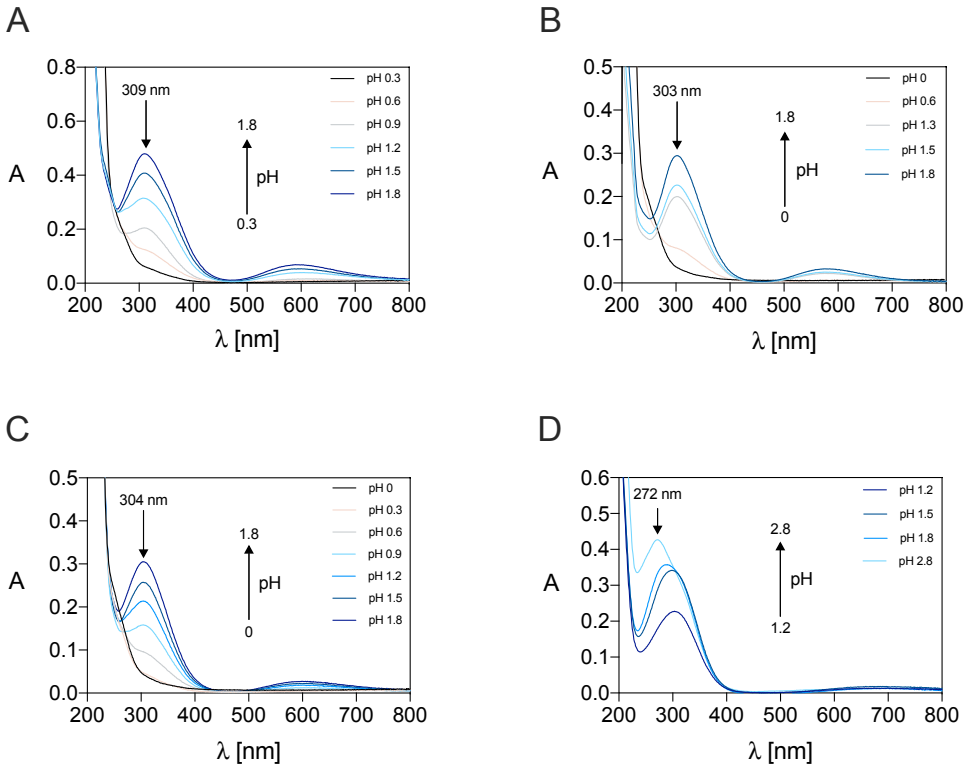

Figure 4.7. UV-Vis spectra at pH < 2 of the Cu^{2+} complexes formed by (A) DO4S ($C_{Cu^{2+}}$ = C_{DO4S} = $1.5 \cdot 10^{-4}$ M), (B) DO3S ($C_{Cu^{2+}}$ = C_{DO3S} = $1.0 \cdot 10^{-4}$ M), (C) DO3SAm ($C_{Cu^{2+}}$ = C_{DO3SAm} = $1.1 \cdot 10^{-4}$ M) and (D) DO2A2S ($C_{Cu^{2+}}$ = C_{DO2A2S} = $0.9 \cdot 10^{-4}$ M) at I = 0.15 M NaCl (for solutions at pH > 0.8) and T = 25°C.

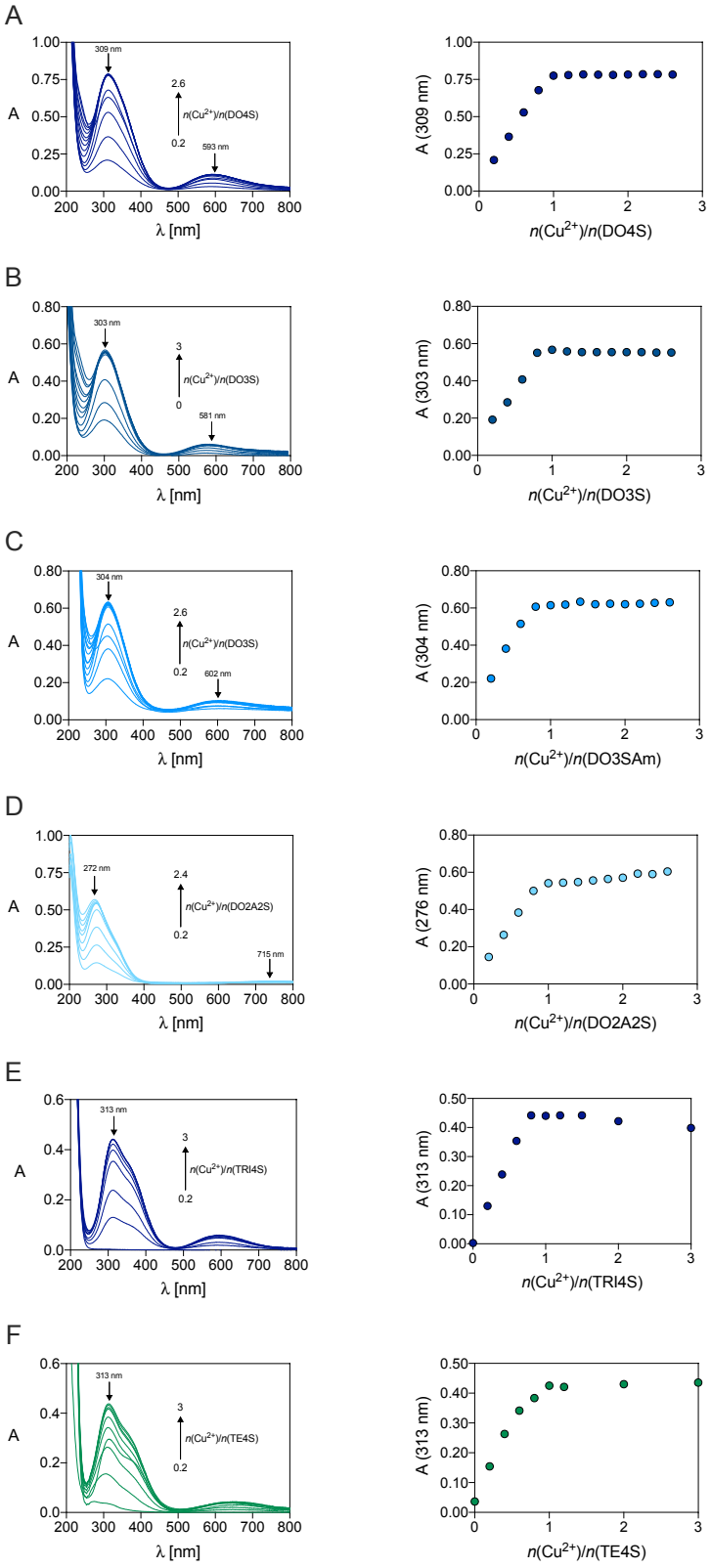

Figure 4.8. UV-Vis titrations by Cu^{2+} of solutions containing (A) DO4S (C_{DO4S} = $2.0 \cdot 10^{-4}$ M, pH 4.8), (B) DO3S (C_{DO3S} = $1.6 \cdot 10^{-4}$ M, pH 4.8), (C) DO3SAm (C_{DO3SAm} = $1.6 \cdot 10^{-4}$ M, pH 4.8), (D) DO2A2S (C_{DO2A2S} = $1.2 \cdot 10^{-4}$ M, pH 4.8), (E) TRI4S (C_{TRI4S} = $1.0 \cdot 10^{-4}$ M, pH 7.5) and (F) TE4S (C_{TE4S} = $1.0 \cdot 10^{-4}$ M, pH 7.5), no ionic strength control and T = 25°C.

Table 4.1. Overall stability constants (logβ) of the Cu^{2+} complexes formed with first- and second-generation ligands at I = 0.15 M NaCl and T = 25°C. Unless otherwise state, values were obtained by UV-Vis spectrophotometric titrations.

Ligand	Equilibrium reaction [a]	logβ				pCu^{2+} [b]
DO4S	$Cu^{2+} + L \leftrightharpoons [CuL]^{2+}$	19.8	±	0.1		17.7
		19.6	±	0.4	[c]	
DO3S	$Cu^{2+} + L \leftrightharpoons [CuL]^{2+}$	20.34	±	0.06		17.5
		20.10	±	0.08	[c]	
DO3SAm	$Cu^{2+} + L \leftrightharpoons [CuL]^{2+}$	19.8	±	0.2		17.2
		19.7	±	0.2	[c]	
DO2A2S	$Cu^{2+} + H^{+} + L^{2-} \leftrightharpoons [CuHL]^{+}$	24.22	±	0.09		19.4
	$Cu^{2+} + L^{2-} \leftrightharpoons [CuL]$	22.05	±	0.3	[c]	
		21.9	±	0.2		
DOTA	$Cu^{2+} + 2H^{+} + L^{4-} \leftrightharpoons [CuH_2L]$	30.8				17.4
	$Cu^{2+} + H^{+} + L^{4-} \leftrightharpoons [CuHL]^{-}$	26.60			[d]	
	$Cu^{2+} + L^{4-} \leftrightharpoons [CuL]^{2-}$	22.30				
TACD3S	$Cu^{2+} + L \leftrightharpoons [CuL]^{2+}$	6.6	±	0.4		6.2
TRI4S	$Cu^{2+} + L \leftrightharpoons [CuL]^{2+}$	18.53	±	0.04		17.0
TE4S	$Cu^{2+} + L \leftrightharpoons [CuL]^{2+}$	17.24	±	0.07		14.5
		17.01	±	0.02	[e]	

[a] L denotes the ligand in its totally deprotonated form. The reported uncertainty was obtained by the fitting procedure and represents one standard deviation unit.
[b] pCu^{2+} calculated at $C_{Cu^{2+}} = 10^{-6}$ M and $C_L = 10^{-5}$ M.
[c] Obtained by Ag^{+}-Cu^{2+} competition (no ionic strength control).
[d] From ref. [37].
[e] Obtained by pH-potentiometric titrations, I = 0.15 M $NaNO_3$.

4.2.5 Comparison of the Thermodynamic Stability of the Cupric Complexes with First- and Second-Generation Ligands

To gain insight into the *in vivo* stability of the cupric complexes and to compare the stability of the Cu^{2+} complexes formed by different chelators, the pCu^{2+} ($pCu^{2+} = -\log[Cu^{2+}]_{free}$) was computed.[38] The pCu^{2+} values of the investigated sulfide-bearing ligands are listed in **Table 4.1** and graphically compared in **Figure 4.10**.

The obtained results revealed that the first-generation series form very stable Cu^{2+} complexes, with a pCu^{2+} value higher or comparable to those of the well-known $^{64/67}Cu^{2+}$ chelators NOTA, DOTA, and TETA (pCu^{2+}_{NOTA} = 18.2; pCu^{2+}_{DOTA} = 17.4; pCu^{2+}_{TETA} = 16.2).

Among those, DO2A2S forms the most stable complexes. Its higher stability, when compared to those of DO4S, DO3S, and DO3SAm, can be attributed to the preference of Cu^{2+} to hard carboxylic donors rather than to soft sulfur ones. If compared to DOTA, the extra-stability of the cupric complexes formed by DO2A2S should be related to the lower basicity of this ligand, which makes it a better complexing agent for Cu^{2+}.

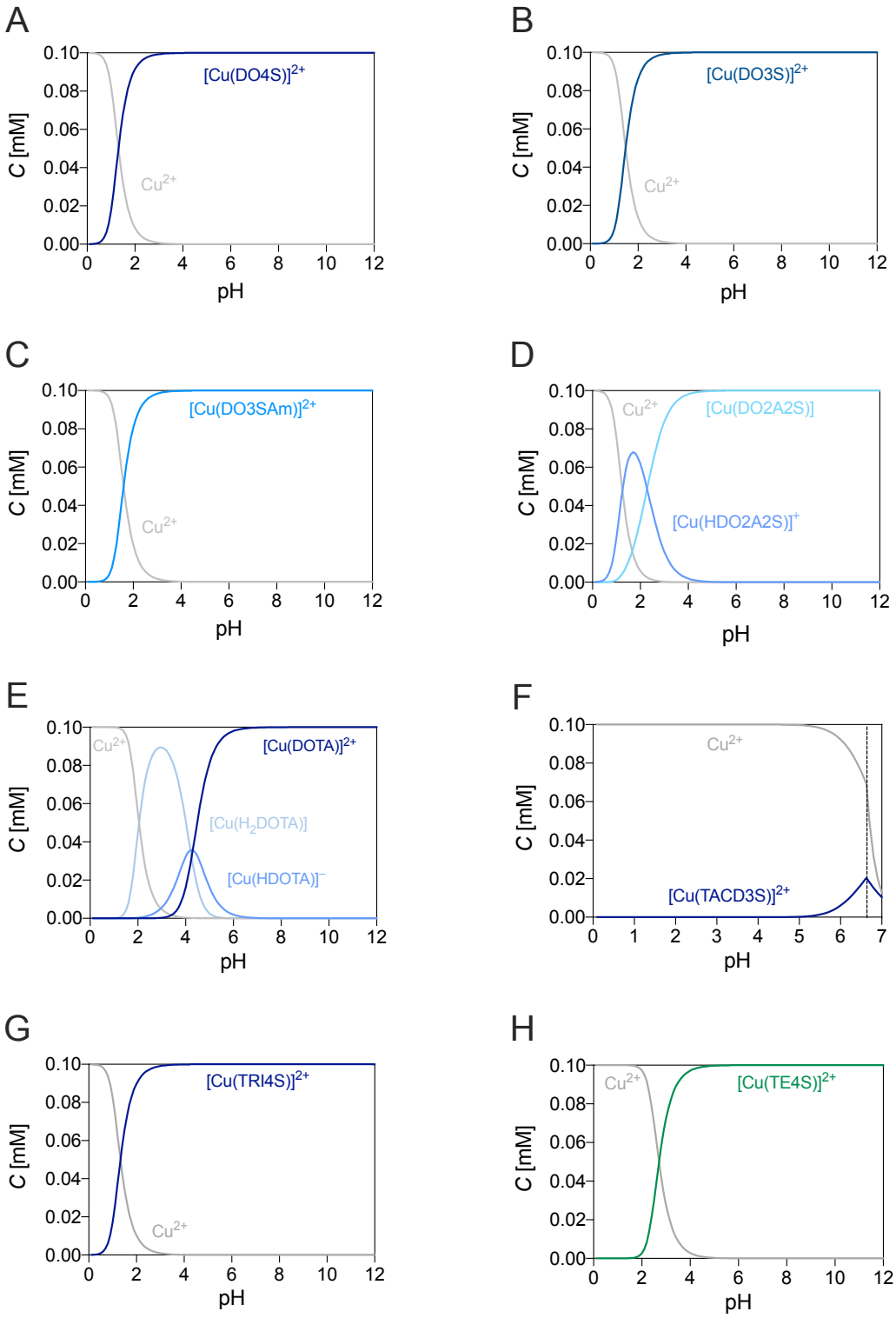

Figure 4.9. Distribution diagrams of (A) Cu^{2+}-DO4S, (B) Cu^{2+}-DO3S, (C) Cu^{2+}-DO3SAm, (D) Cu^{2+}-DO2A2S, (E) Cu^{2+}-DOTA, (F) Cu^{2+}-TACD3S, (G) Cu^{2+}-TRI4S and (H) Cu^{2+}-TE4S at $C_{Cu^{2+}} = C_L = 1.0 \cdot 10^{-4}$ M.

It is also worth to note that the comparable stability of DO4S, DO3S, and DO3SAm indicate that the Cu^{2+} complexation properties are preserved upon the loss of one sulfide arm and *N*-alkylation of the nitrogen atom.

Surprisingly, TACD3S gave a very low pCu^{2+} demonstrating not to be able to complex Cu^{2+} except at nearly neutral pH. It follows that the copresence of four nitrogen atoms is an essential feature in the 12-member ring macrocyclic structure to allow an effective copper coordination when the side chains contain S donors, as the simultaneous removal of a nitrogen donor and a sulfur side chain has a huge impact on the Cu^{2+} coordination. This low Cu^{2+}-complex stability hampered any further investigation with TACD3S. Consequently, this ligand will no longer be considered in the following discussion.

The addition of a ring carbon atom in the DO4S scaffold, leading to TRI4S, only slightly affects the complex stability at physiological pH (pCu^{2+}_{TRI4S} = 17.0 and pCu^{2+}_{DO4S} = 17.7, **Table 4.1**).[39] Contrarily, the further increase of the ring size, leading to TE4S, is detrimental in terms of the stability of the resulting Cu^{2+} complexes, as the pCu^{2+} of TE4S is 2.5 orders of magnitude lower than that of TRI4S (**Table 4.1**). These behaviours are likely related to the worst matching between the size of the metal cation and ring cavity, thus resulting in a stability drop.

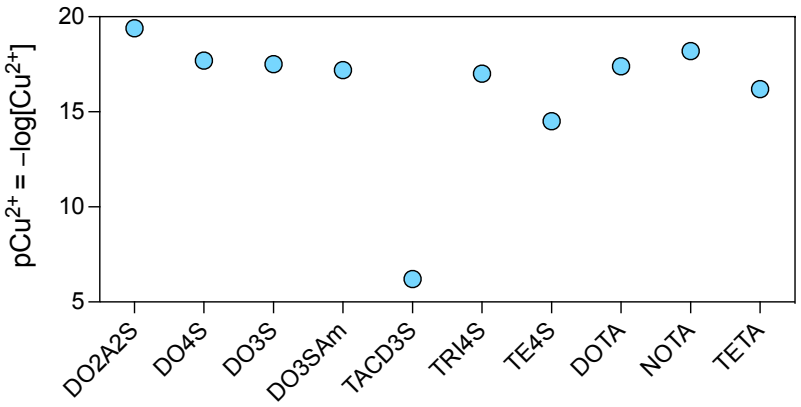

Figure 4.10. Comparison of the pCu^{2+} values at physiological pH for the Cu^{2+} complexes formed with first-, second-generation and state-of-the-art ligands (DOTA, NOTA and TETA).

4.2.6 Solution Structure of the Cupric Complexes with First-Generation Ligands

The UV-Vis absorption spectra of the Cu^{2+} complexes with DO4S, DO3S and DO3SAm (**Figure 4.7** and **Figure C1** - Appendix C) were further examined also to gain insight into their solution structure. Spectra display a strongly intense UV band ($\varepsilon \approx 3.6 \cdot 10^3$ L/cm·mol, **Table C3** - **Appendix C**) centred at 309 nm, 303 nm and 304 nm, respectively. Bosnich *et al.* have assigned the intense band in the 350 nm region in the spectra of square-planar,

square-pyramidal, and tetrahedral amine-thioether donor arrays to a S to Cu^{2+} ligand to metal charge-transfer (LMCT) transition.[40] Therefore, the absorption at around 300 nm for the investigated Cu^{2+}-complexes can be attributed to the same transition. A broadband above 500 nm (**Figure 4.11**) was also found in all solutions ($\varepsilon \approx 4 \cdot 10^2$ L/cm·mol, **Table C3 - Appendix C**), characteristic of the *d-d* orbital transition of the Cu^{2+} ion.

The involvement of the sulfur pendants in the Cu^{2+} coordination sphere is indicated also when the spectra of **Figure 4.7** and **Figure C1** (**Appendix C**) are compared to those of Cu^{2+}-cyclen and Cu^{2+}-DOT-*n*-Bu (**Figure 4.12**), which was considered to compare the electronic effect of secondary (cyclen) and tertiary (DOT-*n*-Bu) amines.[41] The UV absorption peak of Cu^{2+}-DOT-*n*-Bu is red-shifted with respect to that of Cu^{2+}-cyclen, indicating that the replacement of the Cu^{2+}-coordinating secondary amines with tertiary ones has a role in the observed spectral changes. In turn, peaks of Cu^{2+}-DO4S, Cu^{2+}-DO3S, and Cu^{2+}-DO3SAm are red-shifted with respect to that of Cu^{2+}-DOT-*n*-Bu, so that a different coordination mode is suggested when sulfanyl arms replace tert-butyl ones, *i.e.* one or more sulfur atoms should be involved in the metal binding. Conversely, the visible bands attributed to the *d-d* transition (above 500 nm) are much more similar for all ligands.[42–44]

The extinction coefficients in the visible region are remarkably high, which can be explained by the so-called intensity stealing or intensity borrowing of neighbouring higher-energy transitions. A strongly distorted arrangement is thus suggested.[45]

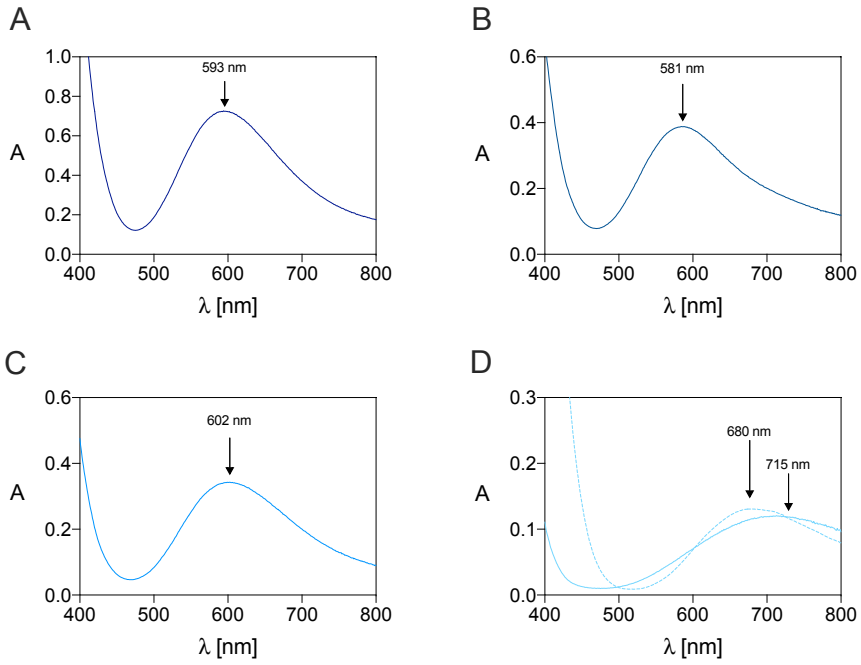

Figure 4.11. *d-d* Band of (A) $[Cu(DO4S)]^{2+}$ ($C_{Cu^{2+}} = C_{DO4S} = 1.2 \cdot 10^{-3}$ M), (B) $[Cu(DO3S)]^{2+}$ ($C_{Cu^{2+}} = C_{DO3S} = 9.2 \cdot 10^{-4}$ M), (C) $[Cu(DO3SAm)]^{2+}$ ($C_{Cu^{2+}} = C_{DO3SAm} = 1.1 \cdot 10^{-3}$ M) and (D) Cu^{2+}-DO2A2S (pH 2.0, $C_{Cu^{2+}} = C_{DO2A2S} = 7.8 \cdot 10^{-4}$ M; pH 1.8 (dotted line), $C_{Cu^{2+}} = C_{DO2A2S} = 9.0 \cdot 10^{-4}$ M) at I = 0.15 M NaCl and T = 25°C.

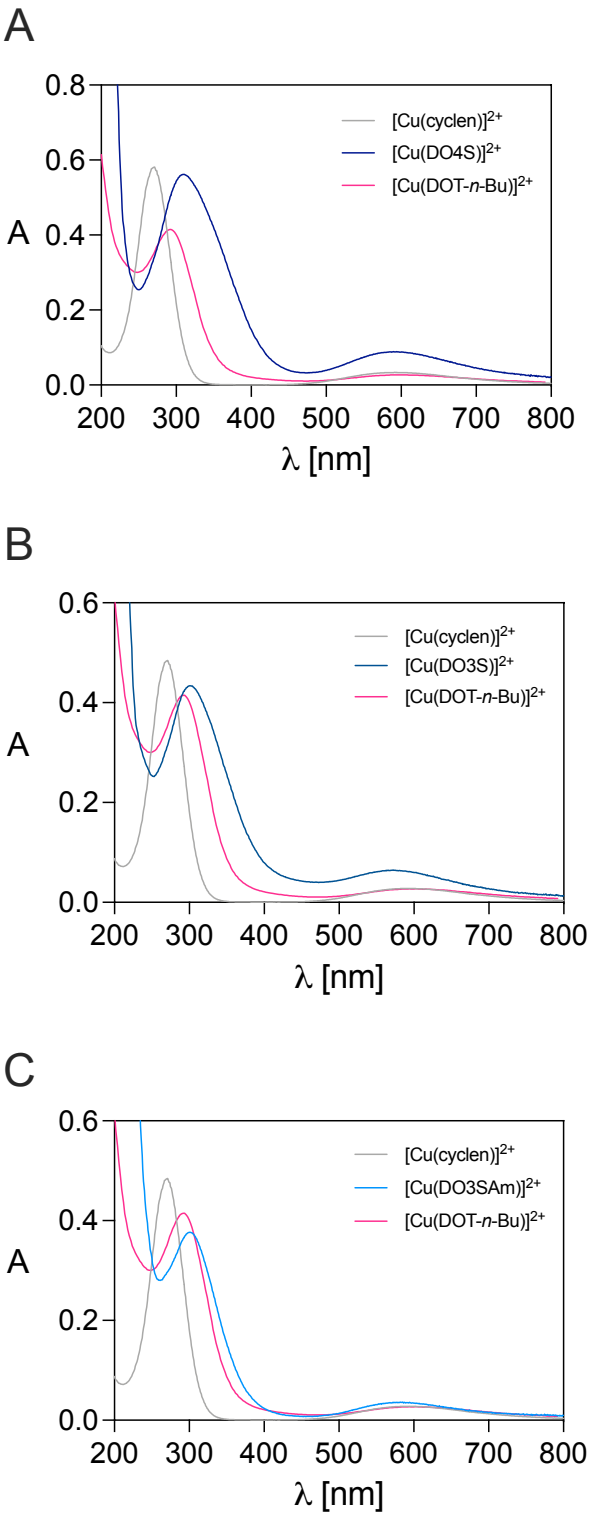

Figure 4.12. Comparison of the electronic spectra of the $[CuL]^{2+}$ complexes formed by (A) DO4S, (B) DO3S and (C) DO3SAm (data from **Figure C1** - **Appendix C**) with those of the same complex formed by cyclen ($C_{Cu^{2+}} = C_{cyclen} = 1.5 \cdot 10^{-4}$ M) and by DOT-*n*-Bu ($C_{Cu^{2+}} = C_{DOT\text{-}n\text{-}Bu} = 2.1 \cdot 10^{-4}$ M).

According to these results, the coordination sphere around the Cu^{2+} center can be depicted either as a distorted square pyramidal or a distorted octahedron.[42]

The involvement of sulfur in the Cu^{2+} coordination can be deduced also if the pCu^{2+} for Cu^{2+}-1,4,7,10-tetramethyl-1,4,7,10-tetrazacyclododecane (Cyc4Me) is compared to that for Cu^{2+}-DO4S (**Table 4.1**), as the former contains tertiary amines but no sulfur donors: the Cu^{2+} complex formed by DO4S is more stable than that formed by Cyc4Me. A DFT calculation was performed to indicate if this difference can be explained only by the electronic effects of the nitrogen atoms. The Gibbs free energies in water (ΔG_{water}) of the two complexes were compared, supposing that both ligands bind the metal ion through all nitrogen atoms, and no sulfur is involved for DO4S. The results (**Table C4** - **Appendix C**) show that the Cu^{2+} complex of DO4S is less stable than that of Cyc4Me by 3.3 kcal/mol. As the experimental result was the opposite, the coordinating role of sulfur(s) is further supported.

To gain additional structural information, the cupric complexes of DO4S and DO3S were studied using EPR spectroscopy. The experimental EPR spectra are presented in **Figure 4.13** together with simulated ones using the parameters summarized in **Table 4.2**.

The room temperature EPR spectra measured for Cu^{2+}-DO4S are unaffected by pH (**Figure 4.13**). This indicates that the metal coordination environment does not change in the investigated pH range (1.61-11.60) as expected. Unfortunately, nitrogen splitting was not well resolved and, consequently, the number of the coordinated nitrogen donor atoms could not be accurately determined; it was assumed this number to be four because also for Cu^{2+}-DOTA and Cu^{2+}-cyclen all four nitrogen atoms are coordinated to the metal center.[44,46]

The measured spectra can be simulated assuming the presence of two isomeric species in a 50:50 ratio, named $[Cu(DO4S)]^{2+}$ (1) and $[Cu(DO4S)]^{2+}$ (2) (**Figure C4** - **Appendix C**). The former was treated with lower g_o value, which indicates a stronger ligand field in the equatorial plane, whilst for the latter a higher g_o was considered (**Table 4.2**).

As for $[Cu(DO4S)]^{2+}$ (2) $g_z > (g_x + g_y)/2$, this Cu^{2+}-DO4S isomer should have elongated axial bonds consistent with distorted square pyramidal or octahedral geometries, as also indicated by UV-Vis.[44,47] Therefore, it is possible to hypothesize that $[Cu(DO4S)]^{2+}$ (1) and $[Cu(DO4S)]^{2+}$ (2) have a [4N] and [4N]S coordination, respectively, and in the latter sulfur should bind copper axially. As a comparison, for the Cu^{2+}-cyclen complex, the geometry is square pyramidal with four nitrogens in the equatorial plane and one O (from H_2O or anions) in apical position, and in this symmetrical arrangement the g_z was found significantly lower and A_z higher (**Table 4.2**).[41]

The spectra recorded at 77 K for Cu^{2+}-DO4S were described with a superposition of a usual spectrum component originated from a Cu^{2+} complex with a distorted geometry and an isotropic singlet spectrum (**Figure 4.13**). The latter can be originated from an aggregation of paramagnetic species in which a dipole-dipole interaction causes the line broadening. For the

usual spectrum, the average g_0 value (2.105) is very close to the measured g_0 of $[Cu(DO4S)]^{2+}$ (2) (2.103) detected at room temperature, so that this isomer likely becomes predominant at 77 K. Differently from the room temperature, at 77 K the ratio of the isotropic spectra varies depending on pH (**Figure C4** - **Appendix C**); however, this change can be due to differences in the freezing conditions.

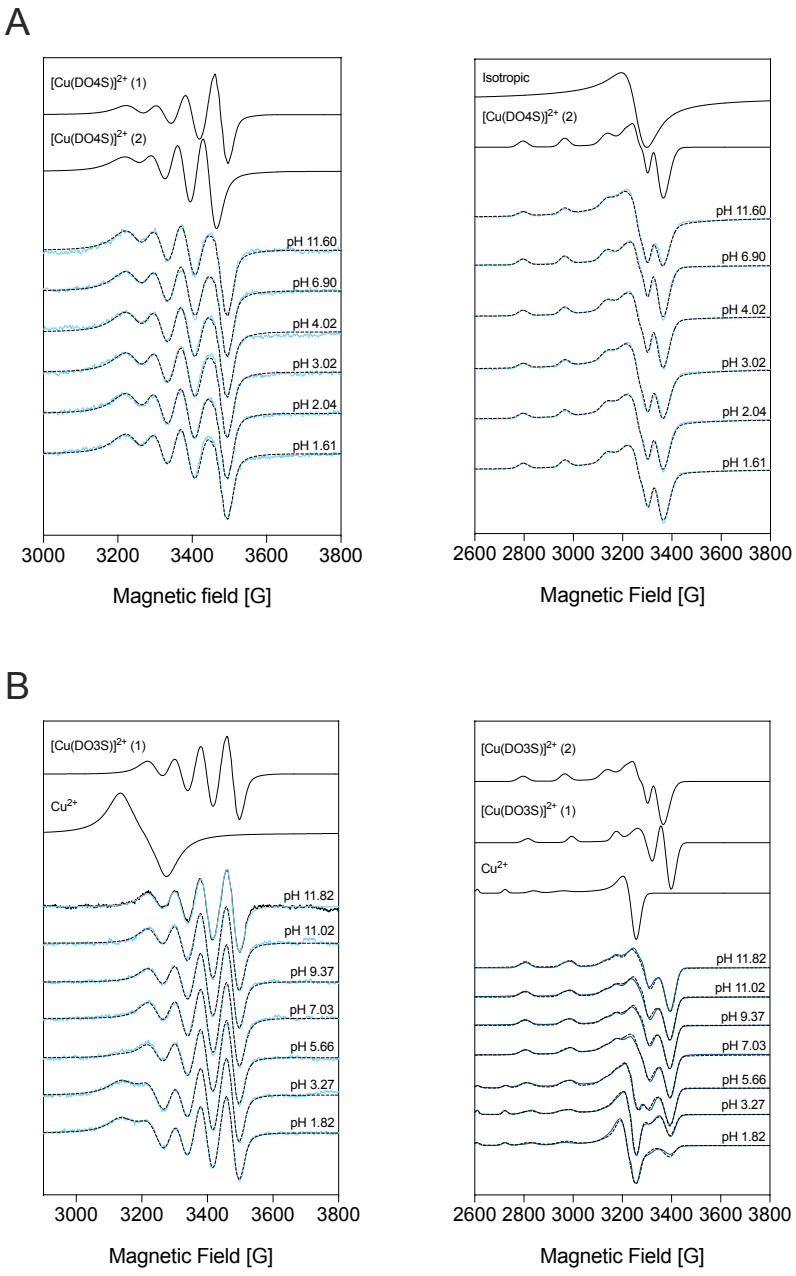

Figure 4.13. Measured (solid lines) and simulated (dotted lines) EPR spectra for solutions containing Cu^{2+} and (A) DO4S ($C_{Cu^{2+}}$ = 1.0·10^{-3} M, C_{DO4S} = 1.3·10^{-3} M), (B) DO3S ($C_{Cu^{2+}}$ = 1.0·10^{-3} M, C_{DO3S} = 1.1·10^{-3} M) at room temperature (left) and 77 K (right). The component spectra obtained from the simulation are shown in the upper part.

Table 4.2. EPR parameters of the components obtained by the simulation of room temperature spectra (isotropic parameters) and 77 K spectra (anisotropic parameters) measured in solutions containing Cu^{2+}-DO4S, Cu^{2+}-DO3S, Cu^{2+}-DO2A2S and Cu^{2+}-TE4S, and suggested coordination. Literature data for Cu^{2+}-DOTA and Cu^{2+}-cyclen are reported for comparison.

	Isotropic parameters [a]		Anisotropic parameters [b]				Calc. [c]	Suggested coordination
	g_0	A_0 ($\cdot 10^{-4}$cm^{-1})	$g_\perp$ *or* g_x, g_y	$g_\parallel$ *or* g_z	$A_\perp$ *or* A_x, A_y ($\cdot 10^{-4}$cm^{-1})	$A_\parallel$ *or* A_z ($\cdot 10^{-4}$cm^{-1})	$g_{0,calc}$	
L = DO4S								
$[CuL]^{2+}$ (1)	2.091	71.7						[4N]
$[CuL]^{2+}$ (2)	2.103	63.6	2.048, 2.058	2.209	20.3, 23.5	171.2	2.105	$[4N]S_{ax}$
L = DO3S								
Cu^{2+}	2.196	34.9	2.085	2.423	11.8	127.2	2.197	
$[CuL]^{2+}$ (1)	2.093	74.0	2.036	2.184	15.6	179.3	2.085	[4N]
$[CuL]^{2+}$ (2)			2.048, 2.058	2.209	20.3, 23.5	171.2	2.105	$[4N]S_{ax}$
L = DO2A2S								
Cu^{2+}			2.085	2.423	11.8	127.2	2.197	
$[CuH_2L]^{2+}$ (1)			2.066	2.257	11.5	158.1	2.129	[3N,S]
$[CuH_2L]^{2+}$ (2)			2.058	2.214	28.7	164,7	2.110	$[4N]S_{ax}$
$[CuHL]^{+}$			2.060	2.234	25.8	161,5	2.118	$[3N,O]N_{ax}$
[CuL]			2.075	2.272	24.5	142.8	2.141	$[2N,2O]2N_{ax}$
L = Cyclen [d]								
$[CuL]^{2+}$			2.040, 2.055	2.197	16.9, 21.0	181.9	2.097	$[4N]H_2O_{ax}$
L = DOTA [e]								
$[CuL]^{2-}$ (1)			2.058	2.301	10.0	150.0	2.139	$[2N,2O]2N_{ax}$
$[CuL]^{2-}$ (2)			2.061	2.241	15.0	157.2	2.121	$[3N,O]N_{ax}$
L = TE4S								
Cu^{2+}	2.194	34.1	2.084	2.423	4.9	126.1	2.197	
[CuL]	2.101	73.3	2.048	2.204	38.2	168.1	2.100	$[4N]S_{ax}$

[a] The experimental error was ± 0.001 for g_0 and ± $1 \cdot 10^{-4}$ cm^{-1} for A_0.
[b] The experimental error was ± 0.002 for g_x, g_y and ± 0.001 for g_z and ± $1 \cdot 10^{-4}$ cm^{-1} for A_x, A_y and A_z.
[c] Calculated by the equation $g_{0,calc} = (g_x+g_y+g_z)/3$ on the basis of anisotropic values.
[d] From reference [44].
[e] From reference [46].

The room temperature EPR spectra of Cu^{2+}-DO3S were simulated with the spectrum of one $[CuL]^{2+}$ species and the spectrum of free copper at the acidic pH range (**Figure 4.13**). As the examined solution was freshly prepared before the measurements, the low complexation rate described above justifies the presence of the free metal ion at low pH.

The obtained g_0 and A_0 values of the $[Cu(DO3S)]^{2+}$ are very close to those of the $[Cu(DO4S)]^{2+}$ (1) isomer, pointing out the same coordination mode (**Table 4.2**). At low temperature, besides the free copper, two isomeric components can be detected for Cu^{2+}-DO3S with a 55:45 ratio (**Figure 4.13** and **Figure C4**). Both spectra show a usual elongated octahedral or square pyramidal geometry, and the calculated g_0 values suggest the same coordination environment as the two isomers $[Cu(DO3S)]^{2+}$ (1) and $[Cu(DO3S)]^{2+}$ (2) observed for DO4S at room temperature.

DFT calculations have been performed on $[Cu(DO4S)]^{2+}$ and $[Cu(DO3S)]^{2+}$ complexes to gain a theoretical support for their structure in solution. A preliminary conformational analysis indicated that the complexes having four coordinated nitrogens are the most stable. These isomers were investigated by evaluating the relative stability of the Cu^{2+} complexes in which zero, one or two sulfide arms, *i.e.* [4N], [4N]S and [4N]2S respectively, are coordinated to the metal center (**Figure 4.14**). The results are shown in **Table 4.3**.

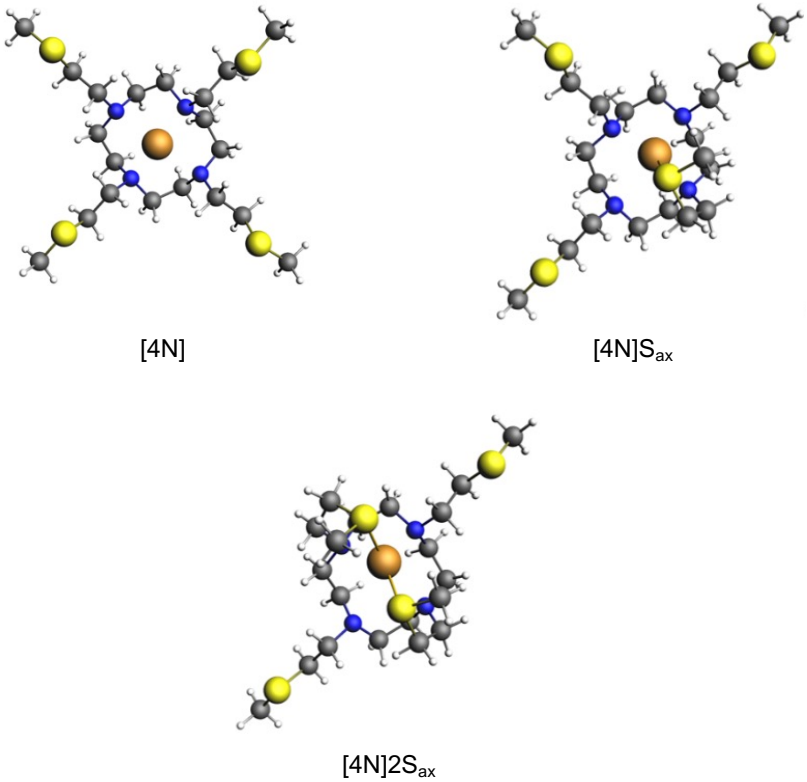

Figure 4.14. DFT-examined isomers of $[Cu(DO4S)]^{2+}$.

Table 4.3. Electronic and Gibbs free energies (in gas-phase and in water) for the cupric and cuprous complexes of DO4S and DO3S. All the energies are in kcal/mol. Level of theory: (COSMO-)ZORA-OPBE/TZ2P//ZORA-OPBE/TZP.

M	Ligand	Coordination	Gas phase		Water	
			Δ*E*	Δ*G*	Δ*E*	Δ*G*
Cu^{2+}	DO4S	[4N]	–412.4	–399.4	–192.7	–179.7
		[4N]S	–417.4	–404.2	–190.9	–177.7
		[4N]2S	–410.1	–396.6	–179.8	–166.2
	DO3S	[4N]	–411.4	–399.5	–196.6	–184.8
		[4N]S	–418.1	–403.8	–197.4	–183.1
		[4N]2S	–411.2	–395.5	–185.9	–170.3
Cu^{+}	DO4S	[4N]	–117.3	–104.7	–60.6	–48.0
		[4N]S	–128.3	–115.4	–68.9	–56.0
		[4N]2S	–122.5	–108.5	–60.6	–46.6
	DO3S	[4N]	–119.7	–108.6	–63.4	–52.4
		[4N]S	–130.6	–117.1	–71.4	–57.9
		[4N]2S	–126.2	–111.4	–63.9	–49.0

For both ligands, the ΔG_{water} values for the [4N] and [4N]S complexes are particularly close: as the accuracy of the computed energies is of the order of ±1 kcal/mol, it is reasonable to assume that both isomers are present in aqueous environment. These two isomers likely correspond to the $[CuL]^{2+}$ (1) and $[CuL]^{2+}$ (2) species detected also by EPR experiments. As well, the S-bonding indicated by the UV-Vis spectra of $[Cu(DO4S)]^{2+}$ and $[Cu(DO3S)]^{2+}$ shown in **Figure 4.7** can now be attributed to the presence in solution of the [4N]S species, which, as seen, accounts for around one-half of the Cu^{2+} complexes. The coordination of a second sulfur atom is disfavored for both ligands because the final [4N]2S complex has a less negative ΔG_{water} of more than 10 kcal/mol compared to those of the [4N] and [4N]S complexes.

The activation strain model (ASM) and the energy decomposition analysis (EDA) have been used in the gas phase to rationalize the origin of the theoretical preference of these Cu^{2+} complexes to bind either zero or one sulfide (**Table C5** - **Appendix C**). The strain energy (ΔE_{strain}) of $[Cu(DO4S)]^{2+}$ increases by a value of 7.5 kcal/mol when passing from [4N] to [4N]S, which is the energy required to bring one extended pendant to the form it has in the coordinated metal complex. However, the [4N]S complex shows a more stabilizing interaction energy (ΔE_{int}) of 12.5 kcal/mol over the [4N] one due mainly to a less destabilizing Pauli repulsion (ΔE_{Pauli}), so that these two complexes result in a similar total energy content. The [4N]2S complex is destabilized when compared to the [4N]S one because it requires an additional strain energy of 6.7 kcal/mol to bend and coordinate a new pendant to the metal, whereas the interaction energy is virtually unaffected. For $[Cu(DO3S)]^{2+}$, energy differences were very similar and can be interpreted analogously as for Cu^{2+}-DO4S.

Attempts were made to obtain suitable crystals for Cu^{2+}-DO4S and for Cu^{2+}-DO3S, to perform structural investigations also in the solid-state through single-crystal X-ray diffraction. Such attempts were successful for Cu^{2+}-DO4S.

A view of the crystal structure of $[Cu(DO4S)(NO_3)]\cdot(NO_3)$ is shown in **Figure 4.15**, and selected bond distances and angles are gathered in **Table 4.4**. Crystal data and refinement details are provided in **Appendix C.**

The complex crystallizes in the monocline space group and the asymmetrical unit contains a $[Cu(DO4S)]^{2+}$ molecule and two nitrate anions. Each Cu^{2+} ion is surrounded by four nitrogens of the macrocyclic ring and a nitrate anion in a square pyramidal geometry. The average bond distances between the metal center and the nitrogen atoms (2.04 Å) are close to those observed for N4-Cu complexes like $[Cu(cyclen)(NO_3)](NO_3)$.[48] Sulfur atoms do not form any bond with Cu^{2+} in the crystal, since they are more than 5.0 Å away from the metal center and together form an S4 plane, coplanar to N4 plane. The structure of $[Cu(DO4S)(NO_3)]\cdot(NO_3)$ likely resembles that of the [4N] isomer $[Cu(DO4S)]^{2+}$ (1) detected in solution by EPR and computed by DFT.

Turning to Cu^{2+}-DO2A2S, **Figure 4.7** and **Figure C1** (**Appendix C**) show that the UV-Vis spectra of Cu^{2+}-DO2A2S solutions at equilibrium are markedly different from those of Cu^{2+}-DO4S, Cu^{2+}-DO3S, and Cu^{2+}-DO3SAm.

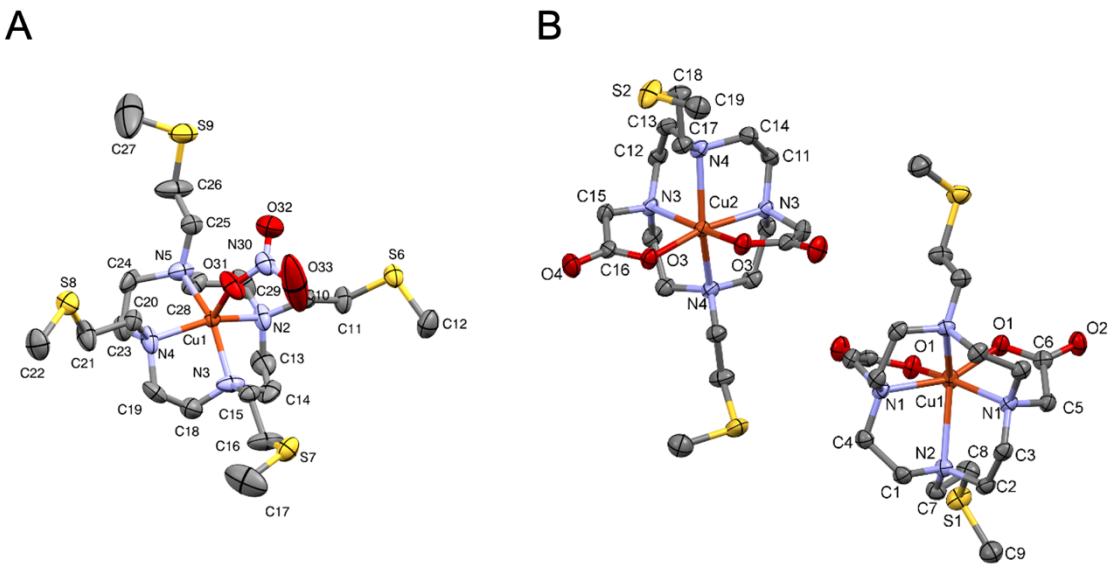

Figure 4.15. ORTEP diagrams of (A) $[Cu(DO4S)(NO_3)]\cdot(NO_3)$ and of (B) [Cu(DO2A2S)] (Cu1 = molecule #1, Cu2 = molecule #2) with atom numbering. Thermal ellipsoids are drawn at the 50% probability level. Water molecules, hydrogen atoms, and non-bonded nitrate anions are omitted for the sake of clarity. Symmetry code for molecules #1 and #2 in [Cu(DO2A2S)] is –x+1,y,–z+1 and –x+2,y,–z+1, respectively.

Table 4.4. Selected bond lengths and angles of the Cu^{2+} coordination environments in the crystal structures of $[Cu(DO4S)(NO_3)]\cdot(NO_3)$ and of both molecules of [Cu(DO2A2S)]. See **Figure 4.15** for atom labelling. Additional data are summarized in **Table C6** - **C8** (**Appendix C**).

$[Cu(DO4S)(NO_3)]\cdot(NO_3)$		[Cu(DO2A2S)]			
		molecule #1		molecule #2	
Bond	**Distance (Å)**	**Bond**	**Distance (Å)**	**Bond**	**Distance (Å)**
Cu1-N5	2.03(7)	Cu1-O1	1.954(2)	Cu2-O3	1.955(2)
Cu1-N3	2.04(7)	Cu1-N1	2.150(3)	Cu2-N3	2.110(3)
Cu1-N2	2.05(7)	Cu1-N2	2.536(3)	Cu2-N4	2.336(3)
Cu1-N4	2.06(7)				
Cu1-O31	2.15(6)				
Bond	**Angle (°)**	**Bond**	**Angle (°)**	**Bond**	**Angle (°)**
N5-Cu1-N2	86.8(3)	O1-Cu1-N1	80.3(1)	O3-Cu2-N3	84.1(1)
N5-Cu1-N3	151.9(3)	N1-Cu1-$N1^{\#1}$	117.2(2)	N3-Cu2-$N3^{\#2}$	103.3(2)
N5-Cu1-N4	87.6(3)	N2-Cu1-$N2^{\#1}$	125.6(2)	N4-Cu2-$N4^{\#2}$	149.9(1)
N5-Cu1-O31	104.6(3)	O1-Cu1-$O1^{\#1}$	87.0(1)	O3-Cu2-$O3^{\#2}$	89.6(1)
N3-Cu1-O31	103.3(3)	O1-Cu1-$N1^{\#1}$	157.49(9)	O3-Cu2-$N3^{\#2}$	169.4(1)
N2-Cu1-O31	110.5(3)				
N4-Cu1-O31	98.7(3)				

Symmetry code for #1 is –x+1, y,–z+1 and for #2 is –x+2, y, –z+1.

At pH > 2, where the complex [Cu(DO2A2S)] exists, a high energy CT absorption band centred at around 272 nm, and a weaker *d-d* transition at 715 nm, were found. The close similarity to the absorption band maxima of the $[Cu(DOTA]^{2-}$ complex (**Figure 4.16**) suggests an analogous distorted octahedral coordination environment where the Cu^{2+} ion is bound with a [2N,2O] equatorial arrangement and with the two other nitrogen donors in axial position ($[2N,2O]2N_{ax}$).[46,49,50] The less prominence of the shoulder at 310 nm (**Figure 4.16**), compared to $[Cu(DOTA]^{2-}$, may indicate that the Jahn-Teller distortion is partially quenched in [Cu(DO2A2S)].

Under highly acidic pH (< 2), the absorbance in the UV region of Cu^{2+}-DO2A2S is slightly dropped with simultaneous broadening and redshift from 276 nm to 303 nm, while in the visible region the band is blue shifted, from 715 nm to 680 nm (**Figure 4.11**). These findings can be attributed to the formation of a different complex, *i.e.* $[Cu(HDO2A2S)]^{+}$ (**Figure 4.9**). Also DOTA forms protonated complexes at acidic pH,[46] but the band shifts observed for DO2A2S were not detected: the Cu^{2+}-DOTA bands only change in intensity due to the lower electron density of the amine groups upon protonation of non-coordinated carboxylates, while the *d-d* band is almost pH-insensitive as the protonation of distant nonbonding carboxylates does not exert a marked influence in the electronic structure of the metal complex.[50]

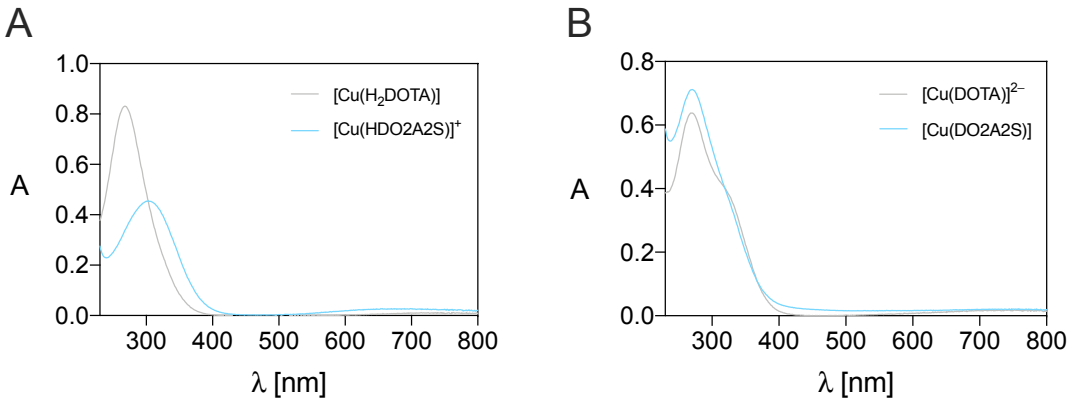

Figure 4.16. Comparison of the UV-Vis spectra of (A) $[Cu(HDO2A2S)]^{+}$ (data from **Figure 4.7**) and $[Cu(H_2DOTA)]$ for DOTA ($C_{Cu^{2+}} = C_{DOTA} = 2.0 \cdot 10^{-4}$ M); (B) [Cu(DO2A2S)] (data from **Figure 4.7**) and $[Cu(DOTA)]^{2-}$ ($C_{Cu^{2+}} = C_{DOTA} = 2.0 \cdot 10^{-4}$ M).

It can be deduced that for Cu^{2+}-DO2A2S the protonation of the carboxylic groups imposes more severe structural changes to the coordination sphere than for Cu^{2+}-DOTA. Interestingly, the UV-Vis absorption spectrum of Cu^{2+}-DO2A2S at highly acidic pH becomes similar to those of the Cu^{2+} complexes formed by the pure sulfur-bearing ligands (DO4S, DO3S, and DO3SAm), so that an analogous coordination geometry may be inferred, *i.e.*, one sulfur atom can be supposed to be involved in the metal coordination. Unlike amines and carboxylates, S donors do not undergo acid-base competitive protonation equilibria and can coordinate metal ions also at strongly acidic pH.

Solutions containing Cu^{2+} and DO2A2S were examined also by EPR, but the signal intensity was very low at room temperature so that it was possible to simulate only the spectra of frozen solutions (**Figure 4.17, Table 4.2**). As comparison, anisotropic EPR parameters of Cu^{2+}-DOTA complexes measured at different pH values were also collected in **Table 4.2**.[46] For Cu^{2+}-DOTA, at pH ~ 7 two differently coordinated isomers were detected, indicated as $[Cu(DOTA)]^{2-}$ (1) and $[Cu(DOTA)]^{2-}$ (2) (**Table 4.2**).

The spectra for Cu^{2+}-DO2A2S show clear pH dependence (**Figure 4.17**), as the increase in proton content causes a noticeable change in the profiles, similarly to what was observed in the UV-Vis investigation. Above pH 3.73, one spectrum becomes predominant and its EPR parameters are near to those of the $[Cu(DOTA)]^{2-}$ (1), suggesting a similar [4N,2O] coordination environment with two axially bound nitrogens ([2N,2O]$2N_{ax}$), as also deduced from the electronic spectra. At pH 2.85, a $[Cu(HDO2A2S)]^{+}$ complex was detected, and its parameters are close to those of the $[Cu(DOTA)]^{2-}$ (2) isomer. At pH 1.94, two-component spectra could be detected which were assigned as $[Cu(H_2DO2A2S)]^{2+}$ (1) and $[Cu(H_2DO2A2S)]^{2+}$ (2) (**Table 4.2** and **Figure C5** - **Appendix C**). The EPR parameters of the latter are similar to those of the $[Cu(DO4S)]^{2+}$ (2) isomer.

The deprotonation of the carboxylate groups causes a substantial rearrangement of the structure which results in higher g_z value compared to the protonated complexes (**Table 4.2**). In the UV-Vis spectra, this appeared as a redshift of the λ_{max} value (**Figure 4.11**) as the g_i and A_i values are related to the electronic transitions by the factors derived from the ligand field theory.[44,51] Differently from the UV-Vis data, EPR reports also the presence of a diprotonated species, and it accounts for this species, rather than for the monoprotonated one, the involvement of sulfur in the coordination sphere. The very large temperature difference (room temperature and 77 K) among the two data sets can explain this disagreement.

The coordination of Cu^{2+}-DO2A2S as a function of pH was further investigated by DFT (**Table 4.5**). When both carboxylates are deprotonated, the most stable structure is achieved through a double coordination by the oxygen donors on the Cu^{2+} metal center: the formed bonds are particularly strong (ΔG_{water} = –206.7 kcal/mol) thanks to the anionic nature of the two pendants. When one of the carboxylates is protonated, the corresponding bond is weakened, as ΔG_{water} is reduced by almost 20 kcal/mol. The detachment of the protonated acetate group is possible and leads to a more stable structure with the remaining anionic carboxylate group coordinated to the metal. In these conditions, no coordination of the sulfur arm is likely to occur, from an energetic point of view, because it does not contribute to the stabilization of the final complex. Such DFT predictions agree very well with the EPR experimental results.

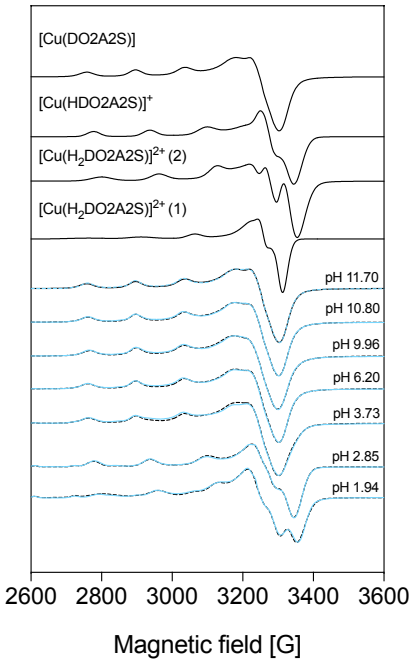

Figure 4.17. Measured (solid lines) and simulated (dotted lines) spectra for solutions containing Cu^{2+} and DO2A2S ($C_{Cu^{2+}}$ = $1.0 \cdot 10^{-3}$ M, C_{DO2AS} = $1.1 \cdot 10^{-3}$ M) at 77 K; the component spectra obtained from the simulation are shown in the upper part.

Table 4.5. Electronic and Gibbs free energies (in gas-phase and in water) for the cupric and cuprous complexes of DO2A2S. All the energies are in kcal/mol. Level of theory: (COSMO-)ZORA-OPBE/TZ2P//ZORA-OPBE/TZP.

M	Coordination	Form [(a)]	Gas phase		Water	
			Δ*E*	Δ*G*	Δ*E*	Δ*G*
Cu^{2+}	[4N,2O]	–	–698.8	–684.7	–220.8	–206.7
	[4N,2O]	H^+	–563.3	–548.3	–202.6	–187.6
	[4N,O]	H^+	–565.7	–550.1	–210.5	–194.9
	[4N,O,S]	H^+	–563.8	–546.4	–201.0	–183.7
	[4N,S]	H^+	–554.6	–539.4	–198.8	–183.6
	[4N,2S]	H^+	–545.5	–528.2	–186.7	–169.4
Cu^+	[4N,2O]	–	–260.6	–260.6	–66.3	–57.2
	[4N,O]	–	–257.7	–257.7	–75.5	–66.0
	[4N,O,S]	–	–253.1	–253.1	–71.4	–61.0
	[4N,S]	–	–248.1	–248.1	–77.8	–67.8
	[4N,2S]	–	–243.7	–243.7	–69.1	–56.2
	[4N,2O]	H^+	–193.4	–193.4	–63.1	–50.5
	[4N,O]	H^+	–203.1	–203.1	–73.1	–59.8
	[4N,O,S]	H^+	–199.6	–199.6	–68.7	–54.1
	[4N,S]	H^+	–188.1	–188.1	–96.9	–82.4
	[4N,2S]	H^+	–184.2	–184.2	–65.2	–48.7

[(a)] The two carboxylates were considered to be either both deprotonated (–) or monoprotonated (H^+).

When both carboxylate arms are protonated (situation not shown in **Table 4.5**), they do not bind the metal center. An analogous situation to that of DO4S and DO3S originates, so that one additional isomer can form involving one sulfur atom in the metal binding, as suggested from the UV-Vis and EPR spectra.

A crystal of Cu^{2+}-DO2A2S suitable for a crystallographic analysis, [Cu(DO2A2S)], was obtained from water at neutral pH. The complex crystallizes in the monocline crystal system in *I*2 space group, and the unit cell contains four neutral [Cu(DO2A2S)] molecules without the inclusion of counter ions or solvent molecules. The crystal structure of [Cu(DO2A2S)] is shown in **Figure 4.15**, and the unit cell and the packing arrangements viewed from the different crystallographic directions are shown in **Figure C6** and **Figure C7** (**Appendix C**). Selected bond distances and angles are gathered in **Table 4.4**. Crystal data and refinement details are provided in **Table C9** - **C11** (**Appendix C**).

The asymmetrical unit contains two complexes (molecule #1 and #2) with slightly different coordination geometry. In both molecules, Cu^{2+} is positioned in a 2-fold rotation axes that mirrors the half of the complexes. Two carboxylates and four nitrogen atoms, but no sulfide, are clearly involved in the metal binding, in agreement with the Cu^{2+}-DO2A2S structural data obtained in solution from UV-Vis, EPR and DFT in similar pH conditions where the crystal was formed. The coordination geometry for both molecules is a distorted octahedron with [2N,2O]$2N_{ax}$ coordination similar to the crystal structure of Cu^{2+}-DOTA.[55] The axial N-Cu-N

angle deviates from the ideal 180° significantly, as it is 129.6(2)° for molecule #1 and 149.9(1)° for molecule #2 (**Table 4.4**). The conformations of the two [Cu(DO2A2S)] molecules and that of Cu^{2+}-DOTA are compared in **Figure C8** (**Appendix C**).

4.2.7 Solution Structure of the Cupric Complexes with Second-Generation Ligands

The analysis of the electronic spectra of the investigated Cu^{2+} complexes allowed to evaluate the structural changes induced by the ring size increase. A comparison between the UV-Vis spectra of the $[Cu(DO4S)]^{2+}$, $[Cu(TRI4S)]^{2}$ and $[Cu(TE4S)]^{2+}$ complexes is reported in **Figure 4.18**. The involvement of the chloride anions in the Cu^{2+} coordination sphere is negligible for both $[Cu(TRI4S)]^{2+}$ and $[Cu(TE4S)]^{2+}$ as the spectra measured upon addition of an excess of NaCl (I = 0.15 M) to aqueous solutions (I = 0 M) do not change (**Figure C9** - **Appendix C**).

Similarly to what was previously found for $[Cu(DO4S)]^{2+}$, $[Cu(TRI4S)]^{2+}$ displays a strongly intense UV transition at 313 nm accompanied by a less intense single broad band in the visible region at 598 nm (**Table C3** - **Appendix C**). The latter absorption is characteristic of the *d-d* transition of the metallic center, whereas the former points out the involvement of sulfur in the coordination as it is attributed to a S-to-Cu^{2+} ligand-to-metal charge-transfer transition (*vide supra*). These similar absorption features suggest a similarity in the Cu^{2+} coordination mode of these two ligands: two different isomers having either [4N]S or [4N] coordination arrangements are thus expected in solution with TRI4S like it was found for the cupric complex of DO4S. When turning to $[Cu(TE4S)]^{2+}$, the maximum absorption is maintained (**Table C3** - **Appendix C**), but a remarkable increase of the shoulder at 370 nm accompanied by a redshift of the *d-d* band (from 598 nm to 626 nm) can be observed, thus suggesting that TE4S binds Cu^{2+} through a different coordination mode.

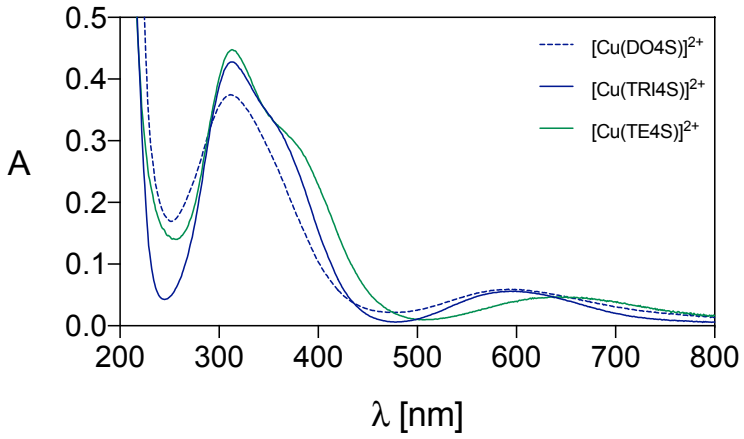

Figure 4.18. Comparison of the electronic spectra of the cupric complexes of DO4S, TRI4S and TE4S ($C_{Cu^{2+}} = C_L = 1.0 \cdot 10^{-4}$ M).

To further investigate this result, an EPR analysis was carried out for Cu^{2+}-TE4S solutions. The EPR spectra recorded at room temperature showed the appearance of free copper ion only below pH 2 (**Figure 4.19**). At higher pH, the $[Cu(TE4S)]^{2+}$ complex spectra were measured, and no further spectral changes were detected, in agreement with the speciation model (**Table 4.1** and **Figure 4.9**). In frozen solution, the complex becomes predominant at higher pH and, at pH 2.76, ~ 30% free copper was detected. The component ratios are shown in **Figure C10** (**Appendix C**).

The obtained EPR parameters are reported in **Table 4.2**. Parameters for $[Cu(TE4S)]^{2+}$ are close to those of $[Cu(DO4S)]^{2+}$ (2), where the coordination of the macrocycle is driven by four nitrogens and complemented axially by a sulfide side chain. However, for Cu^{2+}-TE4S a significantly higher $A_{\perp}$ was detected. This is probably due to the higher symmetrical arrangement of the nitrogen donor atoms in the equatorial sphere, which makes the copper centre in plane with the nitrogen atoms, resulting in higher copper hyperfine coupling values. The observed redshift in the UV-Vis spectra of $[Cu(TE4S)]^{2+}$, when compared to $[Cu(DO4S)]^{2+}$, could be therefore rationalized considering that the UV-Vis spectrum of the latter is a mixture of the spectra deriving from two components, [4N] and $[4N]S_{ax}$, while Cu^{2+}-TE4S contains only $[4N]S_{ax}$. The significantly distended Cu^{2+} cation in the cyclam backbone indicates a mismatch within the ligand metal-binding cleft which could be correlated to the lower thermodynamic stability when compared to DO4S (**Table 4.1**).

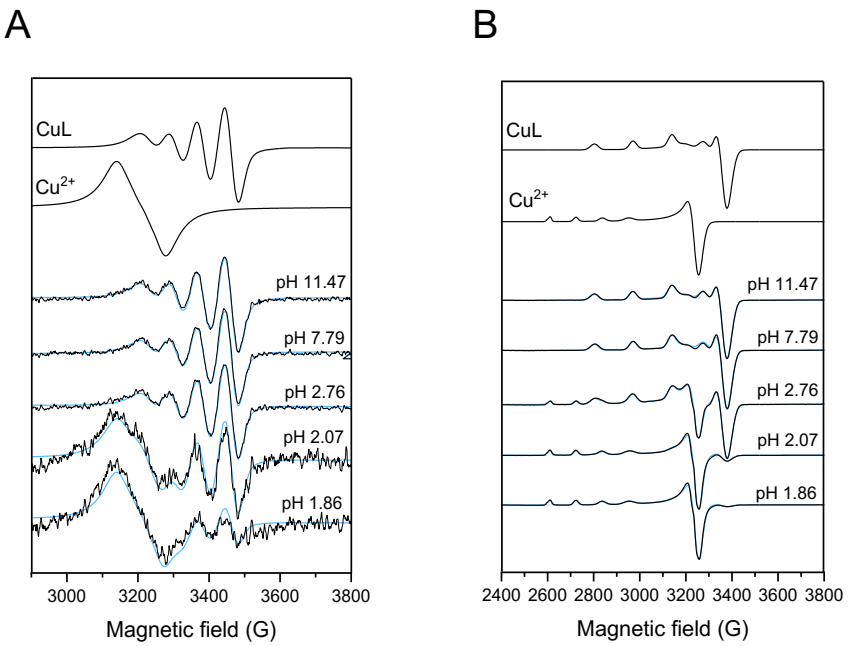

Figure 4.19. Experimental (black) and simulated (light blue) EPR spectra for solutions containing Cu^{2+} and TE4S ($C_{Cu^{2+}}$ = $8.7 \cdot 10^{-4}$ M, C_{TE4S}= $1.08 \cdot 10^{-3}$ M) at (A) room temperature and (B) 77 K. The component spectra obtained from the simulation are shown in the upper part (the spectral intensities were normalized).

4.2.8 Dissociation Kinetics of Cupric Complexes

BFC candidates for radiopharmaceutical applications must exhibit high thermodynamic stability at physiological pH, but also high kinetic inertness toward dissociation.[52] With this regard, the inertness of the Cu^{2+} complexes with first- and second-generation ligands was investigated in harsh conditions by evaluating the acid-assisted dissociation kinetics. Albeit this assay could not predict the *in vivo* integrity of the resulting complex, it is considered a convenient and popular gauge of relative kinetic inertness of copper-tetraamine complexes to Cu^{2+} decomplexation in aqueous media and as a first screening for monitoring the Cu^{2+}-chelator integrity.[53–55] Representative data are shown in **Figure 4.20** - **4.23**. The experimentally observed dissociation rate constants ($^{d}k_{obs}$) and the corresponding half-life ($t_{1/2}$) at different HCl concentrations are compiled in **Table 4.6** and **Table C12** (**Appendix C**) respectively. The observed rate constants ($^{d}k_{obs}$) linearly change with the proton content (**Figure C11** - **Appendix C**), so that the second-order rate constant (^{d}k) was obtained using $^{d}k_{obs} = {}^{d}k\,[H^{+}]$ as fitting equation. The dissociation kinetic of the Cu^{2+} complexes strongly depends on the chelator' sidearms: DO2A2S is the most inert ligand, likely due to the presence of strongly coordinating carboxylates, either in protonated or unprotonated form. Moreover, the obtained results demonstrated that the ring dimension makes the difference in the Cu^{2+} complexes' inertness, because DO4S is kinetically much more inert than the complexes with a larger macrocyclic ring, *i.e.* TRI4S and TE4S. The contrast between related cyclen- and cyclam-based complexes is dramatic since the $[Cu(TE4S)]^{2+}$ complex dissociates within minutes even at the lowest HCl concentrations (**Table 4.6**). Thus, the increase in the ring size not only affects the thermodynamic stability but also the acid-assisted dissociation behaviour of these complexes. If the results of **Tables 4.1** and **4.6** are compared, it follows that the decomplexation rates of the cupric complex in highly acidic solutions are strongly correlated with the complex stabilities. For example, this correlation is clearly visible in **Figure C12** (**Appendix C**) where pCu^{2+} values at physiologic pH are plotted *vs.* $\log t_{1/2}$ at pH 1.

Table 4.6. Acid decomplexation half-life ($t_{1/2}$) of the Cu^{2+} complexes with first- and second-generation ligands and corresponding second order dissociation rate constants (^{d}k).

[HCl] [M]	Half-life ($t_{1/2}$)			
	DO4S [min]	DO2A2S [h]	TRI4S [min]	TE4S [min]
0.1	254	17.8	50.4	1.0
0.2	118	8.8	3.8	0.9
0.4	58.3	4.0	1.4	0.7
0.6	35.3	2.9	0.6	< 30 sec
0.8	25.5	2.3	0.4	
1.0	19.4	1.8	0.3	
^{d}k [M^{-1} s^{-1}]	$(6.1 \pm 0.1)\cdot10^{-4}$	$(10.3 \pm 0.3)\cdot10^{-4}$	$(4.0 \pm 0.2)\cdot10^{-2}$	–

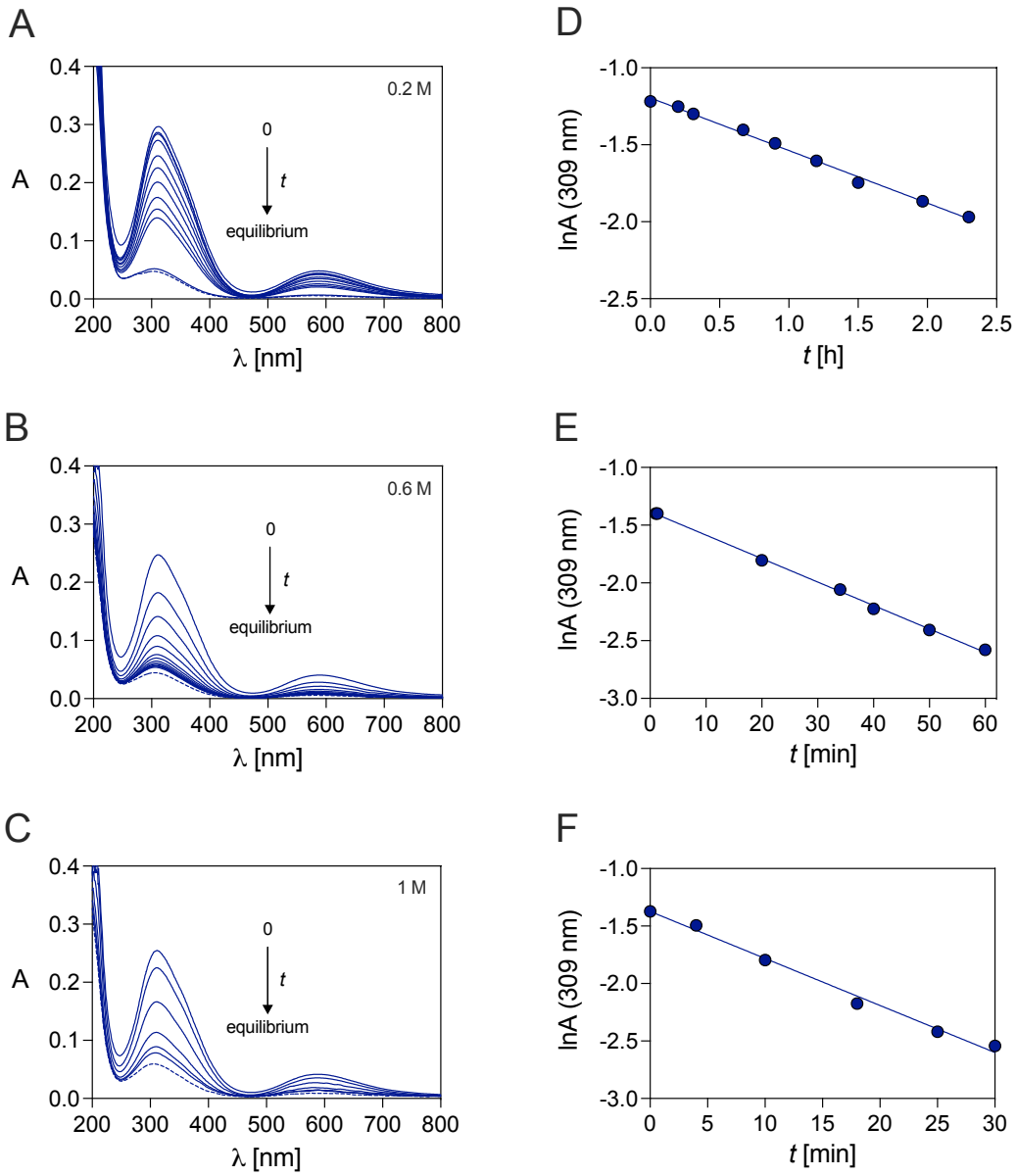

Figure 4.20. (A, B, C) UV-Vis spectra variation during the acid-assisted decomplexation assays for Cu^{2+}-DO4S ($C_{Cu^{2+}} = C_{DO4S} = 1.0 \cdot 10^{-4}$ M) at the given (upper right) HCl concentrations; (D, E, F) ln*A* *vs.* *t* and corresponding fitting line.

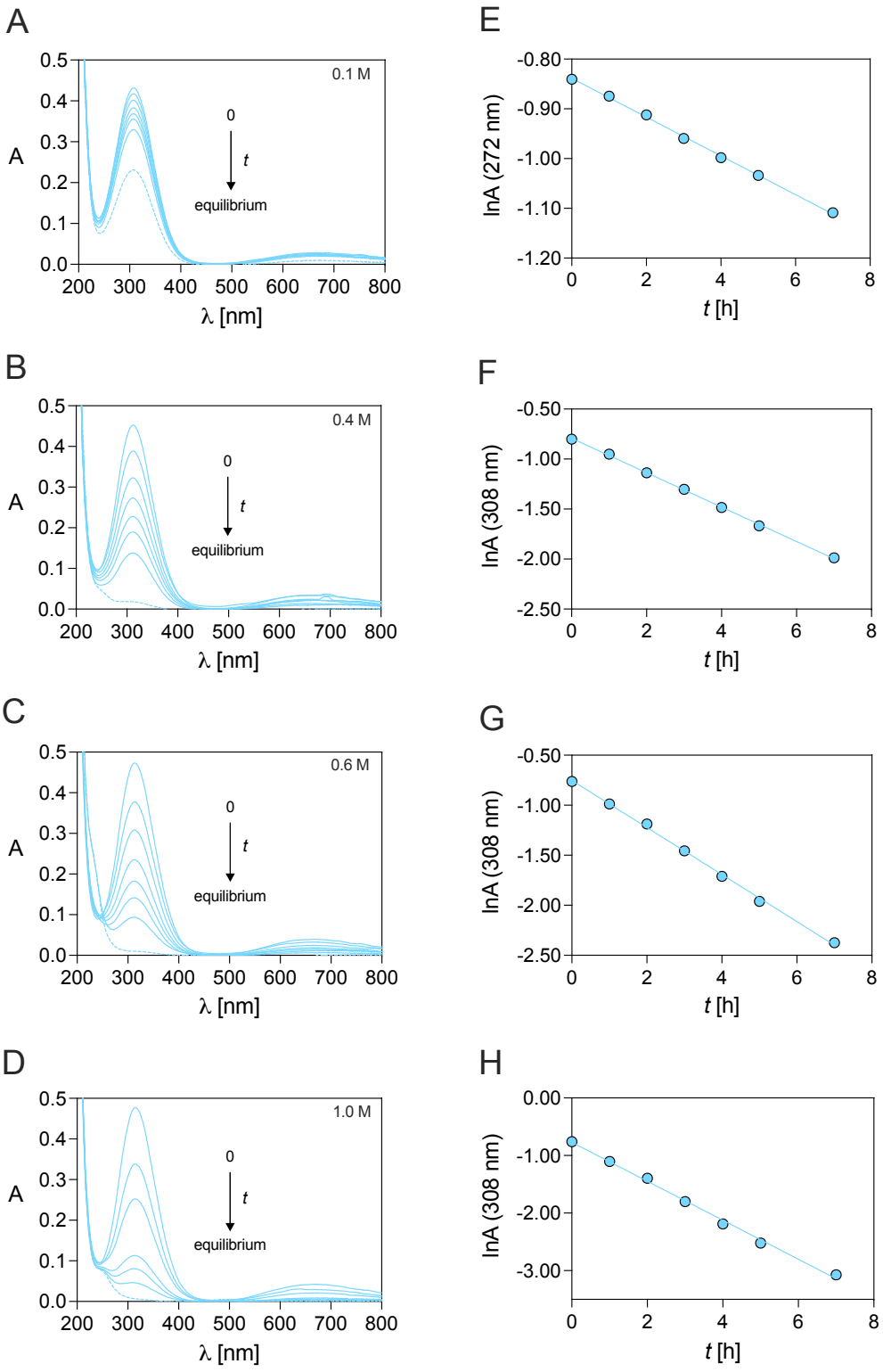

Figure 4.21. (A, B, C, D) UV-Vis spectra variation during the acid-assisted decomplexation assays for Cu^{2+}-DO2A2S ($C_{Cu^{2+}}$ = C_{DO2A2S} = $1.0 \cdot 10^{-4}$ M) at the given (upper right) HCl concentrations (dotted lines correspond to equilibrium conditions); (E, F, G, H) ln*A vs. t* and corresponding fitting line.

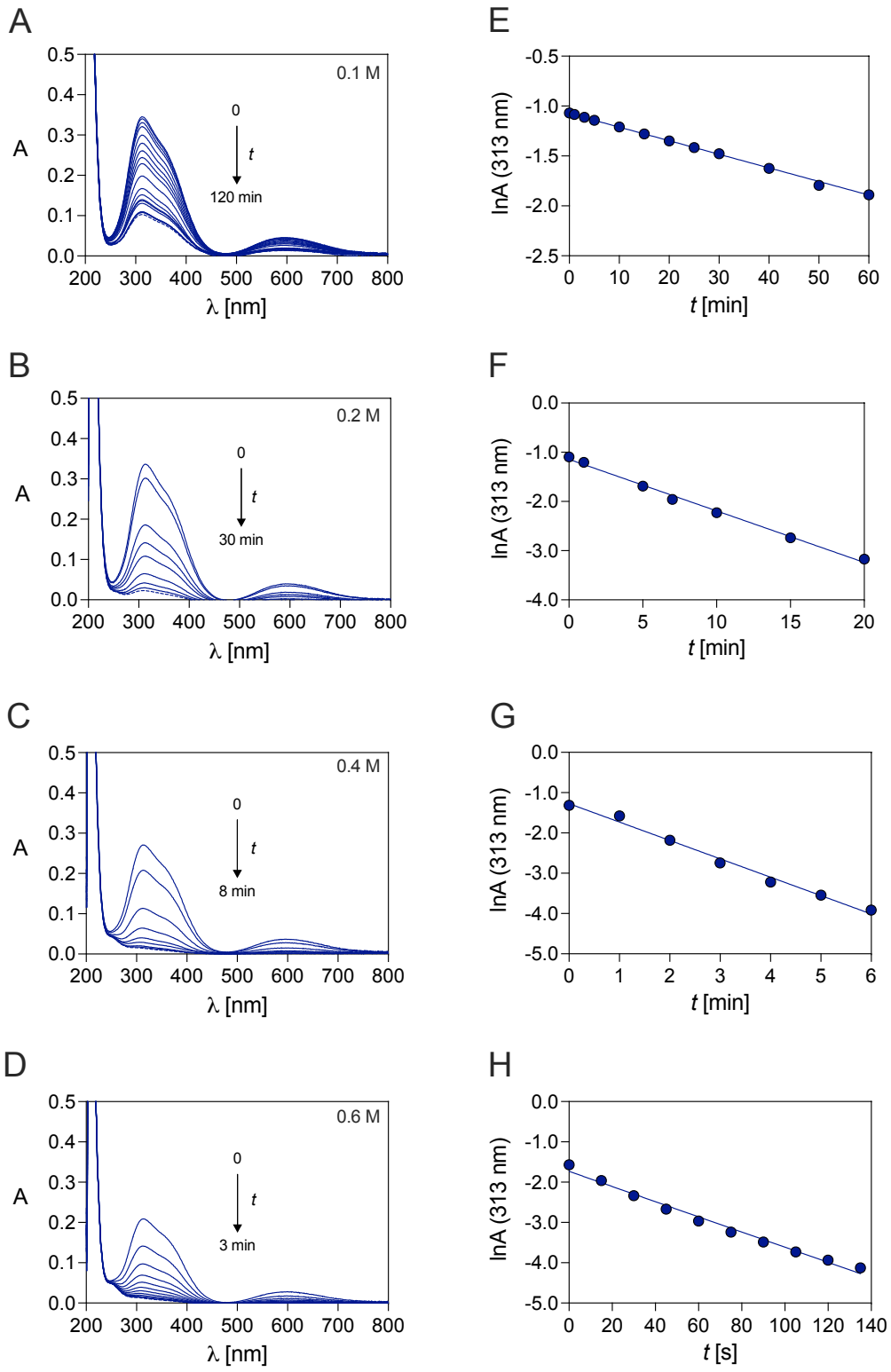

Figure 4.22. (A, B, C, D) UV-Vis spectra variation during the acid-assisted decomplexation assays for Cu^{2+}-TRI4S ($C_{Cu^{2+}}$ = C_{TRI4S} = $1.0 \cdot 10^{-4}$ M) at the given (upper right) HCl concentrations (dotted lines correspond to equilibrium conditions); (E, F, G, H) ln*A vs. t* and corresponding fitting line.

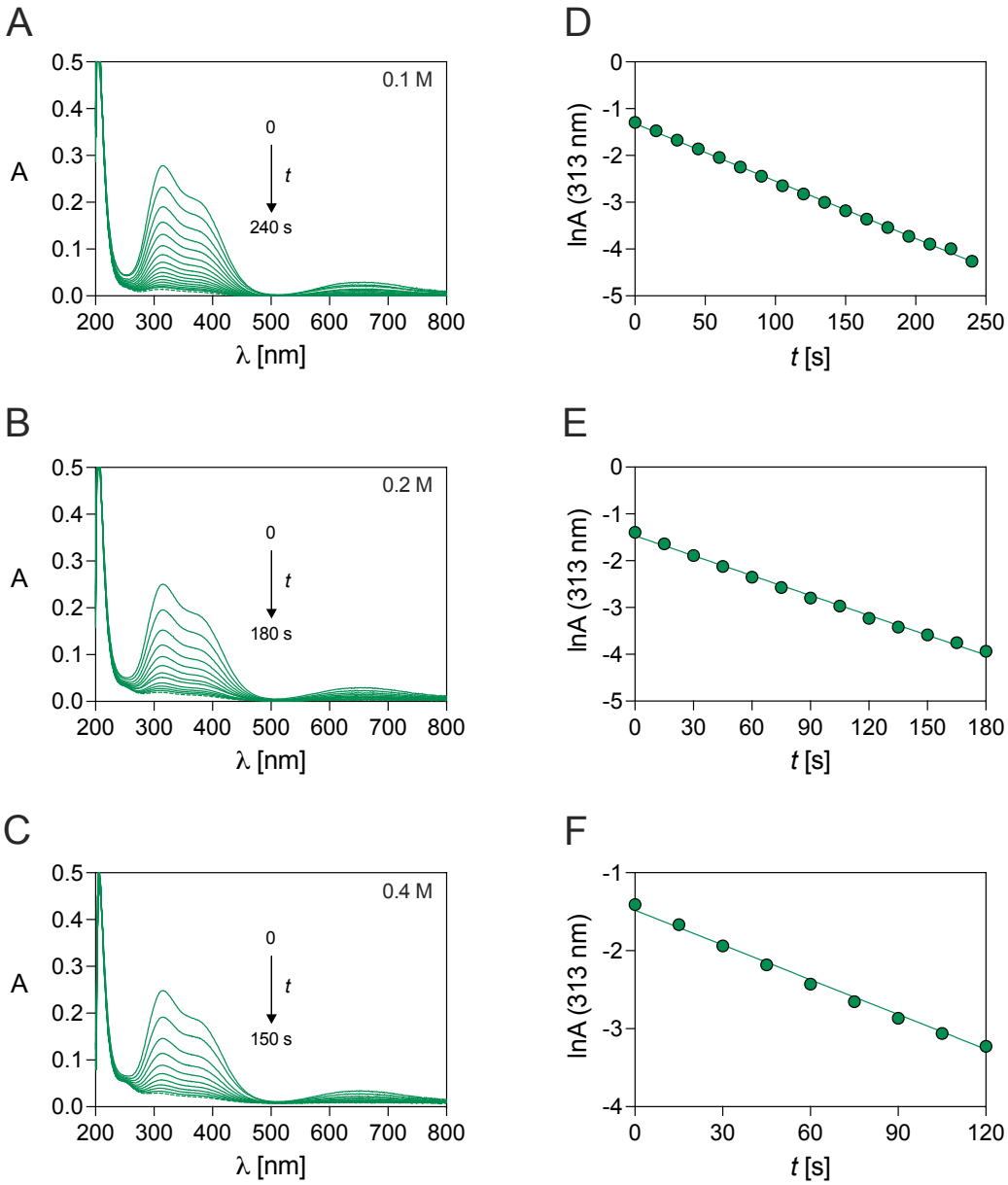

Figure 4.23. (A, B, C) UV-Vis spectra variation during the acid-assisted decomplexation assays for Cu^{2+}-TE4S ($C_{Cu^{2+}}$ = C_{TE4S} = $1.0 \cdot 10^{-4}$ M) at the given (upper right) HCl concentrations (dotted lines correspond to equilibrium conditions); (D, E, F) ln*A vs. t* and corresponding fitting line.

4.2.9 Electrochemical Properties of Cupric and Cuprous Complexes with First-Generation Ligands

The Cu^{2+} complexes formed by DO4S, DO3S, and DO2A2S were examined in aqueous solutions at nearly physiological pH (~ 7) by cyclic voltammetry (CV).

In the cyclic voltammogram of the unbound Cu^{2+} (**Figure C13** - **Appendix C**), a cathodic peak for the reduction of Cu^{2+} to Cu^{+} was observed at about −0.08 V *vs.* saturated calomel electrode (SCE), whilst two overlapping peaks were found on the backward scan due to the oxidation of Cu^{+} and the anodic stripping of Cu^{0} deposited on the electrode because of Cu^{+} dismutation during the scan.

The cyclic voltammograms of the investigated free ligands are shown in **Figure C14** (**Appendix C**). DO4S, DO3S, and DO2A2S demonstrated to be electrochemically inactive in the potential range of Cu^{2+}/Cu^{+} redox couple, *i.e.* from +0.5 to –0.5 V *vs.* SCE. At about 0.8 V *vs.* SCE, DO4S and DO3S showed a small oxidation peak whereas DO2A2S exhibited a well-developed anodic peak. The oxidation processes underlying the former peaks were not further examined because of their low intensity and proximity to the anodic electrolyte discharge. The anodic peak of DO2A2S might be assigned to the oxidation of its carboxylic groups. DO4S and DO3S bear oxidizable thioethers, but the observed anodic peaks cannot be assigned to the oxidation of the sulfanyl side chains because the typical oxidation potentials of these groups are higher than 1.0 V.[56–58] It is more likely that they are due to impurities in the ligands resulting from their synthesis.

Typical cyclic voltammograms of the copper-chelator complexes are presented in **Figure 4.24** while their electrochemical properties are summarized in **Table 4.7**.

At physiological pH, all solutions exhibited two peaks assigned to the redox couple of the Cu^{2+}/Cu^{+} complexes (**Figure 4.24**). This voltammetric behaviour did not change with time or after multiple reduction/oxidation cycles, indicating that no demetallation with copper loss occurs after Cu^{2+} reduction. The long-time stability of Cu^{+} complexes was confirmed by controlled-potential electrolysis, which allowed *in situ* preparation of the chelates, followed by NMR characterization (*vide infra*).

Variation of the scan rate did not modify the voltammetric pattern of Cu-DO4S and Cu-DO3S; only the current intensity changed with the scan rate (**Figure 4.25**). Electron transfer (ET) to Cu^{2+} complexes with these ligands was quite fast with $\Delta E_p = E_{pa} - E_{pc}$ values slightly higher than the canonical 60 mV for Nernstian ET processes. Conversely, ΔE_p for Cu-DO2A2S was much higher than 60 mV and remarkably increased as the scan rate was raised, indicating the occurrence of a quasi-reversible ET. The value of ΔE_p = 155 mV measured at v = 0.01 V/s increased to 260 mV at v = 0.1 V/s. At higher scan rates, the process tended toward the behaviour of an irreversible ET with a drastic decrease of the anodic peak in the reverse scan.

For all complexes the cathodic peak current (i_{pc}) varied linearly with $v^{1/2}$, indicating that all electrode processes are under diffusion control (**Figure 4.26**), and the voltammetric analysis allows to conclude that no demetallation occurs when Cu^{2+} is reduced to Cu^{+}, all ligands being able to accommodate both copper oxidation states.

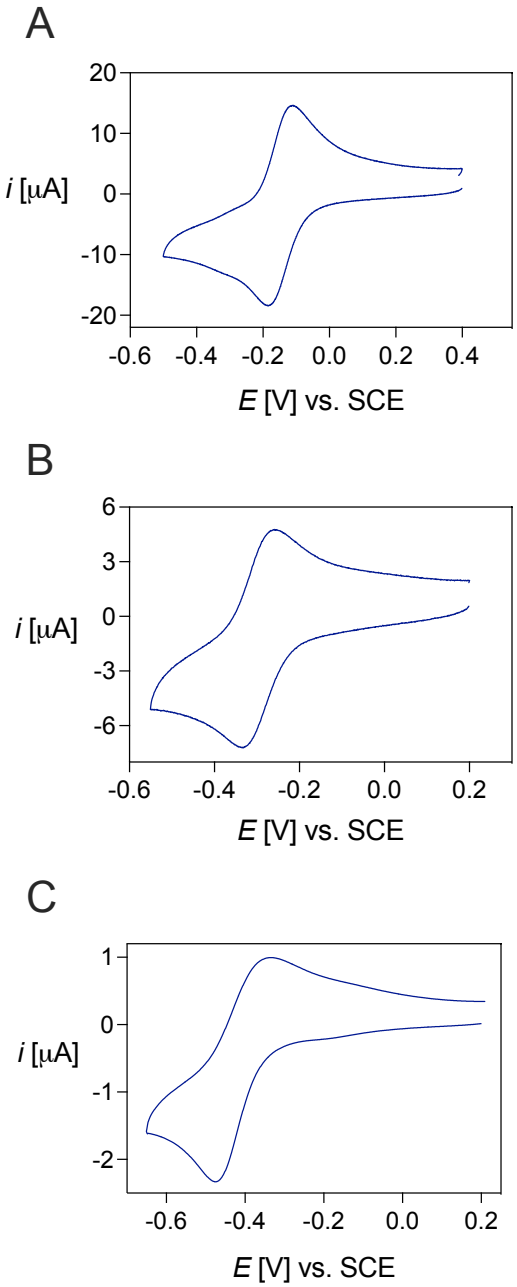

Figure 4.24. Cyclic voltammograms of the copper complexes of (A) DO4S ($C_{[Cu(DO4S)]^{2+}}$ = 1.02·10^{-3} M), (B) DO3S ($C_{[Cu(DO3S)]^{2+}}$ = 1.13·10^{-3} M) and (C) DO2A2S ($C_{[Cu(DO2A2S)]}$ = 6.48·10^{-4} M) in aqueous solution at pH 7, I = $NaNO_3$ 0.15 M and T = 25°C; scan rates: 0.1 V/s (A, B) and 0.01 V/s (C).

Table 4.7. Cathodic peak potential (E_{pc}), anodic peak potential (E_{pa}), and half-wave potential ($E_{1/2}$) for copper complexes of DO4S, DO3S and DO2A2S in aqueous solution at pH 7, I = 0.15 M $NaNO_3$ and T = 25°C.

Complex	E_{pc} [V] *vs.* SCE [(a)]	E_{pa} [V] *vs.* SCE [(a)]	ΔE_p [V] *vs.* SCE [(a)]	$E_{1/2}$ [V] *vs.* SCE [(a)]
Cu-DO4S	−0.182 ± 0.001	−0.115 ± 0.003	0.067	−0.149 ± 0.001
Cu-DO3S	−0.334 ± 0.004	−0.252 ± 0.003	0.082	−0.293 ± 0.005
Cu-DO2A2S	−0.496	−0.341 [(b)]	–0.155	−0.421 ± 0.004
Cu-TRI4S	−0.269 ± 0.001	−0.177 ± 0.006	91	−0.223 ± 0.003
Cu-TE4S	−0.216 ± 0.003	−0.125 ± 0.004	91	−0.170 ± 0.003

[(a)] Average of the values measured at 0.01 ≤ v ≤ 0.2 V/s.
[(b)] Value at v = 0.1 V/s.

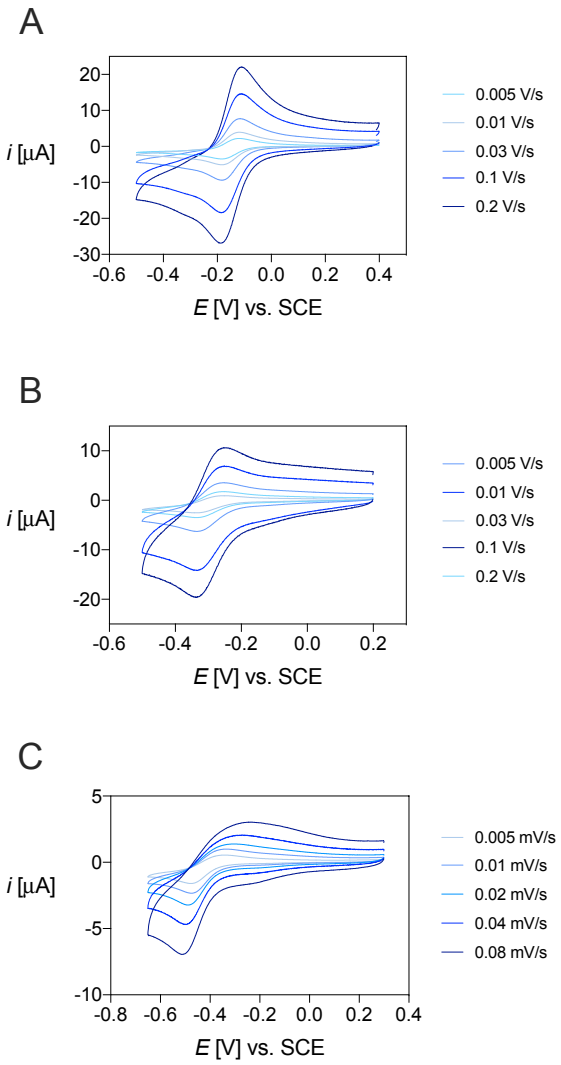

Figure 4.25. Cyclic voltammograms of copper complexes of (A) DO4S ($C_{[Cu(DO4S)]^{2+}}$ = $1.0 \cdot 10^{-3}$ M), (B) DO3S ($C_{[Cu(DO3S)]^{2+}}$ = $1.1 \cdot 10^{-3}$ M) and (C) DO2A2S ($C_{[Cu(DO2A2S)]}$ = $6.48 \cdot 10^{-4}$ M) in aqueous solution at pH 7, I = 0.15 M $NaNO_3$ and T = 25°C at different scan rates (0.005 - 0.2 V/s).

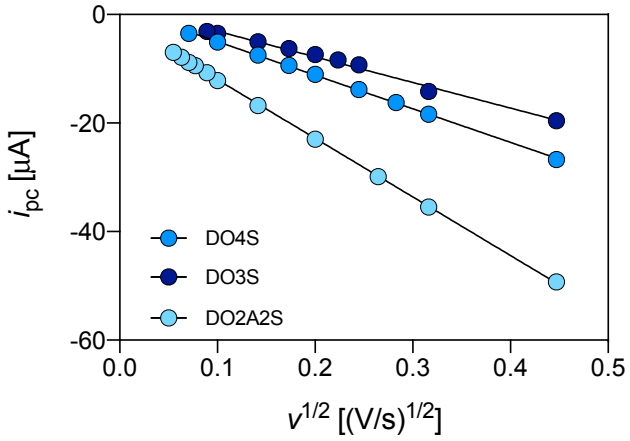

Figure 4.26. Variation of the cathodic current intensity (i_{pc}) with the square root of the scan speed ($v^{1/2}$) for the Cu^{2+} complexes of (A) DO4S, (B) DO3S and (C) DO2A2S, and linear regressions.

Differences were evidenced in the redox kinetics: ET was essentially reversible for the Cu complexes of DO4S and DO3S while sluggish kinetics were observed for Cu-DO2A2S. The activation Gibbs free energy of ET for Cu-DO4S and Cu-DO3S should mainly arise from solvent reorganization, while a significant contribution from inner reorganization is also present in the case of Cu-DO2A2S. A plausible conformational change accompanying ET to Cu^{2+}-DO2A2S might be the decoordination of one or two acetate arms and the simultaneous coordination of one or two sulfurs to form a stable Cu^{+}-DO2A2S complex.

The obtained electrochemical data can also give insights into the ability of the Cu^{2+} complexes to withstand reductive-induced decomplexation *in vivo*. The standard reduction potentials of the Cu^{2+} complexes were calculated from cyclic voltammetry assuming that $E^0 = E_{1/2} = (E_{pa} + E_{pc})/2$ (**Table 4.7**). The estimated threshold for typical bioreductants (E^0 = −0.64 V *vs.* SCE) is more negative than the $E_{1/2}$ values of **Table 4.7**. Therefore, all the investigated copper complexes are likely to be reduced in the presence of biological reductants.[32] However, the stability observed by CV strongly suggests that the resulting Cu^{+} complexes would not undergo demetallation.

Cyclic voltammetry has been previously used to evaluate the ability of Cu^{2+} chelates to withstand reductive-induced demetallation. Several Cu^{2+} complexes with macrocyclic compounds such as TETA and CB-DO2A exhibited irreversible CVs, suggesting instability of electrogenerated Cu^{+} chelates.[4,14] Conversely, all complexes investigated herein undergo one-electron reduction to give highly stable Cu^{+} chelates as shown by cyclic voltammetry and confirmed by controlled-potential electrolysis (*vide infra*).

4.2.10 Solution Thermodynamics and Structural Investigation of Cuprous Complexes with First-Generation Ligands

The stability constants of the Cu^+ complexes of the first-generation ligands were calculated using the electrochemical data and the stability constants of the corresponding Cu^{2+} complexes, as described in **Appendix C**. It was also assumed that the complex formed between Cu^+ and each ligand at pH 7 is $[CuL]^+$, because also Ag^+ form this complex under the same conditions (**Chapter 3**). The results are summarized in **Figure 4.27** and **Table 4.8** together with the calculated pCu^+ values ($pCu^+ = -\log[Cu^+]_{free}$) at physiological pH, which indicate that DO4S forms the most stable Cu^+ complexes.

Bulk electrolyses of Cu^{2+}-DO4S and Cu^{2+}-DO2A2S solutions were performed at nearly neutral pH to isolate and characterize the corresponding Cu^+ complexes. Linear scan voltammetry (LSV) was used to monitor the evolution of the species in solution. A representative example of LSV before and after electrolysis is reported in **Figure 4.28**. The Cu^+ complexes of both ligands remain stable at least for some hours after their formation.

NMR spectra performed on the Cu^+-ligand solution obtained after electrolysis are shown in **Figure 4.29**. The NMR spectral data are summarized in **Table C13** (**Appendix C**), and a comparison between the NMR spectra of the free chelator and the respective Cu^+ complexes, showing significant changes of the proton chemical shifts associated with the complexation event, is reported in **Figure 4.30**.

The ^{1}H-NMR spectrum of $[Cu(DO4S)]^+$ (**Figure 4.29**) is consistent with the formation of a highly symmetric complex as it exhibits only three signals. The singlet at 2.20 ppm was attributed to the SCH_3 protons, whereas those at 2.72 and 2.82 ppm include all other protons. According to the peak integrations, these are the NCH_2 protons of the pendant arms, and the ring NCH_2 together with the SCH_2, but from the mono-dimensional spectrum it is not possible to state which signal belongs to which protons.

Table 4.8. Overall stability constants ($\log\beta$) for the Cu^+ complexes formed by first- and second-generation ligands at I = 0.15 M and T = 25°C, and calculated pCu^+ values.

Ligand	Equilibrium reaction	$\log\beta$	pCu^+ (*)
DO4S	$Cu^+ + L \leftrightharpoons [CuL]^+$	19.8 ± 0.2	17.2
DO3S		17.2 ± 0.2	14.5
DO2A2S	$Cu^+ + L^{2-} \leftrightharpoons [CuL]^-$	16.7 ± 0.1	14.1
TRI4S	$Cu^+ + L \leftrightharpoons [CuL]^+$	16.8 ± 0.1	15.3
TE4S		16.3 ± 0.1	13.6

(*) pCu^+ calculated at $C_{Cu^+} = 10^{-6}$ M and $C_L = 10^{-5}$ M, pH 7.4.

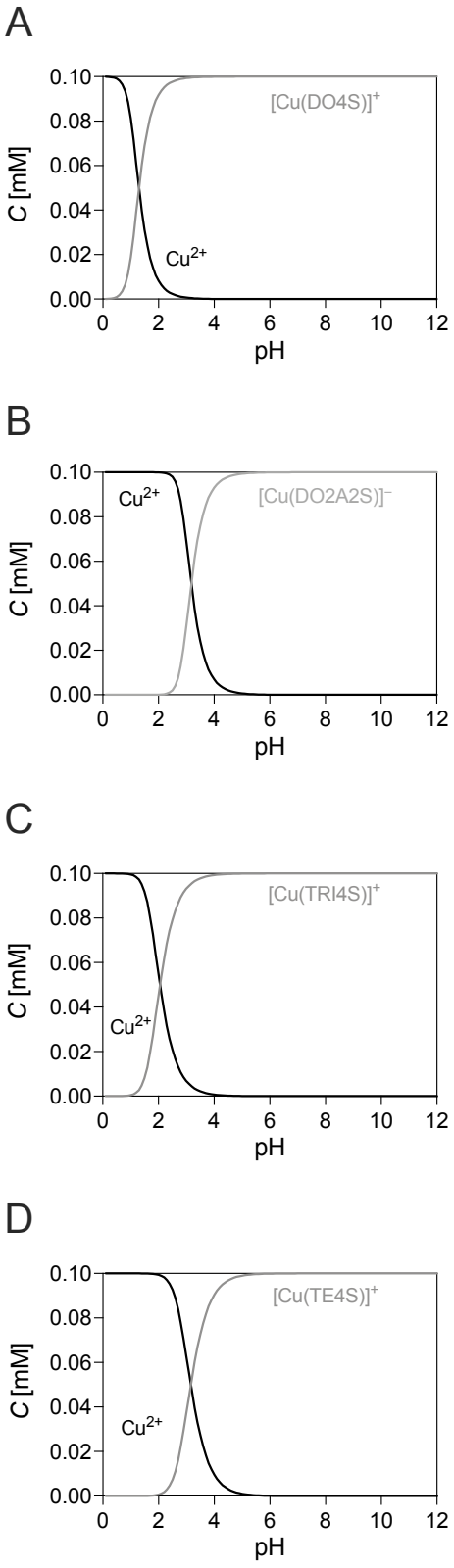

Figure 4.27. Distribution diagrams of (A) Cu^{+}-DO4S, (B) Cu^{+}-DO2A2S, (C) Cu^{+}-TRI4S and (D) Cu^{+}-TE4S at $C_{Cu^{+}} = C_L = 1.0 \cdot 10^{-4}$ M.

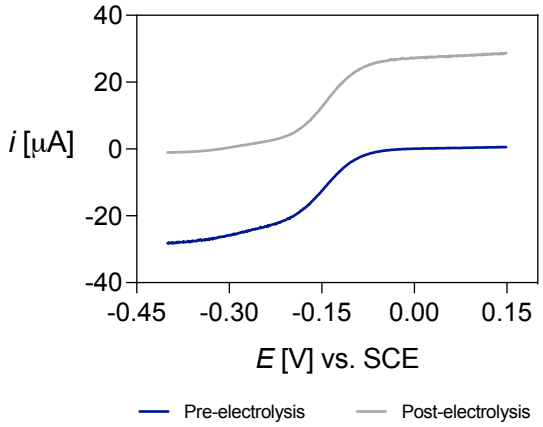

Figure 4.28. LSV of Cu-DO4S before and after electrolysis at E = –0.35 V, performed with a rotating disk electrode at ω = 2000 rpm and v = 0.005 V/s, I = $NaNO_3$ 0.15 M and T = 25°C.

The downfield shift observed for the SCH_3 protons upon Cu^+ complexation (**Figure 4.30**) indicates the formation of Cu^+-S bond(s). Indeed, all S-related signals are equivalent on the NMR timescale, suggesting either that all four sulfurs are bound, or that their exchange is rapid on the NMR timescale. Considering also the reversible voltammetric pattern, which suggests a similar coordination for the Cu^+ and Cu^{2+} complexes, it is possible to argue that all the ring nitrogens and one rapidly exchanging sulfur are present in the metal coordination sphere of $[Cu(DO4S)]^+$. In the case of $[Ag(DO4S)]^+$ solutions, the metal ion was likely bound by two nitrogens and two sulfurs (**Chapter 3**). If the ^{1}H-NMR spectrum of $[Cu(DO4S)]^+$ is compared with that of $[Ag(DO4S)]^+$ (**Figure 4.31**), the metal-coordination seems to be different, as the signals change in shape and position.

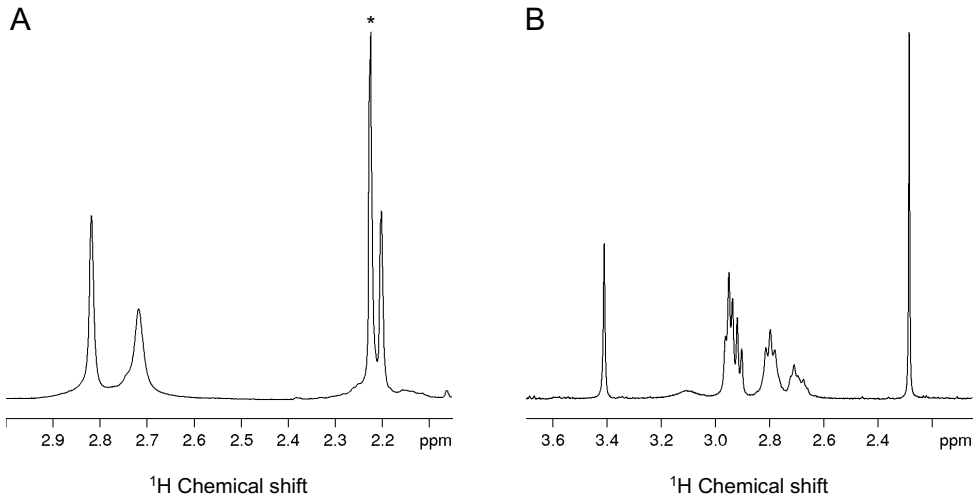

Figure 4.29. ^{1}H-NMR spectra (400 MHz, T = 25°C, H_2O + 10% D_2O) of the *in situ* generated cuprous complexes of (A) DO4S (C_{Cu} = C_{DO4S} = $1.6 \cdot 10^{-3}$ M) and (B) DO2A2S (C_{Cu} = C_{DO2A2S} = $1.4 \cdot 10^{-3}$ M) at pH 7. The signal marked with an asterisk (2.22 ppm) is related to acetone impurity.

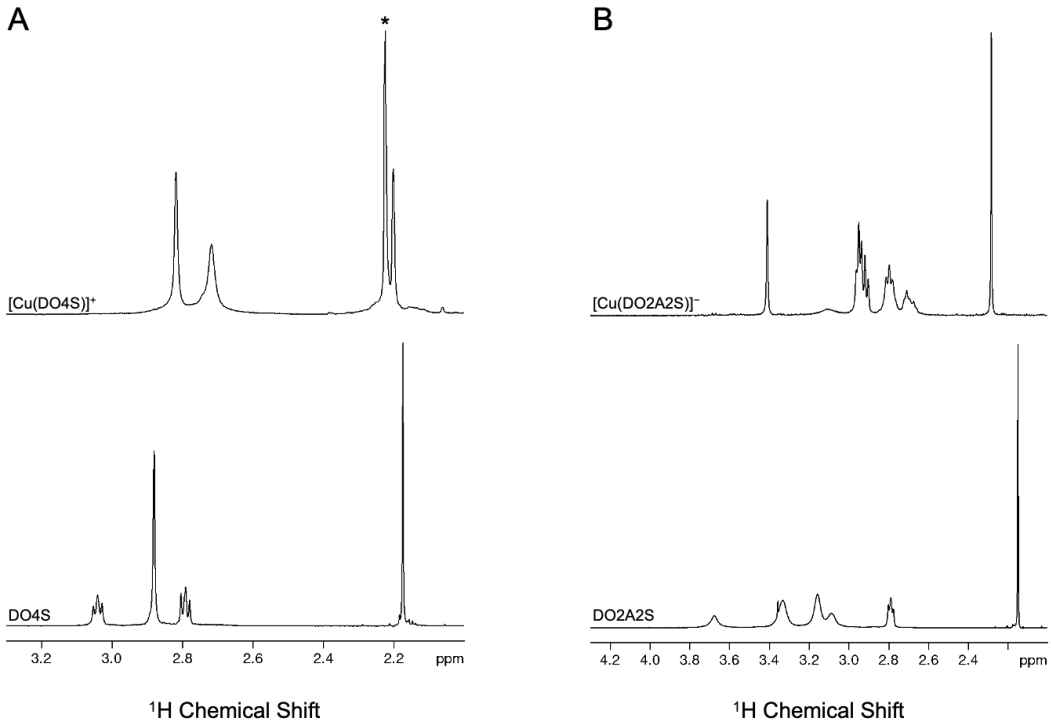

Figure 4.30. Comparison between the ^{1}H-NMR spectra of (A) $[Cu(DO4S)]^{+}$ and (B) $[Cu(DO2A2S)]^{-}$ (400 MHz, T = 25°C, H_2O + 10% D_2O) at pH 7 and free monoprotonated (A) DO4S and (B) neutral DO2A2S (600 MHz, T = 25°C, D_2O). The signal marked with an asterisk (2.22 ppm) is related to acetone impurity.

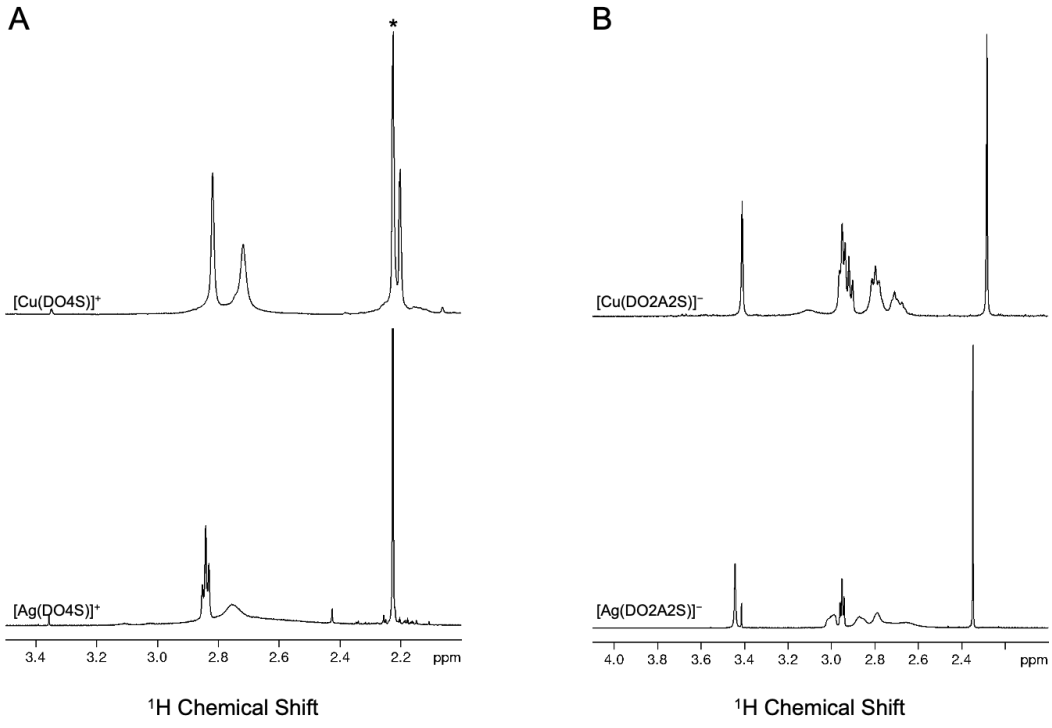

Figure 4.31. Comparison between the ^{1}H-NMR spectra of (A) $[Cu(DO4S)]^{+}$ and (B) $[Cu(DO2A2S)]^{-}$ (400 MHz, T = 25°C, H_2O + 10% D_2O) with the corresponding Ag^{+} complexes (600 MHz, RT, D_2O) at pH 7. The signal marked with an asterisk (2.22 ppm) is related to acetone impurity.

DFT calculations performed on $[Cu(DO4S)]^+$ and $[Cu(DO3S)]^+$ complexes confirm that one sulfur atom is bound to Cu^+ (**Table 4.5**). The cuprous complexes of DO4S and DO3S are stabilized in the [4N]S coordination mode by 6-8 kcal/mol when compared to the [4N] one. The coordination of a second sulfur atom to Cu^+, giving a [4N]2S coordination, is disfavored because a less negative ΔG_{water} is obtained (by ~ 9 kcal/mol if compared to [4N]S). Using ASM and EDA (**Table C5** - **Appendix C**), it can be observed that the stabilization of the [4N]S complex is mainly assigned to the contribution of the interaction energy (ΔE_{int}) and the orbital interaction term (ΔE_{oi}). The destabilization experienced by the addition of a second sulfide is due to an increased strain contribution (ΔE_{strain}).

A Kohn-Sham molecular orbital (KS-MO) analysis has been performed for $[Cu(DO4S)]^+$ to explain the reason behind the more stabilizing ΔE_{oi} of the [4N]S complex compared to the [4N] one. The electron density donation from the HOMO−3 orbital of the ligand (**Figure 4.32**) to the 4*s* orbital of Cu^+ (LUMO) was found to be the strongest interaction and the principal bonding force of the [4N] complex. The same interaction is also present in the [4N]S and [4N]2S complexes with the only difference that the donating orbital is the HOMO−4 and HOMO−5, respectively. This orbital interaction is slightly more efficient in the [4N]S complex because of a lower energy gap and a higher overlap between the metal and ligand orbitals. However, the main ΔE_{oi} stabilization originates from a secondary bonding mode which is active only when a sulfide pendant group directly coordinates the metal center, namely the electron donation that occurs from the HOMO of the ligand to the LUMO+1 ($4p_z$ orbital) of the metal center (**Figure C15** - **Appendix C**).

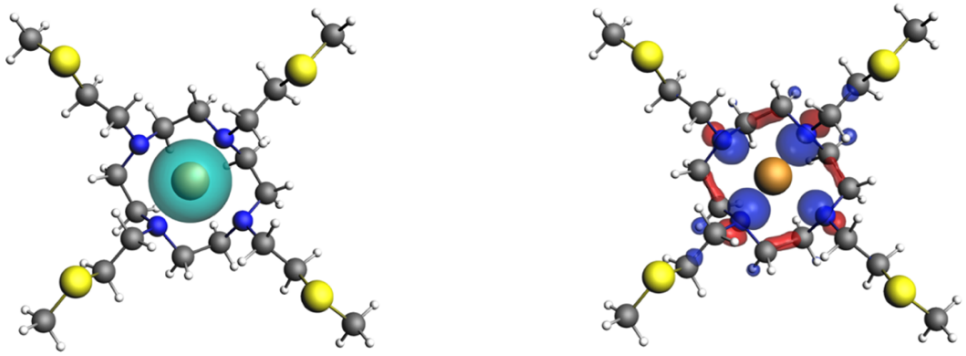

Figure 4.32. Main interacting symmetry-adapted fragment orbitals (SFOs) of the $[Cu(DO4S)]^+$ complex displaying a [4N] coordination mode.

Controlled potential electrolysis of Cu^{2+}-DO2A2S confirmed the formation of a stable $[Cu(DO2A2S)]^-$ species. ^{1}H-NMR spectra for this complex indicate a decreased ligand flexibility upon Cu^+ coordination since both ring and sidearm protons gave signals narrower than those of the free ligand (**Figure 4.30**). The transannular S-donor atoms appear to be involved in the Cu^+ binding since the SCH_3 (2.28 ppm) signals of the complex are significantly downfield shifted when compared to the monoprotonated free chelator (2.15 ppm), and also the SCH_2 signal pattern of the chelator changes considerably upon Cu^+ complexation. This result, combined with the CV data, can represent a proof that a coordination sphere switching occurred when Cu^{2+} was reduced to Cu^+.

The $[Cu(DO2A2S)]^-$ NMR spectra are similar to those obtained for $[Ag(DO2A2S)]^-$ (**Figure 4.31**), but signals are narrower when Cu^+ is coordinated, which might indicate that the cuprous complex is characterized by a slowed-down fluxional interconversion compared to the Ag^+ one.

The stability of the $[Cu(DO2A2S)]^-$ complexes was investigated by DFT, particularly tackling any possible change in coordination due to carboxylate protonation. When no protonation occurs, two structures are predominant and reflect the most probable Cu^+ complex geometries (**Table 4.5**): they are both coordinated in the apical region, *i.e.* above the metal center, by a single chain in which the [4N]S species is ~ 2 kcal/mol more stable than the [4N]O one.

The protonation of a single carboxylate group results in two intriguing effects. First, the relative stability among the different types of coordination does not change with respect to the unprotonated structures. Secondly, the [4N]S complex is now greatly stabilized by 22.6 kcal/mol when compared to the [4N]O one, thus further favouring the formation of the Cu^+ complex with a single sulfur chain coordinated to the metal center.

4.2.11 Electrochemical Properties and Solution Thermodynamics of Cuprous Complexes with Second-Generation Ligands

A CV study was undertaken in water using 0.15 M $NaNO_3$ as a supporting electrolyte to evaluate the stabilities of the second-generation Cu^{2+} complexes upon reduction to Cu^+.

The electrochemical behaviour of the unbound TRI4S and TE4S was firstly assessed: analogously to the first-generation macrocycles, both ligands were demonstrated to be electrochemically inactive in the potential range of the Cu^{2+}/Cu^+ pair (**Figure C16** - **Appendix C**). Representative cyclic voltammograms of the Cu complexes with TRI4S and TE4S acquired at physiological pH and at different scan rates are shown in **Figure 4.33** while the electrochemical properties of their Cu complexes are listed in **Table 4.7**.

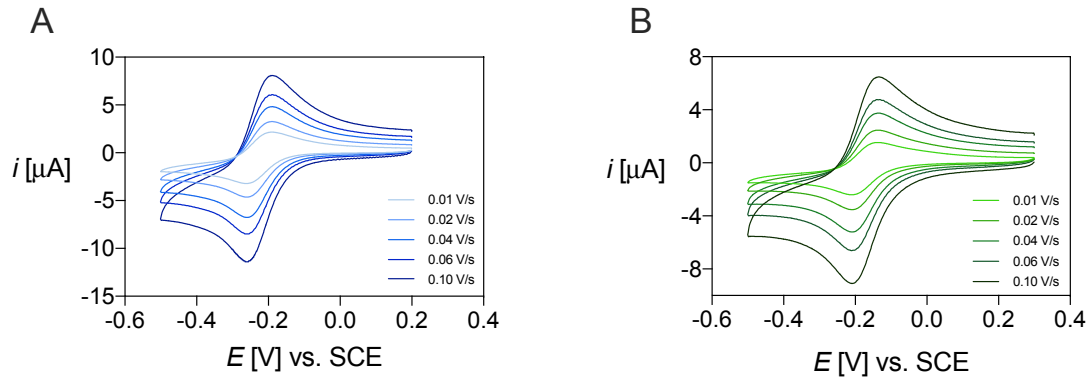

Figure 4.33. Cyclic voltammograms of the copper complexes of (A) TRI4S ($C_{Cu^{2+}}$ = $8.0 \cdot 10^{-4}$ M, C_{TRI4S} = $1.0 \cdot 10^{-3}$ M) and (B) TE4S ($C_{Cu^{2+}}$ = $8.0 \cdot 10^{-4}$ M, C_{TE4S} = $1.1 \cdot 10^{-3}$ M) in aqueous solution at physiological pH, I = $NaNO_3$ 0.15 M and T = 25°C acquired at different scan rates.

Both copper complexes displayed a redox process ascribed to a quasi-reversible one-electron reduction of Cu^{2+} to Cu^{+} at $E_{1/2,\ Cu\text{-}TRI4S}$ = −0.223 ± 0.003 V *vs*. SCE and $E_{1/2,\ Cu\text{-}TE4S}$ = −0.170 ± 0.003 *vs*. SCE. For both metal-ligand solutions, ΔE_p was higher than the canonical 60 mV for Nernstian ET processes (**Table 4.7**), indicating that these processes are quasi-reversible.

The voltammetric pattern was unchanged with multiple reduction/oxidation cycles and at the different scan rates (**Figure 4.34**): in both cases, a linearity between the intensity of the cathodic peak current (i_{pc}) and the square root of the scan rate ($v^{1/2}$) was found (**Figure S32**), indicating that the electrode process is under diffusion control.

Using the thermodynamic cycle described in **Appendix C**, the stability constants of the deprotonated complexes ($[CuL]^{+}$) were determined.

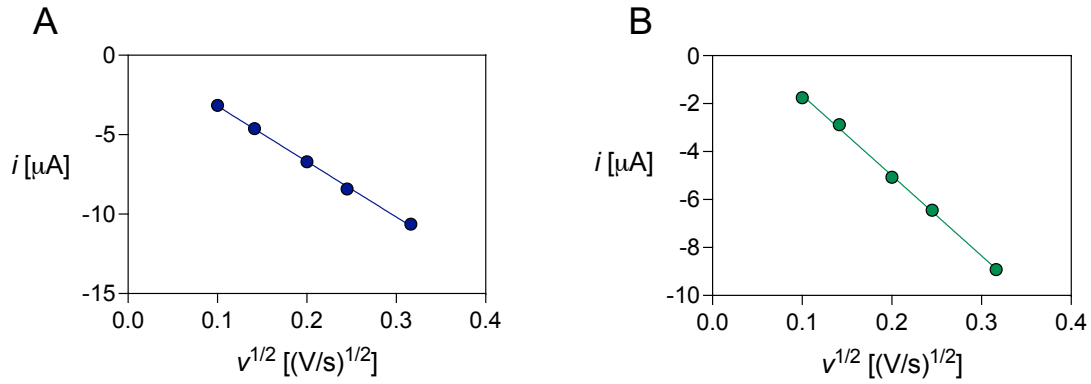

Figure 4.34. Variation of the cathodic current (i_{pc}) (data referred to **Figure 4.33**) with the square root of the scan rate ($v^{1/2}$) for the Cu complexes of (A) TRI4S and (B) TE4S, and corresponding linear regressions.

The complex formed between Cu^{+} and both ligands at pH 7 was initially assumed to be $[CuL]^{+}$ because the first-generation ligands form this complex under the same conditions. This was further confirmed from cyclic voltammograms acquired at different pH which do not show any pH-dependent variation of their pattern (**Figure 4.35**). The results are detailed in **Table 4.8** and the corresponding distribution diagrams are shown in **Figure 4.27**. The calculated pCu^{+} values ($pCu^{+} = -\log[Cu^{+}]_{free}$) indicate that the increase of the ring size from a 12- (DO4S) to a 13- (TRI4S) and then to a 14-member macrocycle (TE4S) corresponds to a progressive decrease of the Cu^{+} complexes stability, likewise to what was found for the +2 oxidation state (*vide supra*).

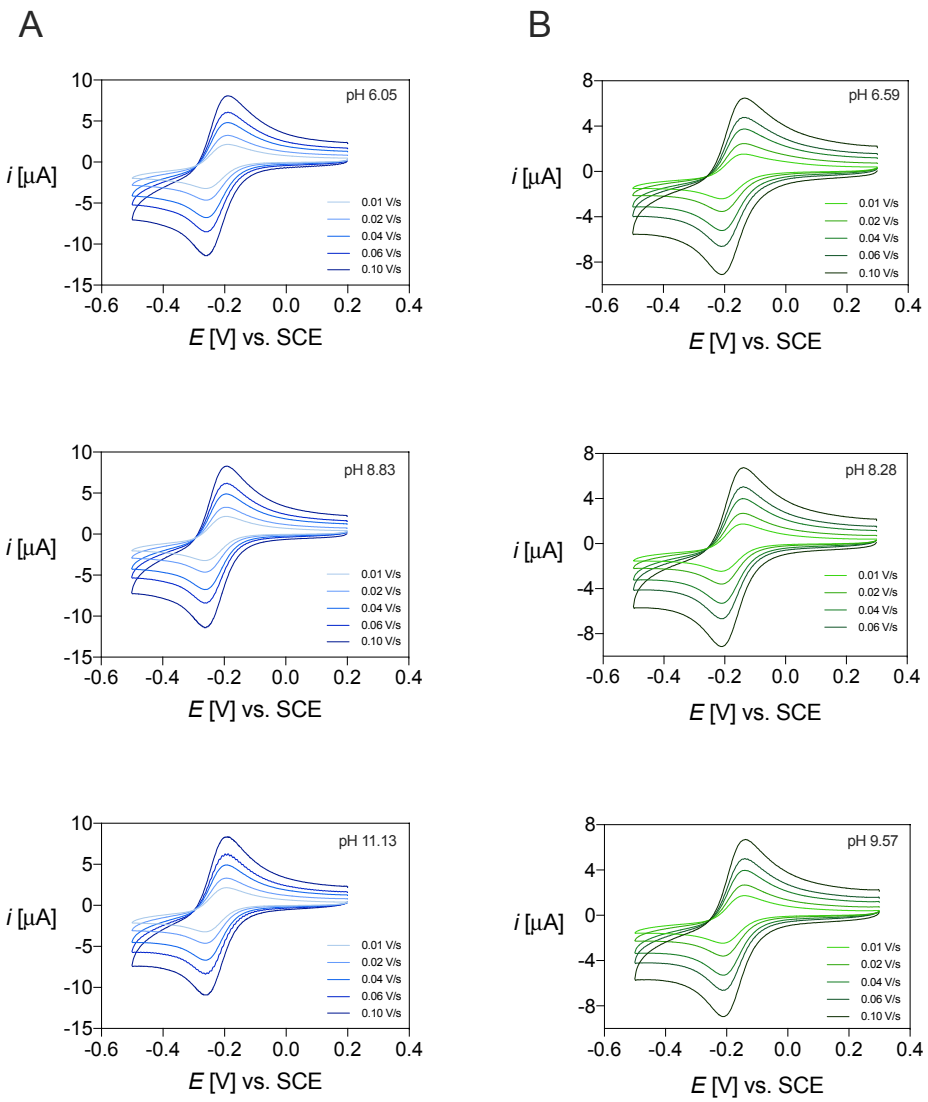

Figure 4.35. Cyclic voltammograms of the copper complexes of (A) TRI4S ($C_{Cu^{2+}} = 8.0 \cdot 10^{-4}$ M, $C_{TRI4S} = 1.0 \cdot 10^{-3}$ M) and (B) TE4S ($C_{Cu^{2+}} = 8.0 \cdot 10^{-4}$ M, $C_{TE4S} = 1.1 \cdot 10^{-3}$ M) in aqueous solution at different pH, I = $NaNO_3$ 0.15 M and T = 25°C acquired at different scan rates.

The reversibility of the CV process indicates that all electrogenerated cuprous complexes are stable and do not dissociate during the CV timescale. The long-term stability of the Cu^{+} complexes was then further confirmed by controlled-potential electrolysis of the Cu^{2+} complexes, which was performed at nearly neutral pH to isolate and characterize the corresponding deprotonated Cu^{+} complexes of TRI4S and TE4S which predominate under physiological conditions. To monitor the reduction processes, LSV was employed (**Figure 4.36**). It was evidenced that both cuprous complexes remained stable at least for some hours after their *in-situ* formation after $[CuL]^{2+}$ reduction. These results demonstrate the ability of TRI4S and TE4S to adapt to both the Cu^{2+} and Cu^{+} coordination requirements, analogously to what was previously found with the first-generation series (*vide supra*).

As previously described, the CV data also allow to obtain information on the ability of the investigated complexes to resist the demetallation process that could be induced *in vivo* by the biologically triggered redox switching between Cu^{2+} and Cu^{+}. The reduction potential ($E^0 = E_{1/2} = (E_{pc} + E_{pa})/2$) for Cu^{2+}-TRI4S and Cu^{2+}-TE4S (**Table 4.7**) are higher than the estimated potential threshold for typical bioreductants (E^0 = −0.64 V *vs.* SCE), which suggests that they would be vulnerable to *in vivo* reduction.[32,39] Nevertheless, the short- and the long-term stability observed in the voltammetric and electrolytic measurements indicate that the resulting Cu^{+} complex would not undergo demetallation and so the copper would remain anchored to the radiopharmaceutical. Thanks to their long-term stability, the Cu^{+}-TRI4S and Cu^{+}-TE4S solutions obtained after electrolysis were characterized by ^{1}H-NMR measurements. ^{1}H NMR spectra of the Cu^{+} complexes, compared with the spectra of the free ligands, are reported in **Figure 4.37**. The signal assignment is presented in **Table C13** (**Appendix C**), supported by the ^{1}H-^{1}H TOCSY spectra in the case of Cu^{+}-TE4S (**Figure C17** - **Appendix C**).

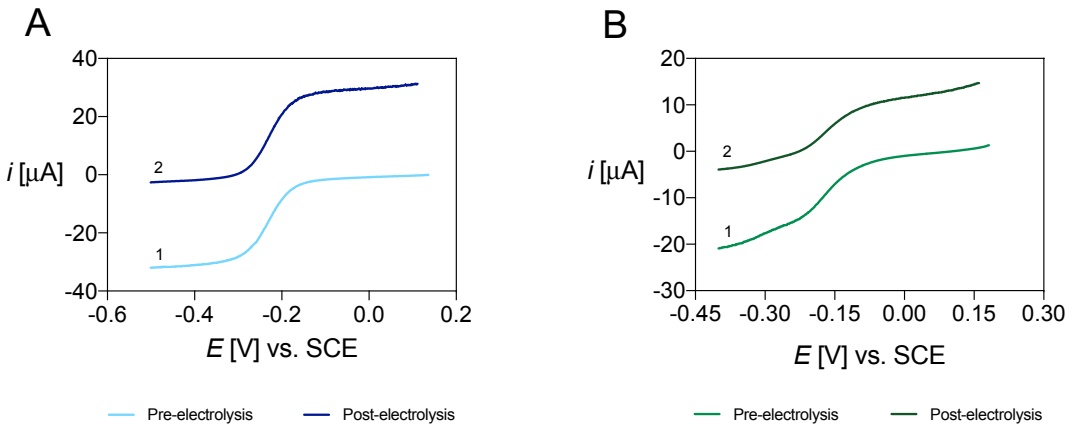

Figure 4.36. LSV of (A) Cu-TRI4S (C_{Cu} = $8.0 \cdot 10^{-4}$ M, C_{TRI4S} = $1.0 \cdot 10^{-3}$ M) and (B) Cu-TE4S (C_{Cu} = $6.0 \cdot 10^{-4}$ M, C_{TE4S} = $7.0 \cdot 10^{-4}$ M) before and after electrolysis at (A) −0.45 V and (B) −0.40 V, performed with a rotating disk electrode at ω = 2000 rpm and v = 0.005 V/s, with I = $NaNO_3$ 0.15 mol/L and T = 25°C.

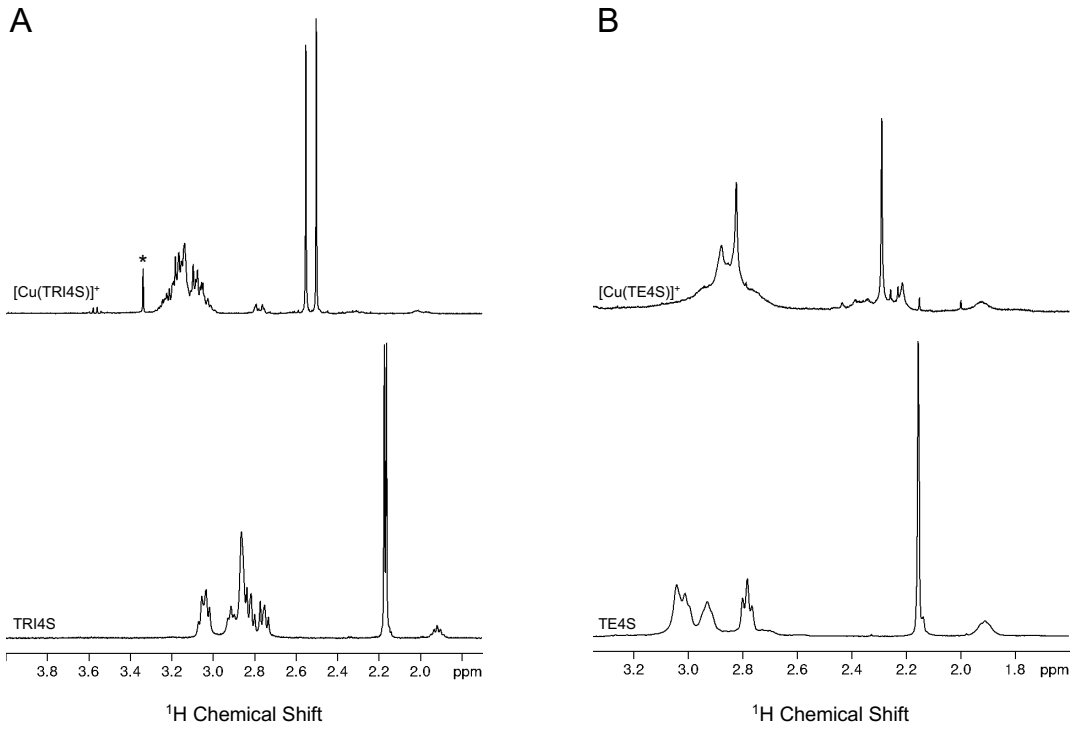

Figure 4.37. ^{1}H NMR spectra (400 MHz, T = 25°C, H_2O + 10% D_2O) of the *in situ* generated Cu^+ complexes of (A) TRI4S (C_{Cu} = $8.0 \cdot 10^{-4}$ M, C_{TRI4S} = $1.0 \cdot 10^{-3}$ M, pH 7) and (B) TE4S (C_{Cu} = $6.0 \cdot 10^{-4}$ M, C_{TE4S} = $7.0 \cdot 10^{-3}$ M, pH 8), and comparison with the ^{1}H NMR spectra of the unbound ligands with the same net charge. The signal marked with an asterisk is related to methanol impurity.

The significant changes in chemical shift and coupling pattern observed among the spectra of the free chelators and those of the Cu^+ complexes undoubtedly confirm the complexation event. All the signals experience a downfield shift upon complexation (more pronounced in the case of $[Cu(TRI4S)]^+$) likely because of the electron density donation from the ligand to the metal ion, thereby suggesting that all the donors are interacting on average with Cu^+.

For $[Cu(TRI4S)]^+$, the SCH_3 protons of the side chains resonate as two narrow singlets with the same intensity at 2.50 and 2.55 ppm (**Table C13** - **Appendix C**). This, combined with the observed downfield shift, is consistent with the involvement of all the S donors in the coordination of Cu^+. Their two-by-two equivalence likely reflects the intrinsic asymmetry of the ligand. For $[Cu(TE4S)]^+$, the methyl groups of the side chains (SCH_3) resonate as a singlet at 2.29 ppm, thus indicating that the S are all involved in the coordination sphere of the metal ion: they can be simultaneously bound to it or in rapid exchange with respect to the NMR timescale.

The signals of the SCH_2 and NCH_2 protons of the side chains and the ring resonate as non-resolved multiplets in both cases (**Table C13** - **Appendix C**). The main difference between the NMR spectra of $[Cu(TRI4S)]^+$ and $[Cu(TE4S)]^+$ is that the latter has broader

signals, suggesting that the Cu^+-TE4S complex is more fluxional and/or its conformational equilibria are slower.

The multiplet attributed to the methylene of the propylenic chain of the ring is split into two very broad signals of equal area only when Cu^+ is coordinated by TRI4S; these two signals have been attributed to axial and equatorial protons of the same molecule, which for conformational constraint become non-magnetically equivalent. If compared with the spectra of the corresponding Ag^+ complexes, *i.e.* $[Ag(TRI4S)]^+$ and $[Ag(TE4S)]^+$ (**Chapter 3**), several spectral features can be recognized, thus indicating a related coordination environment.

4.2.12 Radiolabelling with Copper-64

High molar activity is often crucial when synthesising radiotracers for targeted molecular imaging or therapy since high concentrations of unlabelled targeting agents can lead to receptor blocking and therefore compromise the image interpretation or the therapeutic efficacy. To assess the ability of the first- and second-generation series of sulfur-bearing ligands to chelate $[^{64}Cu]Cu^{2+}$ at extremely low concentrations, radiolabelling experiments were performed under different reaction conditions (high and ambient temperature, neutral and mild-acidic pH), and across six orders of magnitude of chelator concentration (from ~ 10^{-3} M to ~ 10^{-9} M). Similar experiments were also undertaken using the commonly used ligand for $[^{64}Cu]Cu^{2+}$ chelation as NODAGA-RGD, for comparison purposes. Representative radio-chromatograms are shown in **Figure 4.38** - **4.39**.

4.2.12.1 Radiolabelling with First-Generation Ligands

At ambient temperature and pH 4.5, DO2A2S was able to quantitatively chelate $[^{64}Cu]Cu^{2+}$ in 10 min at a molar activity up to 5 MBq/nmol*, a slightly inferior behaviour if compared to NODAGA-RDG which labelled $[^{64}Cu]Cu^{2+}$ at a maximum molar activity equal to 10 MBq/nmol (**Figure 4.40**). Decreasing the ligand concentration dropped the radiochemical yield (RCY) to 82 ± 14% at 10 MBq/nmol, 54 ± 9% at 25 MBq/nmol, 27 ± 6% at 50 MBq/nmol, 14 ± 4% at 100 MBq/nmol and ~ 2% at 250 and 500 MBq/nmol. With NODADA-RDG, the RCY decreased to 58 ± 11% at 25 MBq/nmol and became lower than 5% at molar activities higher than 100 MBq/nmol. Even if the NOTA chelating unit is sufficiently far from the peptide, a slight steric effect of the latter on the RCYs can not be excluded.

The removal of the carboxylate pendants in the macrocyclic structure led to a significant decrease in the labelling performance of the resulting ligands at room temperature. Indeed, DO4S and DO3S were able to quantitatively incorporate $[^{64}Cu]Cu^{2+}$ employing significantly higher chelator concentration (RCY > 99% at 1 MBq/nmol and 0.01 MBq/nmol, respectively) (**Figure 4.40**). At ~ 2.5 MBq/nmol the RCY resulted equal to 82 ± 5% and to ~ 40% and decreased to 75 ± 5% and < 1% at ~ 5 MBq/nmol with DO4S and DO3S, respectively. At molar activities > 25 MBq/nmol, no radiometal incorporation was observed in both cases. An even inferior labelling behaviour was obtained with the amide analogue of DO3S, *i.e.* DO3SAm, which was not able to complex $[^{64}Cu]Cu^{2+}$ at room temperature albeit using the highest ligand concentration assessed.

* Chelator concentrations and amounts corresponding to the different molar activities: 0.1 MBq/nmol: $2 \cdot 10^{-4}$ M, 25 nmol; 1.0 MBq/nmol: $2 \cdot 10^{-5}$ M, 2 nmol; 2.5 MBq/nmol: $8 \cdot 10^{-6}$ M, 1 nmol; 5 MBq/nmol: $4 \cdot 10^{-6}$ M, 0.5 nmol; 10 MBq/nmol: $2 \cdot 10^{-6}$ M, 0.25 nmol; 25 MBq/nmol: $8 \cdot 10^{-7}$ M, 0.10 nmol; 50 MBq/nmol: $4 \cdot 10^{-7}$ M, 0.05 nmol; 100 MBq/nmol: $2 \cdot 10^{-7}$ M, 0.025 nmol; 250 MBq/nmol: $8 \cdot 10^{-8}$ M, 0.010 nmol; 500 MBq/nmol: $4 \cdot 10^{-8}$ M, 0.005 nmol.

This significant difference in RCYs between DO4S and the three-S containing ligands is somewhat surprising given the similarities between their structure.

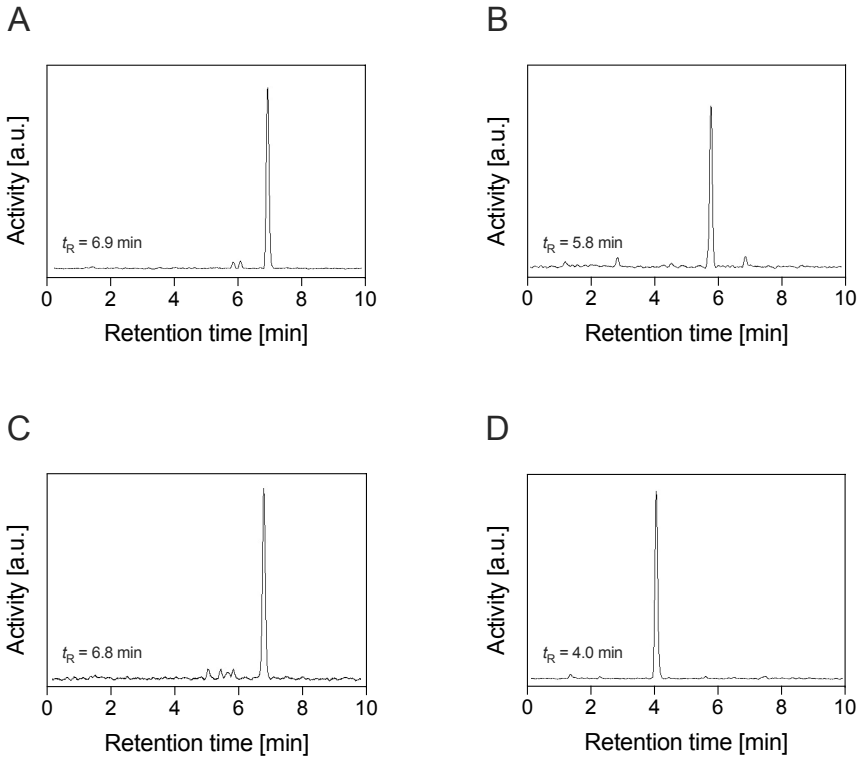

Figure 4.38. Radio-chromatograms of $[^{64}Cu]Cu^{2+}$-labelled first-generation ligands and corresponding retention time (t_R): (A) $[^{64}Cu][Cu(DO4S)]^{2+}$, (B) $[^{64}Cu][Cu(DO3S)]^{2+}$, (C) $[^{64}Cu][Cu(DO3SAm)]^{2+}$ and (D) $[^{64}Cu][Cu(DO2A2S)]$. Free $[^{64}Cu]Cu^{2+}$ elutes near the solvent front (t_R ~ 1 min).

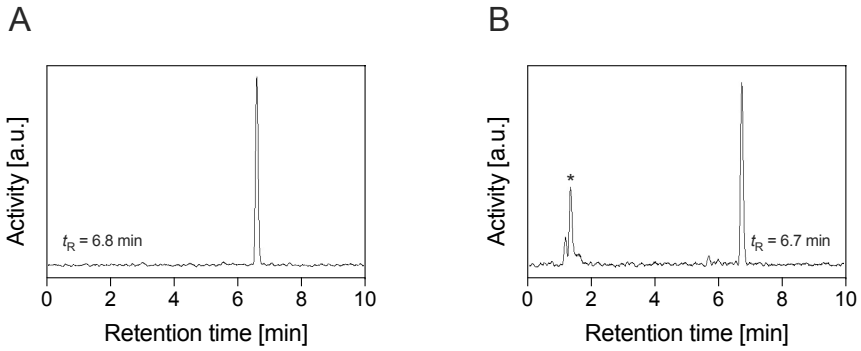

Figure 4.39. Radio-chromatograms of $[^{64}Cu]Cu^{2+}$-labelled second-generation ligands and corresponding retention time (t_R): (A) $[^{64}Cu][Cu(TRI4S)]^{2+}$ and (B) $[^{64}Cu][Cu(TE4S)]^{2+}$. Peak marked with an asterisk is related to unbound $[^{64}Cu]Cu^{2+}$ (t_R ~ 1 min).

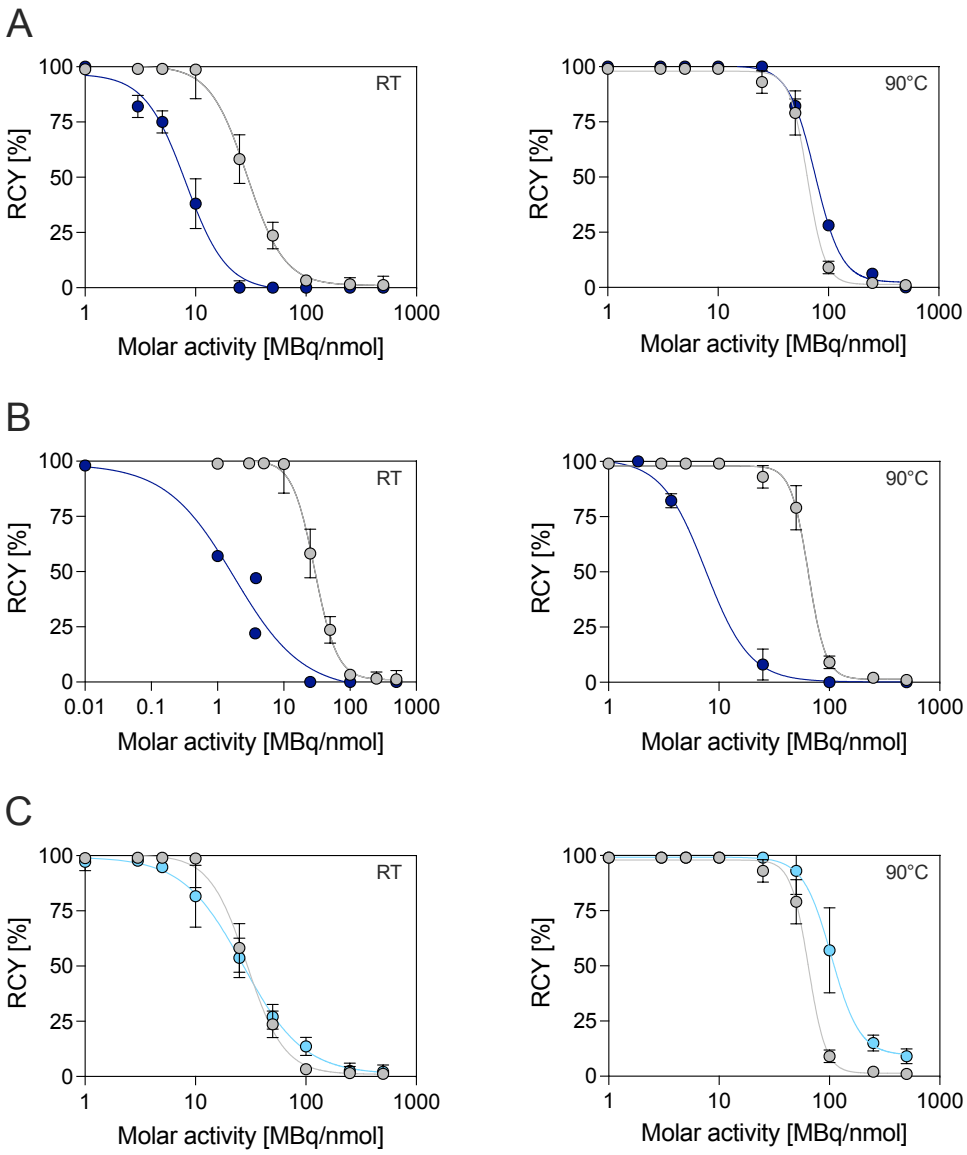

Figure 4.40. Radiochemical yield (RCY%) for [^{64}Cu]Cu^{2+} radiolabelling at different molar activities and temperatures (RT and 90°C) for (A) DO4S, (B) DO3S and (C) DO2A2S at pH 4.5. RCY are compared with those obtained with NODAGA-RDG (grey).

The additional non-coordinating amidic arm of DO3SAm could add a degree of steric hindrance around the metal-binding site (ring N), which may partly justify the lower radiochemical yields obtained with this ligand. On the other hand, the reduced efficiency of DO4S, DO3S and DO3SAm with respect to the carboxylate-containing chelators, *i.e.* DO2A2S and NODAGA, could be rationalized considering the slower kinetics of the complexation reaction (*vide supra*) due to the non-anionic nature of the pendant arms. In fact, as shown in **Figure 4.41**, prolonged reaction times had beneficial effects on RCY with DO4S and DO3S as quantitative incorporation can be obtained after ~ 1 h and ~ 4 h thus suggesting that their labelling efficiencies at pH 4.5 are limited by kinetic barriers.

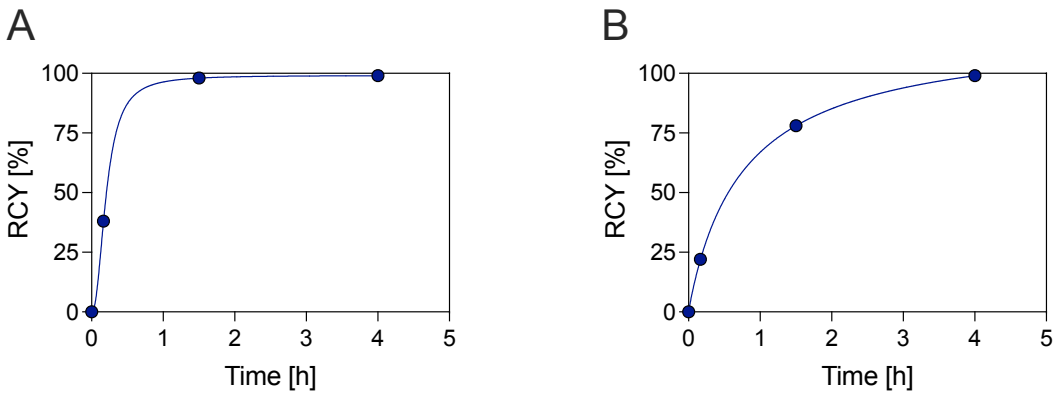

Figure 4.41. Time-dependent radiochemical yield (RCY%) for [^{64}Cu]Cu^{2+} radiolabelling at room temperature with (A) DO4S (10 MBq/nmol) and (B) DO3S (5 MBq/nmol) at pH 4.5.

Similarly, increasing the temperature to 90°C while keeping a short reaction time (10 min), drastically improved the RCY (**Figure 4.40**) with the S-containing ligands. With DO4S, quantitative radiometal incorporation was obtained with a molar activity up to 25 MBq/nmol while RCY became equal to 82 ± 3% at 50 MBq/nmol and < 30% at molar activities higher than 100 MBq/nmol. With DO3S and DO3SAm, quantitative labelling was obtained at 2 MBq/nmol (**Figure 4.40**) The effect of the temperature on the RCY was evaluated also with DO2A2S and NODAGA-RDG (**Figure 4.40**). Also with these ligands, the temperature increase is correlated with an increase of the maximum molar activity associated with a quantitative labelling, which passed from 5 MBq/nmol at room temperature to 50 MBq/nmol at 90°C for DO2A2S and from 10 MBq/nmol to 25 MBq/nmol (**Figure 4.40**) for NODAGA-RDG. With DO2A2S the RCY decreased to 57 ± 20% at 100 MBq/nmol, 15 ± 4% at 250 MBq/nmol and 9 ± 3% at 100 MBq/nmol.

The pH increases from 4.5 to 7 led to a decrease of the maximum ligand concentration to obtain quantitative labelling yields, probably due to the lower competition with the protonated species as emphasized by the previously reported thermodynamic and kinetic data (*vide supra*). At room temperature, DO2A2S gave quantitative incorporation up to 50 MBq/nmol while from 100 MBq/nmol to 500 MBq/nmol, the RCY sequentially dropped to 52 ± 8% and 9 ± 2% (**Figure 4.42**). DO4S possessed lower labelling performance also at neutral pH if compared with DO2A2S, as the maximum molar activity obtained was equal to 10 MBq/nmol. The reduction of the chelator' concentration decreased the RCY to 86 ± 14% at 25 MBq/nmol and < 2% at 100 MBq/nmol. It is worth to note that, when DO4S is compared to NODAGA-RDG (**Figure 4.42**), the same efficacy can be found as maximum molar activity obtained with NODAGA-RDG was equal to 10 MBq/nmol. DO3S and DO3SAm afforded almost quantitative labelling (> 90%) at 1 MBq/nmol.

At neutral pH, no temperature dependence of the labelling yield was found (**Figure 4.42**).

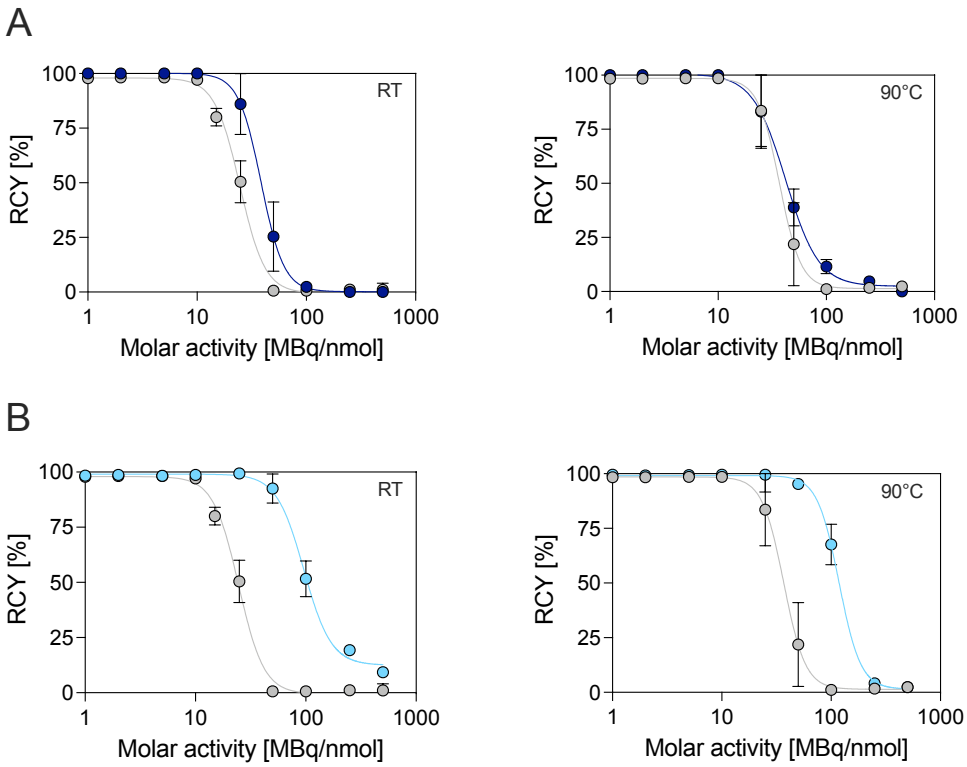

Figure 4.42. Radiochemical yield (RCY%) for [^{64}Cu]Cu^{2+} radiolabelling at different molar activities and temperatures (RT and 90°C) for (A) DO4S and (B) DO2A2S at pH 7. RCY are compared with those obtained with NODAGA-RDG (grey).

4.2.12.2 Radiolabelling with Second-Generation Ligands

Among the different labelling conditions evaluated with the first-generation series of chelators, the neutral pH media proved to be the most suitable. Consequently, the ability of the second generation chelators to complex [^{64}Cu]Cu^{2+} was tested only using this condition which also well-matches with the labelling of thermally- and pH-sensitive targeting vectors.

At room temperature, TRI4S was able to efficiently complex [^{64}Cu]Cu^{2+} with quantitative RCY in less than 10 min up to 10 MBq/nmol while, with increasing molar activities from 25 to 500 MBq/nmol, the RCY dropped from 75% to 0% (**Figure 4.43**). If compared with the cyclen analogue, *i.e.* DO4S, TRI4S demonstrated superior efficiency as a higher molar activity can be obtained (1 MBq/nmol for DO4S *vs.* 10 MBq/nmol for TRI4S). This is likely related to the fastest copper complexation occurring when the ring dimension is increased (*vide supra*).

The 14-member ring analogue of DO4S, *i.e.* TE4S, showed significantly dissimilar labelling performance. Indeed, under the same reaction conditions, TE4S always gave poor RCY (**Figure 4.43**), with only ~ 40% RCYs achieved using the highest chelate concentration assessed. These results suggest a better radiolabelling capacity of TRI4S over TE4S, which could be partially justified by the stronger thermodynamic stability of its Cu^{2+} complex.

In an attempt to force the [^{64}Cu]Cu^{2+} complexation with TE4S, heating was applied resulting in an increased RCY (*e.g.*, from 24% at RT to 74% at 70°C at 25 MBq/nmol) but accompanied with the formation of multiples species which are likely labelling-side-products. The inability of TE4S to quantitatively complex [^{64}Cu]Cu^{2+} under any tested conditions precluded any further evaluation.

4.2.13 Competition Assays

A direct comparison of the labelling efficiency of the investigated chelators was done adding to [^{64}Cu]Cu^{2+} a 1 : 1 mixture containing all the ligands at room temperature. As it is important to observe which complex is formed first ('kinetic product') and whether changes can be detected over time ('thermodynamic product'), the reaction mixture was analyzed at different time point. Representative radio-HPLC chromatograms are shown in **Figure C18** (**Appendix C**). As depicted in **Figure 4.44**, at room temperature DO2A2S confirmed to be the most efficient ligand among the series: the better radiolabelling capacity of the hybrid carboxylate-sulfide derivative, over the pure sulfide analogues, is explained by the synergy between the stronger thermodynamic stability and the faster formation kinetic of its cupric complex. Additional competitive assays were executed using DOTA as a challenging agent as well as metal cations that could outcompete [^{64}Cu]Cu^{2+} for the ligand binding (**Figure C19** - **C20** - **Appendix C**). While at pH 4.5, DOTA was demonstrated to be the most efficient ligand as [^{64}Cu][Cu(DOTA)]$^{2-}$ was the prevalent complexes formed, at neutral pH the sulfur-containing ligands predominated (**Figure 4.44**). This pH-dependent behaviour could be rationalized considering the interplay between the kinetic and thermodynamic factors that drive Cu^{2+} complexes' formation: while at lower pH the low reactivity of the sulfur bearing ligands became the predominant factor, at neutral pH, where the complex formation should occur with comparable rate with respect to DOTA, the higher thermodynamic stability of the first-generation macrocycles should lead to the formation of their complexes.

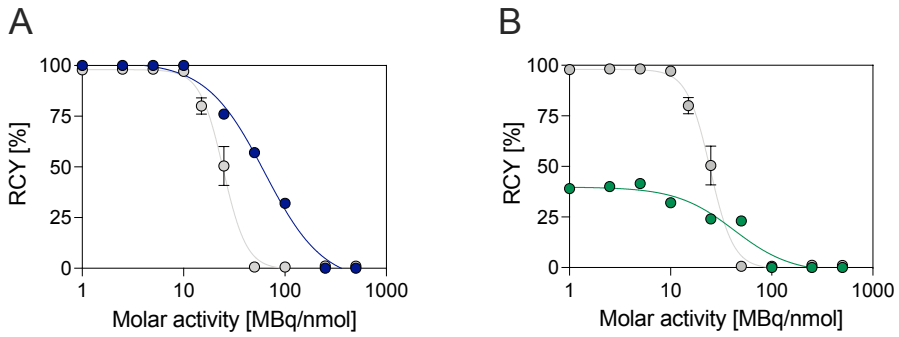

Figure 4.43. Radiochemical yield (RCY%) for [^{64}Cu]Cu^{2+} radiolabelling at different molar activities for (A) TRI4S and (B) TE4S at pH 7 and room temperature. RCY are compared with those obtained with NODAGA-RDG (grey).

The same results were obtained using TRI4S. Furthermore, in metal competition experiments an almost complete [^{64}Cu]Cu^{2+} incorporation was obtained when the pure sulfur-containing ligands were mixed in the presence of a 2-fold molar excess of Zn^{2+} or Ni^{2+} with respect to the chelator (**Table 4.9**).[§§§] These results demonstrated the outstanding selectivity of these ligands for Cu^{2+} relative to other divalent cations, likely related to the harder character of Zn^{2+} and Ni^{2+} which prevent the formation of stable coordination bonds with the borderline/soft donors incorporated in the macrocycles.

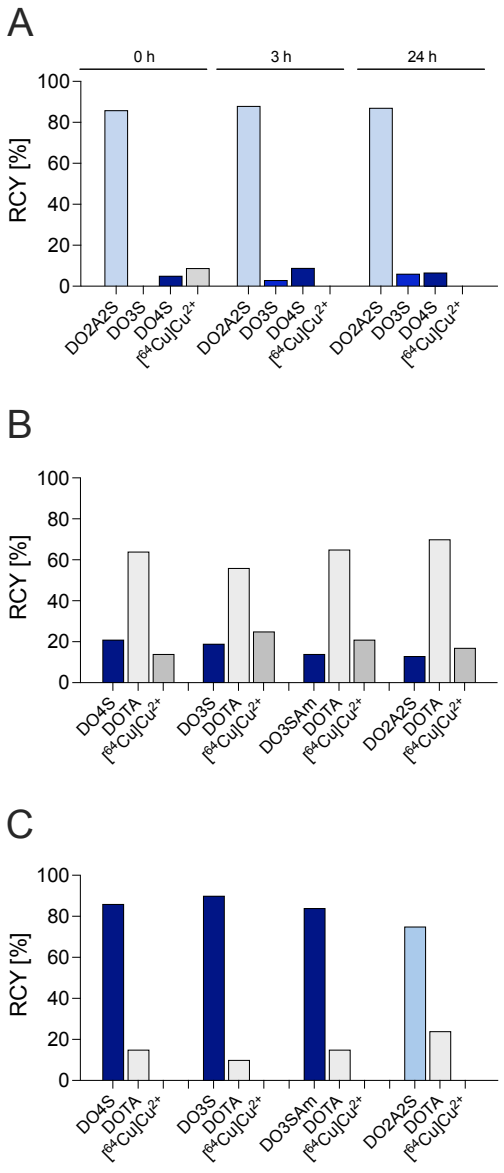

Figure 4.44. (A) Challenge among the chelators (1:1 chelator-to-chelator molar ratio, pH 4.5, RT, 0.5 MBq/nmol) and challenge with DOTA (1:1 chelator-to-DOTA molar ratio, RT, 0.5 MBq/nmol) at (B) pH 4.5 and (C) pH 7.

[§§§] These metal ions were chosen as they are common metallic impurities in radiocopper solutions. Zn^{2+} also represents a biologically relevant cation.[52]

Contrarily, DO2A2S was more affected by the highly challenging environment (**Table 4.9**). Probably the presence of hard carboxylic groups favored the interaction with these competitive hard cations.

4.2.14 Stability Assays

As the kinetic inertness plays a crucial role in metal-based radiopharmaceuticals,[2,27,59] stability assays are an useful tool for predicting the *in vivo* integrity of radiometallic complexes. Consequently, the stability of the [^{64}Cu]Cu^{2+}-complexes was assessed *in vitro* by incubating the preformed [^{64}Cu]Cu^{2+}-complexes in different media.

The [^{64}Cu]Cu^{2+}-labelled complexes were initially subjected to a stability experiment to determine their susceptibility to transchelation using DOTA as challenging chelate. Representative radio-HPLC chromatograms of the DOTA stability assays are presented in **Figure C21** (**Appendix C**). As shown in **Table 4.9**, under these conditions, the complexes demonstrate a remarkable resistance to transchelation, remaining > 80% over 24 h. An exception to this behaviour is represented by DO3SAm as a considerable decrease in complex stability was observed with this ligand. This may suggest that the functionalization of the secondary nitrogen atoms with a non-coordinating arm is negatively affecting the coordination sphere of the metal ion either due to steric bulk or electronic changes from secondary to tertiary amines.

Due to the high level of circulating biomolecules containing thiol groups in human plasma, *e.g.* cysteine and glutathione[60] , any radiometal-chelate complex must be able to withstand transchelation to such proteins in order to successfully deliver the radiotracer to the desired molecular target. Thus, the [^{64}Cu]Cu^{2+}-complexes were incubated with an excess of cysteine at 37°C. The results as shown in **Table 4.9**. All the complexes shown high stability as they remained > 80% intact after 24 h.

Table 4.9. Labelling efficiency in presence of a 2-fold molar excess of Ni^{2+} or Zn^{2+} (2 : 1 metal-to-ligand molar ratio), time-dependent [^{64}Cu]Cu^{2+}-complexes stability in PBS (1: 1 *v*/*v* dilution), in presence of cysteine (1000: 1 Cys-to-ligand molar ratio) and in presence of DOTA (1000: 1 DOTA-to-ligand molar ratio).

Complex	Zn^{2+}	Ni^{2+}	PBS			Cysteine			DOTA		
			0 h	3 h	24 h	0 h	3 h	24 h	0 h	7 h	24 h
[^{64}Cu][Cu(DO4S)]$^{2+}$	100	100	100	100	100	100	100	83	100	92	88
[^{64}Cu][Cu(DO3S)]$^{2+}$	95	91	100	100	100	100	100	100	100	100	100
[^{64}Cu][Cu(DO3SAm)]$^{2+}$	90	99	100	100	100	100	83	72	100	80	38
[^{64}Cu][Cu(DO2A2S)]	64	73	100	100	100	100	85	74	91	90	87
[^{64}Cu][Cu(TRI4S)]$^{2+}$	100	100	100	100	100	–	–	–	–	–	–

Subsequent stability assays performed on the [^{64}Cu]Cu^{2+} complexes, obtained at a specific activity of 25 MBq/nmol and diluted in PBS without radioprotectants addition, demonstrated that they are not stable in these conditions (**Figure 4.45**) (due to the inability of DO3S, DO3SAm and TE4S to reach high molar activities, these experiments were not undertaken with these ligands). In particular, [^{64}Cu][Cu(DO2A2S)] proved to be the most sensitive complex as only 25% remains intact after 24 h of incubation at room temperature. This was attributed to radiolysis phenomena, which cause degradation over time.

To probe that the degradation of the radiometal complexes was related to the activity, the [^{64}Cu]Cu^{2+} complexes, were preprepared at a lower molar activity (0.1 MBq/nmol, 1 MBq). Under these conditions, all the complexes were stable over 24 h in PBS (**Table 4.9**, **Figure C22** - **Appendix C**). In an attempt to mitigate the radiation-induced degradation, radiolysis quenchers, *i.e.* ethanol and ascorbic acid, were added to the incubation solution.

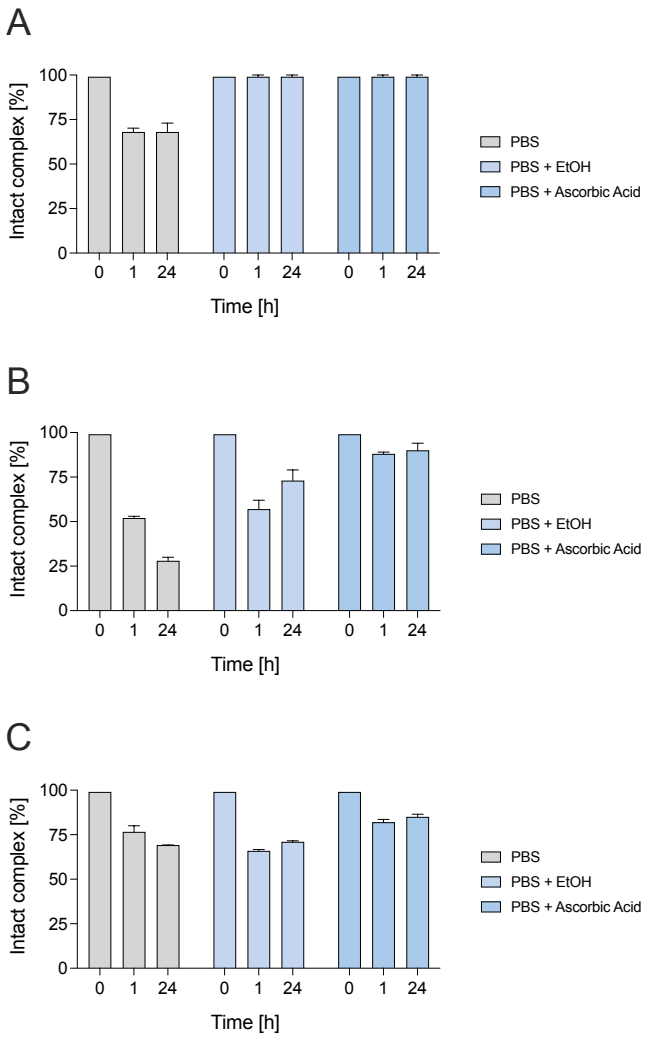

Figure 4.45. Stability of (A) [^{64}Cu][Cu(DO4S)]$^{2+}$, (B) [^{64}Cu][Cu(DO2A2S)] and (C) [^{64}Cu][Cu(DOTA)]$^{2-}$ in PBS with and without the additions of radioprotectants.

The addition of radioprotectant to PBS led to an improvement of the complexes' stability over time. While for $[^{64}Cu][Cu(DO4S)]^{2+}$ no differences in the complex' stability dependent on the radioprotectant were found, for the carboxylate containing ligand, *i.e.* DO2A2S, the highest improvement on the complexes' stability was obtained using ascorbic acid (**Figure 4.45**). The same behaviour was obtained with DOTA.

4.2.15 Human Plasma Stability

Endogenous metal-binding proteins (*e.g.*, superoxide dismutase, metallothionein, ceruloplasmin) can compete with the BFC and displace chelator-bound ^{64}Cu *in vivo*, preventing its successful delivery to the desired target.[22] To gain insight into the stability and inertness of the $[^{64}Cu]Cu^{2+}$ complexes in a biologically relevant environment, human plasma stability assays were performed incubating the radiolabelled complex in human plasma at 37°C. Owing to the poor radiolabelling capacity of DO3S, DO3SAm and TE4S, plasma stability studies were not undertaken with these chelators.

As shown in **Figure 4.46**, $[^{64}Cu][Cu(DO2A2S)]$ was found to be stable over 24 h (> 95% intact complex). In contrast, after 2 hours in human plasma, only ~ 30% and < 5% of the original radioactivity associated with DO4S and TRI4S remained chelated to them. In comparison, NODAGA-RDG exhibited a roughly comparable *in vitro* stability with respect to DO2A2S whilst DOTA showed slightly poorer overall stability. No differences in the % of the intact complex were observed with or without protein precipitation.

The *in vitro* stability of the radioactive cupric complexes was also assessed using an independent method to quantify the activity bound to the human plasma proteins. The results are shown in **Figure 4.47**. $[^{64}Cu][Cu(DOTA)]^{2-}$ confirmed to be overall stable in human plasma as low % of free $[^{64}Cu]Cu^{2+}$ demonstrated to be bound to human plasma protein.

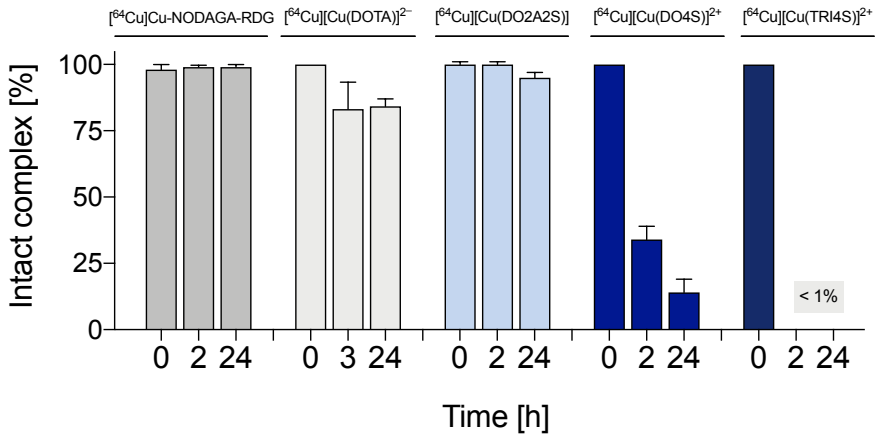

Figure 4.46. Human plasma stability assay for $[^{64}Cu][Cu(DO4S)]^{2+}$, $[^{64}Cu][Cu(DO2A2S)]$, $[^{64}Cu][Cu(TRI4S)]^{2+}$ and comparison with $[^{64}Cu]$-Cu-NODAGA-RDG and $[^{64}Cu][Cu(DOTA)]^{2-}$ (n = 3).

No binding to the filter device for the $[^{64}Cu][Cu(DOTA)]^{2-}$ complex was detected. For $[^{64}Cu][Cu(DO2A2S)]$, ~ 20% and ~ 49% of the activity was bound to the plasma proteins after 20 minutes and 20 hours of incubation, respectively. However, the 'control', *i.e.* $[^{64}Cu][Cu(DO2A2S)$ incubated in PBS, demonstrated 17 ± 0.8% of non-specific binding to the filter device after 20 min. Consequently, the observed instability drop is likely related to this non-specific absorption phenomenon of the intact complex. As for $[^{64}Cu][Cu(DO4S)]^{2+}$, almost all the activity was found to be bound to the plasma proteins likely as a consequence of both the instability of the complexes evidenced with the previous assay as well as to the non-specific binding of the intact complex to the filter device, as also in this case the 'control' demonstrated 19 ± 0.1% of activity bound to it after 20 minutes of incubation.

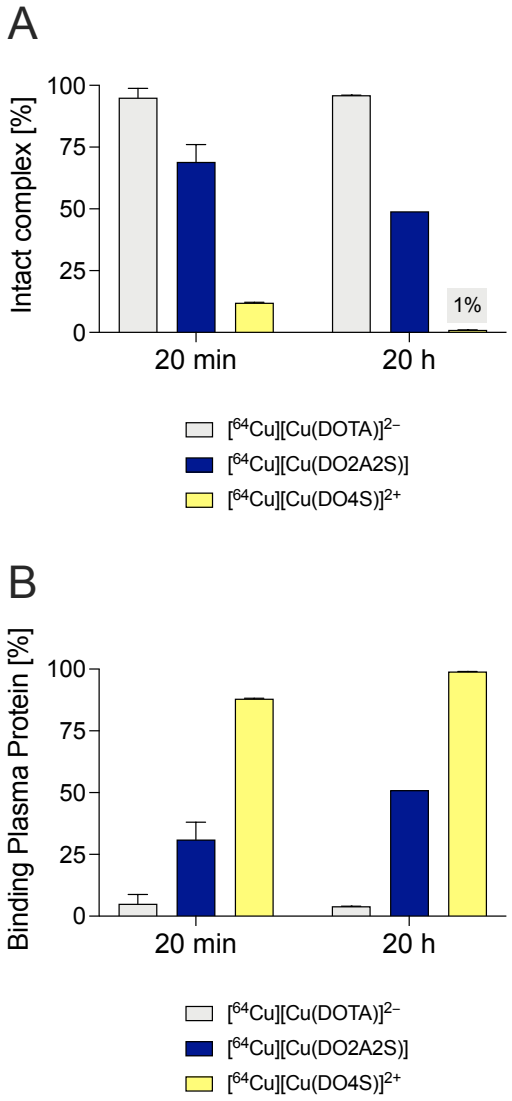

Figure 4.47. (A) Percentage of intact complex and (B) binding to plasma protein for $[^{64}Cu][Cu(DO4S)]^{2+}$ and $[^{64}Cu][Cu(DO2A2S)]$ and comparison with $[^{64}Cu][Cu(DOTA)]^{2-}$ (n = 2).

4.3 Experimental section

4.3.1 Materials and Methods

All chemicals were purchased from commercial suppliers (Sigma Aldrich, Fluka, VWR Chemicals) and were used as received. First- and second-generation ligands were synthesized according to procedures reported in **Chapter 2**. DOTA was obtained from Chematech. NODAGA-RGD (NODAGA-RGD trifluoroacetate) was obtained from ABX GmbH. All solutions were prepared in ultrapure water (18.2 MΩ/cm).

4.3.2 Complexation Kinetics

The kinetics of the reactions between Cu^{2+} and the ligands were investigated using UV-Vis spectroscopy following the increasing intensity of the charge transfer and/or the *d-d* bands of the complexes at the characteristic wavelengths (**Table C3** - **Appendix C**). The electronic spectra were recorded on a Cary 60 UV-Vis spectrophotometer (Agilent) in the range from 200 to 800 nm using a quartz spectrophotometric cell of 1 cm path lengths at room temperature. Equimolar amounts of Cu^{2+} and the corresponding ligand were mixed in buffered aqueous solutions at pH 2.0 ($1.0 \cdot 10^{-2}$ M HCl), 3.0 ($1.0 \cdot 10^{-3}$ M HCl), 4.8 (acetic/acetate), and 7.0 (2-[4-(2-hydroxyethyl)piperazin-1-yl]ethanesulfonic acid - HEPES). Concentrations ranged from $1.0 \cdot 10^{-4}$ M to $1.0 \cdot 10^{-3}$ M. The UV-Vis spectra were collected immediately after the mixing and at different time points.

4.3.3 Thermodynamic Measurements

1 M and 0.1 M hydrochloric acid (HCl, Sigma Aldrich, 37%) and carbonate-free 0.1 M sodium hydroxide (NaOH, Fluka, 99% min) solutions were prepared. The former was standardized against sodium carbonate (Na_2CO_3, Aldrich, 99.95-100.5%) while the latter against 0.1 M HCl. Ligand stock solutions were prepared at ~ $2.0 \cdot 10^{-3}$ M while the Cu^{2+} stock solutions were prepared at ~ $2.0 \cdot 10^{-2}$ M from analytical grade chloride salt ($CuCl_2 \cdot 2H_2O$, Sigma Aldrich, 99.9%) by dissolution of weighted compounds in a calibrated volumetric flask. All stock solutions were stored at 4°C. The ionic strength (I) was fixed to 0.15 M with sodium chloride (NaCl, Fluka, 99%) unless otherwise stated. Each experiment was performed independently at least five times.

Potentiometric Titrations. The potentiometric measurements were carried out as reported in **Chapter 3**. For the first-generation ligands and TRI4S the starting pH was brought to ~ 4 to take into account the slow complexation kinetics.

UV-Vis Titrations. UV-Vis pH-spectrophotometric titrations were carried out by the out-of-cell and in cell methods in the pH range 0-3 (first-generation ligands) and 0-4 (second generation ligands) and from pH ≥ 3 (first-generation ligands) and pH ≥ 4 (second-generation ligands), respectively, at room temperature. In the first method, stock solutions of the ligands and $CuCl_2$ were mixed in independent vials to obtain a 1:1 metal to ligand molar ratio (final concentrations ~ 10^{-4} M), and different amounts of 1 M HCl were added to adjust the pH. The vials were sealed, heated to 80°C in a thermostated bath to ensure complete complexation of Cu^{2+}, and then cooled to room temperature and opened. The absorption spectra were recorded using the same spectrometer of the kinetic measurements. The equilibrium was considered to be reached when no variations of the UV-Vis spectra were detected.

Direct titrations were carried out in a 3 mL water-jacked glass cell maintained at 25.0 ± 0.1°C using a Haake F3 cryostat. The removal of the atmospheric CO_2 prior and during the titration was ensured by a constant flow of purified nitrogen. The ligand concentration in the titration cell varied in the range $5 \cdot 10^{-5}$ - $2 \cdot 10^{-4}$ M and the metal-to-ligand ratios were between 1:1 and 1:2. The solutions were acidified with a known volume of HCl, and the titrations were carried out by accurate NaOH additions (~ µL). The pH was measured with a Mettler Toledo pH-meter equipped with a glass electrode daily calibrated with commercial buffer solutions (pH 4.0, pH 7.0 and pH 9.0), except in very acidic solutions (pH < 2) where it was computed from HCl concentration (pH = $-\log C_{HCl}$). After each addition, the pH was allowed to equilibrate, a sample aliquot was transferred to the spectrophotometric cell, and the spectrum was recorded. The aliquot was transferred back to the titration vessel, and new additions were made up to pH around 12.

Complexes Stoichiometry. UV-Vis spectrophotometric titrations were performed by adding known volumes of a Cu^{2+} solution to the chelator one (~ $1 \cdot 10^{-4}$ M), buffered at pH 4.8 by acetic/acetate (first-generation ligands) or at pH 7.5 by HEPES buffer (second-generation ligands). Metal-to-ligand ratios ranged between 0 and 3. After Cu^{2+} additions, the UV-Vis spectra were recorded, and the stoichiometry was determined by plotting the absorbance at the characteristic wavelength as a function of the metal-to-ligand ratios.

Competitive Titrations. Titrations with Ag^+ as a competitor were performed using UV-Vis spectroscopy at pH 4.8 (acetic/acetate buffer) without control of the ionic strength. Batch titration points were prepared adding varying amounts of Cu^{2+} to a solution containing the preformed Ag^+ complex ($C_{Ag^+} = C_L$ ~ $1 \cdot 10^{-4}$ M). Different metal-to-metal ratios, between 0 and 4, were attained. Due to the slow kinetics of the transmetallation reactions at room temperature, solutions were brought to equilibrium through heating at ~ 55°C before the

UV-Vis spectra measurements. The equilibrium was considered to be reached when the UV-Vis spectra did not change.

Data treatment. The overall equilibrium constants were obtained by refinement of the thermodynamic data using the PITMAP software as described in **Chapter 3**. The errors quoted are the standard deviations calculated by the fitting program. The constants for ligand protonation and, in the case of the competition-titrations, also of the Ag^+ complexes, were taken from **Chapter 2** and **Chapter 3**, respectively, while the formation constants of the Cu^{2+} hydroxo-species were taken from the literature.[41,61,62]

4.3.4 EPR Measurements

All EPR spectra were recorded using a Bruker EleXsys E500 spectrometer (microwave frequency 9.54 GHz, microwave power 13 mW, modulation amplitude 5 G, modulation frequency 100 kHz). The pH-dependent EPR spectra were recorded in a freshly prepared solution containing 1.1 - $1.3 \cdot 10^{-3}$ M DO4S, DO3S and DO2A2S and $1.0 \cdot 10^{-3}$ M $CuCl_2$. The Cu^{2+}-TE4S sample was prepared the day before the measurement and stirred overnight at room temperature to take into account the slow kinetics of complex formation. Variable-pH EPR spectra were measured in the pH range 1.8-12. NaOH or HCl were employed to adjust the pH. The ionic strength was fixed using 0.15 M NaCl.

Room temperature EPR spectra were collected in capillaries recording 12 scans. For the frozen solution spectra, 0.2 mL samples were diluted with 0.05 mL of methanol to avoid crystallization of water and transferred into EPR tubes. Anisotropic EPR spectra were recorded in Dewar containing liquid nitrogen at 77 K. The room temperature spectra were corrected by subtracting the background spectrum of pure water. The spectra were simulated by the 'EPR program' using the parameters g_o, A_o copper hyperfine (I_{Cu} = 3/2) coupling and four linewidth parameters.[63] The anisotropic EPR spectra were analyzed with the same program. Rhombic or axial *g*-tensor (g_x, g_y, g_z) and copper hyperfine tensor (A_x^{Cu}, A_y^{Cu}, A_z^{Cu}) have been used. Orientation dependent parameters (α, β and γ) were used to fit the linewidths through the equation $\sigma_{MI} = \alpha + \beta M_i + \gamma M_i^2$, where M_i denotes the magnetic quantum number of the copper nucleus. Since natural Cu^{2+} was used for the measurements, the spectra were calculated as the sum of the spectra of ^{63}Cu and ^{65}Cu weighted by their natural abundances (69.17% and 30.83%, respectively). The hyperfine and super hyperfine coupling constants and the relaxation parameters were obtained in field units (Gauss = 10^{-4} T).

4.3.5 X-ray Crystal Structure

Blue crystals of [Cu(DO4S)(NO_3)]·NO_3 and [Cu(DO2A2S)] suitable for X-ray diffraction were obtained in solutions containing equimolar amounts of metal and ligand. For DO4S slow evaporation of a methanol solution was performed, whereas for DO2A2S crystals arose in water at pH ~ 7 set with NaOH. X-ray measurements were made at room temperature on a Nicolet P3 (for Cu^{2+}-DO4S) and on Rigaku RAXIS-RAPID II diffractometer (for Cu^{2+}-DO2A2S) using numerical absorption correction with graphite monochromated Mo-K_α radiation.[64] The structures were solved with direct method, missing atoms were determined by difference-Fourier techniques and refined according to the least-squares method against F^2. For Cu^{2+}-DO4S, disordered side chains of molecules have been refined isotropically into two conformations, and all non-hydrogen atoms were refined anisotropically. In general, C-bound H atoms were geometrically located and refined as riding. The isotropic displacement parameters of the hydrogen atoms were approximated from the *U*(eq) value of the atom they were bonded to. For Cu^{2+}-DO4S the Shelx 93 crystallographic software package was used[65], and details about data collection and structure refinement are given in **Table C6** (**Appendix C**). For Cu^{2+}-DO2A2S the software CrystalClear was used.[66] Sir2014[67] and SHELX[68] program package under WinGX[69] software were used to solve the structure and for its refinement. The data collection and refinement parameters are listed in **Table C9** (**Appendix C**). Selected bond lengths and angles of Cu^{2+}-DO2A2S were calculated by PLATON software.[70] The graphical representation and the edition of CIF files were done by Mercury[71] and EnCifer[72] software. The structures were deposited with CCDC number 2036253 for [Cu(DO4S)(NO_3)]·NO_3 and 2078038 for [Cu(DO2A2S)].

4.3.6 Acid-Mediated Decomplexation Kinetics

Acid-mediated decomplexation studies of the Cu^{2+} complexes were performed at room temperature under pseudo-first-order conditions without control of the ionic strength by addition of concentrated HCl (0.01 to 1 M) to aqueous solution of the preformed complexes. The concentration of the Cu^{2+} complexes after the H^+ addition was $1 \cdot 10^{-4}$ M. The reactions were monitored by UV-Vis spectroscopy following the decrease in intensity of the CT transitions of the Cu^{2+} complexes at the characteristic wavelength (**Table C3** - **Appendix C**) at specific time points. The same apparatus described for the formation kinetic measurements was used. The ${}^{d}k_{obs}$ values were calculated from the experimental data using the equation $\ln A_t = \ln A_0 - {}^{d}k_{obs} \cdot t$ where A_t and A_0 are the absorbances at time t and at the beginning of the reaction and ${}^{d}k_{obs}$ is the observed dissociation rate constant. The corresponding half-life were obtained from the equation $t_{1/2} = \ln(2)/{}^{d}k_{obs}$. Each measurement was repeated in triplicate.

4.3.7 Cyclic Voltammetry

Cyclic voltammetry was carried out in a 6-neck cell equipped with three electrodes and connected to an Autolab PGSTAT 302N potentiostat, interfaced with NOVA 2.1 software (Metrohm) at room temperature. The CV experiments were performed using a glassy carbon working electrode (WE) fabricated from a 3 mm diameter rod (Tokai GC-20). The counter electrode (CE) was a platinum wire, and the reference electrode was a saturated calomel electrode (SCE). Before each experiment, the electrode surface was cleaned by polishing with a 0.25 µm diamond paste, followed by ultrasonic rinsing in ethanol for 5 min. All electrochemical experiments were performed in ~ $1 \cdot 10^{-3}$ M aqueous solution of preformed Cu^{2+} complexes. The pH of the solutions was adjusted with NaOH and/or HNO_3 solutions. $NaNO_3$ was used as supporting electrolyte at a 0.15 M concentration without purification. The sample solutions were degassed by bubbling Ar before all measurements and kept under an Ar stream during the measurements. Cyclic voltammograms with scan rates ranging from 0.005 to 0.2 V/s were recorded in the region from –0.5 to 0.5 V. In this potential range, the solvent with the supporting electrolyte and the free ligands were found to be electro-inactive.

4.3.8 Electrolysis and NMR

Exhaustive electrolyses of the pre-formed Cu^{2+} complexes (~ $1 \cdot 10^{-3}$ M) were carried out using a large area glassy carbon WE in a two-compartment cell. The CE was a Pt wire separated from the working solution through a glass double frit (G3) filled with a conductive solution ($NaNO_3$ 0.15 M) and the reference electrode was SCE. The electrolyses were performed at E = −0.35 V for Cu-DO4S, E = −0.75 V for Cu-DO2A2S, E = −0.45 V for Cu-TRI4S and E = −0.40 V for Cu-TE4S. Linear scan voltammetry (LSV) was used to monitor the evolution of the species in solution. Each electrolysis was considered complete when the cathodic current reached < 2% of the initial value.

^{1}H-NMR spectra of the *in situ* generated Cu^+ complexes were recorded on a 400 MHz Bruker Avance III HD spectrometer as described in **Chapter 3**.

4.3.9 Density Functional Theory Calculations

All DFT calculations were performed with the Amsterdam Density Functional (ADF) program.[73–75] The OPBE[76–78] general gradient approximation (GGA) density functional was used, in combination with two basis sets: geometry optimizations and frequency analysis have been carried out with the TZP (triple-ζ quality augmented with one set of polarization functions on each atom), whereas the final energy evaluation has been done with the TZ2P (triple-ζ quality and is augmented with two sets of polarization functions on each atom). Scalar relativistic effects were accounted for using the zeroth-order regular approximation

(ZORA).[79] This level of theory is denoted in the text as ZORA-OPBE/TZ2P//ZORA-OPBE/TZP. All the calculations were performed in gas-phase and water; for the latter case, the solvation effects have been quantified using the COSMO (COnductor-like Screening MOdel) approach (level of theory: COSMO-ZORA-OPBE/TZ2P//ZORA-OPBE/TZP).[80–83] A radius of 1.93 Å and a relative dielectric constant of 78.39 were used. The empirical parameter in the COSMO equation was considered to be 0.0. The radii of the atoms are the classical MM3 radii divided by 1.2. Equilibrium geometries were optimized under no symmetry constraint using analytical gradient techniques. All structures were verified by frequency calculations: for all energy minima, only real frequencies associated with the vibrational normal modes were found.

The activation strain model (ASM) has been used to understand the nature of the metal-ligand chemical bonding. It is a fragment-based approach to understanding chemical reactions and the associated barriers.[84] The starting point is the two separate reactants, which approach from infinity and begin to interact and deform each other. In this model, the energy ΔE is decomposed into the strain energy ΔE_{strain} and the interaction energy ΔE_{int} (eq. 1):

$$\Delta E = \Delta E_{strain} + \Delta E_{int} \quad (1)$$

ΔE_{strain} is the energy associated with the deformation of the reactants from their relaxed geometries into the structure they acquire in the product. ΔE_{int} is the actual interaction energy between the deformed fragments/reactants. This latter can be further analyzed in the framework of the Kohn-Sham Molecular Orbital (KS-MO) model using a quantitative decomposition of the bond into purely electrostatic interaction (ΔV_{elstat}), Pauli repulsion (ΔE_{Pauli}, called also exchange repulsion or overlap repulsion), and (attractive) orbital interactions (ΔE_{oi}) (eq. 2).

$$\Delta E_{int} = \Delta V_{elstat} + \Delta E_{Pauli} + \Delta E_{oi} \quad (2)$$

4.3.10 Copper-64 Radiolabelling, Competitions and *In Vitro* Stability Assays

Caution! ^{64}Cu is a radionuclide that emits ionizing radiation, and it was manipulated in specifically designed facilities under appropriate safety controls.

^{64}Cu Production. Copper-64 chloride ([^{64}Cu]$CuCl_2$) was provided by Advanced Center Oncology Macerata - ACOM (Italy) in 0.5 M HCl or produced at Paul Scherrer Institute (PSI, Switzerland) by irradiation of enriched nichel-64 targets with protons degraded to

approximately 11 MeV at PSI's Inject 2 72 MeV research cyclotron (^{64}Ni(p,n)^{64}Cu reaction) and purified with an automated system according to a previously published protocol.[85] After the separation process, the eluted [^{64}Cu]Cu^{2+} was picked up in 0.05 M HCl.

^{64}Cu Radiolabelling. The chelators DO4S, DO3S, DO3SAm, DO2A2S, TRI4S, TE4S, DOTA and NODAGA-RDG were made up as stock solution (~ 10^{-3} M) in ultrapure water. A serial dilution was used to prepare solutions with ligand concentrations ranging from $1.0 \cdot 10^{-4}$ to $1.0 \cdot 10^{-8}$ M in ultrapure water. Ligand solutions were freshly prepared from stock solutions before each experiment.

Radiolabelling experiments were performed by reacting [^{64}Cu]$CuCl_2$ in 0.05 M hydrochloric acid (~ 2.5 MBq, ~ 2 µL) to an aliquot of a ligand solution (20 µL) of appropriate concentration diluted with a mixture consisting of 0.05 M HCl and 0.5 M sodium acetate in a 5:1 *v*/*v* ratio (~ 98 µL and ~ 20 µL, respectively) to obtain a solution at pH 4.5. Alternatively, sodium phosphate buffer (~ 100 µL) was used (pH 7). The reaction mixtures were agitated briefly and then allowed to react for 10 min at different temperatures (room temperature or 90°C).

The reaction progress was monitored by ultra-high-performance liquid chromatography (UHPLC) or radio thin layer chromatography (TLC). UHPLC was conducted using an Acquity system (Waters, Italy) equipped with a reversed-phase C18 column (1.7 µm, 2.1 mm x 150 mm), an Acquity TUV detector (Waters, Italy) and a Herm LB 500 radiochemical detector (Berthold Technologies, Italy). The mobile phase consisted of 0.1% trifluoroacetic acid (TFA) in water (A) and CH_3CN (B). The elution gradient applied to the UHPLC system includes 3 stages: for the first 2 min, A was kept constant to 5% then from min 2 to min 7, a gradient of 5 to 25% of A was reached and then the initial condition was restored in 2 min. A flow rate of 0.35 mL/min was used. Under these conditions the free [^{64}Cu]Cu^{2+} has a retention time (t_R) equal to ~ 1 min while the [^{64}Cu]Cu^{2+} complexes were retained at t_R = 6.9 min for [^{64}Cu][Cu(DO4S)]$^{2+}$, t_R = 5.8 min for [^{64}Cu][Cu(DO3S)]$^{2+}$, t_R = 6.8 min for [^{64}Cu][Cu(DO3SAm)]$^{2+}$, t_R = 4.0 min for [^{64}Cu][Cu(DO2A2S)], t_R = 6.8 min for [^{64}Cu][Cu(TRI4S)]$^{2+}$ and t_R = 6.7 min for [^{64}Cu][Cu(TE4S)]$^{2+}$. The identity of the radioactive [^{64}Cu]Cu^{2+} complexes was confirmed by the matching of their radio-UHPLC elution profile to the UV-UHPLC chromatogram of the corresponding non-radioactive metal complexes. Their identical retention time demonstrated that the [^{64}Cu]Cu^{2+} species possess the same structure as the previously characterized non-radioactive species.

TLC was carried out using different stationary and mobile phase depending on the ligand. For [^{64}Cu][Cu(DO2A2S)], [^{64}Cu][Cu(DOTA)]$^{2-}$ and [^{64}Cu]-Cu-NODAGA-RDG, TLC silica gel 60 F_{254} plates were used as stationary phase, developed using a mixture of 10% ammonium acetate and methanol (ratio 1:1 *v*/*v*, pH 5.5). Under these conditions the free [^{64}Cu]Cu^{2+} has a retention factor R_f = 0 while the ^{64}Cu complexes migrate with the liquid phase.

For $[^{64}Cu][Cu(DO4S)]^{2+}$, $[^{64}Cu][Cu(TRI4S)]^{2+}$ and $[^{64}Cu][Cu(TE4S)]^{2+}$, RP-silica gel plates were employed as stationary phase and sodium citrate (1 M, pH 4) as eluent. Under these conditions, free $[^{64}Cu]Cu^{2+}$ migrates with the solvent front (R_f = 1) while $[^{64}Cu]Cu^{2+}$-complexes remain at the baseline (R_f = 0). TLC plates were analyzed using a Cyclone Plus Storage Phosphor System (Perkin Elmer) interfaced with the OptiQuant software (version 5.0, Perkin Elmer Inc., USA).

Competition Assays. Competition assay among the chelator was carried out by mixing a 1:1 chelator-to-chelator molar ratio solution with $[^{64}Cu]Cu^{2+}$ (0.5 MBq/nmol, pH 4.5, RT). Competitions studies with DOTA were performed by labelling the ligands (0.5 MBq/nmol, pH 4.5, RT, 10 min) in the presence of a 1:1 DOTA-to-ligand molar ratio. Metal competition studies were performed using the same protocol using a 2:1 metal-to-ligand molar excess of Ni^{2+} or of Zn^{2+}. At different time-point the reaction mixture was analyzed by UHPLC, using the protocol described above.

Cysteine and DOTA stability. The stability of the pre-formed $[^{64}Cu]Cu^{2+}$ complexes in presence of challenging agents was assessed by adding a 1000:1 competitor-to-ligand molar ratio excess of cysteine or DOTA, respectively. With cysteine, the samples were incubated at 37°C to simulate the biological environment. At selected time points, aliquots were taken from the reaction mixtures and analyzed by UHPLC to evaluate the complex integrity.

PBS Stability. The stability of the $[^{64}Cu]Cu^{2+}$ complexes was investigated in phosphate-buffered saline (PBS, pH 7.4) and in presence of radioprotectant (ethanol or ascorbic acid). Both lower molar activity (0.1 MBq/nmol, 1 MBq) and higher molar activity (25 MBq/nmol, 50 MBq) were employed to assess the effect of radiolysis. The stability of $[^{64}Cu][Cu(DO3S)]^{2+}$ and $[^{64}Cu][Cu(DO3SAm)]^{2+}$ was not tested at high molar activities due to the inability of these ligands of label $[^{64}Cu]Cu^{2+}$ under these conditions. Aliquots of each labelled solution were diluted 1:1 *v*/*v* in PBS (pH 7.4), PBS + ethanol (10% *v*/*v*) or PBS + ascorbic acid (10% *v*/*v*). Samples stabilities were investigated at different time points after preparation using the TLC or UHPLC system previously validated.

Human Plasma Stability. *In vitro* human plasma stability assay was performed by incubating the pre-formed $[^{64}Cu]Cu^{2+}$-complexes with human plasma (1:5 *v*/*v* dilution, *i.e.* 50 µL of each labelling solution diluted with 250 µL of human plasma) previously thawed and centrifuged (3 min, 8000 rpm, RT). The samples were vortex and incubated at 37°C. At defined time-point, 50 µL of the plasma containing the labelled complex were added to ~ 200 µL of ice-cold methanol (0.16 MBq/µL final concentration) and centrifuged for 3 min at 8000 rpm. 2 µL of supernatant were subsequently placed on a RP-silica gel TLC plate and

sodium citrate solution (1 M, pH 4) was used as mobile phase. Under these conditions, intact [^{64}Cu]Cu-ligand complexes remained at the baseline of the TLC plate (R_f = 0), while free ^{64}Cu was either bound by plasma proteins or picked up by citrate in the mobile phase and migrated along with the TLC plate (R_f ~ 1). This method was validated by incubating free [^{64}Cu]Cu^{2+} with human plasma.

Dissociation of [^{64}Cu]Cu^{2+} from [^{64}Cu]Cu^{2+} complexes was also monitored at varying time points using the same protocol with the exception that no proteins were precipitated. 2 µL of human plasma containing the labelled complex were directly spotted on a RP-silica gel TLC plate developed using the same mobile phase described above.

Filter Assays. [^{64}Cu]Cu^{2+} (50 MBq) was labelled with each chelator at a molar activity equal to 25 MBq/nmol as previously described. 25 µL of each labelling solution were diluted with 425 µL of PBS to obtain a final activity concentration equal to 0.02 MBq/µL. 25 µL of the diluted complex were added to 250 µL of human plasma previously thaw and centrifuged (RT, 3 min, 3000 rpm), vortexed and incubated at 37°C. At selected time-point, 10 µL of human plasma containing the [^{64}Cu]Cu^{2+}-complex were diluted with 990 µL of PBS ('standard'). The remaining human plasma containing the [^{64}Cu]Cu^{2+}-complex was transferred to a filter (Centrifree®, Merk, Millipore) and centrifuged at 2000 rpm for 30 min at RT. 10 µL of the filtrate were diluted with 990 µL of PBS in a Ria tube ('sample'). 'Standard' and 'sample' were measured using a gamma counter. All measurements were performed in duplicates. The same protocol was repeated using PBS instead of human plasma to evaluated the non-specific binding of the [^{64}Cu]Cu^{2+} complexes to the filter device.

4.4 Conclusions

The stabilization of coordinatively labile and redox-active copper ions in biological environments remains a challenge for the development of improved diagnostic and therapeutic strategies with [$^{64/67}$Cu]Cu^{2+}, as the *in vivo* integrity of these complexes could be thwarted by the bio-induced reduction of Cu^{2+} to Cu^{+} that may bring to demetallation processes. At this purpose, the first- and second-generation ligands bearing borderline N and soft S donors described in **Chapter 2**, were investigated hereby in attempt to stabilize both oxidation states.

The thermodynamic data indicate that the first-generation ligands possess high affinity towards Cu^{2+}, which is a prerequisite for any BFC to securely deliver the radiometals to tumour cells. Complex stability is comparable or even higher than that of state-of-the-art Cu^{2+} chelators like DOTA, NOTA, and TETA. Although DO4S, DO3S and DO2A2S are probably not able to prevent the bioreduction of Cu^{2+}, their Cu^{+} complexes are highly stable due to the

coordination of one sulfur atom to the metal center. This stability might prevent copper demetallation *in vivo*.

Subtle changes of the ligand structure and donor arms can cause drastic changes to the stability of their radiometal complexes so that the effects induced by the modification of the azamacrocyclic ring on the physicochemical properties of the corresponding Cu^{2+} and Cu^{+} complexes were investigated with the second-generation macrocycles. The stability of the Cu^{2+} complexes demonstrated that the increase of one carbon in the azamacrocyclic ring has a negligible influence, as TRI4S forms complexes of comparable stability when compared to DO4S. However, a further increase in the ring size leading to TE4S results in a noticeable drop of the stability. The same trend was observed as regards their inertness towards acid-mediated decomplexations as the Cu^{2+} complexes with first-generation ligands demonstrated to be more inert. The number of carbon between nitrogen donors in the 12-member macrocyclic ring has a major influence on the stability of the Cu^{2+} complexes, as TACD3S was not able to strongly stabilize the metal cation.

On the other hand, the changing ring size did not affect the exceptional inertness of the copper complexes in reductive media as revealed by cyclic voltammetry and electrolysis experiments. While the $E_{1/2}$ still makes these Cu^{2+}-complexes susceptible to *in vivo* reduction, no subsequent Cu^{+} loss should occur.

Radiolabelling studies demonstrated a sharp contrast between the ability of each chelator to complex $[^{64}Cu]Cu^{2+}$. Among all the screened ligands, DO2A2S possessed the highest affinity for this radiometal, achieving high molar activities (50 MBq/nmol) under mild reaction conditions (RT, 10 min) as well as excellent plasma stability over 24 h.

Contrarily, DO4S (as well as its analogues, DO3S and DO3SAm) exhibited an inferior behaviour with respect to DO2A2S as well as poor human plasma stability of the corresponding complex. Although a similar labelling behaviour was achieved with the pure sulfur-bearing chelating agents appended on the larger macrocyclic backbones, the stability of the resulting complex was even worse.

These findings are consistent with the previously determined thermodynamic and kinetic trend and can be related to both the mismatch between the size of the radiometal and the cavity of the azamacrocyclic ring as well as to the difference in hardness/softness and basicity among the ligands. These outcomes clearly highlight the importance of considering the proper backbone as well as the importance of the presence of the carboxylic donors as this feature has been shown to have a noteworthy impact on the chelator performance and the complex' stability.

The excellent properties demonstrated by DO2A2S warrants the further development of a bifunctional derivative. To retain the encouraging properties of the free chelate, this should likely involve the functionalization of the pendant donor groups or the macrocyclic scaffold,

while preserving the two acetate donors, to allow Cu^{2+} complexation, and the two sulfur donors in attempt to obstruct the possible *in vivo* reduction to Cu^{+}.

Author Contributions

M. Tosato designed the experiments, analyzed and interpreted the data. M. Tosato and the Master's students M. Pelosato and E. Berberi and Dr S. Nardella performed the formation kinetic measurements. Solution thermodynamic measurements (UV-Vis, potentiometry *etc.*) were conducted by M. Tosato and partly the students M. Pelosato and E. Berberi and Dr S. Nardella. Cyclic voltammetry and electrolysis experiments were conducted by M. Tosato and the students M. Covolo and M. Pelosato. Prof. A. A. Isse supervised the electrochemical measurements. Prof. P. Pastore and Prof. D. Badocco helped with the electrochemical data interpretation. Decomplexation kinetics measurements were conducted by M. Tosato and Dr S. Nardella and partly by M. Pelosato. All students worked under the supervision of M. Tosato. EPR analysis was conducted by Dr N. May. X-ray crystal structure of [Cu(DO2A2S)] was solved by Dr N. May. Prof. H. Mäcke and Dr A. Alker provided the crystal structure of $[Cu(DO4S)(NO_3)]\cdot(NO_3)$. DFT calculations were performed by Dr M. Dalla Tiezza under the supervision of Prof. L. Orian.
Radiolabelling, competitions and *in vitro* assays with copper-64 were carried out by M. Tosato at Radiopharmaceutical Chemistry Section, Nuclear Medicine Unit, AUSL-IRCCS Reggio Emilia, Reggio Emilia, Italy under the guidance of Dr Mattia Asti and at the Center for Radiopharmaceutical Sciences (CRS) of Paul Scherrer Institute (PSI, Villigen, Switzerland), in the group of Dr Nick van der Meulen. M. Verona, C. Favaretto and Dr Z. Talip gave support and assistance during these experiments. Dr N. van der Meulen was responsible for the production and separation of copper-64 and the radiochemical studies at PSI. Dr M. Asti was responsible for the radiochemical studies. Prof. V. Di Marco oversaw and supervised the study. All the manuscripts were written by M. Tosato.

4.5 References

1 T. J. Wadas, E. H. Wong, G. R. Weisman and C. J. Anderson, *Curr. Pharm. Des*, 2007, **13**, 3-16.

2 T. J. Wadas, E. H. Wong, G. R. Weisman and C. J. Anderson, *Chem. Rev.*, 2010, **110**, 2858-2902.

3 Z. Cai and C. J. Anderson, *J. Label. Compd. Radiopharm.*, 2014, **57**, 224-230.

4 E. Boros, J. F. Cawthray, C. L. Ferreira, B. O. Patrick, M. J. Adam and C. Orvig, *Inorg. Chem.*, 2012, **51**, 6279-6284.

5 C. J. Anderson and M. J. Welch, *Chem. Rev.*, 1999, **99**, 2219-2234.

6 M. Shokeen and C. J. Anderson, *Acc. Chem. Res.*, 2009, **42**, 832-841.

7 F. Borgna, M. Ballan, C. Favaretto, M. Verona, M. Tosato, M. Caeran, S. Corradetti, A. Andrighetto, V. Di Marco, G. Marzaro and N. Realdon, *Molecules*, 2018, **23**, 2437.

8 G. Hao, T. Mastren, W. Silvers, G. Hassan, O. K. Öz and X. Sun, *Sci. Rep.*, 2021, **11**, 3622.

9 I. Carbo-Bague and C. F. Ramogida, in *Encyclopedia of Inorganic and Bioinorganic Chemistry*, 2021.

10 S. C. Srivastava and L. F. Mausner, in *Therapeutic Nuclear Medicine*, Springer-Verlag: Berlin, 2013, 11-50.

11 C. Ramogida and C. Orvig, *Chem. Commun.*, 2013, **49**, 4720-4739.

12 S. Liu, *Adv. Drug Deliv. Rev.*, 2008, **60**, 1347-1370.

13 M. Fani, L. Del Pozzo, K. Abiraj, R. Mansi, M. L. Tamma, R. Cescato, B. Waser, W. A. Weber, J. C. Reubi and H. R. Mäcke, *J. Nucl. Med.*, 2011, **52**, 1110-1118.

14 K. S. Woodin, K. J. Heroux, C. A. Boswell, E. H. Wong, G. R. Weisman, W. Niu, S. A. Tomellini, C. J. Anderson, L. N. Zakharov and A. L. Rheingold, *Eur. J. Inorg. Chem.*, 2005, **2005**, 4829-4933.

15 A. Guillou, L. M. P. Lima, M. Roger, D. Esteban-Gomez, R. Delgado, C. Platas-Iglesias, V. Patinec and R. Tripier, *Eur. J. Inorg. Chem.*, 2017, **2017**, 2435-2443.

16 S. Bhattacharyya and M. Dixit, *Dalton Trans.*, 2011, **40**, 6112-6128.

17 N. Camus, N. Le Bris, S. Nuryyeva, M. Chessé, D. Esteban-Gómez, C. Platas-Iglesias, R. Tripier and M. Elhabiri, *Dalton Trans.*, 2017, **46**, 11479-11490.

18 A. K. Sharma, J. W. Schultz, J. T. Prior, N. P. Rath and L. M. Mirica, *Inorg. Chem.*, 2017, **56**, 13801-13814.

19 L. A. Bass, M. Wang, M. J. Welch and C. J. Anderson, *Bioconjugate Chem.*, 2000, **11**, 527-532.

20 J. L. Dearling, S. D. Voss, P. Dunning, E. Snay, F. Fahey, S. V. Smith, J. S. Huston, C. F. Meares, S. T. Treves and A. B. Packard, *Nucl. Med. Biol.*, 2011, **38**, 29-38.

21 A. Schmidtke, T. Läppchen, C. Weinmann, L. Bier-Schorr, M. Keller, Y. Kiefer, J. P. Holland and M. D. Bartholomä, *Inorg. Chem*, 2017, **56**, 9097-9110.

22 C. F. Ramogida, E. Boros, B. O. Patrick, S. K. Zeisler, J. Kumlin, M. J. Adam, P. Schaffer and C. Orvig, *Dalton Trans.*, 2016, **45**, 13082-13090.

23 M. Le Fur, M. Beyler, N. Le Poul, L. M. P. Lima, Y. Le Mest, R. Delgado, C. P. Iglesias, V. Patineca and R. Tripier, *Dalton Trans.*, 2016, **45**, 7406-7420.

24 S. N. Rylova, C. Stoykow, L. Del Pozzo, K. Abiraj, M. L. Tamma, Y. Kiefer, M. Fani and H. R. Mäcke, *PLoS One*, 2018, **13**, e0195802.

25 S. V. Smith, *J. Inorg. Biochem.*, 2004, **98**, 1874-1901.

26 T. M. Jones-Wilson, K. A. Deal, C. J. Anderson, D. W. McCarthy, Z. Kovacs, R. J. Motekaitis, A. D. Sherry, A. E. Martell and M. J. Welch, *Nucl. Med. Biol.*, 1998, **25**, 523-530.

27 C. A. Boswell, X. Sun, W. Niu, G. R. Weisman, E. H. Wong, A. L. Rheingold and

C. J. Anderson, *J. Med. Chem.*, 2004, **47**, 1465-1474.

28 E. H. Wong, G. R. Weisman, D. C. Hill, D. P. Reed, E. M. Rogers, J. P. Condon, M. A. Fagan, J. C. Calabrese, K. C. Lam, I. A. Guzei and A. L. Rheingold, *J. Am. Chem. Soc.*, 2000, **122**, 10561-10572.

29 R. Ferdani, D. J. Stigers, A. L. Fiamengo, L. Wei, B. T. Y. Li, J. A. Golen, A. L. Rheingold, G. R. Weisman, E. H. Wong and C. J. Anderson, *Dalton Trans.*, 2012, **41**, 1938-1950.

30 D. J. Stigers, R. Ferdani, G. R. Weisman, E. H. Wong, C. J. Anderson, J. A. Golen, C. Moore and A. L. Rheingold, *Dalton Trans.*, 2010, **39**, 1699-1701.

31 E. Boros and A. B. Packard, *Chem Rev.*, 2019, **119**, 870-901.

32 A. Rodríguez-Rodríguez, Z. Halime, L. M. P. Lima, M. Beyler, D. Deniaud, N. Le Poul, R. Delgado, C. Platas-Iglesias, V. Patinec and R. Tripier, *Inorg. Chem.*, 2016, **55**, 619-632.

33 E. Bodio, M. Boujtita, K. Julienne, P. Le Saec, S. G. Gouin, J. Hamon, E. Renault and D. Deniaud, *ChemPlusChem*, 2014, **79**, 1284-1293.

34 S. Shuvaev, E. A. Suturina, N. J. Rotile, C. A. Astashkin, C. J. Ziegler, A. W. Ross, T. L. Walker, P. Caravan and I. S. Taschner, *Dalton Trans.*, 2020, **49**, 14088-14098.

35 R. Ševčik, J. Vanek, P. Lubal, Z. Kotková, J. Kotek and P. Hermann, *Polyhedron*, 2014, **67**, 449-455.

36 S. P. Kasprzyk and R. G. Wilkins, *Inorg. Chem.*, 1982, **21**, 3349-3352.

37 G. Anderegg, F. Arnaud-Neil, R. Delgado and K. Popov, *Pure Appl. Chem.*, 2005, **77**, 1445-1495.

38 M. Tosato and V. Di Marco, *Biomolecules*, 2019, **9**, 269.

39 M. Tosato, M. Dalla Tiezza, N. V. May, A. A. Isse, S. Nardella, L. Orian, M. Verona, C. Vaccarin, A. Alker, H. Mäcke, P. Pastore and V. Di Marco, *Inorg. Chem.*, 2021, **60**, 11530-11547.

40 A. R. Amundsen, J. Whelan and B. Bosnich, *J Am Chem Soc*, 1977, **99**, 6730-6739.

41 M. Tosato, M. Verona, R. Doro, M. Dalla Tiezza, L. Orian, A. Andrighetto, P. Pastore, G. Marzaro and V. Di Marco, *New J. Chem.*, 2020, **44**, 8337-8350.

42 M. C. Styka, R. C. Smierciak, E. L. Blinn, R. E. DeSimone and J. V. Passariello, *Inorg. Chem.*, 1978, **17**, 82-86.

43 J. L. Gray, D. L. Gerlach and E. T. Papisha, *Acta Crystallogr E Crystallogr Commun.*, 2017, **73**, 31-34.

44 S. Lacerda, M. P. Campello, I. C. Santos, I. Santos and R. Delgado, *Polyhedron*, 2007, **26**, 3763-3773.

45 D. E. Nikles, M. J. Powers and F. L. Urbach, *Inorg. Chem.*, 1982, **22**, 3210-217.

46 C. F. G. C. Geraldes, M. P. M.Marques, B. de Castro and E. Pereira, *Eur. J. Inorg. Chem.*, 2000, **2000**, 559–565.

47 L. M. Lima, D. Esteban-Gomez, R. Delgado, C. Platas-Iglesias and R. Tripier, *Inorg. Chem.*, 2012, **51**, 6916-6927.

48 R. Clay, P. Murray-Rust and J. Murray-Rust, *Acta Cryst.*, 1979, **35**, 1894-1895.

49 A. Riesen, M. Zehnder and T. A. Kaden, *Helv. Chim. Acta*, 1986, **69**, 2067-2073.

50 R. Ševčík, J. Vaněk, R. Michalicová, P. Lubal, P. Hermann, I. C. Santos, I. Santos and M. P. C. Campello, *Dalton Trans.*, 2016, **45**, 12723-2733.

51 A. W. Addison, M. Carpenter, L. K. M. Lau and M. Wicholas, *Inorg. Chem.*, 1978, **17**, 1545-1552.

52 R. Gillet, A. Roux, J. Brandel, S. Huclier-Markai, F. Camerel, O. Jeannin, A. M. Nonat and L. J. Charbonniere, *Inorg. Chem.*, 2017, **56**, 11738-11752.

53 J. Kotek, P. Lubal, P. Hermann, I. Císarová, I. Lukes, T. Godula, I. Svobodová, P. Táborský and J. Havel, *Chemistry*, 2003, **9**, 233-248.

54 H. Aneetha, Y. H. Lai, S. C. Lin, K. Panneerselvam, T. H. Lu and C. S. Chung, *J. Chem. Soc., Dalton Trans.*, 1999, 2885-2892.

55 A. V. Dale, G. I. An, D. N. Pandya, Y. S. Ha, N. Bhatt, S. N., H. Lee, H. Ahn, S. Sarkar, W. Lee, P. T. Huynh, J. Y. Kim, M. R. Gwon, S. H. Kim, J. G. Park, Y. R. Yoon and J. Yoo, *Inorg. Chem.*, 2015, **54**, 8177-8186.

56 K. Taras-Goslinska and M. Jonsson, *J. Phys. Chem. A*, 2006, **110**, 9513-9517.

57 B. R. Coleman, R. S. Glass, W. N. Setzer, U. D. G. Prabhu and G. S. Wilson, *Adv. Chem. Ser.* 1982, **201**, 417-441.

58 D. S. Houghton and A. A. Humffray, *Electrochim. Acta*, 1972, **17**, 1421-1433.

59 G. A. Bailey, E. W. Price, B. M. Zeglis, C. L. Ferreira, E. Boros, M. J. Lacasse, B. O. Patrick, J. S. Lewis, M. J. Adam and C. Orvig, *Inorg. Chem.*, 2015, **51**, 12575-12589.

60 S. Lacerda, M. P. Campello, F. Marques, L. Gano, V. Kubıček, P. Fousková, É. Tóth and I. Santos, *Dalton Trans.*, 2009, 4509-4518.

61 M. Tosato, M. Asti, M. Dalla Tiezza, L. Orian, D. Häussinger, R. Vogel, U. Köster, M. Jensen, A. Andrighetto, P. Pastore and V. Di Marco, *Inorg. Chem.*, 2020, **59**, 10907-10919.

62 C. F. J. Baes and R. E. Mesmer, *The Hydrolysis of cations*, New York, 1976.

63 A. Rockenbauer and L. Korecz, *Appl. Magn. Reson.*, 1996, **10**, 29-43.

64 T. Higashi, *NUMABS,* 2002.

65 G. M. Sheldrick, *Acta Cryst.*, 1990, **46**, 467-473.

66 CrystalClear-SM; Version 1.4.0 SP1: Rigaku and Rigaku/MSC, 2008.

67 M. C. Burla, R. Caliandro, B. Carrozzini, G. L. Cascarano, C. Cuocci, C. Giacovazzo, M. Mallamo, A. Mazzone and G. Polidori, *J. Appl. Crystallogr.*, 2015, **48**, 306-309.

68 SHELXL-2013 Program for Crystal Structure Solution; University of Göttingen: Göttingen, Germany, 2013.

69 L. J. Farrugia, *J. Appl. Crystallogr.*, 2012, **45**, 849-854.

70 A. L. Spek, *J. Appl. Crystallogr*, 2003, **36**, 7-13.

71 C. F. Macrae, P. R. Edgington, P. McCabe, E. Pidcock, G. P. Shields, R. Taylor, M. Towler and J. van de Streek, *J. Appl. Crystallogr.*, 2006, **39**, 453-457.

72 F. H. Allen, O. Johnson, G. P. Shields, B. R. Smith and M. Towler, *J. Appl. Cryst.*, 2004,

37, 335-338.

73 G. te Velde, F. M. Bickelhaupt, E. J. Baerends, C. Fonseca Guerra, S. J. A. van Gisbergen, J. G. Snijders and T. Ziegler, *J. Comput. Chem.*, 2001, **22**, 931-967.

74 C. Fonseca Guerra, J. G. Snijders, G. te Velde and E. J. Baerends, *Theor. Chem. Acc*, 1998, **99**, 391-403.

75 ADF2018, SCM, Theoretical Chemistry; Vrije Universiteit, Amsterdam: The Netherlands, http://www.scm.com.

76 J. P. Perdew, K. Burke and M. Ernzerhof, *Phys. Rev. Lett.*, 1996, **77**, 3865-3868.

77 N. C. Handy and A. J. Cohen, *Mol. Phys.*, 2001, **99**, 403-412.

78 M. Swart, A. W. Ehlers and K. Lammertsma, *Mol. Phys.*, 2004, **102**, 2467-2474.

79 E. van Lenthe, E. J. Baerends and J. G. Snijders, *J. Chem. Phys*, 1994, **101**, 9783-9792.

80 N. L. Allinger, X. Zhou and J. Bergsma, *J. Mol. Struct. THEOCHEM*, 1994, **312**, 69-83.

81 J. Ho, A. Klamt and M. L. Coote, *J. Phys. Chem. A*, 2010, **114**, 13442-13444.

82 A. V. Marenich, C. J. Cramer and D. G. Truhlar, *J. Phys. Chem. B*, 2009, **113**, 6378-6396.

83 C. C. Pye and T. Ziegler, *Theor. Chem. Acc.*, 1999, **101**, 396-408.

84 F. M. Bickelhaupt and K. N. Houk, *Angew. Chemie*, 2017, **56**, 10070-10086.

85 N. P. van der Meulen, R. Hasler, A. Blanc, R. Farkas, M. Benešová, Z. Talip, C. Müller and R. Schibli, *J. Label. Compd. Radiopharm.*, 2019, **62**, 460-470.

Chapter 5

Tuning the Softness of Pendant Arms and the Polyazamacrocyclic Backbone to Optimize $^{203/212}$Pb Theranostic Pair Chelation

This chapter is adaptation of a manuscript in preparation and is reproduced in part with the permission from Tosato, M.; Randhawa, P.; Lazzari, L.; McNeil B. L.; Ramogida, C. F. and Di Marco, V. Expected submission: April 2022.

5.1 Introduction

Although β^- emitting radionuclides have proven their usefulness for the eradication of localized macroscopic tumours in TRT, limited successes have been obtained in the case of small clusters or isolated cancer cells.[1] In contrast, targeted alpha therapy (TAT) offers key advantages over TRT with β^- emitters as a potent and localized radiation treatment can be obtained because of the high linear energy transfer (LET) and short-range emission of the α-radiation.[2–4] The higher LET with respect to β^- particles produces more lethal DNA double-strand breaks *per* radiation track when traversing a cell nucleus, while the short-range increases the safety profile of the radiolabelled drug because non-specific irradiation of normal tissue around the target cells is greatly reduced or absent.[3–6] Moreover, the cytotoxicity of the α-emitters is independent of oxygen concentration, dose rate and cell cycle position.[3,6] These features make TAT ideal for the treatment of single tumour cells, micrometastases, lymphatic and vascular tumour cells (*e.g.*, lymphoma and leukaemias) or in the case of residual disease after surgical debulking.[1,4,5,7] However, most of the emerging α-emitters currently under preclinical and clinical investigations such as actinium-225 (^{225}Ac, $t_{1/2}$ 10.0 d), bismuth-212/213 (^{212}Bi, $t_{1/2}$ 60.55 min; ^{213}Bi, $t_{1/2}$ 45.61 min), astatine-211 (^{211}At, $t_{1/2}$ 7.21 h) and thorium-226/227 (^{226}Th, $t_{1/2}$ 30.57 min; ^{227}Th, $t_{1/2}$ 18.70 d) reveals a lack of chemically identical diagnostic isotopes, thus hindering the development of personalized medicine.[8,9]

A rare and unique opportunity of an α-emitter paired with a diagnostic one is represented by lead radioisotopes, lead-203 (^{203}Pb) and lead-212 (^{212}Pb).[10,11] Although ^{212}Pb is a pure β^- emitter ($t_{1/2}$ 51.9 h, $E_{\beta^-,\text{ave}}$ 100 keV, I_{β^-} 100%), it is considered as an *in vivo* α-particle generator through its decay daughter bismuth-212 (^{212}Bi, $t_{1/2}$ 60.5 min, E_α 6.3 MeV, I_α 36%) and the short-lived polonium-212 (^{212}Po, $t_{1/2}$ 0.51 s, E_α 7.4 MeV) (**Figure 5.1**).[12] The *in vivo* generator strategy allows to circumvent the short half-life of ^{212}Bi, which not only poses a logistical dilemma for radiolabelling and drug administration but also limits the time frame for circulation and target accumulation.[3,4,13] Moreover, the *in vivo* ^{212}Pb/^{212}Bi generator allows delivery of up to ten times more doses *per* unit of administered activity compared to ^{212}Bi alone or the α-emitter ^{213}Bi.[8,14,15] On the other hand, ^{203}Pb ($t_{1/2}$ 10.6 h, E_γ 279.1 keV, I_γ 81%) is suitable for SPECT imaging as it releases γ-photons during its decay *via* electron capture to ground state thallium-203 (^{203}Tl) (**Figure 5.1**).[11,12,16–18]

^{212}Pb can be obtained from its parent radionuclides thorium-228 (^{228}Th, $t_{1/2}$ 1.91 y) and radium-224 (^{224}Ra, $t_{1/2}$ 3.64 d) (**Figure 5.2**).[2,11,19–25] Low energy charged particle (proton, deuteron and α particle) bombardment of natural or enriched ^{203}Tl targets yields ^{203}Pb.[11,26,27]

Although it has been clinically demonstrated that lead radioisotopes are very powerful tools for diagnosis and treatment of breast, prostate, neuroendocrine tumours and melanoma, a

few obstacles must be addressed before lead-based radiopharmaceuticals can be translated from the bench into the clinic.[15,28,37–40,29–36] For the successful implementation of theranostic treatment with $^{203/212}$Pb, these radionuclides must be delivered with high specificity and retained within the vicinity of the biological target over the course of its nuclear decay.[41,42] As described in **Chapter 1**, these can be accomplished by the formation of a tight and stable complex with a BFC coupled to the targeting moiety *via* a covalent linkage.[41–46]

Chelation of Pb radioisotopes has been mainly explored with two ligands: DOTA and its tetracetamide derivative 1,4,7,10-tetraazacyclododecane-1,4,7,10-tetraacetic amide (TCMC or DOTAM).[12,47,48] Despite the Pb^{2+}-DOTA complex being stable at biological pH, this ligand is not able to retain the daughter isotope ^{212}Bi which is expelled from the chelate due to the formation of highly ionized daughter atoms associated with the decay of ^{212}Pb to ^{212}Bi, generating off-target toxicity (mainly in kidneys) that can be fatal *in vivo*.[12,23,47–50] Moreover, DOTA is susceptible to acidic conditions which can result in the acid-promoted dissociation of Pb^{2+} in acidic tumour environments.[12,18,49] In TCMC, the replacement of the carboxylates with amides improves the kinetic inertness of Pb^{2+} complexes but the destabilization of the decay daughter from the TCMC complex remains an issue.[12,48,49]

Despite the great potential of $^{203/212}$Pb, limited progress has been made on chelation chemistry improvements for lead radioisotopes, and TCMC persists as the state-of-the-art chelator for these radionuclides. Thus, the issues of the acid-mediated Pb^{2+}-dissociation combined with the stable complexation of its daughter radionuclide ^{212}Bi remain a challenge in the use of ^{212}Pb: a proper ligand that could bind lead ions more strongly and efficiently *in vivo* is still sought and it is the key to boost the advancement of $^{203/212}$Pb towards the clinic.[49,51]

In this context, inspired by the improvement achieved with the replacement of the carboxylates of DOTA with softer amide donors in TCMC, it was hypothesized that the introduction of sulfur donor arms could further improve the performance over their carboxylic acid/amide-bearing counterparts as they could optimally complement with the borderline-soft nature of Pb^{2+}. Hence, the sulfur-bearing chelators described in **Chapter 2** as multipurpose ligands capable to accommodate borderline/soft metals have been considered hereby for lead chelation. It is worth to note that polyazamacrocycles bearing sulfanyl pendant arms have never been used for the complexation of Pb^{2+} radioisotopes so far.

In the present Chapter, the evaluation of the first- and second-generation series of sulfur-containing ligands for the chelation of lead radioisotopes is reported. To investigate the impact of the introduction of sulfur donors on the corresponding complexes' properties, their solution thermodynamic, formation and acid-mediated dissociation kinetics were assessed with non-radioactive Pb^{2+} through a combination of UV-Vis spectrophotometric, pH-potentiometric, and NMR titrations. The solution structures of the Pb^{2+} complexes were

explored using monodimensional, bidimensional and variable-temperature NMR. Radiolabelling experiments were performed with [^{203}Pb]Pb^{2+} to evaluate the complexation efficiency in extremely diluted conditions, and the results were compared with the performance of the current state-of-the-art TCMC. In addition, the *in vitro* human serum stability was investigated to assess the candidacy of these molecules as chelating agents for $^{203/212}$Pb-based theranostic radiopharmaceuticals.

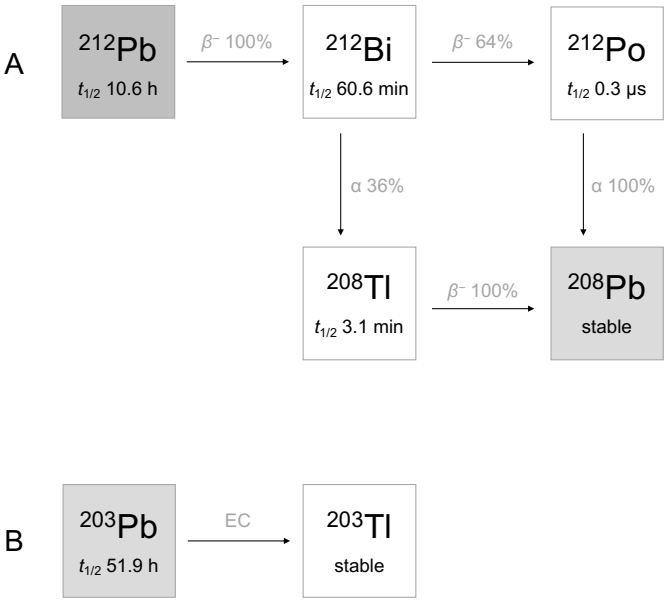

Figure 5.1. Decay scheme of (A) lead-212 and (B) lead-203.

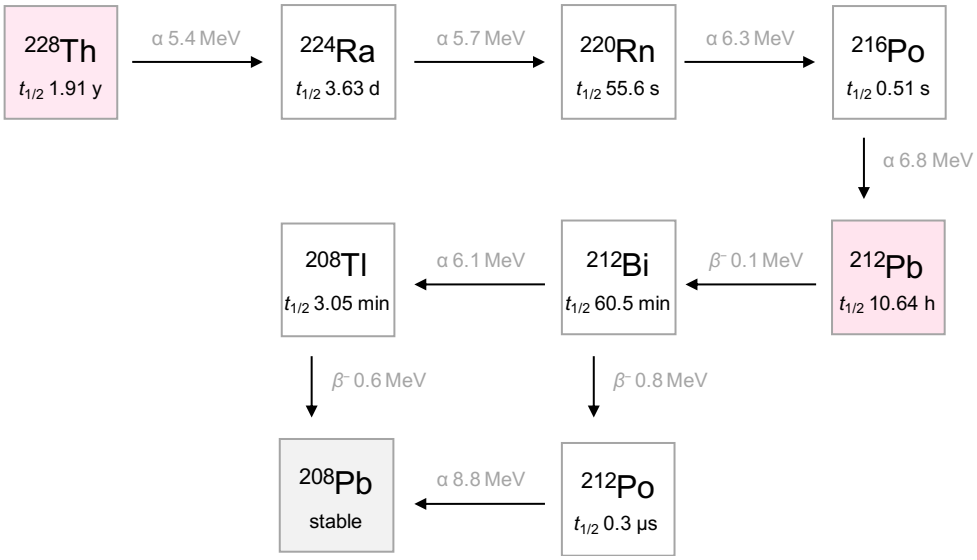

Figure 5.2. Decay scheme of thorium-228.

5.2 Results and Discussion

5.2.1 Complexation Kinetics of Lead Complexes

As a necessary preliminary step, the kinetics of the Pb^{2+}-complexation was assessed at room temperature by UV-Vis and ^{1}H-NMR spectroscopies before the thermodynamic investigation, as the latter requires the knowledge of the time to assure the equilibrium conditions. The UV-Vis spectra and the variation of the absorbance over time for the Pb^{2+} complexation reactions with the first-generation ligands are illustrated in **Figure 5.3**. The estimated complexation times are summarized in **Table D1** (**Appendix D**).

With DO4S, DO3S and DO3SAm, no complex formation was observed below pH ~ 4, neither after 2 weeks at room temperature nor after prolonged heating, as no spectra changes were detected with respect to the free ligands. At pH > 4, the complex formation was found to be rather slow: at pH 5, the time necessary to reach the equilibrium was found to be equal to ~ 1 day and ~ 6 h for DO4S and DO3S, respectively, while at pH 7.4 the Pb^{2+} complex with the former chelator was formed in ~ 1 h and ~ 3 min with the latter (**Figure 5.3**). The addition of oxygen donors in the ligand arms led to an increase in the complexation kinetics (**Table D1** - **Appendix D**). For example, at pH 3.7 the Pb^{2+} complex formation occurred in ~ 30 min for DO2A2S (**Figure 5.3**) while it was instantaneous at pH > 5. At pH 5, the Pb^{2+} complex with DO3SAm was formed in ~ 2 h (**Figure 5.3**). The slowed-down complexation kinetics with the pH decrease can be explained considering the increasingly protonated forms of the ligands present at the equilibrium, which results in an increase in electrostatic repulsions between the cation and donors in the macrocyclic ring, as previously found with Cu^{2+} (**Chapter 4**).[42,52,53] On the other hand, the driving force that speeds up the complexation reaction when the ligand contains oxygen donors can be ascribed to the favourable Coulombic interactions between the negatively charged acetate groups of DO2A2S or the partially negative charged amide group of DO3SAm with the metal cation. These interactions can lead to an increase in the local concentration of Pb^{2+} near the donor atoms due to the formation of an 'out-of-cage' intermediate which is after transformed into the final 'in-cage' product.[42] This does not occur in the presence of the thioether chains as they are not negatively charged.

Increasing the macrocyclic scaffold dimension or decreasing the number of N donors maintaining the total number of ring atoms with respect to the cyclen-analogue have a profound effect on the binding ability of the ligands. The second-generation chelators were demonstrated to not be able to complex Pb^{2+} at pH < 7, thus indicating a low affinity for this cation (**Figure 5.4**). This is likely related to the worst matching between the size of the metal cation and ring cavity. Literature data indicate that the same trend of the binding affinity is

also observed considering the corresponding non-functionalized macrocycles ($\log K_{Pb^{2+}\text{-cyclen}}$ = 15.9 at T = 25°C and I = 0.2 M, $\log K_{Pb^{2+}\text{-cyclam}}$ = 13.48 at T = 25°C and I = 0.15 M $NaNO_3$, $\log K_{Pb^{2+}\text{-13aneN4}}$ = 10.83 at T = 25°C and I = 0.15 M $NaNO_3$).[54] As high thermodynamic stability is a paramount requirement for a ligand to be used as BFC in metal-based radiopharmaceuticals, these chelators were not further considered.

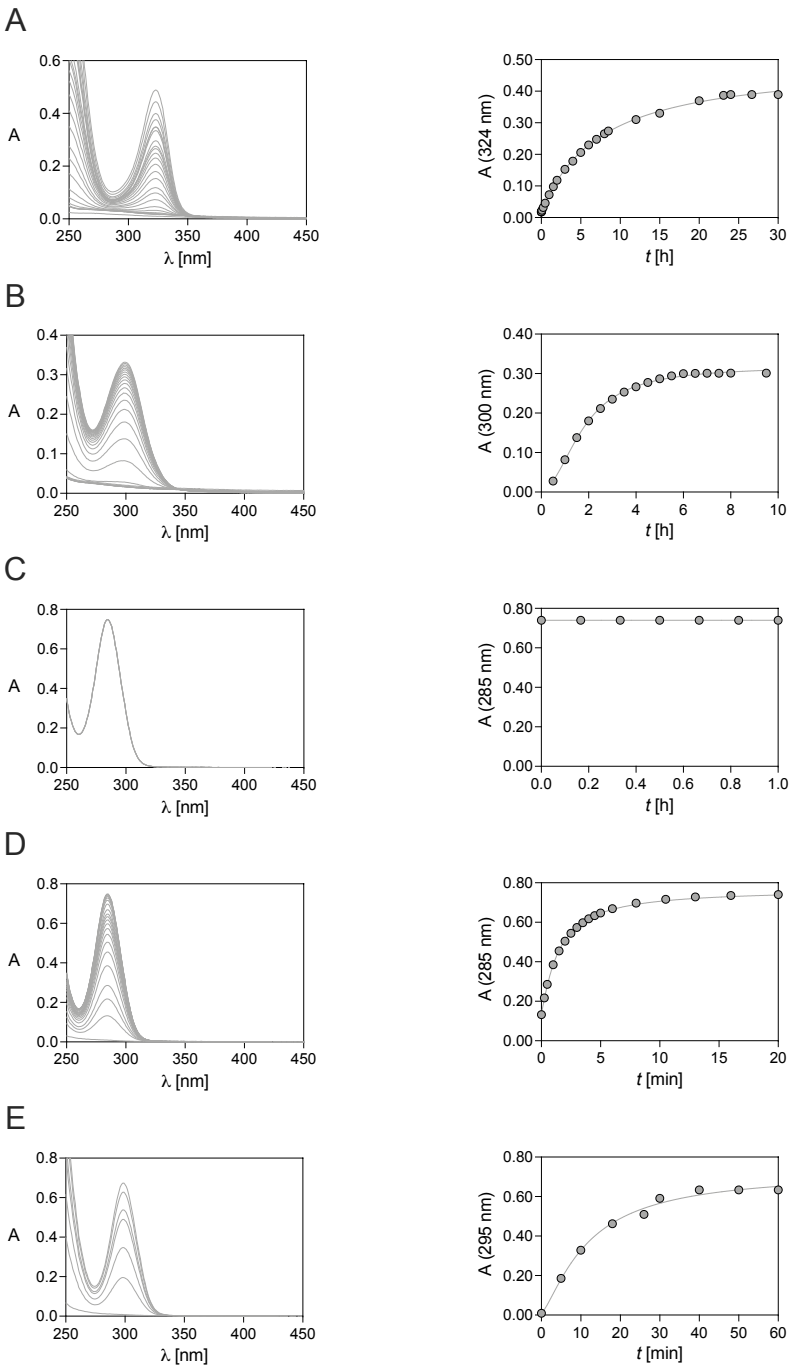

Figure 5.3. UV-Vis spectra (left) and variation of $A_{\lambda max}$ *vs.* time (right) related to the complexation kinetics of the Pb^{2+}-complexes at pH 5 with (A) DO4S, (B) DO3S, (C) DO2A2S and at pH 3.7 with (D) DO2A2S and (E) DO3SAm ($C_{Pb^{2+}} = C_L = 1 \cdot 10^{-4}$ M).

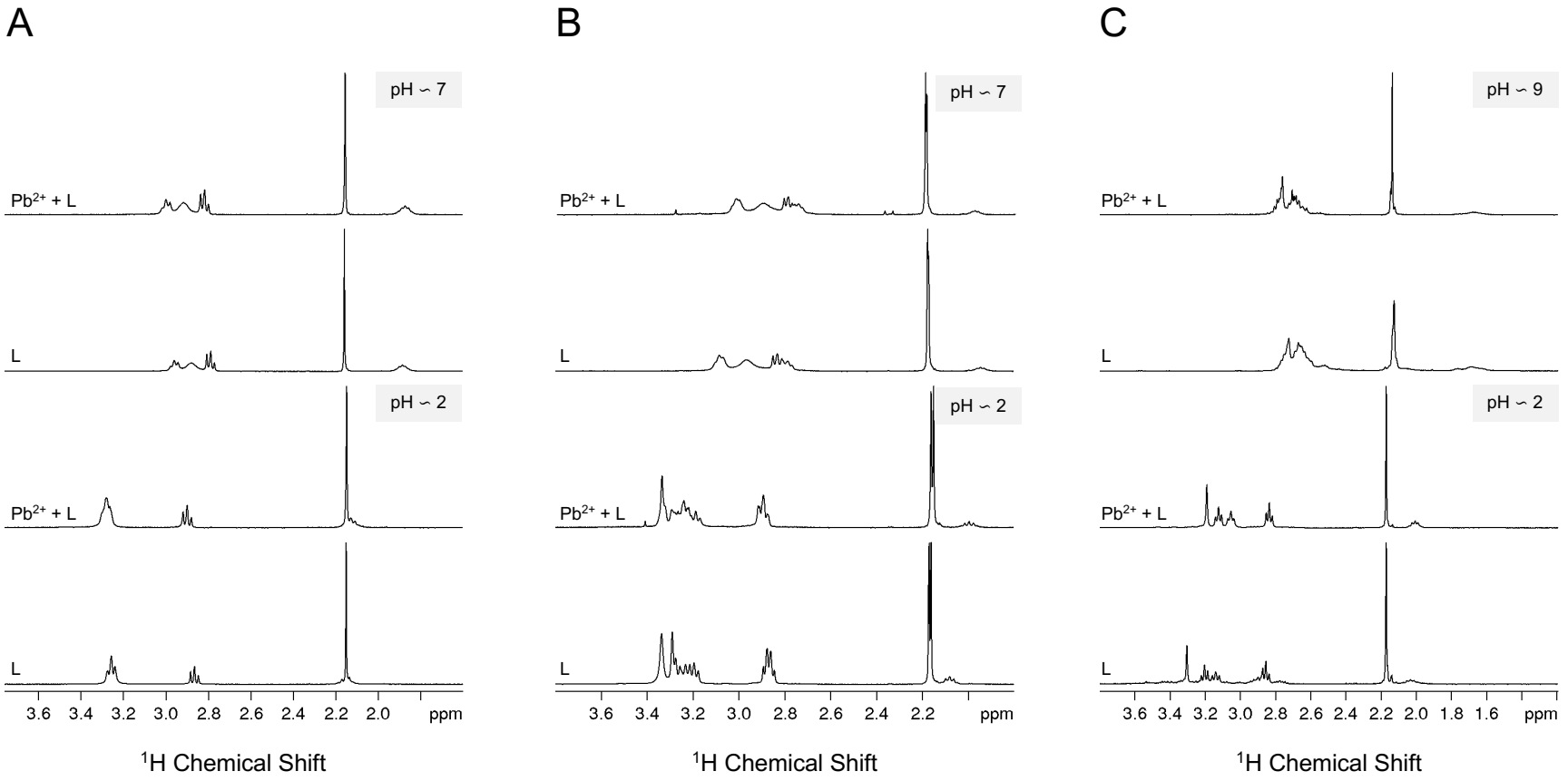

Figure 5.4. Representative ^{1}H-NMR spectra (400 MHz, T = 25°C, H_2O + 10% D_2O) of (A) Pb^{2+}-TACD3S, (B) Pb^{2+}-TRI4S and (C) Pb^{2+}-TE4S at different pH values ($C_{Pb^{2+}} = C_L = 1.0 \cdot 10^{-3}$ M). No complexation was observed as no spectral changes were detected respect to the free ligands.

5.2.2 Solution Thermodynamics of Lead Complexes

The rather slow Pb^{2+} complexation reactions with DO4S and DO3S obviated the use of conventional potentiometric techniques to determine the corresponding formation constants (logβ). Out-of-cell UV-Vis spectrophotometric titrations were therefore employed. With DO2A2S, the equilibrium was reached quickly enough so that additional direct (in-cell) potentiometric measurements were performed. The absorption spectra of solutions containing Pb^{2+} and the first-generation ligands at equilibrium at different pH are reported in **Figure 5.5** while the electronic data are summarized in **Table D2** (**Appendix D**).

When Pb^{2+} was added to the free ligands during the titration experiments, significant spectroscopic changes marked by the appearance of an intense band in the UV-B spectral region (285-325 nm range) were found, indicative of the complexation event. While DO4S, DO3S and DO3SAm coordinate to Pb^{2+} forming only the deprotonated mononuclear complex, *i.e.* $[PbL]^{2+}$, also the monoprotonated species, *i.e.* $[PbHL]^{+}$, was found for DO2A2S. The speciation model and the equilibrium constants for Pb^{2+}-DO2A2S were also confirmed by pH-potentiometric titrations. The obtained formation constants are presented in **Table 5.1** while the corresponding speciation diagrams are shown in **Figure 5.6**.

To compare the chelating ability of the investigated ligands with the state-of-the-art Pb^{2+} chelators, the pPb^{2+} values were computed ($pPb^{2+} = -\log[Pb^{2+}]$).[55] The obtained values are detailed in **Table 5.1**.

The trend of pPb^{2+} values pointed out that the introduction of thioether side chains on the cyclen scaffold induces a remarkable decrease in the stability of the resulting complexes. The pPb^{2+} values for Pb^{2+}-DO4S system are comparable with those of Pb^{2+}-DO3S. On the other hand, the Pb^{2+}-complexes with the two O-containing ligands, *i.e.* DO3SAm and DO2A2S, possess significantly higher pPb^{2+} values than the others but still lower than those characteristics of the current standards for lead chelation, *i.e.* DOTA ($pPb^{2+} = 19.4$) and TCMC ($pPb^{2+} > 18$).[56,57]

5.2.3 Solution Structure of Lead Complexes

To gain insight into the solution structure of the Pb^{2+}-complexes and to further validate the obtained speciation models, variable-pH ^{1}H-NMR titrations were performed. The ^{1}H-NMR spectra at different pH are reported in **Figure 5.7** and **Figure D1** (**Appendix D**) while the spectra assignations are summarized in **Table D3** (**Appendix D**). The assignments were made based on ^{1}H-^{1}H TOCSY and ^{1}H-^{13}C HSQC spectra reported in **Figure 5.8**.

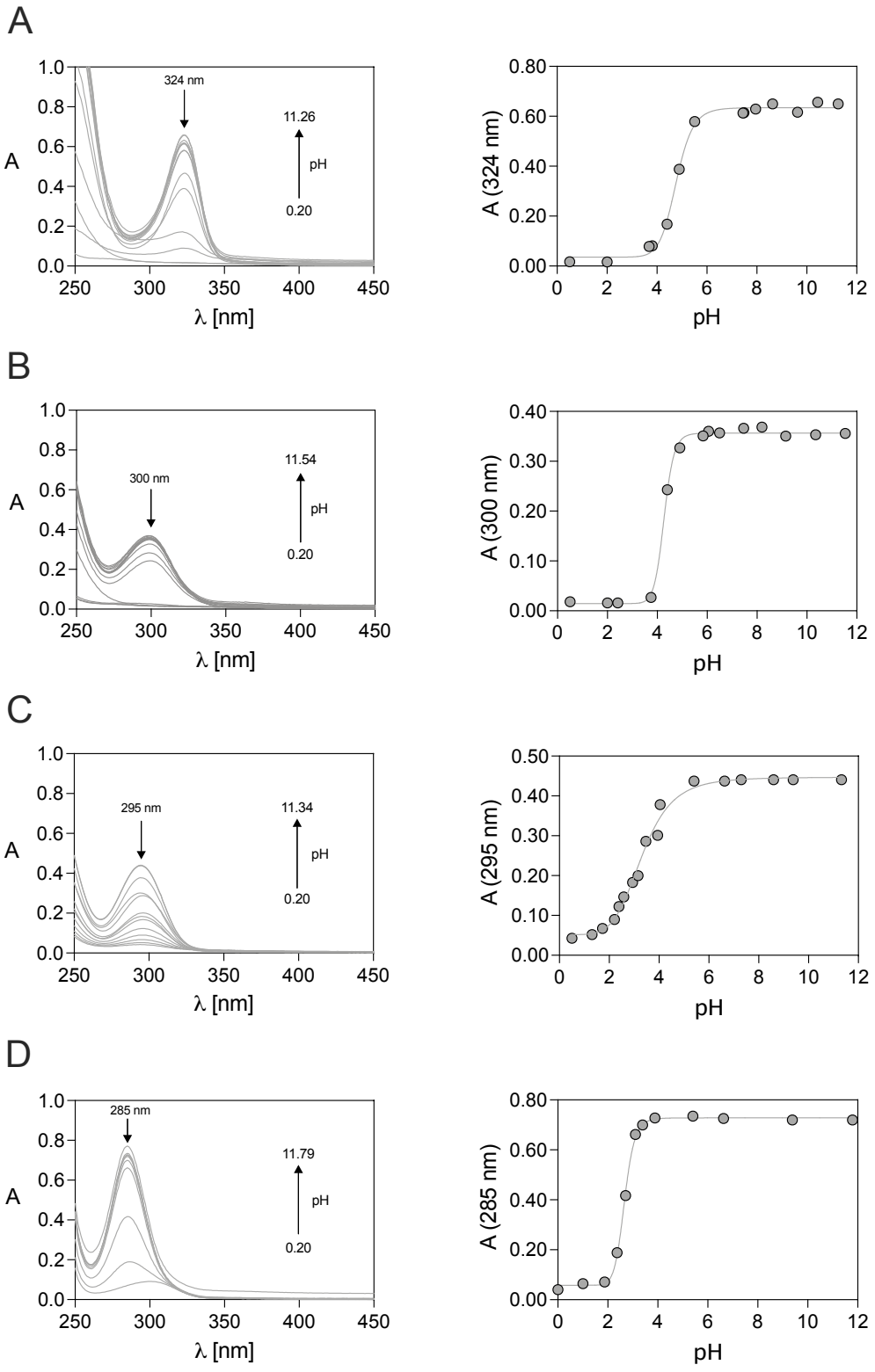

Figure 5.5. Representative variable-pH UV-Vis spectra (left), experimental points and fitting line of A(λ_{max}) *vs.* pH (right) for (A) Pb^{2+}-DO4S, (B) Pb^{2+}-DO3S, (C) Pb^{2+}-DO3SAm and (D) Pb^{2+}-DO2A2S ($C_{Pb^{2+}} = C_L = 1 \cdot 10^{-4}$ M).

Table 5.1. Overall stability constants (logβ) and pPb^{2+} values for the Pb^{2+} complexes with the first-generation ligands at I = 0.15 M $NaNO_3$ and T = 25°C. Unless otherwise stated, the logβ values were obtained by UV-Vis spectroscopy.

Ligand	Equilibrium reaction	logβ				pPb^{2+} [b]
DO4S	$Pb^{2+} + L \leftrightharpoons [PbL]^{2+}$	12.3	±	0.1		10.2
DO3S	$Pb^{2+} + L \leftrightharpoons [PbL]^{2+}$	14.2	±	0.1		11.3
DO3SAm	$Pb^{2+} + L \leftrightharpoons [PbL]^{2+}$	16.8	±	0.1		14.2
DO2A2S	$Pb^{2+} + H^{+} + L^{2-} \leftrightharpoons [PbHL]^{+}$	20.89	±	0.07	[a]	15.7
	$Pb^{2+} + L^{2-} \leftrightharpoons [PbL]$	18.2	±	0.1	[a]	
		18.3	±	0.1		

[a] Obtained by pH-potentiometry, I = 0.15 M $NaNO_3$, T = 25°C.
[b] pPb^{2+} calculated at $C_{Pb^{2+}} = 10^{-6}$ M and $C_L = 10^{-5}$ M and pH 7.4.

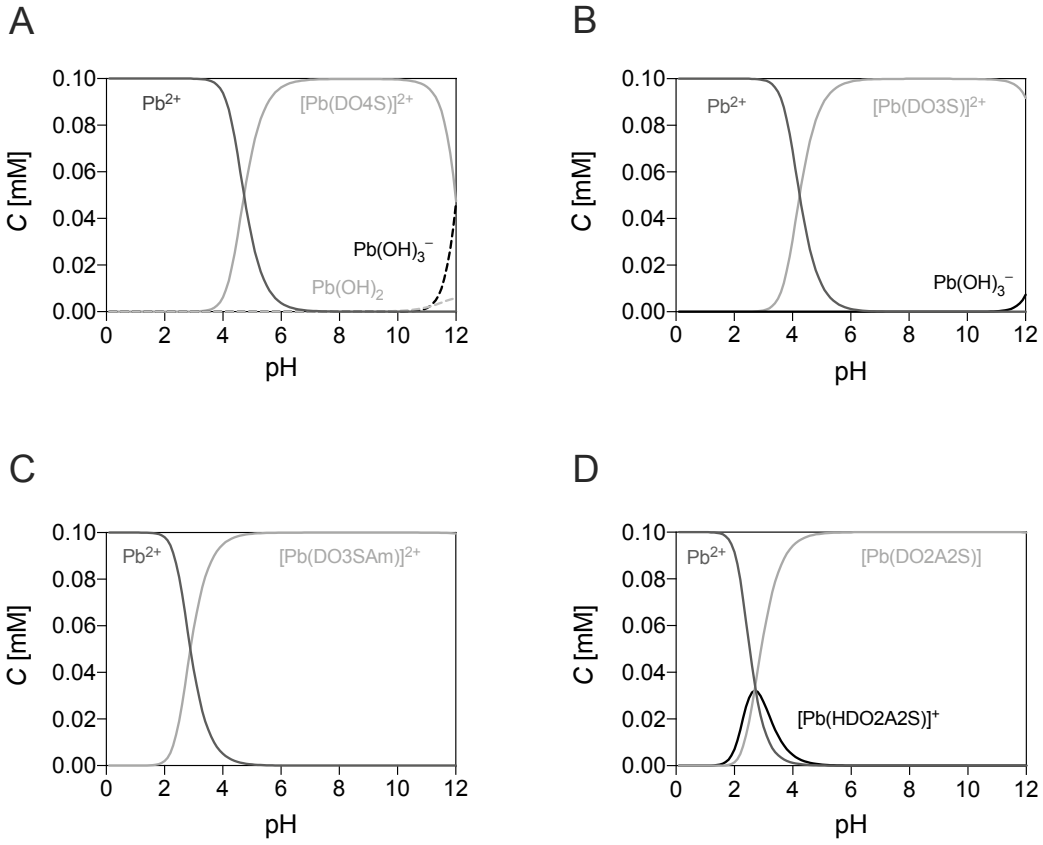

Figure 5.6. Distribution diagrams of (A) Pb^{2+}-DO4S, (B) Pb^{2+}-DO3S, (C) Pb^{2+}-DO3SAm and (D) Pb^{2+}-DO2A2S at $C_{Pb^{2+}} = C_L = 1 \cdot 10^{-4}$ M.

Comparison between the spectra of the free ligands and the Pb^{2+}-chelate undoubtedly probe the complexation as significant changes in chemical shift and coupling pattern are recognizable (**Figure 5.9** and **Figure 5.10**). In the pH range where the non-quantitative formation of the Pb^{2+}-complexes is expected from the speciation models (**Figure 5.6**), the spectra always appear as the convolution of those of the free ligands and the complexes.

With DO4S, DO3S and DO3SAm no proton content dependency of the ^1H NMR spectra was observed, indicating that a single species, *i.e.* $[PbL]^{2+}$, is involved in the equilibrium over the examined pH range, in agreement with the potentiometric and spectrophotometric data (*vide supra*). On the other hand, for Pb^{2+}-DO2A2S, the resonance of the CH_2 protons of the acetate side chains experienced a significant shift towards lower ppm with the pH increase, as shown in **Figure D2** (**Appendix D**). This is attributable to the chemical exchange between the monoprotonated and the deprotonated form of the complex, *i.e.* $[PbHL]^-$ and [PbL], which are simultaneously present at the equilibrium between pH 2 and 4 according to the previously described speciation model (**Figure 5.6**). The pK_a of the deprotonation process ($[PbHL]^+ \leftrightharpoons [PbL] + H^+$) estimated from the ^1H NMR data (pK_a = 2.6 ± 0.1), is in good agreement with the potentiometric data (**Table 5.1**).

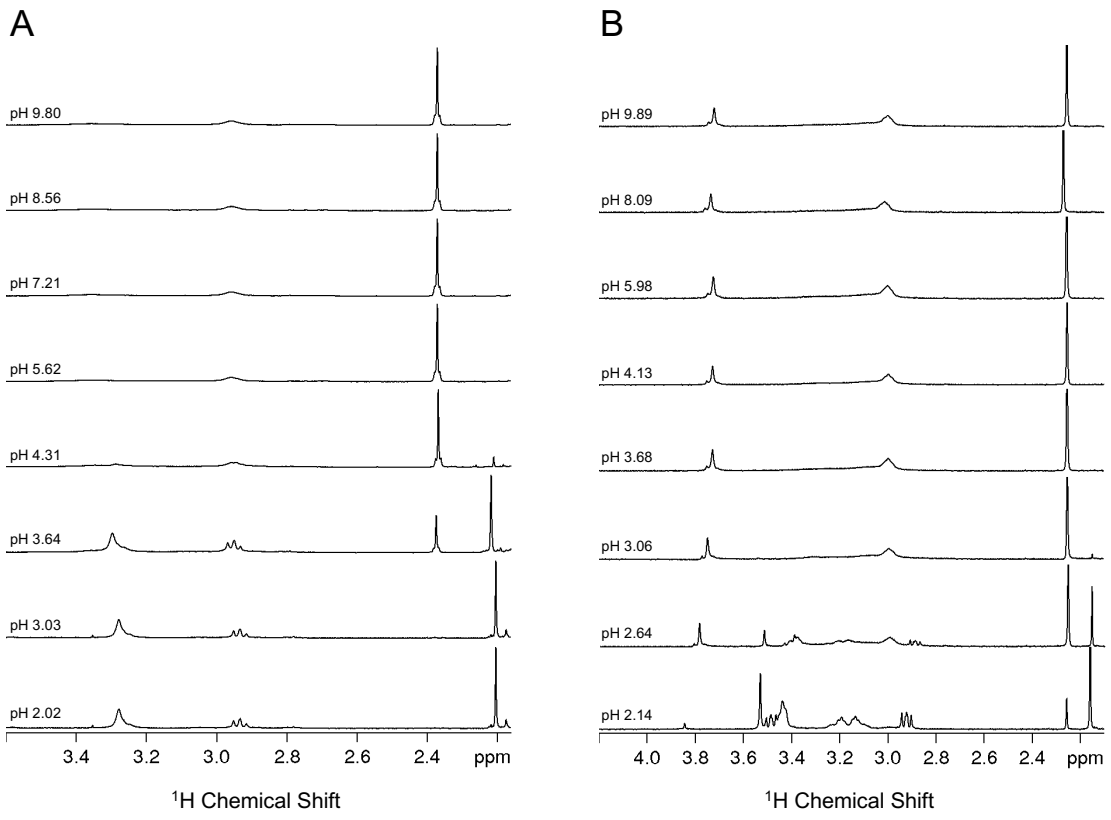

Figure 5.7. Variable-pH ^1H NMR spectra of (A) Pb^{2+}-DO4S and (B) Pb^{2+}-DO2A2S (400 MHz, T = 25°C, H_2O + 10% D_2O, $C_{Pb^{2+}} = C_L = 1.0 \cdot 10^{-3}$ M).

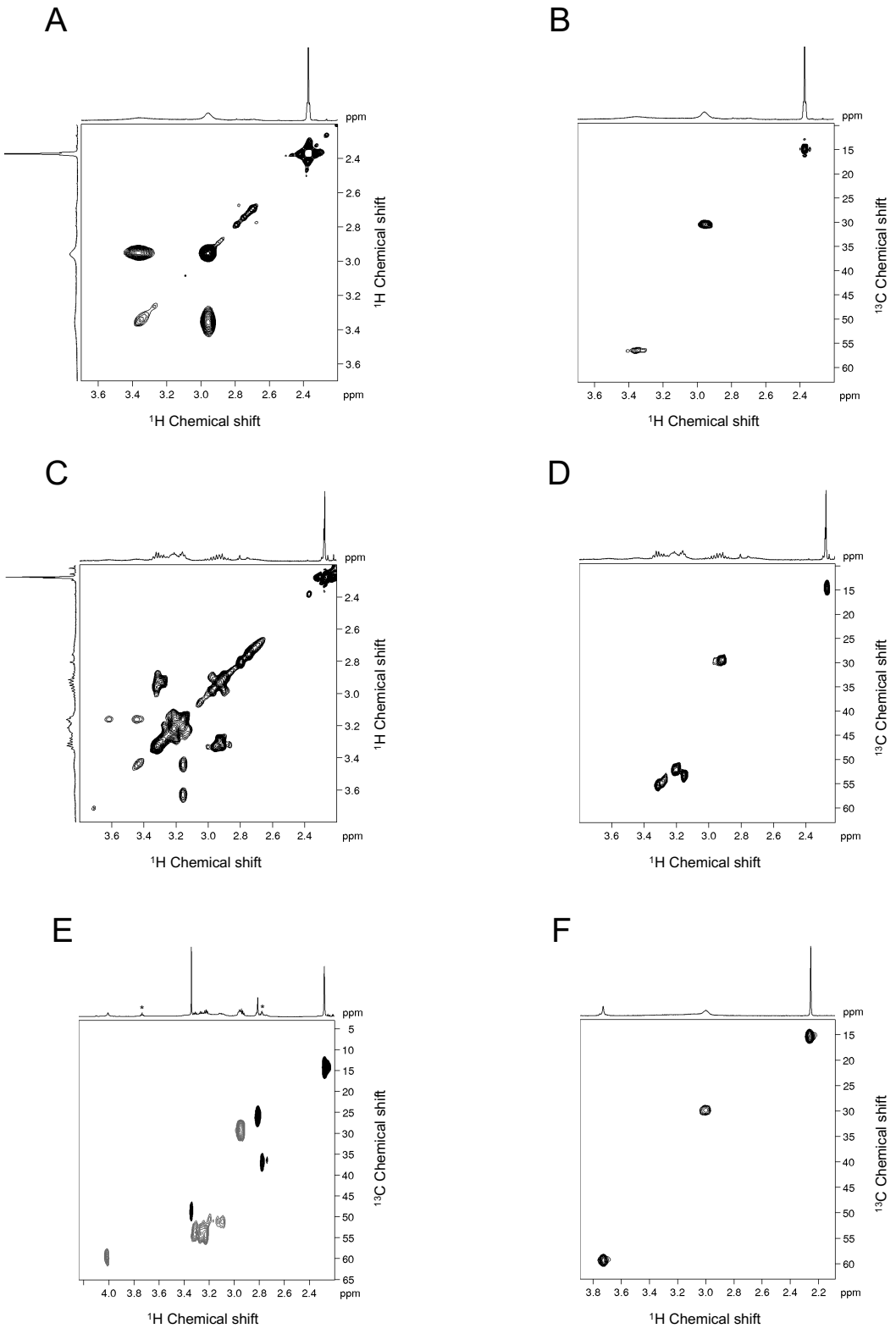

Figure 5.8. (A) ^{1}H-^{1}H TOCSY and (B) ^{1}H-^{13}C HSQC NMR spectra of $[Pb(DO4S)]^{2+}$ (400 MHz, *T* = 25°C, H_2O + 10% D_2O); (C) ^{1}H-^{1}H TOCSY and (D) ^{1}H-^{13}C HSQC NMR spectra of $[Pb(DO3S)]^{2+}$ (400 MHz, *T* = 25°C, H_2O + 10% D_2O); ^{1}H-^{13}C HSQC NMR spectra of (E) $[Pb(DO3SAm)]^{2+}$ (600 MHz, *T* = 25°C, H_2O + 10% D_2O) and (F) $[Pb(DO2A2S)]^{2+}$ (400 MHz, *T* = 25°C, H_2O + 10% D_2O).

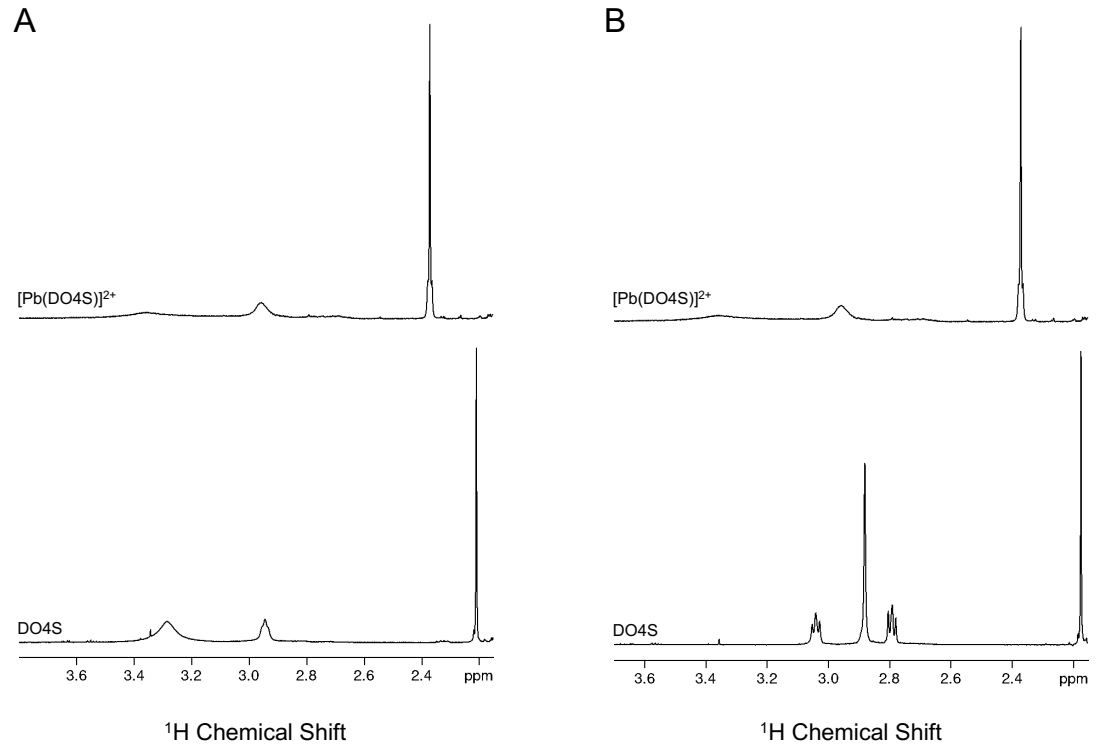

Figure 5.9. Comparison of the ^{1}H NMR spectra of free DO4S and $[Pb(DO4S)]^{2+}$ (400 MHz, *T* = 25°C, H_2O + 10% D_2O) at (A) pH 5 and (B) pH 9.

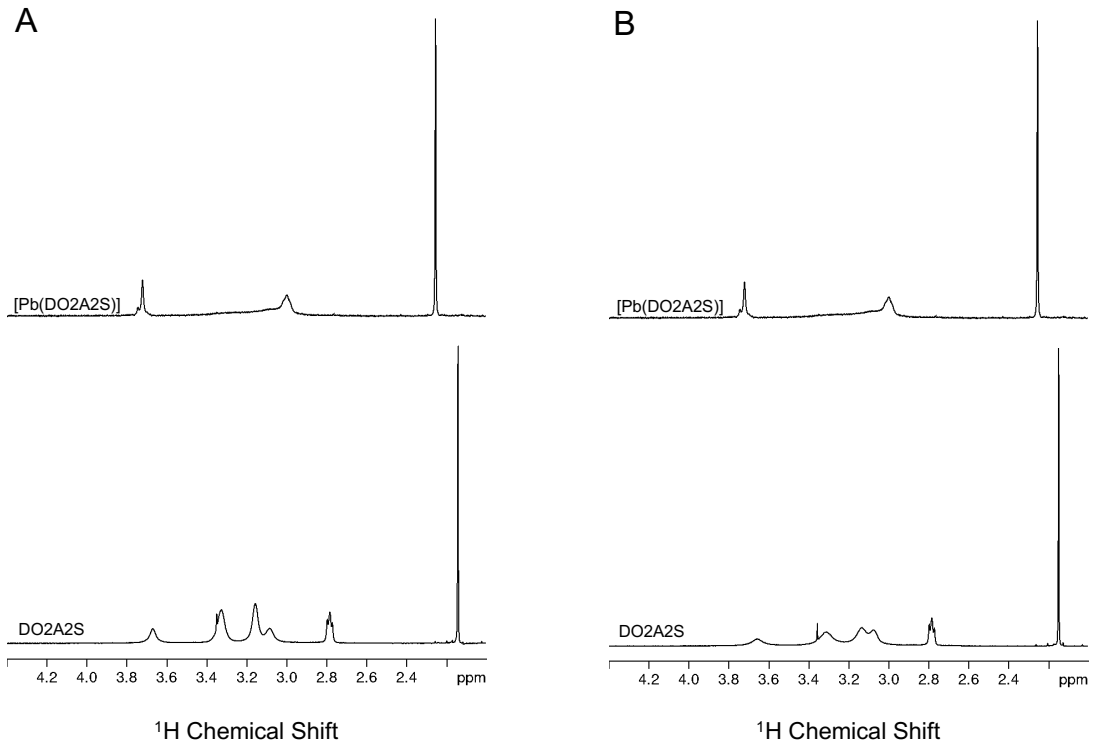

Figure 5.10. Comparison of the ^{1}H NMR spectra of free DO2A2S and [Pb(DO2A2S)] (400 MHz, *T* = 25°C, H_2O + 10% D_2O) at (A) pH 5 and (B) pH 9.

The ^{1}H-NMR spectra of $[Pb(DO4S)]^{2+}$ and [Pb(DO2A2S)] consist in a low number of extremely broad signals (**Figure 5.7**), presumably as a consequence of a high degree of symmetry combined with a fluxional solution behaviour. While the coordination of Pb^{2+} resulted in a significant local effect on shifts and broadening of macrocyclic ring and pendant nitrogen resonances, it had a less marked effect on resonances broadening of sulfanyl (SCH_3 and SCH_2) and acetate protons ($\underline{CH_2}COOH$). All the signals experience significant downfield shift upon complexation (**Figure 5.9** and **Figure 5.10**) likely because of the electron density donation from the ligand to the metal ion. This, combined with the Pb^{2+} coordination number preferences, suggests that both the cyclen core and the pendant arms are interacting on average with the metal ion to form an 8-coordinate structure. In $[Pb(DO4S)]^{2+}$, the simultaneous involvement of all the sulfur donors in the lead coordination can be undoubtedly stated by the appearance of two satellite peaks at 2.36 and 2.38 ppm (^{3}J = 6.1 Hz, abundance ~ 23%) around the SCH_3 singlet (δ_{SCH_3} = 2.37 ppm) which arise as a consequence of the ^{1}H-^{207}Pb coupling through sulfur atoms, Pb-S-CH_3, (**Figure 5.11**) being the isotope lead-207 an NMR-active nucleus (natural abundance: 22%, I = + 1/2). For [Pb(DO2A2S)], no satellites can be recognized for the SCH_3 protons (δ_{SCH_3} = 2.25 ppm) while for the CH_2COOH protons (δ_{CH_2COOH} = 3.72 ppm) they are present (**Figure 5.7**). These features suggest that the acetate arms are bound to Pb^{2+} in a non-fluxional mode while the SCH_3 are exchanging faster on the NMR timescale. Alternatively, the absence of coupling could be justified considering that the observed ^{3}J could be zero due to bond angle constraint. In contrast, the ^{1}H NMR spectra of $[Pb(DO3S)]^{2+}$ and $[Pb(DO3SAm)]^{2+}$ exhibited a more complicated pattern characterized by a higher number of sharper signals (**Figure D1** - **Appendix D**).

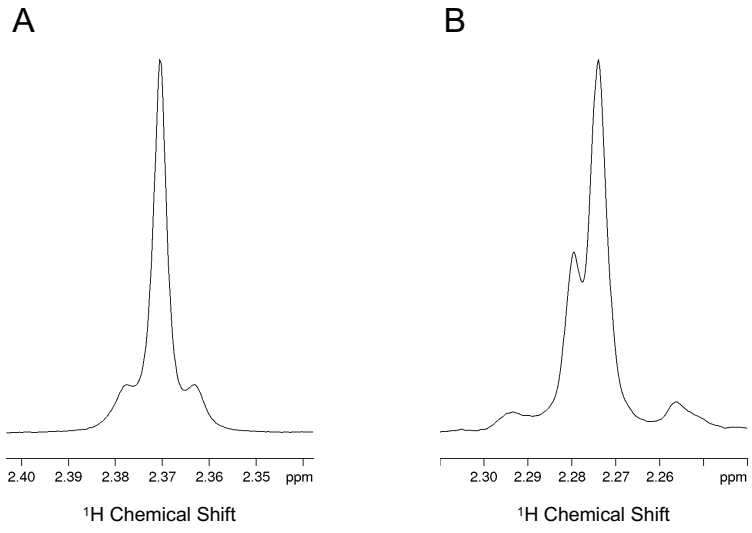

Figure 5.11. SCH_3 satellites of (A) $[Pb(DO4S)]^{2+}$ and (B) $[Pb(DO3S)]^{2+}$.

The former feature could arise from the lower symmetry of the ligands themself while the latter could suggest a slowed-down complex fluxionality with respect to DO4S and DO2A2S. For $[Pb(DO3S)]^{2+}$, the ^{1}H signals from chemically inequivalent N_1, N_7 and N_4 S-methyl groups resulted in almost coincident resonances but remain chemically distinct thus suggesting an asymmetry in the complex solution state ($\delta_{N_1,N_7\,SCH_3}$ = 2.27 ppm and $\delta_{N_3\,SCH_3}$ = 2.28 ppm) (**Figure D1** - **Appendix D**). The two satellites peaks at 2.25 and 2.29 ppm indicate the ^{207}Pb-SCH_3 coupling (^{3}J = 15 Hz). It is worth noting that the coupling is recognizable for the SCH_3 protons on N_1 and N_7 arms, thereby indicating that only the two opposite donors are statically bound to the metal ion with respect to the NMR timescale (**Figure 5.11**). The asymmetric arm may not be involved in the Pb^{2+} coordination or can be in a fast exchange or the coupling could be absent for geometrical reasons which induce a J = 0. The signal of $[Pb(DO3S)]^{2+}$ showed downfield shifts within the cyclen unit, and the pendants compared to the uncoordinated ligand, thereby indicating that each heteroatom is interacting on average to form a heptacoordinate solution structure. For $[Pb(DO3SAm)]^{2+}$, a slight inequivalence of the sulfanyl arms is pointed out by the presence of two singlets for the SCH_3 protons (**Table D3** - **Appendix D**). The absence of any ^{1}H-^{207}Pb coupling pattern, combined with the deshielding of the resonance with respect to the unbound ligand suggest that all the S donors are bound to the Pb^{2+} center but in a rapid exchange.

To further probe the coordination structure of the Pb^{2+} complexes, variable-temperature NMR (VT-NMR) were performed. For $[Pb(DO4S)]^{2+}$ and [Pb(DO2A2S)], the signals broadening observed at room temperature can be related to the fluxionality of the complexes in aqueous solution, which can include decoordination-coordination flip of the side chains, macrocycle ring turns, or both processes. As depicted in **Figure 5.12**, acquiring spectra at higher temperatures, from 5 to 65°C, resulted in signal sharpening. At 65°C, the extremely broad singlet, centred at 3.36 ppm for $[Pb(DO4S)]^{2+}$ and at 3.12 ppm for [Pb(DO2A2S)] at room temperature, split in two different groups of signals: a triplet at 3.37 ppm for the former and at 3.70 ppm for the latter and two broad quasi-symmetrical multiplets centred at 3.23 ppm and 3.29 ppm, respectively (**Figure 5.12**). While the triplet is attributed to the nitrogen-bound protons of the pendant arms, the multiplet arose from the non-equivalent proton environments of the NCH_2 groups of the cyclen ring (**Table D4** - **Appendix D**). As these signals resemble the simpler spectra of $[Pb(cyclen)]^{2+}$, where the multiplets arose from neighbouring protons on the macrocyclic scaffold becoming diasterotopic upon Pb^{2+} coordination and coupling to each other, the involvement of all N in the metal coordination sphere is further supported.[58] Similarly, the SCH_2 protons of the pendant arms resonate as triplets at 2.97 ppm for DO4S and 2.98 ppm for DO2A2S (**Table D4** - **Appendix D**). In both cases, below 25°C, all the nitrogen-bound protons coalesced in a single extremely broad singlet to such an extent that they nearly disappeared from the spectrum (**Figure 5.12**).

Contrarily, the SCH_3 protons of both complexes do not experience any variation with the temperature as they always resonate as a singlet. A slight peak broadening combined with the loss of the satellite peaks is observed at $T > 45°C$ for $[Pb(DO4S)]^{2+}$. This could suggest that at higher temperatures the sulfanyl side chains are not statically bound to the metal center but became chemically equivalent through fast intramolecular exchange on the NMR timescale.

When Pb^{2+} is bound to DO2A2S, the ^{1}H-^{207}Pb satellite peaks related to the acetate groups are present at $T > 25°C$ (^{3}J = 19 Hz), indicating that these donors are statically bound to Pb^{2+}. At 5°C, this signal became broader and starts to split: a slower transient dissociation and re-coordination of O-donors can be deduced. Combining these results, the lead coordination sphere in $[Pb(DO4S)]^{2+}$ and [Pb(DO2A2S)] can be depicted as a highly fluxionally octacoordinated environment.

$[Pb(DO3S)]^{2+}$ and $[Pb(DO3SAm)]^{2+}$ did not show a significant temperature-dependent variation of their resonances, suggesting a more rigid coordination environment. The solution fluxionality seems therefore to be correlated with the symmetry of the ligands themselves as only DO4S and DO2A2S possess this dynamic behaviour.

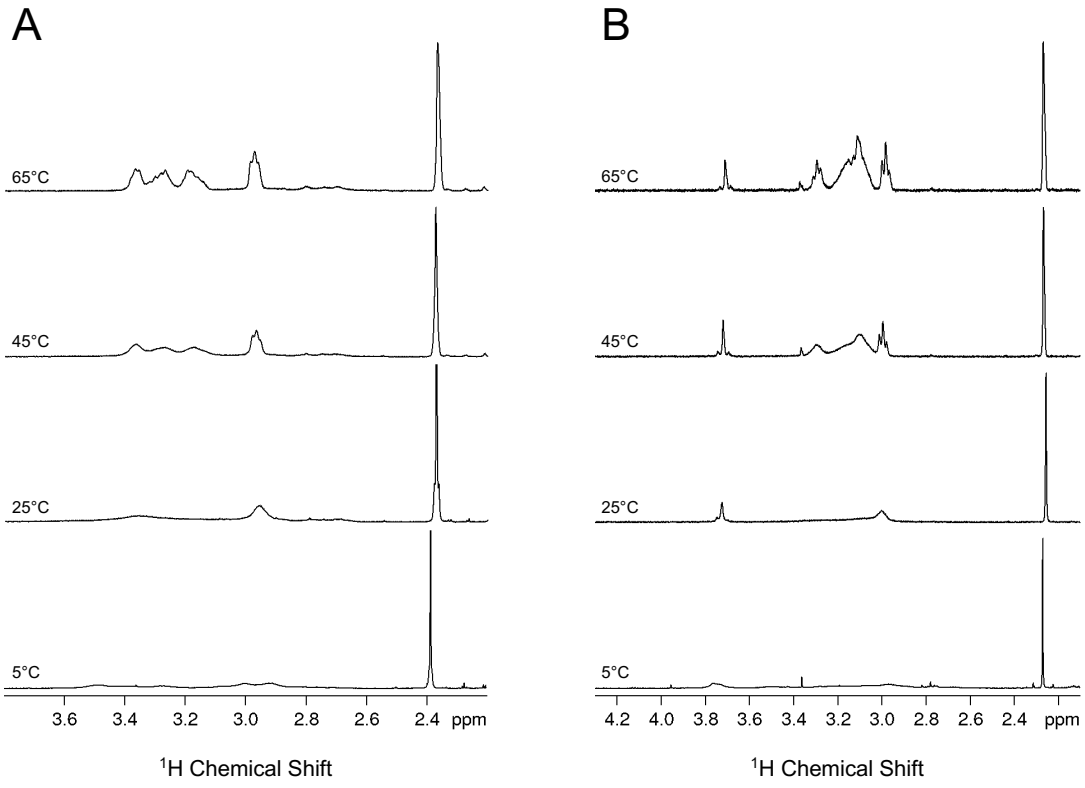

Figure 5.12. Variable-temperature NMR spectra of (A) $[Pb(DO4S)]^{2+}$ and (B) [Pb(DO2A2S)].

The role of the sulfanyl arms in the Pb^{2+} coordination is also supported by the observed absorption maxima shift towards higher wavelengths that occurs in the electronic spectra of the lead complexes as the set of sulfur donor atoms increases from DOTA to DO4S (**Figure 5.13**). The absorption band, attributed to the $6s^2 \rightarrow 6sp$ transition of the metallic centre, experiences a shift that resembles what happens on substituting water ligands on the Pb^{2+} ion with more covalently binding donors as reported in the literature for different ligands.[59] Consequently, the transition shift to lower energy, due to the increasing covalency of the Pb-L bond, can be justified if the involvement of more covalently binding S-donors in the lead coordination sphere is considered.

5.2.4 Acid-Mediated Dissociation Kinetics

Although thermodynamic parameters are very valuable as a first gauge to assess the performance of a chelating agent, they not always correlate to the *in vivo* stability as other factors (*e.g.*, competitive reactions) may become prevalent: the kinetic inertness of the complexes is another important property to be satisfied to ensure that the radiometal is not released *in vivo*.[60]

To complement the equilibrium studies, the kinetic inertness of the Pb^{2+} complexes was assessed by investigating their dissociation in acidic media at room temperature in differently concentrated HCl solutions by UV-Vis spectroscopy. These very low pH do not have a physiological equivalent, apart in particular intracellular environments which are generally difficult to reach; the study, therefore, aims to evaluate the behaviour of the complex in highly competitive conditions which can compromise their integrity, thus representing an indicator of their lability.

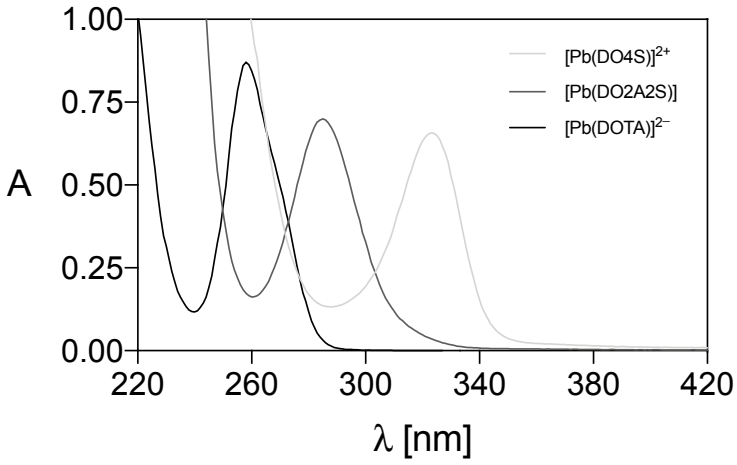

Figure 5.13. Comparison of the electronic spectra of $[Pb(DO4S)]^{2+}$, [Pb(DO2A2S)] and $[Pb(DOTA)]^{2-}$.

Representative spectral changes during the acid decomplexation assays are reported in **Figure 5.14** - **5.16**. The observed dissociation rates ($^{d}k_{obs}$) and the corresponding half-life ($t_{1/2}$) are collected in **Table 5.2** and **Table D5** (**Appendix D**), respectively.

While the Pb^{2+} complexes with DO2A2S only partially decomplex at 0.01 M HCl, a progressively faster and quantitative decomplexation is observed at higher proton concentration, in agreement with the thermodynamic data (**Figure 5.6**). $[Pb(DO4S)]^{2+}$, $[Pb(DO3S)]^{2+}$ and $[Pb(DO3SAm)]^{2+}$ quantitatively decomplex in all the tested conditions as predicted from their speciation (**Figure 5.6**). $[Pb(DO4S)]^{2+}$ demonstrated to be the most inert with respect to acid-mediated dissociation along the series as its $t_{1/2}$ was found to be ~ 4 h at 0.01 M HCl and decreased to ~ 1 min at 1 M HCl (**Table 5.2**). The corresponding values obtained for $[Pb(DO3S)]^{2+}$, $[Pb(DO3SAm)]^{2+}$ and [Pb(DO2A2S)] were lower and fairly similar; indeed, they presented an average $t_{1/2}$ of ~ 15 min already in 0.01 M HCl (**Table 5.2**).

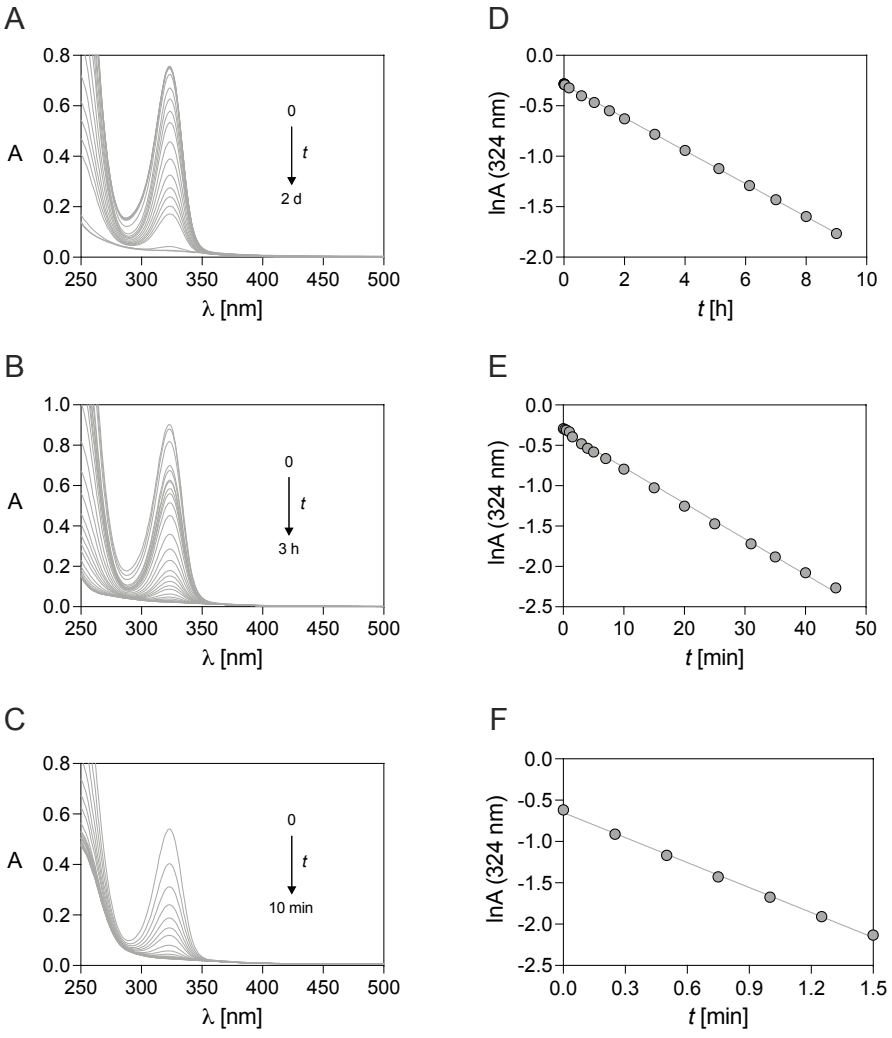

Figure 5.14. Acid decomplexation assay of $[Pb(DO4S)]^{2+}$ at (A) pH 2, (B) pH 1 and (C) pH 0; (D, E, F) ln*A vs. t* and corresponding fitting lines.

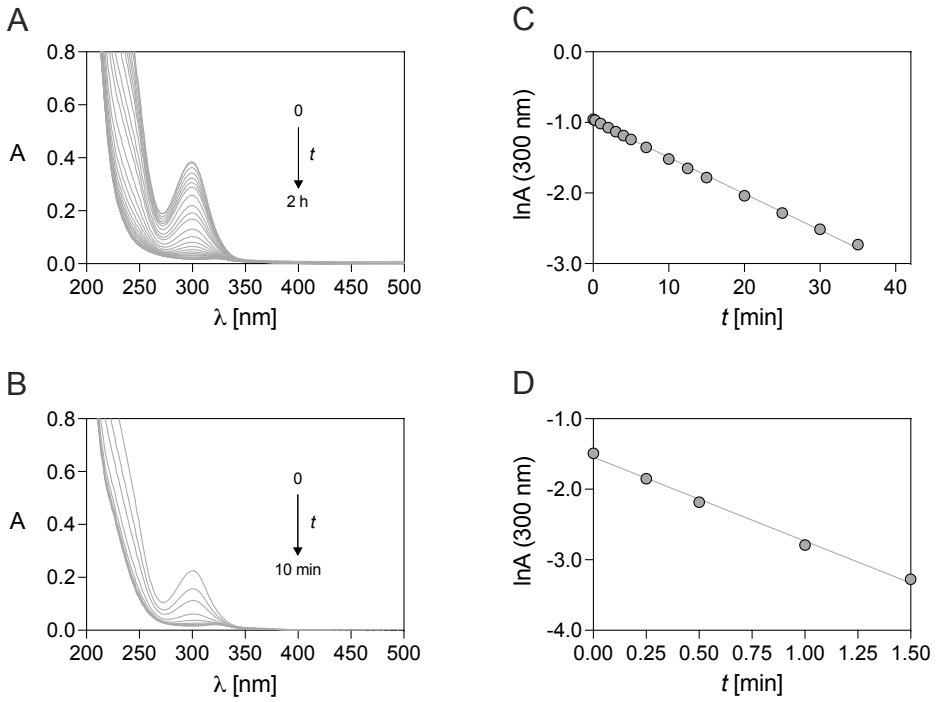

Figure 5.15. Acid decomplexation assay of $[Pb(DO3S)]^{2+}$ at (A) pH 2 and (B) pH 1; (C, D) ln*A vs. t* and corresponding fitting lines.

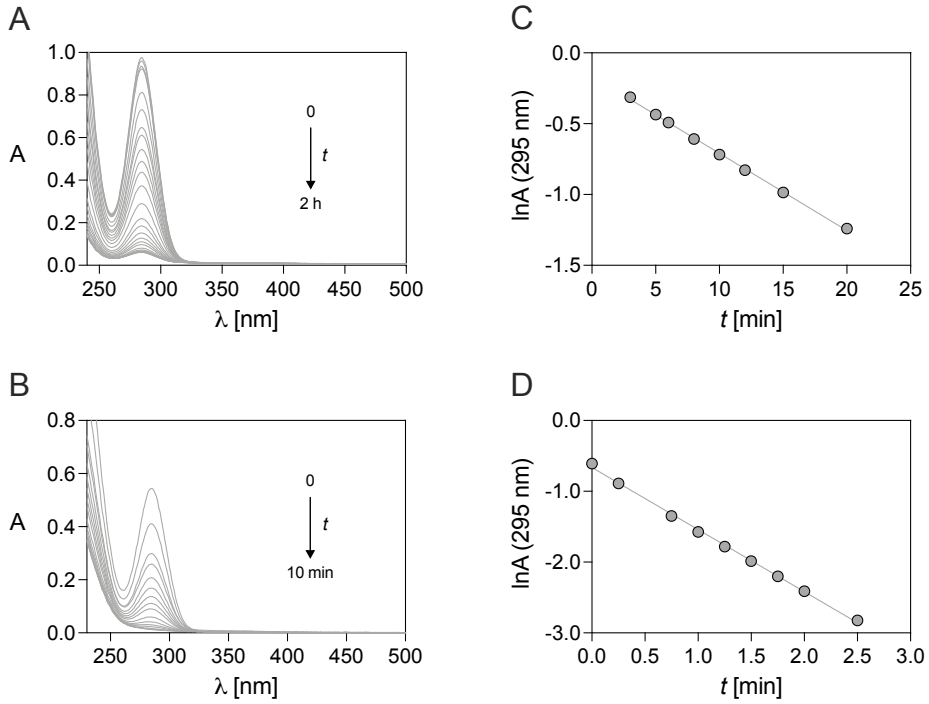

Figure 5.16. Acid decomplexation assay of [Pb(DO2A2S)] at (A) pH 2 and (B) pH 1; (C, D) ln*A vs. t* and corresponding fitting lines.

While the presence of O-donors in the pendant arms of DO2A2S and DO3SAm increase the complexes' stability, the highest number of S-donors in DO4S increases its inertness likely because of the absence of acid-base competitive equilibria on the binding moiety SCH_3. The comparable inertness of $[Pb(DO3S)]^{2+}$ with respect to the carboxylic/amide derivatives could be related to the non-fully saturated coordination sphere around the metal centre.
However, if the dissociation properties are compared with the values of Pb^{2+}-DOTA, it is evident that all the sulfur-bearing Pb^{2+}-complexes are more labile in acidic conditions compared to the former. This is likely related to the higher thermodynamic stability of the Pb^{2+}-DOTA complex.

Table 5.2. Half-life ($t_{1/2}$) for the acid-assisted dissociation reactions of the Pb^{2+} complexes with first-generation ligands in aqueous HCl at room temperature. Data for Pb^{2+}-DOTA are reported for comparison purposes.

HCl [M]	$t_{1/2}$ [min]				
	$[Pb(DO4S)]^{2+}$	$[Pb(DO3S)]^{2+}$	$[Pb(DO3SAm)]^{2+}$	[Pb(DO2A2S)]	$[Pb(DOTA)]^{2-}$
0.01	240 ± 25	12 ± 2	22 ± 4	15 ± 4 [(a)]	[(a)]
0.1	18 ± 3	0.47 ± 0.09	1.6 ± 0.2	1.1 ± 0.4	33 ± 2
1	0.66 ± 0.03	[(b)]	[(b)]	[(b)]	3.8 ± 0.2

[(a)] Not quantitative decomplexation.
[(b)] Instantaneous decomplexation during the reagent mixing time.

5.2.5 Lead-203 Radiolabelling

Concentration-dependent radiolabelling with $[^{203}Pb]Pb^{2+}$ was conducted under mild reaction conditions (room temperature, pH 7, 1 h) to determine the chelating ability of the sulfur bearing ligands in extremely low concentrations. The obtained results are shown in **Figure 5.17**. The state-of-the-art ligand for Pb^{2+} complexation, *i.e.* TCMC, gave quantitative radiochemical yields (RCY) at ligand concentrations higher than 10^{-6} M while the RCY dropped to 41 ± 1% lowering its concentration to 10^{-7} M. When the amide donors of TCMC were replaced by sulfanyl arms in DO4S and DO3S, the RCY reduced sequentially to 81 ± 10%, 55 ± 2%, 16 ± 3%, 1.4 ± 0.4% from 10^{-4} to 10^{-7} M for the former and to 88 ± 1%, 55 ± 10%, 15 ± 4%, 2 ± 1% for the latter. The presence of carboxylic/amide donors in DO2A2S and DO3SAm drastically improved the RCY when compared with the pure sulfur bearing analogues. Indeed, both the chelators were able to efficiently complex $[^{203}Pb]Pb^{2+}$ at ligand concentrations of 10^{-4} M and 10^{-5} M (RCYs > 90%). At 10^{-6} M and 10^{-7} M, the RCY decreased to 68 ± 1% and 56 ± 4% for the former and 68 ± 4% and 14 ± 4% for the latter.

DOTA was previously found to be able to complex $[^{203}Pb]Pb^{2+}$ with radiochemical yields of 96 ± 1%, 76 ± 9%, 3 ± 1%, and 1.5 ± 0.2% at concentrations from 10^{-4} M to 10^{-7} M, respectively.[11] The obtained results pointed out that, under these conditions, DO2A2S and DO3SAm are superior to DOTA but slightly less efficient than TCMC at complexing $[^{203}Pb]Pb^{2+}$. As shown in **Figure 5.18**, shortening the reaction times had no negative effect on RCY with DO2A2S and DO3SAm as well as for TCMC. On the other hand, DO4S and DO3S demonstrated a slowed-down reactivity as the RCY increased from ~ 35% after 5 min to ~ 81% after 1 h for the former and from ~ 65% after 5 min to ~ 88% after 1 h for the latter. The reactivity trend observed during the $[^{203}Pb]Pb^{2+}$ labelling experiments entirely reflects the results obtained during the kinetic evaluation with the stable Pb^{2+} (*vide supra*).

Radiolabelling studies with TACD3S, TRI4S and TE4S revealed a poor ability to coordinate $[^{203}Pb]Pb^{2+}$ as no radiometal incorporation was observed at room temperature albeit using the highest ligand concentration assessed (10^{-4} M). RCYs were only slightly improved through heating at 80°C (**Figure 5.19**). These results are consistent with a low thermodynamic stability of the Pb^{2+} complexes with non-cyclen-based scaffolds (*vide supra*).

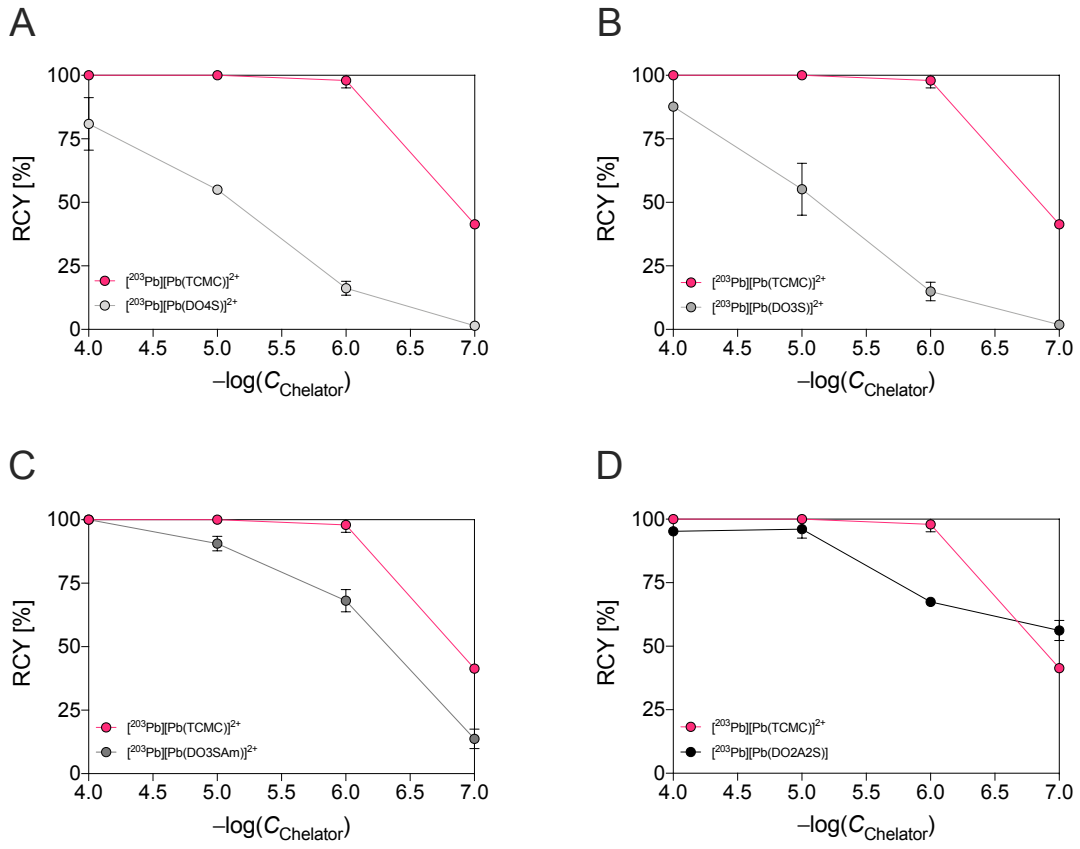

Figure 5.17. Concentration-dependent radiolabelling of the first-generation ligands at pH 7 with $[^{203}Pb]Pb^{2+}$ (124 kBq) after 1 hour at room temperature (n = 3).

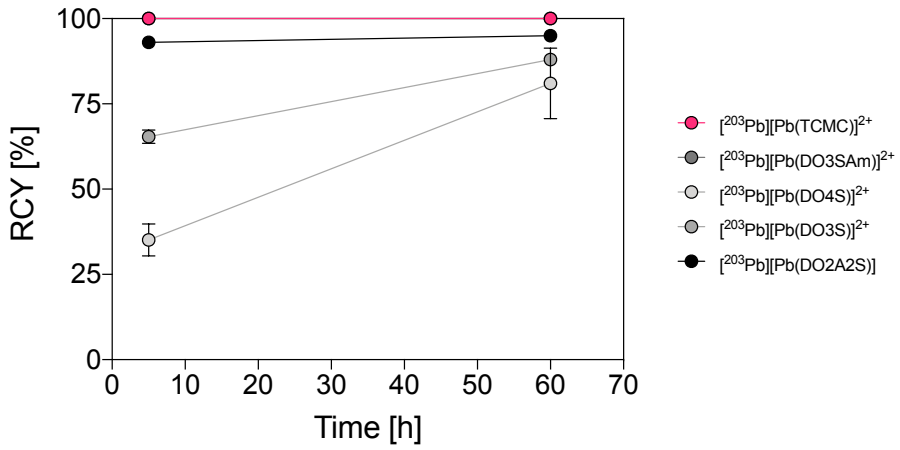

Figure 5.18. Time-dependent radiochemical yields at room temperature for $[^{203}Pb][Pb(DO4S)]^{2+}$, $[^{203}Pb][Pb(DO3S)]^{2+}$, $[^{203}Pb][Pb(DO3SAm)]^{2+}$, $[^{203}Pb][Pb(DO2A2S)]$, $[^{203}Pb][Pb(TCMC)]^{2+}$ (124 kBq $[^{203}Pb]Pb^{2+}$, pH 7, $C_L = 10^{-4}$ M).

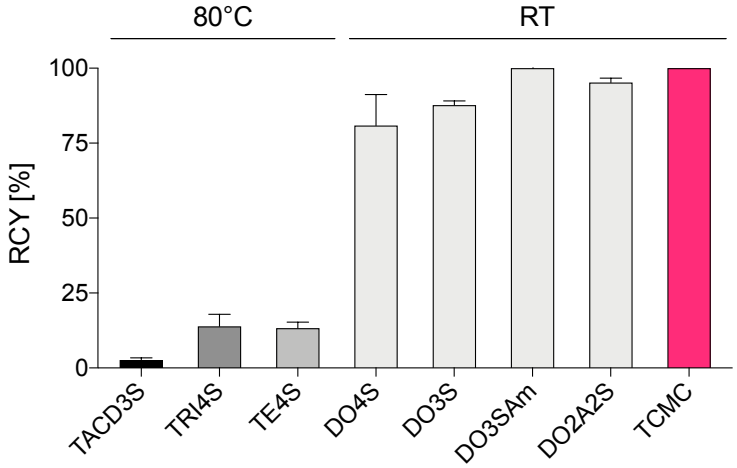

Figure 5.19. Comparison of the radiochemical yields of $[^{203}Pb][Pb(TACD3S)]^{2+}$, $[^{203}Pb][Pb(TRI4S)]^{2+}$, $[^{203}Pb][Pb(TE4S)]^{2+}$ and first-generation ligands (124 kBq $[^{203}Pb]Pb^{2+}$, $C_L = 10^{-4}$ M) at pH 7 after 1 h.

5.2.6 *In Vitro* Human Serum Stability

The *in vitro* human serum stability of $[^{203}Pb][Pb(DO4S)]^{2+}$, $[^{203}Pb][Pb(DO3SAm)]^{2+}$ and $[^{203}Pb][Pb(DO2A2S)]$ was evaluated to assess their integrity in presence of biologically relevant substrates that can compete and displace chelator bound metal ions *in vivo*. The obtained results are shown in **Figure 5.20**.

$[^{203}Pb][Pb(DO2A2S)]$ and $[^{203}Pb][Pb(DO3SAm)]^{2+}$ retained favourable integrity over the course of 24 h, with ≤ 5% transchelation to serum proteins.

After 72 h, there is a progressive decrease of the percentage of intact complex (84 ± 8% for DO3SAm and 70 ± 4% for DO2A2S). In comparison, the state-of-the-art, TCMC, was found to be slightly more robust compared to DO3SAm.
$[^{203}Pb][Pb(DO4S]^{2+}$ was only moderately stable in human serum, remaining 80 ± 5% intact after 24 h while significant decomplexation was observed over 72 h (53 ± 3%).

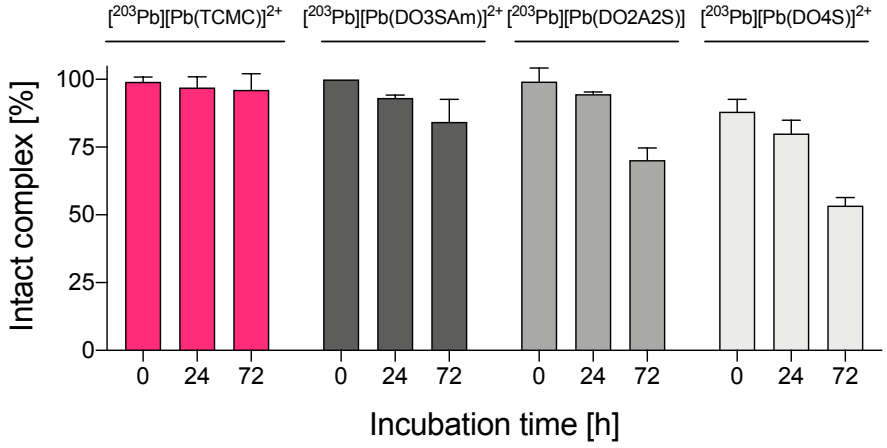

Figure 5.20. Human serum stability of $[^{203}Pb]Pb^{2+}$ complexes at 37°C over 3 days (*n* = 3 *per* time points).

5.3 Experimental Section

5.3.1 Materials and Methods

All chemicals were obtained from commercial suppliers and were used as received without further purification. DOTA and TCMC were purchased from Chematech. DO4S, DO3S, DO3SAm, DO2A2S, TACD3S, TRI4S and TE4S were synthesized according to the procedures reported in **Chapter 2**. Lead chloride ($PbCl_2$) and lead nitrate ($Pb(NO_3)_2$) were purchased from Sigma-Aldrich. All solutions were prepared using ultrapure water (18.2 MΩ cm^{-1}) purified using a Purelab Chorus (Veolia) or a Milli-Q Millipore system.

5.3.2 Lead Complexation Kinetics

The formation kinetics of the Pb^{2+} complexes was evaluated at room temperature by UV-Vis or NMR spectroscopies as described in **Chapter 4**. A typical experiment was performed by mixing equimolar amounts of metal and ligand solutions (final concentrations: $C_{Pb^{2+}} = C_L = 10^{-4}$ M for the UV-Vis measurements; $C_{Pb^{2+}} = C_L = 10^{-3}$ M for the NMR measurements) in buffered media at pH 2 (HCl 10^{-2} M), pH 3.7 (acetic/acetate buffer), pH 5 (formic/formiate buffer) and pH 7.4 (2-[4-(2-hydroxyethyl)piperazin-1-yl]ethane sulfonic acid - HEPES -

buffer). To prevent the formation of $PbCO_3$ (K_s = $7.4 \cdot 10^{-14}$), water was boiled before the measurements.

The electronic and ^{1}H-NMR spectra were collected using the same set-up described in the previous chapters and the complexation reactions were monitored by the increase of the absorption peaks diagnostic of the Pb^{2+}-ligand complex formation at the characteristic wavelength (**Table D2** - **Appendix D**) over time.

5.3.3 Thermodynamic Measurements

The experimental procedures[****], the details of the apparatus as well as the data processing for the pH-potentiometric, UV-Vis spectrophotometric and NMR titrations followed those reported in **Chapter 3** and **Chapter 4**. Variable-temperature NMR were performed as described in **Chapter 3**.

5.3.4 Acid-mediated Dissociation Kinetics

The dissociation kinetics of the Pb^{2+} complexes were studied under pseudo-first-order conditions in aqueous solution at room temperature without control of the ionic strength by addition of concentrated aqueous solution of HCl (0.01 to 1 M) to aqueous solution of the preformed complexes. The concentration of the Pb^{2+} complexes after the H^+ addition was $1 \cdot 10^{-4}$ M. Dissociation reaction was followed by the decreasing intensity of the absorption band of the complexes at the characteristic wavelength (**Table D2** - **Appendix D**) using the same apparatus described in **Chapter 4** for the acid-mediated dissociation kinetics of the Cu^{2+} complexes.

5.3.5 Lead-203 Radiolabelling and Human Serum Stability

Caution! ^{203}Pb is a radionuclide that emits ionizing radiation, and it was manipulated in a specifically designed facility under appropriate safety controls.

^{203}Pb Production. ^{203}Pb was produced *via* the ^{203}Tl (p,n)^{203}Pb reaction at TRIUMF's TR13 cyclotron following a previously reported method.[11] Lead was obtained as [^{203}Pb]$Pb(OAc)_2$ in 1 M ammonium acetate (pH 7) solution.

^{203}Pb Radiolabelling. Stock solutions of the ligands (10^{-3} M) were prepared in ultrapure deionized H_2O and diluted appropriately to give serial dilution series (10^{-4} - 10^{-6} M).

[****] Lead solutions were preprepared from analytical grade chloride ($PbCl_2$, Sigma Aldrich, 99%) or nitrate ($Pb(NO_3)_2$, Sigma Aldrich, 99%) salts and standardized using complexometric titrations with ethylenediaminetetraacetic acid (EDTA) with xylenole orange as indicator.

Concentration-dependent radiolabelling were performed by addition of [^{203}Pb]Pb^{2+} (10 µL, 124 kBq) to a solution containing the ligand (10 µL, 10^{-3} - 10^{-6} M) diluted in ammonium acetate buffer (80 µL, 1 M, pH 7). Water was used instead of the ligands as a negative control. All the radiolabelling for the first-generation macrocycles were performed at room temperature and monitored at 5 min and 1 h time points whereas heating at 80°C was employed for second-generation ligands. All radiolabelling reactions were repeated at least in triplicate. Radiochemical yields (RCY%) were determined *via* instant thin-layer chromatography (iTLC) with silicic acid (SA)-impregnated paper TLC plates (iTLC-SA, Agilent Technologies, USA). EDTA (50 mM, pH 5.5) was used as eluent. Under these conditions free [^{203}Pb]Pb^{2+} migrates with the solvent front (R_f = 1) while [^{203}Pb]Pb^{2+}-complexes remain at the baseline (R_f = 0). iTLC-plates were analyzed on an Eckert & Ziegler AR-2000 TLC scanner and all the data were processed with Eckert & Ziegler WinScan software. Representative TLC radiochromatograms are presented in **Figure D3** (**Appendix D**).

Human serum stability. The stability of the [^{203}Pb]Pb^{2+}-complexes, prepared using the radiolabelling protocol described above, was assessed by incubation in human plasma at 37°C (1:1 *v*/*v* dilution) at varying time points. The metal-complex stability was monitored over the course of 3 days *via* iTLC using the same protocol described for the radiolabelling studies.

5.4 Conclusion

A series of polyazamacrocycles incorporating S-donor pendants were investigated in the present chapter as potential ligands for [$^{203/212}$Pb]Pb^{2+} theranostic pair chelation. The rationale behind the selection of the investigated chelators was the hypothesis that the introduction of sulfanyl pendants could have improved the stability and the inertness of the resulting Pb^{2+} complexes over their carboxylic acid/amide-bearing counterparts as softer donors could have optimally complemented the borderline-soft nature of Pb^{2+}.

Contrary to the initial naive expectations, combined UV-Vis spectrophotometric and pH-potentiometric titrations revealed that the introduction of S-donors on the pendant arms on the cyclen scaffold induces a progressive drop of their thermodynamic stability, by about 5 log units from DO2A2S (pPb^{2+} = 15.7) to DO4S (pPb^{2+} = 10.2). On the other hand, the highest number of S-donors in DO4S increases its kinetic inertness in highly acidic environments with respect to the O-containing analogues, *i.e.* DO2A2S and DO3SAm, likely because of the absence of acid-base competitive equilibria on the binding moiety SCH_3.

The lower inertness of Pb^{2+}-DO3S with respect to DO4S could be related to the non-functionalized N that restricts DO3S to an heptadentate coordination mode.

Furthermore, variable-temperature NMR studies gave insights into the geometry of the Pb^{2+}-complexes, indicating that an averaged highly fluxional symmetric octa-coordinated complex is formed in solution when Pb^{2+} is bound to DO4S or DO2A2S. On the other hand, the introduction of asymmetry in the ligand structure in DO3S and DO3SAm afforded a more static coordination environment.

No complexation was observed when the cyclen core was substituted with a larger ring in TRI4S and TE4S or fewer nitrogen donors in TACD3S, likely a result of a mismatch between the metal ion and the ring cavity. This highlights the importance of considering the correct macrocyclic platform for the future development of macrocyclic chelators for $[^{203/212}Pb]Pb^{2+}$.

To evaluate the complexation efficiency of the first-generation ligands in extremely diluted conditions, concentration-dependent radiolabelling with $[^{203}Pb]Pb^{2+}$ were performed. While DO4S and DO3S displayed modest labelling performances, DO2A2S and DO3SAm demonstrated quantitative radiochemical yields under mild conditions (room temperature, 1 h) at a chelator concentration as low as 10^{-6} M.

As a final assessment of the potential of these chelators for $[^{203/212}Pb]Pb^{2+}$ theranostic pair chelation, the *in vitro* serum stability was evaluated. $[^{203}Pb][Pb(DO4S)]^{2+}$ was only moderately inert (80 ± 5%, n = 3) whereas $[^{203}Pb][Pb(DO3SAm)]^{2+}$ (93 ± 1%, n = 3) and $[^{203}Pb][Pb(DO2A2S)]$ (94 ± 1%, n = 3) demonstrated favorable robustness over 24 h.

Despite the lower thermodynamic stability and kinetic inertness of the Pb^{2+} complexes with the S- and O-containing macrocycles, *i.e.* DO3SAm and DO2A2S, compared to the state-of-the-art $[^{203}Pb]Pb^{2+}$ chelators, *i.e.* DOTA and TCMC, their ability to form an inert complex in serum at least for 24 h makes them viable candidates for nuclear medicine applications.

Author Contributions

M. Tosato designed the experiments, analyzed and interpreted the data. UV-Vis and NMR spectroscopic measurements and potentiometric titrations were conducted by the Master's student L. Lazzari under the supervision of M. Tosato. Lead-203 was produced and separated by B. L. McNeil and P. Randhawa at TRIUMF (Vancouver, BC, Canada). Radiolabelling and human serum stability experiments were performed by P. Randhawa at TRIUMF (Vancouver, BC, Canada). Prof. C. F. Ramogida was responsible of the radiochemistry experiments. Prof. V. Di Marco oversaw and supervised the study. The draft of the manuscript was written by M. Tosato.

5.5 References

1 F. Guérard, J. F. Gestin and M. W. Brechbiel, *Cancer Biother. Radiopharm.*, 2013, **28**, 1-20.

2 A. K. H. Robertson, B. L. McNeil, H. Yang, D. Gendron, R. Perron, V. Radchenko, S. Zeisler, P. Causey and P. Schaffer, *Inorg. Chem.*, 2020, **59**, 12156-12165.

3 M. Miederer, D. Scheinberg and M. McDevitt, *Adv. Drug Deliv. Rev.*, 2008, **60**, 1371-1382.

4 L. Li, J. Rousseau, M. de Guadalupe Jaraquemada-Peláez, X. Wang, A. Robertson, V. Radchenko, P. Schaffer, K.S. Lin, F. Bénard and C. Orvig, *Bioconjugate Chem*, 2020, **32**, 1348-1363.

5 M. McDevitt, D. Ma, J. Simon, R. Frank and D. Scheinberg, *Appl. Radiat. Isot.*, 2002, **57**, 841-847.

6 H. Yang, C. Zhang, Z. Yuan, C. Rodriguez-Rodriguez, A. Robertson, V. Radchenko, R. Perron, D. Gendron, P. Causey, F. Gao, F. Bénard and P. Schaffer, *Chemistry*, 2020, **26**, 11435-11440.

7 F. Guerard, J. Barbet, J. F. Chatal, F. Kraeber-Bodere, C. M. and F. Haddad, *J. Nuc. Med. Mol. Imaging*, 2015, **59**, 161-167.

8 M. G. Ferrier, V. Radchenko and D. S. Wilbur, *Radiochim. Acta*, 2019, **107**, 1065-1085.

9 A. Ingham, T. I. Kostelnik, B. L. McNeil, B. O. Patrick, N. Choudhary, M. de Guadalupe Jaraquemada-Peláez and C. Orvig, *Dalton Trans.*, 2021, **50**, 11579-11595.

10 D. Màthe, K. Szigeti, N. Hegedűs, I. Horvath, D. S. Veres, B. Kovacs and Z. Szűcs, *Appl. Radiat. Isot.*, 2016, **114**, 1-6.

11 B. L. McNeil, A. K. H. Robertson, W. Fu, H. Yang, C. Hoehr, C. F. Ramogida and P. Schaffer, *EJNMMI Radiopharm. Chem.*, 2021, **6**, 6.

12 I. Carbo-Bague and C. F. Ramogida, in *Encyclopedia of Inorganic and Bioinorganic Chemistry*, 2021.

13 L. M. P. Lima, M. Beyler, R. Delgado, C. Platas-Iglesias and R. Tripier, *Inorg. Chem.*, 2015, **54**, 7045-7057.

14 M. G. Ferrier, Y. Li, M. K. Chyan, R. Wong, L. Li, S. Spreckelmeyer, D. K. Hamlin, T. Mastren, M. E. Fassbender, C. Orvig and D. S. Wilbur, *J. Label. Compd. Radiopharm.*, 2020, **63**, 502-516.

15 K. Yong and M. W. Brechbiel, *Dalton Trans.*, 2011, **40**, 6068-6076.

16 C. G. Pippin, T. J. McMurry, M. W. Brechbiel, M. McDonald, R. Lambrecht, D. Milenic, M. Roselli, D. Colcher and O. A. Gansow, *Inorg. Chim. Acta*, 1995, **239**, 43-51.

17 E. Horak, F. Hartmann, K. Garmestani, C. C. Wu, M. W. Brechbiel, O. A. Gansow, N. F. Landolfi and T. A. Waldmann, *J. Nucl. Med.*, 1997, **38**, 1944-1950.

18 G. Ruble, C. Wu, R. A. Squire, O. A. Gansow and M. Strand, *Int. J. Radiat. Oncol*, 1996, **34**, 609-616.

19 S. A. Hassfjell, *Appl. Radiat. Isot.*, 2001, **55**, 433-439.

20 S. P. Hassfjell and P. A. Hoff, *Appl. Radiat. Isot.*, 1994, **45**, 1021-1025.
21 G. L. Zucchini and A. M. Friedman, *Int J Nucl Med Biol*, 1982, **9**, 83-84.
22 S. Mirzadeh, *Appl. Radiat. Isot.*, 1998, **49**, 345-349.
23 B. Bartoś, K. Lyczko, A. Kasperek, S. Krajewski and A. Bilewicz, *J. Radioanal. Nucl. Chem*, 2013, **295**, 205-209.
24 K. E. Baidoo, D. E. Milenic and M. W. Brechbiel, *Nucl Med Biol*, 2013, **40**, 592-599.
25 M. Li, X. Zhang, T. P. Quinn, D. Lee, D. Liu, F. Kunkel, B. E. Zimmerman, D. McAlister, K. Olewein, Y. Menda, S. Mirzadeh, R. Copping, F. L. Johnson and M. K. Schultz, *Appl. Radiat. Isot.*, 2017, **127**, 52-60.
26 P. L. Horlock, M. L. Thakur and I. A. Watson, *Postgrad. Med. J.*, 1975, **51**, 751-754.
27 K. Garmestani, D. E. Milenic, E. D. Brady, P. S. Plascjak and M. W. Brechbiel, *Nucl. Med. Biol.*, 2005, **32**, 301-305.
28 R. F. Meredith, J. Torgue, M. T. Azure, S. Shen, S. Saddekni, E. Banaga, R. Carlise, P. Bunch, D. Yoder and R. Alvarez, *Cancer Biother. Radiopharm.*, 2014, **29**, 12-17.
29 R. F. Meredith, J. J. Torgue, T. A. Rozgaja, E. P. Banaga, P. W. Bunch, R. D. Alvarez, J. M. Straughn, M. C. Dobelbower and A. M. Lowy, *Am J Clin Oncol.*, 2018, **41**, 716-721.
30 K. J. Yong, D. E. Milenic, K. E. Baidoo and M. W. Brechbiel, *Mol Cancer Ther.*, 2012, **11**, 639-648.
31 K. J. Yong, D. E. Milenic, K. E. Baidoo and M. W. Brechbiel, *Int J Radiat Oncol Biol Phys*, 2013, **85**, 1119-1126.
32 K. J. Yong, D. E. Milenic, K. E. Baidoo and M. W. Brechbiel, *Br J Cancer*, 2013, **108**, 2013-2020.
33 K. J. Yong, D. E. Milenic, K. E. Baidoo and M. W. Brechbiel, *PLoS One*, 2014, **9**, e108511.
34 D. E. Milenic, K. Garmestani, E. D. Brady, P. S. Albert, A. Abdulla, J. Flynn and M. W. Brechbiel, *Clin. Cancer Res.*, 2007, **13**, 1926-1935.
35 J. C. Dos Santos, M. Schäfer, U. Bauder-Wüst, W. Lehnert, K. Leotta, A. Morgenstern, K. Kopka, U. Haberkorn, W. Mier and C. Kratochwil, *Eur J Nucl Med Mol Imaging*, 2019, **46**, 1081-1091.
36 V. Y. Stenberg, A. Juzeniene, Q. Chen, X. Yang, Ø. S. Bruland and R. H. Larsen, *J. Label. Compd. Radiopharm.*, 2020, **63**, 129-143.
37 A. L. S. R. Banerjee, I. Minn, V.Kumar, A. Josefsson, C. B. M. Brummet, J. Chen, A. P. Kiess, K. Baidoo, R. F. H. and R. C. Mease, M. Brechbiel, G. Sgouros and M. G. Pomper, *J. Nucl. Med.,* 2020, **61**, 80-88.
38 H. S. Chong, H. A. Song, X. Ma, D. E. Milenic, E. D. Brady, S. Lim, H. Lee, K. Baidoo, D. Cheng and M. W. Brechbiel, *Bioconjugate Chem.*, 2008, **19**, 1439-1447.
39 Y. Miao, M. Hylarides, D. R. Fisher, T. Shelton, H. Moore, D. W. Wester, A. R. Fritzberg, C. T. Winkelmann, T. Hoffman and T. P. Quinn, *Clin. Cancer Res.*, 2005, **11**, 5616-5621.
40 C. Zhang, K. S. Lin and F. Bénard, *Mol Imaging*., 2017, **16**, 1536012117737919.
41 M. Tosato, M. Asti, M. Dalla Tiezza, L. Orian, D. Häussinger, R. Vogel, U. Köster,

M. Jensen, A. Andrighetto, P. Pastore and V. Di Marco, *Inorg. Chem.*, 2020, **59**, 10907-10919.

42 M. Tosato, M. Dalla Tiezza, N. V. May, A. A. Isse, S. Nardella, L. Orian, M. Verona, C. Vaccarin, A. Alker, H. Mäcke, P. Pastore and V. Di Marco, *Inorg. Chem.*, 2021, **60**, 11530-11547.

43 L. Li, M. G. de Jaraquemada-Peláez, H.T. Kuo, H. Merkens, N. Choudhary, K. Gitschalter, U. Jermilova, N. Colpo, C. Uribe-Munoz, V. Radchenko, P. Schaffer, K. S. Lin, F. Benard and C. Orvig, *Bioconjugate Chem.*, 2019, **30**, 1539-1553.

44 R. Ševčíková, P. Lubal, M. P. C. Campello and I. Santos, *Polyhedron*, 2013, **62**, 268-273.

45 S. Spreckelmeyer, C. F. Ramogida, J. Roussea, K. Arane, I. Bratanovic, N. Colpo, U. Jermilova, G. M. Dia, I. Dud, M. de G. Jaraquemada-Peláez, F. Bénar, P. Schaffer and C. Orvig, *Bioconjugate Chem.*, 2017, **28**, 2145-2159.

46 J. Notni, J. Simecek and H. J. Wester, *ChemMedChem*, 2014, **9**, 1107-1115.

47 V. Y. Stenberg, A. Juzeniene, Ø. S. Bruland and R. H. Larsen, *Curr Radiopharm.*, 2020, **13**, 130-141.

48 L. L. Chappell, K. A. Deal, E. Dadachova and M. W. Brechbiel, *Bioconjugate Chem*, 2000, **11**, 510-519.

49 L. L. Chappell, E. Dadachova, D. E. Milenic, K. Garmestani, C. Wu and M. W. Brechbiel, *Nucl Med Biol*, 2000, **27**, 93-100.

50 S. Mirzadeh, K. Kumar and O. A. Gansow, *Radiochim. Acta*. 1993, **60**, 1-10.

51 K. Lyczko, M. Lyczko and M. Pruszynski, *Polyhedron*, 2020, **192**, 114822.

52 M. Tosato, M. Verona, R. Doro, M. Dalla Tiezza, L. Orian, A. Andrighetto, P. Pastore, G. Marzaro and V. Di Marco, *New J. Chem.*, 2020, **44**, 8337-8350.

53 M. Tosato, M. Pelosato, S. Franchi, A. A. Isse, N. V. May, G. Zanoni, F. Mancin, P. Pastore, D. Badocco, M. Asti and V. Di Marco, 2022, *Submitted manuscript*.

54 A. Bianchi, M. Micheloni and P. Paoletti, *Coord. Chem. Rev.*, 1991, **110**, 17-113.

55 M. Tosato and V. Di Marco, *Biomolecules*, 2019, **9**, 269.

56 C. G. Pippin, T. J. McMurry, M. W. Brechbiel, M. McDonald, R. Lambrecht, D. Milenic, M. Roselli, D. Colcher and O. A. Gansow, *Inorg. Chim. Acta*, 1995, **239**, 43-51.

57 F. Cuenot, M. Meyer, E. Espinosa, A. Bucaille, R. Burgat, R. Guilard and C. Marichal-Westrich, *Eur. J. Inorg. Chem*, 2008, **2008**, 267-283.

58 M. Litecká, R. Gyepes, Z. Vargová, M. Vilková, M. Almáši, M. Walko and J. Imrich, *J. Coord. Chem.*, 2017, **70**, 1698-1712.

59 J. W. Nugent, H. S. Lee, J. H. Reibenspies and R. D. Hancock, *Polyhedron*, 2015, **91**, 120-127.

60 M. Le Fur, M. Beyler, N. Lepareur, O. Fougère, C. Platas-Iglesias, O. Rousseaux and R. Tripier, *Inorg. Chem.*, 2016, **55**, 8003-8012.

Chapter 6

Exploring the Chelation of the Exotic Meitner-Auger Emitter Mercury-197 With Sulfur-Rich Macrocycles

This chapter is adaptation of a manuscript in preparation and is reproduced in part with the permission from Tosato, M.; Randhawa, P.; Menegazzo, I.; Chen, S.; Radchenko, V.; Ramogida, C. F. and Di Marco., V. Expected submission: April 2022.

6.1 Introduction

Meitner-Auger electrons are low-energy electrons (1-10 keV) that are emitted by radionuclides during electron capture (EC) and/or internal conversion (IC) decay processes.[12] The majority of the Meitner-Auger electrons deposit their energy over short distances in tissues (≤ 1-20 μm, < 1 cell diameter).[2] These exceedingly short-range emissions possess high linear energy transfer (1 and 23 keV/μm), which is potentially very effective for generating clustered damage in cancer cells if they are emitted nearby cell sensitive targets such as the DNA and the cell membrane.[3,4] As the decay range occurs within a short path distance, Meitner-Auger electrons can cause lethal damage at subcellular level, thus being optimal for the treatment of small or metastatic tumours owing to the minimal irradiation of the surrounding sites, with the notable caveat that highly specific biological targeting remains a nontrivial prerequisite.[2]

Although these particles show promising therapeutic applications for incorporation into cutting-edge radiopharmaceuticals, they are virtually unexplored.[3] In fact, despite almost half of the medically interesting radioisotopes are Meitner-Auger emitters (*e.g.*, indium-111, gallium-67, technetium-99m, iodine-123/125), most of them are not suitable for Meitner-Auger therapy due to other accompanying emissions or non-compatible half-life.[3] A rare and unique opportunity of a Meitner-Auger emitter with suitable decay properties is represented by the exotic isomers mercury-197m (^{197m}Hg, $t_{1/2}$ 23.8 h) and mercury-197 (^{197}Hg, $t_{1/2}$ 64.14 h). They are also a promising matched theranostic pair since the former is a γ-emitter suitable for SPECT imaging and both emit the cascade of conversion and Meitner-Auger electrons that can be used for therapy.[5] As depicted in **Figure 6.1**, ^{197m}Hg predominantly decays by isomeric transition (IT) (branching ratio 94.68%) to the ground state ^{197g}Hg, emitting monoenergetic conversion electrons (CE) (E_{CE} 82 keV, I_{CE} 20%; E_{CE} 119 keV, I_{CE} 33%; E_{CE} 150 keV, I_{CE} 50%), high-energy gamma rays (E_γ 134 keV, I_γ 34.8%; E_γ 165 keV, I_γ 0.28%) as well as low energy Meitner-Auger electrons (E_{ave} 7.1 keV).[36] Concurrently, X-rays (10-70 keV) are released.[3,5–8] The minor route (branching ratio 5.32%) implicates the decay by electron capture (E_{EC} 499 keV, I_{EC} 5.32%) to the excited state gold-197 (^{197}Au*) which decays by isomeric transition to stable ^{197}Au. The decay is accompanied by the emission of high-energy γ-rays (E_γ 130 keV, I_γ 0.17%; E_γ 408 keV, I_γ 0.0057%; E_γ 279 keV, I_γ 3.79%; E_γ 201.4 keV, I_γ 0.054%), conversion electrons (E_{CE} 116 keV, I_{CE} 6%), low-energy Meitner-Auger electrons (E_{ave} 7.6 keV) as well as X-rays (10-70 keV).[3,5–8] On the other hand, the ground state ^{197}Hg decays to an excited state of ^{197}Au* by electron capture (E_{EC} 523 keV, I_{EC} 100%). The latter decays by isomeric transition to stable ^{197}Au emitting conversion electrons (E_{CE} 63 keV, I_{CE} 60%), low-energy gamma rays (E_γ 77 keV, I_γ 0.0143%; E_γ 268.78 keV, I_γ 0.0393%; E_γ 191.44 keV, I_γ 0.632%)

and Meitner-Auger electrons (E_{ave} 7.4 keV). Analogously to ^{197m}Hg decay, also in this case X-rays are coemitted (10-68 keV).[3,5–8] It is worth pointing out that, owing to the high number of emitted Meitner-Auger electrons from $^{197m/g}$Hg, the dose *per* decay, in a small radius of 1 μm, is ten times higher than the dose of the routinely used lutetium-177 (^{177}Lu): this should produce higher therapeutic effectiveness compared to the latter. However, the $^{197m/g}$Hg γ-dose is six times higher compared to ^{177}Lu as a result of the higher number of emitter photons but much lower than those of the clinically employed iodine-131 (^{131}I).[5,7,9] Moreover, $^{197m/g}$Hg has demonstrated to deposit a 2-fold higher dose in comparison to the Meitner-Auger emitter indium-111 (^{111}In), thus emphasizing its great therapeutic potential.

$^{197m/g}$Hg were first produced from neutron irradiation on natural Hg *via* the ^{196}Hg(n,γ)^{197}Hg reaction in the 1950s and used for brain scanning and cancer imaging when incorporated into 3-chloromercury-2-methoxyprop-1-yl (chlormerodrin) (**Figure 6.2**).[10,11]

However, their medical application was virtually finished due to the neurotoxic side effects deriving from both the *in vivo* stability of the ^{197}Hg-labelled compounds and the low molar activity of the radiometal itself as the product was contaminated by the long-lived isotope mercury-203 (^{203}Hg).[12] In fact, Rhoton *et al.* reported the localization of intracranial tumours using chlormerodrin but significant uptake of ^{197}Hg in neoplasms of the brain, skin, bones, eye, pancreas and breast/prostate.[13] As a result of these drawbacks, the use of ^{197}Hg was replaced with the SPECT radioisotope technetium-99m (^{99m}Tc).[7]

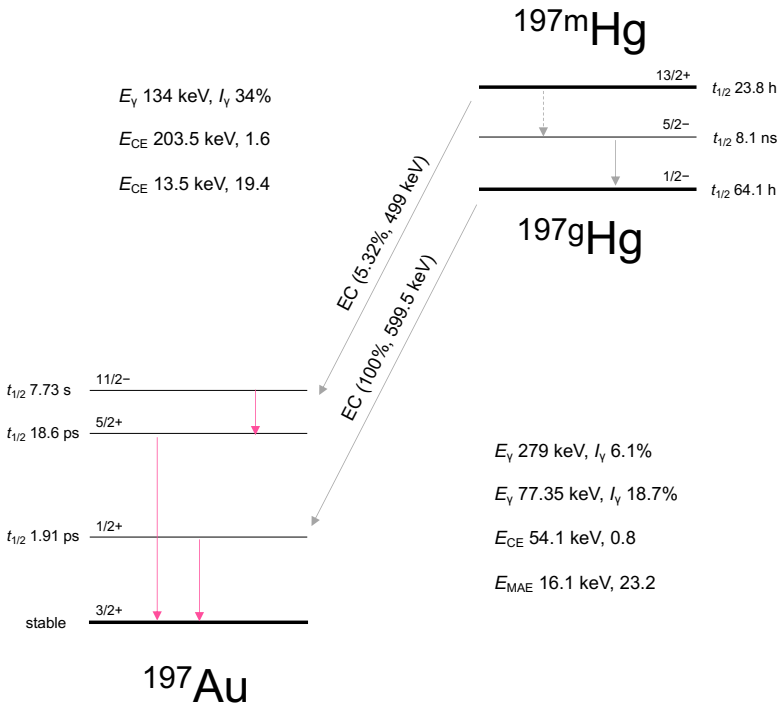

Figure 6.1. Decay scheme of $^{197m/g}$Hg. The useful γ emissions for SPECT imaging, the average number of Meitner-Auger electrons (MAE) and conversion electrons (CE) and their emission energies are reported.

In recent years, there has been a resurgence of interest in mercury for use as a theranostic radionuclide.[14] Consequently, alternative production pathways were explored to obtain $^{197m/g}$Hg with higher specific activities[††††] and in larger quantities.[5,15,16] The most effective way to produce $^{197m/g}$Hg nowadays is by proton or deuteron irradiation of natural Au target (^{197}Au(p,n)$^{197m/g}$Hg reaction).[17] This route is also less expensive than previous approaches that used enriched Hg targets because ^{197}Au is 100% abundant so that the use of enriched target is unecessary.[15] Deuteron bombardment of gold targets *via* the ^{197}Au(d, 2n)$^{197m/g}$Hg reaction has a higher cross-section although its application is restricted to fewer cyclotrons due to the use of high energy deuterons.[18] Alternative production routes include platinum foils irradiation *via* ^{194}Pt(α,n)$^{197m/g}$Hg and ^{195}Pt(α,2n)$^{197m/g}$Hg nuclear reactions or by spallation of lead targets.[19,20]

Despite its theranostic potential, $^{197m/g}$Hg BFC chemistry is virtually unexplored as only one ^{197}Hg-labelled trithiamacrocycle conjugated to an antibody[‡‡‡‡] has been reported (**Figure 6.2**) to date.[21] The development of appropriate chelating platforms for ^{197}Hg is therefore essential to harness its theranostic power.

Hg^{2+} is classified as a soft Lewis acid according to the HSAB theory. Due to its d^{10} electronic configuration, it generally displays a flexible coordination environment with a huge diversity of geometry and coordination numbers (from tetra to octa-coordinated geometry).[3] Owing to its extraordinary chemical softness, the formation of stable complexes with the sulfur-bearing ligands developed in **Chapter 2** was hypothesized hereby.

In this Chapter, the thermodynamic and structural properties of the Hg^{2+} complexes with the first- and the second-generation ligands are reported as well as the ^{197}Hg labelling and the *in vitro* stability investigation of the resulting radioactive complexes.

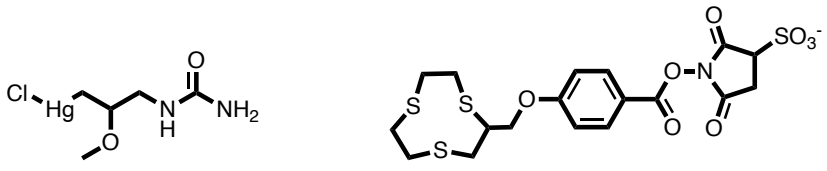

Chlormerodrin S_3 macrocycle

Figure 6.2. Structure of chlomerodrin for brain scanning and state-of-the-art trithiamacrocycle for ^{197}Hg-labelling.

[††††] Notably, based on the potential therapeutic doses (ng - μg), only trace amounts of ^{197}Hg will be required for therapy if the latter is produced at high specific activity. This amount is far below the safe concentration limit of Hg in the blood set by the USA (0.7 μg/kg body weight), Europe (1.6 μg/kg) and Canada (0.1 μg/kg), implying that there is no risk of mercury poisoning in patients.[3]

[‡‡‡‡] This macrocyclic thioether ligand was conjugated with rabbit IgG and labelled with ^{197}Hg. However, most of the radioactivity was found associated in the protein fractions during stability assays, thus demonstrating the instability of the Hg complexes formed by this ligand.

6.2 Results and Discussion

6.2.1 Thermodynamics of Mercuric Complexes with First- and Second-Generation Ligands

The family of first-generation sulfur-bearing polyazamacrocyclic ligands instantaneously formed highly stable complexes with Hg^{2+}, likely as a consequence of the extreme affinity of this metal ion for the soft-sulfur donors on the pendant arms combined with a proper macrocyclic cavity. Consequently, only a lower limit for the binding constants was estimated from pH-potentiometric titration experiments.[§§§§] Analogously to the other divalent cations investigated in this work (**Chapter 4** and **Chapter 5**), the determined speciation model with the pure sulfur-bearing cyclen-based ligands (DO4S and DO3S) involves the presence of the 1:1 metal-to-ligand deprotonated complex*, i.e.* $[HgL]^{2+}$, while for the carboxylate bearing DO2A2S also the monoprotonated complex, *i.e.* $[HgHL]^{+}$, exist under acidic conditions. DOTA and the unsubstituted macrocycle, *i.e.* cyclen, were studied as well as only a few works have investigated their mercuric thermodynamic properties and coordination chemistry. DOTA was also considered as it is a generally employed chelating agent in nuclear medicinal chemistry. As reported in **Table 6.1**, the same speciation model of the pure sulfur-containing macrocycles and the carboxylate one was found with cyclen and DOTA, respectively. It is worth to note that, while the speciation model obtained for the former is in agreement with the literature data, for the latter, the monoprotonated complex ($[Hg(HDOTA)]^{-}$) was also detected. This is incongruent with the previously reported data according to which its mercuric complex exists only in the deprotonated form ($\log K_{[Hg(DOTA)]^{2-}}$ = 26.4 in I = 0.20 M KNO_3 and T = 25°C). Different competitive titration experiments were attempted to determine the exact values of the formation constants with the first-generation ligands. Initially, ^{1}H-NMR titrations in highly competitive acidic environments were performed using HNO_3 to increase the proton concentration. The spectra recorded in the 0-12 pH range are reported in **Figure 6.3** - **6.4**. As illustrated in **Figure E1** - **E5** (**Appendix E**), the spectra are markedly different than those of the free ligands, indicating the metal binding event.

The absence of any variation on the resonances with the proton content of the solution demonstrated that the same Hg^{2+} complexes with the pure sulfur-containing ligands, *i.e.* DO4S and DO3S, exist also in extremely forcing conditions (pH << 2) thus confirming the speciation determined by pH-potentiometric titrations and indicating an exceptionally high

[§§§§] Preliminary NMR measurements of solutions containing Hg^{2+} and the ligands at different pH ($C_{Hg^{2+}} = C_L = 1 \cdot 10^{-3}$ M) demonstrated that all the complexation reactions were quickly enough (< 5 min) to be investigated by means of pH-potentiometric titrations.

thermodynamic stability.[*****] This clearly hampered the determination of the logβ values through this approach.

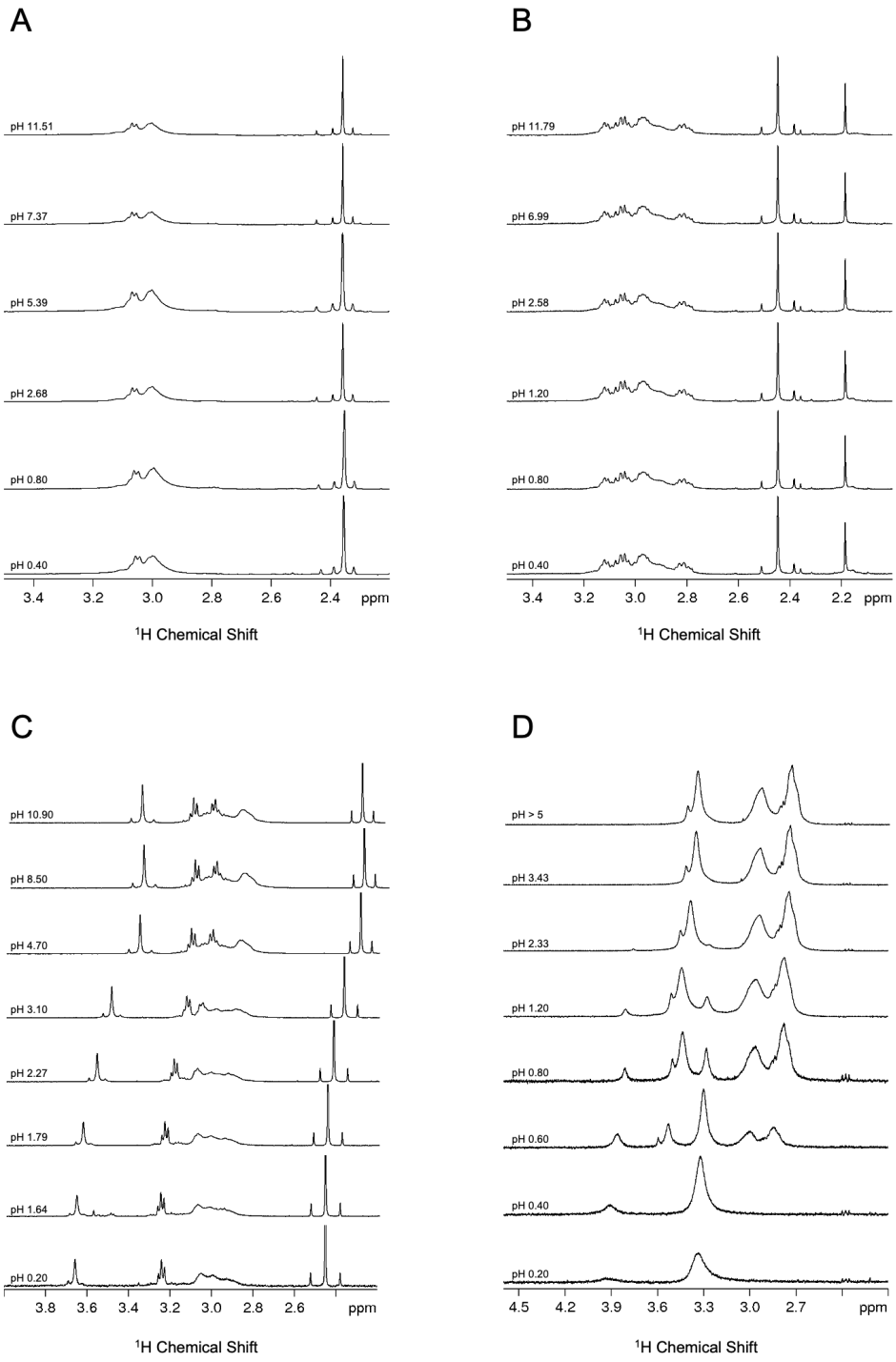

Figure 6.3. Variable-pH ^{1}H NMR spectra of (A) Hg^{2+}-DO4S, (B) Hg^{2+}-DO3S, (C) Hg^{2+}-DO2A2S and (D) Hg^{2+}-DOTA (400 MHz, T = 25°C, I = 0.15 M $NaNO_3$ (pH > 1), H_2O + 10% D_2O, $C_{Hg^{2+}} = C_L = 1.0 \cdot 10^{-3}$ M).

[*****] No changes in the ^{1}H NMR spectra were detected nor after several months at room temperature nor after prolonged heating.

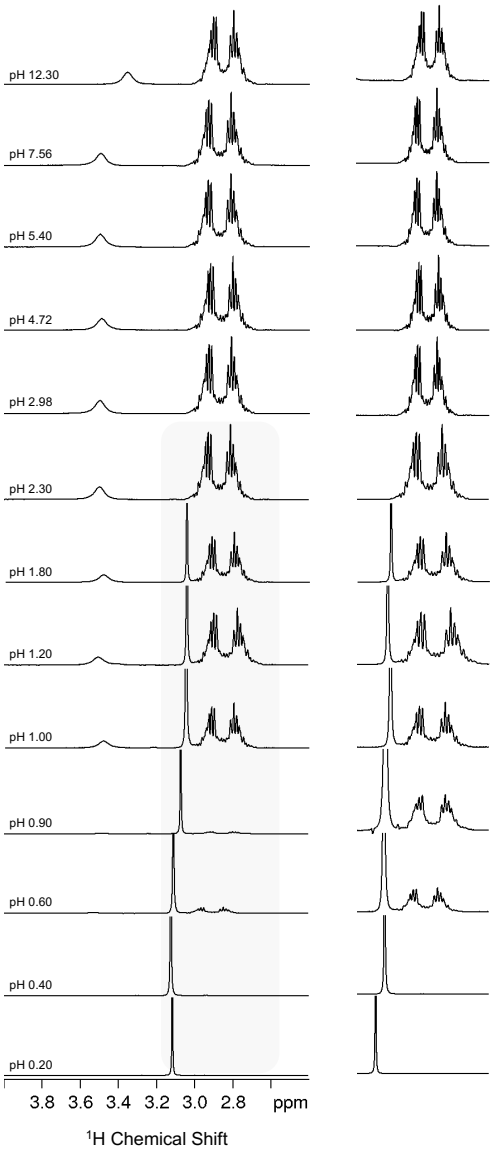

Figure 6.4. Variable-pH ^{1}H NMR spectra of Hg^{2+}-cyclen (400 MHz, T = 25°C, I = 0.15 M $NaNO_3$ (pH > 1), H_2O + 10% D_2O, $C_{Hg^{2+}} = C_{cyclen} = 2.0 \cdot 10^{-3}$ M). An enlargement of the 2.6-3.0 ppm spectral region is reported on the right (spectra are not in scale).

With DO2A2S, besides the absence of free ligand throughout the investigated pH range, at increasingly proton content, different signal shifts are also recognizable because of the presence of the monoprotonated complex, $[Hg(HDO2A2S)]^+$ (**Figure 6.3**). ^{1}H chemical shift variations as a function of pH are shown in **Figure E6** (**Appendix E**). These data allowed to estimate the pK_a associated with the deprotonation process ($[HgLH] \leftrightharpoons [HgHL]^+ + H^+$), which is in good agreement with that determined by pH-potentiometry (**Table 6.1**).

Only for Hg^{2+}-cyclen and Hg^{2+}-DOTA it was possible to recognize the signals of the free ligand at a rather acidic pH (**Figure 6-3** - **6.4**), thus allowing to define the values of the formation constants (**Table 6.1**).

Table 6.1. Stability constants (logβ) and pHg^{2+} values for the Hg^{2+} complexes with first-, second-generation ligands, DOTA and cyclen at T = 25°C.

Ligand	Equilibrium reaction	logβ				pHg^{2+} [a]
Cyclen	$Hg^{2+} + L \leftrightharpoons [HgL]^{2+}$	23.8	±	0.1	[b]	19.4
		25.5			[c]	21.1
DO4S	$Hg^{2+} + L \leftrightharpoons [HgL]^{2+}$	32.5	±	0.1	[d]	30.5
DO3S	$Hg^{2+} + L \leftrightharpoons [HgL]^{2+}$	32.3	±	0.1	[d]	29.4
DO2A2S	$Hg^{2+} + H^{+} + L^{2-} \leftrightharpoons [HgHL]^{+}$	34.59	±	0.08	[e]	29.2
		34.5	±	0.1	[b]	
	$Hg^{2+} + L^{2-} \leftrightharpoons [HgL]$	31.7	±	0.1	[d]	
DOTA	$Hg^{2+} + H^{+} + L^{4-} \leftrightharpoons [HgHL]^{-}$	31.84	±	0.02	[e]	25.8
		32	±	0.1	[b]	
	$Hg^{2+} + L^{4-} \leftrightharpoons [HgL]^{2-}$	29.0	±	0.1	[b]	
TACD3S	$Hg^{2+} + L \leftrightharpoons [HgL]^{2+}$	16.02	±	0.06	[f]	15.1
TE4S	$Hg^{2+} + L \leftrightharpoons [HgL]^{2+}$	19.52	±	0.2	[b]	16.8

[a] pHg^{2+} calculated at $C_{Hg^{2+}} = 10^{-6}$ M and $C_L = 10^{-5}$ M and pH 7.4.
[b] Obtained by ^{1}H-NMR competitive titrations with H^+ (HNO_3), T = 25°C.
[c] From ref. [22] at I = 0.20 M $NaClO_4$ and T = 25°C by polarography.
[d] Obtained by competitive titrations with chloride, no ionic strength control, T = 25°C.
[e] Obtained by combining the pH-potentiometric logβ value of $[HgLH]^-$ at I = 0.15 M $NaNO_3$ and T = 25°C with the value determined at [b] or [d].
[f] Obtained by pH-potentiometry at I = 0.15 M $NaNO_3$ and T = 25°C.

Analogously to Hg^{2+}-DO2A2S, also for Hg^{2+}-DOTA the recognizable peak shift toward higher chemical shifts with the pH decrease corroborates the speciation model as it is indicative of the co-presence of the monoprotonated ($[HgHL]^-$) and deprotonated ($[HgL]^{2-}$) complexes.
Not even the competition with Ag^+, which is a cation that forms very stable complexes with these S-containing ligands (**Chapter 3**), allowed to obtain the values of the formation constants, since the addition of Hg^{2+} to the solution of the preformed Ag^+ complexes produced the complete transmetallation at all the investigated Ag^+-to-Hg^{2+} molar ratio as depicted in **Figure E7** - **E8** (**Appendix E**). The addition of Ag^+ on solution of preformed Hg^{2+} complexes did not produce any spectral changes albeit the high competitor concentrations used (Ag^+-to-Hg^{2+} molar ratios > 20). These results further substantiated an exceptionally high stability of the mercuric complexes with the investigated S-rich ligands. Competition titrations with chloride, which forms highly stable complexes with Hg^{2+} (**Table 6.2**), allowed to obtain reliable values of the formation constants. Indeed, as shown in **Figure 6.5**, only under forcing conditions it was possible to obtain the complexes' demetallation. Representative titrations curves are reported in **Figure E9** (**Appendix C**) while the logβ values are shown in **Table 6.1**. The corresponding distribution diagrams are displayed in **Figure 6.6**. The same speciation model of the pure sulfur-containing first-generation ligands was preserved with the analogues with the different macrocyclic backbones. For TACD3S, the formation constant of the monomercuric complex ($[Hg(TACD3S)]^{2+}$) was readily accessible by pH-potentiometric measurements. On the other hand, for Hg^{2+}-TE4S, competition measurements, in a strongly acidic environment, support the potentiometric data. The obtained formation constants are detailed in **Table 6.1** while the distribution diagrams are shown in **Figure 6.6**.

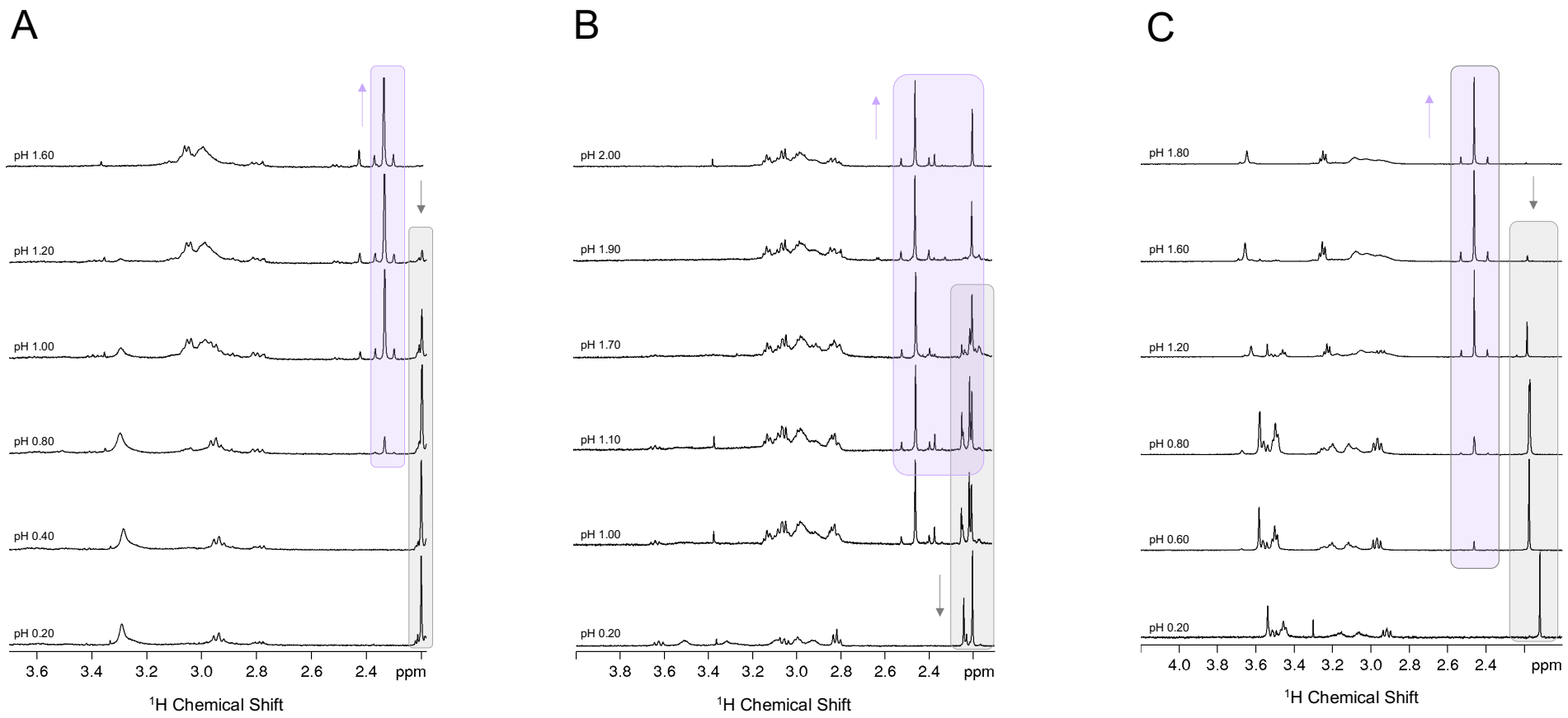

Figure 6.5. Competitive titrations with Cl^- of (A) Hg^{2+}-DO4S, (B) Hg^{2+}-DO3S and (C) Hg^{2+}-DO2A2S (400 MHz, T = 25°C, H_2O + 10% D_2O, $C_{Hg^{2+}} = C_L = 6.0 \cdot 10^{-4}$ M). The signals related to the Hg^{2+} complexes are highlighted in purple and those representative of the free ligand signals in grey.

Table 6.2. Recommended IUPAC values for the Hg^{2+}-Cl^- complexes at T = 25°C and I = 0.1 mol/kg $NaClO_4$.[23]

Reaction	log*K*
$Hg^{2+} + Cl^- \leftrightharpoons HgCl^+$	7.31
$Hg^{2+} + 2Cl^- \leftrightharpoons HgCl_{2\,(aq)}$	14.00
$HgCl_{2\,(aq)} + Cl^- \leftrightharpoons HgCl_3^-$	0.925
$HgCl_3^- + Cl^- \leftrightharpoons HgCl_4^{2-}$	0.61

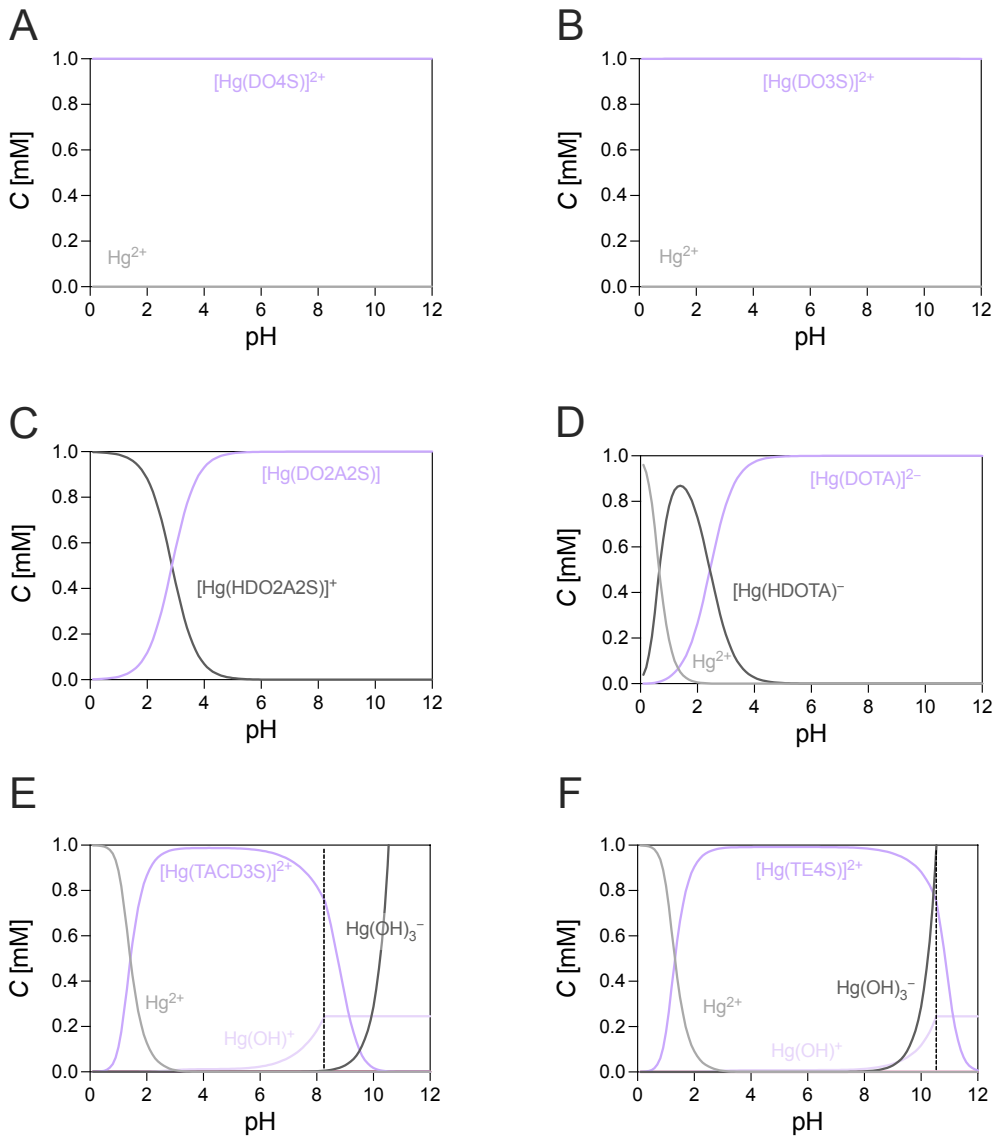

Figure 6.6. Distribution diagrams of (A) Hg^{2+}-DO4S, (B) Hg^{2+}-DO3S, (C) Hg^{2+}-DO2A2S, (D) Hg^{2+}-DOTA, (E) Hg^{2+}-TACD3S and (F) Hg^{2+}-TE4S at $C_{Hg^{2+}} = C_L = 1 \cdot 10^{-3}$ M. The dashed lines in (E) and (F) show the theoretical start of $Hg(OH)_2$ precipitation, which was never experimentally observed.

6.2.2 Comparison of the Thermodynamic Stability of the Mercuric Complexes with First- and Second-Generation Ligands

In **Figure 6.6** a graphical comparison of the pHg^{2+} values is shown to compare the thermodynamic stability of the investigated ligands: the presence of sulfur clearly induces an extraordinary increase in the stability of the resulting mercuric complexes when compared with the non-functionalized macrocycle, *i.e.* cyclen, or to the pure carboxylic analogue, *i.e.* DOTA, as a result of the high affinity of the metallic center for the softer sidearms. Similarly to what was previously found with Ag^{+} (**Chapter 3**), the stability of the mercuric complexes is governed by the number of S donors, as $[Hg(DO4S)]^{2+}$ is the most stable species along the series. However, differently from Ag^{+}, the presence of an asymmetrical sidechain in the macrocyclic backbone (*i.e.* without the opposite arm) generates a complex of comparable stability with respect to the ligand containing only two opposite sulfur (pHg^{2+}_{DO3S} = 29.4 *vs.* pHg^{2+}_{DO2A2S} = 29.2). This can be partially attributed to the ligand's asymmetry which likely induces a geometrical constraint that does not allow the binding of the third S as also demonstrated by NMR (*vide infra*).

The overall results obtained by varying the macrocyclic backbone are similar to those obtained with the other metal cations investigated in this work (**Chapter 3**, **Chapter 4** and **Chapter 5**): variation of the nitrogen donors array, as well as the increase in the ring size, have an extremely detrimental effect on the stability of the resulting complexes. Similarly to what has been previously stated, this effect has to be attributed to non-ideal matching between the cavity of the cation and ring pocket. The stability trend was further experimentally confirmed by ^{1}H-NMR competitive measurements of 1:1 ligand-to-ligand mixtures: the complex that forms with all the tested ligand combinations (DO4S *vs.* cyclen/DOTA/TACD3S/TE4S) is always $[Hg(DO4S)]^{2+}$ (data not shown).

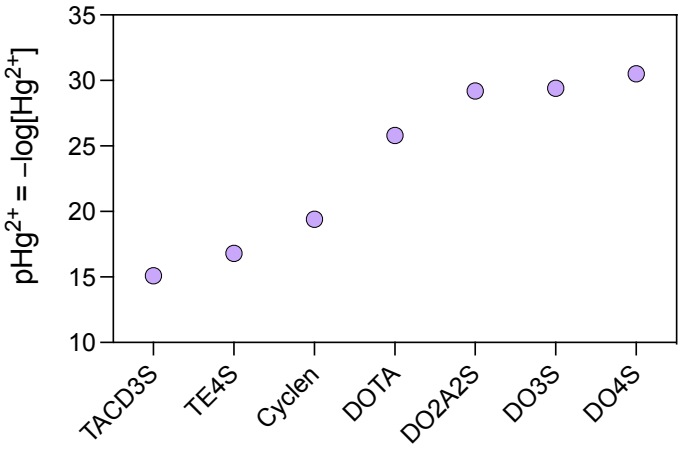

Figure 6.7. Comparison of the pHg^{2+} values at physiological pH for the Hg^{2+} complexes formed with the investigated ligands.

6.2.3 Solution Structure of Mercuric Complexes with First-Generation Ligands

The ^{1}H NMR spectra of the Hg^{2+} complexes with the first-generation ligands (**Figure 6.3** - **6.4**) were further examined to gain insight into their solution structure. Signal assignments, performed with the aid of ^{1}H-^{1}H COSY and ^{1}H-^{13}C HMQC reported in **Figure 6.8** - **6.9** and **Figure E10** (**Appendix E**), are summarized in **Table E1** (**Appendix E**).

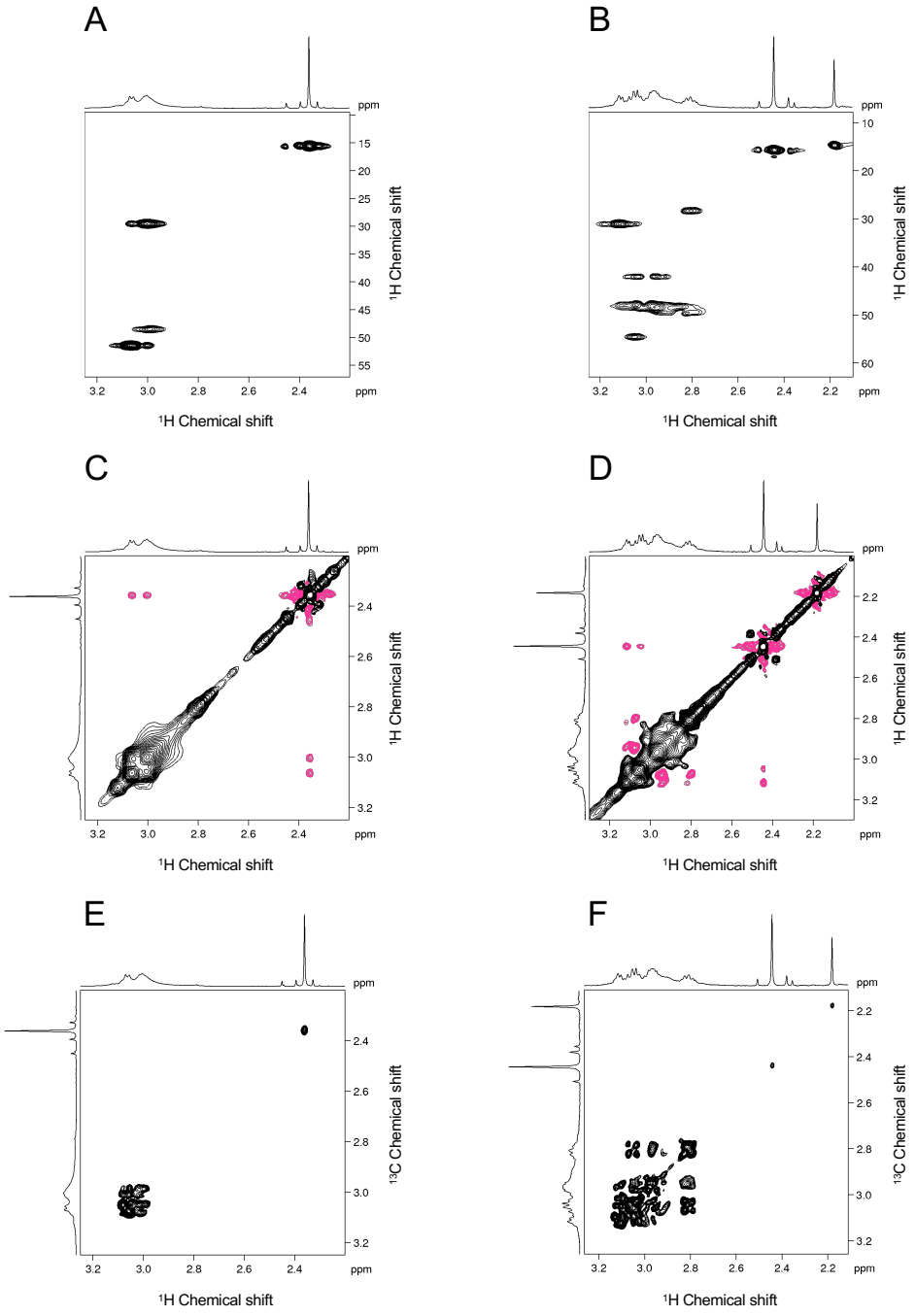

Figure 6.8. ^{1}H-^{13}C HMQC spectrum of (A) $[Hg(DO4S)]^{2+}$ and (B) $[Hg(DO3S)]^{2+}$; NOESY spectrum of (C) $[Hg(DO4S)]^{2+}$ and (D) $[Hg(DO3S)]^{2+}$, and ^{1}H-^{1}H COSY spectrum of (E) $[Hg(DO4S)]^{2+}$ and (F) $[Hg(DO3S)]^{2+}$.

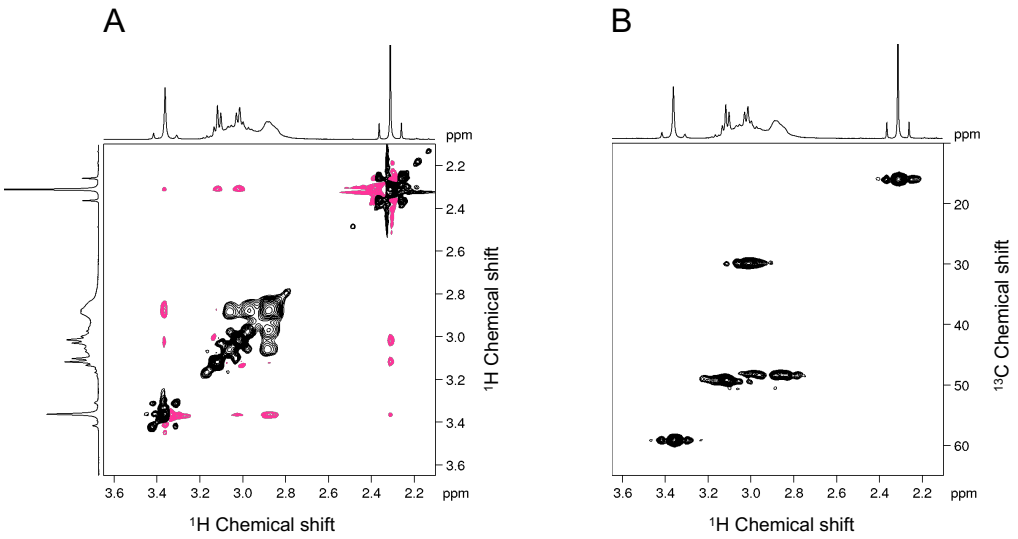

Figure 6.9. (A) NOESY and (B) ^{1}H-^{13}C HMQC spectrum of [Hg(DO2A2S)].

The spectra of $[Hg(DO4S)]^{2+}$ display only two resonances presumably as a consequence of a high degree of symmetry in solution: an enlarged multiplet at 2.90-3.20 ppm attributed to SCH_2 and ring and arms NCH_2 protons, and a sharp singlet at 2.36 ppm ascribed to the SCH_3 protons of the side arms (**Figure 6.3**). The latter is accompanied by two satellite signals at 2.32 and 2.39 ppm ($^3J_{^1H\text{-}^{199}Hg}$ = 30 Hz) having approximately one-fifth of the area of the main resonance (δ_{SCH_3} = 2.36 ppm), and arising from the presence of the NMR active nucleus ^{199}Hg at natural abundance.[††††] This coupling, combined with the significant downfield shift upon complexation observed with respect to the free ligand (**Figure E1** - **Appendix E**) represents a direct proof that all the sulfur donors are statically bound to Hg^{2+} on the NMR timescale. Indeed, rapid exchange between various SCH_3 environments (as previously observed with other cations, *e.g.* Ag^+ - **Chapter 3**) would have precluded the detection of the ^{1}H-^{199}Hg coupling.

^{1}H-^{199}Hg Heteronuclear Single Quantum Coherence (^{1}H-^{199}Hg HSQC) experiments allowed to probe the Hg^{2+} coordination in solution. As it can be deduced from **Figure 6.10**, in $[Hg(DO4S)]^{2+}$ all the donors are involved in the metal binding as all proton resonances give correlation peaks with the ^{199}Hg resonance at −1275 ppm (**Table 6.3**): a [4N]4S octa-coordination is therefore likely occurring. The absence of ligand exchange processes was further confirmed by the lack of temperature-dependent effect on the line widths when variable-temperature NMR were performed (data are not reported as spectra are identical to the ones at RT).

[††††] ^{199}Hg: 16.84% natural abundance, nuclear spin I = ½, magnetogyric ratio $4.8154 \cdot 10^7$ rad/T·s, relative sensitivity (^{1}H = 1.00) $5.67 \cdot 10^{-3}$.

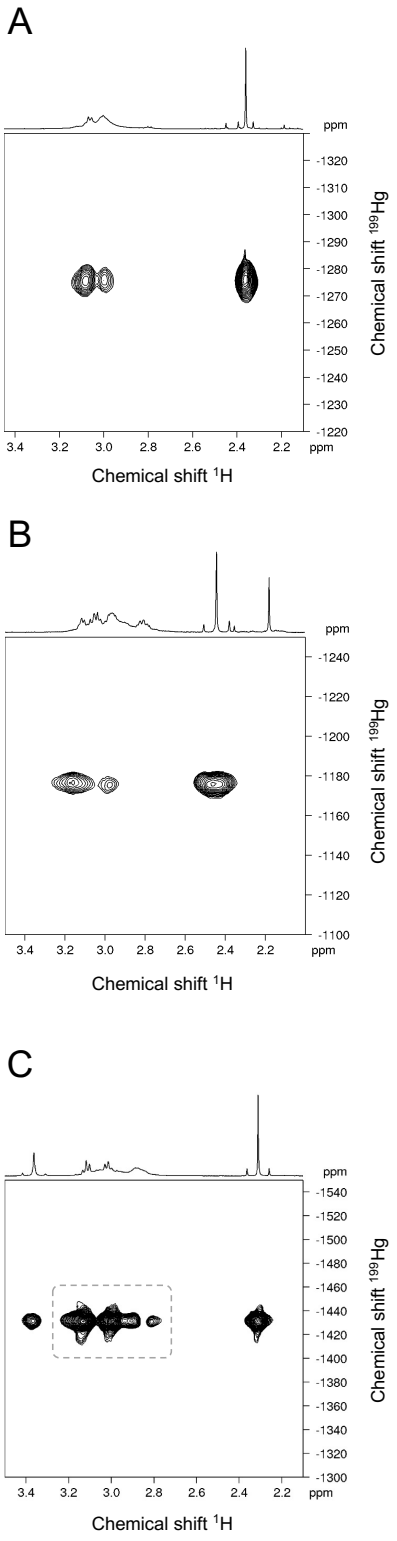

Figure 6.10. Decoupled ^{1}H-^{199}Hg of (A) $[Hg(DO4S)]^{2+}$, (B) and $[Hg(DO3S)]^{2+}$ and (C) [Hg(DO2A2S)]. Non-decoupled ^{1}H-^{199}Hg spectra are shown in **Figure E11** (**Appendix E**).‡‡‡‡‡

‡‡‡‡‡ Intensity scale for the signals inside and outside the box is different.

Table 6.3. NMR coupling constants and ^{199}Hg chemical shift for the first-generation mercuric complexes. DOTA and cyclen are reported for comparison purposes.

Complex	$J^{1}_{H\text{-}^{199}Hg}$ [Hz]	^{199}Hg Chemical Shift [ppm]
[Hg(cyclen)]$^{2+}$	55 [(a, b)]	−1117
[Hg(DO3S)]$^{2+}$	52 [(c)]	−1176
[Hg(DO4S)]$^{2+}$	30 [(c)]	−1275
[Hg(DO2A2S)]	42 [(c)] 44 [(d)]	−1431
[Hg(DOTA)]$^{2-}$	48 [(a, b)] 52 [(a, d)]	−1828

[(a)] From ^{1}H-^{199}Hg HSQC spectra.
[(b)] Coupling with NCH_2 protons.
[(c)] Coupling with SCH_3 protons.
[(d)] Coupling with CH_2COOH protons.

The binding of the mercuric ion into the ligand's cleft is also supported by the spectral variations observed in the corresponding NOESY spectrum (**Figure 6.8**): while the free ligand assumes a folded geometry in solution (**Chapter 2**), the protons of the ring lose this property when they are blocked by the bonding to the metallic center.

The descent in symmetry in the DO3S and DO2A2S ligands is reflected onto the corresponding Hg^{2+} complexes as a relatively more complicated resonance pattern is displayed (**Figure 6.3**). However, the ^{1}H-^{199}Hg satellite coupling peaks can be recognized also in this case. Independently on the protonation states, in Hg^{2+}-DO2A2S both the SCH_3 and the acetate groups show the presence of a $J^{1}_{H\text{-}^{199}Hg}$ ($^{3}J^{1}_{H\text{-}^{199}Hg\ SCH_3}$ = 42 Hz; $^{3}J^{1}_{H\text{-}^{199}Hg\ CH_2COOH}$ = 44 Hz - **Table 6.3**): both acetate and sulfanyl arms are consequently bound to the metal ion (at least in the timescale of the NMR experiment). As already stated, the protonation induces the upfield shift of the signals of both the carboxyl chain and the S donors: since these groups are involved in the Hg^{2+} coordination sphere (**Figure 6.3**), it is reasonable to expect that the protonation induces a great conformational (and consequently spectral) change.

Noteworthily, for [Hg(DO3S)]$^{2+}$ only the SCH_3 signal of the N_1 and N_7 arms displays the ^{1}H-^{199}Hg coupling ($^{3}J^{1}_{H\text{-}^{199}Hg}$ = 52 Hz - **Table 6.3**), thereby indicating that only the two symmetric donors are statically bound to the metal ion with respect to the NMR timescale. The N_4 sulfur donor is likely not involved in the coordination since its chemical shift is virtually unchanged with respect to the free ligand (**Figure E2** - **Appendix E**). In fact, the SCH_3 signals involved in the metal coordination in [Hg(DO3S)]$^{2+}$ are more deshielded than those in [Hg(DO4S)]$^{2+}$ (2.45 ppm *vs.* 2.36 ppm), and this could be justified considering that in DO3S the 2+ charge of the metal ion is shared with two donors while in DO4S it is shared with four. Clearly, the asymmetric arm could also be in a fast exchange, or the coupling could be absent for geometrical reasons which generate a $J^{1}_{H\text{-}^{199}Hg}$ = 0. However, these hypotheses seem implausible.

For both $[Hg(DO3S)]^{2+}$ and [Hg(DO2A2S)], ^{1}H-^{199}Hg HSQC experiments (**Figure 6.10**) allowed to prove that the cyclen cores are also interacting with the metal ion to form a 6- and 8-coordinate structure, respectively. The [4N]2S2O coordination geometry in [Hg(DO2A2S)] is further suggested from its NOESY (**Figure 6.9**) spectrum as, in this case, the SCH_3 protons are spatially close to those of the acetic chains as a consequence of the octacoordinated geometry that occurs in solution. Interestingly, in $[Hg(DO3S)]^{2+}$ the non-bonded sulfur side chain is not spatially close to the other protons (**Figure 6.8**).

When Hg^{2+} is bound to DOTA, the spectrum of the deprotonated complex appears markedly different with respect to those characteristic of the sulfur-containing ligands (**Figure 6.3**). All the signals are very broad, probably as a consequence of a highly dynamic solution behaviour. Moreover, the signals attributed to the ring protons are split into two coupling multiplets (**Figure E10** - **Appendix E**) indicating that, after the metal coordination, these protons became non-magnetically equivalent, differentiating both sides of the cyclen ring. The same splitting-effect is obtained with the non-functionalized macrocycle, *i.e.* cyclen, even if in this case the resonances are much narrower, thus indicating a slowed-down fluxionality. This pattern was previously observed with cyclen and other divalent cations (*e.g.,* Zn^{2+} and Cd^{2+}).[24] The ^{1}H-^{199}Hg HSQC spectra (**Figure 6.11**) are consistent with the involvement of all donors in the Hg^{2+} coordination sphere, *i.e.* [4N]4O with DOTA and [4N] with cyclen since all proton signals give cross-peaks with the Hg resonances. The latter structure is in agreement with the crystalline structure reported in the literature for the complex $[Hg(cyclen)(NO_3)]NO_3$ where the cation assumes a distorted trigonal-prismatic coordination environment as it is also bound to the counterion (**Figure 6.12**).

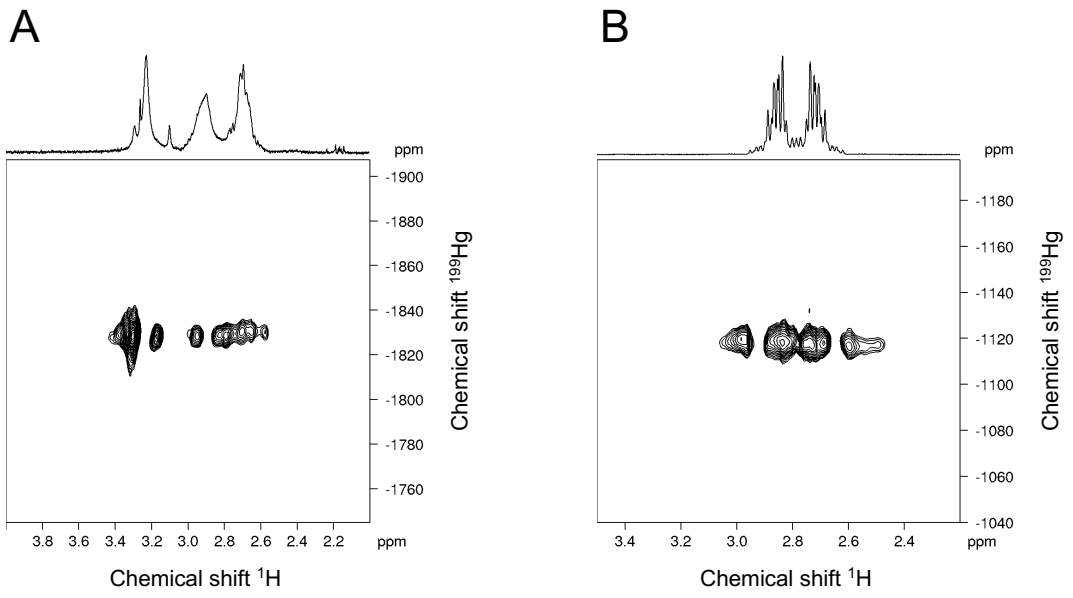

Figure 6.11. Non-decoupled ^{1}H-^{199}Hg spectra of (A) $[Hg(DOTA)]^{2-}$ and (B) $[Hg(cyclen)]^{2+}$.

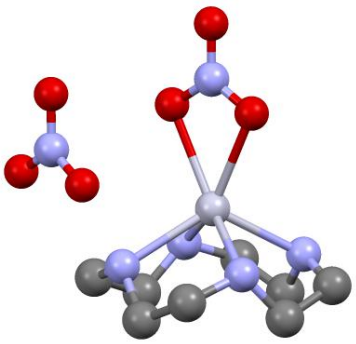

Figure 6.12. X-ray structure of [Hg(cyclen)(NO_3)]NO_3 obtained by Liteckà *et al.*[24]

6.2.4 Solution Structure of Mercuric Complexes with Second-Generation Ligands

The ^{1}H NMR spectra of Hg^{2+}-TACD3S and Hg^{2+}-TE4S are reported in **Figure 6.13** while the spectra assignations are summarized in **Table E2** (**Appendix E**). The assignments were based on ^{1}H-^{1}H TOCSY and ^{1}H-^{13}C HSQC spectra reported in **Figure E12** (**Appendix E**).

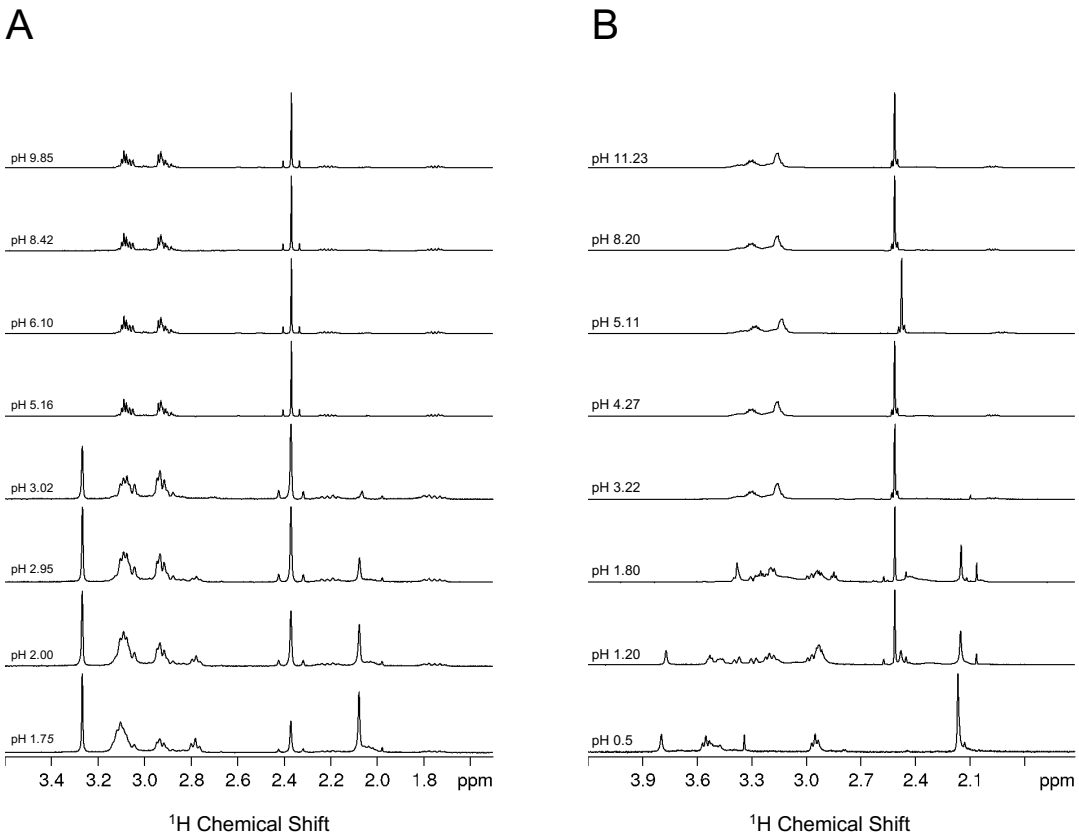

Figure 6.13. Variable-pH ^{1}H NMR spectra of (A) Hg^{2+}-TACD3S and (B) Hg^{2+}-TE4S (600 MHz, T = 25°C, I = 0.15 M $NaNO_3$ (pH > 1), H_2O + 10% D_2O, $C_{Hg^{2+}}$ = C_L = $1.0 \cdot 10^{-3}$ M). Signals at 3.3 ppm are attributed to methanol impurities.

The pH-dependent spectra of the mercuric complexes with the second-generation ligands corroborate the previously obtained speciation model since the proton resonances are pH-insensitive, consistently with the existence of a single complex, *i.e.* $[HgL]^{2+}$, in the investigated pH range (**Figure 6.13**). At acidic pH, the presence of the free chelator is recognizable for both ligands (**Figure 6.13**). Indeed, this feature was exploited to determine the formation constant of formation of $[Hg(TE4S)]^{2+}$ (*vide supra*). With regards to Hg^{2+}-TACD3S, the percentages of free ligand calculated are in good agreement with those determined by pH-potentiometry.

Even with the second-generation ligands, the ^{1}H-^{199}Hg satellite peaks with respect to the SCH_3 signals are recognizable (**Figure 6.13**): the simultaneous and static coordination of all the sulfur chains is therefore maintained unperturbed in these cases ($^{3}J_{^{1}H\text{-}^{199}Hg}$ = 42 Hz for $[Hg(TACD3S)]^{2+}$ and $^{3}J_{^{1}H\text{-}^{199}Hg}$ = 20 Hz for $[Hg(TE4S)]^{2+}$). However, the change of the backbone's properties imposes considerable structural variations with respect to the first-generation series. Indeed, it is intriguing to note that all the resonance (in particular in $[Hg(TACD3S)]^{2+}$) are markedly narrow, indicating an absence of fluxionality in the ring. This was confirmed by the absence of spectral variations at different temperatures ($5 \leq T \leq 65$°C).

In $[Hg(TACD3S)]^{2+}$, the SCH_2 and NCH_2 protons are symmetrically split, resembling the coupling pattern of $[Hg(cyclen)]^{2+}$ (*vide supra*). Furthermore, even the CH_2 protons of the propylic fragment are split into two coupling multiplets of equal area: the introduction of the metal center induces the differentiation of the two sides of the ring, making the corresponding protons (axial and equatorial) non-equivalent. It is therefore reasonable to suppose that the N donors are involved in the coordination sphere: the drastic stability drop with respect to the 12-member analogue, *i.e.* DO4S, should, therefore, be attributed to the smaller number of donors present. Similar considerations also apply to $[Hg(TE4S)]^{2+}$ (**Figure 6.13**), even if in this case the proton splitting is asymmetric, probably because it reflects the lower symmetry of the ligand itself.

6.2.5 Mercury-197 Radiolabelling

The $[^{197m/g}Hg]Hg^{2+}$ labelling ability of the first- and second-generation ligands was explored. This study was also performed with the amido derivative of DO3S, *i.e.* DO3SAm, in order to mimic the effects on the ability to bind mercury once the chelating agent is conjugated to a targeting vector. The results obtained are summarized in **Figure 6.14** and **Figure 6.15**.

Initially, the labelling efficiency was assessed at room temperature and pH 7, which are mild reaction conditions compatible with the use of heat- and pH-sensitive biovectors. However, after 10 minutes of reaction, the RCYs were rather low (< 20%) albeit using a high chelator concentration (10^{-3} M).

An increase in the reaction time led to an increased RCY, thus suggesting that their labelling efficiencies at pH 7 are limited by kinetic barriers. Unfortunately, the incorporation was never quantitative even after 1 hour. Heating to 50°C led to a significant increase in RCY (**Figure 6.14**). With the first-generation chelators, quantitative yields were obtained after 1 hour at 10^{-3} M. When the ligand concentration was decreased to 10^{-4} M, the RCY dropped to 11 ± 1, 33 ± 6 and 9 ± 4% for DO4S, DO3SAm and DO2A2S. Unexpectedly, with DO3S the RCYs were never higher than 20%. Intriguingly, no [$^{197m/g}$Hg]Hg^{2+} incorporation was observed with DOTA after 1 hour, neither at ambient nor at higher temperatures (80°C). This variation in RCY has to be attributed to the difference in the softness of the donor arms, thus emphasizing that the sulfur-containing side arms play a crucial role in radiometal coordination. With the second-generation chelators, the incorporation was slightly increased at 50°C but it was never quantitative (**Figure 6.14**). Not even prolonged heating to higher temperatures (80°C) led to the complete incorporation of the radionuclide (**Figure 6.15**): the influence of ring size variation and the nitrogen donor array on the thermodynamic stability of the Hg^{2+} complexes is straightforwardly reflected in their labelling capabilities. The inability of the second-generation ligands to quantitatively complex [^{197}Hg]Hg^{2+} under any tested conditions precluded any further evaluation.

6.2.6 *In Vitro* Human Serum Stability by SDS-PAGE

Radiopharmaceuticals are administered *via* intravenous injection into the bloodstream. Under these conditions, the concentration of the radiotracers may become so low that the dissociation of the [$^{197m/g}$Hg]Hg^{2+} from the chelating unit will eventually become favoured, thus significantly increasing the accumulation of radioactivity in non-target organs. These reactions can also be promoted by the competition with endogenous ligands (in particular, for Hg^{2+}, sulfur-containing species). To evaluate the stability/inertness of the resulting [$^{197m/g}$Hg]Hg^{2+} complexes, *in vitro* human serum stability assays were carried out. A plethora of different techniques (*e.g.*, HPLC, iTLC, ultrafiltration devices *etc.*) have been tried to achieve this goal as many difficulties have been encountered in differentiating between chelated and protein-bound activity. The use of the iTLC with quenching technique with dimercaptosuccinic acid (DMSA) did not prove to be suitable for the *in vitro* human assays in serum as, in 'control' samples (free [^{197}Hg]Hg^{2+} incubated with human serum), DMSA demonstrated to be not able to transchelate the [$^{197m/g}$Hg]Hg^{2+} bound to serum proteins. The filter assays used in **Chapter 4** with [^{64}Cu]Cu^{2+} were therefore tested. With these ultrafiltration devices, the activity bound to the chelator should pass through the filter while the one bound to the serum proteins should remain trapped into the device thus allowing to distinguish the two contributions by means of γ-spectroscopy measurements.

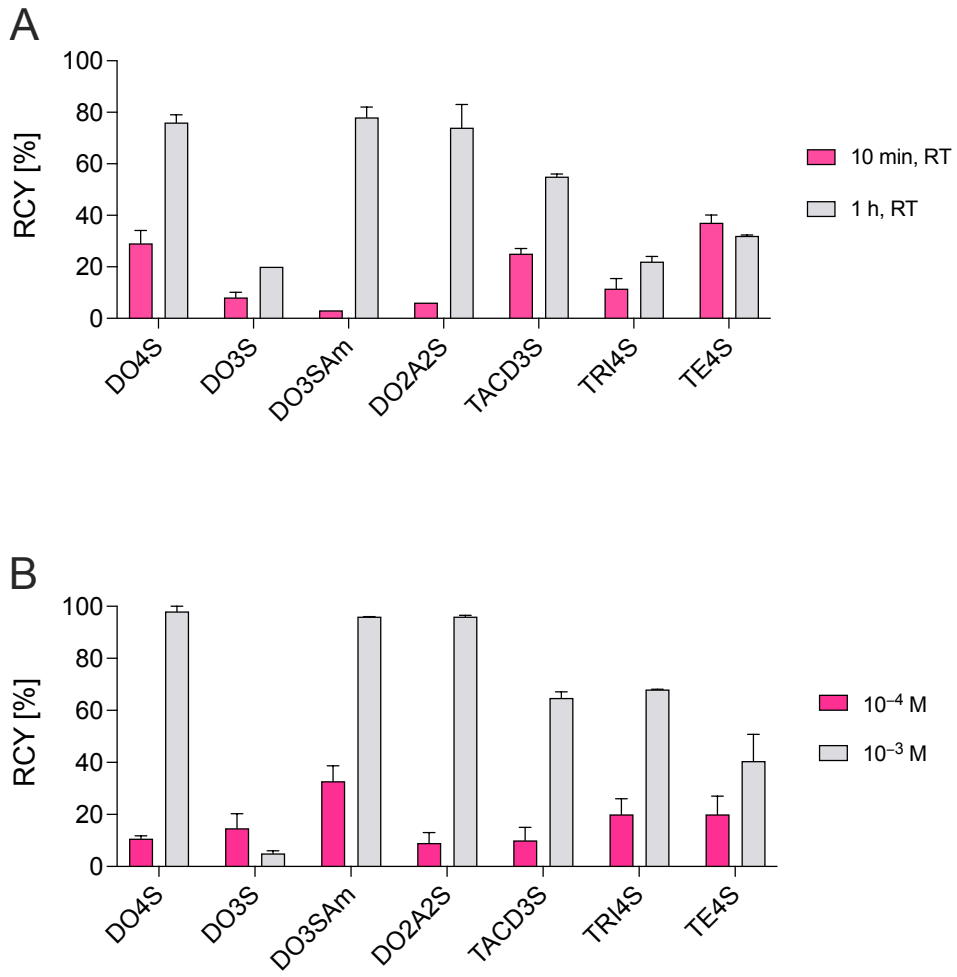

Figure 6.14. [^{197m,g}Hg]Hg^{2+} radiochemical yield (RCY %) for first- and second-generation ligands at (A) RT (ligand concentration 10^{-3} M) and (B) 50°C at pH 7. TRI4S was included as well in this experiment despite the thermodynamic properties of its Hg^{2+} complexes have not yet been determined.

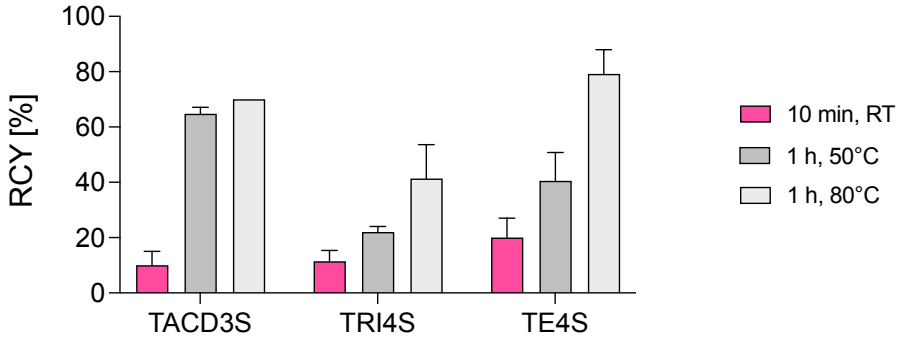

Figure 6.15. [^{197m,g}Hg]Hg^{2+} radiochemical yield (RCY %) for second-generation ligands at different temperatures and pH 7 (ligand concentration 10^{-3} M).

However, the [$^{197m/g}$Hg]Hg^{2+} complexes diluted in PBS and placed in contact with the filter ('control') were found to be completely attached to the device likely due to non-specific interactions. A similar behaviour, albeit much less evident, was also evidenced with the [^{64}Cu]Cu^{2+} complexes (**Chapter 4**) and is therefore partially attributable to the properties of the sulfur-containing macrocycles.

The only technique that proved to be suitable was the Sodium Dodecyl Sulfate - PolyAcrylamide Gel Electrophoresis (SDS-PAGE) as it allowed to differentiate the metal-bound to the proteins and the chelator-bound one. As shown in **Figure 6.16**, the electrophoretic migration of the free [$^{197m/g}$Hg]Hg^{2+} incubated in serum ('control'), the [$^{197m/g}$Hg]Hg^{2+} complex incubated in PBS ('control') and the [$^{197m/g}$Hg]Hg^{2+} complex incubated in serum are different. From the integration of the signals, it was, therefore, possible to obtain the percentages of the intact [$^{197m/g}$Hg]Hg^{2+} complex over time. The obtained results are summarized in **Figure 6.17**. All the [$^{197m/g}$Hg]Hg^{2+} complexes demonstrated to be kinetically inert upon challenged with human serum proteins at 37°C over 24 h, rendering them promising for further biofunctionalization and *in vivo* evaluation.

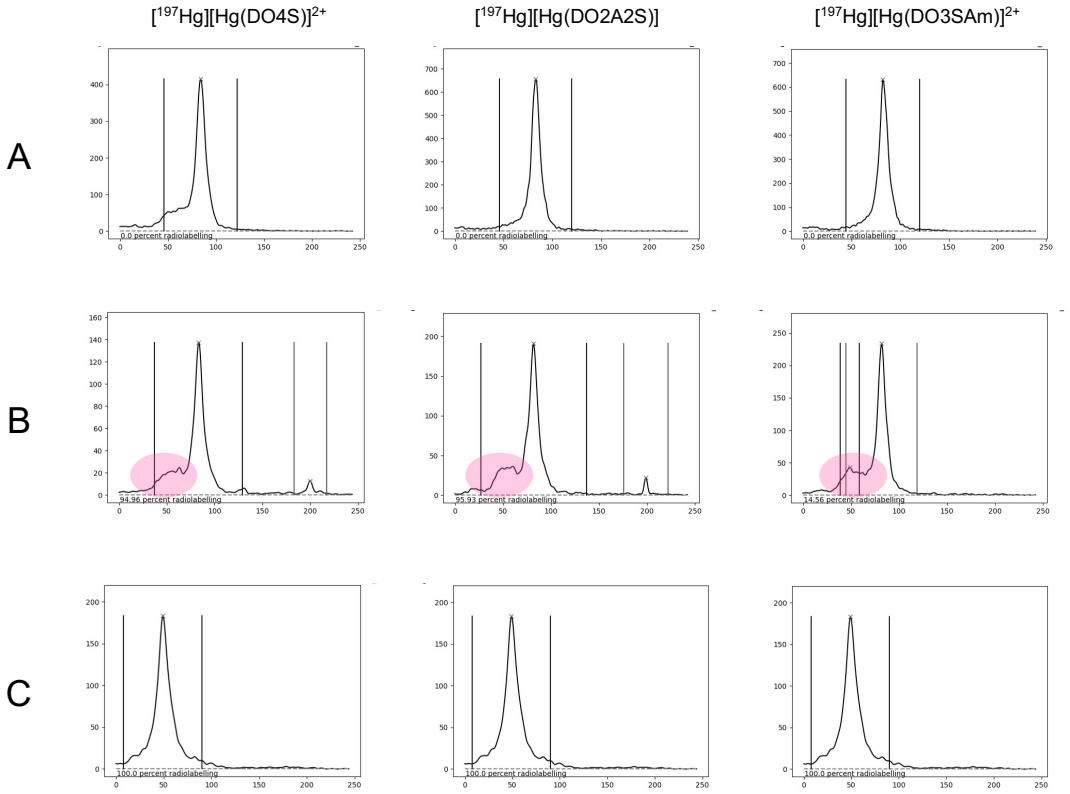

Figure 6.16. Representative SDS-PAGE radioactive scans of the [^{197}Hg]Hg^{2+} complexes with the first-generation ligands incubated in (A) PBS and (B) human serum and comparison with (C) free [^{197}Hg]Hg^{2+} incubated in human serum. Free [^{197}Hg]Hg^{2} transchelated to proteins is highlighted in pink.

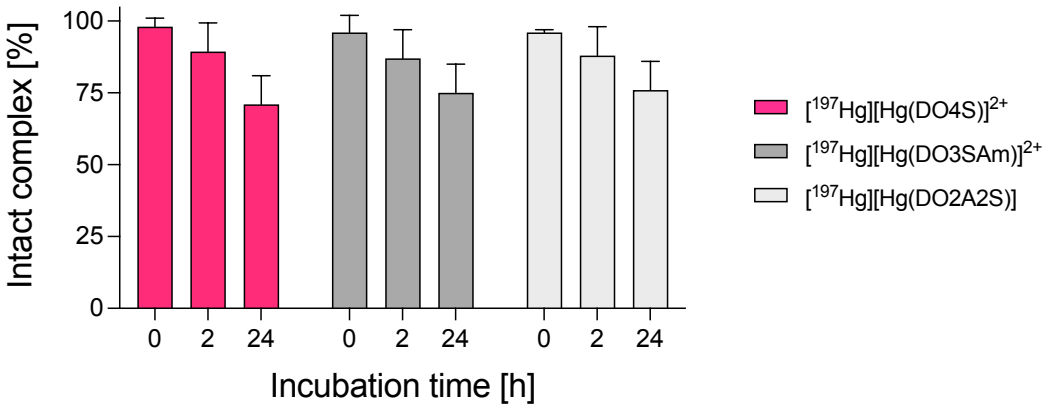

Figure 6.17. Human serum stability of $[^{197}Hg]Hg^{2+}$ complexes at 37°C over 2 days.

6.3 Experimental Section

6.3.1 Materials and Methods

All chemicals were obtained from commercial suppliers and were used as received without further purification. 1,4,7,10-Tetraazacyclododecane (cyclen) and 1,4,7,10-tetraazacyclododecane-1,4,7,10-tetraacetic acid (DOTA) was purchased from Chematech. DO4S, DO3S, DO3SAm, DO2A2S, TACD3S, TRI4S and TE4S were synthesized according to the procedures reported in **Chapter 2**. Mercury nitrate ($Hg(NO_3)_2$) was purchased from Sigma-Aldrich. All solutions were prepared using ultrapure water (18.2 MΩ/cm) purified using a Purelab Chorus (Veolia) or a Milli-Q Millipore system.

6.3.2 Thermodynamic Measurements

The experimental procedures, the details of the apparatus as well as the data processing for the pH-potentiometry and NMR (1D, 2D and VT) followed those reported in **Chapter 3**. ^{1}H-^{199}Hg HSQC NMR data were acquired in non-uniform sampling (NUS) mode (20%) for ^{199}Hg over a ^{1}H frequency width of 10 ppm and a ^{199}Hg frequency width of 1400 ppm. Both experiments were adjusted for a $^{3}J(^{1}H,^{199}Hg)$ coupling of 28-50 Hz, depending on the mercuric complex (**Table 6.3**).

6.3.3 Mercury-197m/g Radiolabelling and *In Vitro* Human Serum Stability

Caution! $^{197m/g}Hg$ is a radionuclide that emits ionizing radiation, and it was manipulated in a specifically designed facility under appropriate safety controls.

^{197}Hg Production. ^{197}Hg was produced on the TR13 (13 MeV) cyclotron at TRIUMF *via* the ^{197}Au(p,n)^{197}Hg nuclear reaction using solid gold targets. The target was irradiated at a beam current of 20 µA for up to four hours. Target removal was performed the next day to lower the radiation exposure to cyclotron operators. ^{197}Hg was separated from the target material by extraction chromatography on LN resin using a previously published procedure.[25] After the separation process, the eluted [^{197}Hg]Hg^{2+} was picked up in 0.01 M HCl. The radionuclidic purity of the obtained [^{197}Hg]Hg^{2+} was confirmed using γ-ray spectroscopy on a high purity germanium (HPGe) gamma spectrometer (Canberra, Mirion Technologies, USA). Spectra were processed using Genie-2000 software.

^{197}Hg Radiolabelling. Stock solutions of the ligands (10^{-2} M) were prepared in ultrapure deionized H_2O + 20% CH_3OH and diluted appropriately to give serial dilution series (10^{-3} - 10^{-4} M). Concentration-dependent radiolabelling was performed by addition of [^{197}Hg]Hg^{2+} (1 - 5 µL, 1 MBq) to a solution containing the ligand (10 µL, 10^{-2} - 10^{-4} M) diluted in ammonium acetate buffer (85 µL, 1 M, pH 7). Water was used instead of the ligands as a negative control. The influence of the temperature on the reaction yield was evaluated by incubating the reaction mixtures at different temperatures (RT, 50°C and 80°C). Radiolabelling reactions were performed at least in triplicate.
The radiolabelling reactions were monitored by quenching an aliquot (10 µL) of the reaction mixture and diluting it with an equal volume of dimercaptosuccinin acid solution (DMSA, $5{\cdot}10^{-2}$ M, pH 5). The quenched solution was mixed, and a portion (10 µL) was spotted onto a silica-impregnated instants thin-layer chromatography paper plate (iTLC-SG, Agilent technologies, USA). DMSA ($5{\cdot}10^{-2}$ M, pH 5) was used as mobile phase. Under these conditions unlabelled [^{197}Hg]Hg^{2+} migrates with the solvent front (R_f = 1) while [^{197}Hg]Hg^{2+}-complexes remain at the baseline (R_f = 0). iTLC-SG plates were analyzed on an Eckert & Ziegler AR-2000 TLC scanner. All data were processed with Eckert & Ziegler WinScan software (USA).

***In Vitro* Human Serum Stability.** The stability of the [^{197}Hg]Hg^{2+}-complexes, prepared using the radiolabelling protocol described above, was assessed by incubation in human plasma at 37°C (1:1 *v*/*v* dilution) at varying time points. The metal-complex stability was monitored over the course of two days *via* SDS-PAGE. An aliquot of labelled complex (5 µL) was diluted with PBS and added to 2×Laemmli (5% *β*-mercaptoethanol) (10 µL), and then the mixture was loaded onto the SDS-PAGE gels. The SDS-PAGE was run at RT and 80 V until the dye front reached the resolving gel. After electrophoresis, the gel was scanned with the radio-TLC scanner described above.

6.4 Conclusion

There has been an increased interest in Meitner-Auger emitters for micrometastatic and small undetectable tumours, as the short path-length and high LET of their emission result in minimal toxicity to surrounding healthy tissue and strong tumour growth inhibition.

Among the Meitner-Auger emitters, mercury isotopes are very promising as they also represent a theranostic pair. However, their clinical application is slowed down by the absence of selective and stable chelating agents.

Herein, the first- and second-generation ligands were investigated with Hg^{2+} as it was postulated the high number of sulfur-donors should allow the formation of stable and inert complexes with this radiometal based on the HSAB theory. Non-radioactive complexation studies, as well as radiolabelling investigations, demonstrated that the introduction of S has a profound effect on increasing the complexes' stability if the cyclen backbone is employed. A combination of monodimensional, bidimensional and variable-temperature NMR allowed to gain insight into the solution structure of the Hg^{2+} complexes with the investigated ligands. ^{1}H-^{199}Hg heteronuclear single quantum coherence experiments allowed to demonstrate the Hg^{2+} coordination in solution. For DO4S and DO2A2S, all the donors are involved in the metal binding ([4N]4S and [4N]2O2S coordination mode, respectively). In DO3S the absence of a sulfur-bearing counter arm on the opposite nitrogen induces remarkable structural difference with respect to DO4S, *e.g.* only two among the four S are involved in the coordination. With a larger ring or fewer nitrogen donors, the thermodynamic stabilities, as well as the corresponding labelling performance, drastically decreased. This highlights the importance of considering the correct macrocyclic platform for the future development of chelators for $[^{197}Hg]Hg^{2+}$.

The high stability encountered with the first-generation ligands opens the way to the potential application of mercury-197 as a theranostic radionuclide bound to biological vectors.

Author Contributions

M. Tosato designed and conducted all the experiments, analyzed and interpreted the data. Dr I. Menegazzo provided guidance for the ^{1}H-^{199}Hg HMQC experiments. Mercury-197 was produced and separated from the gold target by S. Chen, P. Randhawa and M. Tosato at TRIUMF (Vancouver, BC, Canada). Radiolabelling and human serum stability experiments were performed by M. Tosato with assistance from P. Randhawa at TRIUMF (Vancouver, BC, Canada). Prof. C. F. Ramogida was responsible and provide guidance for the radiochemistry experiments together with Prof. V. Radchenko. Prof. V. Di Marco oversaw and supervised the study. The draft of the manuscript was written by M. Tosato.

6.5 References

1 J. A. O' Donoghue and T. E. Wheldon, *Phys. Med. Biol.,* 1996, **41**, 1973-1992.

2 A. Ku, V. J. Facca, Z. Cai and R. M. Reilly, *EJNMMI Radiopharm. Chem.*, 2019, **4**, 27.

3 P. Randhawa, A. P. Olson, S. Chen, K. L. Gower-Fry, C. Hoehr, J. W. Engle, C. F. Ramogida and V. Radchenko, *Curr Radiopharm.*, 2021,**14**, 394-419.

4 A. I. Kassis, *Radiat. Prot. Dosimetry*, 2011, **143**, 241-247.

5 M. Walther, S. Preusche, S. Bartel, G. Wunderlich, R. Freudenberg, J. Steinbach and H. J. Pietzsch, *Appl. Radiat. Isot.* 2015, **97**, 177-181.

6 O. Lebeda and J. Červenák, *Nucl. Instruments Methods Phys. Res. Sect. B Beam Interact. with Mater. Atoms*, 2020, **478**, 85-91.

7 R. Freudenberg, R. Apolle, M. Walther, H. Hartmann and J. Kotzerke, *EJNMMI Phys.*, 2018, **5**, 15.

8 O. Lebeda, F. G. Kondev and J. Červenák, *Nucl. Instruments Methods Phys. Res. Sect. A Accel. Spectrometers, Detect. Assoc. Equip.*, 2020, **959**, 163481.

9 Z. Cai, N. Al-Saden, C. J. Georgiou and R. M. Reilly, *Int. J. Radiat. Biol.*, 2020, 1-22.

10 M. C. Overton, T. P. Haynie and S. R. Snodgrass, *Jama,* 1965, **191**, 431-436.

11 R. L. Greif, W. J. Sullivan, G. S. Jacobs and R. F. Pitts, *J. Clin. Invest.,* 1956, **35**, 38-43

12 G. G. Somjen, S. P. Herman, R. Klein, P. E. Brubaker, W. H. Briner, J. K. Goodrich, M. R. Krigman and J. K. Haseman, *J. Pharmacol. Exp. Ther.*, 1973, **187**, 602-611.

13 A. L. Rhoton, J. Eichling and M. M. Ter-Pogossian, *J. Nucl. Med.*, 1966, **7**, 50-59.

14 J. R. Ribeiro Guevara S, Zizek S, Repinc U, Perez CS and H. M., *Anal Bioanal Chem*, 2007, **387**, 2185-2197.

15 E. Boros and A. B. Packard, *Chem Rev.*, 2019, **119**, 870-901.

16 M. Sadeghi, M. Bakhtiari, M. K. Bakht, M. Anjomrouz and L. Mokhtari, *Phys. Rev. C Nucl. Phys.*, 2012, **C 85**, 034605.

17 I. Carbo-Bague and C. F. Ramogida, in *Encyclopedia of Inorganic and Bioinorganic Chemistry*, 2021.

18 O. Lebeda and J. Cervenak, *Nucl. Instrum. Methods Phys. Res. B*, 2020, **478**, 85-91.

19 J. D. Despotopulos, K. N. Kmak and D. A. Shaughnessy, *J. Radioanal. Nucl. Chem.* 2018, **317**, 985-989.

20 M. Gloris, R. Michel, F. Sudbrock, U. Herpers, P. Malmborg and B. Holmqvist, *Nucl. Instrum. Methods Phys. Res. A*, 2001, **463**, 593-633.

21 P. J. Blower, R. J. Smith and C. Jolley, *Nucl. Med. Commun.*, 1992, **13**, 231.

22 A. Bianchi, M. Micheloni and P. Paoletti, *Coord. Chem. Rev.*, 1991, **110**, 17-113.

23 K. J. Powell, P. L. Brown, R. H. Byrne, T. Gajda, G. Hefter, S. Sjöberg and H. Wanner, *Pure Appl. Chem.*, 2005, **77**, 739-800.

24 M. Litecká, R. Gyepes, Z. Vargová, M. Vilková, M. Almáši, M. Walko and J. Imrich, *J. Coord. Chem.*, 2017, **70**, 1698-1712.

25 M. Walther, O. Lebeda, S. Preusche, H. J. Pietzsch and J. Steinbach, *AIP Conf. Proc.*, 2017, **1845**, 11-15.

Appendix

Appendix A

Supplementary Data for Chapter 2

Table A1. Electronic and Gibbs free energies (in gas-phase and in water) for nine conformers of cyclen. All the energies are in kcal/mol and refer to the most stable structure (given in bold). Level of theory: COSMO-ZORA-OPBE/TZ2P//ZORA-OPBE/DZP. The infill of the circles denotes the position of the nitrogen atoms: a solid infill (black circle) indicates that the atoms are below the molecular plane; conversely, an empty infill indicates that the atoms are above the molecular plane. The cyclen conformer with two adjacent nitrogen atoms above the molecular plane (and the other two below the plane) with all four hydrogens inside the ring was not located on the potential energy surface (PES).

	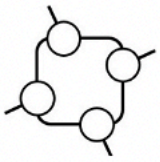		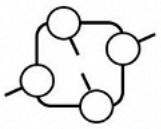
ΔE	12.1	8.9	**0.0**
ΔE_{H2O}	7.0	5.8	**0.0**
ΔG	9.8	8.4	**0.0**
ΔG_{H2O}	4.7	5.3	**0.0**
Point Group	C_4	C_2	**C_2**
	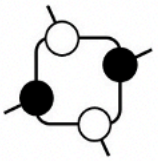		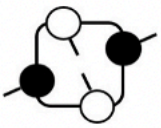
ΔE	10.0	13.9	4.2
ΔE_{H2O}	13.8	13.6	4.7
ΔG	9.1	11.4	3.3
ΔG_{H2O}	13.0	11.2	3.8
Point Group	C_2	C_2	C_2
	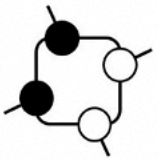	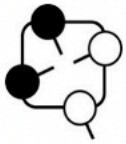	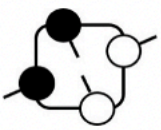
ΔE	10.4	8.0	10.7
ΔE_{H2O}	9.9	8.2	9.9
ΔG	9.4	6.7	9.4
ΔG_{H2O}	9.0	6.9	8.6
Point Group	C_1	C_1	C_1

Table A2. Electronic and Gibbs free energies (in gas-phase and in water) for three monoprotonated and two bis-protonated forms of cyclen. All the energies are in kcal/mol and are relative to the most stable structure (in bold). Level of theory: COSMO-ZORA-OPBE/TZ2P//ZORA-OPBE/DZP.

	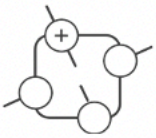		
ΔE	**0.0**	11.5	–5.3
ΔE_{H2O}	**0.0**	9.8	2.3
ΔG	**0.0**	10.6	–5.5
ΔG_{H2O}	**0.0**	8.9	2.0
Point Group	**C_1**	C_1	C_1

		
ΔE	27.9	**0.0**
ΔE_{H2O}	19.6	**0.0**
ΔG	26.3	**0.0**
ΔG_{H2O}	18.1	**0.0**
Point Group	C_2	**C_1**

Table A3. Calculated pK_a and ΔG_{H2O} (kcal/mol) for cyclen. Level of theory: COSMO-ZORA-OPBE/TZ2P//ZORA-OPBE/DZP.

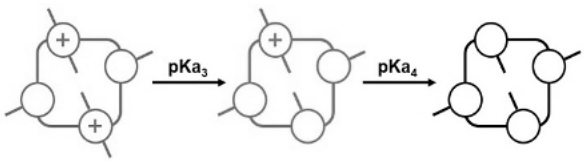

	pK_{a3}	**ΔG_{H2O}**	**pK_{a4}**	**ΔG_{H2O}**	**ΔpK_a**
Method 1	9.0	12.2	11.5	15.7	2.5
Method 2	7.9	13.2	10.4	16.6	2.5

Table A4. Calculated pK_a and ΔG_{H2O} (kcal/mol) values for DO3S using paths A, B and C. Level of theory: COSMO-ZORA-OPBE/TZ2P//ZORA-OPBE/DZP.

path A	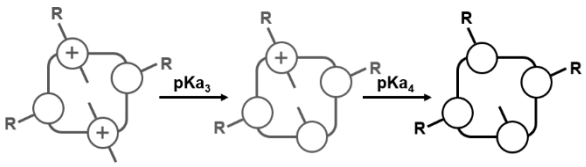				
	pK_{a3}	ΔG_{H2O}	pK_{a4}	ΔG_{H2O}	ΔpK_a
Method 1	4.7	6.4	8.5	11.6	3.8
Method 2	3.7	7.4	7.5	12.6	3.8
path B	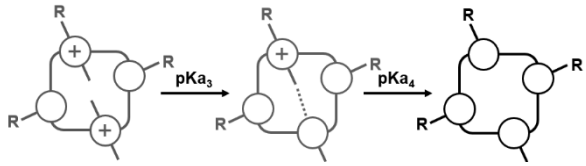				
	pK_{a3}	ΔG_{H2O}	pK_{a4}	ΔG_{H2O}	ΔpK_a
Method 1	3.4	4.6	16.4	22.3	13.0
Method 2	2.3	5.5	15.3	23.3	13.0
path C	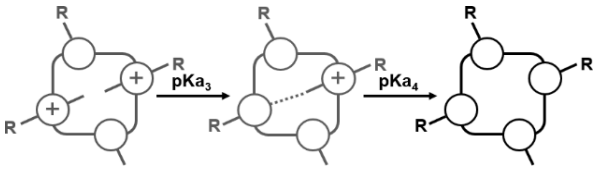				
	pK_{a3}	ΔG_{H2O}	pK_{a4}	ΔG_{H2O}	ΔpK_a
Method 1	3.9	5.3	14.1	19.3	10.2
Method 2	2.9	6.3	13.1	20.2	10.2

Table A5. Calculated pK_a and ΔG_{H2O} (kcal/mol) for DO4S. Level of theory: COSMO-ZORA-OPBE/TZ2P//ZORA-OPBE/DZP.

	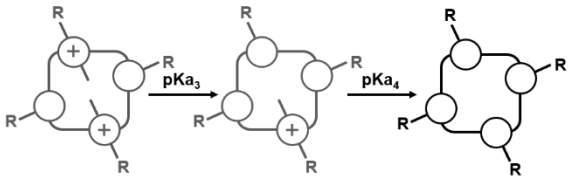				
	pK_{a3}	**ΔG_{H2O}**	**pK_{a4}**	**ΔG_{H2O}**	**ΔpK_a**
Method 1	3.8	5.2	13.0	17.8	9.2
Method 2	2.8	6.1	12.0	18.7	9.2

Table A6. Chemical shift, multiplicity, area, and ^1H resonance assignments for DO4S.

Species	δ [ppm]	Multiplicity	Area	Assignation
HL^+	2.17	s	12	SCH_3
	2.79	t	8	SCH_2
	2.88	s	16	NCH_2 ring
	3.05	t	8	NCH_2 arms
H_2L^{2+}	2.20	s	12	SCH_3
	2.94	m	8	SCH_2
	3.28	m br	24	NCH_2 ring + NCH_2 arms

m = multiplet; m br = multiplet broad; s = singlet; t = triplet

Table A7. Chemical shift, multiplicity, area, and ^1H resonance assignments for DO3S.

Species	δ [ppm]	Multiplicity	Area	Assignation
HL^+	2.15	s	6	N_1, N_7 - SCH_3
	2.17	s	3	N_4 - SCH_3
	2.70 - 2.86	m	22	SCH_2 + NCH_2 ring + NCH_2 arms
	3.00 - 3.07	m	6	NCH_2 arms
H_2L^{2+}	2.18	s	6	N_1, N_7 - SCH_3
	2.22	s	3	N_4 - SCH_3
	2.79	t	4	SCH_2 (^1H_a)
	2.87	m br	2	NCH_2 arm (^1H_b)
	2.94	m br	8	NCH_2 arm (^1H_b) + NCH_2 ring (^1H_e)
	3.03	t	2	SCH_2 (^1H_c)
	3.07	m br	2	
	3.20	m br	2	
	3.37	m br	2	NCH_2 ring (^1H_e)
	3.45	m br	2	
	3.52	m br	2	
	3.61	t	2	SCH_2 (^1H_d)

m = multiplet; m br = multiplet broad; s = singlet; t = triplet

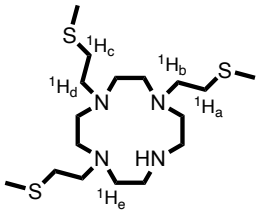

Table A8. Chemical shift, multiplicity, area, and ^1H resonance assignments for DO3SAm.

Species	δ [ppm]	Multiplicity	Area	Assignation
	2.16	s	6	N_1, N_7 - SCH_3
	2.20	s	3	N_4 - SCH_3
HL^+	2.65 - 3.21	m br	28	SCH_2 + NCH_2 ring + NCH_2 arms
	2.80	s	3	NCH_3 arms (^1H_a)
	3.30	m br	2	CH_2 (^1H_b)
	2.19	s	9	SCH_3
H_2L^{2+}	2.82 - 3.56	m br	28	SCH_2 + NCH_2 ring + NCH_2 arms
	2.81	s	3	NCH_3 arms (^1H_a)

m = multiplet; m br = multiplet broad; s = singlet

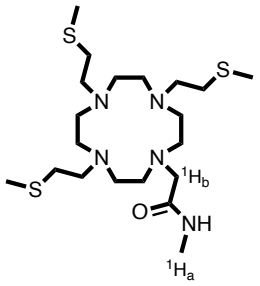

Table A9. Chemical shift, multiplicity, area, and ^1H resonance assignments for DOT-*n*-Bu.

Species	δ [ppm]	Multiplicity	Area	Assignation
	0.94	t	12	CH_3 (^1H_a)
	1.36	q	8	CH_2 (^1H_b)
HL^+	1.58	q	8	CH_2 (^1H_c)
	2.80	m	8	NCH_2 arms (^1H_d)
	2.98	s	16	NCH_2 ring (^1H_e)
	0.94	t	12	CH_3 (^1H_a)
	1.37	q	8	CH_2 (^1H_b)
H_2L^{2+}	1.60	q	8	CH_2 (^1H_c)
	2.97	m	8	NCH_2 arms (^1H_d)
	3.21	s	16	NCH_2 ring (^1H_e)

m = multiplet; m br = multiplet broad; s = singlet; t = triplet; q = quintet

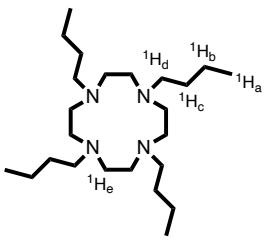

Table A10. Chemical shift, multiplicity, area, and ^{1}H resonance assignments for DO2A2S.

Species	δ [ppm]	Multiplicity	Area	Assignation
H_2L	2.15	s	6	SCH_3
	2.79	t	4	SCH_2
	3.08	s br	4	NCH_2 arms
	3.16	s br	8	NCH_2 ring (^1H_a)
	3.33	s br	8	NCH_2 ring (^1H_b)
	3.67	s br	4	CH_2 arms (^1H_c)
H_3L^+	2.16	s	6	SCH_3
	2.93	t	4	SCH_2
	3.11	m	4	NCH_2 ring (^1H_a)
	3.21	m	4	NCH_2 ring (^1H_a)
	3.45	s	8	NCH_2 ring (^1H_b)
	3.50	t	4	CH_2 arms
	3.54	s	4	CH_2 arms (^1H_c)

m = multiplet; m br = multiplet broad; s = singlet; t = triplet

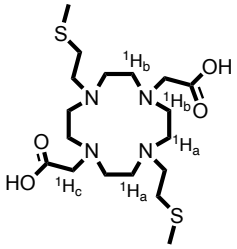

Table A11. Chemical shift, multiplicity, area, and ^{1}H resonance assignments for DO4S4Me.

Species	δ [ppm]	Multiplicity	Area	Assignation
HL^+	1.04	m br	12	CH_3 (^1H_e)
	2.19	m br	12	SCH_3
	2.60 - 3.18	m br	24	SCH_2 (^1H_a) + NCH_2 arms (^1H_b) + NCH_2 ring (^1H_c)
	3.27	m br	4	NCH_2 ring (^1H_d)
H_2L^{2+}	1.22	d	12	CH_3 (^1H_e)
	2.21	s	12	SCH_3
	2.80	m	4	NCH_2 ring (^1H_c)
	2.99	m	8	SCH_2 (^1H_a)
	3.00	m	4	NCH_2 ring (^1H_c)
	3.26	m br	8	NCH_2 arms (^1H_b)
	3.59	m br	2	NCH_2 ring (^1H_d)
	3.84	m br	2	NCH_2 ring (^1H_d)

d = doublet; m = multiplet; m br = multiplet broad; s = singlet

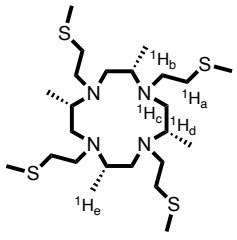

Table A12. Lowest and most intense computed excitation energies (level of theory: COSMO-ZORA-SAOP/QZ4Pae//ZORA-OPBE/DZP) of cyclen, DO3S and DO4S.

		COSMO-TD-DFT Values	Electronic transitions [% assignment]
Cyclen	**L**	5.5175 eV (0.0344) - 225 nm 6.54765 eV (0.10040) - 200 nm	HOMO → LUMO (98%) HOMO → LUMO+6 (96%)
	HL^+	5.6636 eV (0.00479) - 219 nm 6.7329 eV (0.08054) - 184 nm	HOMO → LUMO (99%) HOMO → LUMO+5 (85%)
	H_2L^{2+}	6.1566 eV (0.0141) - 201 nm 7.5958 eV (0.24039) - 163 nm	HOMO → LUMO (99%) HOMO → LUMO+9 (97%)
DO3S	**L**	4.4605 eV (0.00689) - 278 nm 5.31891 eV (0.02905) - 233 nm	HOMO → LUMO (100%) HOMO-3 → LUMO+4 (66%)
	HL^+	4.8827 eV (0.000354) - 254 nm 5.98296 eV (0.02545) - 207 nm	HOMO → LUMO (100%) HOMO-1 → LUMO+10 (95%)
	H_2L^{2+}	4.7593 eV (0.00220) - 260 nm 6.05491 eV (0.07081) - 205 nm	HOMO → LUMO (97%) HOMO-3 → LUMO+3 (95%)
DO4S	**L**	4.3251 eV (0.00194) - 287 nm 4.78384 eV (0.02606) - 259 nm	HOMO → LUMO (100%) HOMO-2 → LUMO+1 (61%)
	HL^+	4.8627 eV (0.000335) - 255 nm 5.60689 eV (0.01931) - 221 nm	HOMO → LUMO (98%) HOMO-5 → LUMO+6 (100%)
	H_2L^{2+}	4.7426 eV (0.00333) - 261 nm 5.67375 eV (0.03349) - 219 nm	HOMO → LUMO (100%) HOMO-4 → LUMO (98%)

Table A13. Chemical shift, multiplicity, area, and ^1H resonance assignments for TACD3S.

Species	δ [ppm]	Multiplicity	Area	Assignation
L	1.51 - 1.71	m	6	CH_2 ring
	2.15	s	9	SCH_3
	2.43 - 2.83	m	24	SCH_2 + NCH_2 ring + NCH_2 arms
HL^+	1.85 - 1.93	m	6	CH_2 ring
	2.16	s	9	SCH_3
	2.79	t	6	SCH_2
	2.83 - 2.93	m	12	NCH_2 ring
	2.93 - 3.01	m	6	NCH_2 arms
H_2L^{2+}	2.04 - 2.12	qn	6	CH_2 ring
	2.15	s	9	SCH_3
	2.84	t	6	SCH_2
	3.10 - 3.19	m	18	NCH_2 ring + NCH_2 arms
H_3L^{3+}	2.15	s	9	SCH_3
	2.27 - 2.35	qn	6	CH_2 ring
	2.92	t	6	SCH_2
	3.46 - 3.54	m	18	NCH_2 ring + NCH_2 arms

m = multiplet; qn = quintet; s = singlet; t = triplet

Table A14. Chemical shift, multiplicity, area, and ^1H resonance assignments for TRI4S.

Species	δ [ppm]	Multiplicity	Area	Assignation
L	1.65	m	2	CH_2 ring
	2.14	s	12	SCH_3
	2.61	m	4	NCH_2 ring
HL^+	1.89	m	2	CH_2 ring
	2.16	s	6	SCH_3
	2.17	s	6	SCH_3
	2.72 - 2.89	m	24	SCH_2 + NCH_2 ring + NCH_2 arms
	2.98 - 3.03	m	8	
H_2L^{2+}	2.00	m	2	CH_2 ring
	2.18	s	6	SCH_3
	2.19	s	6	SCH_3
	2.86	t	8	SCH_2
	3.05 - 3.26	m	24	NCH_2 ring + NCH_2 arms
H_3L^{3+}	2.16	s	6	SCH_3
	2.17	s	6	SCH_3
	2.25	m	2	CH_2 ring
	2.87	t	4	SCH_2
	2.93	t	4	SCH_2
	3.21	t	4	NCH_2 arms
	3.34	s	4	NCH_2 ring (^1H_b)
	3.47 - 3.53	m	12	NCH_2 arms + NCH_2 ring (^1H_a + ^1H_c)
	3.67	t	4	NCH_2 ring (^1H_a)

m = multiplet; s = singlet; t = triplet

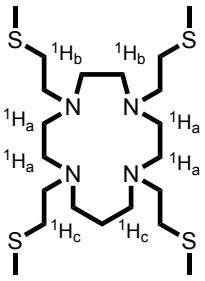

Table A15. Chemical shift, multiplicity, area, and ^1H resonance assignments for TE4S.

Species	δ [ppm]	Multiplicity	Area	Assignation
L	1.70	m	4	CH_2 ring
	2.13	s	12	SCH_3
	2.55 - 2.81	m	4	SCH_2 + NCH_2 ring + NCH_2 arms
HL^+	2.00	m br	4	CH_2 ring
	2.16	s	12	SCH_3
	3.02	m	4	SCH_2 + NCH_2 ring + NCH_2 arms
H_2L^{2+}	2.00	m	4	CH_2 ring
	2.16	s	12	SCH_3
	2.83	t	8	SCH_2
	3.11	m	8	NCH_2 ring (^1H_b)
	3.03	m	8	NCH_2 arms
	3.17	s	8	NCH_2 ring (^1H_a)
H_3L^{3+}	2.16	s	12	SCH_3
	2.16	m	4	CH_2 ring
	2.95	t	8	SCH_2
	3.58	m	8	NCH_2 ring (^1H_b)
	3.53	m	8	NCH_2 arms
	3.84	s	8	NCH_2 ring (^1H_a)

m = multiplet; m br = multiplet broad; s = singlet; t = triplet

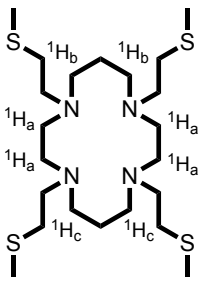

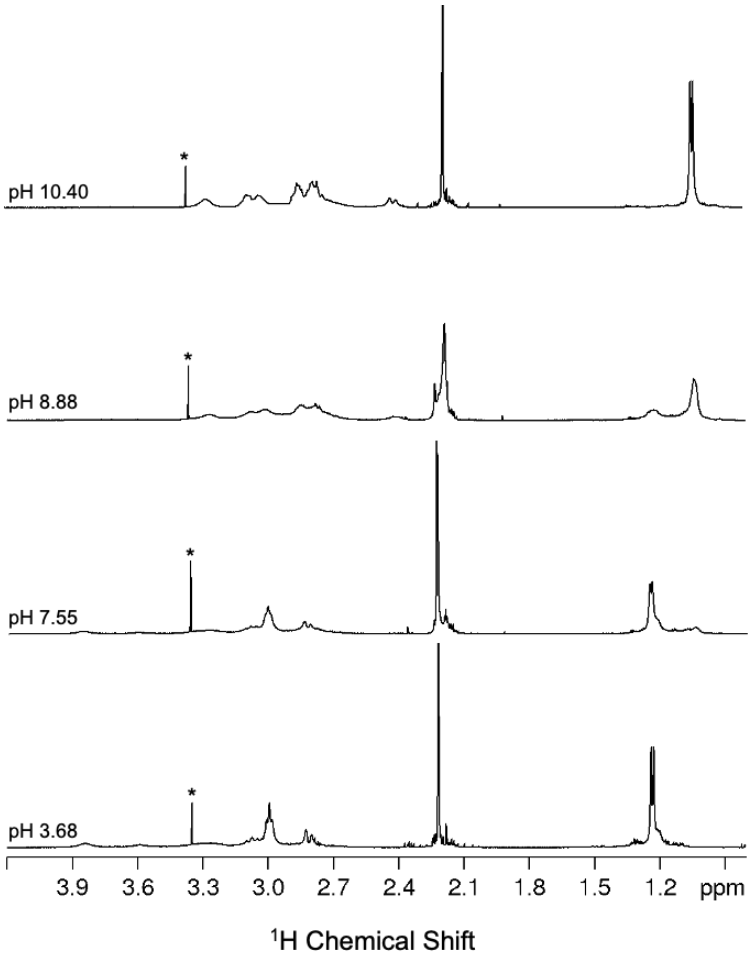

Figure A1. Variable-pH ^{1}H NMR spectra of DO4S4Me (600 MHz, H_2O + 10% D_2O, T = 25°C, $C_{DO4S4Me}$ = $1.0 \cdot 10^{-3}$ M). The signals marked with an asterisk are related to a methanol impurity.

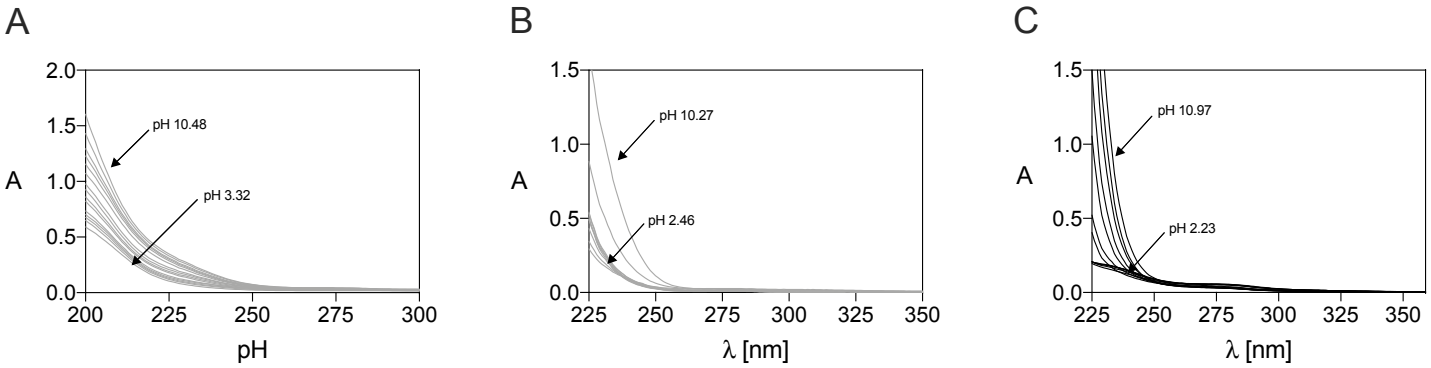

Figure A2. UV-Vis spectra of (A) DO4S4Me ($C_{DO4S4Me}$ = 1.14·10^{-3} M), (B) DO2A2S (C_{DO2A2S} = 1.345·10^{-3} M) and (C) cyclen (C_{cyclen} = 1.39·10^{-2} M) at different pH.

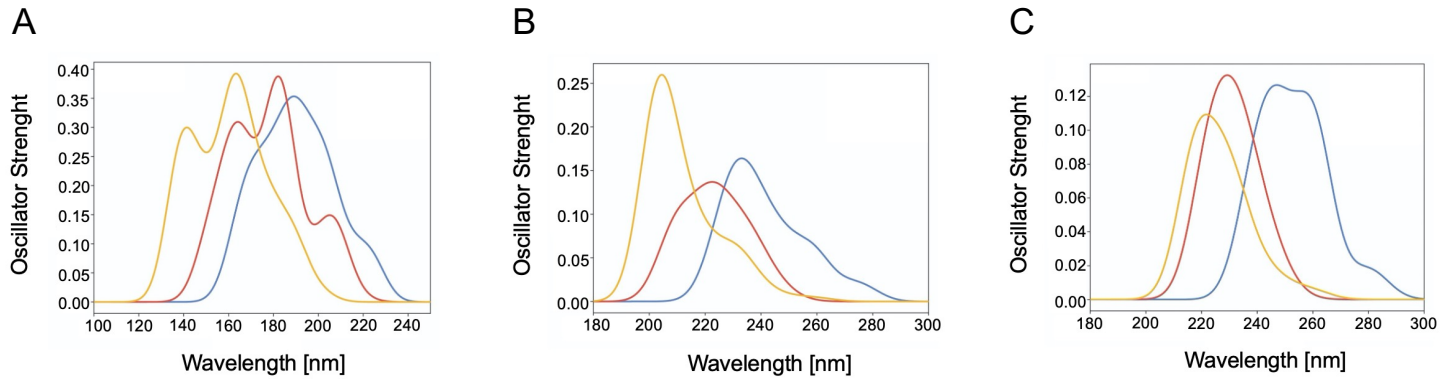

Figure A3. Predicted UV-Vis spectrum (level of theory: COSMO-ZORA-SAOP/QZ4Pae//OPBE/DZP) for (A) cyclen, (B) DO3S and (C) DO4S in three different protonation states (L in blue, HL^+ in red, H_2L^{2+} in yellow).

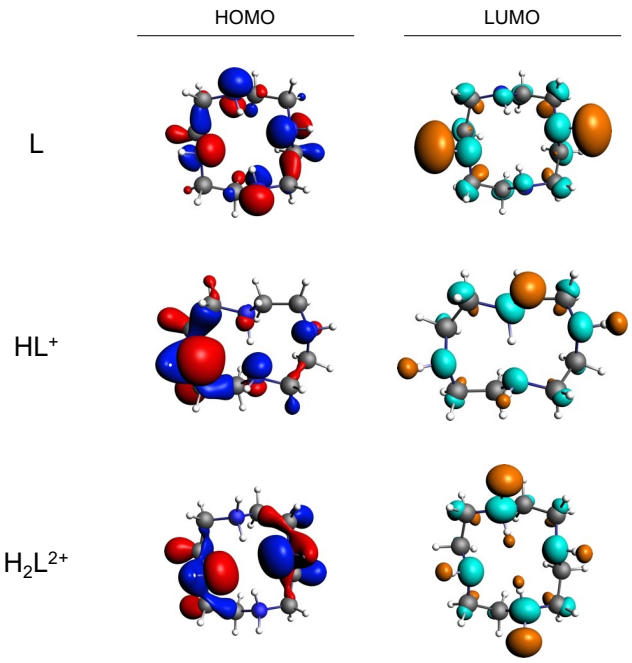

Figure A4. HOMO and LUMO for differently protonated species of cyclen (level of theory: COSMO-ZORA-SAOP/QZ4Pae//ZORA-OPBE/DZP).

Appendix B

Supplementary Data for Chapter 3

Table B1. Chemical shift, multiplicity, area, and ^{1}H resonance assignments for Ag^{+} complexes formed by DO4S.

Species	pD	δ [ppm]	Multiplicity	Area	Assignation
$[Ag(DO4S)]^{+}$	≥ 6.0	2.22	s	12	SCH_3
		2.75	s br	24	NCH_2
		2.84	t	8	SCH_2
$[Ag(DO4S)]^{+}$ (58%) + $[Ag(HDO4S)]^{2+}$ (41%)	4.4	2.20	s	12	SCH_3
		2.73	s br	24	NCH_2
		2.82	t	8	SCH_2
		2.30	s	12	SCH_3
		2.97	s br	24	NCH_2
		3.04	t	8	SCH_2
$[Ag(DO4S)]^{+}$ (37%) + $[Ag(HDO4S)]^{2+}$ (62%)	3.6	2.20	s	12	SCH_3
		2.72	s br	24	NCH_2
		2.82	t	8	SCH_2
		2.30	s	12	SCH_3
		2.97	s br	24	NCH_2
		3.04	t	8	SCH_2
H_2DO4S^{2+} (14%) + $[Ag(HDO4S)]^{2+}$ (86%)	2.1	2.20	s	–	SCH_3
		2.32	s	12	SCH_3
		2.98	s br	8	NCH_2
		3.05	s br	24	SCH_2

s = singlet; t = triplet; br = broad

Table B2. Chemical shift, multiplicity, area, and ^{1}H resonance assignments for Ag^{+} complexes formed by DO3S.

Species	pD	δ [ppm]	Multiplicity	Area	Assignation
$[Ag(DO3S)]^{+}$	≥ 7.8	2.19	s	3	SCH_3
		2.23	s	6	SCH_3
		2.44-2.90	m br	28	$SCH_2 + NCH_2$
$[Ag(HDO3S)]^{2+}$	5.4 4.2	2.33	s	9	SCH_3
		2.46-3.05	m br	28	$SCH_2 + NCH_2$

m = multiplet; s = singlet; br = broad

Table B3. Chemical shift, multiplicity, area, and ^{1}H resonance assignments for Ag^{+} complexes formed by DO3SAm.

Species	δ [ppm]	Multiplicity	Area	Assignation
$[Ag(DO3SAm)]^{+}$	2.39	s	6	SCH_3
	2.45	s	3	SCH_3
	2.58-3.28	m br	31	$SCH_2 + NCH_2 + NCH_3$
	2.73	s	2	$\underline{CH_2}CONHCH_3$
$[Ag(HDO3SAm)]^{2+}$	2.35	s	9	SCH_3
	2.66-3.25	m br	31	$SCH_2 + NCH_2 + NCH_3$
	3.53	s	2	$\underline{CH_2}CONHCH_3$

m = multiplet; s = singlet; br = broad

Table B4. Chemical shift, multiplicity, area, and ^{1}H resonance assignments for Ag^{+} complexes formed by DO2A2S.

Species	δ [ppm]	Multiplicity	Area	Assignation
$[Ag(DO2A2S)]^{-}$	2.30	s	6	SCH_3
	2.60 + 2.80 + 2.95	s br	24	NCH_2
	2.90	t	4	SCH_2
	3.39	s	4	$\underline{CH_2}COOH$
[Ag(HDO2A2S)]	2.30	s	6	SCH_3
	2.80 + 3.10	s br	24	NCH_2
	2.92	t	4	SCH_2
	3.55	s br	4	$\underline{CH_2}COOH$
$[Ag(H_2DO2A2S)]^{+}$	2.30	s	6	SCH_3
	2.80 + 3.15	s br	24	NCH_2
	2.92	t	4	SCH_2
	3.65	s br	4	$\underline{CH_2}COOH$

s = singlet; t = triplet; br = broad

Table B5. Chemical shift, multiplicity, area, and ^{1}H resonance assignments for the Ag^{+} complexes formed by DO4S4Me.

Species	pH	δ [ppm]	Multiplicity	Area	Assignation
AgL^{+}	≥ 2.86	0.93	d	12	CH_3
		2.39	s	3	SCH_3
		2.40	s	9	SCH_3
		2.68	m	2	NCH2 ring
		2.82	m	8	NCH_2 ring + SCH_2
		2.90	m	2	NCH_2 side arm
		3.01	m	6	NCH_2 side arm
		3.16	m	6	SCH_2
		3.23	m	3	NCH ring
		3.31	m	1	NCH ring
$AgHL^{2+}$ + $AgHL^{2+}$	≥ 2.86	0.91	d	12	CH_3
		2.40	s	3	SCH_3
		2.44	s	9	SCH_3
		2.67	m	2	NCH_2 ring
		2.80	m	8	NCH_2 ring + SCH_2
		2.88	m	2	NCH_2 side arm
		3.09	m	2	NCH_2 side arm
		3.16	m	6	SCH_2
		3.23	m	3	NCH ring
		3.31	m	1	NCH ring
		1.08	d	-	CH_3
		2.37	s	-	SCH_3
		3.52	s	-	CH

s = singlet; d = doublet; m = multiplet

Table B6. Chemical shift, multiplicity, area, and ^{1}H resonance assignments for the Ag^{+} complexes formed by TACD3S.

Species	δ [ppm]	Multiplicity	Area	Assignation
[AgL(OH)]	1.53 - 1.67	m, br	3	CH_2 ring
	1.92 - 2.06	m, br	3	CH_2 ring
	2.24	s	9	SCH_3
	2.64	t	6	NCH_2 arms
	2.66 - 2.78	m	12	NCH_2 ring
	2.89	t	6	SCH_2
$[AgL]^{+}$	1.54 - 1.73	m br	3	CH_2 ring
	1.87 - 2.04	m br	3	CH_2 ring
	2.22	s	9	SCH_3
	2.61 - 2.82	m	18	NCH_2 ring + NCH_2 arms
	2.82 - 2.92	m	6	SCH_2
$[AgHL]^{2+}$	1.85 - 2.12	m br	6	CH_2 ring
	2.26	s	9	SCH_3
	2.85 - 3.10	m	24	SCH_2 + NCH_2 ring + NCH_2 arms

s = singlet, t = triplet, m = multiplet, br = broad

Table B7. Chemical shift, multiplicity, area, and ^{1}H resonance assignments for the Ag^{+} complexes formed by TRI4S.

Species	δ [ppm]	Multiplicity	Area	Assignation
$[AgL]^{+}$	1.68 - 1.78	m br	1	CH_2 ring
	1.82 - 1.94	m br	1	CH_2 ring
	2.21	s	6	SCH_3
	2.23	s	6	SCH_3
	2.58-2.86	m	32	SCH_2 + NCH_2 ring + NCH_2 arms
$[AgHL]^{2+}$	-	-	-	CH_2 ring not visible
	2.20	m br	6	SCH_3
	2.30	s	6	SCH_3
	2.60 - 3.30	m	32	SCH_2 + NCH_2 ring + NCH_2 arms

s = singlet, m = multiplet, br = broad

Table B8. Chemical shift, multiplicity, area, and ^{1}H resonance assignments for the Ag^{+} complexes formed by TE4S.

Species	δ [ppm]	Multiplicity	Area	Assignation
$[AgL]^{+}$	1.77	m br	1	CH_2 ring
	1.91	m br	1	CH_2 ring
	2.24	s	12	SCH_3
	2.52 - 2.97	m	32	SCH_2 + NCH_2 ring + NCH_2 arms
$[AgHL]^{2+}$	2.03	m br	2	CH_2 ring
	2.24	s	6	SCH_3
	2.60 - 3.22	m	32	SCH_2 + NCH_2 ring + NCH_2 arms

s = singlet, m = multiplet, br = broad

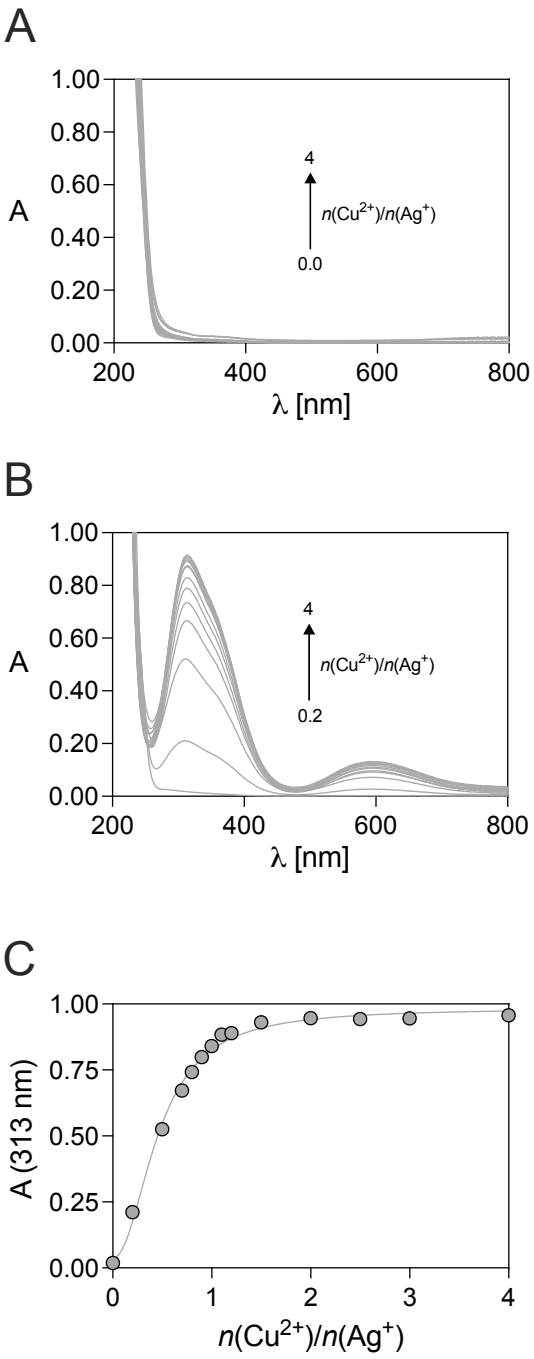

Figure B1. UV-Vis spectra of the preformed Ag^+ complex with TRI4S (C_{Ag^+} = C_{TRI4S} = $1.0 \cdot 10^{-4}$ M, pH 3.7) (A) immediately after the addition of variable equivalents of Cu^{2+} (t = 0) and (B) at equilibrium during the competition titrations; (C) representative A *vs.* $n(Cu^{2+})/n(Ag^+)$ profile obtained during the Ag^+-Cu^{2+} competitions measurements and corresponding fitting lines.

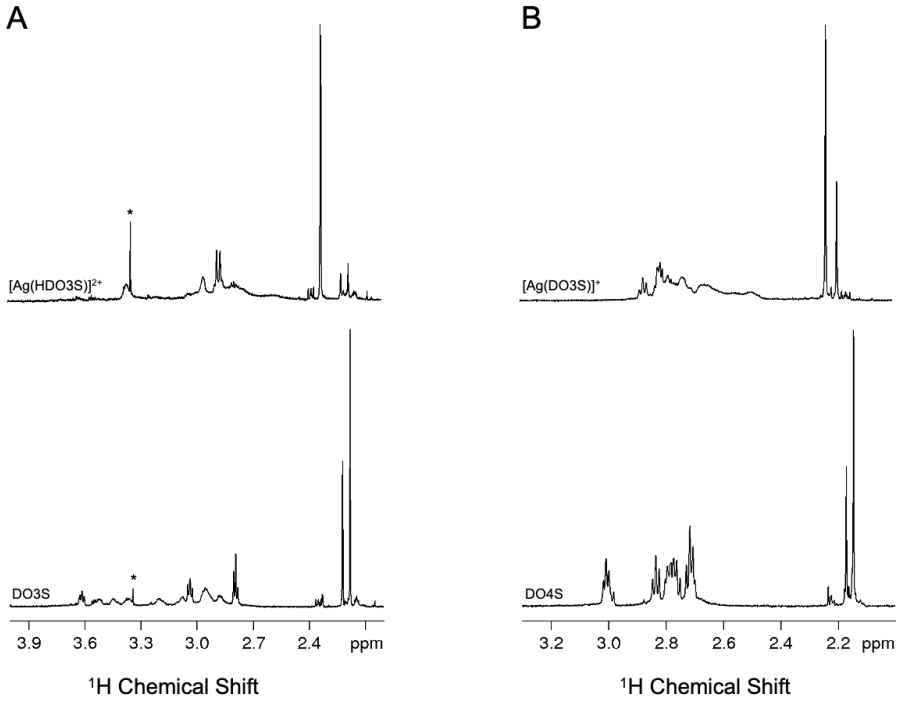

Figure B2. Comparison of the ^{1}H NMR spectra (600 MHz, T = 25°C, D_2O) of (A) bis-protonated DO3S and $[Ag(HDO3S)]^{2+}$ and (B) monoprotonated DO3S and $[Ag(DO3S)]^{+}$. The signals marked with an asterisk are related to methanol impurities.

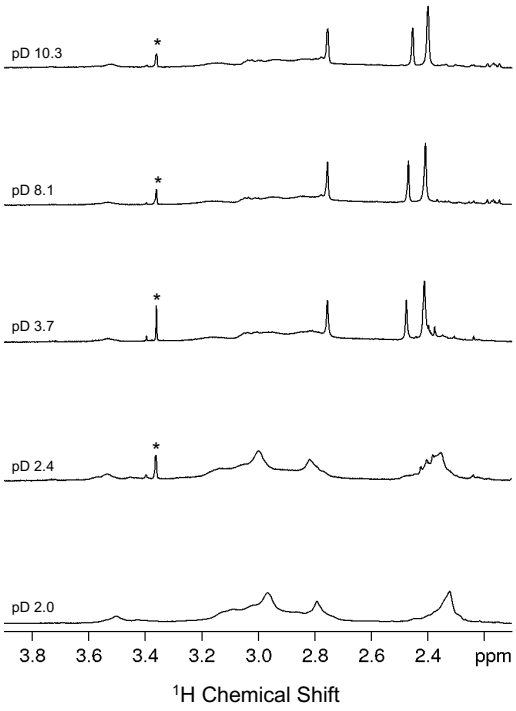

Figure B3. Variable-pH ^{1}H NMR spectra of Ag^+-DO3SAm (400 MHz, T = 25°C, D_2O, $C_{Ag^+} = 8.6 \cdot 10^{-4}$ M, $C_{DO3SAm} = 8.5 \cdot 10^{-4}$ M). The signals marked with an asterisk are related to a methanol impurity.

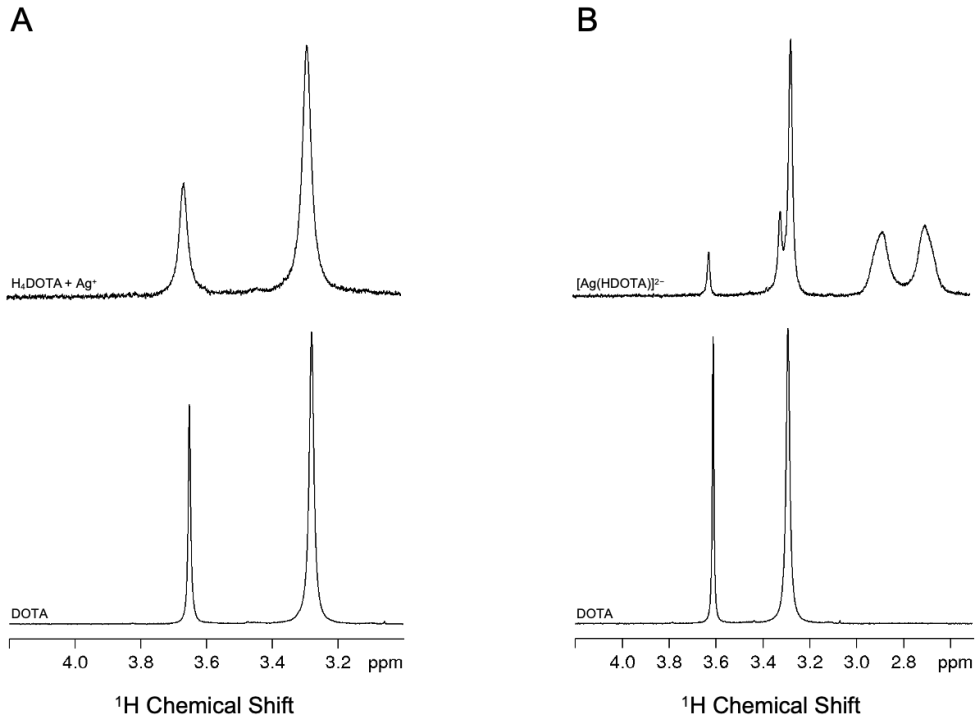

Figure B4. Comparison of the ^{1}H NMR spectra (400 MHz, RT, H_2O + 10% D_2O) of Ag^{+}-DOTA and free DOTA at (A) pH 4.15 and (B) pH 6.20.

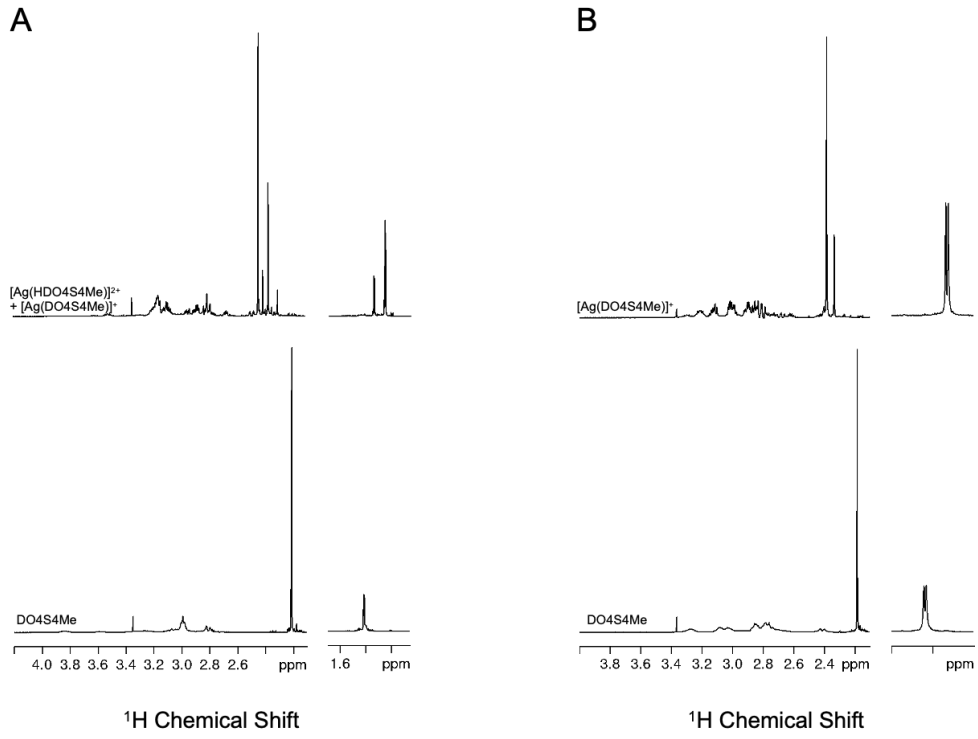

Figure B5. Comparison between the ^{1}H NMR spectra (600 MHz, 25°C, H_2O + 10% D_2O) of $[AgL]^{+}$ and free ligand at pH ~ 9. The signals marked with an asterisk are related to a methanol impurity.

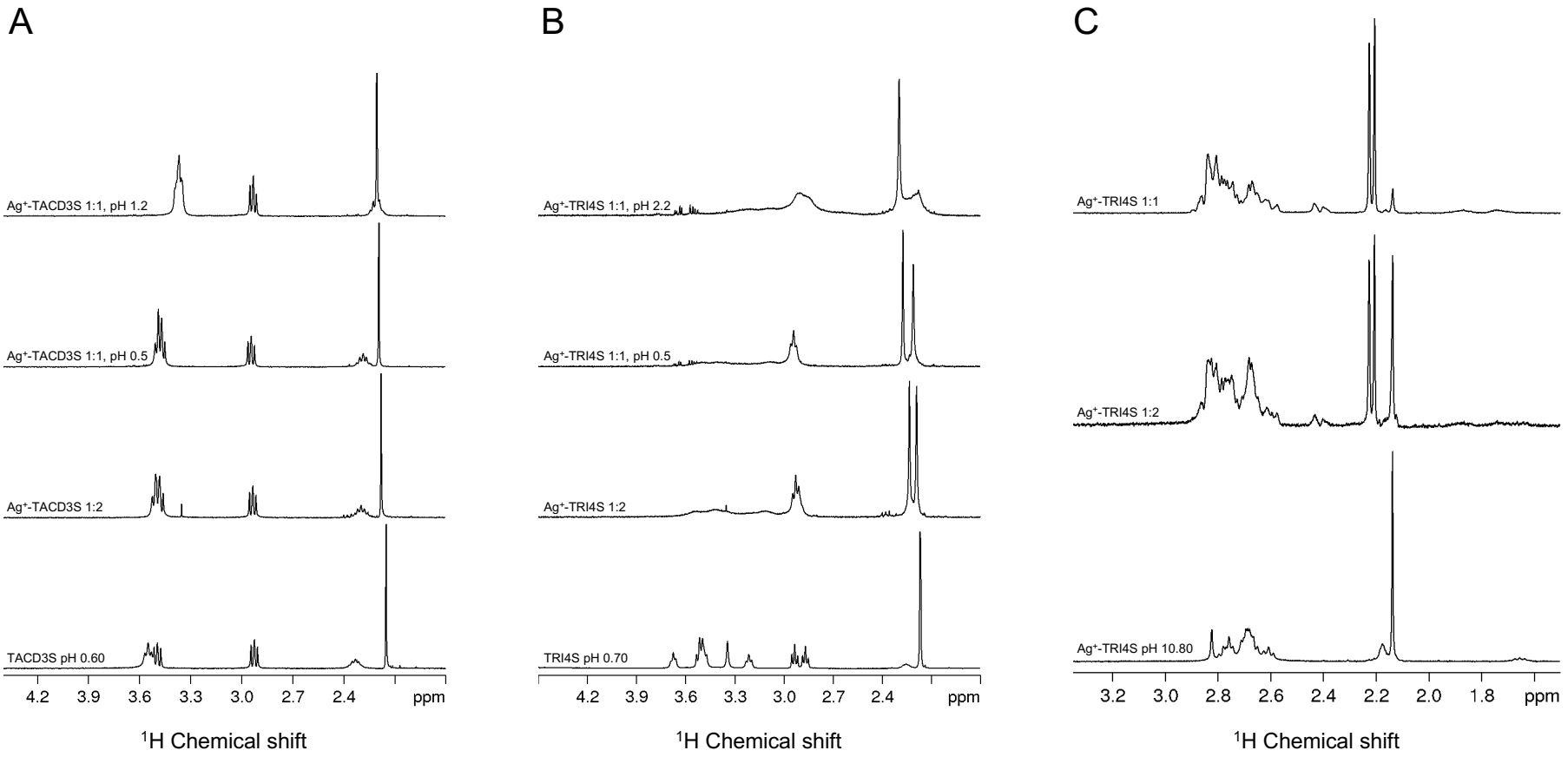

Figure B6. Comparison of the ^{1}H NMR spectra (400 MHz, T = 25°C, H_2O + 10% D_2O) of (A) Ag^{+}-TACD3S (pH 0.5), (B) Ag^{+}-TRI4S (pH 0.5) and (C) Ag^{+}-TRI4S (pH 12.0) at 1:2 metal-to-ligand ratio with the spectra of free ligands and those at 1:1 metal-to-ligand ratio.

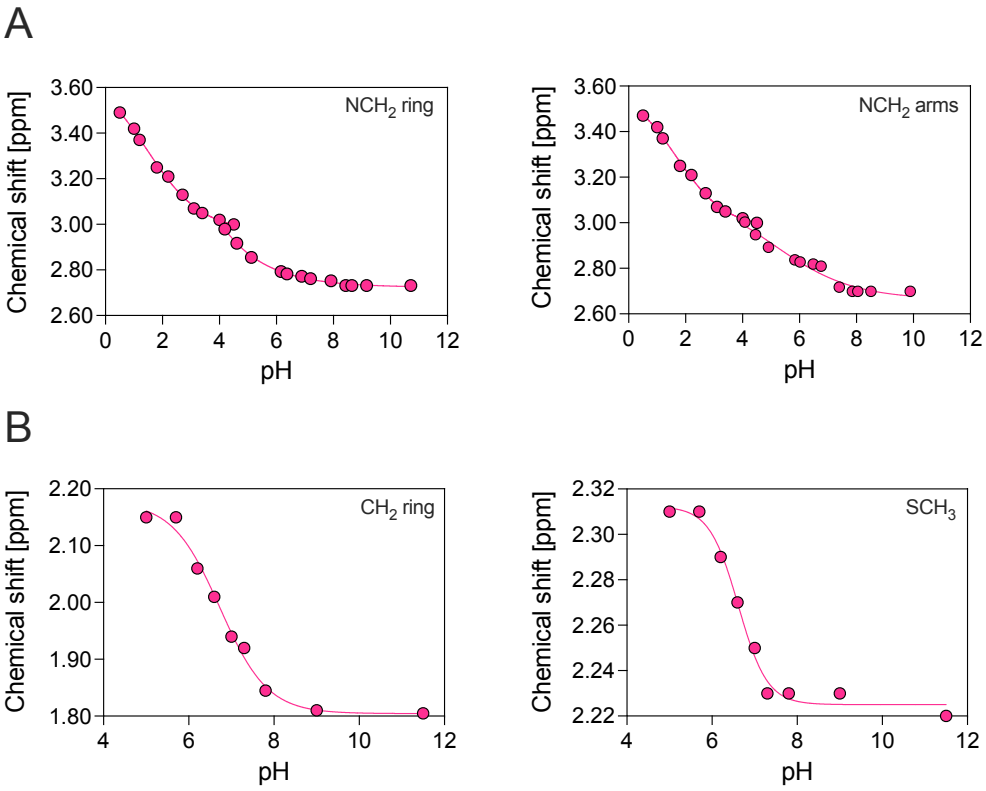

Figure B7. Representative ^{1}H-NMR titration curves and corresponding fitting lines of (A) Ag^{+}-TACD3S and (B) Ag^{+}-TRI4S (data points were taken from **Figure 3.16**).

Appendix C

Supplementary Data for Chapter 4

Table C1. Approximate time required to reach equilibrium during the reaction between Cu^{2+} and first-/second-generation ligands at RT and various pH. Data were taken from **Figures 4.2** - **4.6** (**Chapter 4**).

pH	Equilibration time							
	DO4S	**DO3S**	**DO3Sam**	**DO2A2S**	**DOTA**	**TACD3S**	**TRI4S**	**TE4S**
2.0	~ 10 d	~ 10 d	~ 10 d	~ 4 h	~ 1 h	[a]	2 d	[a]
3.0	~ 20 h	~ 20 h	~ 10 h	~ 10 min	~ 5 min	[a, b]	40 min [b]	20 min [b]
4.8	~ 50 min	~ 30 min	~ 1 h	< 10 sec	< 10 sec	–	–	–
7.0	< 10 sec	< 10 sec	< 10 sec	< 10 sec	< 10 sec	< 10 sec [b]	< 10 sec	< 10 sec

[a]: No Cu^{2+} complex formation.
[b]: pH 3.7.
[b]: Not quantitative.

Table C2. Approximate time required to reach equilibrium during the reaction between Cu^{2+} and first-generation ligands at various pH.

pH	Equilibration time		
	DO4S	**DO3S**	**DO2A2S**
2.0 [a]	–	–	~ 20 min
3.0 [b]	~ 2 h	~ 5 h	< 1 min
4.8 [c]	~ 3 min	~ 2 min	< 10 sec
7.0 [d]	< 10 sec	< 10 sec	< 10 sec

[a] pH 2.0: $C_{DO2A2S} = C_{Cu^{2+}} = 1.0 \cdot 10^{-3}$ M.
[b] pH 3.0: $C_{DO4S,\ DO3S} = C_{Cu^{2+}} = 9.0 \cdot 10^{-4}$ M; $C_{DO2A2S} = C_{Cu^{2+}} = 8.0 \cdot 10^{-4}$ M.
[l] pH 4.8: $C_{DO4S} = C_{Cu^{2+}} = 1.2 \cdot 10^{-3}$ M; $C_{DO3S,\ DO2A2S} = C_{Cu^{2+}} = 1.1 \cdot 10^{-3}$ M.
[d] pH 7.0: $C_{DO4S,\ DO3S,\ DO2A2S} = C_{Cu^{2+}} = 1.0 \cdot 10^{-3}$ M.

Table C3. UV-Vis spectroscopic data of the Cu^{2+} complexes with first- and second-generation ligands.

Complex	Transition	λ_{max} [nm]	ε calculated [L/cm·mol]
$[Cu(DO4S)]^{2+}$	CT	309	$(3.6 \pm 0.9)\cdot10^{3}$ [(a)]
	d-d	593	$5.3\cdot10^{2}$ [(b)]
$[Cu(DO3S)]^{2+}$	CT	303	$(3.6 \pm 0.2)\cdot10^{3}$ [(a)]
	d-d	581	$4.3\cdot10^{2}$ [(b)]
$[Cu(DO3SAm)]^{2+}$	CT	304	$(3.7 \pm 0.8)\cdot10^{3}$ [(a)]
	d-d	602	$3.2\cdot10^{2}$ [(b)]
[Cu(DO2A2S)]	CT	272	$(5.0 \pm 0.2)\cdot10^{3}$ [(a)]
	d-d	715	$1.6\cdot10^{2}$ [(b)]
$[Cu(HDO2A2S)]^{+}$	CT	303	$(4.0 \pm 0.9)\cdot10^{3}$ [(a)]
	d-d	680	–
$[Cu(TRI4S)]^{2+}$	CT	313	$(4.6 \pm 0.4)\cdot10^{3}$ [(a)]
	d-d	598	$6.9\cdot10^{2}$ [(b)]
$[Cu(TE4S)]^{2+}$	CT	313	$(4.5 \pm 0.5)\cdot10^{3}$ [(a)]
	d-d	626	$4.1\cdot10^{2}$ [(b)]

[(a)]: Obtained from the UV-Vis data fitting aimed at the determination of the equilibrium constants.
[(b)]: Estimated from the UV-Vis spectra.

Table C4. Electronic and Gibbs free energies (in gas-phase and in water) for the cupric complexes of Cyc4Me and DO4S, supposing no sulfur coordination in the latter. All the energies are in kcal/mol. Level of theory: (COSMO-)ZORA-OPBE/TZ2P//ZORA-OPBE/TZP.

Ligand	Gas phase		Water	
	ΔE	ΔG	ΔE	ΔG
Cyc4Me	–402.5	–387.1	–198.4	–183.0
DO4S	–412.4	–399.4	–192.7	–179.7

Table C5. Activation Strain Model (ASM) and Energy Decomposition Analysis (EDA) of the cupric and cuprous complexes of DO4S and DO3S. All the energies are in kcal/mol. Level of theory: ZORA-OPBE/TZ2P//ZORA-OPBE/TZP.

M	Ligand	coordination	ΔE	ΔE_{strain}	ΔE_{int}	ΔE_{Pauli}	ΔV_{elstat}	ΔE_{oi}
Cu^{2+}	DO4S	[4N]	–412.4	13.7	–426.1	166.5	–234.6	–358.0
		[4N]S	–417.4	21.2	–438.6	142.7	–228.3	–353.0
		[4N]2S	–410.1	27.3	–437.4	96.6	–198.0	–336.1
	DO3S	[4N]	–411.4	12.4	–423.8	168.2	–241.6	–350.4
		[4N]S	–418.1	21.1	–439.2	153.0	–241.3	–350.9
		[4N]2S	–411.2	27.8	–439.0	111.0	–214.3	–335.6
Cu^{+}	DO4S	[4N]	–117.3	5.6	–122.9	157.3	–171.1	–109.0
		[4N]S	–128.3	13.7	–142.0	161.0	–179.5	–123.5
		[4N]2S	–122.5	21.8	–144.3	141.7	–164.9	–121.2
	DO3S	[4N]	–119.7	4.9	–124.5	158.9	–176.3	–107.2
		[4N]S	–130.6	13.4	–144.1	160.3	–182.3	–122.1
		[4N]2S	–126.2	18.0	–144.2	140.7	–166.4	–118.5

Table C6. Crystallographic data and refinement details for $[Cu(DO4S)(NO_3)]\cdot(NO_3)$.

Empirical formula	$C_{20}H_{44}CuN_6O_6S_4$
Formula weight	656.39 g/mol
Temperature	183 (2)
Radiation and wavelength	Mo-Kα, λ = 0.71073 Å
Crystal system	Monoclinic
Space group	P2 (1)
Unit cell dimension	*a* = 8.128 Å *α* = 90.0° *b* = 14.879 Å *β* = 102.86° *c* = 12.373 Å γ = 90.0°
Volume	1458.8 $Å^3$
Z	2
Density (calculated)	1.494 Mg/cm^3
Absorption coefficient, μ	1.080 mm^{-1}
F(000)	694
Crystal colour	blue
Crystal size	0.6 × 0.4 × 0.4 mm
θ area data collection	1.69 to 27.52°
Index area	0 ≤ h ≤ 10, 0 ≤ k ≤ 19, −16 ≤ l ≤15
Reflections collected	3760
Independent reflections	3462 [R(int) = 0.02951]
Refinement method	Full-matrix least squares on F^2
Data/restraints/parameters	3462/1/336
Final R indices [I <2σ(I)]	R_1 = 0.0570, wR_2 = 0.1387
R indices (all data)	R_1 = 0.0736, wR_2 = 0.1527
Absolute structure parameter	0.00 ± 3
Extinction coefficient	0.00 ± 2
Differential signals	0.842 and −0.575 e.$Å^{-3}$

$R_1 = \Sigma\, ||F_0|-|F_c||/\Sigma\, |F_0|$
$wR_2 = \{\Sigma\, [w(|F_0|^2-|F_c|^2)^2/\Sigma\, [w(F_0^4)]\}^{1/2}$

Table C7. Bond lengths of [Cu(DO4S)(NO_3)]·(NO_3).

Bond	Bond length [Å]	Bond	Bond length [Å]
Cu(1)-N(5)	2.029(7)	S(7)-C(16)	1.773(10)
Cu(1)-N(3)	2.035(7)	S(8)-C(22)	1.784(11)
Cu(1)-N(2)	2.053(7)	S(8)-C(21)	1.805(10)
Cu(1)-N(4)	2.057(7)	S(9)-C(27)	1.690(2)
Cu(1)-O(31)	2.149(6)	S(9)-C(26)	1.799(10)
N(2)-C(13)	1.447(12)	C(10)-C(11)	1.525(11)
N(2)-C(10)	1.469(10)	C(13)-C(14)	1.420(2)
N(2)-C(29)	1.599(13)	C(15)-C(16)	1.518(11)
N(3)-C(18)	1.425(12)	C(18)-C(19)	1.423(14)
N(3)-C(15)	1.477(10)	C(20)-C(21)	1.524(12)
N(3)-C(14)	1.611(12)	C(23)-C(24)	1.453(13)
N(4)-C(23)	1.459(12)	C(25)-C(26)	1.515(13)
N(4)-C(20)	1.482(10)	C(28)-C(29)	1.447(14)
N(4)-C(19)	1.573(12)	N(39)-O(33)	1.168(14)
N(5)-C(28)	1.470(12)	N(30)-O(32)	1.174(14)
N(5)-C(25)	1.482(10)	N(30)-O(31)	1.229(9)
N(5)-C(24)	1.579(13)	N(34)-O(35)	1.194(11)
S(6)-C(12)	1.765(11)	N(34)-O(36)	1.228(12)
S(6)-C(11)	1.811(9)	N(34)-O(37)	1.245(10)
S(7)-C(17)	1.736(14)		

Table C8. Bond angles of [Cu(DO4S)(NO_3)]·(NO_3).

Angle	[°]	Angle	[°]
N(5)-Cu(1)-N(3)	151.9(3)	C(25)-N(5)-C(24)	110.4(7)
N(5)-Cu(1)-N(2)	86.8(3)	C(28)-N(5)-Cu(1)	101.9(6)
N(3)-Cu(1)-N(2)	86.7(3)	C(25)-N(5)-Cu(1)	114.4(5)
N(5)-Cu(1)-N(4)	87.6(3)	C(24)-N(5)-Cu(1)	103.3(5)
N(3)-Cu(1)-N(4)	84.8(3)	C(12)-S(6)-C(11)	101.4(5)
N(2)-Cu(1)-N(4)	150.7(3)	C(17)-S(7)-C(16)	102.1(8)
N(5)-Cu(1)-O(31)	104.6(3)	C(22)-S(8)-C(21)	100.9(8)
N(3)-Cu(1)-O(31)	103.3(3)	C(27)-S(9)-C(26)	99.7(8)
N(8)-Cu(1)-O(31)	110.5(3)	N(2)-C(10)-C(11)	114.2(6)
N(4)-Cu(1)-O(31)	98.7(3)	C(10)-C(11)-S(6)	109.8(6)
C(13)-N(2)-C(10)	115.8(7)	C(14)-C(13)-N(2)	108.4(8)
C(13)-N(2)-C(29)	110.9(8)	C(13)-C(14)-N(3)	111.0(8)
C(10)-N(2)-C(29)	108.8(7)	N(3)-C(15)-C(16)	115.6(6)
C(13)-N(2)-Cu(1)	102.0(6)	C(15)-C(16)-S(7)	111.9(6)
C(10)-N(2)-Cu(1)	115.4(5)	C(19)-C(18)-N(3)	108.2(8)
C(29)-N(2)-Cu(1)	103.1(5)	C(18)-C(19)-N(4)	111.2(7)
C(18)-N(3)-C(15)	116.6(7)	N(4)-C(20)-C(21)	114.2(7)
C(18)-N(3)-C(14)	109.2(7)	C(20)-C(21)-S(8)	109.2(6)
C(15)-N(3)-C(14)	108.8(7)	C(24)-C(23)-N(4)	108.8(7)
C(18)-N(3)-Cu(1)	102.7(6)	C(23)-C(24)-N(5)	110.9(7)
C(15)-N(3)-Cu(1)	116.0(4)	N(5)-C(25)-C(26)	114.2(7)
C(14)-N(3)-Cu(1)	102.6(5)	C(25)-C(26)-S(9)	112.1(7)
C(23)-N(4)-C(20)	114-1(7)	C(29)-C(28)-N(5)	110.5(9)
C(23)-N(4)-C(19)	111.2(7)	O(33)-N(30)-O(32)	120.6(12)
C(20)-N(4)-C(19)	110.7(7)	O(33)-N(30)-O(31)	118.2(11)
C(23)-N(4)-Cu(1)	101.1(5)	O(32)-N(30)-O(31)	120.0(11)
C(20)-N(4)-Cu(1)	115.3(5)	N(30)-O(31)-Cu(1)	136.1(5)
C(19)-N(4)-Cu(1)	103.5(5)	O(35)-N(34)-O(36)	120.0(9)
C(28)-N(5)-C(25)	115.4(8)	O(35)-N(34)-O(37)	120.2(9)
C(28)-N(5)-C(24)	110.5(7)	O(36)-N(34)-O(37)	119.7(8)

Table C9. Crystal data and structure refinement for [Cu(DO2A2S)].

Empirical formula	$C_{18}H_{34}CuN_4O_4S_2$
Formula weight	498.15
Temperature	295(2)
Radiation and wavelength	Mo-Kα, λ =0.71073 Å
Crystal system	monoclinic
Space group	*I* 2
Unit cell dimensions	*a* = 16.1921(10) Å *α* = 90.0° *b* = 6.7295(4) Å *β* = 91.554(10)° *c* = 19.970(3) Å γ = 90.0°
Volume	2175.2(4) Å^3
Z/*Z'*	4/1
Density (calculated)	1.521 Mg/m^3
Absorption coefficient, μ	1.228 mm^{-1}
F(000)	1052
Crystal colour	blue
Crystal description	block
Crystal size	0.30 × 0.30 × 0.20 mm
Absorption correction	numerical
Max. And min. Transmission	0.928, 0.966
θ range for data collection	3.195 ≤ θ ≤ 27.468°
Index ranges	0 ≤ *h* ≤ 10, 0 ≤ *k* ≤ 19, −16 ≤ *l* ≤15
Reflections collected	23317
Completeness to 2*θ*	0.998
Independent reflections	4964 [*R*(int) = 0.0421]
Reflections *I*>2σ(*I*)	4599
Refinement method	full-matrix least-squares on F^2
Data / restraints / parameters	4964 /1 /266
Goodness-of-fit on F^2	1.038
Final *R* indices [*I*>2σ(*I*)]	R_1 = 0.0298, wR_2 = 0.0616
R indices (all data)	R_1 = 0.0345, wR_2 = 0.0628
Max. And mean shift/esd	0.000; 0.000
Largest diff. Peak and hole	0.396; –0.202 e.Å^{-3}

Table C10. Bond lengths for [Cu(DO2A2S)].

Bond	Bond length [Å]	Bond	Bond length [Å]
Cu1-O1#1	1.954(2)	Cu1-O1	1.955(2)
Cu1-N1#1	2.150(3)	Cu1-N1	2.150(3)
S1-C9	1.789(4)	S1-C8	1.813(3)
O1-C6	1.283(4)	O2-C6	1.231(4)
N1-C5	1.481(4)	N1-C3	1.482(4)
N1-C4#1	1.490(4)	N2-C2	1.461(4)
N2-C1	1.476(4)	N2-C7	1.478(4)
C1-C4	1.514(4)	C2-C3	1.521(5)
C5-C6	1.510(5)	C7-C8	1.515(5)
Cu2-O3#2	1.955(2)	Cu2-O3	1.955(2)
Cu2-N3#2	2.110(3)	Cu2-N3	2.110(3)
Cu2-N4#2	2.336(3)	Cu2-N4	2.336(3)
S2-C19	1.785(4)	S2-C18	1.812(4)
O3-C16	1.277(4)	O4-C16	1.229(4)
N3-C15	1.485(4)	N3-C12	1.489(4)
N3-C11	1.490(4)	N4-C14	1.463(4)
N4-C13	1.479(4)	N4-C17	1.489(4)
C11-C14#2	1.523(4)	C12-C13	1.528(5)
C15-C16	1.526(5)	C17-C18	1.521(4)

Table C11. Bond angles for [Cu(DO2A2S)].

Angle	[°]	Angle	[°]
O1#1-Cu1-O1	87.0(1)	O1#1-Cu1-N1#1	80.3(1)
O1-Cu1-N1#1	157.49(9)	O1#1-Cu1-N1	157.49(9)
O1-Cu1-N1	80.3(1)	N1#1-Cu1-N1	117.2(2)
C9-S1-C8	101.2(2)	C6-O1-Cu1	118.0(2)
C5-N1-C3	110.3(2)	C5-N1-C4#1	107.1(3)
C3-N1-C4#1	110.8(3)	C5-N1-Cu1	102.5(2)
C3-N1-Cu1	114.5(2)	C4#1-N1-Cu1	111.1(2)
C2-N2-C1	109.9(2)	C2-N2-C7	111.4(2)
C1-N2-C7	110.1(2)	N2-C1-C4	111.1(2)
N2-C2-C3	110.9(2)	N1-C3-C2	111.6(3)
N1#1-C4-C1	112.0(3)	N1-C5-C6	110.4(2)
O2-C6-O1	125.3(3)	O2-C6-C5	119.6(3)
O1-C6-C5	115.1(3)	N2-C7-C8	112.5(3)
C7-C8-S1	112.9(2)	O3#2-Cu2-O3	89.6(1)
O3#2-Cu2-N3#2	84.1(1)	O3-Cu2-N3#2	169.4(1)
O3#2-Cu2-N3	169.4(1)	O3-Cu2-N3	84.1(1)
N3#2-Cu2-N3	103.3(2)	O3#2-Cu2-N4#2	107.21(9)
O3-Cu2-N4#2	94.2(1)	N3#2-Cu2-N4#2	79.70(9)
N3-Cu2-N4#2	81.75(9)	O3#2-Cu2-N4	94.2(1)
O3-Cu2-N4	107.21(9)	N3#2-Cu2-N4	81.75(9)
N3-Cu2-N4	79.70(9)	N4#2-Cu2-N4	149.9(1)
C19-S2-C18	102.2(2)	C16-O3-Cu2	117.2(2)
C15-N3-C12	111.2(2)	C15-N3-C11	111.2(3)
C12-N3-C11	110.4(3)	C15-N3-Cu2	104.3(2)
C12-N3-Cu2	109.7(2)	C11-N3-Cu2	109.8(2)
C14-N4-C13	114.6(3)	C14-N4-C17	113.2(3)
C13-N4-C17	112.5(2)	C14-N4-Cu2	101.4(2)
C13-N4-Cu2	107.6(2)	C17-N4-Cu2	106.5(2)
N3-C11-C14#2	111.3(2)	N3-C12-C13	112.0(3)
N4-C13-C12	113.4(2)	N4-C14-C11#2	111.4(2)
N3-C15-C16	113.7(3)	O4-C16-O3	125.8(4)
O4-C16-C15	118.1(3)	O3-C16-C15	116.0(3)
N4-C17-C18	115.2(3)	C17-C18-S2	111.1(2)

Symmetry codes to generate equivalent atoms: #1 –x+1,y,–z+1 and #2 –x+2,y,–z+1

Table C12. $^{d}k_{obs}$ values for the Cu^{2+} complexes of DO4S, DO2A2S, TRI4S and TE4S in HCl at different concentrations.

[HCl] [M]	$^{d}k_{obs} \cdot 10^{5}$ [s^{-1}]			
	DO4S	**DO2A2S**	**TRI4S**	**TE4S**
0.1	4.5 ± 0.8	1.08 ± 0.02	22.9 ± 0.3	1100 ± 100
0.2	9.8 ± 0.2	2.20 ± 0.03	300 ± 9	1300 ± 100
0.4	19.8 ± 0.3	4.78 ± 0.05	800 ± 60	1520 ± 50
0.6	33 ± 3	6.5 ± 0.1	1830 ± 70	–
0.8	45 ± 1	8.2 ± 0.1	2800 ± 100	–
1.0	59 ± 6	10.4 ± 0.3	3400 ± 300	–

Table C13. ^{1}H-NMR resonance assignments for the Cu^{+} complexes formed by DO4S and DO2A2S.

Complex	δ [ppm]	Multiplicity	Area	Proton Assignation
$[Cu(DO4S)]^{+}$	2.20	s	12	SCH_3
	2.72	s br	16	SCH_2 + NCH_2 arms or NCH_2 ring
	2.82	s b	16	NCH_2 ring or SCH_2 + NCH_2 arms
$[Cu(DO2A2S)]^{-}$	2.28	s	6	SCH_3
	2.71	m	4	SCH_2
	2.80	t	8	NCH_2 ring
	2.92	m	4	NCH_2
	2.94	t	8	NCH_2 ring
	3.41	s	4	CH_2COOH
$[Cu(TRI4S)]^{+}$	2.00	s	1	$CH_{2,ax/eq}$
	2.31	s	1	$CH_{2,ax/eq}$
	2.50	s	6	SCH_3
	2.55	s	6	SCH_3
	2.96-3.30	m	32	SCH_2 + NCH_2 arms + NCH_2 ring
$[Cu(TE4S)]^{+}$	1.93	s br	4	CH_2
	2.29	s	12	SCH_3
	2.63-3.10	m br	32	SCH_2 + NCH_2 arms + NCH_2 ring

s = singlet; br = broad; t = triplet; m = multiplet

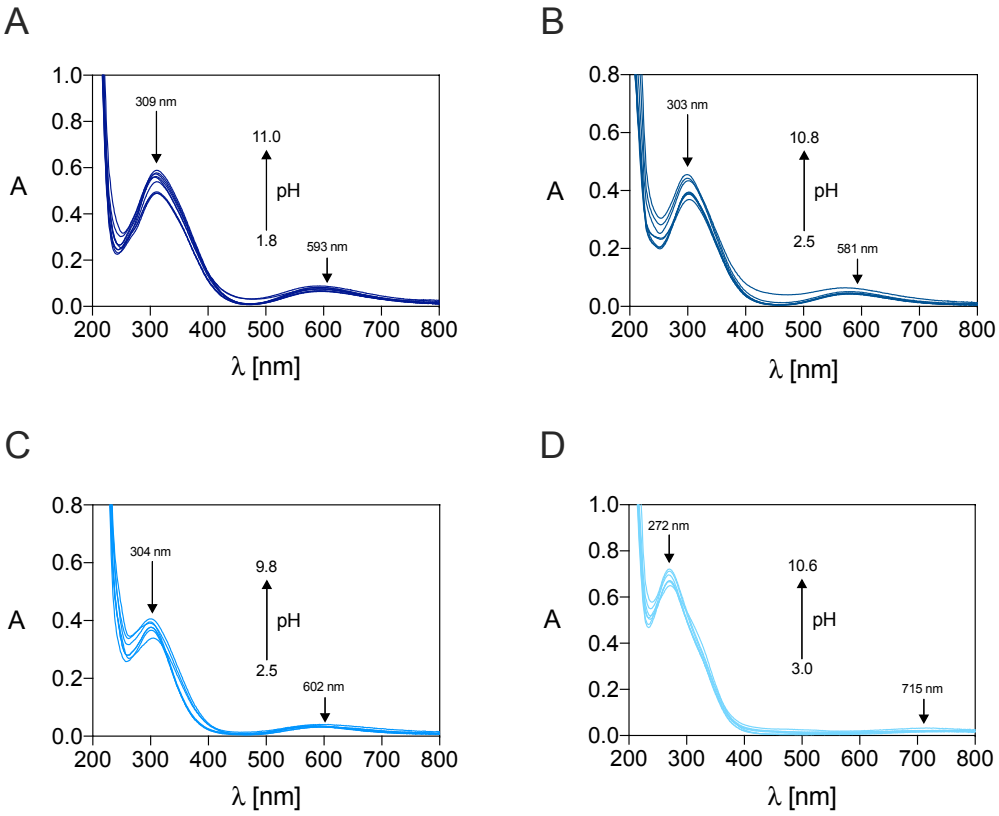

Figure C1. Selected UV-Vis spectra at pH > 2 of the Cu^{2+} complexes with (A) DO4S ($C_{Cu^{2+}}$ = C_{DO4S} = $1.5 \cdot 10^{-4}$ M), (B) DO3S ($C_{Cu^{2+}}$ = C_{DO3S} = $1.1 \cdot 10^{-4}$ M), (C) DO3SAm ($C_{Cu^{2+}}$ = C_{DO3SAm} = $1.0 \cdot 10^{-4}$ M) and (D) DO2A2S ($C_{Cu^{2+}}$ = C_{DO2A2S} = $1.4 \cdot 10^{-4}$ M) at I = 0.15 M NaCl and T = 25°C.

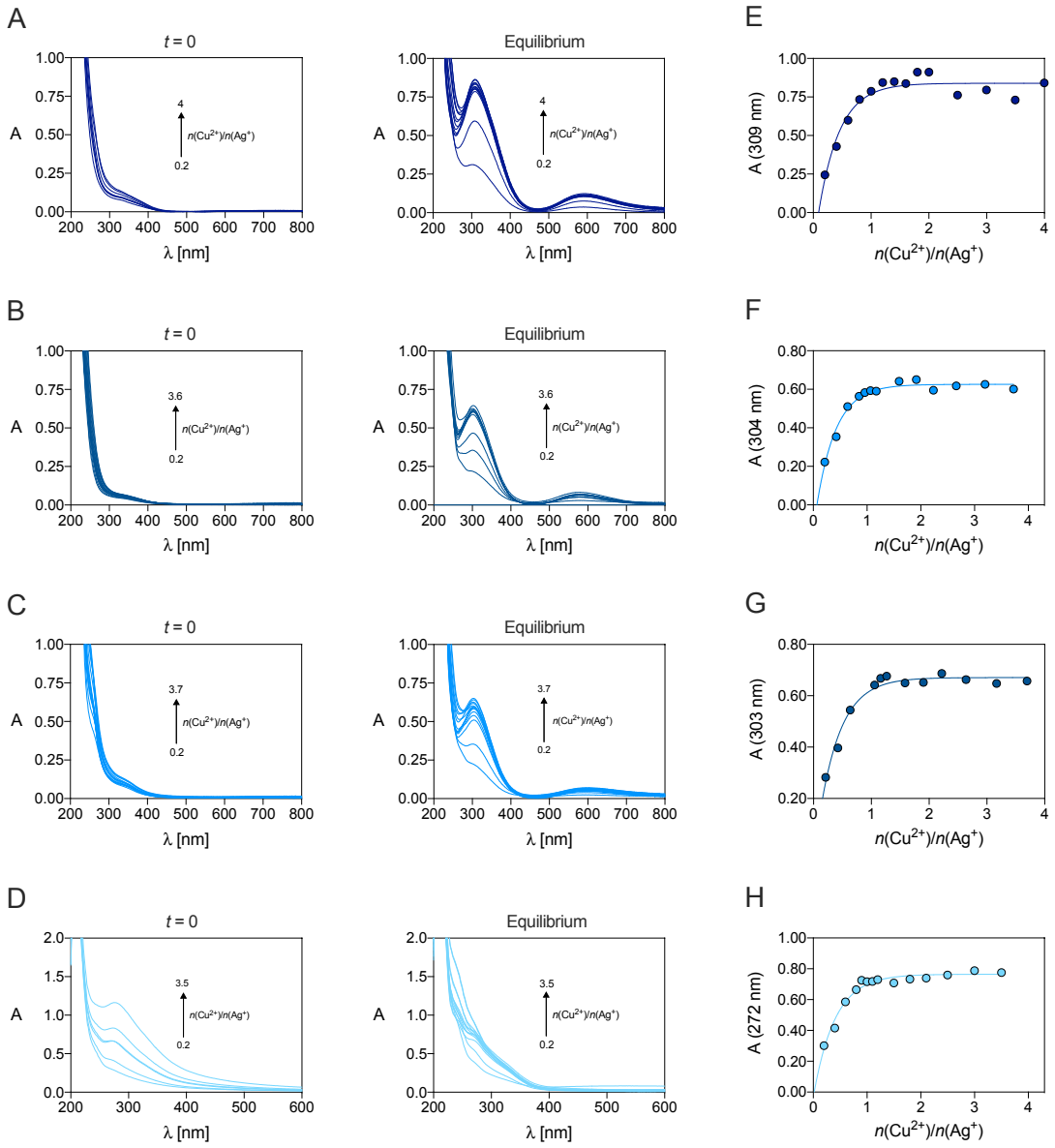

Figure C2. UV-Vis spectra at pH 4.8 of the preformed Ag^+ complex with (A) DO4S (C_{Ag^+} = C_{DO4S} = $2.2 \cdot 10^{-4}$ M), (B) DO3S (C_{Ag^+} = C_{DO3S} = $1.5 \cdot 10^{-4}$ M), (C) DO3SAm (C_{Ag^+} = C_{DO3SAm} = $1.6 \cdot 10^{-4}$ M) and (D) DO2A2S (C_{Ag^+} = C_{DO2A2S} = $1.2 \cdot 10^{-4}$ M) immediately after the addition of variable equivalents of Cu^{2+} (t = 0) and at equilibrium during the competition titrations. (E, F, G, H) Representative A *vs.* $n(Cu^{2+})/n(Ag^+)$ profiles obtained during the Ag^+-Cu^{2+} competitions measurements and corresponding fitting lines.

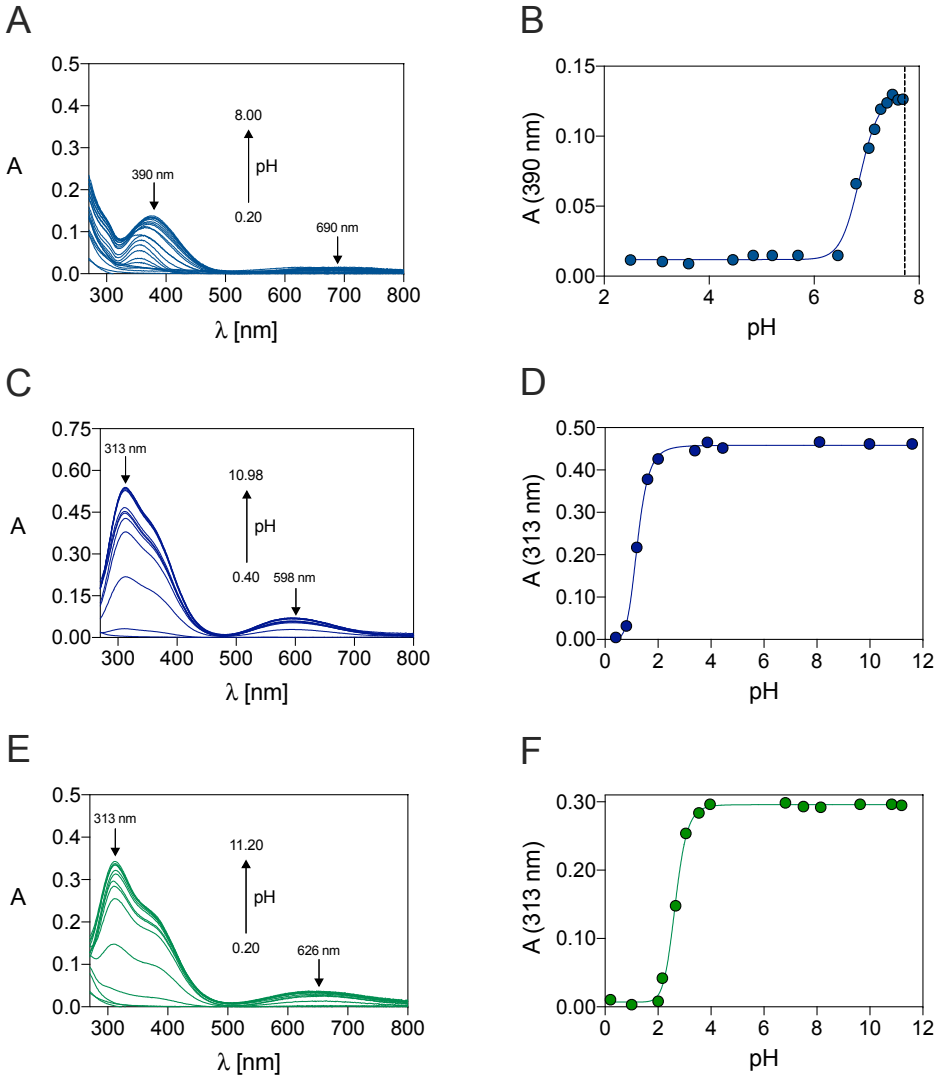

Figure C3. Representative UV-Vis spectrophotometric titrations of the Cu^{2+} complexes with (A) TACD3S ($C_{Cu^{2+}}$ = C_{TACD3S} = $1.0 \cdot 10^{-4}$ M), (B) TRI4S ($C_{Cu^{2+}}$ = C_{TRI4S} = $1.0 \cdot 10^{-4}$ M) and (C) TE4S ($C_{Cu^{2+}}$ = C_{TE4S} = $7.0 \cdot 10^{-5}$ M) at I = 0.15 M NaCl and T = 25°C.

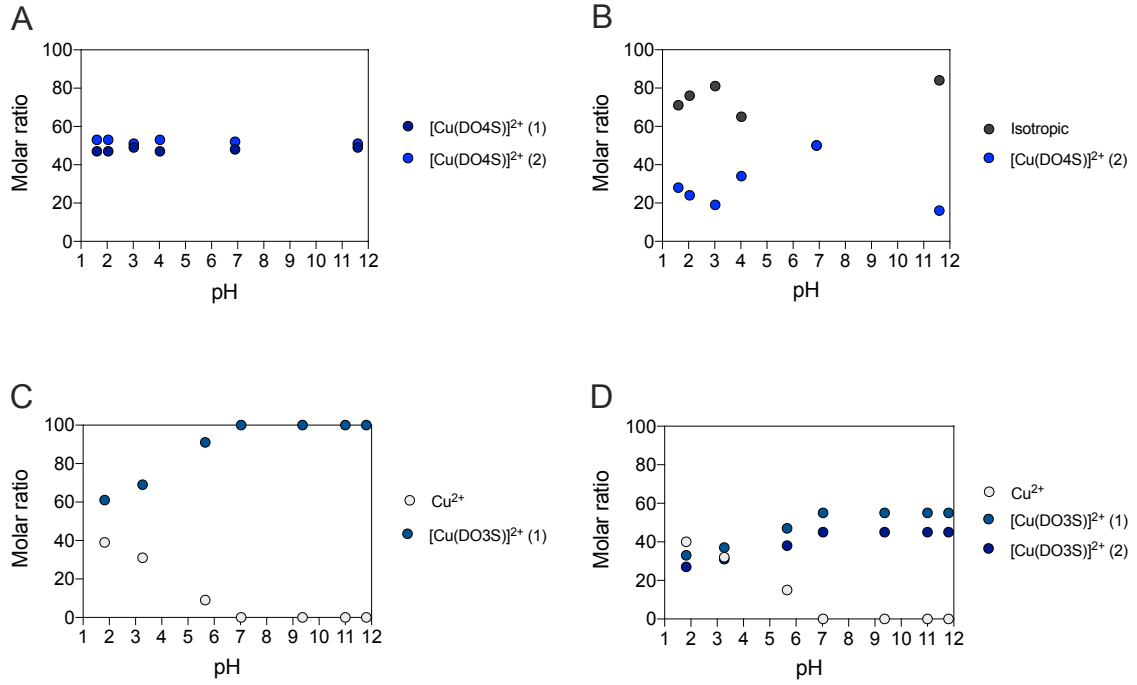

Figure C4. Component ratios obtained from the simulation of Cu^{2+}-DO4S EPR spectra recorded at (A) room temperature and (C) 77 K and of Cu^{2+}-DO3S EPR spectra recorded at (B) room temperature and (D) 77 K.

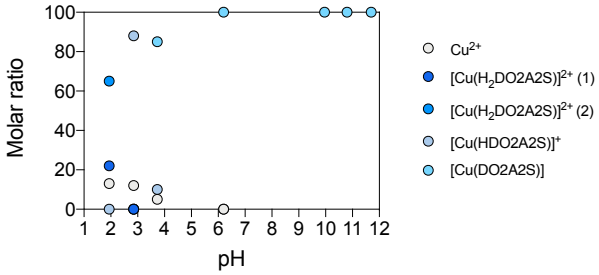

Figure C5. Component ratios obtained from the simulation of Cu^{2+}-DO2A2S EPR spectra recorded at 77 K.

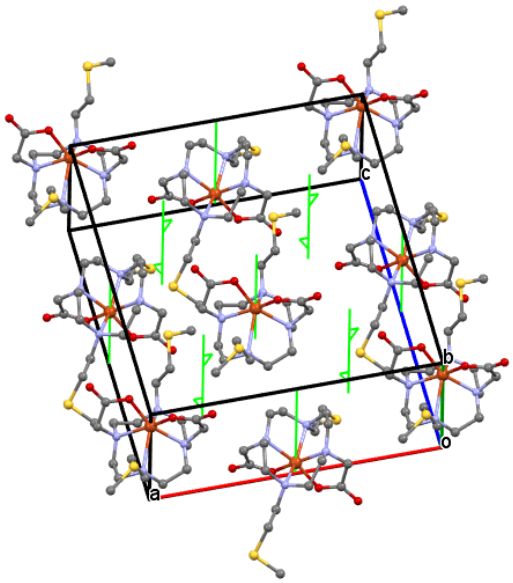

Figure C6. Unit cell of crystal [Cu(DO2A2S)] showing the 2-fold rotation and screw axes.

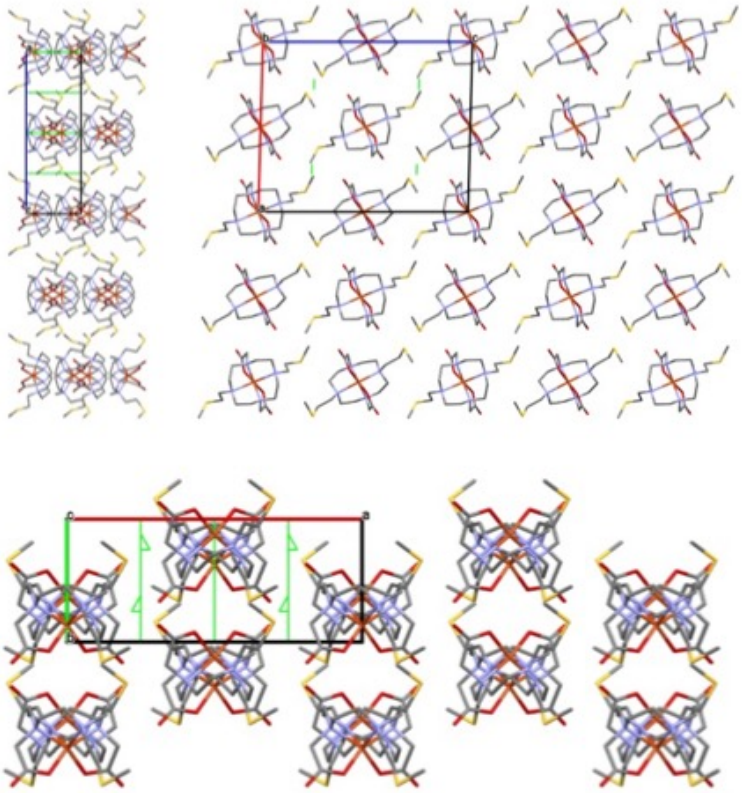

Figure C7. Packing arrangements in crystal [Cu(DO2A2S)] viewed from the crystallographic directions 'a', 'b' and 'c'.

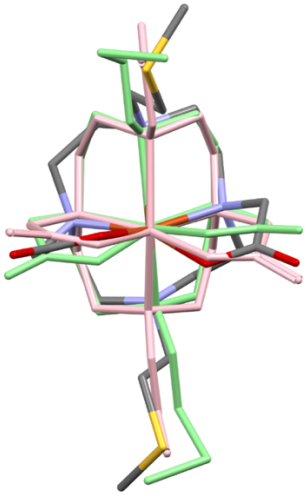

Figure C8. Comparison of the conformation of molecules in the asymmetrical unit of crystal [Cu(DO2A2S)] by overlay of the two molecules (molecule #1 is coloured by element, and #2 is green) together with crystal structure of Cu-DOTA (pink, Ref. Code FEKVAS).

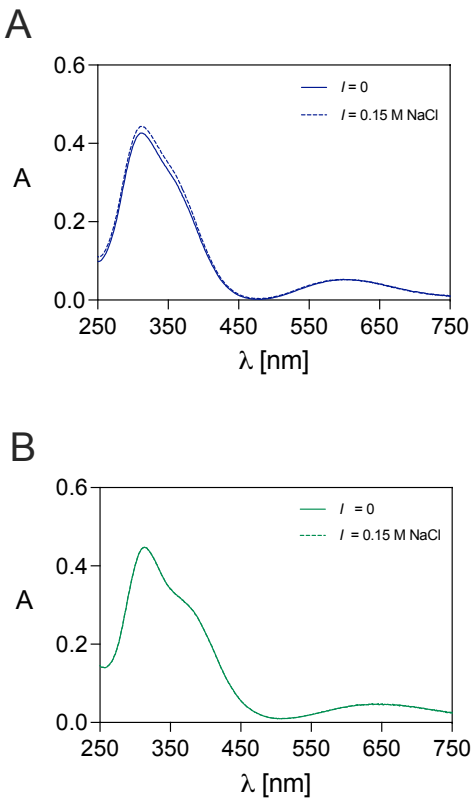

Figure C9. Comparison of the UV-Vis spectra of the Cu^{2+} complexes with (A) TRI4S and (B) TE4S ($C_{Cu^{2+}} = C_L = 1.0 \cdot 10^{-4}$ M) at I = 0 M and I = 0.15 M NaCl and T = 25°C.

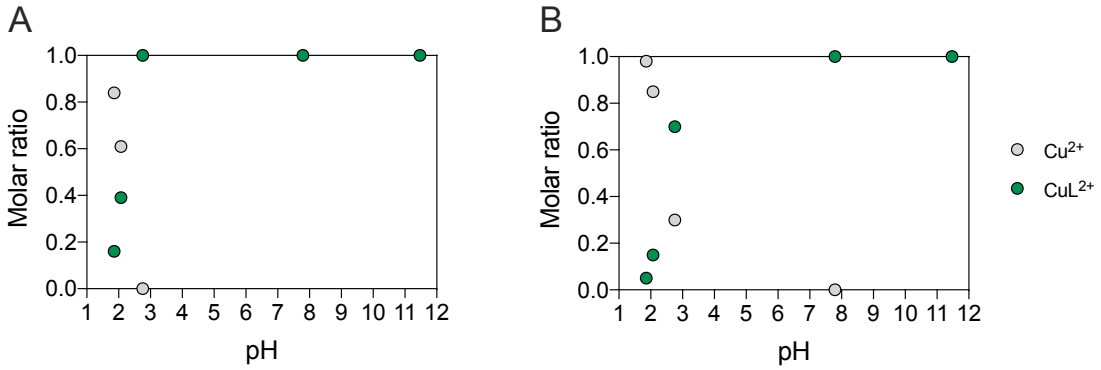

Figure C10. Component ratios obtained from the simulation of Cu^{2+}-TE4S EPR spectra at room temperature (left) and frozen solution at 77 K (right).

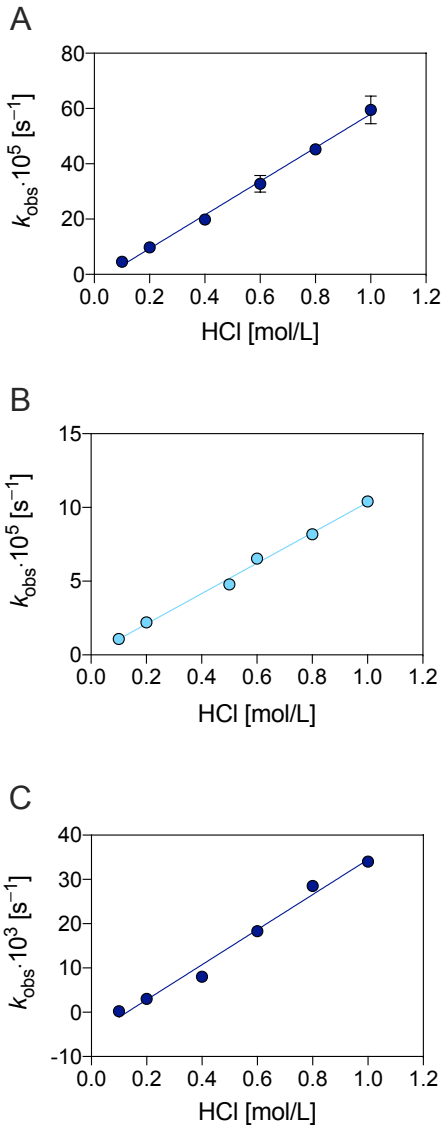

Figure C11. pH-Dependence of $^{d}k_{obs}$ for acid-mediated decomplexation of the Cu^{2+} complexes with (A) DO4S, (B) DO2A2S and (C) TRI4S at room temperature, and corresponding fitting lines.

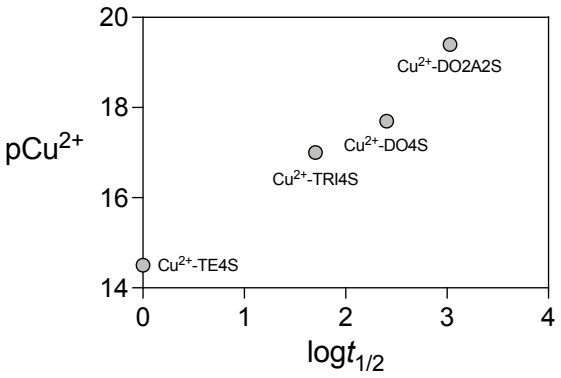

Figure C12. Correlation between pCu^{2+} values and $\log t_{1/2}$ at pH 1.

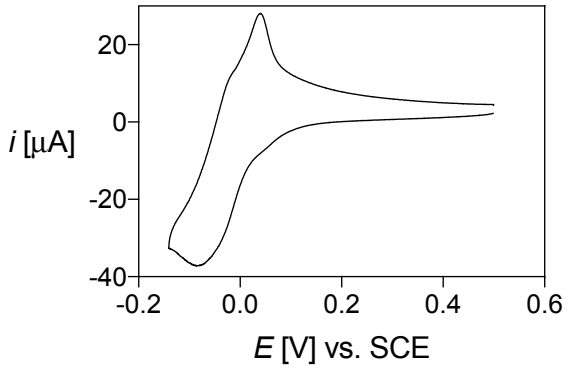

Figure C13. Cyclic voltammogram of unbound Cu^{2+} ($C_{Cu^{2+}}$ = $2.3 \cdot 10^{-3}$ M) in aqueous solution at pH 7, I = 0.15 M $NaNO_3$ and T = 25°C, acquired at a scan rate of 0.1 V/s.

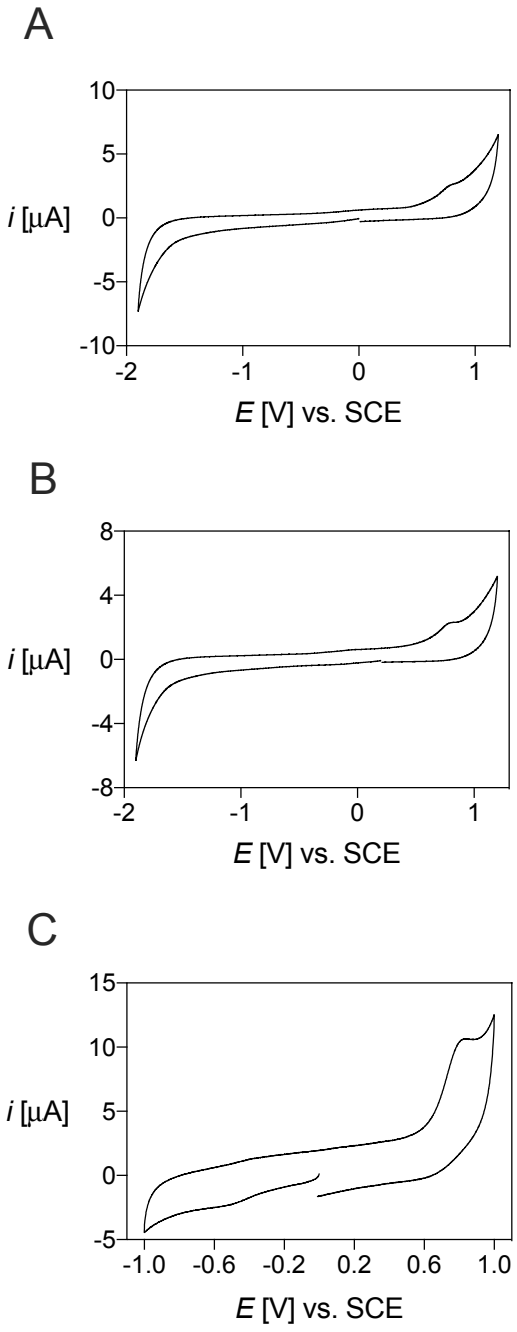

Figure C14. Cyclic voltammogram of (A) DO4S (C_{DO4S} = 1.0·10^{-3} M), (B) DO3S (C_{DO3S} = 1.1·10^{-3} M) and (C) DO2A2S (C_{DO2A2S} = 1.0·10^{-3} M) in aqueous solution at pH 7, I = 0.15 M $NaNO_3$ and T = 25°C, acquired at a scan rate of 0.1 V/s.

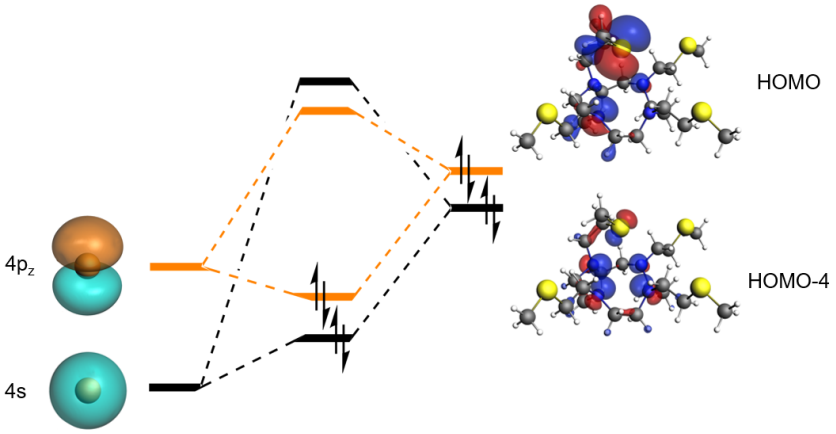

Figure C15. Molecular orbital diagram showing the two main bonding modes of the $[Cu(DO4S)]^+$ complex displaying a [4N]S coordination mode. On the left, symmetry-adapted fragment orbitals (SFOs) representing the 4*s* and the 4p_z orbitals located on the metal center. On the right, ligand SFOs involved in the primary (black) and secondary (orange) molecular bonding and antibonding orbital.

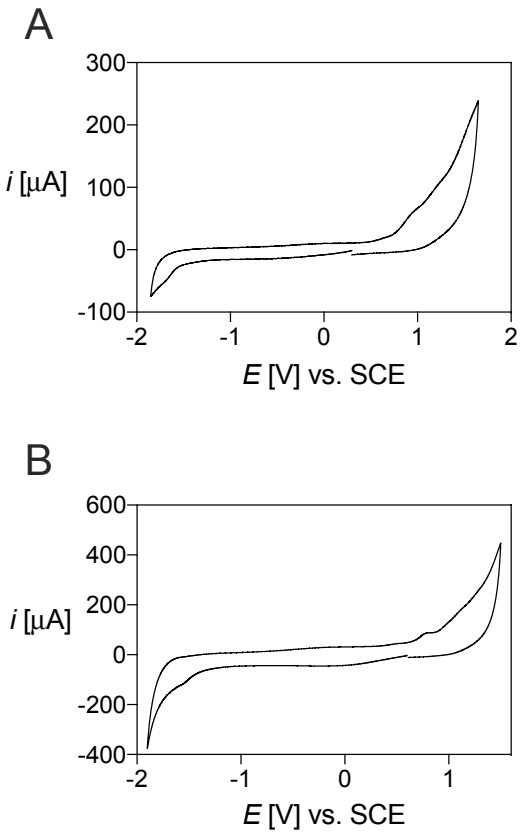

Figure C16. Cyclic voltammograms of free (A) TRI4S (C_{TRI4S} = 9.85·10^{-4} M) and (B) TE4S (C_{TE4S} = 8.80·10^{-4} M) in aqueous solution, *I* = 0.15 M $NaNO_3$ and *T* = 25°C acquired at a scan rate of 0.1 V/s.

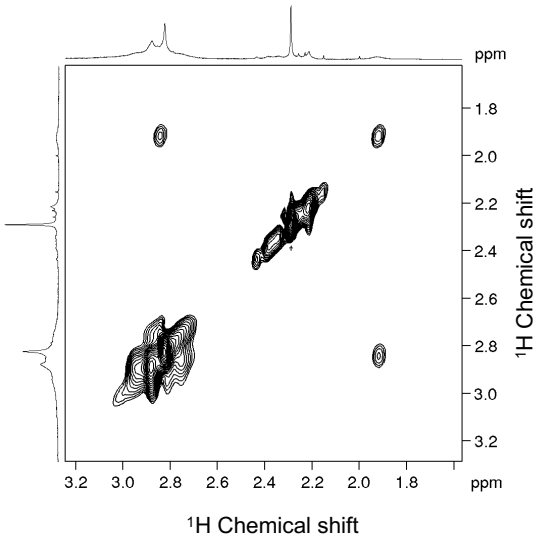

Figure C17. TOCSY spectra of $[Cu(TE4S)]^+$ (C_{Cu} = 6.0·10^{-4} M, C_{TE4S} = 7.0·10^{-4} M).

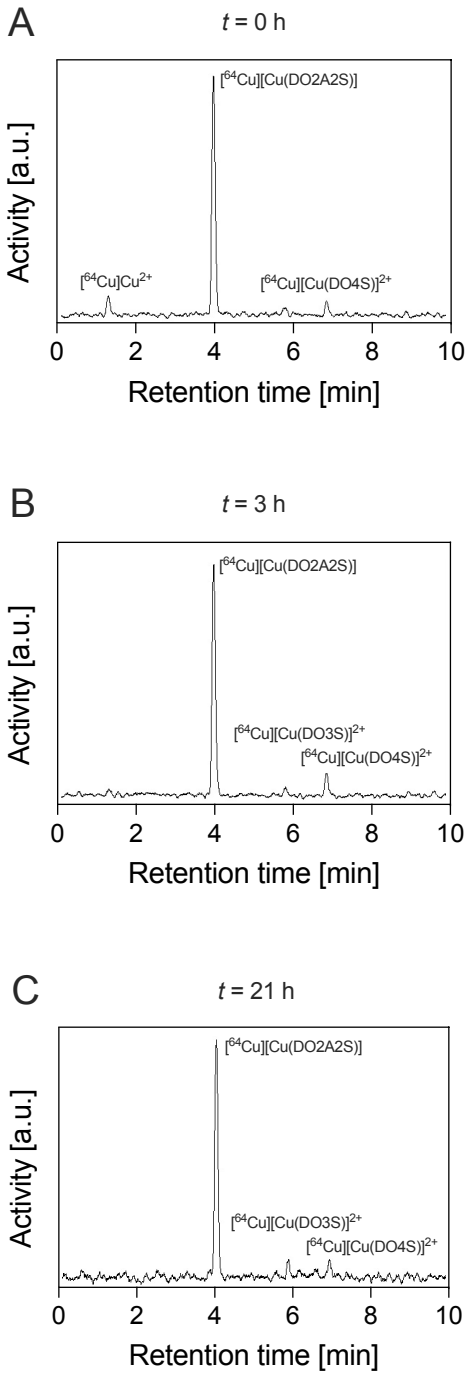

Figure C18. Radio-chromatograms related to the competition assay among the first-generation chelators (1:1 chelator-to-chelator molar ratio) at pH 4.5.

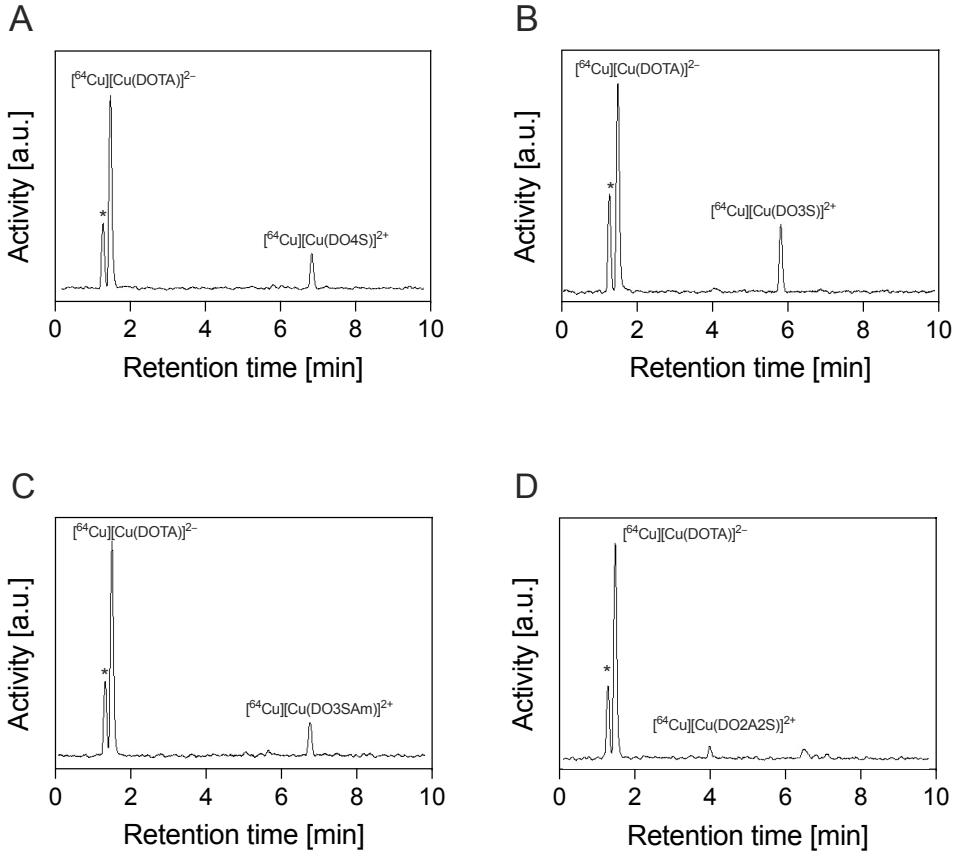

Figure C19. Radio-chromatograms related to the DOTA competition assays (1:1 DOTA-to-ligand molar ratio) with (A) DO4S, (B) DO3S), (C) DO3SAm and (D) DO2A2S at pH 4.5

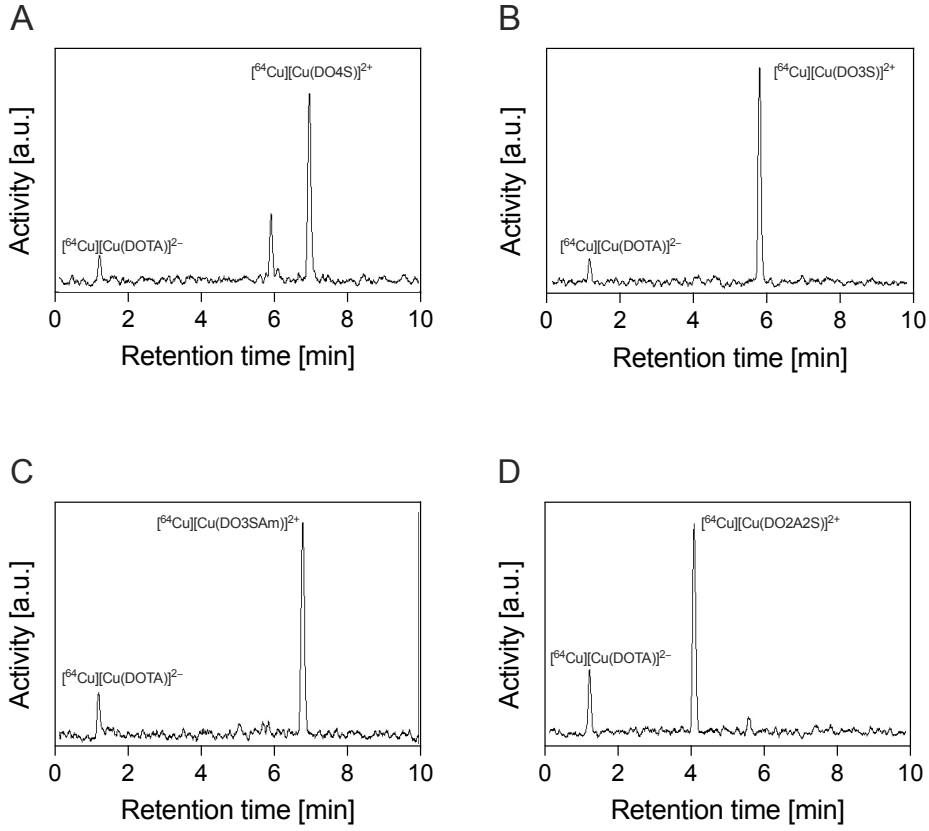

Figure C20. Radio-chromatograms related to the DOTA competition assays (1:1 DOTA-to-ligand molar ratio) with (A) DO4S, (B) DO3S), (C) DO3SAm and (D) DO2A2S at pH 7.

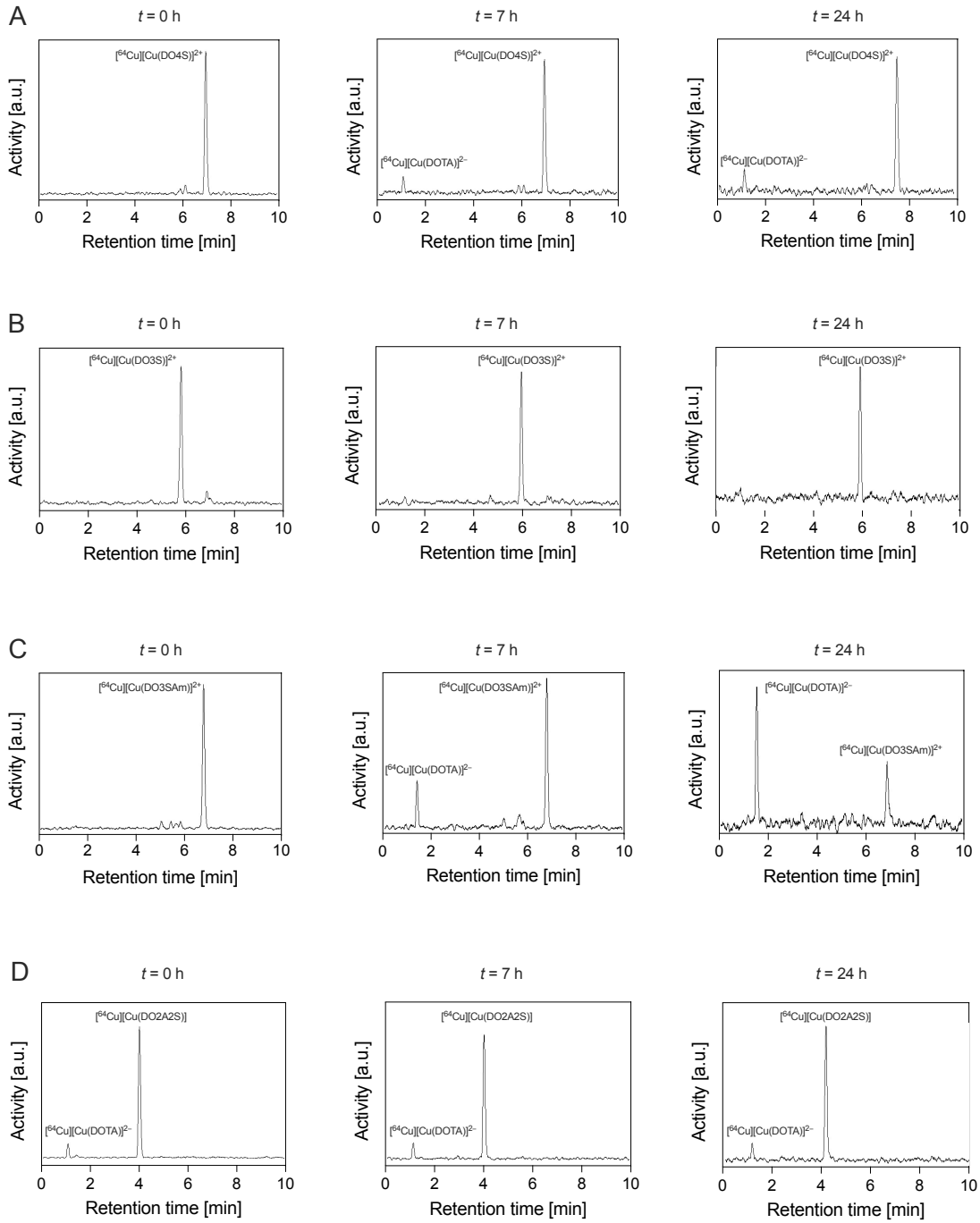

Figure C21. Radio-chromatograms related to the DOTA stability assay (1000:1 DOTA-to-ligand molar ratio) of (A) $[^{64}Cu][Cu(DO4S)]^{2+}$, (B) $[^{64}Cu][Cu(DO3S)]^{2+}$, (C) $[^{64}Cu][Cu(DO3SAm)]^{2+}$ and (D) $[^{64}Cu][Cu(DO2A2S)]$.

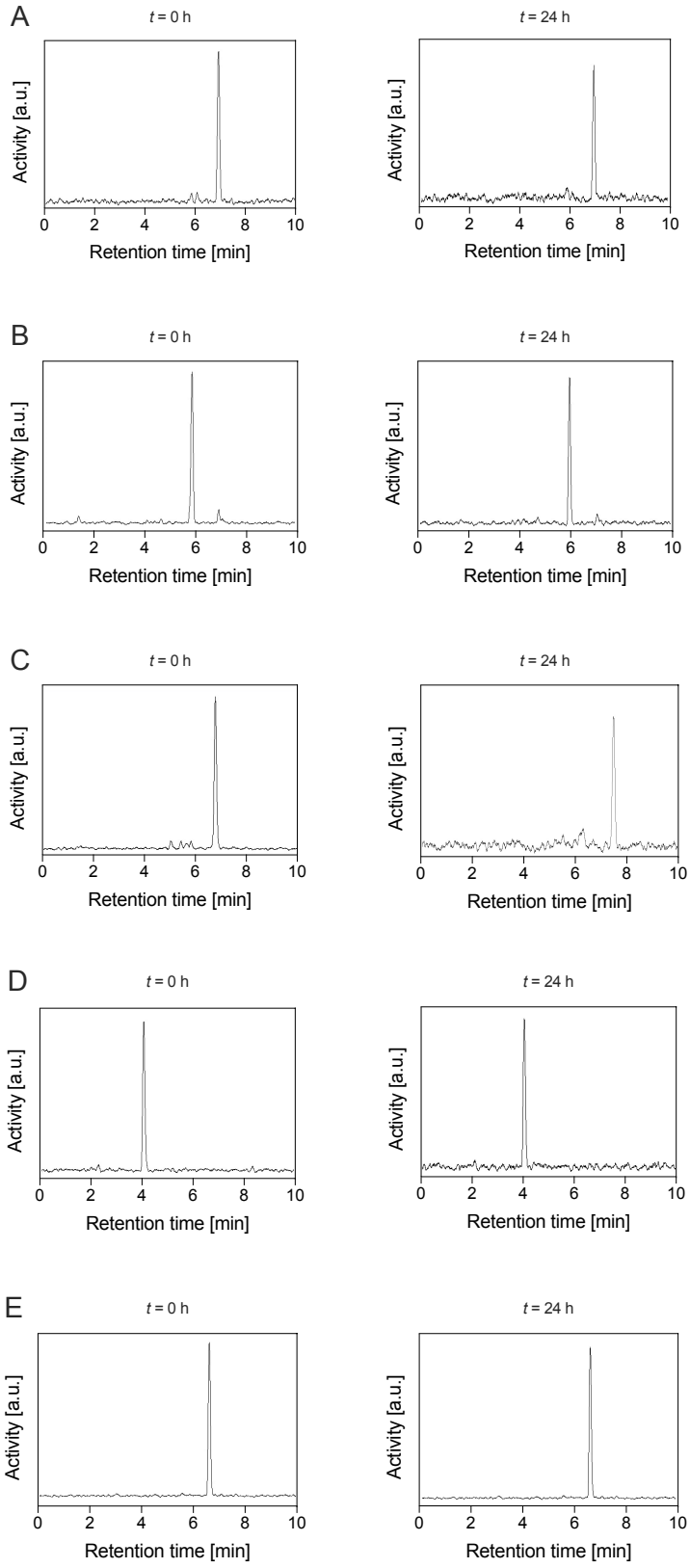

Figure C22. Radio-chromatograms related to the PBS stability assays of: (A) $[^{64}Cu][Cu(DO4S)]^{2+}$, (B) $[^{64}Cu][Cu(DO3S)]^{2+}$, (C) $[^{64}Cu][Cu(DO3SAm)]^{2+}$, (D) $[^{64}Cu][Cu(DO2A2S)]$ and (E) $[^{64}Cu][Cu(TRI4S)]^{2+}$.

Determination of the Stability Constants of the Cu^{+} Complexes from Voltametric Data

The relationship between the stability constants of the Cu^{2+} and Cu^{+} complexes with the ligand L was obtained using the following thermodynamic cycle:

1)	Cu^{2+}	+ L	⇋	CuL^{2+}	ΔG_1^0	=	$-RT\ln(\beta_{II})$
2)	CuL^{2+}	+ e^-	⇋	CuL^{+}	ΔG_2^0	=	$-nF\,E_2^0$
3)	Cu^{2+}	+ e^-	⇋	Cu^{+}	ΔG_3^0	=	$-nF\,E_3^0$
4)	Cu^{+}	+ L	⇋	CuL^{+}	ΔG_4^0	=	$-RT\ln(\beta_{I})$

where n = 1, β_{II} and β_{I} represent the formation constants of CuL^{2+} and CuL^{+}, respectively, and $E°_2$ is the standard potential for the unbound Cu^{2+}/Cu^{+} redox couple. It was assumed that the experimental $E_{1/2}$ values approximate the standard potentials ($E°_3$).

The stability constants for the Cu^{+} complexes were obtained from:

$$\Delta G_4^0 = \Delta G_1^0 + \Delta G_2^0 - \Delta G_3^0 \tag{6}$$

so that:

$$\ln(\beta_I) = \ln(\beta_{II}) + \frac{nF}{RT}(E_2^0 - E_3^0) \tag{7}$$

Appendix D

Supplementary Data for Chapter 5

Table D1. Time required to reach the equilibrium during the Pb^{2+} complexes formation reactions at various pH with first-generation ligands.

pH	Equilibration time			
	DO4S	**DO3S**	**DO3SAm**	**DO2A2S**
2.0	[a]	[a]	[a]	~ 3 h [b]
3.7	[a]	[a]	–	~ 20 min
5.0	~ 1 d [b]	~ 6 h [b]	~ 2 h [c]	< 30 s [c]
7.4	~ 70 min	~ 3 min	< 30 s [c]	< 30 s [c]

[a] No complex formation.
[b] Complexation not quantitative.
[c] Complex formation during the mixing time of the two reagents.

Table D2. UV-Vis spectroscopic data of the Pb^{2+} complexes with first-generation ligands.

Complex	**$[Pb(DO4S)]^{2+}$**	**$[Pb(DO3S)]^{2+}$**	**$[Pb(DO3SAm)]^{2+}$**	**[Pb(DO2A2S)]**
λ_{max} [nm]	324	300	295	285
ε [L/cm·mol]	$6.5 \cdot 10^3$	$4.5 \cdot 10^3$	$4.0 \cdot 10^3$	$7.0 \cdot 10^3$

Table D3. Chemical shift, multiplicity, area, and ^{1}H resonance assignments for Pb^{2+}-complexes with first-generation ligands.

Complex	^{1}H			^{13}C	
	δ [ppm]	Multiplicity	Area	δ [ppm]	Assignation
$[Pb(DO4S)]^{2+}$	2.37	s	12	14.94	SCH_3
	2.96	m br	8	30.49	SCH_2
	3.04 - 3.70	m br	24	56.72	NCH_2 ring + arms
$[Pb(DO3S)]^{2+}$	2.27	s	6	14.61	SCH_3
	2.28	s	3		SCH_3
	2.85 - 3.02	m	8	29.61	SCH_2
	3.07-3.26 + 3.39-3.70	m	16	52.3 - 55.15	NH_2 ring
	3.27 - 3.37	m	24		NCH_2 arms
$[Pb(DO3SAm)]^{2+}$	2.28	s	9	14.5	SCH_3
	2.81	s	3	2.81	$CONHCH_3$
	2.95	m	6	2.95	SCH_2
	3.06 - 3.38	m	22	51.1 - 53.6	NCH_2
	4.00	s	2	59.8	$-CH_2CO$
[Pb(DO2A2S)]	2.25	s	6	15.4	SCH_3
	3.00	m	4	30.1	SCH_2
	2.65 - 3.40	m br	20	–	NCH_2 ring + arms
	3.72	s	4	59.5	CH_2COOH

m br = multiplet broad; s = singlet

Table D4. Chemical shift, multiplicity, area, and ^{1}H resonance assignments for $[Pb(DO4S)]^{2+}$ and [Pb(DO2A2S)] at T = 65°C.

Complex	δ [ppm]	Multiplicity	Area	Assignation
$[Pb(DO4S)]^{2+}$	2.37	s	12	SCH_3
	2.97	t	8	SCH_2
	3.11 - 3.23	m br	8	NCH_2 ring
	3.3 - 3.34	m br	8	NCH_2 ring
	3.34 - 3.43	m br	8	NCH_2 arms
[Pb(DO2A2S)]	2.26	s	6	SCH_3
	2.98	t	4	SCH_2
	3.02 - 3.23	m br	16	NCH_2 ring
	3.29	t	4	NCH_2 arms
	3.70	s	4	CH_2COOH

m br = multiplet broad; t = triplet, s = singlet

Table D5. $^{d}k_{obs}$ for the acid-assisted dissociation of the Pb^{2+} complexes with DO4S, DO3S, DO3SAm and DO2A2S in aqueous HCl at room temperature. Data for Pb^{2+}-DOTA are reported for comparison purposes.

HCl [M]	$^{d}k_{obs}$ [min^{-1}]				
	$[Pb(DO4S)]^{2+}$	**$[Pb(DO3S)]^{2+}$**	**$[Pb(DO3SAm)]^{2+}$**	**[Pb(DO2A2S)]**	**$[Pb(DOTA)]^{2-}$**
0.01	$(29 \pm 3)\cdot10^{-4}$	$(6 \pm 1)\cdot10^{-2}$	$(3.0 \pm 0.2)\cdot10^{-2}$	$(4.6 \pm 1.3)\cdot10^{-2}$ [(a)]	$(2.1 \pm 0.1)\cdot10^{-2}$
0.1	$(3.8 \pm 0.7)\cdot10^{-2}$	1.5 ± 0.3	0.43 ± 0.02	0.7 ± 0.3	0.18 ± 0.01
1	1.04 ± 0.05	[(b)]	[(b)]	[(b)]	[(b)]

[(a)] Non-quantitative decomplexation.
[(b)] Instantaneous decomplexation after HCl addition.

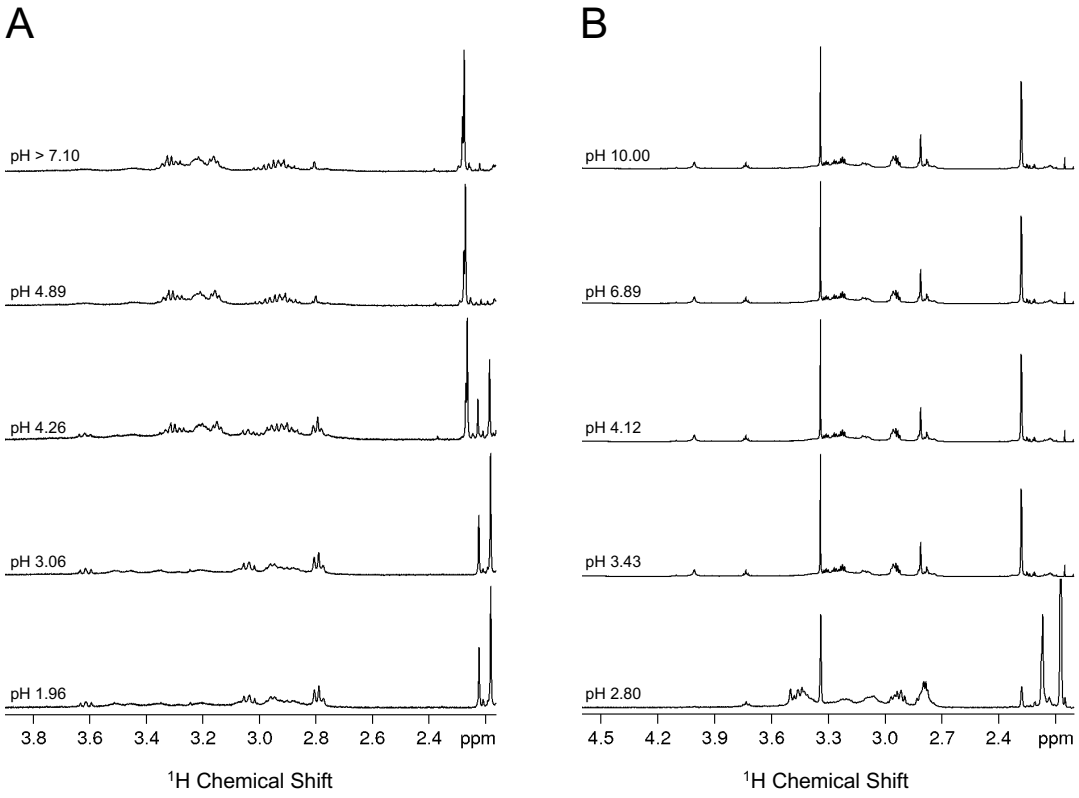

Figure D1. Variable-pH ^{1}H NMR spectra of (A) Pb^{2+}-DO3S (400 MHz, T = 25°C, H_2O + 10% D_2O, $C_{Pb^{2+}} = C_{DO3S} = 1.0 \cdot 10^{-3}$ M) and (B) Pb^{2+}-DO3SAm (600 MHz, T = 25°C, H_2O + 10% D_2O, $C_{Pb^{2+}} = C_{DO3SAm} = 8.0 \cdot 10^{-4}$ M). The signals at 2.72 ppm and 3.73 ppm have been tentatively attributed to impurities. The signal at 3.34 ppm is related to residual methanol.

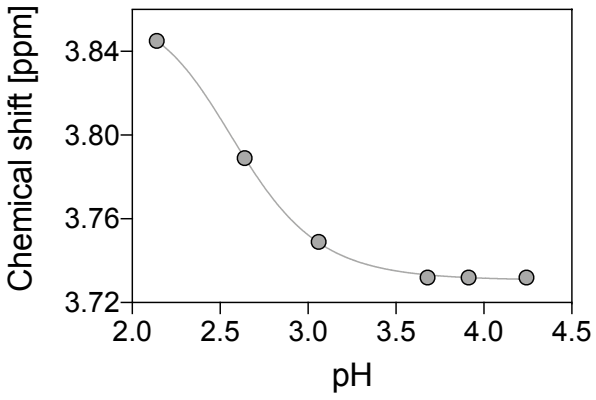

Figure D2. Variation of the chemical shift of the acetate protons of Pb^{2+}-DO2A2S as a function of pH and corresponding fitting line.

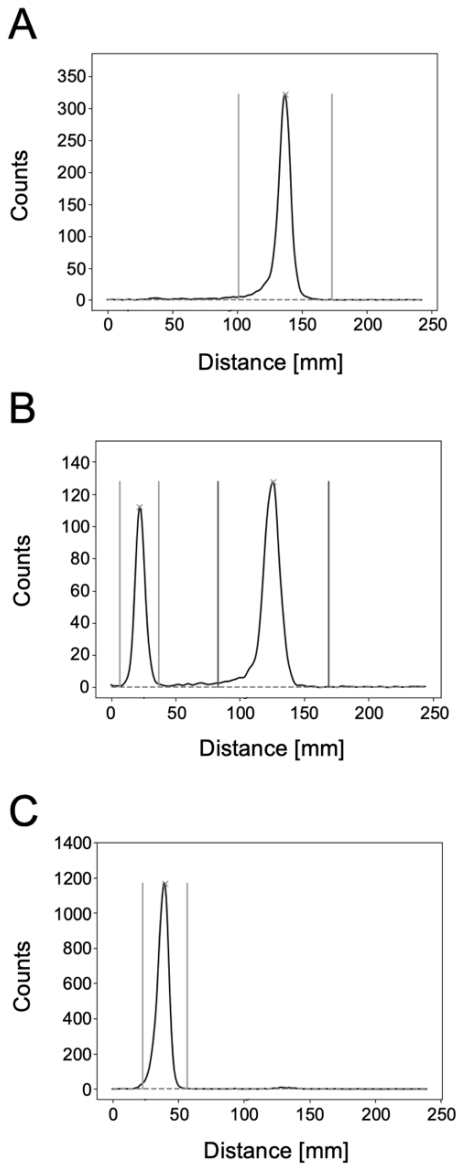

Figure D3. Representative iTLC radio-chromatograms of (A) unlabelled [^{203}Pb]Pb^{2+}, (B) non-quantitative labelling reaction and (C) quantitative labelling reaction.

Appendix E

Supplementary Data for Chapter 6

Table E1. NMR chemical shift, multiplicity, area, ^{1}H and ^{13}C resonance assignments for Hg^{2+}-complexes with first-generation ligands, DOTA and cyclen.

Complex	^{1}H			^{13}C	
	δ [ppm]	Multiplicity	Area	δ [ppm]	Assignation
$[Hg(DO4S)]^{2+}$	2.36	s	12	15.6	SCH_3
			8	29.7	SCH_2
	2.88 - 3.17	m br	24	48.6 + 51.6	NCH_2 ring + arms
$[Hg(DO3S)]^{2+}$	2.18	s	3	9.8	N_4 - SCH_3
	2.44	s	6	10.7	N_1, N_7 - SCH_3
	2.71 - 2.85	m	28	28.4	SCH_2 (H_a)
				48.1	NCH_2 ring (H_e)
	2.86 - 3.09			42.1	NCH_2 ring (H_e)
				48.1	NCH_2 arm (H_c + H_b)
				54.7	
	3.09 – 3.15			30.98	SCH_2 (H_d)
[Hg(DO2A2S)]	2.31	s	6	15.8	SCH_3
	3.01	t	4	29.8	SCH_2
	2.78 - 3.08	m	16	48.6	NCH_2 ring
	3.12	t	4	49.6	NCH_2 arms
	3.41	s	4	59.5	CH_2COOH
$[Hg(HDO2A2S)]^{+}$	2.46	s	6	-	SCH_3
	2.82 - 3.12	m br	20	-	NCH_2 ring + arms
	3.25	t	4	-	SCH_2
	3.66	s	4	-	CH_2COOH
$[Hg(DOTA)]^{2-}$	2.69	m	8	-	NCH_2
	2.90	m	8	-	NCH_2
	3.25	s br	8	-	CH_2COOH
	3.31			-	
$[Hg(cyclen)]^{+}$	2.80	m	8	-	NCH_2
	2.91	m	8	-	NCH_2
	3.50	s br	1	-	NH

m br = multiplet broad; s = singlet; t = triplet

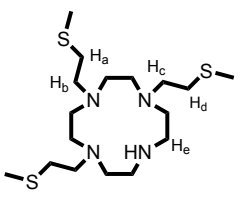

Table E2. Chemical shift, multiplicity, area, ^{1}H and ^{13}C resonance assignments for Hg^{2+}-complexes with second-generation ligands.

Complex	^{1}H			^{13}C	
	δ [ppm]	**Multiplicity**	**Area**	**δ [ppm]**	**Assignation**
$[Hg(TACD3S)]^{2+}$	1.75	qn	3	-	CH_2
	2.21	qn	3	-	CH_2
	2.37	s	9	-	SCH_3
	2.83 - 2.97 + 3.01 - 3.15	m	12	-	SCH_2 + NCH_2 ring + arms
			12	-	
$[Hg(TE4S)]^{2+}$	1.70	m	2	-	CH_2
	2.08	m	2	-	CH_2
	2.24	s	12	15.9	SCH_3
	2.83 - 3.02	m	32	28.3	SCH_2
				51.9 54.0 59.1	NCH_2 ring + arms

m = multiplet; s = singlet; qn = quintet

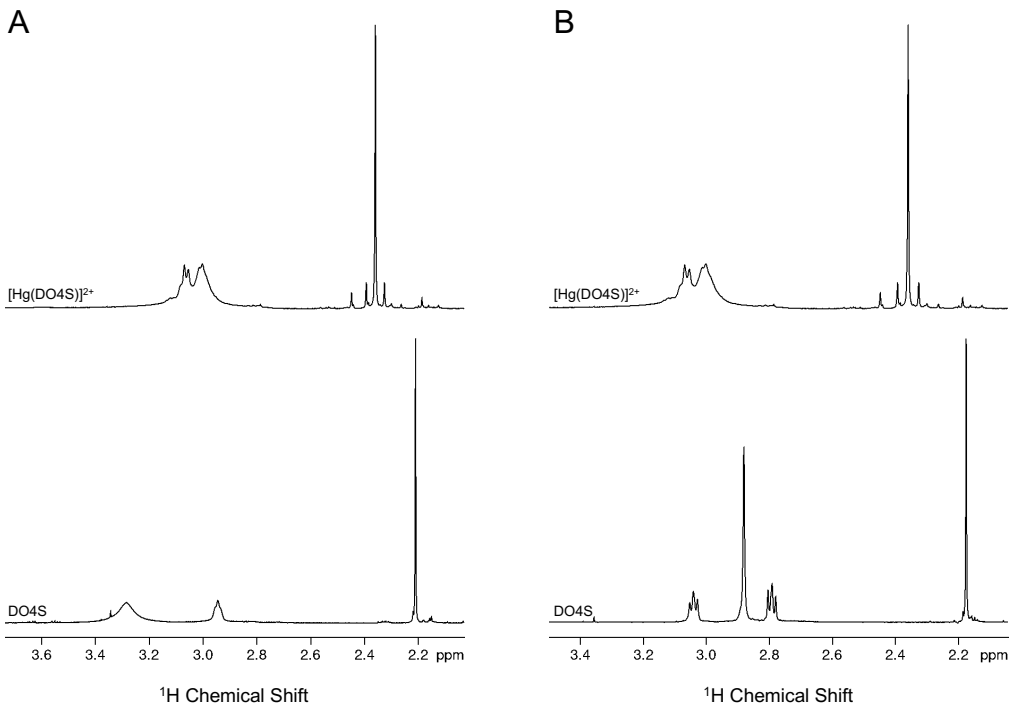

Figure E1. Comparison of the ^{1}H NMR spectra of $[Hg(DO4S)]^{2+}$ (400 MHz, T = 25°C, H_2O + 10% D_2O) and free (A) diprotonated and (B) monoprotonated DO4S (600 MHz, T = 25°C, D_2O).

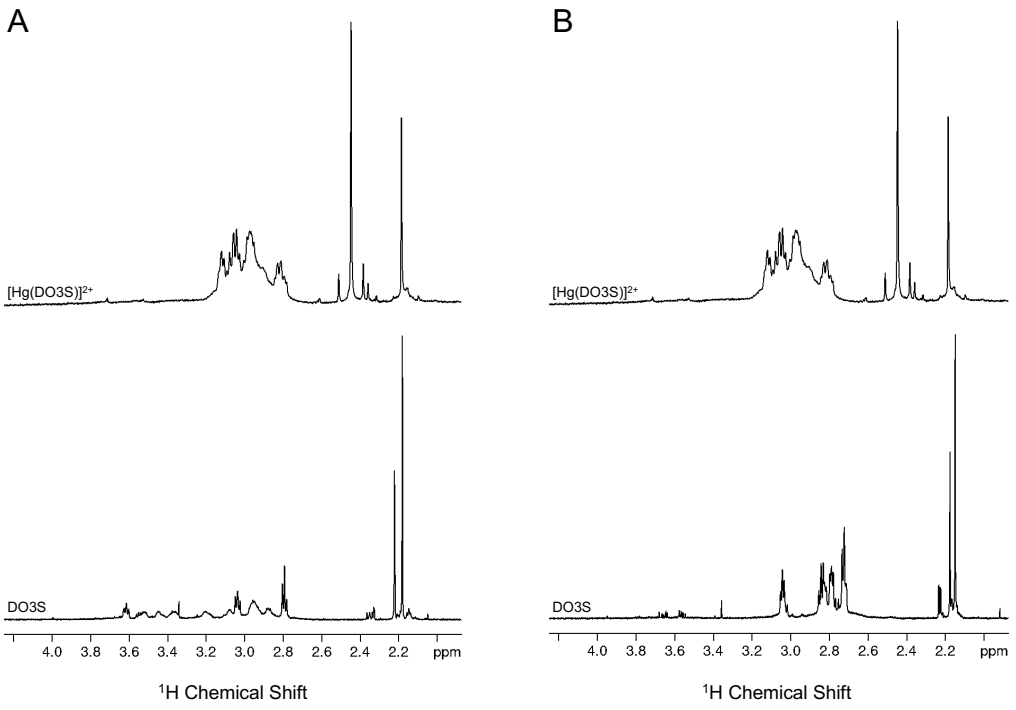

Figure E2. Comparison of the ^{1}H NMR spectra of $[Hg(DO3S)]^{2+}$ (400 MHz, T = 25°C, H_2O + 10% D_2O) and free (A) diprotonated and (B) monoprotonated DO3S (600 MHz, T = 25°C, D_2O).

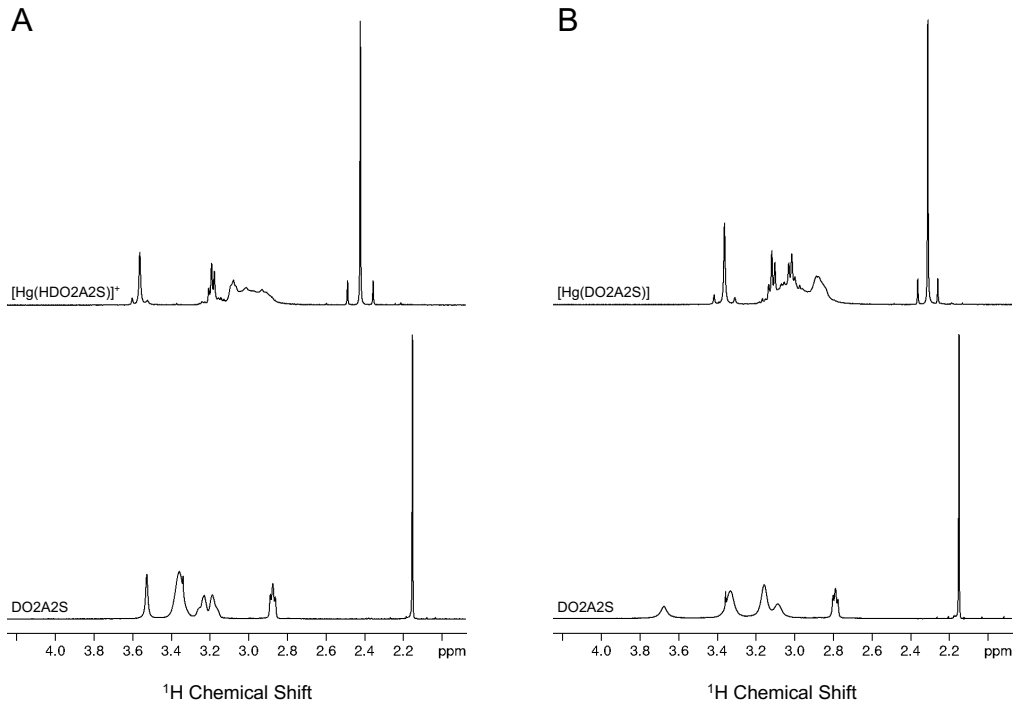

Figure E3. Comparison of the ^{1}H NMR spectra of (A) $[Hg(HDO2A2S)]^+$ (400 MHz, T = 25°C, H_2O + 10% D_2O) and free monoprotonated DO2A2S (600 MHz, T = 25°C, D_2O) and (B) [Hg(DO2A2S)] and free diprotonated DO2A2S.

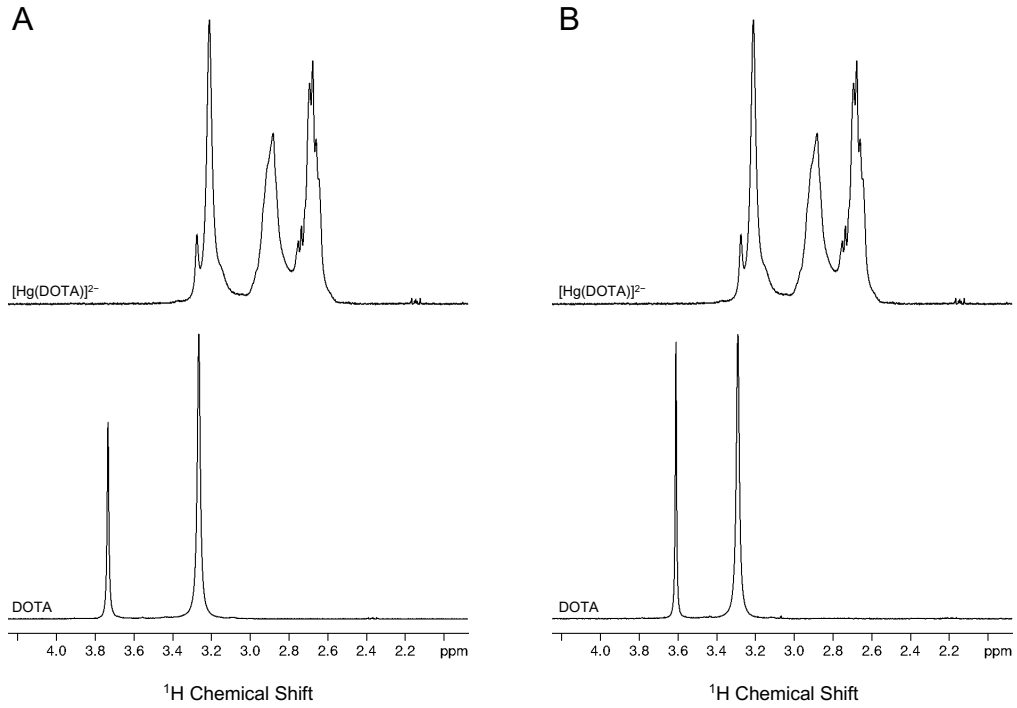

Figure E4. Comparison of the ^{1}H NMR spectra of (A) $[Hg(DOTA)]^{2-}$ and free (A) tetraprotonated and (B) diprotonated DOTA (400 MHz, T = 25°C, H_2O + 10% D_2O).

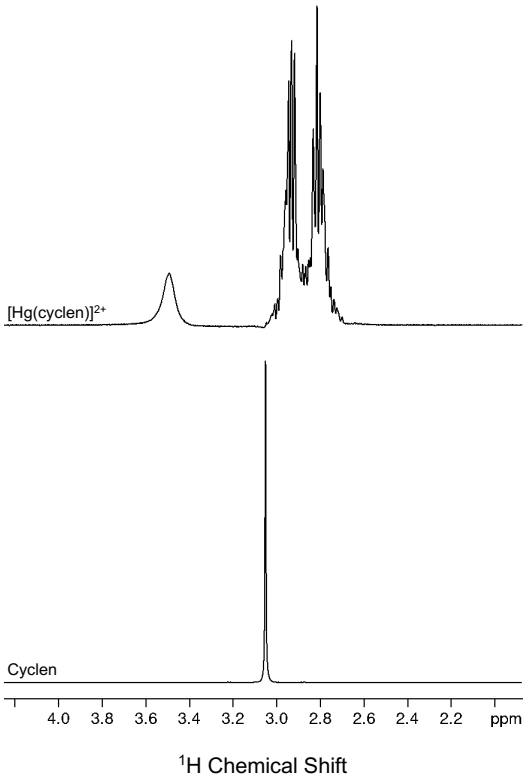

Figure E5. Comparison of the ^{1}H NMR spectra of $[Hg(cyclen)]^{2+}$ and free diprotonated cyclen (400 MHz, T = 25°C, H_2O + 10% D_2O).

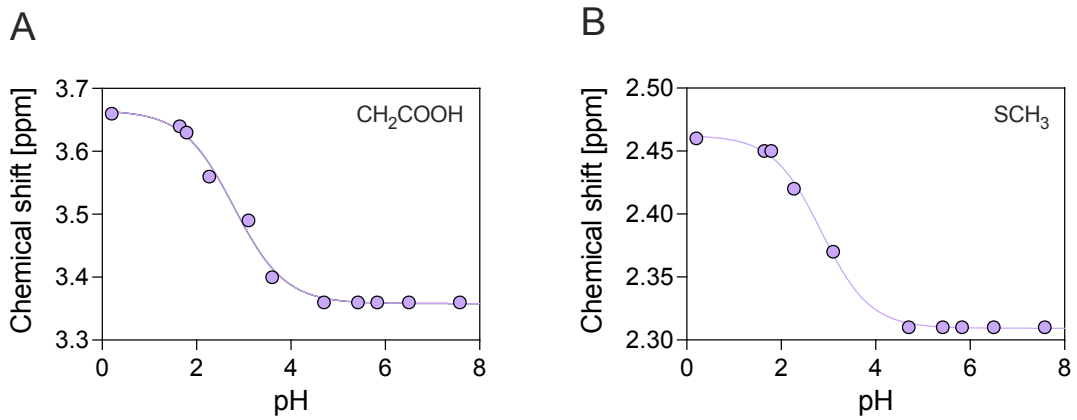

Figure E6. Variation of the chemical shift of (A) acetate and (B) SCH_3 protons of Hg^{+}-DO2A2S as a function of pH and corresponding fitting line.

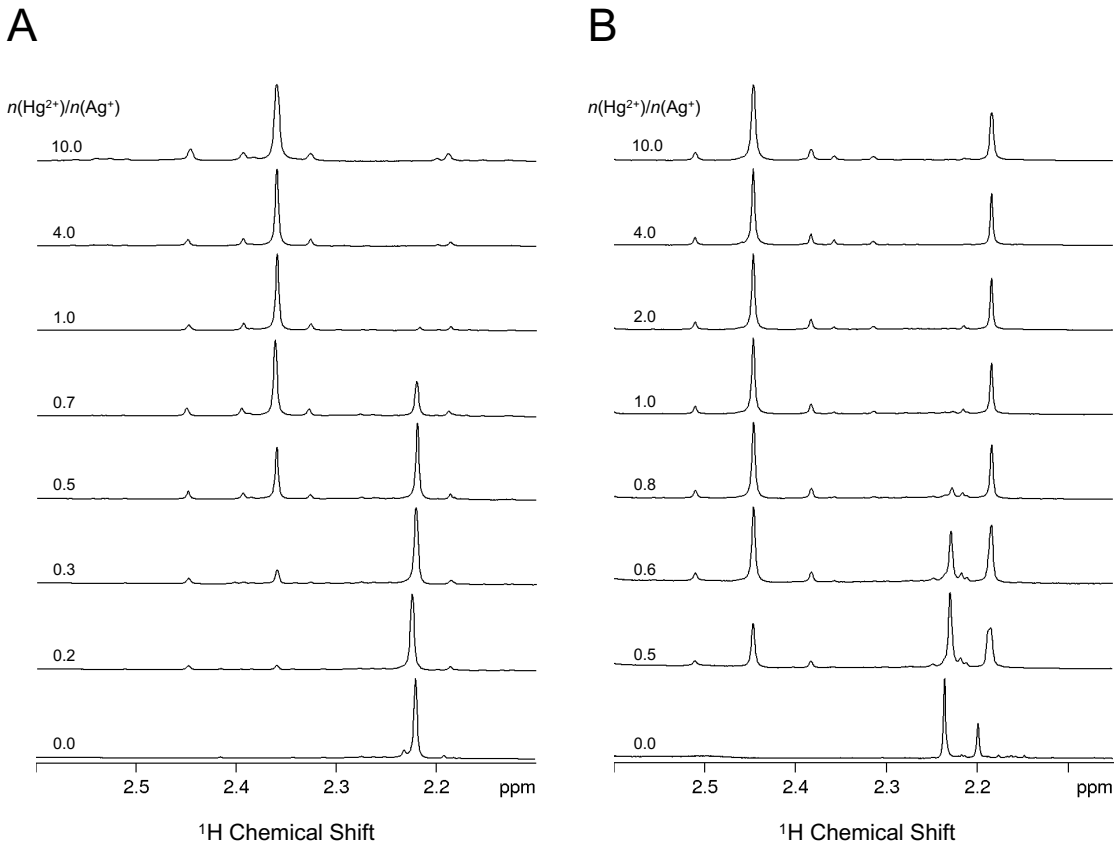

Figure E7. Representative competitive titrations of (A) $[Ag(DO4S)]^+$ ($C_{[Ag(DO4S)]^+}$ = $2.25 \cdot 10^{-3}$ M) and (B) $[Ag(DO3S)]^+$ ($C_{[Ag(DO3S)]^+}$ = $1.36 \cdot 10^{-3}$ M) with $HgNO_3$.

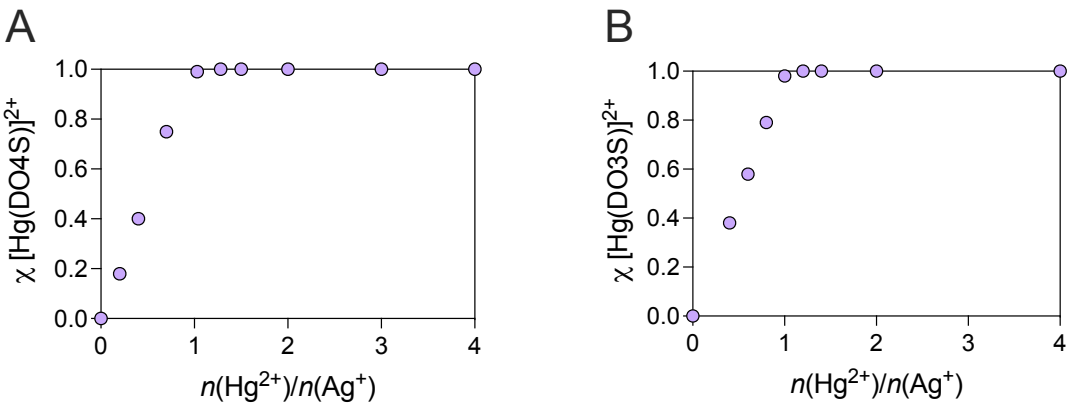

Figure E8. Representative χ *vs.* $n(Hg^{2+})/n(Ag^+)$ profile obtained during the Hg^{2+}-Ag^+ competitions measurements indicating the complete transmetallation (data were taken from **Figure E7**).

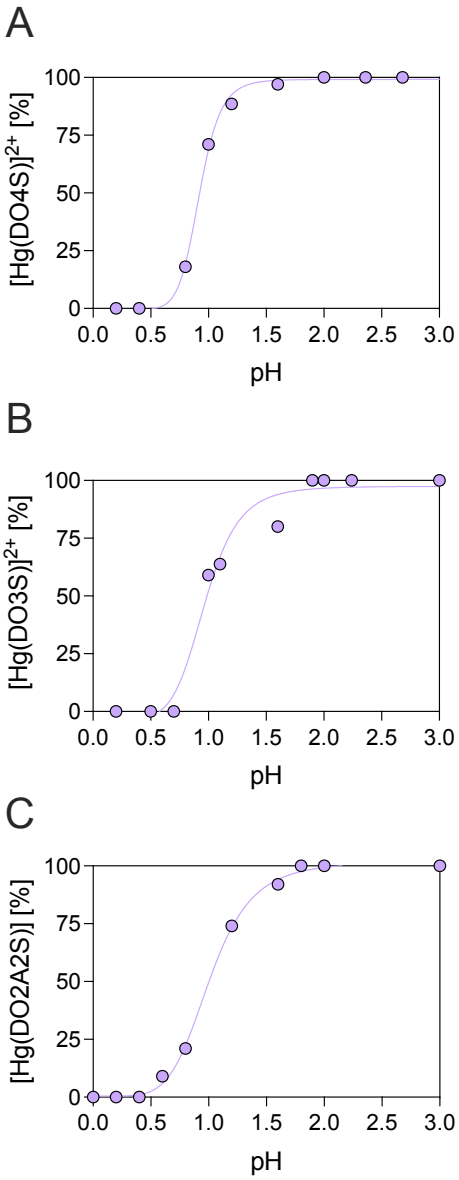

Figure E9. Representative profile obtained during the Hg^{2+}-Cl^{-} competition titrations of (A) Hg^{2+}-DO4S, (B) Hg^{2+}-DO3S and (C) Hg^{2+}-DO2A2S (data were taken from **Figure 6.5**).

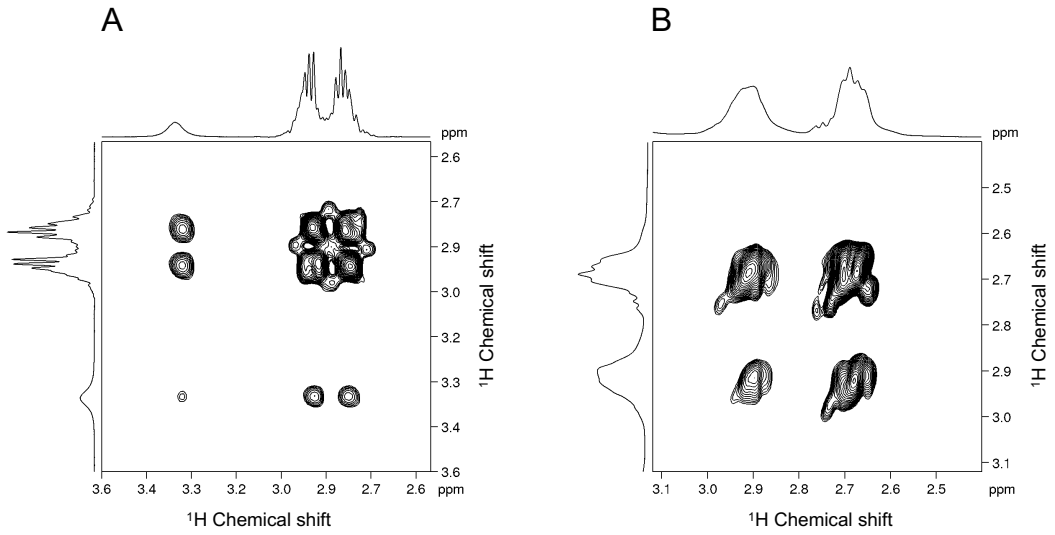

Figure E10. ^{1}H-^{1}H COSY spectrum of (A) $[Hg(cyclen)]^{+}$ and (B) $[Hg(DOTA)]^{2-}$.

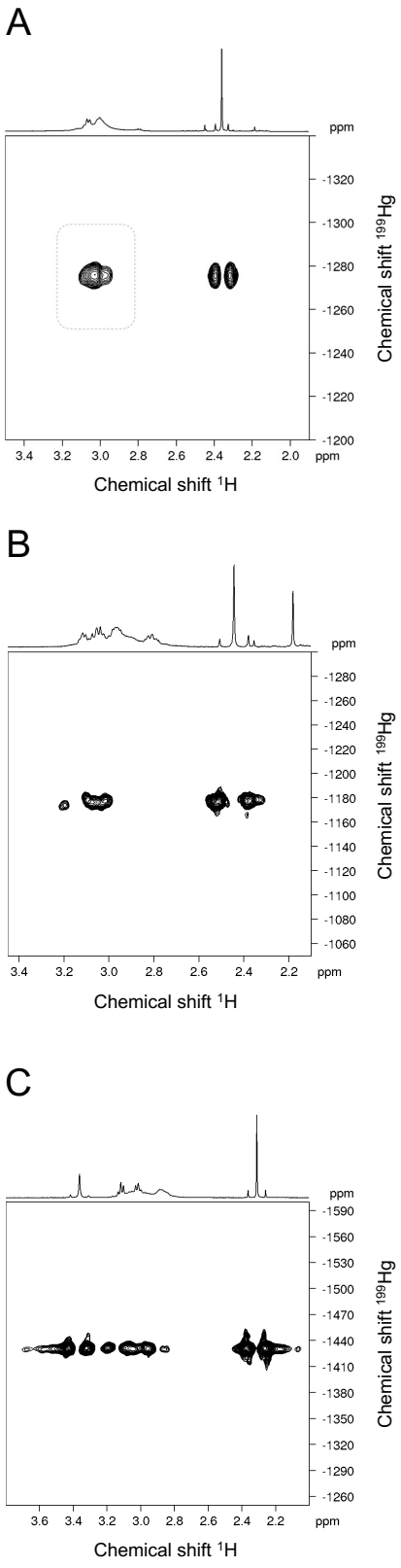

Figure E11. Non-decoupled ^{1}H-^{199}Hg NMR spectrum of (A) $[Hg(DO4S)]^{2+}$, (B) and $[Hg(DO3S)]^{2+}$ and (C) [Hg(DO2A2S)].

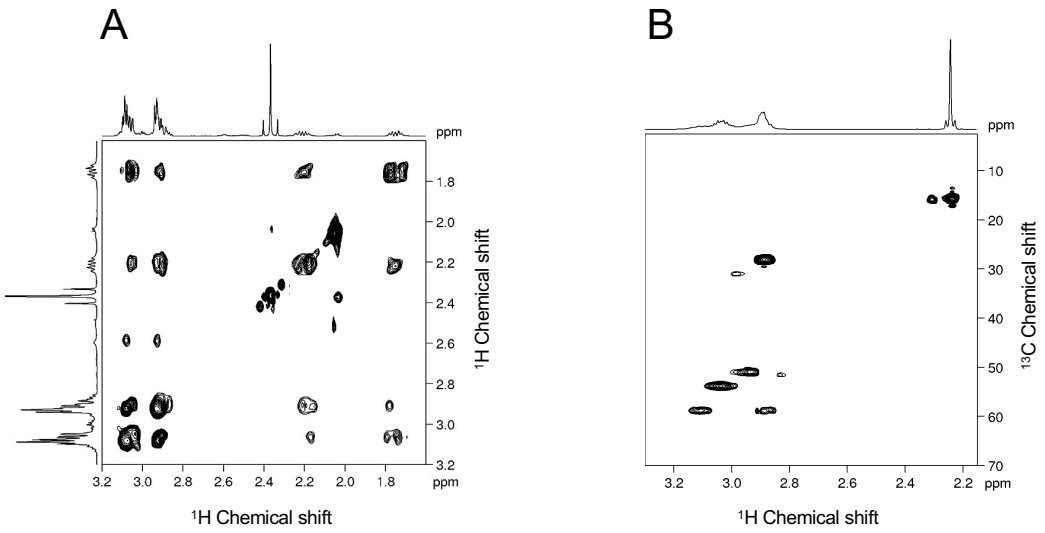

Figure E12. (A) ^{1}H-^{1}H TOCSY spectrum of $[Hg(TACD3S)]^{2+}$ and (B) ^{1}H-^{13}C HMQC spectrum of $[Hg(TE4S)]^{2+}$.